MoDOT

Research, Development and Technology

University of Missouri-Rolla

RDT 04-016

High Performance Concrete for Bridge A6130-Route 412, Pemiscot County, MO

RI 00-002

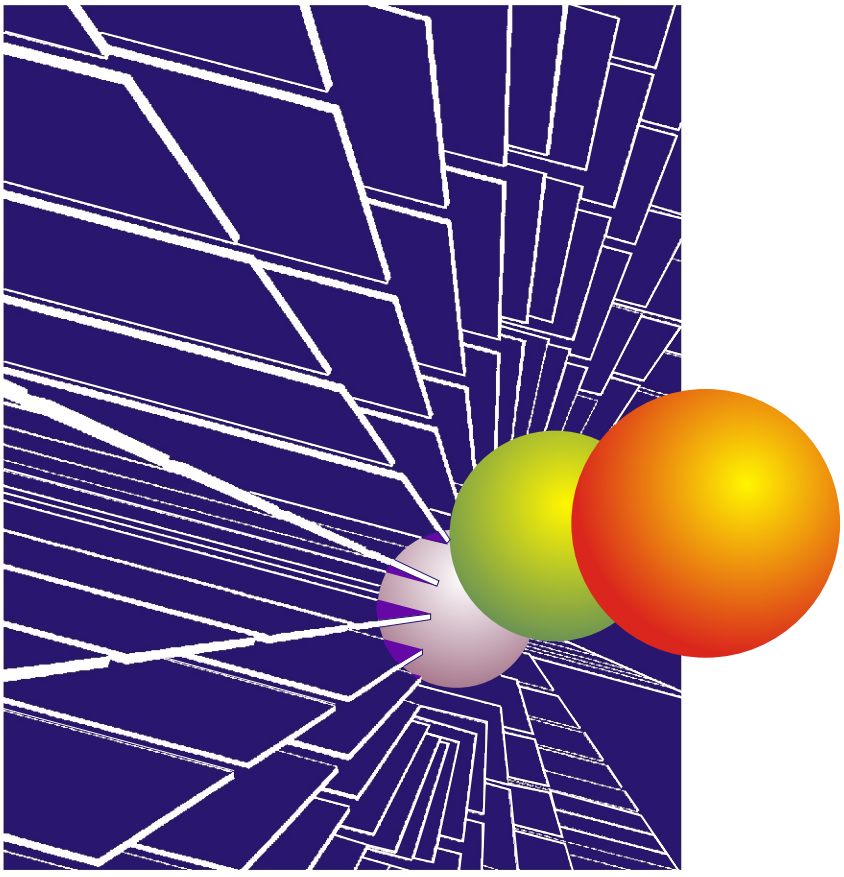

June, 2004

TECHNICAL REPORT DOCUMENTATION PAGE

1. Report No. RDT 04-016	2. Government Accession No.	3. Recipient's Catalog No.
4. Title and Subtitle High Performance Concrete for Bridge A6130-Route 412, Pemiscot County, MO		5. Report Date June 2004
		6. Performing Organization Code University of Missouri-Rolla
7. Author(s) John Myers, Yumin Yang – University of Missouri-Rolla		8. Performing Organization Report No. RDT 04-016 / RI 00-002
9. Performing Organization Name and Address University of Missouri-Rolla Dept. of Civil Engineering 111 Butler-Carlton Hall Rolla, Missouri 65409-0030		10. Work Unit No. 11. Contract or Grant No.
12. Sponsoring Agency Name and Address Missouri Department of Transportation Research, Development and Technology Division P. O. Box 270-Jefferson City, MO 65102		13. Type of Report and Period Covered Final Report, Sep. 1, 2000 – Dec. 31, 2003 14. Sponsoring Agency Code MoDOT

15. Supplementary Notes
The investigation was conducted in cooperation with the University Transportation Center at University of Missouri – Rolla, Federal Highway Administration.

16. Abstract

For its significant economical savings and greater design flexibility, high performance concrete (HPC) is becoming more widely utilized in highway bridge structures. High performance bridges with HPC and large diameter prestressed strands are becoming attractive to designers.

A prestressed high performance concrete (HPC) highway bridge was constructed in Missouri utilizing concrete with 56 day strength of up to 86 MPa (12,500 psi). The utilization of HPC allowed for larger girder spacing and longer spans than typically used in conventional prestressed concrete bridges. This project is sponsored by the Missouri Department of Transportation (MoDOT), the Federal Highway Administration and the University Transportation Center at the University of Missouri-Rolla.

The Bridge A6130, in Pemiscot County near Hayti, Missouri, is a five-span simply-supported for dead load HPC highway bridge over main ditch, drainage ditch No.8 carrying Route 412. The span lengths for the bridge are 15.5 m (50.85 ft), 17.0 m (55.77 ft), 17.0 m (55.77 ft), 17.0 m (55.77 ft) and 15.5 m (50.85 ft). The bridge was designed with MoDOT type 2 I-girder in conjunction with HPC and 15.2 mm (0.6 in.) diameter prestressing strands.

HPC materials for both girders and cast-in-place deck are studied for both mechanic and material properties including compressive strength, modulus of elasticity, splitting strength, freeze-thaw, abrasion resistance, de-icing scaling, ponding chloride, rapid chloride permeability, creep, shrinkage, and coefficient of thermal expansion.

The completed bridge was instrumented to measure temperature and strain variations. This was combined with deformation measurements to determine how the bridge behaves in response to temperature changes, dead load, live load, creep, and shrinkage. Measured thermal behavior, strain behavior, prestress losses, camber and deflection are investigated by comparing with theoretical estimation for both early-age and later-age. Modified theoretical methods based on the test results were recommended.

In addition, a live load test was completed for the bridge to study the load distribution and structure behavior due to live load. Two simplified models were developed and compared with measured values to investigate the continuity level of the MoDOT interior bent detail.

MoDOT girder cross sections were studied for cost effectiveness by using high strength concrete. The objectives are to identify the limitations of the sections relative to the use of high-strength concrete in simple span structures and to examine the feasibility of modified cross sections that can be used to take advantage of the higher strength concrete that are currently available.

Construction for HPC Bridge related issues were documented to give a reference for later construction for HPC bridges. The summary, conclusions and recommendations were given for HPC highway bridges in Missouri and for general HPC structures in US considering design, fabrication, construction and research.

17. Key Words Bridges Instrumentation High Performance Concrete Precast Girders Prestress Loss Load Test	18. Distribution Statement No restrictions. This document is available to the public through National Technical Information Center, Springfield, Virginia 22161

19. Security Classification (of this report) Unclassified	20. Security Classification (of this page) Unclassified	21. No. of Pages 447	22. Price

Investigation Number RI00-002

FIELD AND LABORATORY PERFORMANCE OF PRESTRESSED HIGH PERFORMANCE CONCRETE GIRDERS FOR MISSOURI BRIDGE STRUCTURES

Final Report for
High Performance Concrete For Bridge A6130
–– Route 412 Pemiscot County, MO

CIVIL ENGINEERING

UNIVERSITY OF MISSOURI-ROLLA

June 2004

EXECUTIVE SUMMARY

The first fully high performance concrete (HPC) bridge A6130 was constructed in Missouri utilizing concrete with 56 day design strength of 70 MPa (10,152 psi) and 15.2 mm (0.6 in.) diameter prestressing strands. HPC materials for both girders and cast-in-place deck were studied for both mechanical and material properties.

The completed bridge was instrumented to measure temperature and strain variations. This was combined with deformation measurements to determine the bridge response to temperature changes, dead load, live load, creep, and shrinkage. Measured thermal behavior, strain behavior, prestress losses, camber and deflection were investigated by comparing to theoretical estimate at both early-age and later-age. Modified theoretical methods based on the test results were recommended. In addition, a live load test was completed for the bridge to investigate the load transfer, structure behavior due to live load, and the continuity level of the MoDOT interior bent detail.

MoDOT girder cross sections were investigated to identify the limitations of the sections relative to the use of high-strength concrete in simple span structures and to examine the feasibility of modified cross sections that can be used to take advantage of higher strength concrete that are currently available.

Construction related issues for HPC Bridges were documented to provide a reference for future HPC bridges. The summary, conclusions and recommendations were given for HPC highway bridges in Missouri and for general HPC structures in the United States considering design, fabrication, construction and the research program undertaken.

ACKNOWLEDGMENTS

The authors would like to acknowledge the financial support of the Missouri Department of Transportation, the Federal Highway Administration and the University Transportation Center at University of Missouri – Rolla. Special thanks are given to Patricia L. Lemongelli, Timothy M. Chojnacki, Scott Breeding, Lynelle Skouby Luther, Brian Holt, and Chris J. Chriswell from the Missouri Department of Transportation.

TABLE OF CONTENTS

Page

LIST OF ILLUSTRATIONS

Figure Page

LIST OF TABLES

Table Page

NOTATIONS

A	Area, mm^2 (in^2)
A_c	Net concrete area, mm^2 (in^2)
A_g	Area of gross section, mm^2 (in^2)
A_t	Area of transformed section, mm^2 (in^2)
C_c	Creep coefficient
C_{ct}	Creep coefficient at time t
C_{cu}	Ultimate creep coefficient
e	Eccentricity, mm (in.)
e_t	Eccentricity of prestress strands, mm (in.)
E_{ci}	Modulus of elasticity of concrete at release, Pa (psi)
E_c	Modulus of elasticity of concrete, Pa (psi)
E_s	Modulus of elasticity of steel, Pa (psi)
E_{ps}	Modulus of elasticity of prestress strand, Pa (psi)
f'_c	Compressive strength of concrete, Pa (psi)
f_{cgs}	Stress in concrete at c.g. of strands, Pa (psi)
f_{py}	Yield stress of prestress strand, Pa (psi)
f_{pu}	Nominal ultimate strength of prestress strand, Pa (psi)
f_r	Flexural tensile strength of concrete, Pa (psi)
f_{sp}	Splitting tensile strength of concrete, Pa (psi)
h	Depth of section, mm (in.)
I	Moment of inertia, mm^4 (in^4)

I_c	Moment of inertia of net concrete, mm^4 (in^4)
I_g	Moment of inertia of gross section, mm^4 (in^4)
I_t	Moment of inertia of transformed section, mm^4 (in^4)
m	Number of time intervals used to reach time t
M	Moment, N·m (lb·in)
M_{max}	Maximum moment, N·m (lb·in)
$M_{self-wt}$	Moment caused by self weight, N·m (lb·in)
n	Modular ratio of steel to concrete
P_0	Prestress force at release, N (lb)
P_e	Effective prestress force, N (lb)
r	Radius of gyration of section, mm (in.)
S_b, S_t	Section modulus for bottom fibers and top fibers, respectively, mm^3 (in^3)
t	Time, hour or day
T	Temperature, °C (°F)
$T_{July,\max}$	Average daily maximum ambient temperature in July, °C (°F)
$T_{Jan,\min}$	Average daily minimum ambient temperature in January, °C (°F)
$T_{all-time,\max}$	Maximum ambient temperature ever recorded, °C (°F)
$T_{all-time,\min}$	Minimum ambient temperature ever recorded, °C (°F)
w	Concrete density, kg/m^3 (lb/ft^3)
y_t, y_b	Distance from c.g. to top and bottom fibers, respectively, mm (in.)
α	Efficiency ratio for girder cross section
α_{gauge}	Coefficient of thermal expansion of strain gauge, $\mu\varepsilon$/°C ($\mu\varepsilon$/°F)

α_{ps}	Coefficient of thermal expansion of prestress strand, $\mu\varepsilon$/°C ($\mu\varepsilon$/°F)
β	Constant factor for calculation of prestress loss before release
ε	Strain, mm/mm (in/in)
ε_{sh}	Shrinkage strain, mm/mm (in/in)
$\varepsilon_{sh,t}$	Shrinkage strain at time *t*, mm/mm (in/in)
ε_{shu}	Ultimate shrinkage strain, mm/mm (in/in)
σ	Stress, Pa (psi)
τ	Differential length of time for a time interval, hour or day
Δ	Deflection or camber, mm (in.)
$\Delta_{erection}$	Deflection at erection of girders, mm (in.)
$\Delta_{long\text{-}term}$	Long-term deflection of girders, mm (in.)
Δ_{p}	Camber due to eccentric prestress, mm (in.)
Δ_{sw}	Deflection due to self-weight, mm (in.)
Δ_{cd}	Deflection due to weight of composite deck, mm (in.)
Δ_{deck}	Deflection due to of deck, mm (in.)
Δ_{sdl}	Deflection due to superimposed dead loads, mm (in.)
Δf_{ps}	Prestress loss, Pa (psi)
$\Delta f_{ps,Diff\text{-}sh}$	Prestress loss due to differential shrinkage, Pa (psi)
$\Delta f_{ps,DL}$	Prestress loss due to superimposed loads, Pa (psi)
$\Delta f_{ps,ES}$	Prestress loss due to elastic shortening, Pa (psi)
$\Delta f_{ps,RE}$	Prestress loss due to strand relaxation, Pa (psi)
$\Delta f_{ps,SH}$	Prestress loss due to shrinkage, Pa (psi)

$\Delta f_{ps,TD}$	Time-dependent prestress loss, Pa (psi)
$\Delta f_{ps,thermal}$	Prestress loss due to thermal effect, Pa (psi)
ΔT	Change in temperature, °C (°F)
ρ	Efficiency factor for girder cross section

1. INTRODUCTION

1.1. BACKGROUND

Civil Engineering is a very important field due to its tremendous impact on any nation. Infrastructure including buildings, bridges and roads play an important role in a country's development and productivity. Highway structures including bridges in particular, are vital to the transportation system.

From ancient time, different kinds of materials have been employed in bridge structures. Stone, timber, iron and steel has been used for bridge construction during different historic periods in time. Today, portland cement concrete, is the most widely used material in bridge construction. It is most widely used as reinforced concrete (RC) and prestressed concrete (PC).

Even though RC and PC have proven to be the most durable materials for highway bridge structures, studying new materials including high performance materials can improve the service life and reduce the maintenance costs of new structures. High Performance Concrete (HPC) is one of these new materials.

In recent years, the use of HPC for highway bridges structures has increased due to its extended service life, reduced maintenance requirements and flexibility for designers. Since the first HPC bridges were constructed in Texas in the late 1990's, more and more projects have been constructed or are in the design or construction phases around US. In Missouri, the first HPC Girder Bridge (Bridge A5529) was constructed in Jefferson County, Missouri, in 1998.

Due to its low permeability, HPC exhibits excellent resistance to physical and chemical agents responsible for concrete deterioration. The increased durability of HPC

translates into a longer service life and fewer repair, leading to reduced life-cycle costs. It is anticipated that the use of HPC in highway bridges will yield significant economical savings. HPC has higher compressive strength, which allows larger vertical clearance underneath the bridge, lighter and more slender girders and consequently a reduced number of supports. It also has increased modulus of elasticity (MOE) such that deflections and elastic shortening losses at prestress transfer are reduced. The increased tensile strength of HPC increases permissible stress range at service. Its lower creep and shrinkage reduces prestress losses over time.

The enhanced performance characteristics of HPC are usually obtained by adding various cementitious materials and chemical admixtures to conventional concrete mix designs, and by modifying curing procedures. For example, the addition of fly ash and micro silica to concrete reduces the porosity of the concrete and increases its durability. Super plasticizers can be used to reduce the water to cement ratio (w/cm) and thereby increase the concrete compressive strength. However, even if the target properties are achieved, it is important to thoroughly test a new mix. Changes in mixes rarely affect only the target properties, in this case strength and durability, but they also affect other material properties, such as creep, shrinkage, modulus of elasticity, and coefficient of thermal expansion.

With use of chemical and mineral admixtures and proper batching techniques HPC can reach specified aims such as high strength, high elastic modulus, high permeability, freeze-thaw resistance and so on. This means designers can choose any type of HPC as they want for high capacity or high durability. It also allows designers design for aesthetics.

1.2. LITERATURE RESEARCH OF HPC

During the 1980's research began focusing on High Strength Concrete (HSC) where the driver was strength development. HSC was used in highway structures for its high compressive strength development which resulted in cost effective designs. In addition to strength, other concrete properties including modulus of elasticity, creep, shrinkage, etc. are known to have an important role on the overall behavior of concrete members. The definition of HPC therefore has subsequently been expanded to incorporate other performance characteristics including elasticity, freezing/thawing durability, chloride permeability, abrasion resistance, scaling resistance, shrinkage, and creep.

1.2.1. Definition of HPC. Zia et al. (1997) defined HPC as "Any concrete which satisfies certain criteria proposed to overcome limitations of conventional concretes may be called High-Performance concrete (HPC)." It may include concrete which provides either substantially improved resistance to environmental influences (durability in service) or substantially increased structural capacity while maintaining adequate durability. It may also include concrete which significantly reduces construction time to permit rapid opening or reopening of roads to traffic, without compromising long-term serviceability. Therefore, it is not possible to provide a unique definition of HPC without considering the performance requirements of the intended use of the concrete.

Forster (1994) defined HPC as "a concrete made with appropriate materials combined according to a selected mix design and properly mixed, transported, placed, consolidated, and cured so that the resulting concrete will give excellent performance in the structure in which it will be exposed, and with the loads to which it will be subjected

for its design life." In discussing the meaning of HPC, Aitcin and Neville (1993) stated that "in practical application of this type of concrete, the emphasis has in many cases gradually shifted from the compressive strength to other properties of the material, such as a high modulus of elasticity, high density, low permeability, and resistance to some forms of attack."

A more broad definition of HPC was adopted by the American Concrete Institute (ACI). HPC was defined as concrete which meets special performance and uniformity requirements that cannot always be achieved routinely by using only conventional materials and normal mixing, placing, and curing practices. The requirements may involve enhancements of characteristics such as placement and compaction without segregation, long-term mechanical properties, early-age strength, volume stability, or service life in severe environments. Concretes possessing many of these characteristics often achieve higher strength. Therefore, HPC is often of high strength, but high-strength concrete may not necessarily be categorized as high performance.

For the purpose of the SHRP C-205 project (Zia et al. 1993), HPC was defined in terms of certain target strength and durability criteria as shown in Table 1.1. In this definition, the target minimum strength should be achieved in the specified time after water is added to the concrete mixture. The compressive strength is determined from 100 x 200 mm (4 x 8 in.) cylinders tested with neoprene caps. The water to cement ratio is based on all cementitious materials. The minimum durability factor should be achieved after 300 cycles of freezing and thawing according to ASTM C 666 (AASHTO T 161), procedure A.

Table 1.1. Definition of HPC according to SHRP C-205 (Zia et al. 1993)

Category of HPC	Minimum Compressive Strength	Maximum Water/ Cement Ratio	Min. Frost Durability Factor
Very early strength (VES)			
Option A (with Type III cement)	2000 psi (14 MPa) in 6 hours	0.40	80%
Option B (with PBC-XT cement)	2500 psi (17.5 MPa) in 4 hours	0.29	80%
High early strength (HES) (with Type III cement)	5000 psi (34.5 MPa) in 24 hours	0.35	80%
Very high strength (VHS) (with Type I cement)	10,000 psi (70 MPa) in 28 hours	0.35	80%

Based on the results of SHRP C-103 and SHRP C-205 research, the Federal Highway Administration (FHwA) proposed criteria for four different performance grades of HPC (Goodspeed et al. 1996). The criteria are expressed in terms of eight performance characteristics including strength, elasticity, freezing/thawing durability, chloride permeability, abrasion resistance, scaling resistance, shrinkage, and creep as shown in Table 1.2.

Depending on a specific application for different structures in different environmental conditions, a given high performance concrete may require different grade of performance for each performance characteristics. For example, a bridge located in an urban area with moderate climate may require Grade 3 performance for compressive strength, modulus of elasticity, shrinkage, creep, and abrasion resistance, but only Grade 1 performance for freezing/thawing durability, scaling resistance, and chloride permeability.

Table 1.2. Definition of HPC according to FHwA (Goodspeed et al. 1996)

Performance characteristics	Standard test method	FHwA HPC performance grade			
		1	2	3	4
Freeze-thaw durability	AASHTO T161 ASTM C666 Procedure A	60%<X1<80%	80%<X1		
Scaling resistance	ASTM C672	X2=4, 5	X2=2, 3	X2=0, 1	
Abrasion resistance	ASTM C944	2.0>X3>1.0	1.0>X3>0.5	0.5>X3	
Chloride penetration	AASHTO T277 ASTM C 1202	3000>X4>2000	2000>X4>800	800>X4	
Strength	AASHTO T2 ASTM C39	41<X5<55	55<X5<69	69<X5<97	97<X5
Elasticity	ASTM C469	28<X6<40	40<X6<50	50<X6	
Shrinkage	ASTM C157	800>X7>600	600>X7>400	400>X7	
Specific creep	ASTM C512	75>X8>60	60>X8>45	45>X8>30	30 >X8

Note:

X1 = relative dynamic modulus of elasticity after 300 cycles

X2 = visual rating of the surface after 50 cycles

X3 = avg. depth of wear in mm (1 mm = 0.03937 in.)

X4 = coulombs

X5 = compressive strength in MPa (1MPa = 145.0377 psi)

X6 = modulus in GPa (1GPa = 145.0377 ksi)

X7 = microstrain

X8 = microstrain per MPa (1MPa = 145.0377 psi)

1.2.2. QC/QA of HPC. For the application of concrete to real construction activities, the quality control and quality assurance is critically important for the producing of the required concrete. It is important for engineers to realize its increased importance for HPC compared to the conventional concrete.

1.2.2.1 Introduction. For the successful implementation of HPC, quality assurance (QA) and quality control (QC) are very important. They are defined by ACI Committee 116 - Terminology and Notation (ACI 116R-90 1990) as:

Quality assurance—actions taken by an owner or the owner's representative to provide assurance that what is being done and what is being provided are in accordance with the applicable standards of good practice for the work.

Quality control—actions taken by a producer or contractor to provide control over what is being done and what is being provided so that the applicable standards of good practice for the work are followed.

Use and incorporation of performance based specification systems are recommended rather than prescriptive based specification systems. Through this methodology, "engineered concrete" mix designs which have been optimized to satisfy a specific mechanical and or material criterion are more likely to result. The resulting optimized mix designs are a more economic use of materials.

1.2.2.2 Preparation. A preconstruction meeting with project participants should be held to talk about and make clear the following items: contract requirements; placing conditions and procedures; testing programs and criteria; effects on concrete of temperature, placing, consolidation, time and curing; prequalification of the work force, staff and facilities; lines of communication and identification of responsibilities.

Historical data can be used as guidance on proportioning high-strength concrete mixtures if available. If historical data are not available the development of an optimum mixture requires a large number of trial batches. Firstly, mix design for appropriate material proportions should be determined in the laboratory with sufficient trials to meet

project requirements. Secondly, based on the laboratory results, production-sized batches should be conducted because different production mixers can lead to different properties of concrete.

For concrete with a specified strength of 70 MPa (10,000 psi) or higher or at least 7 MPa (1000 psi) higher than previously produced in the market local to the project, bidders should be prequalified before being offered the supply contract. All bidders should make the specifications clear, which may include trial batches, in-place strength, air entrainment and temperature considerations.

If there is no usable data for mix proportions and constituents of the high performance concrete, mix design and optimization are needed to assure the required properties. In an effort to develop a HPC mix which is economical, the use of locally available materials is emphasized. Coarse aggregate, sand, portland cement, fly ash and chemical admixtures are the main materials for these mix designs. Usually, laboratory mix designs and field trial mixes are then initiated to develop the promising mix designs.

1.2.2.3 Producing. Related detailed guidelines can be found in *Guide to Quality Control and Testing of High-Strength Concrete* (ACI 363.2R-98 1998) reported by ACI Committee 363 - High-Strength Concrete, here gives some aspects that are important for practitioners.

Spot checking the plant is recommended unless the complexities of the project demand full-time monitoring. In many cases, full-time inspection at the batching facility is not necessary. Full-time inspection is recommended for concretes with design strengths greater than 70 MPa (10,000 psi). Adequate job control must be established to prevent delays that may cause slump loss and result in lower workability. At the job site,

preparations should be made as detailed as possible. Different strength concretes should be marked clearly to avoid mixing in construction.

In ACI 363.2R-98, water curing of high-strength concrete is recommended because of the low water-cementitious materials ratios employed.

In research conducted on the first HPC bridge in North America, Louetta Road Overpass Bridge Project in Houston, Texas (Myers 1998), match curing technology was found to be beneficial to the fabricator since it increases plant productivity and allows for the monitoring of the concrete maturity to more accurately estimate concrete strength at release. The system incorporates steel molds that include internal coils that cure the cylinders at the same temperature profile as the thermocouple location in the member. Test data indicates the match cured cylinders best represented the concrete in the Texas U-beam members used in this project. It also resulted in a more accurate representative of mechanical and material properties of the concrete which allows the design engineer to more precisely predict short and long-term structural performance.

1.2.2.4 Testing. One of the objectives of QA/QC is to produce HPC with expected mechanical and material properties so that the design considerations can be met. Compared with conventional concrete, HPC is found to be more sensitive to testing variables. The tests may include compressive strength, modulus of elasticity, flexural strength, splitting tensile strength, creep, shrinkage, freeze-thaw resistance, rapid chloride permeability, chloride ponding concentration, abrasion resistance, scaling de-icing resistance, etc. These tests can be performed according to ASTM. Test time and curing conditions may be considered as variables for all kinds of specimens for different tests each pour.

1.2.3. Material Properties of HPC. For designers and practitioners, it is very helpful to get an overall conception about the properties of high performance concrete. These properties relate to strength, serviceability, and durability and include compressive strength, tensile strength, modulus of elasticity, creep, shrinkage, permeability, freeze-thaw resistance and abrasion resistance as examples. Selection of materials to produce high quality HPC is important in meeting any design needs. To date AASHTO format specifications do not specifically address mechanical property guidelines for high-strength concrete, thus the state-of-the-art from ACI and other sources is presented herein. It may be noted that several NCHRP research projects have been let with the ultimate goal in developing AASHTO format specifications related to HSC and HPC.

1.2.3.1 Strength. Concrete properties such as elastic modulus, tensile or flexural strength, shear strength, stress–strain relationships and bond strength are usually expressed in terms of uniaxial compressive strength of 150 x 300 mm (6 x 12 in.) cylinders, moist cured to 28 days. For high performance concrete of higher strength, the shape of the ascending part of the curve becomes more linear and steeper, the strain at maximum stress is slightly higher, and the slope of the descending part becomes steeper.

According to the research conducted by Myers (1998), the temperature development within precast members dramatically influenced the long term strength gain of the concrete within the member. Thus the various curing conditions yield quite different results. The member cured cylinders used to determine release of prestressing strands underestimated the compressive strength of the member by as much as 27.9% when compared to the match cured cylinders. The ASTM moist cured cylinders used to verify the design strength of the member at 56 days overestimated the compressive

strength of the member by as much as 15.9% when compared to the match cured cylinders. This is particularly important for designing HPC components where current code empirical equations are based on a function of the compressive strength of the concrete.

The tensile strength is important for the cracking behavior and other properties such as stiffness, damping action, bond to embedded steel, and durability of concrete. The relationship between tensile and compressive strength is not simplistic in nature. It depends on the age and strength of concrete, the type of aggregate, the amount of air entrainment and the degree of compaction. The tensile strength can be determined by direct tensile tests or by indirect tensile tests such as flexural or split cylinder tests.

For concrete with compressive strengths in the range of 20.7 MPa (3000 psi) to 82.7 MPa (12,000 psi), ACI committee 363 (1992) proposed:

$$f_{sp} = 7.4(f'_c)^{0.5} \text{ psi} \qquad \text{Equation 1.1}$$

$$f_r = 11.7(f'_c)^{0.5} \text{ psi} \qquad \text{Equation 1.2}$$

where, f_{sp} is splitting tensile strength, f'_c is compressive strength; f_r is the flexural tensile strength.

1.2.3.2 Modulus of elasticity. The modulus of elasticity of concrete is one of the most important mechanical properties of concrete since it impacts the serviceability and the structural performance of reinforced concrete structures. The modulus of elasticity is generally related to the compressive strength of concrete. Empirical equations for the elastic modulus in terms of the compressive strength in the range of 20.7 MPa (3000 psi) to 82.7 MPa (12,000 psi) were presented by the ACI 363 (1992) as shown in Equation 1.3.

$$E_c = 40{,}000(f'_c)^{0.5} + 10^6 \text{ psi} \qquad \text{Equation 1.3}$$

where, E_c is modulus of elasticity, f'_c is compressive strength.

High performance concrete with high modulus of elasticity can be achieved in two ways as shown in Figures 1.1 and 1.2. One method is to increase the coarse aggregate content of the mix. The other method is to select hard dense aggregate sources that are compatible with the paste matrix characteristics (Myers 1999).

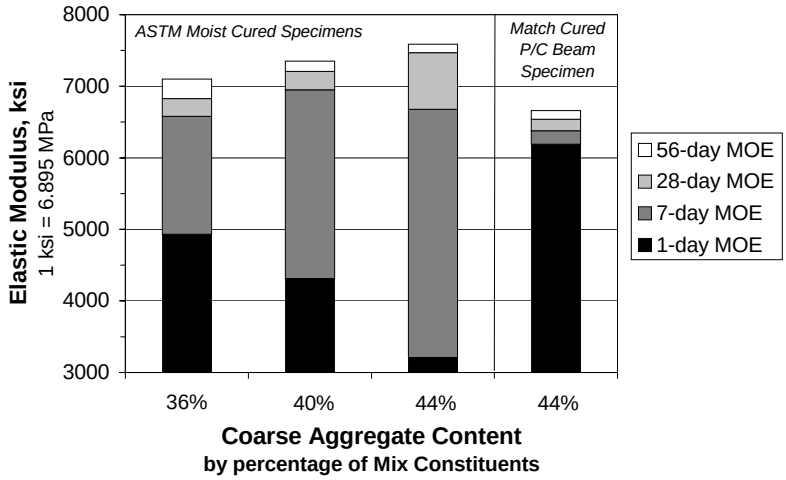

Figure 1.1. Elastic Modulus versus Coarse Aggregate Content and Curing Condition (Myers 1999)

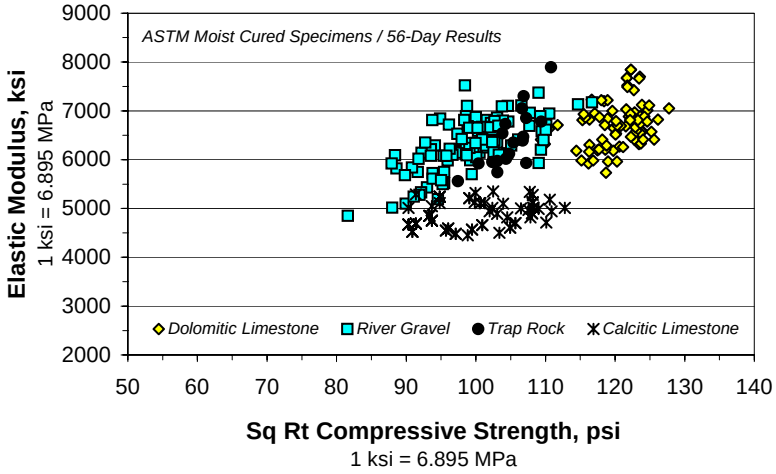

Figure 1.2. Elastic Modulus versus Sq. Rt. Compressive Strength by Coarse Aggregate Type (Myers 1999)

1.2.3.3 Creep and shrinkage. Creep and shrinkage are important for both conventional and high performance concrete. Creep is defined as the time-dependent increase in strain of hardened concrete subjected to sustained stress. It is usually determined by subtracting the sum of the initial instantaneous strain from the total measured strain in a loaded specimen. The sum of the initial instantaneous strain are those strains due to sustained stress, the shrinkage, and any thermal strain in an identical load-free specimen subjected to the same history of relative humidity and temperature conditions.

Shrinkage is the decrease of concrete volume with time. This decrease is due to changes in the moisture content of the concrete and physicochemical changes, which occur without stress attributable to actions external to the concrete. Swelling is the increase of concrete volume with time.

Measured shrinkage strain and predicted shrinkage using the current method suggested by ACI Committee 209 - Creep and Shrinkage in Concrete (ACI 209R-92 1992) are quite different as shown in Figure 1.3 based on research conducted on HPC bridges in Texas. The fitted curve quantifies the measured results for the HPC mix design and is defined by the following empirical Equation 1.4:

$$\varepsilon_{sh} = (0.000510)\frac{t}{35+t} \qquad \text{Equation 1.4}$$

Figure 1.4 outlines the measured creep coefficient and current ACI 209 (1992) prediction for the creep coefficient. The fitted curve quantifies the measured results for the creep coefficient for the HPC mix design and is defined by empirical Equation 1.5 as follows:

$$C_{ct} = (1.95)\frac{t^{0.6}}{10 + t^{0.6}} \qquad \text{Equation 1.5}$$

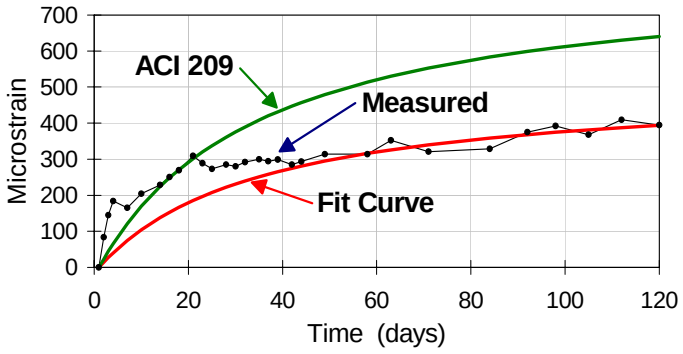

Figure 1.3. Average Shrinkage Strain for Concrete Sampled From the Precast U-Beam Members (Myers 1998)

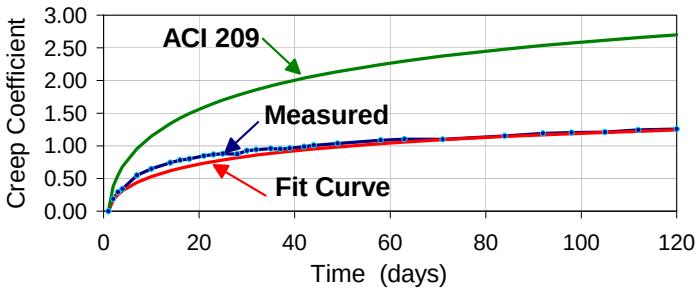

Figure 1.4. Creep Coefficient for Concrete Sampled From the Precast U-Beam Members (Myers 1998)

It has been found that both creep and shrinkage are largely dependent on the amount of mix water and are less than predicted by the ACI 209 (1992) “standard” values (Gross, 1999). This may lead to lower prestress losses than the values determined by prediction method for conventional concrete. Thus for designers to predict prestress losses more accurately, empirical models specific to HPC are required.

1.2.3.4 Permeability. Permeability of high-strength concrete, which is considered to be a good indicator of its durability and long term performance, has been the topic of a large number of research studies and investigations. The main reason for this concern is that permeability has been shown to directly affect the durability of concrete (Mindness and Young, 1981). To date, there is no recognized standard test method to measure the permeability of concrete. In general, there are three categories of methods: air (or gas) permeability, hydraulic permeability, and chloride ion permeability. High performance concrete with low permeability is desired in bridge decks.

Research has concluded by Myers (1998) and others that a water to cementitious (w/cm) ratio can no longer be used effectively to predict the durability or permeability performance of a concrete mix design with the use of today's mineral and chemical admixtures. Varying degrees of permeability performance at any single w/cm ratio were exhibited depending on the mixture constituents and characteristics. The variation of the permeability due to changing the coarse aggregate type was minimal. Decreasing the w/cm ratio while keeping all other properties constant was not effective in decreasing the permeability. Myers (1998) also found the use of a Class C fly ash replacement reduced the permeability of the high performance concrete mixes.

1.2.3.5 Freeze-thaw resistance. Damage of concrete under repeated cycles of freezing and thawing (frost attack) is a major problem of durability. Stark (1989) found that long freeze-thaw cycles were more severe than short freeze-thaw cycles for same number of cycles, even where air void spacing factors were no greater than 0.2 mm (0.008 in.). Cohen et al. (1992) concluded that while an explanation for this phenomenon requires further study of the microstructure, it appears clear that the concrete

deterioration process during freezing and thawing cycles had reached a stage that the normal relationship between the compressive strength and the modulus could no long hold true.

Many studies have found that HPC has improved freeze-thaw resistance compared to conventional concretes. Enhanced strength characteristics associated with the HPC had a minor influence on the overall freeze-thaw resistance of the concrete as long as the concrete incorporated sound materials and an adequate well distributed air void system. As found by Myers (1998), HPC with a 50% increase in strength had only a 5% change in freeze-thaw performance. The high strength associated with many HPC's resulted in slightly less visible surface damage, but similar freeze-thaw durability performance (Nawy, 2001).

1.2.3.6 Abrasion resistance. Abrasion is wearing due to repeated rubbing and friction. For pavements, abrasion results from traffic wear. From the standpoint of safety, adequate abrasion resistance during the service life of the wearing surface is important for pavements and bridge decks. Abrasion resistance of concrete is a direct function of its strength, and thus its w/cm ratio and constituent materials (Mindness and Young, 1981). High quality paste and strong aggregates are essential to produce an abrasion resistant concrete. In our study, higher strength concrete can be expected to result in reduced ware resistance for mix designs with similar constituents assuming they are finished and cured under similar conditions.

1.2.3.7 Scaling resistance. Scaling is a problem of durability caused by repeated application of deicing salts. A study found that strength had little influence on the scaling resistance of the concrete (Mindness and Young, 1981). The concrete that had the lowest

strength actually exhibited the best scaling resistance. Rather than strength, the primary factors affecting scaling resistance are mixture characteristics, curing and curing procedures, air entrainment, aging effects and sealers.

1.2.4. HPC Bridges. High performance concrete has been used in columns of high rise buildings dating back to the 1980's, but only recently have the benefits of HPC seen application to bridge structures.

As one of AASHTO's lead states, Texas has been at the forefront in application of HPC in bridge structures. The Louetta Road Overpass in Houston, Texas, a bridge constructed in 1997, utilized HPC in most aspects of the bridge design including the piers, girders and deck. Required concrete strengths for the girders were 48.9 MPa (7000 psi) at transfer and ranged between 69.9 MPa (10,000 psi) and 90.8 MPa (13,000 psi) at design. Twelve of the thirty three girders in the bridge were instrumented. Gauges used were strain gauged bars, vibrating wire strain gauges, and thermocouples. Demountable mechanical (DEMEC) strain gauges were used to measure surface strains and a piano wire deflection system was used to measure deflections. Four CR10 data loggers from Campbell Scientific and nine AM416 multiplexers were used to acquire data from the gauges. The San Angelo bridge, the second HPC bridge in the United States and Texas was constructed with 15.2 mm (0.6 in.) diameter strands. Required concrete strength at transfer was 62.2 MPa (8900 psi) and the 56-day strength was 102.7 MPa (14,700 psi) at design. The compressive strength of the concrete at one year was reported in excess of 117.2 MPa (17,000 psi). Similar instrumentation programs with the Louetta Road Overpass were implemented for this bridge project. To date, this bridge incorporated the highest design compressive strength produced in the United States and perhaps the world.

Following these two HPC bridges, other bridges utilizing HPC were constructed in Virginia, Nebraska, New Hampshire, Washington, and so on. Most of these bridges were studied under the Strategic Highway Research Program (SHRP). These bridges are summarized in Table 1.3 and Table 1.4.

Table 1.3. Summary of HPC Bridges in U.S.

State	Bridge Name	Girder Type	Max. Span, ft	Max. Spacing, ft	Dia. of Strands, in	Design Strength, psi	Actual Strength, psi
AL	AL 199	BT-54	114	8.75	0.6	10,000	NA
Co	Yale Av.	BOX	112	Adjacent	0.6	10,000	14,000
GA	SR 920	II, IV	127.1	7.6	0.6	10,000	NA
LA	Charenton	III	72	10	0.5	10,000	12,023
MO	A5529	Type 6	82	8.67	0.5	10,000	12,365
NE	120th St.	NU1100	75	12.4	0.5	12,000	13,944
NH	Route 104	III	65	12.5	0.5	8000	7755
NH	Route 3A	NE 1000	60	11.5	0.6	8000	11,200
NC	U.S. 401	IV, III	91.9	10.2	0.6	10,000	15,000
OH	U.S. 22	B42-48	115.5	Adjacent	0.6	10,000	12,920
SD	I29 NB	II	61	11.4	0.5	9900	15,900
SD	I29 SB	II	61	11.4	0.5	9900	13,250
TN	Porter	BT-72	159	8.33	0.6	10,000	NA
TN	Hichman	BT-72	151.3	8.33	9/16	10,000	NA
TX	Louetta-NB	U54	136.5	12.94	0.6	13,100	14,440
TX	Louetta-SB	U54	134	16.62	0.6	13,100	14,550
TX	SA-EB	IV	157	11	0.6	14,000	15,240
TX	SA-WB	IV	140.3	8.26	0.5	8900	10,130
VA	Route 40	IV	80	10	0.5	8000	11,490
VA	VA Av.	III	74	9.25	0.6	10,000	11,200
WA	SR 18	W74G	137	8	0.6	10,000	12,220
Conversion Factors: 1 ft = 0.3048 m; 1 in = 25.4 in; 1 psi = 0.00689 MPa NA – Not Available							

Table 1.4. Summary of Structural Design and Instrumentation of HPC Bridges

Bridge Name	Deck (1)	Deck (2)	Live Loads	Prestress Loss, psi	Instrumentation
AL 199	7	NA	NA	NA	Temp., strain, camber, load test
Yale Av.	11.5	NA	HS 25	65,753	Temperature, strain, camber
SR 920	8	2000	MS 18	64,500	Temp., strain, camber, initial prestressing force, frequency
Charenton	8	2000	HS 20	49,500	NA
MO	NA	None	NA	NA	Temp., strain, camber, load test
120th St.	7.5	1800	HS 20	NA	Temp. strain, camber, rotation, prestressing force
Route 104	9	1000	HS 25	NA	Temp. strain
Route 3A	9	1000	HS 25	48,800	Temp. strain
U.S. 401	8.5	NA	MS18	35,585	Temp. strain, camber, rotation, prestressing force, transfer length
U.S. 22	5.5	NA	HS 25	19.6%	Temp. strain, camber, rotation, prestress loss, DL, load test
I29 NB, SB	9	NA	HS 25	28%	NA
Porter	8.25	1500	HS 20	NA	NA
Hichman	8.25	1500	HS 20	NA	NA
Louetta	7.25	NA	HS 20	55,390	Temperature, strain, camber, rotation, prestressing force, transfer length, load test
SA-EB	7.5	NA	HS 20	49,070	
SA-WB	7.5	NA	HS 20	47,910	
Route 40	8.5	2500	HS 20	28%	None
VA Av.	8.5	2500	HS 20	30.81%	Transfer and development length
SR 18	7.5	NA	HL 93	41,100	Temp., strain, force, camber

Deck (1): Deck thickness in inch; Deck (2): Specified permeability in coulombs.

Except bridge SR 18 using AASHTO LRFD design code, the other bridges were designed according to AASHTO Standard Specification; NA – Not Available

1 psi = 0.00689 MPa; Temp.: Temperature; DL: Development length

1.2.5. Behavior of HPC Structures. The simplified AASHTO and PCI equations for prestress losses were found inappropriate for HPC. Gross (1999) proposed a

modified general form of these component methods. Actually, the accurate prediction of prestress losses is largely dependent on the accurate estimation of material properties.

The long-term deflection behavior of HPC girders are often designed to exhibit a small upward camber (< span length / 800) under full dead load in the composite bridge (AASHTO, 1996). Long-term deflection behavior is extremely sensitive for HPC girders compared to girders with conventional concrete. Small variations in material properties and prestress losses can have significant impact (± 50%) on deflection behavior of HPC girders (Myers and Yang, 2001).

The effect of thermal gradients during hydration and differential shrinkage before release contributes to the significant difference between measured camber and predicted values using measured parameters. Thermal gradients in composite and non-composite HPC girders have a significant influence on behavior, especially measured deflections and concrete strains in the deck (Myers and Kleinhans, 2003).

Hydration temperatures for girders are generally rather high for high performance concrete, which reached 130°F - 210°F (54°C – 99°C), and thus cracking can result before release (Myers, 1999). It should be avoided by releasing the prestress for these girders as soon as possible after the required release strength is obtained and side forms are stripped. More accurate methods to estimate extreme bridge temperatures are needed to study the sensitivity of hydration temperature on HPC.

HPC designs are more sensitive to variations in material properties and other design parameters including the magnitudes of prestress forces and all dead loads. Often, it is difficult to make accurate estimation of prestress losses and deflection behavior. Care

must be exercised in designing HPC highway structures and designers must be aware of the increased sensitivity (Myers and Yang 2001).

Live load tests are usually necessary to investigate the behavior of a bridge under live load and check the design assumptions. As listed in Table 1.4, live load tests have been implemented for several HPC bridges. For issues related to the behavior of a structure, such as the continuity between adjacent spans, load tests play an important role.

Previous studies identified the advantages of utilizing high-strength concrete in highway bridges (Rabbat and Russell 1982). Comparisons showed that by increasing the girder concrete compressive strength from 35 to 48 MPa (5000 to 7000 psi), the maximum span capability of AASHTO girders was increased by about 15%. In the project studied by Carpenter (1980), it indicated that span capabilities of various girder cross sections could be increased through the utilization of higher strength concretes. For the same span length, the number of girders in a cross section could be reduced by utilizing a high-strength concrete. It was found that at the higher concrete strength levels, the maximum available prestressing force limited the advantages of high-strength concrete.

In the study by Construction Technology Laboratories (CTL) reported in 1997 (Russell et al. 1997), it indicated that the use of existing girder cross sections with concrete compressive strengths up to 69 MPa (10,000 psi) allow longer span lengths by 18% and more economical structures by 17%. To effectively utilize high-strength concretes, additional prestressing force must be applied to the cross section. This can be obtained by modifying the cross section geometry or strands layout in the members.

1.3. RESEARCH PROGRAM

1.3.1. Program Team. Dr. John Myers at University of Missouri-Rolla (UMR) served as the principal investigator. The lead graduate research assistant, Yumin Yang, devoted much of his research time to this project. Other UMR graduate students including Ji Shen, Ishwor Gurung and many other undergraduate students have also participated in this project. The project was sponsored by Missouri Department of Transportation (MoDOT), Federal Highway Administration (FHwA) and the University Transportation Center (UTC) at the University of Missouri-Rolla.

1.3.2. Design Details of the Bridge. A description of this high performance bridge is presented in this Section. The HPC bridge for this study has a National Bridge Inventory (NBI) structure number of A6130, located in Pemiscot County near Hayti, Missouri. It spans drainage ditch No.8 carrying Route 412 as shown in Figure 1.5.

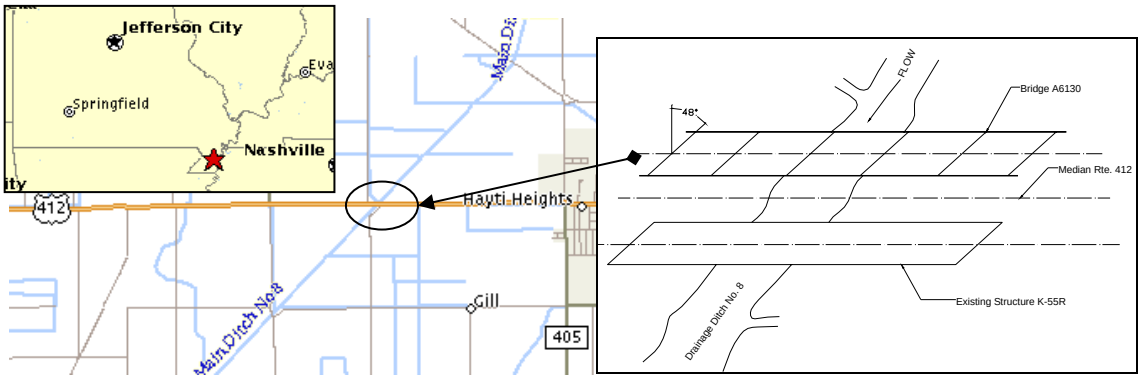

Figure 1.5. Bridge Location

There is an existing bridge on the south of Bridge A6130 that is scheduled for replacement in 2003 - 2004. The Existing bridge has five spans with span length as

14.320 m (46.98 ft), 16.161 m (53.02 ft), 16.002 m (52.50 ft), 16.161 m (53.02 ft), 14.320 m (46.98 ft). It consists of steel girders with a section depth of 838 mm (33 in.).

The new bridge, A6130, also has five spans, 15.5 m (50.85 ft), 17.0 m (55.77 ft), 17.0 m (55.77 ft), 17.0 m (55.77 ft), 15.5 m (50.85 ft). The bridge has a skew of 48°. A plan view of half of the bridge is shown in Figure 1.6. A cross-section of the bridge is presented in Figure 1.7.

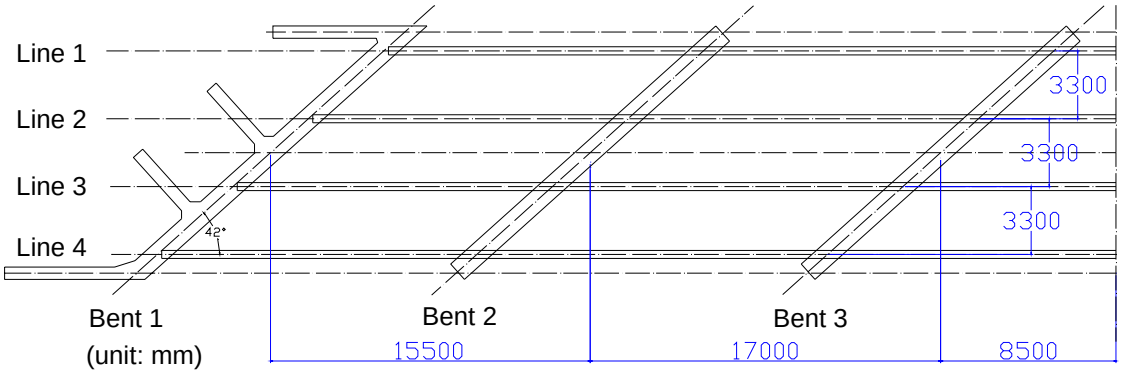

Figure 1.6. Bridge A6130 Alignment

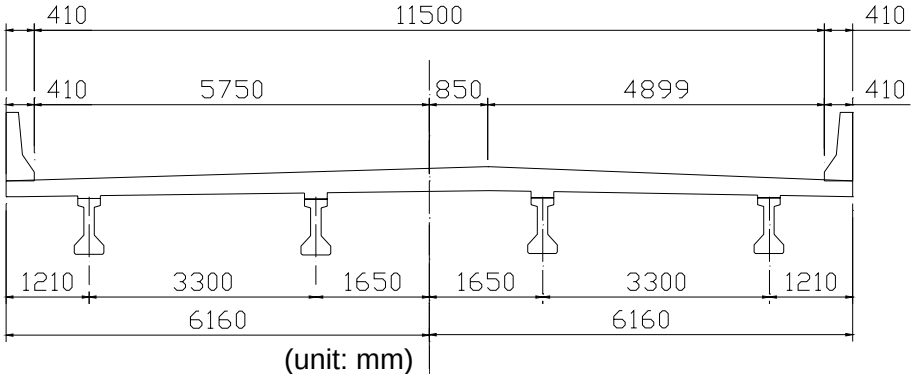

Figure 1.7. Cross-Section of Bridge A6130

The unsymmetrical roadway width is 11.4 m (37.73 ft), plus 410 mm (16.14 in.) safety barrier curbs, and adds 100 mm (3.94 in.) bridge width on the right side of the

bridge parallel to back tangent of curve to allow the curved roadway to fit on a tangent bridge. The loading criteria for the bridge is MoDOT MS18 modified (AASHTO HS20 modified). The substructure uses cast-in-place (CIP) concrete piles. The superstructure uses high performance concrete (HPC) in prestressted precast I-girders and a CIP deck.

One of the unique features of this HPC bridge is that it is designed with a continuity detail (see Figure 1.8) that was developed in the 1970's in Missouri for conventional normal strength prestressed / precast concrete members. This research study will provide the opportunity to investigate the behavior of this detail in conjunction with HPC and 15.24 mm (0.6 in.) diameter prestressing strands. As later-age load tests are conducted, the softening of this detail may be studied over time providing important information for designers.

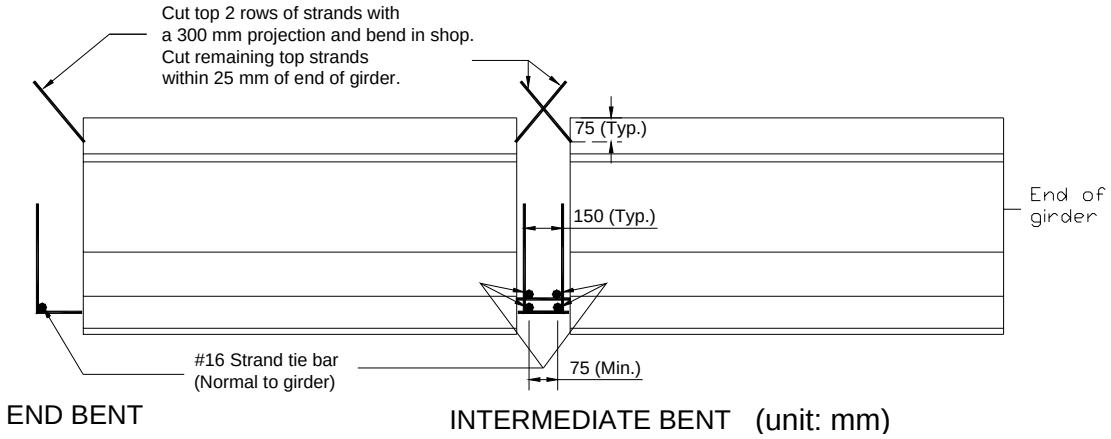

Figure 1.8. Intermediate Bent / End Bent Continuity Detailing

The girders were fabricated by Egyptian Concrete Company located in Bonne Terre, Missouri during the months of June and July in 2001. Construction of the bridge

started in the summer of 2001 and was complete in December 2001. It opened to traffic in October 2002.

1.3.2.1 Prestressed / Precast I girder. The PC girders are MoDOT Type 2 girders. The dimensions of a Type 2 girder are shown in Figure 1.9. The concrete compressive strength for design was required to be 70 MPa (10,152 psi) at 56 days, and a compressive strength of 52 MPa (7542 psi) was required at transfer.

The strands used were 15.24 mm (0.6 in.), seven wires, low relaxation, Grade 1860 prestressing strands. The strands layout is shown in the Figures 1.10 and 1.11. For Span (1-2) and Span (5-6), there are 18 strands with an initial prestress force of 3486 kN (779.6 kips). Eight strands are draped at end span. For the other three spans, 20 strands were used with an initial prestress force of 3770 kN (847.5 kips). Only 4 of 20 strands are draped at the end span.

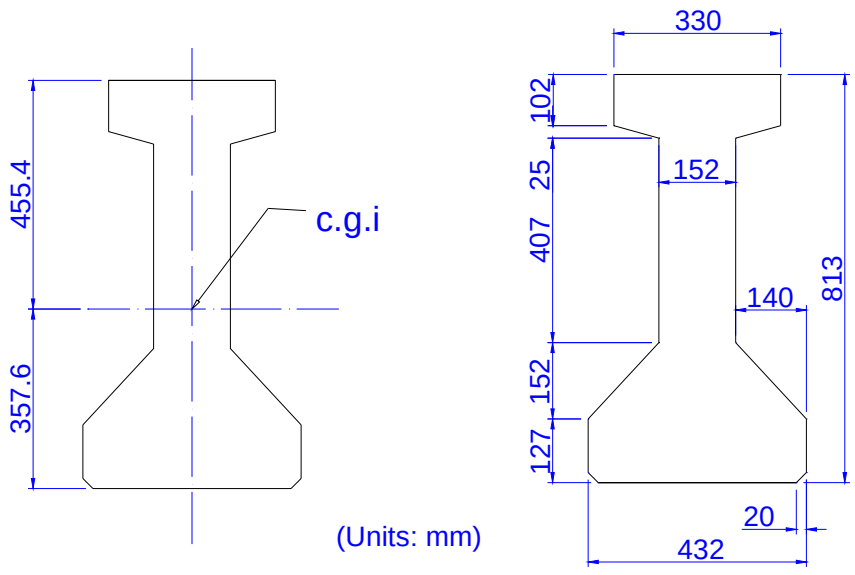

Figure 1.9. Type 2 I-Girder Section

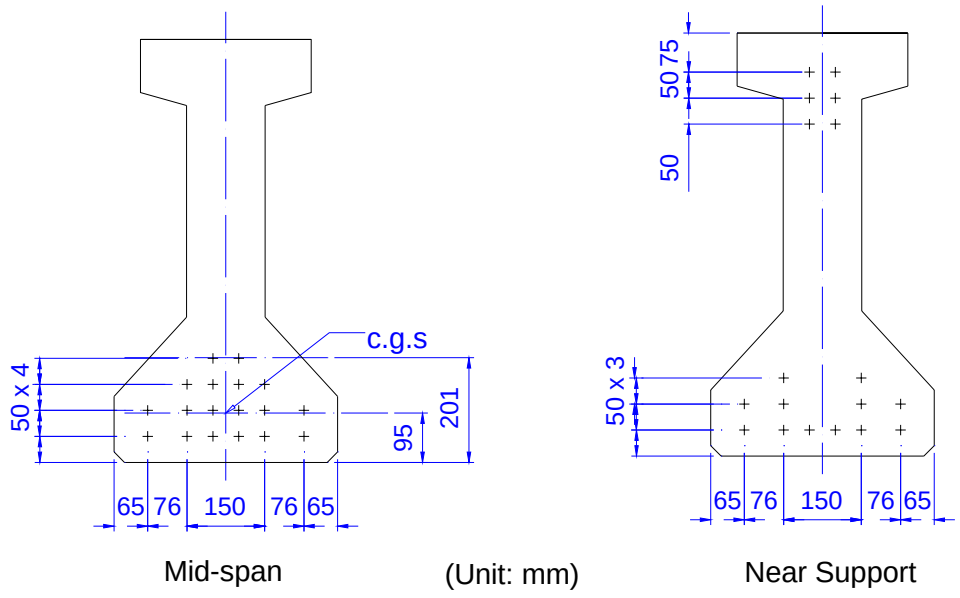

Figure 1.10. Strands Layout for Span (1-2) and Span (5-6)

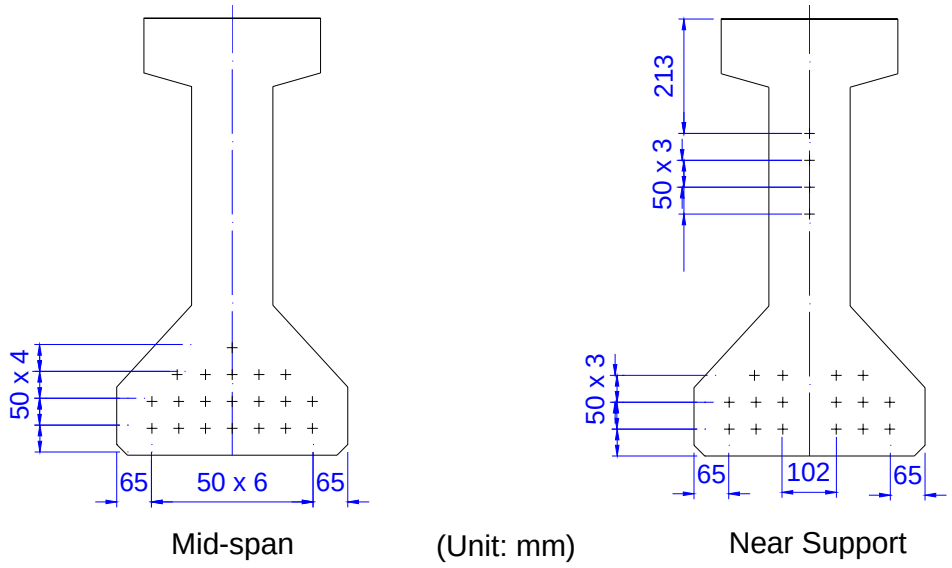

Figure 1.11. Strands Layout for Span (2-3), (3-4) and (4-5)

1.3.2.2 HPC bridge deck. The CIP deck was designed as an HPC deck to improve long-term durability performance. A performance permeability was required by

the owner, MoDOT, to meet service life goals. The slab thickness is 230 mm (9.055 in.). The design compressive strength for the CIP deck was 28 MPa (4000 psi) at 28 days.

1.3.3. Bridge Elements Numbering. The girders and deck are numbered as shown in Figure 1.12. The other half bridge is numbered in sequential order respectively.

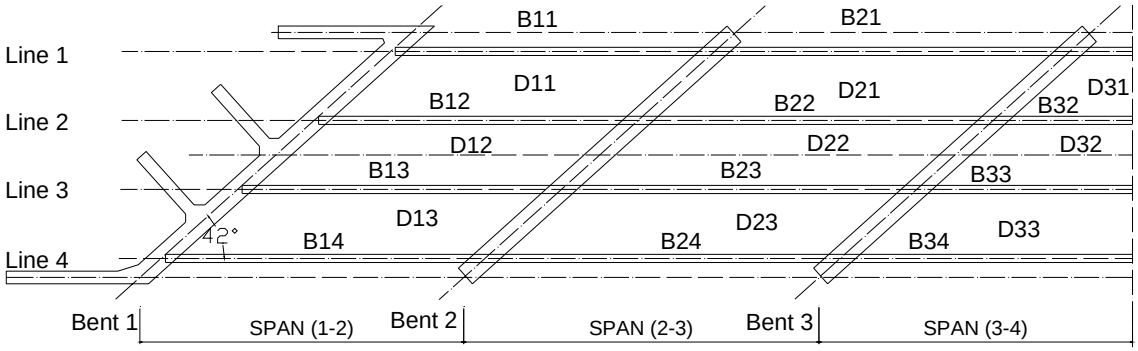

Figure 1.12. Numbering of the Bridge Components (Half Bridge)

1.4. SCOPE OF THE REPORT

A flow chart for the project is presented in Figure 1.13. HPC materials for girders and cast-in-place deck were studied for both mechanical and material properties including compressive strength, modulus of elasticity, splitting strength, freeze-thaw, abrasion resistance, de-icing scaling, ponding chloride, rapid chloride permeability, creep, shrinkage, and coefficient of thermal expansion.

The completed bridge was instrumented to measure temperature and strain variations. This was combined with deformation measurements to determine how the bridge behaves in response to temperature changes, dead load, live load, creep, and shrinkage. Measured thermal behavior, strain behavior, prestress losses, camber and

deflection were investigated by comparing with theoretical estimation for both early-age and later-age. Modified theoretical methods based on the test results were recommended.

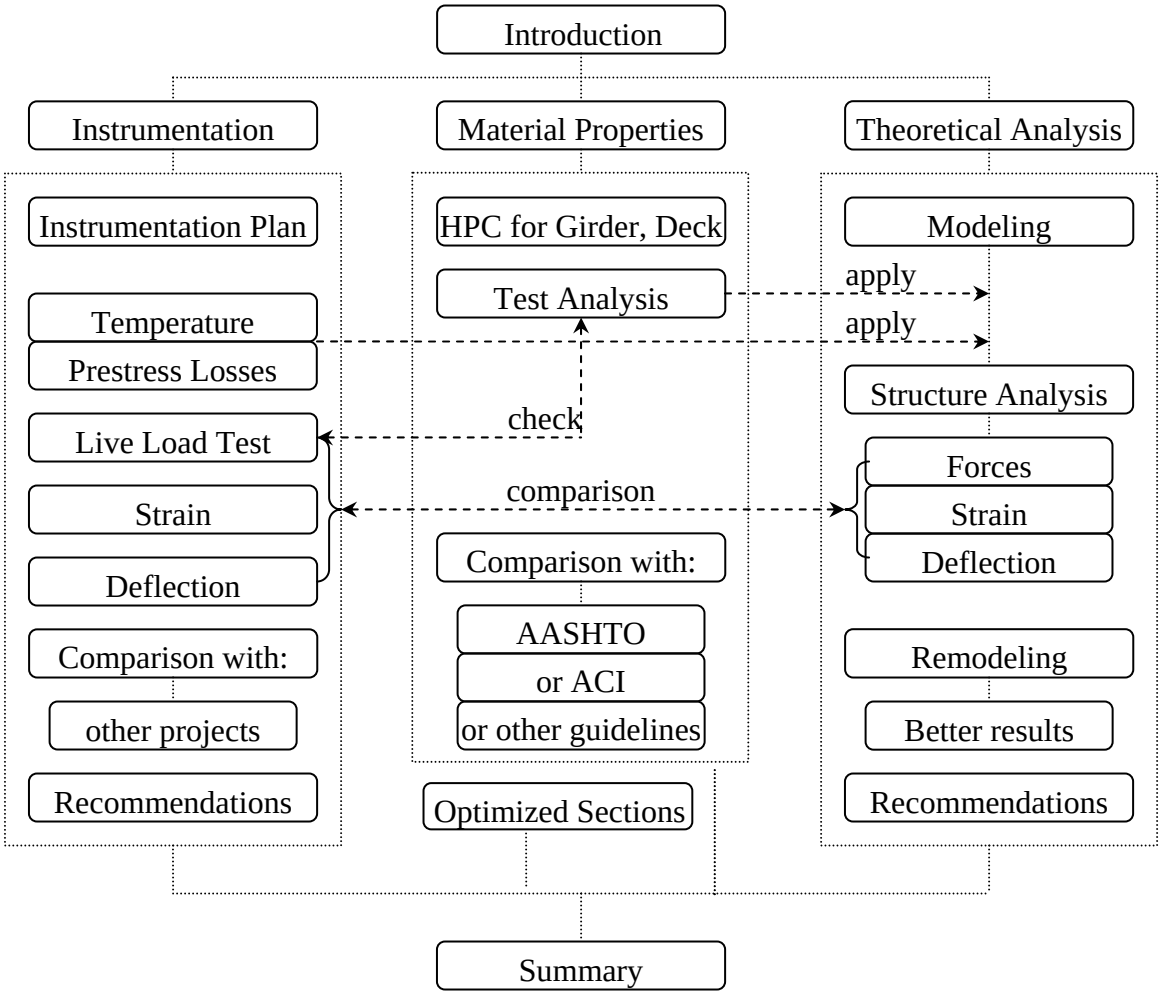

Figure 1.13. Flow Chart for the Project

In addition, a live load test was completed for the bridge to study the load distribution and structure behavior due to live load. Two simplified models were developed and compared with measured values to investigate the continuity level of the MoDOT interior bent detail. MoDOT girder cross sections were studied for cost

effectiveness by using high-strength concrete. The objectives were to identify the limitations of the sections relative to the use of high-strength concrete in simple span structures and to examine the feasibility of modified cross sections that can be used to take advantage of the higher strength concretes that are currently available. Construction for HPC Bridge related issues are documented to provide a reference for the construction of future HPC bridges. The summary, conclusions and recommendations were given for HPC highway bridges in Missouri and for general HPC structures in the United States considering design, fabrication, construction and the research conducted herein.

1.5. ORGANIZATION OF THE REPORT

An introduction related to research conducted on HPC and HPC bridges is summarized including previous project details. Section 2 lists the material testing program for both the prestressed girders and the CIP deck. Section 3 presents the instrumentation plans and procedures used. Section 4 discusses the results of the mechanical and material test program. Section 5, Section 6, Section 7, and Section 8 investigate the temperature, strain, prestress losses, camber and deflection behavior of the HPC bridge, respectively. Section 9 discusses construction and fabrication concerns for this bridge project. A static live load test is presented in Section 10. Optimized MoDOT cross sections are studied and presented in Section 11. Finally, the summary, conclusions and recommendations were given for HPC highway bridges in Missouri and for general HPC structures in the United States considering design, fabrication, construction and the research conducted herein in Section 12.

2. MATERIAL TESTING PROGRAM

2.1. INTRODUCTION

For HPC, empirical equations are generally used for the calculation of mechanical or material properties. For HPC with high compressive strength, current empirical equations developed for conventional strength concrete generally do not predict accurate mechanical properties. Accurate mechanical and material properties are critically important to predict the actual behavior of HPC bridges.

For the HPC used in both precast prestress girders and cast-in-place deck, mechanical and material tests were completed to obtain accurate HPC properties that could be used throughout later stages of the study to predict the behavior of the bridge.

In this Section, a mechanical and material testing program is listed including compressive strength, modulus of elasticity, splitting strength, ponding chloride concentration, rapid chloride ponding, freeze-thaw, de-icing scaling, creep, shrinkage, and coefficient of thermal expansion tests.

2.1.1. Member Cast. Precast girders were fabricated at Egyptian Concrete Company, Inc., which is located in Bonne Terre, MO. The deck was cast-in-place (CIP). The mix design constituents were materials that were commercially available in Missouri to produce a cost effect mix design.

All precast prestress girders specimens were fabricated in a single bed in a series of casting dates. In total, 5 casting dates were performed to produce all 20 girders as shown in Table 2.1. Several different curing conditions were studied. The CIP deck was cast from the east side to the west side of the bridge after erection of girders at the site.

The specimens were also cast right beside the deck. The QC/QA specimens that were cast for mechanical and material characterization are illustrated in Figures 2.1 and 2.2.

Table 2.1 Bridge Construction Date

Pour #	Date	Time	Girders Were Cast
Girder Pour 1	6/6/2001	6:30am-9:00am	Cast B41, B42, B43, B44
Girder Pour 2	6/13/2001	6:30am-9:00am	Cast B21*, B22*, B31, B32
Girder Pour 3	6/20/2001	6:30am-9:00am	Cast B23*, B24*, B33, B34
Girder Pour 4	6/26/2001	6:30am-9:00am	Cast B51, B52, B53, B54
Girder Pour 5	7/3/2001	6:30am-9:00am	Cast B11, B12, B13*, B14*
Deck Pour	9/11-9/12, 2001	6:30pm-5:00am	Cast CIP deck
* Girders which are instrumented			

Figure 2.1. Specimens Cast at Precast Plant

Figure 2.2. Specimens Cast at Bridge Jobsite

2.1.2. Mix Design. The mix design for precast prestress girders and CIP deck are listed in Tables 2.2 and 2.3. The provisions that MoDOT specified for the mix design were different than those usually used for a prestressed concrete girder using Normal Strength Concrete (NSC). Some of the special provisions are summarized in the aforementioned tables.

2.1.3. Curing Conditions. Curing conditions play a very important role in the material and mechanical property development. Several different curing conditions were considered and studied for the HPC material properties and mechanical property development.

2.1.3.1 Precast concrete. The following curing conditions were investigated for the precast concrete.

ASTM Moist Cured: In ASTM moist cured condition, the specimens were kept in a 21.1 °C (70 °F) room for approximately 24 hours after casting at which time they were demolded and cured in a moist-curing room (see Figure 2.3) until testing. The moist-curing room had a temperature of 21.1 °C (70 °F) and a humidity of 100%. This group of specimens was cured according to ASTM C31/31M-95 specification and was intended to serve as the control group.

Member Cured: In this condition, the specimens were kept along the bed of the precast girders until the forms for the member were stripped (see Figure 2.4). After releasing the prestressing strands for the precast member, the specimens were stored in an ambient condition adjacent to the precast member until testing. The member cured specimens were intended to be representative of the concrete in the member by curing at a similar temperature profile as the concrete in the member.

Table 2.2. Mix Designs for Precast Prestress Girders

		Cast 1	Cast 2	Cast 3	Cast 4	Cast 5
Casting data		**6/6/2001**	**6/13/2001**	**6/20/2001**	**6/26/2001**	**7/3/2001**
Mix Proportions						
Coarse Aggregate,	Type	Iron MT Trap Rock	Iron MT Trap Rock	Iron MT Trap Rock	Iron MT Trap Rock	Iron MT Trap Rock
	Quantity lbs/cy	2000	1993	1987	2000	2013
Fine aggregate,	Type	Missippi river sand CL-A	Missippi river sand CL-A	Missippi river sand CL-A	Missippi river sand CL-A	Missippi river sand CL-A
	Quantity lbs/cy	927	933	927	933	927
Water	Type	City of Bonne Terre	City of Bonne Terre	City of Bonne Terre	City of Bonne Terre	City of Bonne Terre
	Quantity lbs/cy	225	225	225	225	225
Cement	Type	River Cement-- Type I	River Cement-- Type I	River Cement-- Type I	River Cement-- Type I	River Cement-- Type I
	Quantity lbs/cy	850	853	850	852	848
Silica Fume	Type	Force 10000	Force 10000	Force 10000	Force 10000	Force 10000
W.R.Grace, microsilica	Quantity lbs/cy	50	50	50	50	50
Retarder	Type	Daratard 17	Daratard 17	Daratard 17	Daratard 17	Daratard 17
W.R.Grace, ASTM C-494 Type D	Quantity fl.oz/cy					
HRWR	Type	Adva Cast	Adva Cast	Adva Cast	Adva Cast	Adva Cast
W.R.Grace, ASTM C-494 Type F	Quantity fl.oz/cy	90	90	90	90	90
Air Entrainment	Type	Daravair 1400	Daravair 1400	Daravair 1400	Daravair 1400	Daravair 1400
W.R.Grace, ASTM C-260	Quantity fl.oz/cy	49	51	51	51	51
Fresh Concrete Properties						
W/Cm (C+FA)		0.25	0.25	0.25	0.25	0.25
slump in.		8	8	8	7.75 - 8	8
Air content %		5.1 - 6.7	4.5 - 5.9	5.5 - 6.5	5.0 - 6.9	6.3 - 6.7
Temperature °F	Ambient	69	74	74	64	66
Temperature °F	Concrete	74 - 82	77 – 80	77 - 81	73 - 79	76 - 82

Table 2.3. Mix Designs for the Cast-in-place Deck

		Trial Mix 1	**Trial Mix 2**	**Deck cast Mix 1**	**Deck cast Mix 2**
Casting data		4/23/2001	7/12/2001	9/11/2001	9/11/2001
Mix Proportions					
Coarse Aggregate,	Type	Grad D porphyry for PCCP and Masonry			
	Quantity lbs/cy	1687	1687	1684	1684
Fine aggregate,	Type	Class A Natural Sand	Class A Natural Sand	Class A Natural Sand	Class A Natural Sand
	Quantity lbs/cy	1086	1086	1078	1078
Water	Type				
	Quantity lbs/cy	289	289	290	262
Cement	Type	Type I	Type I	Type I	Type I
	Quantity lbs/cy	543	558	558	558
Fly Ash	Type	class "C" Fly Ash	class "C" Fly Ash	class "C" Fly Ash	class "C" Fly Ash
	Quantity lbs/cy	138	105	105	105
Microsilica	Type	Microsilica	Microsilica	Microsilica	Microsilica
	Quantity lbs/cy	43	43	42	42
Retarder (pozzolith 300 M master Builder)	Type	300 R	300 R	300 R	300 R
	Quantity oz/cy	3	3	20	32
Air Entrainment MB AE 90 Master Builders	Type				
	Quantity oz/cy	18	18	6	6.5
HRWR Rheobuild 1000 Master Builders	Type				
	Quantity oz/cy	25	25	25	25
Fresh Concrete Properties					
W/Cm (C+FA)		0.40	0.41	0.41	0.37
slump in.		8	2.5	5.2	5.2
Air content %		6.2	5.6	6.5	5.4
Temperature °F	Ambient	72	69	NA	58
Temperature °F	Concrete	74	81	NA	82

Figure 2.3. ASTM Moist Curing Room

Figure 2.4. Member-Cured Specimens

Match Cured: By curing cylinders at the exact temperature profile in the member, match cured specimens were selected to more precisely simulate the actual concrete in various locations of the member. The match curing system and match-cured specimens are shown in Figure 2.5. These specimens were cured in steel match curing molds at the exact temperature profile until release of the strands. Representative cylinders were tested for properties at transfer and others were stored in an ambient condition for later-age property evaluation.

2.1.3.2 Cast-in-place concrete. The following curing conditions were investigated for the CIP concrete.

ASTM Moist Cured: Under ASTM moist cured condition, the specimens were kept in a 21.1 °C (70 °F) room for approximately 24 hours after casting at which time they were demolded and cured in a moist-curing room (see Figure 2.3) until testing. This group of specimens was cured according to ASTM C31/31M-95 specification and was intended to serve as the control group.

Figure 2.5. Match Curing System and Specimens

Field Cured: In this condition, the specimens were kept along the CIP deck until testing (see Figure 2.6). The specimens were intended to be representative of the concrete in the member by curing at a similar temperature profile as the concrete in the member.

Figure 2.6. Member-Cured Specimens for CIP Deck

2.1.4. Overview of the Testing Program. Table 2.4 listed the material testing for the precast girders and CIP deck.

Table 2.4. Summary of Material Testing Program

HPC Girders	HPC CIP Deck
C, E, T	C, E, T
PC, RP, FT, DI, AB	PC, RP, FT, DI, AB
CR, SH, CTE	CR, SH, CTE
C - Compressive Strength E – Elastic Modulus T – Tensile Strength PC – Chloride Ponding RP – Rapid Chloride FT – Freeze-Thaw DI – De-icing Scaling CTE – Coefficient of Thermal Expansion CR – Creep SH – Shrinkage AB – Abrasion Resistance	

2.2. COMPRESSIVE STRENGTH

The compressive strength tests were performed in accordance with ASTM C39-94 "Standard Test Method for Compressive Strength of Cylindrical Concrete Specimens." The cylinder specimens used were 100 mm (4 in.) diameter by 200 mm (8 in.) high.

The compressive strength at transfer was tested at Egyptian Concrete Company in Bonne Terre, MO immediately before releasing the prestress strands (see Figure 2.7). The machine used there was hydraulically operated compression test machine. All of the later-age compressive strength cylinders were tested in the Butler-Carlton Civil Engineering Materials Load Frame Laboratory at University of Missouri-Rolla (see Figure 2.8). The machine used at UMR was a 5338 kN (1200 kips) Forney compression machine. The specimens were loaded at a rate of 241 ± 103 kPa per second (35 ± 15 psi per second), which means 440 ± 188 lb/s loading. Neoprene pads inserted in steel retaining caps were used in lieu of sulfur mortar caps. For HSC neoprene pads had a

manufacturer stated minimum hardness of 70 durameter. Table 2.5 summarizes the specimens that were cast and tested for compressive strength and elastic modulus tests.

Figure 2.7. Compressive Strength and Elastic Modulus Test at Egyptian Concrete

Figure 2.8. Compressive Strength and Elastic Modulus Test at UMR

Table 2.5. Specimens Compressive Strength and Elastic Modulus

HPC GIRDER (PER CAST DATE)			CIP DECK	
Moist Cured	Member Cured	Match Cured	Moist Cured	Member Cured
Release 28 days 56 days Erection Slab Cast Completion* 1 year 2 years	Release 28 days 56 days Erection Slab Cast Completion* 1 year 2 years	Release 56 days (Using match curing system)	3 days 28 days 56 days Completion* 1 year 2 years	3 days 28 days 56 days Completion* 1 year 2 years
24 Cylinders	24 Cylinders	12 Cylinders	18 Cylinders	18 Cylinders
Girders: 60 cylinders/pour; Deck: 36 cylinders. Total specimens: 276 cylinders				
The specimens for girders are for instrumented girder pouring date, i.e., Pour 2, Pour 4, Pour 5. For the other pouring date, specimens were only cast for release, 3 days, 7 days, 14 days, 28 days and 56 days. Completion* - Bridge Completion, right before open to traffic.				

2.3. MODULUS OF ELASTICITY

Modulus of Elasticity (MOE) is a very important mechanical property of concrete since it affects the serviceability and performance of RC/PC structures. Major factors affecting MOE are aggregate stiffness, shape, size and quantity, cement paste and method of determining modulus.

Modulus of elasticity tests were performed in accordance with ASTM C469-94 “Standard Test Method for Static Modulus of Elasticity and Poisson’s Ratio of Concrete in Compression.” The cylindrical specimens used were also 100 mm (4 in.) diameter by 200 mm (8 in.). A loading at a rate of 241 ± 103 kPa/s (35 ± 15 psi/s) was used identical

to the compression testing. The compressive strength f_{c1} was recorded when deformation reached Δ_1 = 0.0005 in and 0.4 f'_c namely deformation Δ_2. The modulus of elasticity was the calculated as (0.4 f'_c - f_{c1}) * h / (Δ_2 - Δ_1).

2.4. SPLITTING TENSILE STRENGTH

The splitting tensile strength tests were performed in accordance with ASTM C496-96 “Splitting Tensile Strength of Cylindrical Concrete Specimens.” The specimens used were 100 mm (4 in.) diameter by 200 mm (8 in.) high cylinders. The tests were done at UMR in the Engineering Research Laboratory (ERL) Structural Engineering Laboratory with a hydraulically operated Tinius-Olsen testing machine as shown in Figure 2.9. The specimens were loaded at a continuous rate of 517 ± 103 kPa per minute (75 ± 15 psi per minute) until failure. Table 2.6 shows the specimens that were cast and tested for splitting tensile strength.

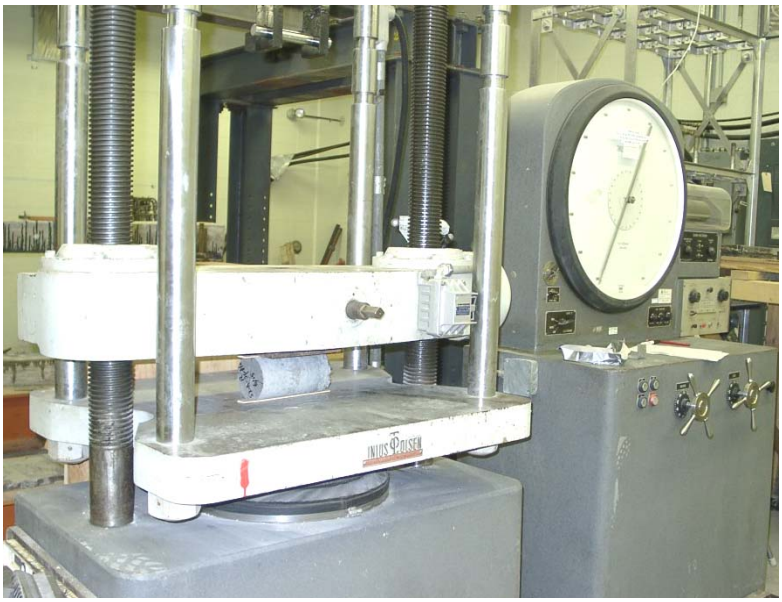

Figure 2.9. Splitting Tensile Strength

Table 2.6. Specimen for Splitting Tests

HPC GIRDER (PER CAST DATE)		CIP DECK	
Moist Cured	Member Cured	Moist Cured	Member Cured
Release 28 days 56 days Erection Slab Cast Completion* 1 year 2 years	Release 28 days 56 days Erection Slab Cast Completion* 1 year 2 years	3 days 28 days 56 days	3 days 28 days 56 days
16 Cylinders	16 Cylinders	6 Cylinders	6 Cylinders
Pour 5: 60 cylinders; Pour 2, Pour 3: 12 cylinders/pour; Deck: 12 cylinders. Total: 96 cylinders			
The specimens for girders listed are for Pour 5. For the other pouring date, specimens were only cast for release date and 56 days. Completion* - Bridge Completion, right before open to traffic.			

2.5. CREEP

Creep is defined as continued deformation under a constant stress. It also affects serviceability and performance of RC/PC structures. Mix composition, curing condition, loading conditions, member geometry, service exposure conditions and amount of reinforcing are major factors affecting creep.

ASTM C512 test procedure was followed with a few basic modifications. A single long specimen, 100 × 600 mm (4 × 24 in.) cylinder, was used in lieu of stacking multiple short specimens, such as three 100 × 200 mm (4 × 8 in.) cylinders with one exception. For the deck, the long cylinders cast for creep (C), shrinkage (S) and coefficient of thermal expansion (T) were damaged during transportation to UMR due to

a vehicular accident. Therefore, for deck concrete, three 100 × 200 mm (4 × 8 in.) cylinders were stacked as one creep specimen. The broken long specimen could still be used for shrinkage measurement. The length of these specimens allowed for the measurement of surface strains during the test using a DEMEC mechanical strain gauge with a 200 mm (8 in.) gauge length.

Four specimens were cast for HPC girder casting dates 4 and 5. Table 2.7 lists the curing regimes and tests investigated for the two casting dates. The shrinkage specimen cast to study effects under moist cured conditions did not yield results as the DEMEC points were not durable in the high moisture level.

Table 2.7. Specimens for C/S/T

	Pour 4	Pour 5	CIP Deck
Creep	S4-AC-Creep	S5-AC-Creep	SD-AC-Creep SD-MC-Creep
Shrinkage	S4-AC-Sh S4-AC-Sh/Th	S5-AC-Sh S5-AC-Sh/Th	S5-AC-Sh-1 S5-AC-Sh-6
CTE	S4-AC-Sh/Th	S5-AC-Sh/Th	
AC: air cured; MC: moist cured. CTE – Coefficient of Thermal Expansion.			

Precut segments of PVC pipe and 100 mm (4 in.) plastic caps were used to form the specimens. Concrete was placed in 100 to 150 mm (4 to 6 in.) layers and each layer was rodded 25 times. A set of C/S/T specimens is shown in Figure 2.10.

Specimens were capped to prevent moisture loss and were stored alongside the structure for 8 to 16 hours and then they were shipped to the laboratory in UMR.

About 24 hours after casting of the specimens, the PVC molds were removed and DEMEC points were fixed to the surface using quick-set epoxy gel. The arrangement of the points and the specimens are shown in Figure 2.10.

The creep specimens were then sulfur capped to ensure smooth ends for the loading frame. And the DEMEC points allowed setting overnight.

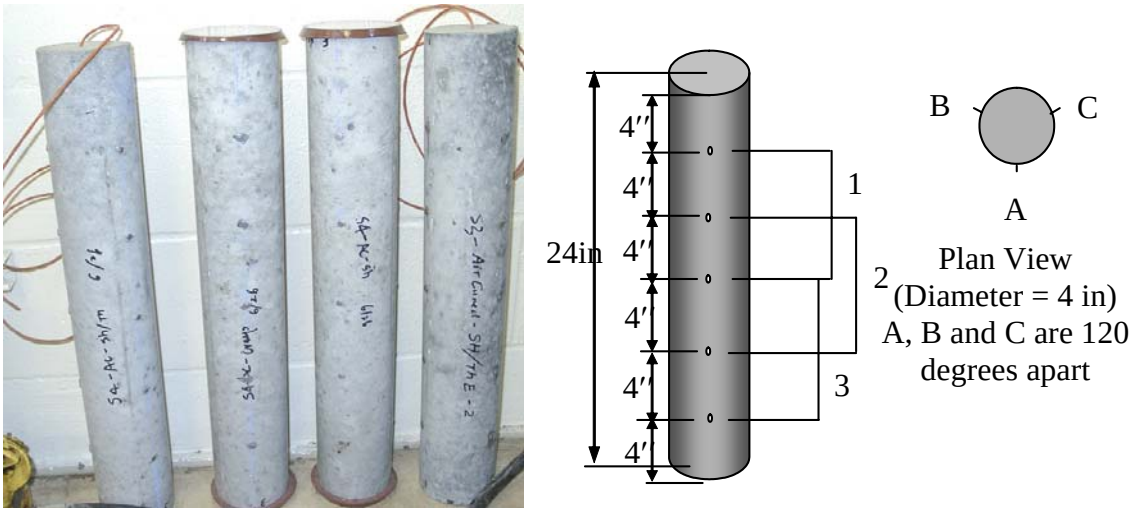

Figure 2.10. C/S/T Specimens and DEMEC Points Arrangement

The loading frames for the creep test are shown in Figure 2.11. They were constructed in accordance with the creep test specification of ASTM. The principle of the design is to apply a constant load to a stack of cylinders between two steel plates by applying pressure with a pump beneath the lower plate and then locking in the load.

Four sets of coil springs were used for each creep rig to maintain a constant load as the specimens shortened. The springs had a maximum compression of 50 mm (2 in.) with an approximate stiffness of 1.612 kN/mm (9.205 k/in.). The springs had an inside diameter of 108 mm (4.25 in.) and an outside diameter of 178 mm (7.0 in.). Thus, the

total stiffness of the four set of springs was 6.448 kN/mm (36.82 k/in.). The rig was designed to support another set of spring so that capacity of the frame could support higher strength concrete at a future time.

A jack and a load cell were used to stress the creep rigs (as shown in Figure 2.12). When the correct load was reached, the nuts below the bottom plate were tightened. The specimens for the HPC girder mix were loaded 2 days after casting to 40% of nominal design compressive strength of the mix. For the cast-in-place specimens, one was air cured in the testing room and the other was moist cured prior to be loaded at 28 days.

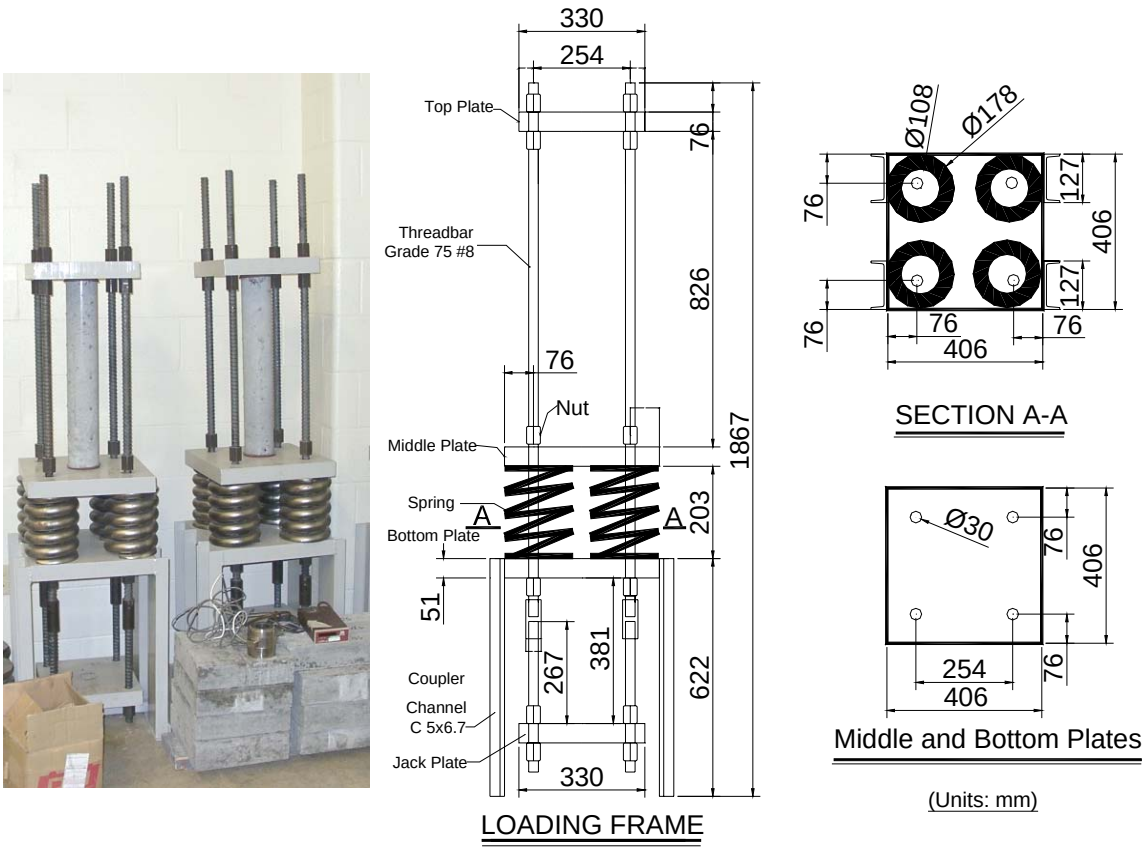

Figure 2.11. Creep Loading Frame and Specimens

Figure 2.12. Creep Loading Frames and Specimens

The applied load for each specimen was maintained throughout the tests using test frames. The loss of load with time, due to the shortening of the specimens and consequential elongation of the springs could be determined by monitoring the spring elongation since the stiffness of the springs was known. When 2% of the initial load was lost, the load was reapplied using the pump and ram.

Readings were taken every day for the first week after loaded, every few days for the first 28 days and every few weeks thereafter.

2.6. SHRINKAGE

Shrinkage is broadly defined as the decrease in volume of a concrete element when it loses moisture by evaporation. The major factors affecting drying shrinkage are curing conditions, member size, member shape, amount of reinforcing, temperature, and mix composition including aggregate type, w/cm ratio, and admixtures.

The shrinkage test was performed in accordance with ASTM C157 “Test Method for Length Change of Hardened Hydraulic-Cement Mortar and Concrete.” Readings were taken every day for the first week after molds were removed, every few days for the first 28 days and every few weeks thereafter. Shrinkage specimens were kept in a controlled environment. Relative humidity was found to average 55%. The room temperature was kept at 21.1 °C (70 °F).

For each specimen at each measurement interval, the average of the nine individual gauge readings was computed to determine the total strain on the specimen.

2.7. COEFFICIENT OF THERMAL EXPANSION

The coefficient of thermal expansion of concrete is a function of the coefficients of both the aggregate and paste. However, because aggregates generally make up the bulk of the concrete mix, the coefficient of thermal expansion of concrete is most influenced by the coefficient of the aggregate, as well as the quantity of aggregate in the mix.

The coefficient of thermal expansion test was performed in accordance with ASTM C 490 with some modifications. Coefficient of thermal expansion was measured on 5 specimens for the HPC girder concrete. Specimens were of the same dimension as for the creep and shrinkage tests. Cylinder molds were stripped approximately 24 hours after casting, and then were air cured in the lab. DEMEC mechanical strain gauge points were attached to the surface of each specimen as for creep and shrinkage. Cylinders were then pre-cycled to ensure that the specimens had reached the extreme test temperatures at least once prior to actual testing. During testing, specimens were cycled between extreme temperatures of 4.4 °C (40 °F) and 48.9 °C (120 °F). Thermocouples placed in the center

of the specimens during casting were used to determine when the specimens had stabilized at the extreme temperature. A standard environmental chamber in UMR (as illustrated in Figure 2.13) was used to control temperature and relative humidity during each test cycle.

A set of DEMEC strain gauge readings was recorded during a cycle after specimens stabilized at the extreme temperatures. The internal specimen temperatures were also recorded at the time of each strain measurement. The coefficient of thermal expansion was then determined for each specimen cycle by dividing the change in strain by the change in temperature over the cycle.

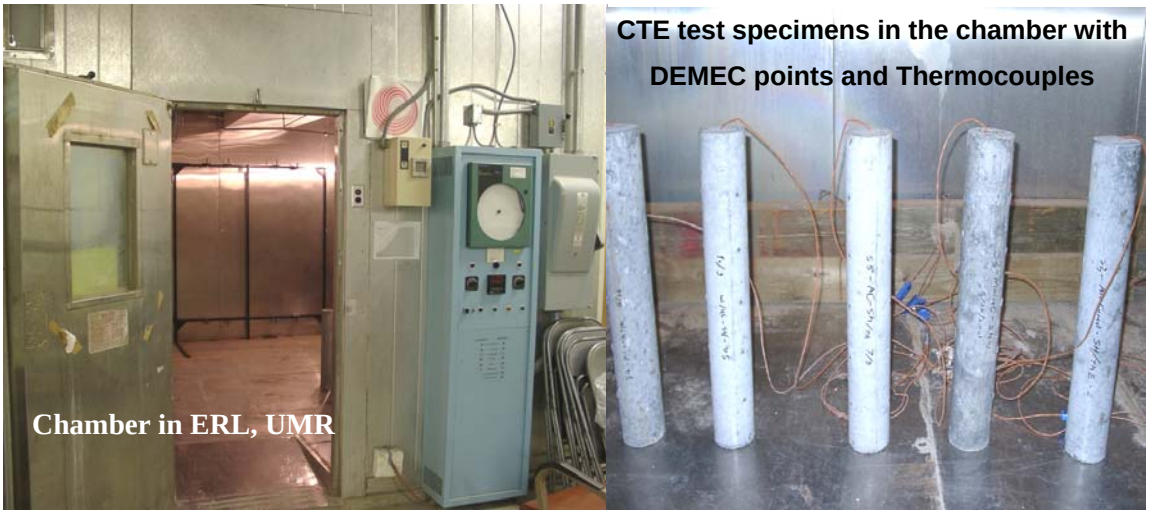

Figure 2.13. Coefficient of Thermal Expansion (CTE) Test at UMR

2.8. FREEZE–THAW DURABILITY

The resistance to freezing and thawing of the concrete was performed in accordance with ASTM C666 “Standard Test Method for Resistance of Concrete to Rapid Freezing and Thawing.” Three 76 mm × 76 mm × 406 mm (3 in. × 3 in. × 16 in.)

specimens were cast for each pour in which freeze-thaw resistance was to be determined as shown in Figure 2.14. Concrete was placed and vibrated in two layers. The blocks were demolded at 24 hours. Weight measurements were made at every 20 cycles until 300 cycles. The final freeze-thaw resistance values were obtained in terms of mass losses. The tests were done in the Butler-Carlton Civil Engineering Material Laboratory at UMR as shown in Figure 2.15. Table 2.8 summarizes the specimens that were cast and tested for freeze-thaw tests. Totally, there were nine specimens, three for each concrete casting date.

Figure 2.14. F-T Test Specimens

Figure 2.15. F-T Test Machine

Table 2.8. Specimens for Freeze-Thaw

	Pour 3	Pour 5	CIP DECK
Numbering	S3-FT-1 S3-FT-2 S3-FT-3	S5-FT-1 S5-FT-2 S5-FT-3	SD-FT-1 SD-FT-2 SD-FT-3
FT: freeze-thaw. SD is also called CIP somewhere.			

2.9. RAPID CHLORIDE PERMEABILITY

The rapid chloride permeability testing of the concrete was performed in accordance with AASHTO T277 “Standard Method of Test for Rapid Determination of the Chloride Permeability of Concrete.” Two 100 mm × 200 mm (4 in. × 8 in.) cylinders were cast for each pour in which rapid chloride permeability was to be determined. The cylinders were demolded at 24 hours. For HPC girder concrete one was moist cured and the other was member cured for 56 days equivalent to the design strength time requirements. For the CIP deck concrete, one cylinder was moist cured and the other was field cured for 28 days equivalent to the design strength time requirements. The tests were performed by the MoDOT Research Development & Technology materials laboratory in Jefferson City, MO. Table 2.9 summarizes the specimens that were cast and tested for rapid chloride permeability tests.

Table 2.9. Specimens for Rapid Chloride Permeability

	Pour 3	Pour 5	CIP DECK
Numbering	S3- RP -1 S3- RP -2	S5- RP -1 S5- RP -2	SD- RP -1 SD- RP -2
RP: rapid chloride.			

2.10. CHLORIDE PONDING

The chloride ponding test for the concrete was performed in accordance with AASHTO T259 “Resistance of Concrete to Chloride Ion Penetration.” Three 305 mm × 305 mm × 89 mm (12 in. × 12 in. × 3.5 in.) specimens were cast for each pour in which chloride resistance was to be determined as shown in Figure 2.16. Concrete was placed and vibrated in two layers. The blocks were demolded at 24 hours. Table 2.10 summarizes the specimens that were cast and tested for chloride ponding tests.

After 14 days moist curing, the specimens were air cured until ponded. The ponding block’s surface was cleaned of loose particles and roughened using a wire brush to remove loose surface concrete. Then the blocks were ponded with 7.5% NaCl solution in the constant temperature lab for 90 days.

Figure 2.16. Ponding Chloride Test Specimens

Table 2.10. Specimens for Chloride Ponding

	Pour 3	Pour 5	CIP DECK
Numbering	S3- PC -1 S3- PC -2 S3- PC -3	S5- PC -1 S5- PC -2 S5- PC -3	SD- PC -1 SD- PC -2 SD- PC -3
PC: chloride ponding.			

Concrete powder samples for were sampled using a hammer drill by drilling 5 holes to various depths as follows: 1.65 to 12.7 mm (0.065 to 0.5 in.), 12.7 to 25.4 mm (0.5 to 1.0 in.) and 25.4 to 38.1 mm (1.0 to 1.5 in.). The powered samples from each depth range was mixed and then weighed 3.0 gram (0.1058 oz.) as a sample. The sample was dissolved in the extraction liquid. A CL-2000 chloride test system, manufactured by James Instruments Inc., was used to measure the percentage by weight of chloride penetrated in concrete as shown in Figure 2.17.

Figure 2.17. Ponding Chloride Test

2.11. SCALING RESISTANCE

The scaling resistance test was performed in accordance with ASTM C672 “Standard Test Method for Scaling Resistance of Concrete Surfaces Expose to Deicing Chemicals.” Two 305 mm × 152 mm × 76 mm (12 in. × 6 in. × 3 in.) specimens were cast for each pour in which scaling resistance was to be determined as shown in Figure 2.18. Concrete was placed and vibrated in two layers. The blocks were demolded at 24 hours. The tests were performed by the MoDOT Research Development & Technology

materials laboratory in Jefferson City, MO. Table 2.11 summarizes the specimens that were cast and tested for scaling resistance tests.

Figure 2.18. Scaling Resistance Test Specimen

Table 2.11. Specimens for Scaling Resistance

	Pour 3	Pour 5	CIP DECK
Numbering	S3- DI -1 S3- DI -2	S5- DI -1 S5- DI -2	SD- DI -1 SD- DI -2
DI: scaling de-icing.			

2.12. ABRASION RESISTANCE

The abrasion resistance test was performed in accordance with ASTM C944 "Standard Test Method for Abrasion Resistance of Concrete or Mortar Surfaces by the Rotating Cutter Method." Three 305 mm × 305 mm × 76 mm (12 in. × 12 in. × 3 in.) specimens were cast for each pour. Concrete was placed and vibrated in two layers. The blocks were demolded at 24 hours. The tests were conducted at UMR in the ERL

Structural Engineering Laboratory as shown in Figure 2.19 and Figure 2.20. Table 2.12 summarizes the specimens for abrasion resistance tests.

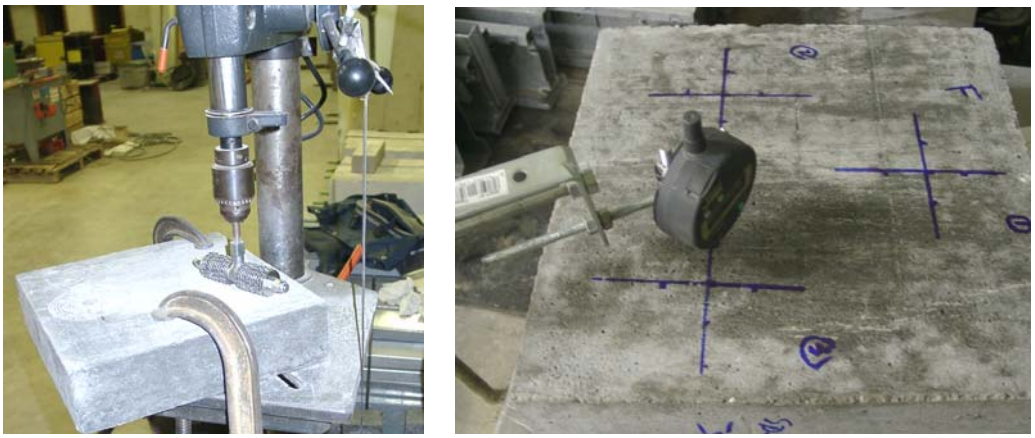

Figure 2.19. Abrasion Test Set-Up

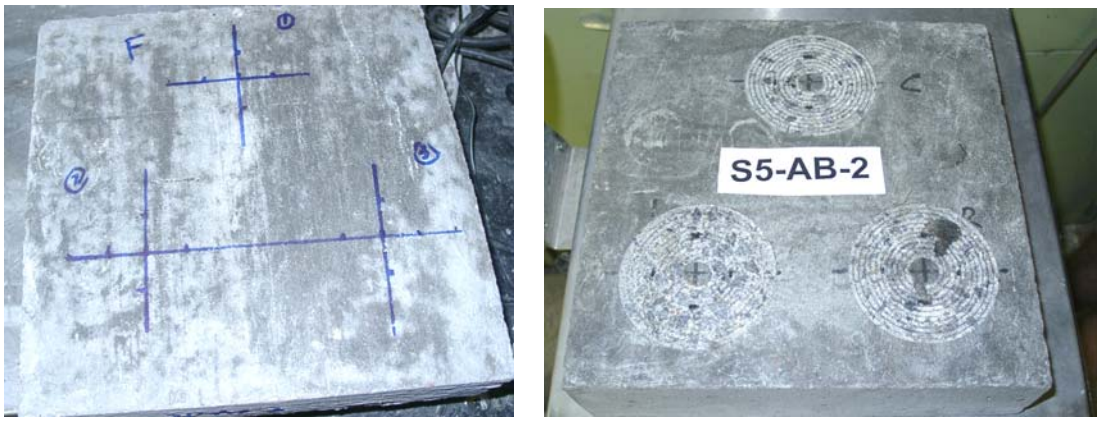

Figure 2.20. Abrasion Test Specimen Before and After Test

Table 2.12. Specimens for Abrasion Resistance

	Pour 3	Pour 5	CIP DECK
Numbering	S3- AB -1 S3- AB -2 S3- AB -3	S5- AB -1 S5- AB -2 S5- AB -3	SD- AB -1 SD- AB -2 SD- AB -3
AB: abrasion resistance.			

2.13. SUMMARY OF MATERIAL TESTING PROGRAM

In this Section, a material testing program for the HPC used in this project is presented including compressive strength, modulus of elasticity, splitting strength, ponding chloride concentration, rapid chloride ponding, freeze-thaw, de-icing scaling, creep, shrinkage, and coefficient of thermal expansion tests. The test program is summarized in Tables 2.13 and 2.14.

Table 2.13. Summary of Material Testing Program

Time	HPC Girders					CIP Deck
	Pour 1	Pour 2	Pour 3	Pour 4	Pour 5	
Release	C, E	C, E, T	C, E	C, E, T	C, E, T	
3 Days	C, E		C, E			C, E, T
7 Days	C, E		C, E			
14 Days	C, E		C, E			
28 Days	C, E	C, E	C, E	C, E	C, E, T	C, E, T
56 Days	C, E	C, E, T	C, E	C, E, T	C, E, T	C, E, T
Girder Erection		C, E		C, E	C, E, T	
Slab Casting		C, E		C, E	C, E, T	
Bridge Completion		C, E		C, E	C, E, T	C, E
1 Year		C, E		C, E	C, E, T	C, E
2 Years		C, E		C, E	C, E, T	C, E
Additional			CP RP FT DI AB	CTE	CTE CP RP FT DI AB	CTE CP RP FT DI AB
Continuous				CR SH	CR SH	CR SH

C - Compressive Strength E – Elastic Modulus T – Tensile Strength

CP – Chloride Ponding RP – Rapid Chloride FT – Freeze-Thaw

DI – De-icing Scaling CTE – Coefficient of Thermal Expansion

CR – Creep SH – Shrinkage AB – Abrasion Resistance

Table 2.14. Summary of Material Testing Program

Tests	Test Method	Specimens	Curing Conditions	
			HPC Girders	HPC CIP Deck
Compressive Strength	ASTM C39	4"×8" cylinder	Member Curing Moist Curing Match Curing	Field Curing Moist Curing Match Curing
Modulus of Elasticity	ASTM C469			
Splitting Tensile Strength	ASTM C496	4"×8" cylinder	Member Curing Moist Curing	Field Curing Moist Curing
Rapid Chloride Ion Penetration	AASHTO T277 ASTM C1202			
Creep	ASTM C512	4"×24" cylinder	24 hours demold and then lab cured	24 hours demold and then lab cured
Shrinkage	ASTM C157			
Coefficient of Thermal Expansion	ASTM C490			
Ponding Chloride Ion	AASHTO T259	12"×12"×3.5" block	Moist curing for 14 days and then air dry for required days	Moist curing for 14 days and then air dry for required days
Freeze-Thaw Resistance	ASTM C666	3"×3"×16" block		
Abrasion Resistance	ASTM C944	12"×12"×3" block		
Scaling Resistance	ASTM C672	12"×6"×3" block		

3. INSTRUMENTATION PLANS AND PROCEDURES

3.1. INTRODUCTION

In Section 3, a brief overview of the types of measurements, gauges, and other instrumentation systems is presented. The data acquisition system used for collecting data is also discussed. Then the preparation and installation of gauges are discussed. Finally a summary of problems encountered is presented. This should serve as a record for future monitoring projects on items that can occur during field related projects.

An instrumentation program was developed to monitor components of the bridge superstructure during early-age and later-ages, identify trends in measured and observed behavior, examine applicability of current design procedures and assumptions for high performance concrete designs with 15.2 mm (0.6 in.) diameter prestressing strands and provide recommendations for design of future HPC bridges in Missouri with 15.2 mm (0.6 in.) diameter prestressing strands as warranted. The primary goals of the instrumentation plan may be summarized as follows:

1. Monitor deflections from transfer through service life and compare predicted and measured deflections;
2. Monitor stresses along spans due to prestressing, applied loads, and thermal effects;
3. Develop stress blocks (strain blocks) along depth of members near support and at mid-span;
4. Monitor thermal gradients at similar cross-sections, for both interior and exterior spans;
5. Evaluate distribution of loading between adjacent interior and exterior sections of the same span through a live load test after construction has been completed;

3.2. MEASUREMENT TYPES

There are three basic measurements for the instrumentation program: concrete temperatures, concrete strains, and camber or deflection of bridge girders as listed in Table 3.1.

Table 3.1. Types of Measurements

Measurement Type	Gauges and Instrumentation System	Data from Measurements
Concrete Strains	• Vibrating Wire Strain Gauges • Electrical Resistance Strain Gauges • Surface Mechanical Strain Gauges	• Girder Curvatures • Live load Response • Prestress Losses
Concrete Temperatures	• Thermocouples • Thermistors	• Thermal Gradients • Extreme Seasonal Bridge Temperatures • Hydration Temperatures • Corrections for Strain and Deflection Measurements
Girder Camber/ Deflection	• Tensioned-Wire System • Precise Surveying	• Elastic Responses to Prestress, Deck Loads, etc. • Time-Dependent Behavior due to Creep • Live load Response

3.2.1. Concrete Temperatures. Concrete temperatures were measured in selected prestressed girders and selected location in the cast-in-place deck. Two types of gauges were used for the temperature measurements. One was thermocouples. The other was thermistors which were integrally attached to the vibrating wire strain gauges (VWSG).

Hydration behavior of the concrete mixes was measured using thermocouples and thermistors. Thermocouples were embedded in various depths of the girders and deck to

obtain thermal gradients of the bridge. Maximum and minimum seasonal bridge deck temperatures were also determined from collected data. Temperature data was also used to correct for variations in strain and deflection measurements due to temperature effects. Hydration behavior of the concrete mixes was measured using thermocouples and thermistors during casting and at early-ages.

3.2.2. Concrete Strains. Concrete strains were also measured in selected prestressed girders and selected locations in the cast-in-place deck. Two main types of gauges were used for the strain measurements. Vibrating wire strain gauges and electrical resistance strain gauges were embedded in both girders and the deck. Surface concrete strain was measured using mechanical strain gauges (DEMEC) as a backup system.

The strain profile was determined with strain measurements at various locations through the depth of the girder sections. Elastic curvature changes and time-dependent curvature changes resulting from creep and shrinkage were moniotered using the measured concrete strains. The strain changes for the live load tests were also monitored.

3.2.3. Girder Camber/Deflection. Deflection behavior for several girders of the bridge was monitored throughout construction and service. Girder camber or deflection was recorded at release of prestress, storage at the prestressing plant, before erection at jobsite, casting of the bridge deck and some other intervals between these specific stages.

Two types of systems were used for girder camber or deflection measurement. Tensioned-wire method was developed in UMR and used before the girders were erected. Precise surveying method was used after the girder erection. The precise surveying method was also used for the live load test.

3.3. GAUGES AND MEASUREMENT SYSTEMS

The gauges used for the instrumentation were selected considering cost, reliability, accuracy, installation and compatibility with the data acquisition system.

3.3.1. Thermocouples. Thermocouples are very simple temperature measuring devices. The voltage drop is proportional to the temperatures using formulas or data tables developed for the specific combination of two metals. These wires are coupled simply by tightly twisting thermocouple wire. The length for twisting is about 13 to 25 mm (0.5 to 1.0 in.) as shown in Figure 3.1.

The thermocouple used in this project was produced by OMEGA, Inc. The model number is TT-T-20-TWSH. TT is for thermocouple grade PFA Teflon. T means type T (copper-constantan). 20 is for 20 AWG (American Wire Gauge), which refers to the conductor size that is 0.813 mm (0.032 in.). TWSH means twisted/shielded thermocouple. The temperature range is reported to be -267 – +260 °C (-450 – +500 °F) by the manufacturer. The accuracy of measurements was stated to be ± 1.0 °C (± 1.8 °F) for the thermocouple used (www.omega.com/pptst/TT-J-TWSH.html).

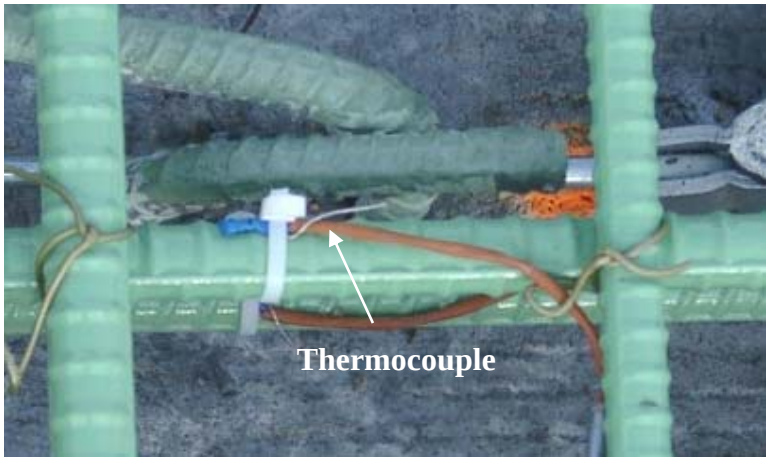

Figure 3.1. Thermocouple

3.3.2. Vibrating Wire Strain Gauges. A vibrating wire strain gauge (VWSG) designed for embedment in concrete measures strain caused by stress variations. The specific VWSG used was EM-5 manufactured by Roctest, Inc, as shown in Figure 3.2.

The EM-5 is composed of two end pieces joined by a tube that protects a length of steel wire. The wire is sealed in the tube by a set of o-rings on each end piece. Both end pieces have a flat circular flange to allow transfer of concrete deformation to the wire. An electromagnet is fitted at the center of the gauge. Strain developing in the concrete modifies the tension in the wire and its resonant frequency, which is read by the electromagnet. A thermistor incorporated into the EM measures the temperature of the specimen.

The EM-5 has an adjustable 3000 microstrain range with an accuracy of 1 microstrain. This is usable mircostrain limit of the EM-5 VWSG. The operating temperature range reported by manufacturer is -50 °C to +60 °C (-122 °F – +140 °F).

Specific cable length was provided for each gauge when it was ordered. The gauges with cable were attached to a rebar and then located to the specific location in the concrete.

Vibrating wire strain gauges are extremely durable and reliable for several years under field conditions, a primary reason why they were selected for this project. They also have the benefit of having an integrally attached thermistor for temperature measurement at the gauge location. Their only drawback is their expense, which is $76 each, higher compared to other types of gauges ($10 - $50) used for internal concrete strains measurement.

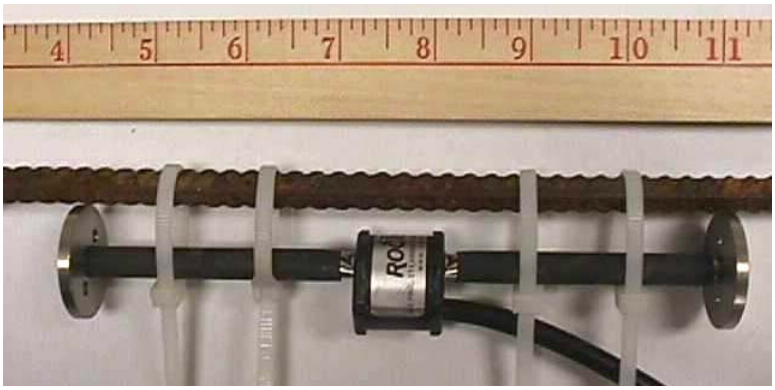

Figure 3.2. Vibrating Wire Strain Gauges

3.3.3. Electrical Resistance Strain Gauges. The specific electrical resistance strain gauge used was EGP-5-350. As listed in Figure 3.3, the gauge length is 100 mm (4 in.). The normal usage temperature range is -5 °C to +50 °C (-25 °F – +125 °F). The resistance is 350 ± 0.8% ohms.

The EGP-Series Embedment Strain Gauge is specially designed for measuring mechanical strains inside concrete structures. The sensing grid, constructed of a nickel-chromium alloy (similar to Karma), has an active gauge length of 100 mm (4 in.) for averaging strains in aggregate materials. A rugged 130 mm (5 in.) outer body of proprietary polymer concrete resists mechanical damage during pouring, minimizes reinforcement of the structure, and provides protection from moisture and corrosive attack. The grid, cast within the polymer concrete to ensure maximum strain sensitivity, is self-temperature-compensated to minimize thermal output when installed in concrete structures. Each gauge incorporates a heavy-duty 3 m (10 ft) cable with 22-AWG (0.643 mm diameter) leadwires; a three-wire construction to the sensing grid helps minimize temperature effects in the instrumentation leads.

Because the attached wire was only 3 m (10 ft), extension wire was needed. Belden 3 conductor unshielded circuit cable (No. 9493) was used as extension wire with the ERSG. The wire splice was waterproofed using a layer of nitrile rubber and a layer of electrical tape.

These gauges are not very durable or reliable for use in the field. Gross (1999) reported that only 50% of these ERSG gauges were functioning at 1 years. Measurement repeatability is difficult in the field because the resistance-based measurement is sensitive to the connection of lead wires to the data acquisition system. The preparation of these gauges is labor intensive.

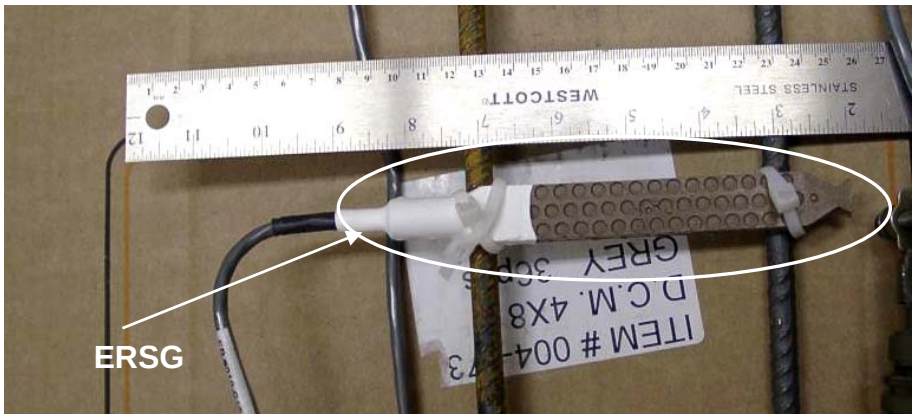

Figure 3.3. Electrical Resistance Strain Gauges

3.3.4. Demountable Mechanical Strain Gauge. The demountable mechanical strain gauge was developed at the Cement and Concrete Association to enable strain measurements to be made at different parts of a structure using a single instrument. The DEMEC consists of a standard or a digital dial gauge attached to an invar bar that supports the digital dial gauge as shown in Figure 3.4. A fixed conical point is mounted at one end of the bar, and a moving conical point is mounted on a knife edge pivot at the

opposite end. The pivoting movement of this second conical point is measured by the dial gauge.

Figure 3.4. DEMEC Strain Gauge and Discs

A setting out bar is used to position pre-drilled stainless steel discs which are attached to the structure using a suitable adhesive. Each time a reading has to be taken, the conical points of the gauge are inserted into the holes in the discs and the reading on the dial gauge noted. In this way, strain changes in the structure are converted into a change in the reading on the dial gauge.

The gauge has been designed so that only minor temperature corrections are required for changes in ambient temperature, and an Invar reference bar is provided for this purpose. The gauge and stainless steel target discs used were manufactured by Mastrad Inc. The gauge was 200 mm (8 in.) long. The discs were fixed to the concrete surface using a five-minute epoxy gel. Points were allowed to set for 10 to 20 minutes before a set of initial readings was performed.

The DEMEC system was not appropriate for long-term outdoor measurements especially when the girders were curing with water. The high humidity caused some discs, sometimes referred to as “DEMEC points” to debond. This issue is more related to the epoxy system that bonds the points. The accuracy of the system was reported to be approximately 16 microstrains. Important baseline readings must be taken when the girders were cooling quickly after form removal since the temperature changes affected the readings. The system was not used during later stages of the instrumentation program. However, the system was applicable for creep and shrinkage tests because the temperature and humility was stable in the lab [Temperature = ± 5°F (2.8°C), RH = ± 5%].

3.3.5. Loadcell for Prestress Losses. A loadcell was used for the prestress losses before the strands were released. As shown in Figure 3.5, a 444.8 kN (100 kips) loadcell was connected with data acquisition system for force monitoring. A same load cell was used for creep loading.

Figure 3.5. Load Cell for Prestress Losses

3.3.6. Tensioned-Wire Deflection Measuring System. The tensioned-wire system was used for all camber reading at the precast plant. As shown in Figure 3.6, it was a manual deflection measurement system. A precision scale was fixed at the mid-span of the girder. The system is simple and reliable. One person could perform the readings without assistance. The system used was based on the systems previously used at the University of Texas at Austin by Gross (1999).

Right after the molds were removed, a precision scale was fixed to mid-span of the girder as shown in Figure 3.7. Then anchor bolts were inserted into the concrete as illustrated in Figure 3.8. In the field, the system was set up as shown in Figures 3.9 through 3.11. The precision stainless steel scales had 0.25 mm (0.01 in.) divisions. Two small piece of aluminum plates were attached to the concrete using epoxy as the scale support. Then the scale was fixed to the plates vertically using quick set epoxy. Anchor bolts used were Hilti HSL M10/20. They were anchored into both ends for the tensioned-wire system. A hammer drill was used to drill holes for the inserts. Size #6 piano wire was used as the tensioned wire. The diameter of the piano wire is 0.41 mm (0.016 in.). A 15.06 kg (33.20 lb) weight was used to tension the piano wire. The dead weight was a steel cylinder with diameter of 127 mm (5 in.) and a height of 152.4 mm (6 in.).

A baseline reading was taken just before release of prestress with the assumption that the prestress bed was perfectly level. The later stages measurements can be compared to the baseline reading to determine the girder camber at that stage.

The wire often corroded during storage of the girders and thus was replaced periodically. The drawback of the system is it is entirely based on measurements relative

to the initial reading. If the scale becomes unbonded for any reason, the system will fail. Fortunately, this did not occur during this study.

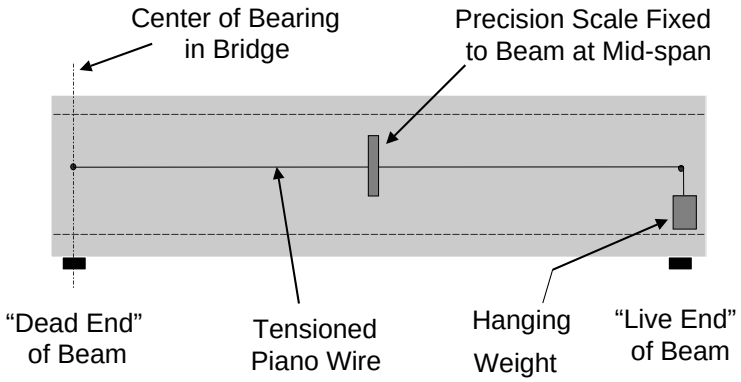

Figure 3.6. Tension-Wire System for Deflection

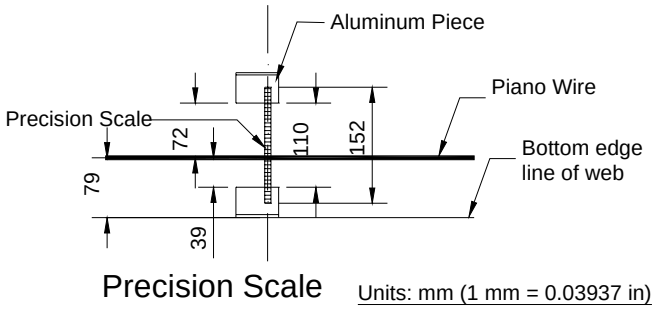

Figure 3.7. Precision Scale Details for Tension-Wire System

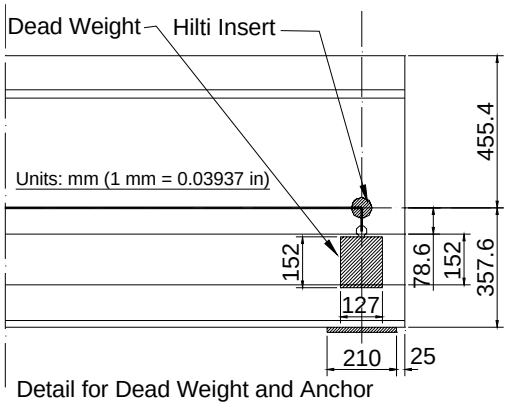

Figure 3.8. Dead Weight and Anchor Details for Tension-Wire System

Figure 3.9. Precision Scale for Tension-Wire System

Figure 3.10. Anchor for Tension-Wire System

Figure 3.11. Dead Weight for Tension-Wire System

3.3.7. Precise Surveying System. After erection of the girders at the jobsite, the tensioned wire system was no longer applicable due to the continuity and construction related issues with the bridge. A precise surveying system was now used for the later age deflection measurements. It is based on basic surveying principles. Some minor modifications were introduced to increase accuracy. As shown in the Figures 3.12 and 3.13, the system including a level, a tripod for the level, a sighting rod and several precision scales. The precision scales are attached to the rod to increase the number of measurement divisions.

Figure 3.12. Precision Surveying System for Deflection Monitoring before Deck Casting

A relative elevation method was used to make measurements of girder camber and deflection. The differences in elevation between a point at mid-span and points at each end of the girder were measured.

Before the decks were complete, the measurements were taken under the bridge. The points measured were marked at the bottom of the girders. After completion of the

decks, measurements were performed on the top surface of the bridge deck. The switch to the top surface eliminated the requirement for the dry embankment when taking measurements, although traffic control may be required for future periodic measurements.

The precise surveying system was inexpensive since the level and sighting rod can be borrowed from the Civil Engineering Department in UMR. The precise scales (less than $20 total) were the only equipment that was purchased. Because the system was not based on a baseline measurement, it can not fail unless the reference points (painted measurement marks on the deck surface) are removed.

Figure 3.13. Precision Surveying System for Deflection Monitoring after Deck Casting

3.4. DATA ACQUISITION

3.4.1. Data Acquisition System. A data acquisition system (DAS) was custom-built by the researchers at University of Missouri-Rolla (UMR). The system was selected to function with a number of gauges used in the instrumentation plan including thermocouples, vibrating wire strain gauges and resistance strain gauges. The specific components used for the DAS were supplied by Campbell Scientific, Inc.

The DAS boxes were fabricated in Civil Engineering Department at UMR. As shown in Figure 3.14, there were six boxes in total. One was for datalogger CR23X as shown in Figure 3.15. Four boxes were used for VWSG channels. One was for a power charger and battery. There was one access box for data downloading using laptop.

During precasting of the girders, part of DAS channels were used for different casting dates as shown in Figures 3.16 through 3.18. Figure 3.19 shows the DAS hooking up for the casting of the deck and after construction. Channels needed for different stages of the instrumentation program were list in Table 3.2 and Table 3.3.

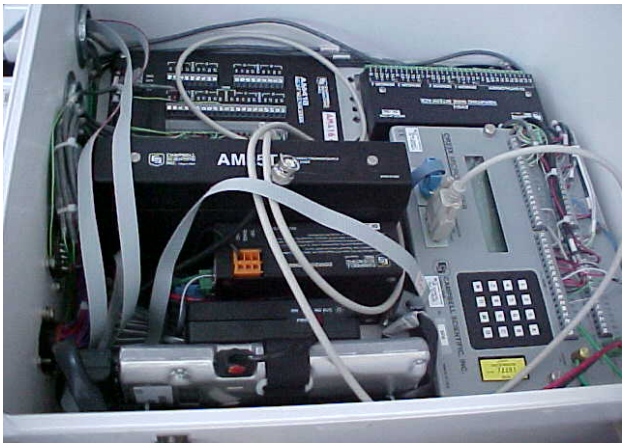

Figure 3.14. Data Acquisition System

Figure 3.15. Data Acquisition System Boxes

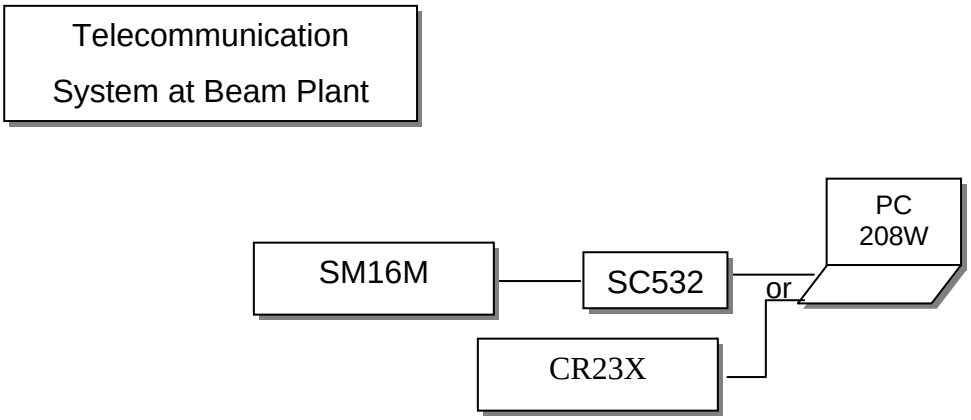

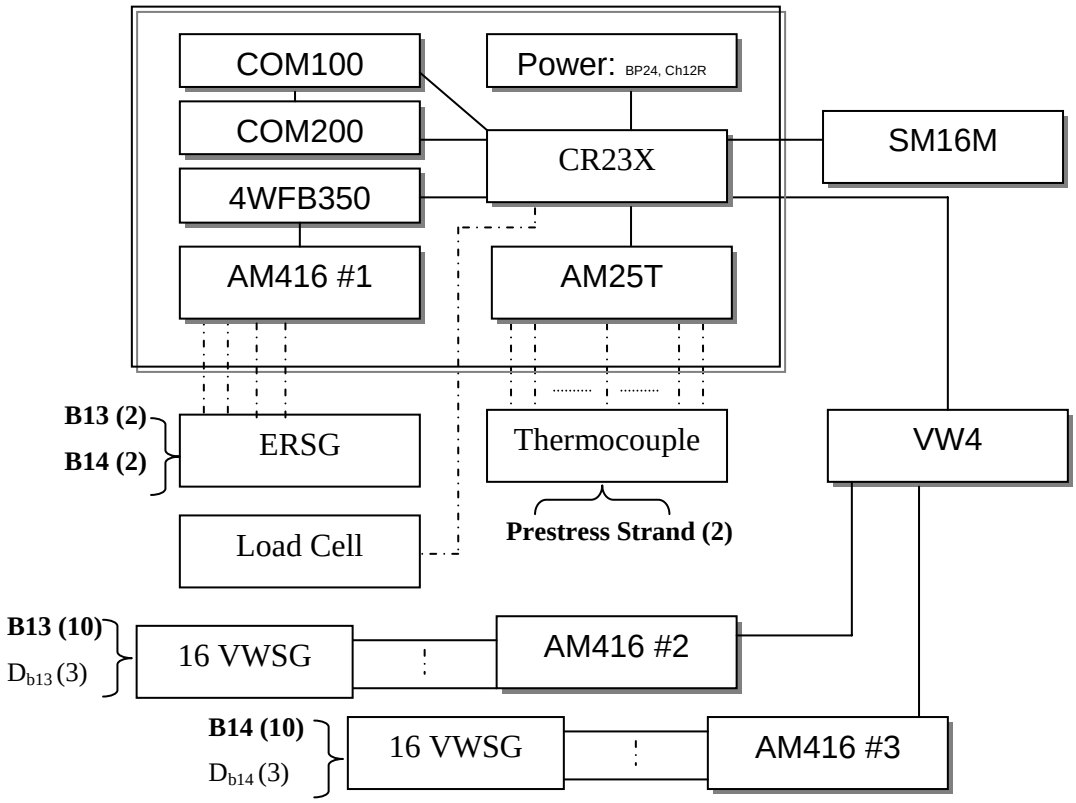

Figure 3.16. DAS Components and Gauges for Girders B13, B14

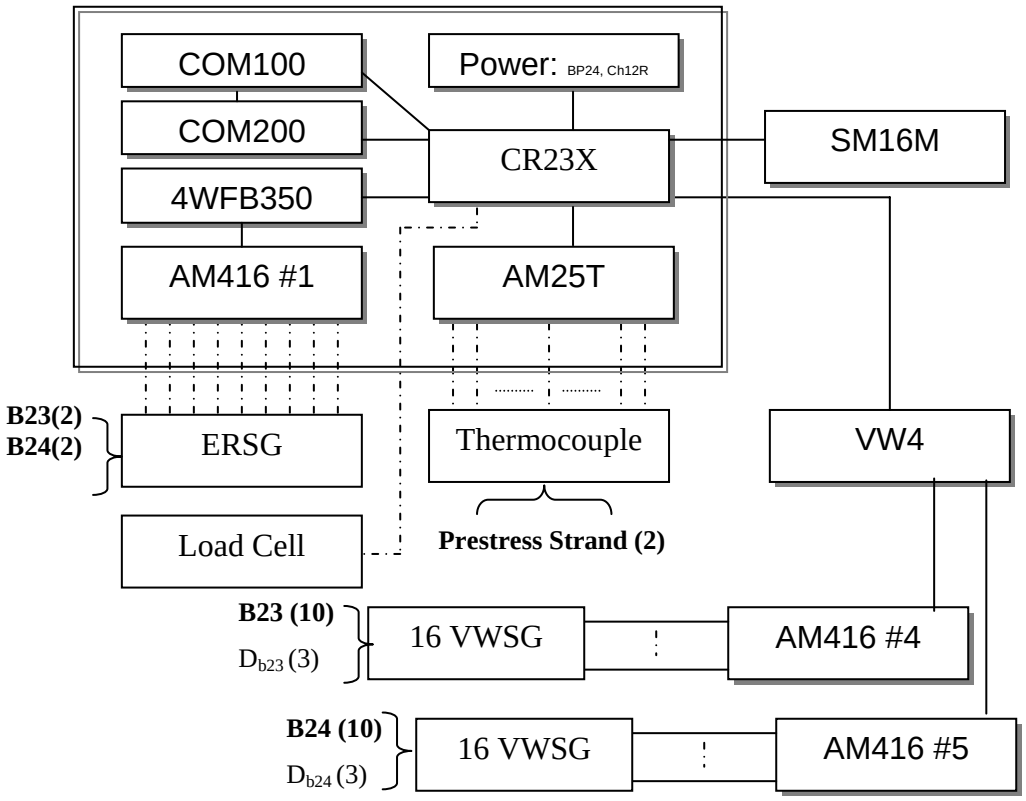

B23, B24 Instrumentation

Figure 3.17. DAS Components and Gauges for Girders B23, B24

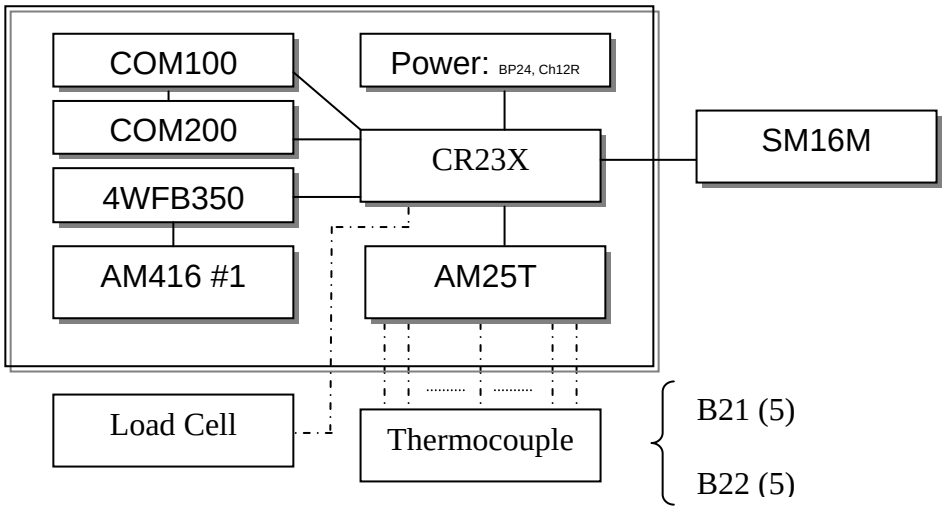

B21, B22 Instrumentation

Figure 3.18. DAS Components and Gauges for Girders B21, B22

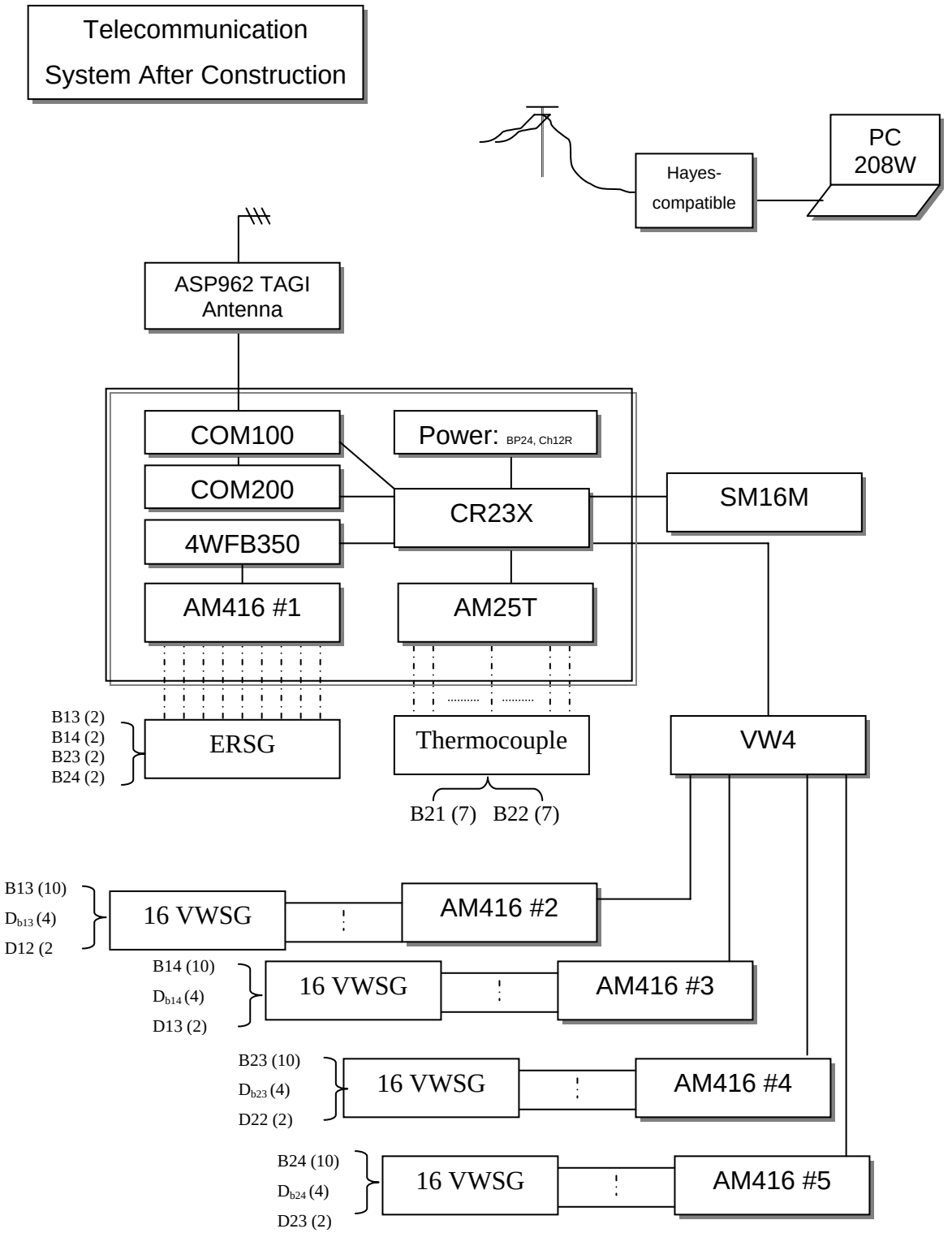

Figure 3.19. DAS Components and Gauges for Girders and Deck

Table 3.2. Channels Needed for Gauges Precasting Girders in Plant

Pour	Girders	Gauges for each girder		Channels	Total channels
1	B13, B14	VWSG	10	20	27
		ERSG	2	4	
		Thermocouple	2	2	
		Load cell	1	1	
2	B23, B24	VWSG	10	20	27
		ERSG	2	4	
		Thermocouple	2	2	
		Load cell	1	1	
3	B21, B22	Thermocouple	5	10	13
		Thermocouple	2	2	
		Load cell	1	1	

Table 3.3. Channels Needed for Gauges Casting Deck in Site

	Girders	Gauges for each		Channels	Total channels
CIP Deck	Above B21, B22	Thermocouple	2	4	28
	Other location	VWSG	12	24	
Girders	B13, B14	VWSG	10	20	24
		ERSG	2	4	
	B23, B24	VWSG	10	20	24
		ERSG	2	4	
	B21, B22	Thermocouple	5	10	10
Girders connection	B13 and B23	ERSG	3	3	3
	B14 and B24	ERSG	3	3	3
Total channels for long term					92

3.4.2. Programming and Data Collection. A personal computer and the PC208W software package supplied with the datalogger were used for datalogger programming and collection of stored data. Programs were written and downloaded to the datalogger by personal computer or storage module. A sample program written by the author for all gauges and channels can be found in Appendix C. The data can be downloaded to the computer or storage module. As shown in Figure 3.20 and Figure 3.21, data downloading was performed with laptop in the precast plant and the bridge jobsite.

Figure 3.20. Data Acquisition System at Precast Plant

Figure 3.21. Data Acquisition System at Jobsite

3.5. INSTRUMENTATION PLAN

3.5.1. Instrumentation Equipment and Gauges. In Table 3.4, a summary of all instrumentation equipment and gauges used for the project is presented. A total of 64 vibrating wire strain gauges (VWSG), 14 electrical resistance strain gauges (ERSG) and 16 thermocouples were embedded in the girders and decks. A data acquisition system (DAS) with enough channels was assembled for the project. The VWSG can then provide a profile of strain along the depth of the section as well as the temperature profiles. This type of strain gauges has proven very reliable. ERSG were used as back up gauges for strain measurement in the event of VWSG malfunction. Thermocouples have also proven very reliable in measuring the temperature in the girder for thermal gradients (Byle and Burns, 1998). A load cell was set up to monitor prestress losses before the strands are released. A tension wire system was set up for early-age deflection measurement. For later-age, precise surveying equipment was used for deflection as described previously.

Table 3.4. Instrumentation Equipment and Gauges

Equipment & gauges	Quantity	Description
DAS	1	Acquiring data from all sensors
Thermocouples	16	Monitoring temperature
Vibrating wire strain gauges (VWSG)	64	Monitoring strain
Electrical resistance strain gauges (ERSG)	14	Monitoring strain
DEMEC strain gauge	1	Measure transfer and development length
Load cell	1	Measure prestress losses before release
Tension-wire deflection system	4	Measure deflection before the girders are erected
Precision deflection system	1	Measure deflection after girders are erected

3.5.2. Instrumentation Location. As illustrated in Figure 3.22, 6 precast / prestressed girders were instrumented at the precast plant. 14 cast-in-place deck locations

were instrumented. VWSG and ERSG were embedded in girders B13, B14, B23 and B24 at mid-span section and near support section. Thermocouples were embedded in girders B21 and B22 at a section 2 m (6.56 ft) from the end of the girder. Sketches with gauge locations for every girder and cast-in-place deck span with instrumentation are presented in Appendix A and B. Typically, the locations of sensors along cross sections of girders were top flange (TF), top of web (TW), middle of web (MW), bottom of web (BW), center of gravity of noncomposite girder (CGI), center of gravity of prestressed strands (CGS), and bottom flange (BF) as shown in Figure 3.23.

As mentioned previously, DEMEC strain gauge was used for the girder end surface strain. After the girder forms were stripped the girder lower flange surface was cleaned and the DEMEC points were mounted. Both ends of six instrumented girders were placed with discs on both sides. The location and numbering of DEMEC points were shown in Figure 3.24.

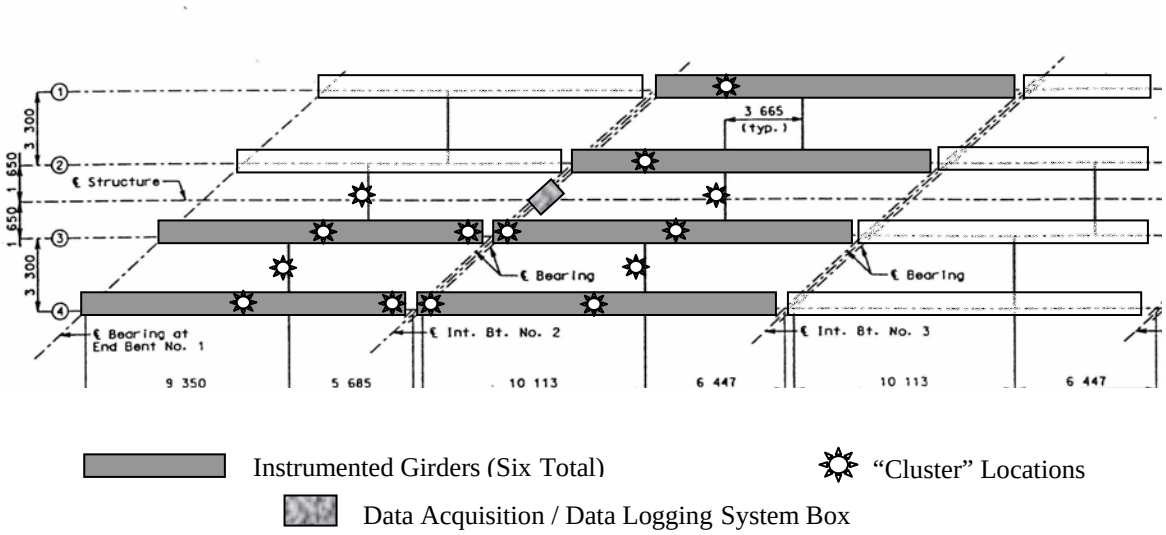

Figure 3.22. Plan Illustrating Girders Instrumented and "Cluster" Locations

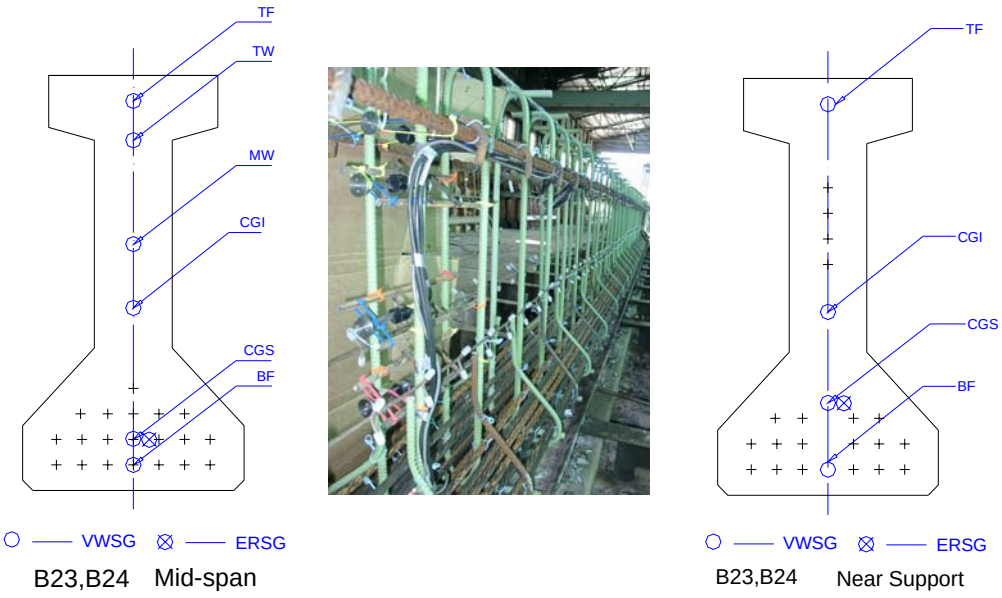

Figure 3.23. Location of Sensors along Cross Section of Girders

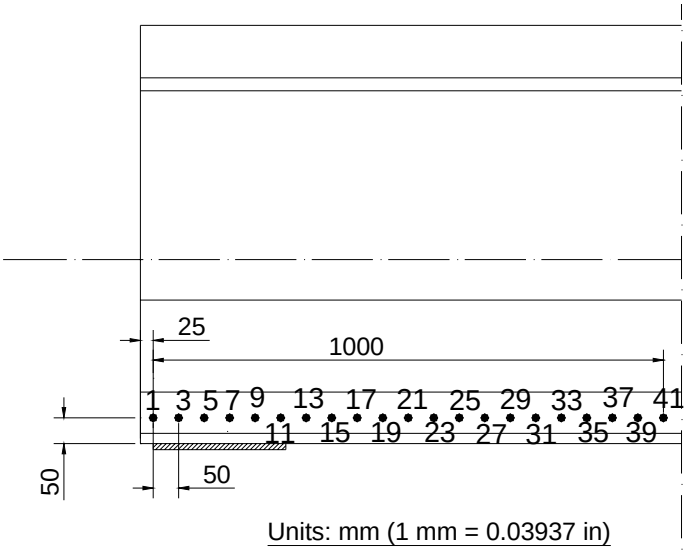

Figure 3.24. Location of DEMEC Points

3.5.3. Gauge Numbering and Identification. Because the instrumentation program is somewhat complicated, a complete identification of each gauge was necessary to minimize confusion. In Table 3.5, gauge identification designations are listed.

Table 3.5. Gauge Identification Designations

ITEMS	IDENTIFICATION		
Embedded Gauge Number	Type	Range	Named
	Deck VW	001-100	001-008
	Girder VW	101-200	101-156
	Girder ER	201-250	201-208
	Girder TC	251-300	251-257; 261-267
	Deck TR	301-400 (Corresponding VW # + 300)	301-308
	Girder TR	401-500 (Corresponding VW # + 300)	401-456
Girders and Decks Designation	Girder: *Bmn* CIP Deck: *Dmn*	Where *B* = beam, *m* = span #, *n* = beam line # Separate the deck as several small decks between bents and girders Where *D* = deck, *m* = span #, *n* = small beam line # of the two lines	
Embedded Gauge Depth	TD	Top Deck (2 in. below top fiber of deck)	
	BD	Bottom Deck (2 in. above bottom of deck)	
	TF	Top Flange (2 in. below top fiber)	
	TW	Top of Web	
	MW	Middle of Web	
	BW	Bottom of Web	
	CGI	c.g. of Noncomposite I-shaped Girder	
	CGS	c.g. of Prestressed Strands	
	BF	Bottom Flange (2 in. above bottom surface)	
Longitudinal Location of Gauges	M	Mid-span	
	Sm	Near the Support at Bent *m*	
	Sm,n	Near Bent *m, n* meters. from end of girder	
Gauge Type	Embedded Gauges	VW	Vibrating Wire Strain Gauge
		TC	Thermocouple
		ER	Bonded Electric Resistance Strain Gauge
		TR	Thermistor (integral with Vibrating Wire Strain Gauge)
	Other Gauges	DEMEC	Surface Mechanical Strain Gauges
		T-W	Tensioned – Wire Deflection System
		PSS	Precise Survey System of Deflection
		LC	Load Cells
DAS	CR23X		

3.6. PREPARATION AND FIELD INSTALLATION

3.6.1. Embedded Gauges Preparation. All gauges were prepared in ERL at UMR prior to installation in the field. The first step was dealing with individual gauges. As discussed before, resistance strain gauges required extensive preparation such as connecting with extension wire. Thermocouples needed to be cut to a specific length for different locations and one end of the wire was twisted. Vibrating wire strain gauges did not require significant prep work. The only prep work required a final lead connection to the DAS in the field. After final preparation, all of the wires were numbered. The second step was the grouping of individual gauges. For each location of girders and the deck, all the gauges that would go to this location were bond together as a cluster, as shown in Figure 3.25 and Figure 3.26. Then, vibrating wire gauges and resistance strain gauges were soldered with connectors, which connected with the DAS. The free end of thermocouple was inserted into a connector using special tools, as shown in Figure 3.27. The gauges were arranged in groups for different casting dates as shown in Figure 3.28. For field installation, a steel cage was welded as a support for the required gauge location as shown in Figure 3.29.

Figure 3.25. Gauges Numbering and Grouping

Figure 3.26. Gauges Groups for Different Locations

Figure 3.27. Gauges and Connectors for the DAS

Figure 3.28. DAS and Gauges Ready for the Instrumentation

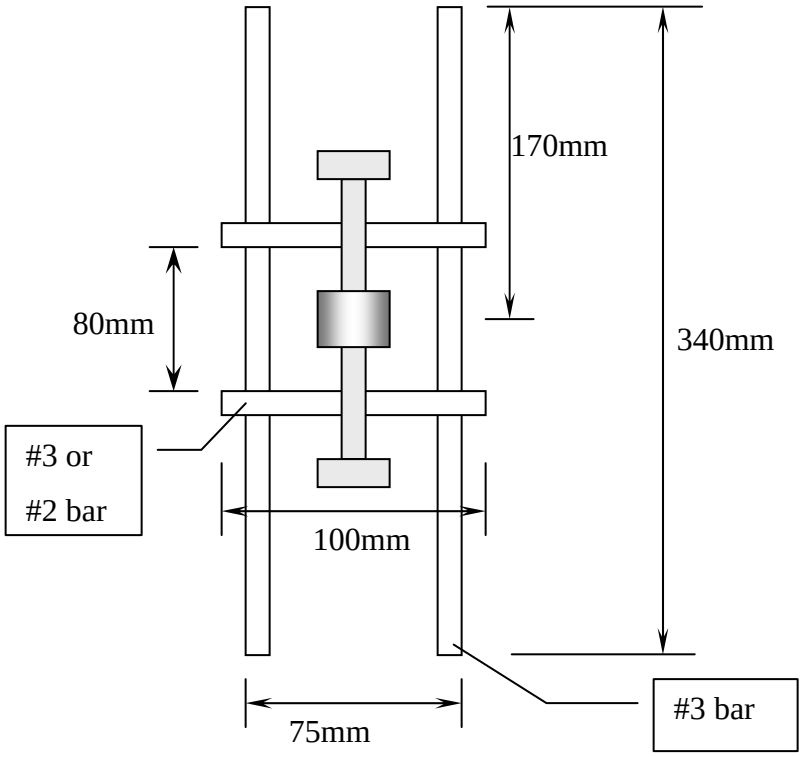

Figure 3.29. Welded Grid Rebar Cage for VWSG

3.6.2. Preparation for Tensioned-Wire System. Before going to the plant, the piano wire, dead weight, hilti anchors, hammer drill, aluminum pieces, quick set epoxy and precision scales were all prepared for the field use as discussed in Section 3.3.6.

3.6.3. Field Installation.

3.6.3.1 Prestressed girders. Before the strands were tensioned, a load cell was installed to the end of one strand, as shown in Figure 3.30. After all strands were tensioned, usually about two days prior to casting, placement of the mild steel reinforcement began by the fabricator. The installation of embedded sensors in prestressed girders was generally performed after this procedure was complete because the steel reinforcement was used as a framework for the placement of gauges. The

process of placing a gauge is shown in Figure 3.31. The installed gauges in the girder can be seen in Figure 3.32. After all gauges were installed for a casting date, the gauges were connected with the DAS, which was protected with wood plate and placed beside the casting bed as shown in Figure 3.33. The layout for the instrumentation in the precast plant can be seen in Figure 3.34.

Usually 2 days later, the fabricator removed the formwork. Before the strands were released, the DEMEC points were fixed to the concrete surface as discussed previously. After the epoxy was set the initial reading was taken as shown in Figure 3.35. The tensioned-wire deflection system was also installed for each instrumented girder and the baseline reading was taken. Following this, the strands were released by the fabricator. The second set of readings was performed for the DEMEC points and tension-wire systems. For the later age instrumentation, the DAS was moved out to the girders to obtain readings.

Figure 3.30. Installation of Loadcell

Figure 3.31. Gauges Installation

Figure 3.32. Gauges Installed at Designed Locations

Figure 3.33. Protected DAS during Concrete Placement

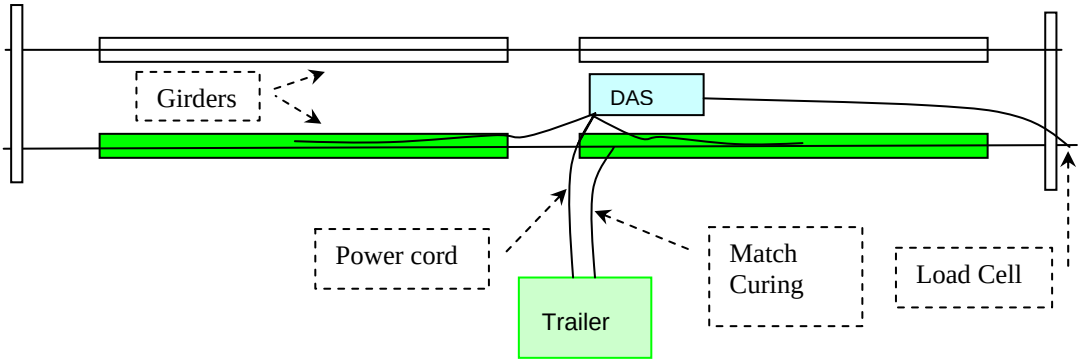

Figure 3.34. Layout for Instrumentation in Precast Plant

Figure 3.35. DEMEC Reading

Figure 3.36. Instrumentation When the Girders Were Stored in Precast Plant

3.6.3.2 Instrumentation during shipping. Two girders were instrumented during shipping to the jobsite. Before shipping the deflection readings were taken using the tensioned-wire deflection system on the girders. The DAS was fixed beside the girders on the trailer and connected with the strain gauges as shown in Figure 3.37 and Figure 3.38.

Figure 3.37. Preparing for Shipping of the Girders to the Bridge Jobsite

Figure 3.38. Shipping of the Girders to the Bridge Jobsite

3.6.3.3 Cast-in-place deck. In this section, field work for the instrumentation programs is presented. Girders were erected and braced by the contractor. Then the researchers placed the DAS on the bent for monitoring as shown in Figure 3.39. The DAS box was mounted after erection of all girders and removal of backfill around the bent to prevent potential vandalism. The mounting location of DAS on the bent was illustrated in Figure 3.40. The power was connected to the nearest utility pole through a power cord buried under ground. The trench for the power supply cord was dug by the contractor as shown in Figure 3.41.

Then cast-in-place (CIP) deck forms were set by the contractor and reinforcement was placed by the contractor. The researchers installed the CIP sensors in the cluster locations prior to casting that section of the deck as shown in Figure 3.42 and Figure 3.43. It was desirable that the sensors be placed as close to the casting of the deck as possible to avoid potential damage to sensors. After the bridge was completed, additional

readings were taken by the researchers periodically. The DAS was protected by the construction of a wood box as illustrated in Figure 3.44.

Figure 3.39. Data Reading for Girders and Deck with DAS

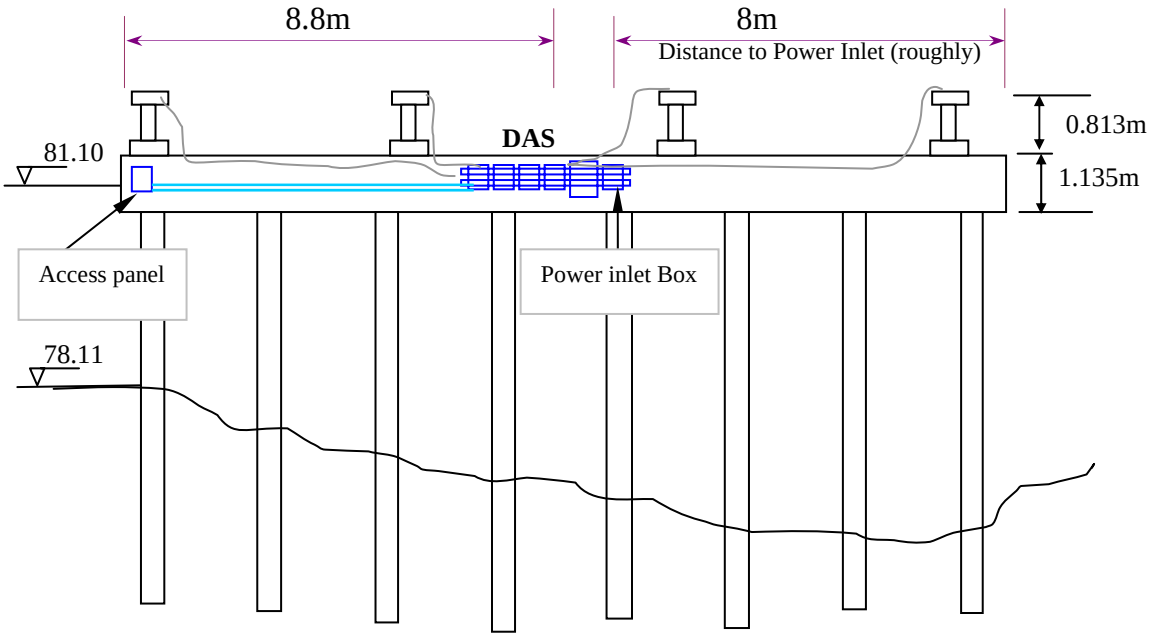

Figure 3.40. Mounting Location of DAS on the Bent

Figure 3.41. Trench Preparation for DAS Power Source

Figure 3.42. Bonding Strain Gauges and Thermocouples to the Steel

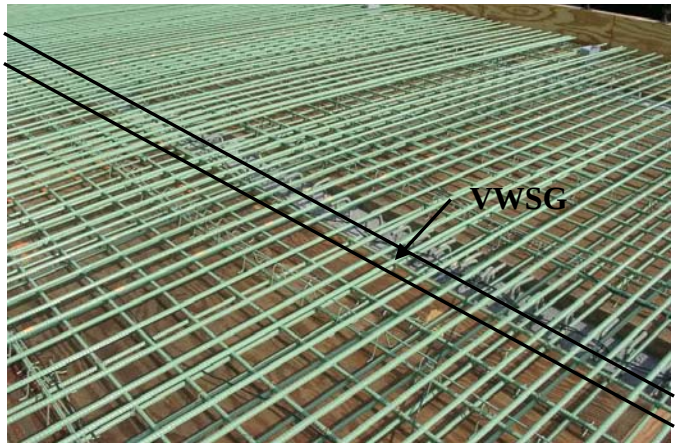

Figure 3.43. Sensors Embedded in the DECK

Figure 3.44. Wood Box for DAS

3.7. PROBLEMS ENCOUNTERED

The instrumentation at the precast plant for the girder was installed successfully and took approximately 4 hours per girder. Field instrumentation including the CIP deck and routing of wiring was also installed successfully taking approximately 12 hours. However, there were some problems encountered throughout the instrumentation program. In this Section a summary of problems encountered is presented. The DEMEC points worked well prior to moist curing of the girders. The high humidity of the water curing resulted in debonding of several DEMEC points as shown in Figure 3.45. During storage of the girders at the precast plant, as shown in Figure 3.46, the girders were placed so close that the DEMEC points were impacted by an adjacent member. This also caused debonding of several points.

The power supply for the DAS at the jobsite cost one thousand dollars, which was an expense not anticipated by the research team. Several outages in power were encountered due to contractor error and failure of the power supply; however, these did not affect the research study to a significant degree. This included a time period from

August 7th to August 21st, 2001, which was caused by improper wiring of the power supply to the DAS by the contractor.

Figure 3.45. Water Curing of the Girders

Figure 3.46. Girders Stored in Precast Plant

Power to the DAS was accidentally turned off at the jobsite by the contractor during the initial monitoring period. Data was lost for approximately a month during the

initial monitoring period. Undoubtedly, some freeze-thaw cycles that occurred on the bridge were not recorded. However, it did not dramatically affect the research study because the data were obtained for extreme temperatures and thermal gradients, strain analysis, and prestress losses. Freeze-thaw cycles were not the major research objective.

Field trips were time consuming because the distance between the bridge site and UMR. Travel time between the university and bridge site was 4.5 hours. Anticipating the field conditions prior to departure and arrival were difficult. Sometimes unexpected conditions occurred in the field such as heavy storms.

Figure 3.47 illustrates a site visit on November 10, 2001. As shown, high water levels made data transfer very difficult and challenging, however in the end transfer was successful. Water level at this height was not expected or planned for in the monitoring program based on available flood stage levels.

Figure 3.47. Data Downloading

4. MATERIAL TEST RESULTS AND DISCUSSION

4.1. INTRODUCTION

The material test program was initiated for this project in June 2001 in the materials and structural engineering labs of Butler-Carlton Civil Engineering Hall at UMR. These tests include compressive strength, modulus of elasticity, splitting strength, freeze-thaw, rapid chloride permeability, chloride ponding, scaling resistance, abrasion resistance, de-icing scaling, creep, shrinkage and coefficient of thermal expansion tests as summarized in Section 2. In Section 4, the material tests results are presented and discussed.

4.2. COMPRESSIVE STRENGTH

The test results for compressive strength with time were plotted and illustrated in Figures 4.1 through 4.6. Curves were fit to represent the measured data as shown in the figures at 56-day strength and long-term strength. For the late-age strength, the specimens were tested about two years after the concrete casting. ASTM moist cured and member cured specimens were tested for each concrete casting date. The fit curves for concrete strength development were used in the time-step method for prestress losses and deflection calculation in Section 7 and 8.

In Figure 4.7, 28-day compressive strength and 56-day compressive strength were compared to 2-year compressive strength for HPC used in bridge A6130. It was observed that 56-day strength was more than 90% of the 2-year strength and thus could be used as design strength.

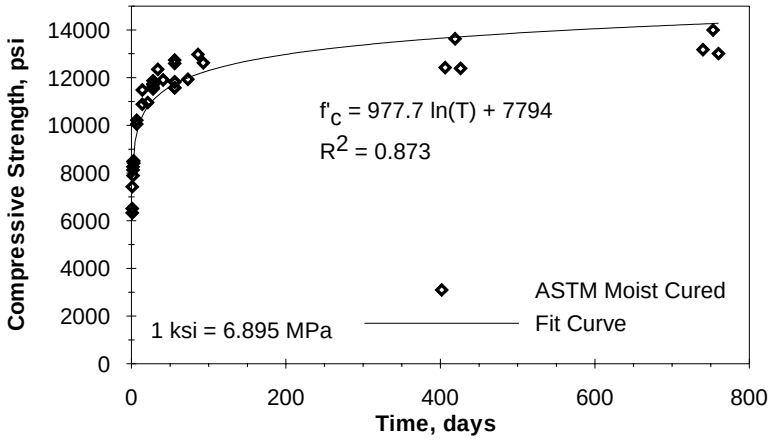

Figure 4.1. Late-Age Compressive Strength of Girder Concrete - ASTM Moist Cured

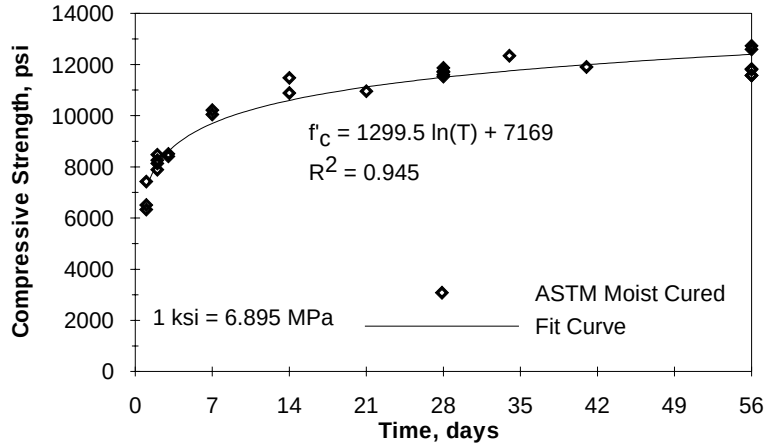

Figure 4.2. 56-Day Compressive Strength of Girder Concrete - ASTM Moist Cured

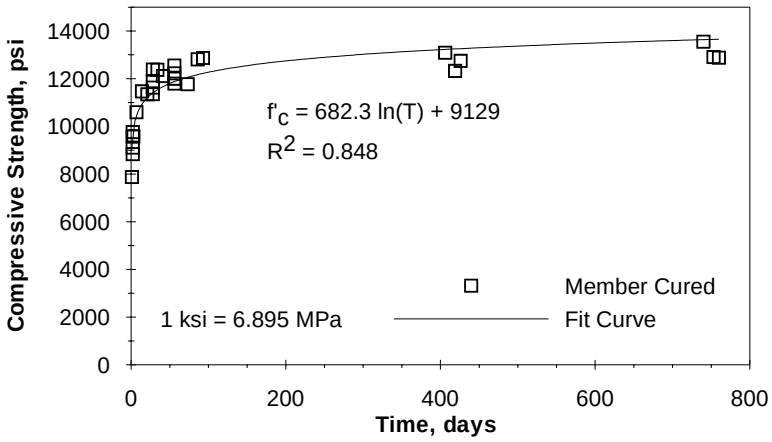

Figure 4.3. Late-Age Compressive Strength of Girder Concrete - Member Cured

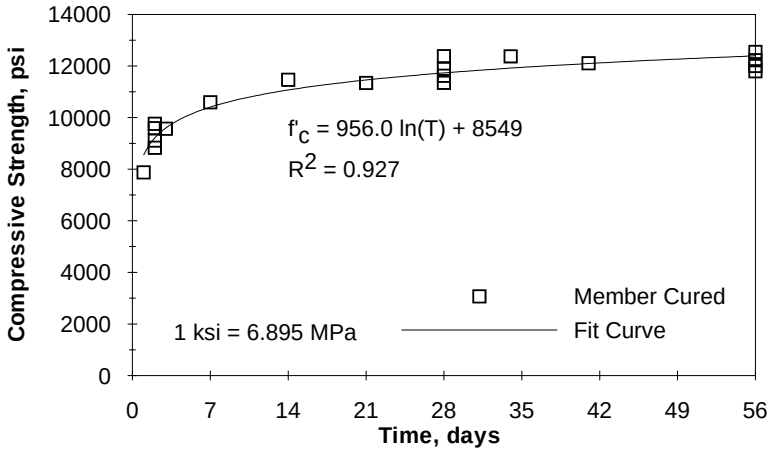

Figure 4.4. 56-Day Compressive Strength of Girder Concrete - Member Cured

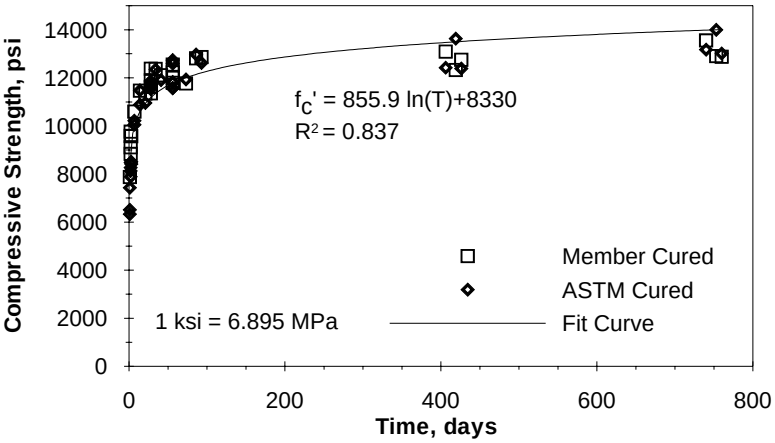

Figure 4.5. Late-Age Compressive Strength Development for Girder Concrete

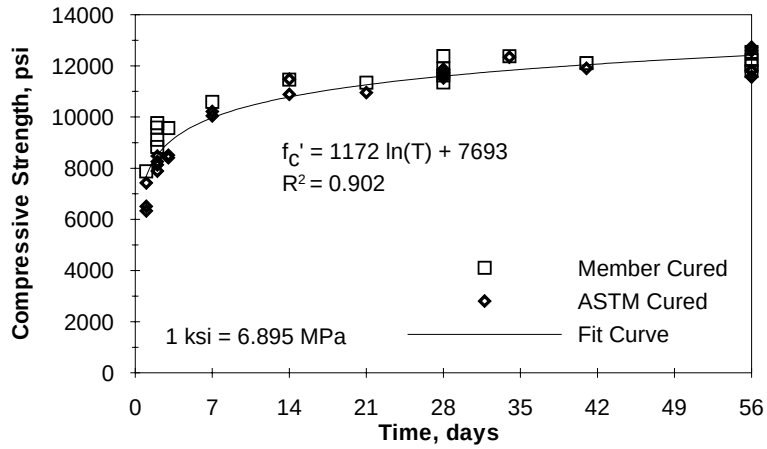

Figure 4.6. 56-Day Compressive Strength Development for Girder Concrete

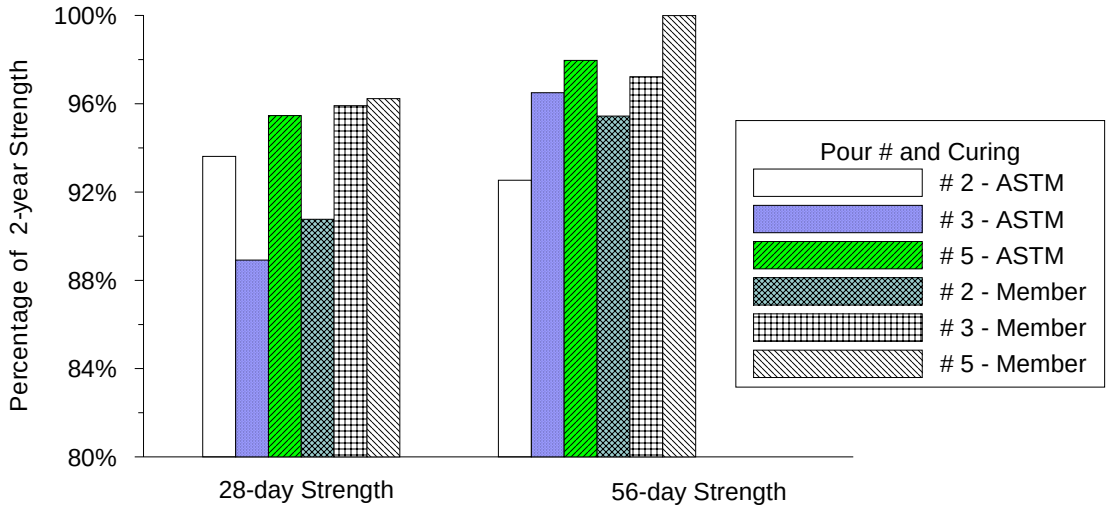

Figure 4.7. Ratio of 28-day and 56-day Strength to 2-year Strength

4.3. MODULUS OF ELASTICITY

Figure 4.8 illustrates modulus of elasticity test results of the specimens cast for this project. It can be found that most of test results were higher than those predicted using empirical equations suggested by ACI 363 (ACI 363R-92 1992) or ACI Committee 318 - Standard Building Code (ACI 318-02 2002).

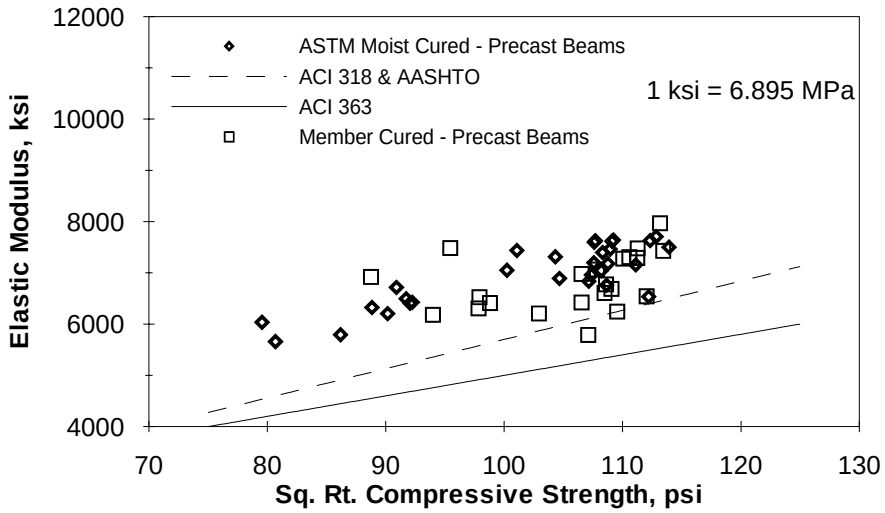

Figure 4.8. Modulus of Elasticity for Precast Girder

Figure 4.9 presents a large amount of test data reported by many researchers as well as the author. Some recommended empirical equations between MOE and compressive strength are shown in the figure. It is clear that these equations did not represent the measured data, especially when the strengths were high. Figure 4.10 and Figure 4.11 show the data and a fitted curve based on the data for light weight and normal weight concrete, respectively. Two equations that fit the data best are shown in Equation 4.1 and Equation 4.2. These are not intended to be specific to a given mix design/mix constituent, but rather an average starting empirical equation for the design engineer with limited mix design/mix constituent information.

For light weight concrete:

$$E_c = (w/145)^{1.5}[42090(f_c^{'})^{0.5} + 854100]\ (psi) \qquad \text{Equation 4.1}$$

For normal weight concrete:

$$E_c = (w/145)^{1.5}[43780(f_c^{'})^{0.5} + 141300]\ (psi) \qquad \text{Equation 4.2}$$

4.4. SPLITTING TENSILE STRENGTH

Figure 4.12 summarizes a large amount of test data for splitting tensile strength including test results obtained from this study. Three predicting equations for splitting tensile strength including that recommended by ACI 363 (1992) are shown in the figure and found not to be appropriate for high-strength concrete. Based on the data a fit curve was obtained as shown in Figure 4.13. The following expression is recommended based on the large database of information collected. This is a recommended starting point for the design engineer with limited mix design/mix constituent information.

$$f_{sp} = 2.59(f_c^{'})^{0.62}\ (psi) \qquad \text{Equation 4.3}$$

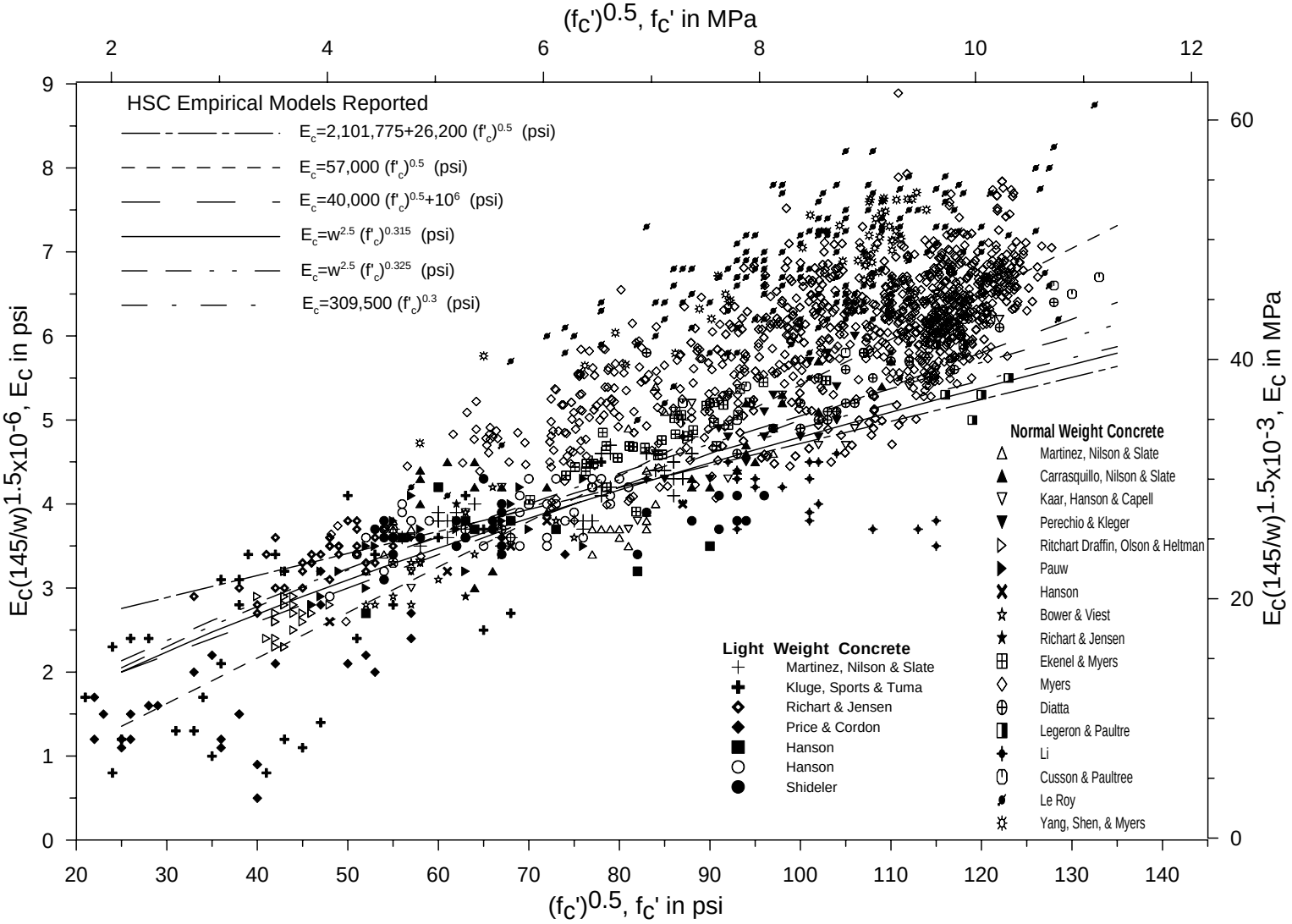

Figure 4.9. Modulus of Elasticity versus Concrete Strength

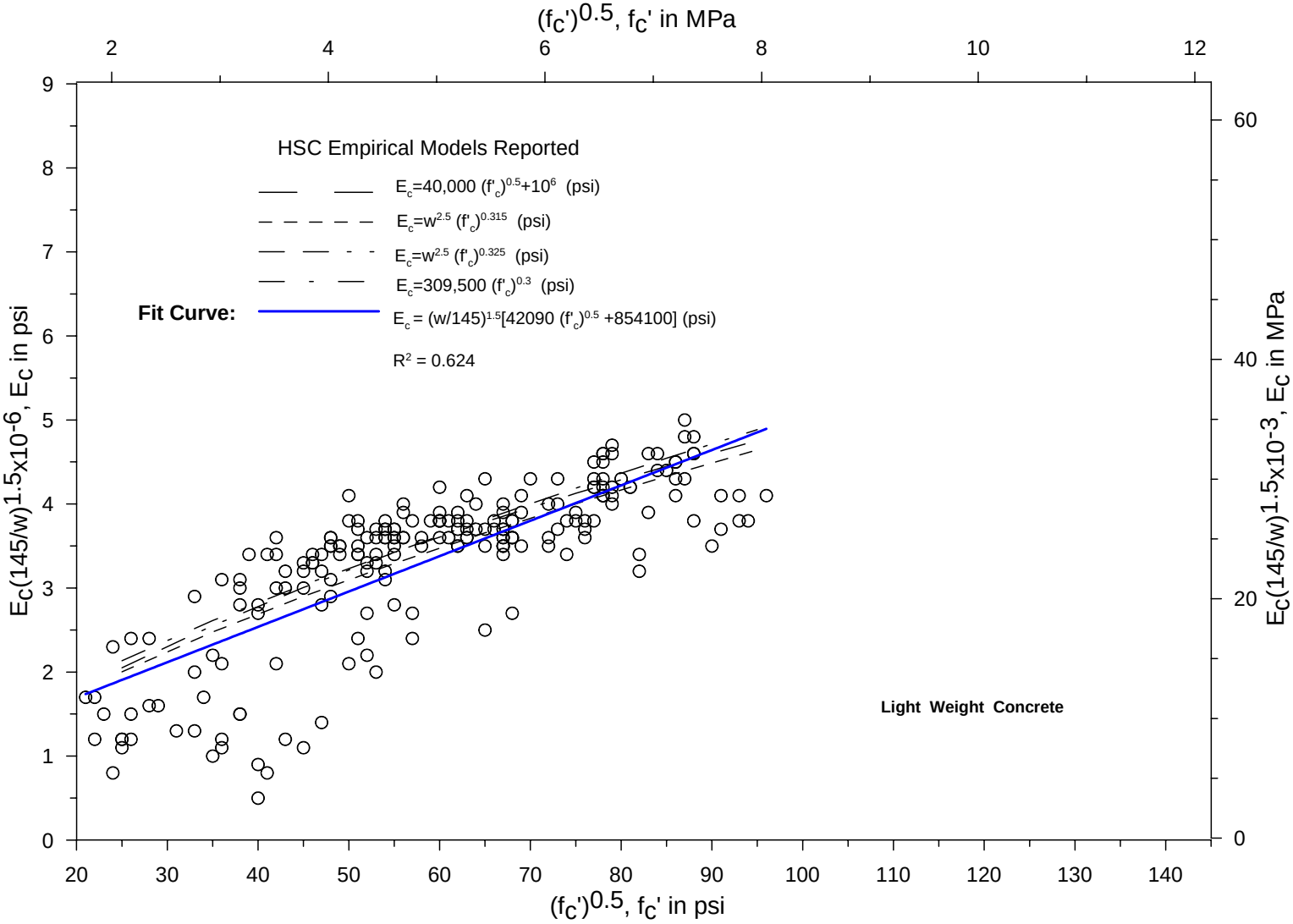

Figure 4.10. Modulus of Elasticity versus Concrete Strength for Light Weight Concrete

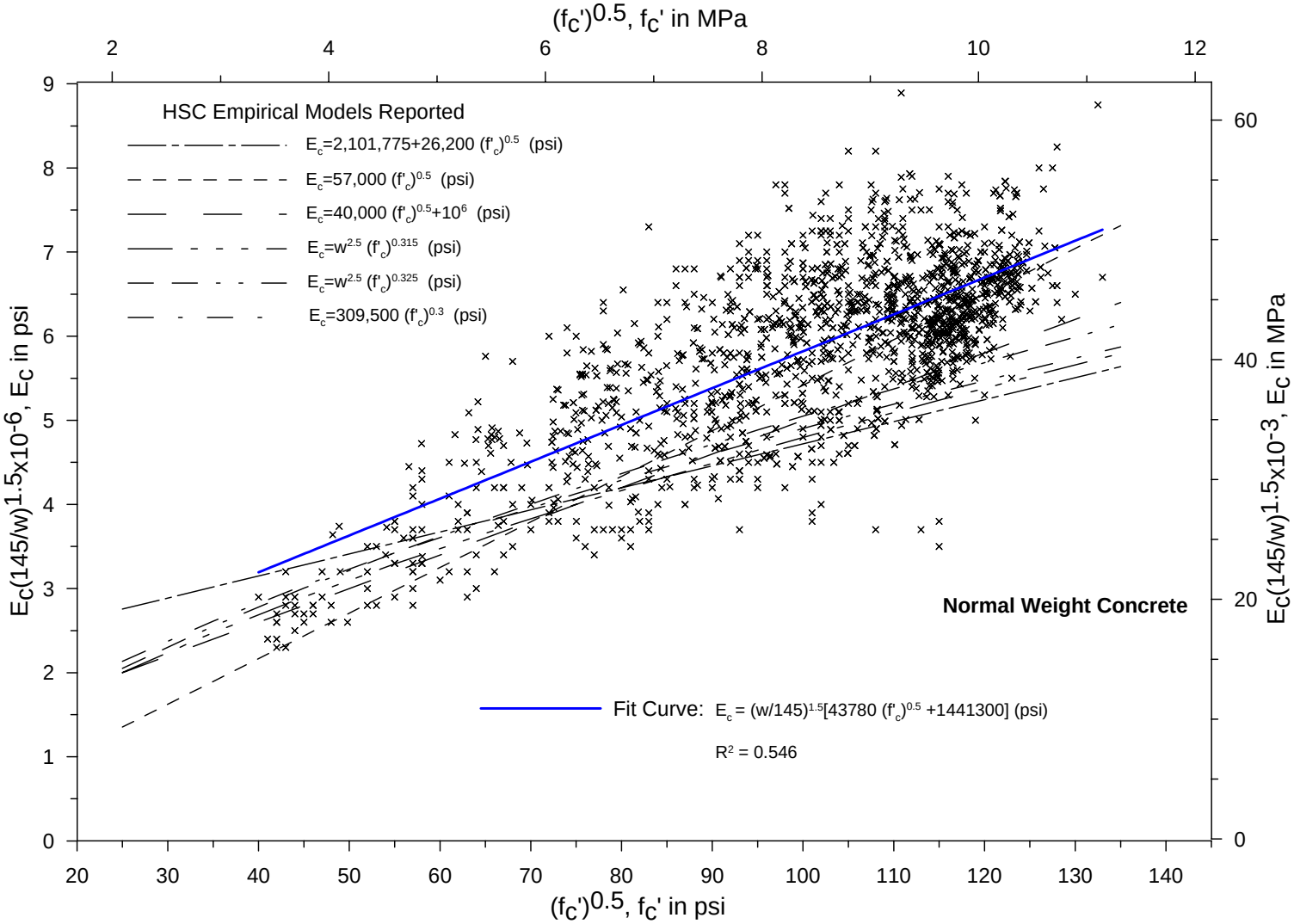

Figure 4.11. Modulus of Elasticity versus Concrete Strength for Normal Weight Concrete

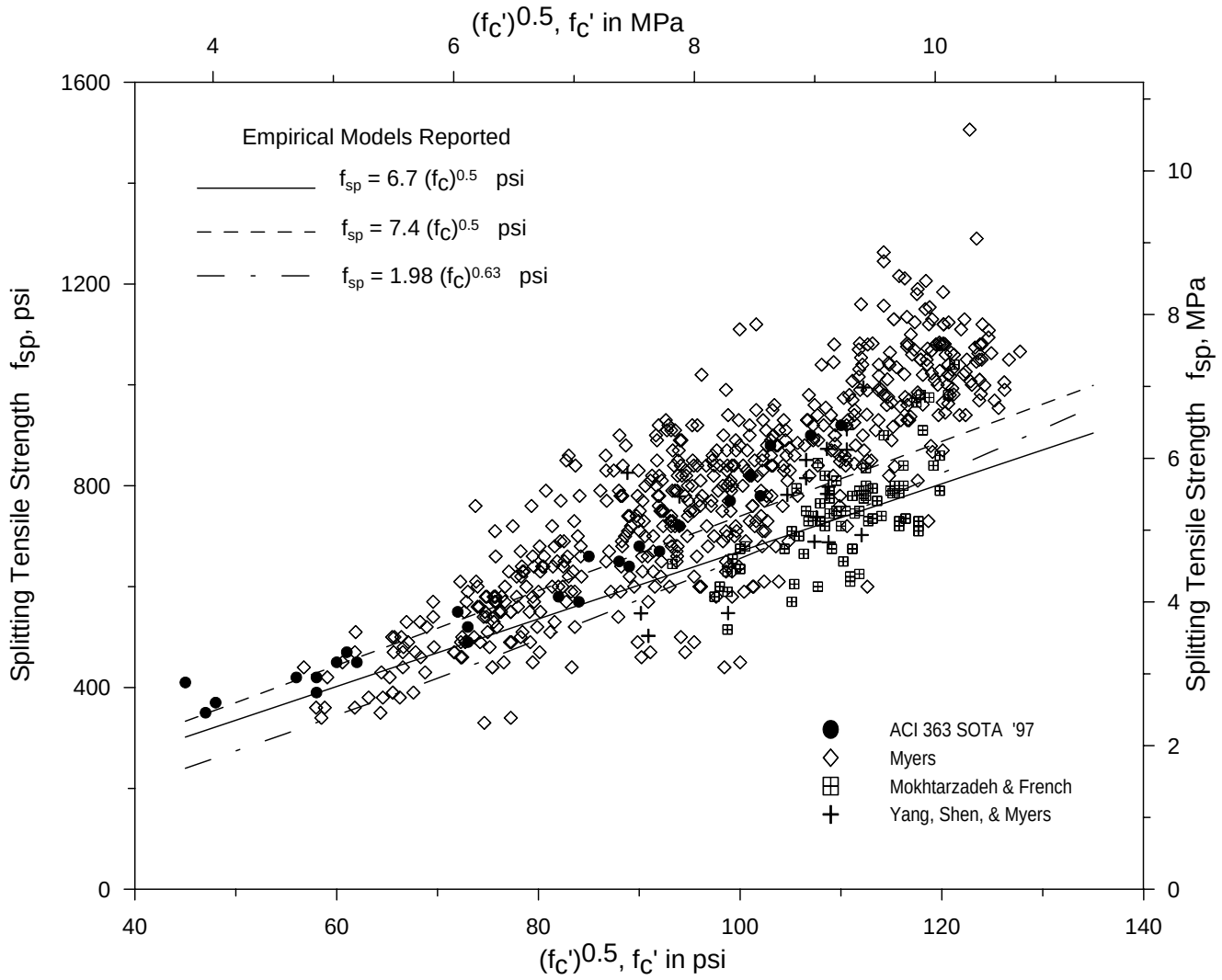

Figure 4.12. Splitting Tensile Strength versus Concrete Strength

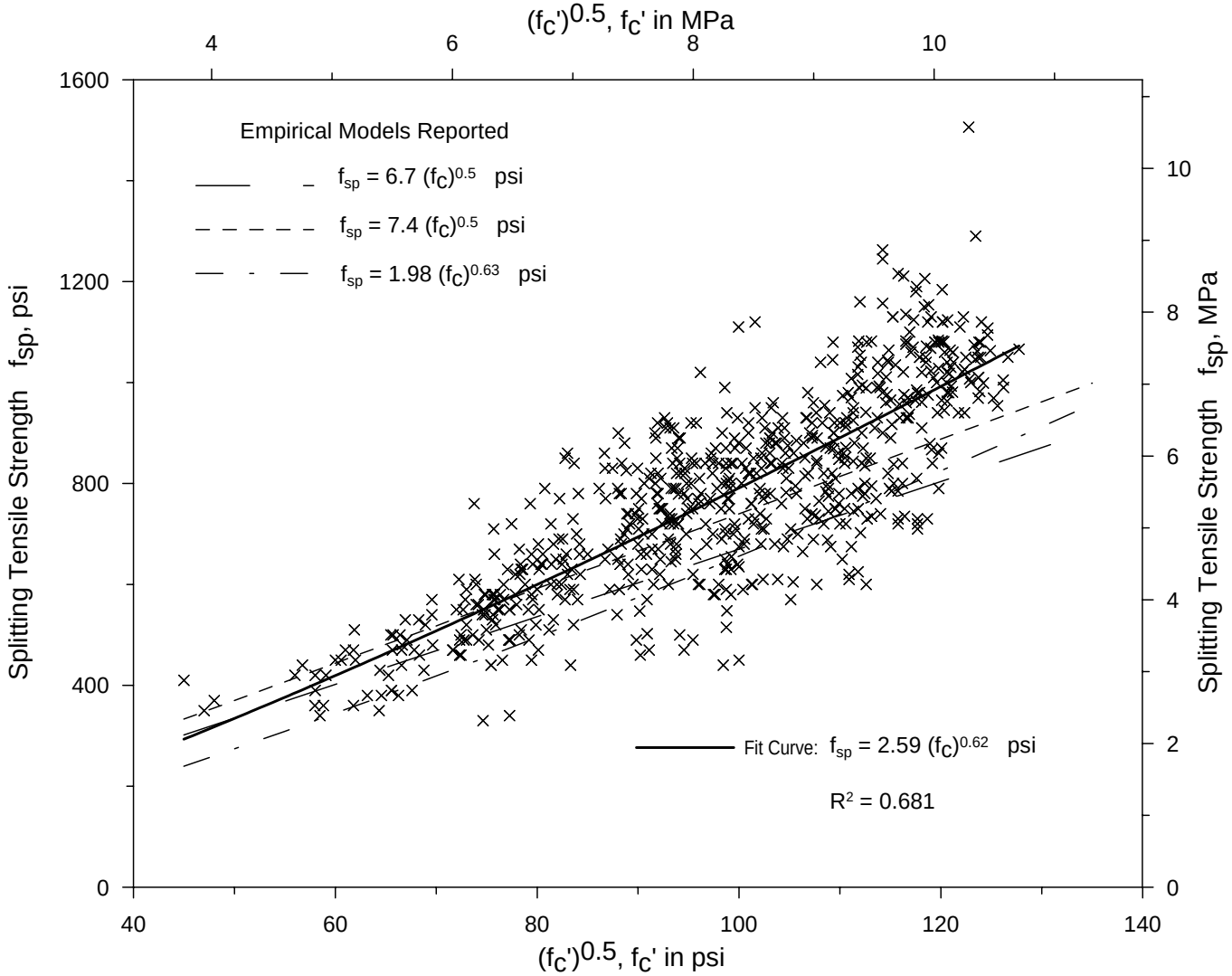

Figure 4.13. Splitting Tensile Strength versus Concrete Strength

4.5. CREEP

Creep is defined as continued deformation under a constant stress. For HPC girder concrete, strain was measured immediately prior to loading and immediately after loading to determine the elastic strain during loading. For the CIP deck pour concrete, however, three short specimens were stacked and bonded together for creep. The elastic strain was determined by the loading force and the MOE when the specimens were loaded. The following Equation 4.4 was used to determine the creep coefficient.

$$C_{ct} = \frac{(t - t_0)^c}{d + (t - t_0)^c} \cdot C_{cu} \qquad \text{Equation 4.4}$$

where, C_{ct} is the creep coefficient at time *t*; C_{cu} is the ultimate creep coefficient; *c*, *d* is constant.

Table 4.1 summarizes the creep tests that were performed at UMR for both the girder concrete and deck concrete. Table 4.2 and Table 4.3 present the creep coefficients and specific creep based on measured data obtained.

Table 4.1. Summary of Creep Tests

Specimen ID (specimen #)	Casting Date	Design Compressive Strength (MPa)	Loading Force (kN)	Stress Level (MPa)
S4-AC-Creep	6-26-01	68.95	223.6	27.6
S5-AC-Creep	7-3-01	68.95	223.6	27.6
SD-AC-Creep	9-11-01	27.58	89.54	11.0
SD-FC-Creep		27.58	89.54	11.0
1 kN = 224.8 lb; 1 MPa = 145.04 psi; AC – Air cured; FC – Field cured				

Table 4.2. Measured Creep Coefficients

Specimen ID (specimen #)	Casting Date	Creep Coefficient			
		7 days	28 days	56 days	180 days
S4-AC-Creep	6-26-01	1.19	1.58	1.73	2.04
S5-AC-Creep	7-3-01	0.66	0.87	0.96	1.12
Average for HPC girders		**0.93**	**1.22**	**1.34**	**1.58**
% of Creep at 180 days		**59**	**77**	**85**	**100**
SD-AC-Creep	9-11-01	1.16	1.60	1.81	2.53
SD-FC-Creep		1.06	1.55	1.76	2.59
Average for the CIP deck		**1.11**	**1.58**	**1.79**	**2.56**
% of Creep at 180 days		**43**	**62**	**70**	**100**
1 kN = 224.8 lb; 1 MPa = 145.04 psi; AC – Air cured; FC – Field cured Days used here are days after loading					

Table 4.3. Measured Specific Creep

Specimen ID (specimen #)	Casting Date	Specific Creep (με/psi)			
		7 days	28 days	56 days	180 days
S4-AC-Creep	6-26-01	0.113	0.150	0.164	0.194
S5-AC-Creep	7-3-01	0.113	0.148	0.163	0.189
Average for HPC girders		**0.113**	**0.149**	**0.164**	**0.192**
SD-AC-Creep	9-11-01	0.206	0.284	0.320	0.448
SD-FC-Creep		0.184	0.270	0.306	0.450
Average for the CIP deck		**0.195**	**0.277**	**0.313**	**0.449**
1 kN = 224.8 lb; 1 MPa = 145.04 psi; AC – Air cured; FC – Field cured Days used here are days after loading					

Measured average creep coefficient at 180 days was 1.58, which is lower than a predicted value of 1.63 using the ACI Committee 209 report method (ACI 209R-92

1992). These low creep coefficients can have a great impact on prestress losses as discussed in Section 7. Percentages of the measured creep at 180 days that occurred 7, 28, 56 days after loading are also listed in Table 4.2. The clear trend is that creep occurred much more quickly in the precast mixes than the cast-in-place mixes. This attributed to earlier loadings more pronounced temperature effects and the higher strength of the precast mixes. Creep coefficients for pour 4, pour 5 and the deck pour are summarized in Appendix E.

Equation 4.4 was used to fit the measured data. Three types of regression analysis were compared as listed in Tables 4.4 through 4.6. Figure 4.14 illustrates a typical creep coefficient curve fit. It maybe observed that the general form fits the data to the highest R^2 value. When the power *c* is fixed at 0.6, parameter *d* is 10 and C_{cu} is 2.35, then the equation is the same as in ACI 209 (1992). This is the ACI empirical equation illustrated in Figure 4.14 and it was found to highly overestimate creep relationships obtained in this study by 44%. The fit curve using general form was used for prestress loss and camber analysis in Section 7 and Section 8 of this study.

Table 4.4. Creep-Time Regression Curve Parameters (General Form)

Specimen ID (specimen #)	Casting Date	General Form of Equation 4.4			
		c	d	C_{cu}	R^2
S4-AC-Creep	6-26-01	0.4	3.8	3.20	0.982
S5-AC-Creep	7-3-01	0.4	3.1	1.63	0.990
Average for HPC girders		**0.3**	**3.6**	**2.54**	**0.987**
SD-AC-Creep	9-11-01	0.4	7.7	4.34	0.991
SD-FC-Creep		0.4	9.2	4.74	0.993
Average for the CIP deck		**0.4**	**8.4**	**4.53**	**0.993**

Table 4.5. Creep-Time Regression Curve Parameters (Power Fixed)

Specimen ID (specimen #)	Casting Date	General Form of Equation 4.4			
		c	d	C_{cu}	R^2
S4-AC-Creep	6-26-01	0.6	3.7	2.31	0.972
S5-AC-Creep	7-3-01	0.6	3.0	1.24	0.982
Average for HPC girders		0.6	**3.5**	**1.79**	**0.974**
SD-AC-Creep	9-11-01	0.6	6.7	3.09	0.987
SD-FC-Creep		0.6	7.7	3.19	0.990
Average for the CIP deck		0.6	**7.2**	**3.14**	**0.989**

Table 4.6. Creep-Time Regression Curve Parameters (Parameters Fixed)

Specimen ID (specimen #)	Casting Date	General Form of Equation 4.4			
		c	d	C_{cu}	R^2
S4-AC-Creep	6-26-01	0.6	10	3.26	0.765
S5-AC-Creep	7-3-01	0.6	10	1.81	0.707
Average for HPC girders		0.6	10	**2.52**	**0.693**
SD-AC-Creep	9-11-01	0.6	10	3.54	0.984
SD-FC-Creep		0.6	10	3.58	0.983
Average for the CIP deck		0.6	10	**3.57**	**0.980**

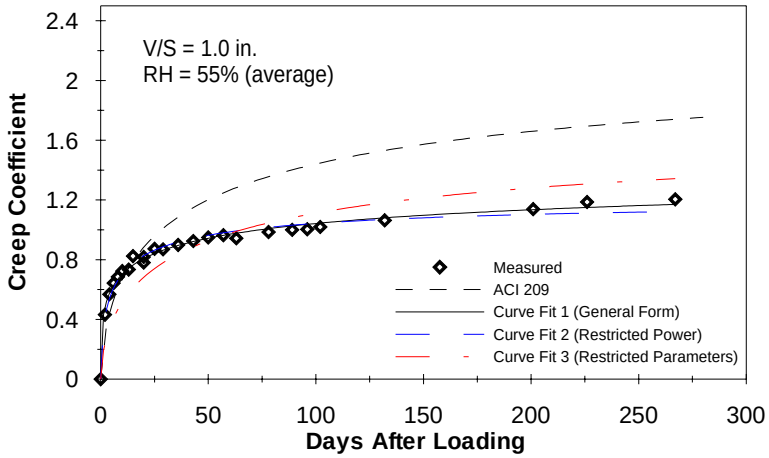

Figure 4.14. Typical Creep Coefficient Curve Fits from Regression Analysis

4.6. SHRINKAGE

Shrinkage is broadly defined as the decrease in volume of a concrete element when it loses moisture by evaporation. Table 4.7 summarized the measured shrinkage strains for both girder concrete and deck concrete.

Measured shrinkage for the precast girder concrete at 180 days ranged from 268 to 277 microstrain, which was much lower than a value of 653 microstrain predicted by ACI 209 (1992). For the deck concrete, an average measured shrinkage of 411 microstrain, which was also much lower than ACI 209 predicted. Shrinkage strains for pour 4, pour 5 and the deck pour are summarized in Appendix E.

Table 4.7. Measured Shrinkage Strain

Pour #	Casting Date	Shrinkage Strain (με)			
		7 days	28 days	56 days	180 days
Girder Pour 4	6-26-01	115	170	206	277
Girder Pour 5	7-3-01	122	148	187	268
Average for HPC girders		**119**	**159**	**197**	**273**
% of Shrinkage at 180 days		**43**	**58**	**72**	**100**
Deck Pour	9-11-01	95	270	316	411
% of Shrinkage at 180 days		**23**	**66**	**77**	**100**
Days used here are days after stripping					

Equation 4.5 was used to fit the measured data. Three types of regression analysis were compared as listed in Tables 4.8 through 4.10. Figure 4.15 illustrates a typical shrinkage strain curve fit. ACI 209 (1992) predicted curve for shrinkage is also shown in Figure 4.15 and found to overestimate the shrinkage to a high degree (up to 138%). The

fit curve using general form was used for prestress loss and camber analysis in Section 7 and Section 8.

$$\varepsilon_{sh,t} = \frac{(t-t_1)^e}{f+(t-t_1)^e} \cdot \varepsilon_{shu} \qquad \text{Equation 4.5}$$

where, $\varepsilon_{sh,t}$ is shrinkage at time t; ε_{shu} is the ultimate shrinkage of concrete; e, f is constant.

Table 4.8. Shrinkage-Time Regression Curve Parameters (General Form)

Pour #	Casting Date	General Form of Equation 4.5			
		e	f	$\varepsilon_{sh,u}$	R^2
Girder Pour 4	6-26-01	0.4	9.6	674	0.966
Girder Pour 5	7-3-01	0.3	13.0	982	0.971
Deck Pour	9-11-01	1.0	20.8	454	0.987

Table 4.9. Shrinkage-Time Regression Curve Parameters (Power Fixed)

Pour #	Casting Date	General Form of Equation 4.5			
		e	f	$\varepsilon_{sh,u}$	R^2
Girder Pour 4	6-26-01	1.0	12.5	266	0.891
Girder Pour 5	7-3-01	1.0	9.6	249	0.881
Deck Pour	9-11-01	1.0	21.0	452	0.987

Table 4.10. Shrinkage-Time Regression Curve Parameters (Power Fixed)

Pour #	Casting Date	General Form of Equation 4.5			
		e	f	$\varepsilon_{sh,u}$	R^2
Girder Pour 4	6-26-01	1.0	35	344	0.710
Girder Pour 5	7-3-01	1.0	35	332	0.654
Deck Pour	9-11-01	1.0	35	526	0.936

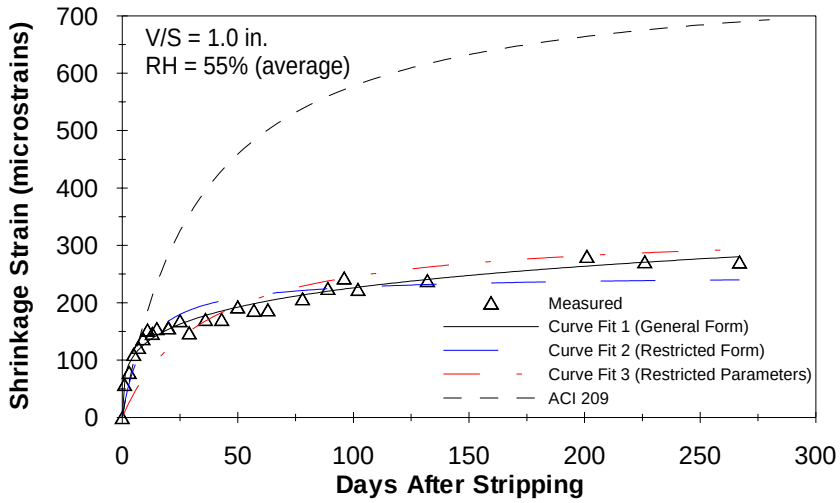

Figure 4.15. Typical Shrinkage Curve Fits from Regression Analysis

4.7. COEFFICIENT OF THERMAL EXPANSION

The coefficient of thermal expansion (CTE) of concrete is a function of the coefficients of both the aggregate and paste. The CTE of aggregate ranges from 7 με/°C (3.9 με/°F) to 13 με/°C (7.2 με/°F) and that of paste ranges from 18 με/°C (10 με/°F) to 20 με/°C (11 με/°F). However, because aggregates generally make up about 70% of the bulk of the concrete mix, the coefficient of thermal expansion of concrete is most influenced by the coefficient of the aggregate, as well as the quantity of aggregate in the mix (Nawy, 2001).

There were five specimens tested for coefficient of thermal expansion for HPC girder concrete mix. The results are shown in the Table 4.11. Measured coefficients fell within the range of 8.7 to 11.6 με/°C (4.8 to 6.5 με/°F), which falls into the range of values suggested by Mindess and Young (1981) for all concretes. The measured CTE were used for thermal behavior analysis of the bridge in Section 5.

Table 4.11. Measured Coefficient of Thermal Expansion

Specimen ID (specimen #)	Casting Date	CTE	
		με/°F	με/°C
S3-MC-SH-1	6-20-01	5.36	9.66
S3-AC-SH/TH-2	6-20-01	4.86	8.75
S4-MC-SH/TH	6-26-01	5.49	9.88
S4-AC-SH/TH	6-26-01	5.18	9.32
S5-AC-Creep	7-3-01	6.42	11.55
Average for HPC girders		5.46	9.83
SH - Shrinkage; TH - Thermal; AC – Air cured; FC – Field cured			

4.8. FREEZE–THAW DURABILITY

Freeze-thaw resistance was investigated for both girder and deck concrete. In lieu of obtaining the relative dynamic modulus of elasticity, mass changes were measured. The test results for each specimen are presented in Table 4.12. Figure 4.16 illustrates the mass change versus freeze-thaw cycles for the test specimens.

Table 4.12. Test Results for Freeze-Thaw

Specimen ID (specimen #)	Casting Date	Total Freeze-Thaw Cycles	Mass Change (percent)
S3-FT-1	6-20-01	300	0.25
S3-FT-2		300	0.31
S5-FT-1	7-3-01	300	0.32
S5-FT-2		300	0.27
Average of all specimens for HPC for girders			**0.29**
SD-FT-1	9-11-01	300	1.12
SD-FT-2		300	0.69
Average of all specimens for the CIP deck			**0.91**

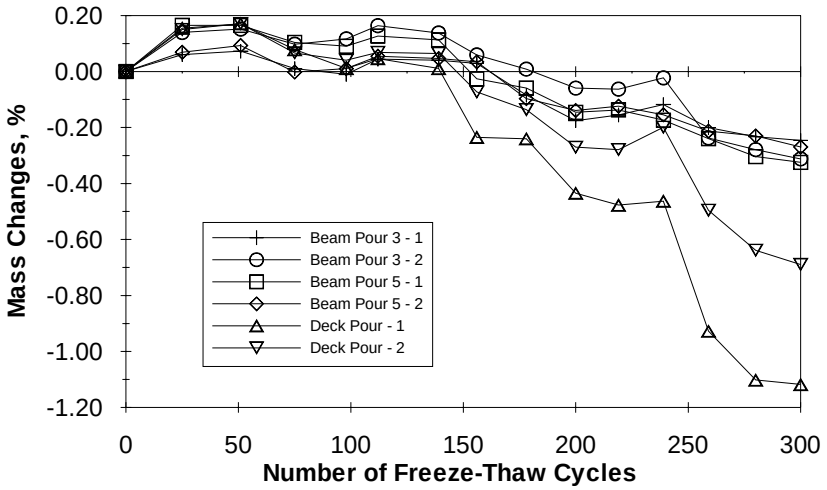

Figure 4.16. Mass Change versus Number of Freeze – Thaw Cycles

The mass loss for the girder concrete varied between 0.25 and 0.32% and for deck concrete, the loss ranged from 0.69 to 1.12%. In terms of mass loss, comparing that of conventional concrete (from 5 to 15%), both of these mixes performed very well and can be expected to have excellent Free-Thaw resistance and correspond to a durability factor above 85% based on ACI criteria (Nawy, 2001).

4.9. RAPID CHLORIDE PERMEABILITY

The rapid chloride permeability testing (RCPT) was performed for both HPC girders and the CIP deck concrete. The results are presented in Figures 4.17 and 4.18. For the precast prestress girders, the ASTM moist cured and member cured cylinders resulted in an average RCPT of 123 and 78 coulombs respectively, both average values in the very low classification.

For the CIP deck concrete at 29 days, the ASTM moist cured and field cured cylinders resulted in an average RCPT of 1789 and 3084 coulombs respectively. Moist cured average values are in the low classification. Field cured average values are in the

moderate classification. Conventional concrete has RCPT higher than 4000 coulombs, which is in the high classification (Nawy, 2001).

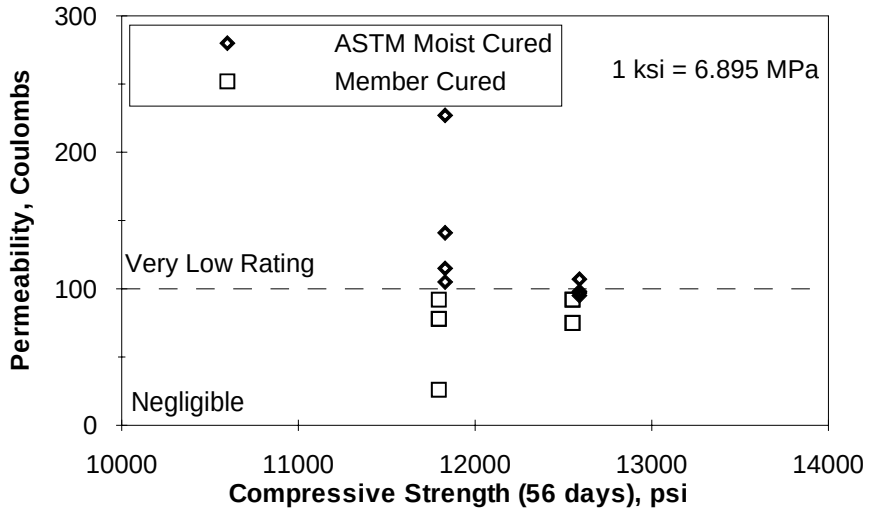

Figure 4.17. Rapid Chloride Permeability (56 Days) for HPC Precast Girders

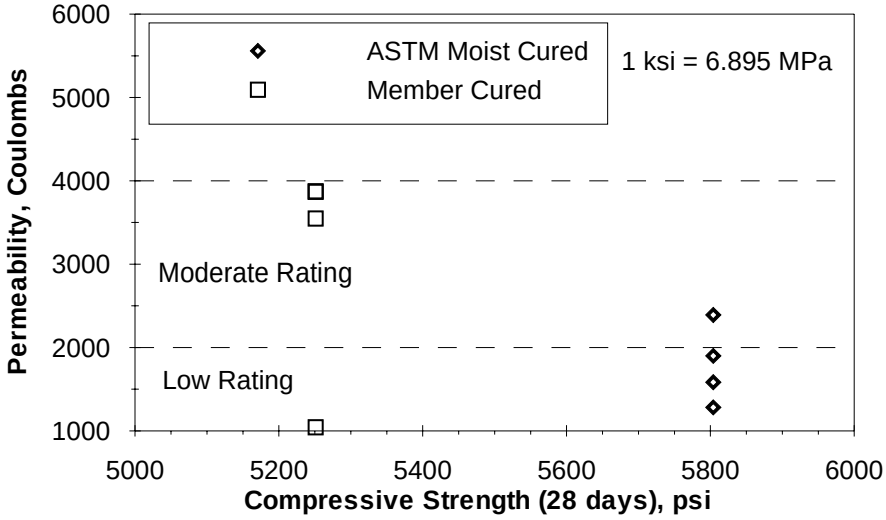

Figure 4.18. Rapid Chloride Permeability (29 Days) for CIP Deck

4.10. CHLORIDE PONDING

The chloride ponding test for the concrete was performed in accordance with AASHTO T259 "Resistance of Concrete to Chloride Ion Penetration." The test results are summarized in Table 4.13. Figure 4.19 illustrates the chloride concentration versus depth. It may be observed that the chloride percentage by weight at 50.8 mm (2.0 in.) is negligible. For conventional concrete, total integral chloride to 38.1 mm (1.5 in.) depth is higher than 0.8% (Myers, 1998).

Table 4.13. Test Results for Chloride Ion Penetration

Specimen ID (specimen #)	Casting Date	Chloride Percent (% by weight)		
		Depth from the Surface of the specimens		
		0.065 to 0.5 in.	0.5 to 1.0 in.	1.0 to 1.5 in.
S3- PC -1	6-20-01	0.143	0.037	0.012
S5- PC -1	7-3-01	0.136	0.020	0.008
Average for HPC for girders		**0.140**	**0.029**	**0.010**
SD- PC -1	9-11-01	0.161	0.045	0.022
Average for the CIP deck		**0.161**	**0.045**	**0.022**

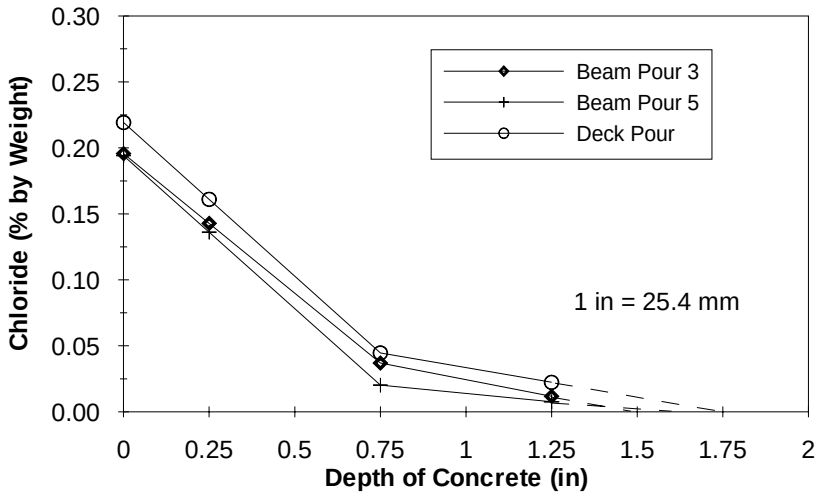

Figure 4.19. Ponding Chloride for HPC Precast Girders

4.11. SCALING RESISTANCE

The scaling resistance test results for each specimen are presented in Table 4.14. A representative specimen after 50 cycles is shown in Figure 4.20.

The average visual condition rating was 2 for the specimens sampled from HPC mix design used in precast girders. Based on ASTM C672 rating scale 0-5, the average visual condition rating was 0 for the specimens sampled from HPC mix design for CIP deck, which meant no scaling. These test results demonstrate the high scaling resistance of HPC.

Table 4.14. Test Results for Scaling De-Icing Resistance

Specimen ID (specimen #)	Casting Date	Weight Loss after 50 Cycles	Condition of Surface after 50 Cycles
S3-DI-1	6-20-01	10.3%	3
S3-DI-2		2.7%	0
S5-DI-1	7-3-01	11.3%	2
S5-DI-2		13.8%	2
Average of all specimens for HPC for girders			**2**
SD-DI-1	9-11-01	4.6%	0
SD-DI-2		4.7%	0
Average of all specimens for the CIP deck			**0**

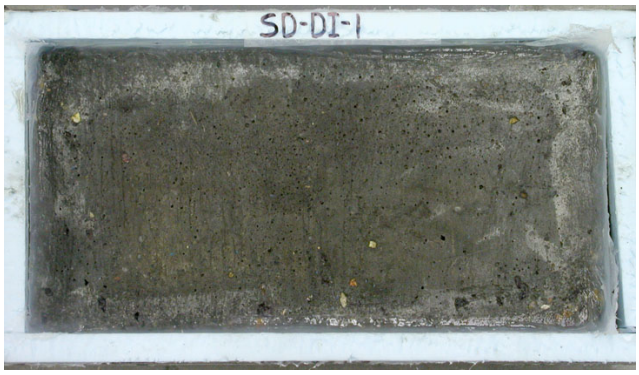

Figure 4.20. Deicer Scaling Resistance for CIP Deck (Visual Rating = 0)

4.12. ABRASION RESISTANCE

A representative specimen after abrasion is illustrated in Figure 4.21. The abrasion resistance test results are listed in following Table 4.15.

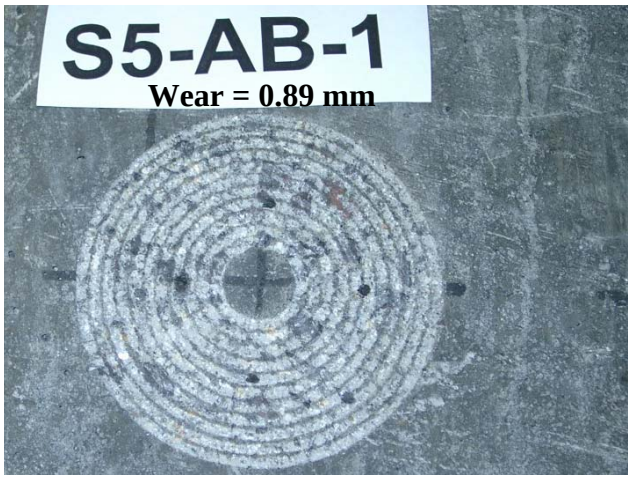

Figure 4.21. Abrasion Resistance Test

Table 4.15. Test Results for Abrasion Resistance

Specimen ID (specimen #)	Casting Date	Weight Loss		Depth of Wear (in.)
		(lb.)	Percent	
S3-AB-1	6-20-01	0.10	0.26	0.014
S3-AB-2		0.05	0.13	0.015
S3-AB-3		0.30	0.76	0.036
S5-AB-1	7-3-01	0.10	0.26	0.035
S5-AB-2		0.05	0.13	0.020
S5-AB-3		0.10	0.26	0.036
Average for HPC for girders		**0.12**	**0.30**	**0.026 (0.66 mm)**
SD-AB-1	9-11-01	0.15	0.41	0.062
SD-AB-2		0.15	0.41	0.050
SD-AB-3		0.15	0.40	0.045
Average for the CIP deck		**0.15**	**0.41**	**0.054 (1.36 mm)**
AB: abrasion resistance. 1 inch = 25.4 mm; 1 pound = 0.4536 kg				

4.13. SUMMARY

Based on the test results for the girder concrete and deck concrete, the HPC used for the bridge can be defined according FHwA grade as shown in Table 4.16.

As a result, based on the FHwA HPC performance grade (Goodspeed et al. 1996), the precast girder concrete may be classified as Grade 2 HPC and the cast-in-place deck concrete may be classified as Grade 1 HPC.

The relationships between modulus of elasticity, splitting tensile strength and compressive strength were studied for both lightweight concrete and normal weight concrete. Fit curves gave a better prediction than existing empirical equations.

Creep and shrinkage were found lower than predicted by ACI 209 (1992). Fit curves represent the data well and can be used to calculate creep coefficient and shrinkage strain.

Table 4.16. HPC Used in Bridge A6130 According to FHwA(Goodspeed et al. 1996)

Performance characteristics	FHwA HPC performance grade				Concrete Grade	
	1	2	3	4	Girder	Deck
Freeze-thaw durability	60%<X1<80%	80%<X1			2	2
Scaling resistance	X2=4, 5	X2=2, 3	X2=0, 1		2	3
Abrasion resistance	2.0>X3>1.0	1.0>X3>0.5	0.5>X3		2	1
Chloride penetration	3000>X4>2000	2000>X4>800	800>X4		3	1
Strength	41<X5<55	55<X5<69	69<X5<97	97<X5	3	1
Elasticity	28<X6<40	40<X6<50	50<X6		2	1
Shrinkage	800>X7>600	600>X7>400	400>X7		3	2
Specific creep	75>X8>60	60>X8>45	45>X8>30	30 >X8	4	1

Note:

X1 = relative dynamic modulus of elasticity after 300 cycles

X2 = visual rating of the surface after 50 cycles

X3 = avg. depth of wear in mm (1 mm = 0.03937 in.)

X4 = coulombs

X5 = compressive strength in MPa (1MPa = 145.0377 psi)

X6 = modulus in GPa (1GPa = 145.0377 ksi)

X7 = microstrain

X8 = microstrain per MPa (1MPa = 145.0377 psi)

5. TEMPERATURE MEASUREMENTS

5.1. INTRODUCTION

5.1.1. General. Temperature can have a significant impact on concrete highway bridge structures. Large stresses and strains may results as a structure heats or cools, depending on the distribution of temperature and level of restraint present in the structure (Gross 1999). Large stresses may result from the restraint of movement in an indeterminate structure and large strains and deflections may result from the heating or cooling of the structure in a determinate structure (Reynolds and Emanuel 1974). Since a real structure is rarely completely free to move or completely restrained, a combination of strain and stress is usually present. Thermal strains and stresses may result in thermal cracking. The ultimate strength of the bridge components is not generally affected by thermal cracking. However, the serviceability of the structure may be significantly affected because thermal cracking makes the corrosion of reinforcing steel occur and thus reduces the service life of the structure.

High hydration temperatures from 54°C (130 °F) to 99 °C (210 °F) are often developed in members using high-strength concrete (HSC) since large quantities of cementitious materials (up to 60% by weight more than conventional concrete) are typically used. High temperature development during hydration can have a significant impact on the early-age and long-term strength gain of the concrete (Myers, 1998). In regards to structure behavior, high hydration temperatures can result in permanent deformations when the structure cools. In addition, if the cooling of a member shortly after hydration is restrained, thermal cracking may result.

Continual transfer of heat between a bridge structure and the surrounding environment occurs throughout the structure service life. Radiation, conduction and convection all contribute to this transfer of heat energy, but radiation is generally considered to be the most important of these three mechanisms (Imbsen et al. 1985). The heating of the superstructure is thus influenced by several factors, including solar radiation, ambient temperature, wind speed, material properties, surface characteristics, and section geometry (Priestly 1978). Variations in environmental conditions lead to two basic thermal cycles for any bridge structure: the seasonal (or annual) cycle, and the diurnal (or daily) cycle (Gross 1999).

The seasonal cycle is governed mainly by the Earth's orientation and orbit. Ambient temperatures are highest during the summer months and lowest during the winter months. Average bridge temperatures follow the same basic trend. Bridge structures must be designed to accommodate the axial movements associated with this seasonal cycle, which in real design is stress resulting from the restraint of these movements.

The daily temperature cycle is mainly governed by the path of the sun in the sky at the bridge site and the changes in ambient conditions during the course of the day and night. In a typical morning and afternoon, the surface of the bridge deck heats up by 30 – 50 % rapidly due to the solar radiation and the increase in ambient temperature (Gross, 1999). The lower portions of the superstructure are shaded from direct sunlight and thus warm much more slowly. This uneven heating results a non-uniform temperature distribution, or temperature gradient, through the depth of the superstructure. Similarly, an opposite gradient may be produced around sunset. Thermal gradient produce a

combination of axial and flexural stresses and strains through the depth of the structure. Though these stresses and strains are temporary in nature, their magnitude can exceed those produced from live loads in certain cases (Radolli and Geen 1975).

For bridge A6130, there is no asphalt wearing surface. The concrete deck is under direct sunlight. This would decrease the deck temperatures.

5.1.2. Ambient Temperature Data. Measurement of ambient temperature requires an instrument shelter which is well-ventilated and protects the temperature measuring device from any exposure to radiation. Since there was no convenient location at a jobsite to properly measure ambient temperature in an automated fashion, the ambient temperature at the jobsite was not measured as part of the instrumentation program. Ambient temperature data was obtained from the National Climatic Data Center (NCDC) monitoring station close to the bridge site. Although the measurements do not represent exact jobsite conditions, the differences are less than 1.5°C (2.7°F) as stated by NCDC.

5.2. HYDRATION TEMPERATURES

5.2.1. Background. The hydration of portland cement is highly exothermic and can be summarized as a process occurring in five phases (Gross, 1999). Phase one is a period in which heat is rapidly evolved during initial mixing. Phase two is a dormant period of several hours during which the concrete remains plastic. Phase three is an acceleration phase when the calcium silicate in the cement begins to react vigorously with water until a maximum rate of heat evolution is reached. Then the rate of heat evolution slows but the generated heat continues to raise the concrete temperature until

the peak hydration temperature occurs. In phase five, heat generation is minimal and the concrete loses heat until a state of equilibrium is reached with the surrounding environment (Lachemi et al. 1996).

High strength concrete (HSC) exhibits relatively high hydration temperature development due to their high cementitious contents, which has peak hydration temperature higher than 66 °C (150 °F) (Gross, 1999). According to ACI Committee 363 (ACI 363R-92 1992), temperature rise during hydrating for high-strength concretes ranges from 10 to 14 °C per 100 kg/m^3 of cement (11 to 15 °F per 100 lb/yd^3 of cement). Some other researchers have recorded peak hydration temperatures in massive HSC columns and footings in the range of 66 to 95 °C (150 to 203 °F).

Hydration temperature and compressive strength are related both at early-age and later-age. During placing and setting a high temperature will increase the early-age strength, but may adversely affect the strength after about seven days (Neville 1981). High hydration temperatures can lead to cracking in structural members when restraint is present.

5.2.2. Measurements. As described in Section 3, hydration temperatures were measured using thermocouples and thermistors every 6 minutes. A thermocouple, labeled as EX-BS, was tied to an external bottom strand, which was between two girder ends on the same prestressing bed outside the girder mold but inside the curing tarps. It also considered the effect of steam curing. The hydration curve for the concrete at the bottom strand level was collected using a thermocouple attached to one bottom strand in the girder, at a section 3.05 m (10 ft) away from the girder end as shown in Figure 5.1. The thermocouple was labeled as IN-BS.

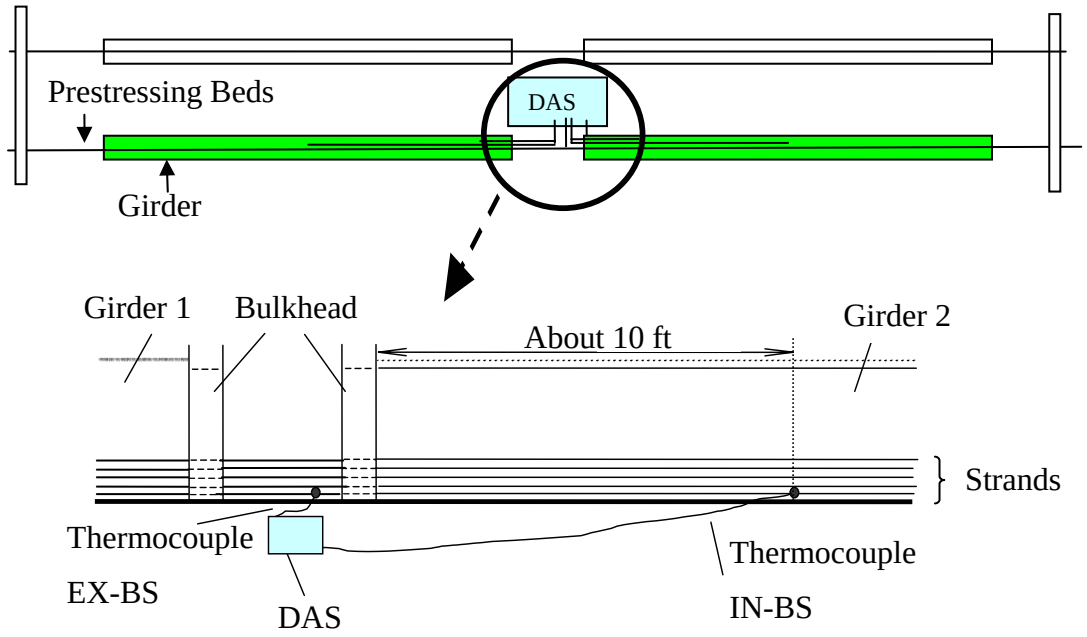

Note: Drapped strands and other gagues not shown for clarity.

Figure 5.1. Thermocouples EX-BS and IN-BS

Based on the data collected at the precast plant, typical hydration curves for the HPC MoDOT Type 2 girders are shown in Figures 5.2 and 5.3. Since all the casting beds had an indoor environment, the temperature in the casting plant was relatively stable (± 2.5 °C). Therefore, hydration curves were similar in shape to what might be expected under adiabatic conditions because the hydration development was not affected by environmental temperature.

In Figure 5.2, hydration profiles at the mid-span section of girder B23 are presented. Six locations were instrumented with VWSG along the height of the section as previously described. These include the top flange, top web, middle web, c.g of the section, c.g of prestressing strands, and bottom flange. In addition, the temperature inside mold and outside mold was also monitored and recorded using thermocouples EX-BS and IN-BS. The temperature increased up to a peak temperature of 53 °C (127 °F) during

hydration for girder B23 concrete. The variation in temperature distribution within the member was about 9 °C (16 °F), which is not dramatic due to the size and shape of the member. That is consistent with other studies on similar type I-shaped sections (Burns et al. 1997).

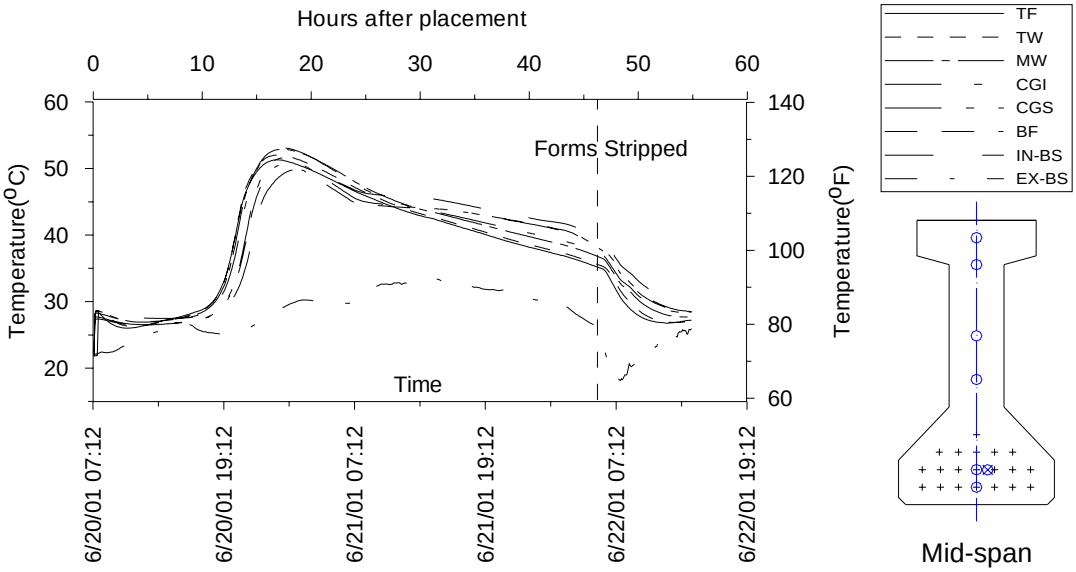

Figure 5.2. Measured Hydration Temperatures in Mid-Span Section of Girder B23

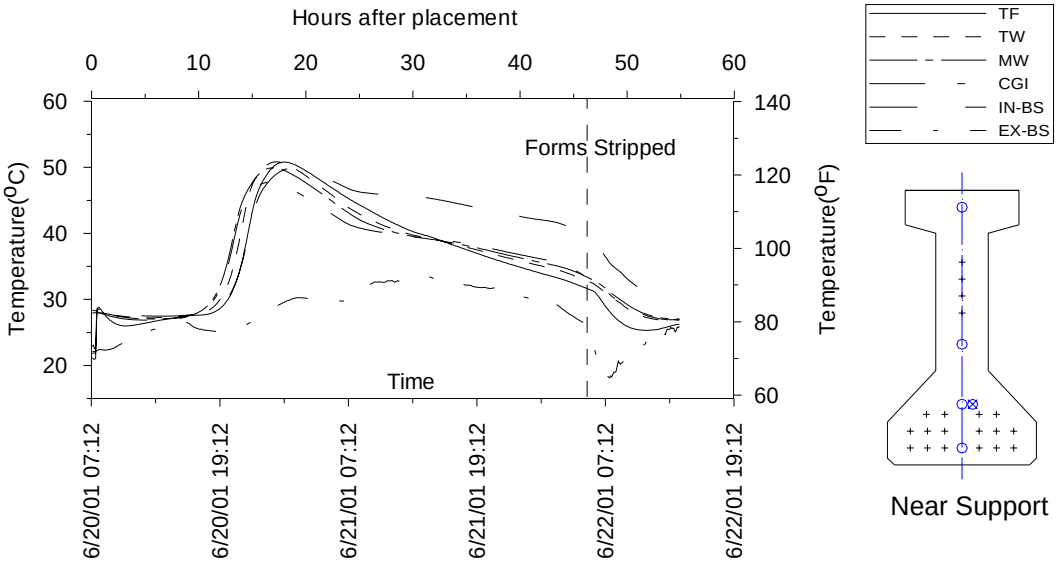

Figure 5.3. Measured Hydration Temperatures in Near Support Section of Girder B23

Table 5.1. Summary of Measured Hydration Temperatures for HPC Girders

Girder	B21	B22	B23	B24	B13	B14
Casting Date	6/13/01	6/13/01	6/20/01	6/20/01	7/3/01	7/3/01
Placement Time	7:30 am	7:45 am	7:10 am	7:30 am	7:20 am	7:00 am
Avg. Placement Temp.	85 °F	85 °F	82 °F	81 °F	81 °F	80 °F
Avg. Temp. at End of Dormant Phase	86 °F	86 °F	82 °F	82 °F	83 °F	82 °F
Peak Hydration Temp.	134 °F	135 °F	127 °F	134 °F	133 °F	135 °F
Location of Peak Hydration Temp.	MW	MW	CGI	MW	TW	TW
Max. Temp. Rise after Dormant	48 °F	50 °F	46 °F	51 °F	49 °F	53 °F
Maximum Gradient	9 °F	13 °F	16 °F	13 °F	15 °F	15 °F
Maximum Gradient Location	TF-BF	TW-BF	TW-BF	MW-BF	TF-BF	CGI-BF
Temperature: °F = (1.8 * (°C)) + 32; Temp. Change: °F = 1.8 °C						

For the other girders, the measurement results are summarized in Table 5.1. The peak temperature during hydration was 57 °C (135 °F) for girder B14 and girder B22. Maximum hydration temperatures in the six monitored HPC girders ranged from 53 °C to 57 °C (127 °F to 135 °F). The peak temperature was recorded by gauges at the TW or the MW location for most of the girders.

Maximum temperature rise after the dormant period ranged from 26 °C to 29 °C (46 °F to 53 °F). Maximum gradients for most of the girders occurred prior to or at peak hydration temperature. A maximum gradient of 9 °C (16 °F) was observed between the TW and BF gauges locations in girder B23.

The effect of the removal of curing tarps and forms is obvious as shown in Figures 5.2 and 5.3. After removing the tarps and forms, a sharp temperature drop occurred across the depth of the section.

Hydration temperatures were measured in the instrumented CIP bridge decks. Temperatures were measured during hydration in all instrumented spans. The CIP decks were cast on November 11th to 12th 2001 followed by a sunny day. The deck was cast in a single placement operation. A typical hydration profile is shown in Figure 5.4. A summary of all data is presented in Table 5.2.

The average placement temperature and average temperature at the end of dormant phase for the CIP deck were 26 °C (79 °F) and 28 °C (82 °F), respectively. Peak hydration temperature occured at 51 mm (2 in.) below top of deck surface with a value of 48 °C (119 °F). Maximum temperature rise after the dormant period was approximately 18 °C (32 °F).

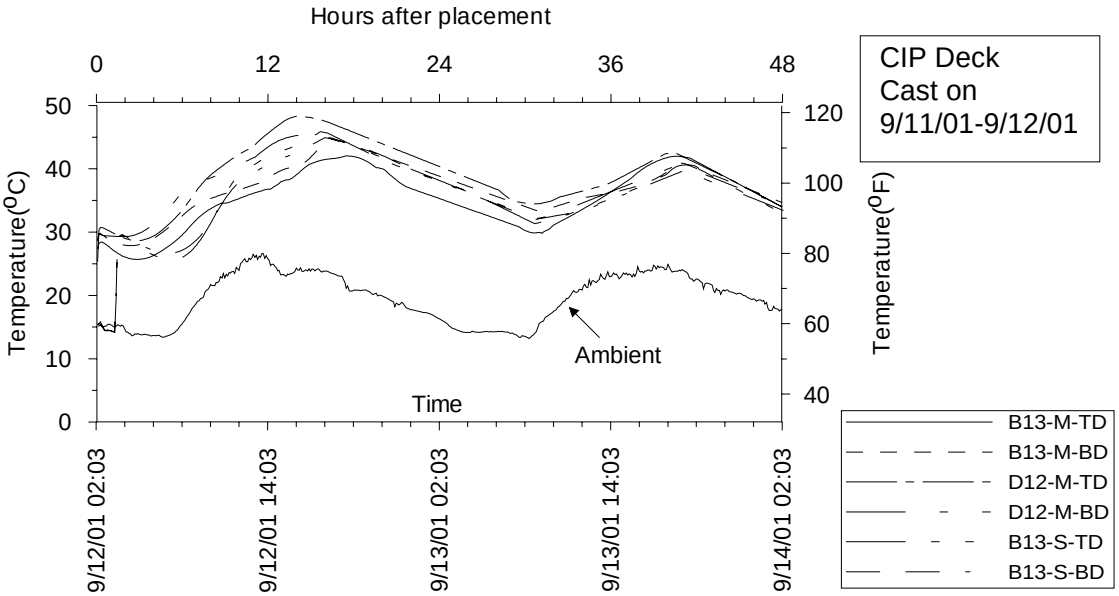

Figure 5.4. Measured Hydration Temperatures in CIP Deck

Table 5.2. Summary of Measured Hydration Temperatures for CIP Deck

Items	CIP Deck
Casting Date and Placement Time	6:30 pm, 9/11/01 – 5:00 am, 9/12/01
Avg. Placement Temperature	79 °F
Avg. Temp. at End of Dormant Phase	82 °F
Peak Hydration Temperature	119 °F
Location of Peak Hydration Temperature	2 inches below top of deck surface
Maximum Temp. Rise after Dormant Period	32 °F
Maximum Gradient	6 °F
Temperature: °F = (1.8 * (°C)) + 32; Temp. Change: °F = 1.8 °C	

5.2.3. Discussion. The maximum measured hydration temperature in the HPC prestressed girders was 57 °C (135 °F) and the measured temperature gains after the end of the dormant period ranged from 26 °C (46 °F) to 29 °C (53 °F). Equivalent maximum temperature rises ranged from 5.1 to 5.9 °C per 100 kg/m^3 (5.4 to 6.2 °F per 100 lb/yd^3) of cement. For the HPC CIP deck, maximum temperature rise after dormant period was about 18 °C (32 °F). Equivalent maximum temperature rises 5.4 °C per 100 kg/m^3 (5.7 °F per 100 lb/yd^3) of cement, or 4.6 °C per 100 kg/m^3 (4.8 °F per 100 lb/yd^3) of total cementitious material. These equivalent maximum temperatures are well below (by 45-60%) values suggested by ACI Committee 363 (1992).

The maximum hydration temperature developed is lower in part due to the use of supplementary cementitious materials and the less massive section shape.

All the girders were cast early in the morning, from 7:00 am to 8:00 am, when the ambient temperature was still mild. This helped to reduce the prestress losses before prestress release. Further discussion is presented in Section 7 on this topic.

Cracking was observed on almost all instrumented girders as a result of the restraint provided by the bed against contraction due to cooling and drying shrinkage coupled with the time of release. However, these cracks closed entirely after release. No structural impact was observed as a result of this cracking and none should be expected. This phenomenon is further discussed in Section 6.

5.3. MEAN BRIDGE TEMPERATURES

5.3.1. Background. It is important for designers to realize the importance of mean bridge temperatures, which is essential for the prediction of axial bridge movements during the seasonal temperature cycle. Usually, the axial movements are accommodated by the use of expansion joints and/or flexible supports, such as sliding plates and elastomeric bearing pads. Analysis of expected forces and deformations required that approximate values of the extreme average bridge temperatures be known, as well as the approximate average temperatures of the structure at the time of girder erection and deck casting.

The AASHTO Standard Specifications (1996), Section 3.16, addresses:

> 3.16 THERMAL FORCES
>
> Provision shall be made for stresses or movements resulting from variations in temperature. The rise and fall in temperature shall be fixed for the locality in which the structure is to be constructed and shall be computed from an assumed temperature at the time of erection. Due consideration shall be given to the lag between air temperature and the interior temperature of massive concrete members or structures.
>
> The range of temperatures shall generally be as follows:

Metal Structures

Moderate climate, from 0 to 120 °F
Cold climate, from -30 to 120 °F

Concrete Structures

	Temperature Rise	Temperature Fall
Moderate climate	35 °F	45 °F
Cold climate	35 °F	45 °F

Note that the moderate and cold climate designations are not defined in either the AASHTO code or the commentary. Thermal load is to be considered in three service load combinations, as specified in Section 3.22 of the AASHTO Standard Specifications. Design for axial temperature effects is also mentioned briefly in the section of the AASHTO Standard Specifications dealing with prestressed concrete as in Section 9.5.1. It states that in all bridges provisions shall be made in the design to resist thermal stresses induced, or means shall be provided for movement caused by temperature changes.

For uniform temperature changes, the AASHTO LRFD Specifications (1994), Section 3.12.2, addresses:

3.12.2 Uniform Temperature

3.12.2.1 TEMPERATURE RANGES
In the absence of more precise information, the ranges of temperatures shall be as specified below. The difference between the extended upper or lower boundary and the base construction temperature assumed in the design shall be used to calculate thermal deformation effects.

Temperature Ranges

CLIMATE	STEEL OR ALUMINUM	CONCRETE	WOOD
Moderate	0 to 120 °F	10 to 80 °F	10 to 75 °F
Cold	-30 to 120 °F	0 to 80 °F	0 to 75 °F

The AASHTO LRFD Specification (1994) introduced the concept of a setting temperature and clearly stated that the temperature ranges are intended only to be a general guide in the absence of more precise information.

In the AASHTO LRFD Specification, uniform temperature effects are considered in all strength and service load combinations. A load factor of 1.2 is specified for deformation considerations and 1.00 for all other effects in the service limit states. In the strength limit states, load factors of 1.20 for deformation considerations and 0.50 for all other effects are specified. These load combinations and factors represent the fact that temperature effects are always present in a structure, but reflects the low probability that maximum loading of all types, including uniform temperature loading, will act on a structure simultaneously. The lower load factors for the strength limit states reflect the fact that temperature effects will generally cause serviceability damage to a structure, but not significantly reduce the ultimate strength.

National Cooperative Highway Research Program (NCHRP) Report 276 (Imbsen et al. 1985) examined the effects of thermal effects in concrete bridge superstructures. This report recommended that all concrete bridges shall be designed to accommodate the stresses and movements resulting from a fluctuation in the effective bridge temperature. The values for the anticipated minimum and maximum effective bridge temperatures are dependent on the type of construction and on the minimum and maximum normal air temperatures at the bridge site. If more precise climatic data is unavailable, the normal daily minimum temperature for January and the normal daily maximum temperature for July can be estimated at a given location in the United States using two isotherm maps provided in the guidelines.

With the construction of the first HPC bridge in Texas, thermal behavior of the bridges was studied including mean bridge temperature and thermal gradients (Gross 1999). A simple method for estimating bridge mean temperature was recommended by Gross (1999). In this method, the design maximum temperature for a bridge was suggested as 2.8 °C (5 °F) higher than the average of daily maximum ambient temperature in July and the maximum ambient temperature ever recorded at the bridge location. Similarly, the minimum design temperature is computed as the average of daily minimum ambient temperature in January and the minimum ambient temperature ever recorded at the bridge location.

5.3.2. Measurements. Bridge temperatures were measured using thermocouples and thermistors after the bridge was constructed. Temperatures were generally recorded every 15 minutes or every one hour at later-ages. During the monitoring period, there are some days without valid data because the power for the DAS was accidentally turned off by the contractor. However, during this period, at least one set of valid data were obtained for all months of a year.

For each set of readings at a composite section of a girder and corresponding deck portion, an average bridge temperature was calculated. The average bridge temperature can be defined as a weighted mean of the temperatures at different depths of the composite cross-section, and is computed as the sum of the products of each measured temperature within the cross-section and its given weights. Weights were computed for each layer using the proportion of the total transformed area present in the given layer. Weights used for calculating the bridge mean temperature can be found in Table 5.3. It

was found that total contribution of the deck temperatures to the average bridge temperatures was about 70%.

Table 5.3. Weights Used for Calculation of Average Bridge Temperature

Layer	Weight	CIP Deck
Layer 1	0.350	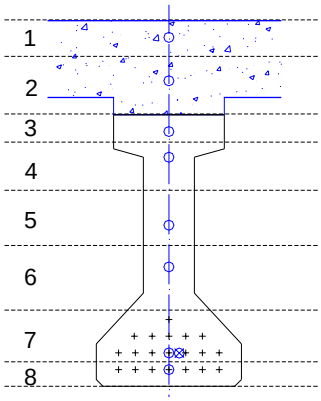
Layer 2	0.370	
Layer 3	0.035	
Layer 4	0.030	
Layer 5	0.030	
Layer 6	0.060	
Layer 7	0.074	
Layer 8	0.051	

Daily maximum and minimum temperatures for girder B13 are shown in Figure 5.5 and Figure 5.6, respectively, from September 2001 through February 2003. General trends may be observed in these figures, especially the difference during the summer as discussed in the next paragraph. Average daily maximum and minimum temperatures for girder B13 were computed for each calendar month and illustrated in Figure 5.7 and Figure 5.8. The maximum temperatures tend to occur during the middle of the summer, typically in July. During this period, the maximum average bridge temperature tended to be approximately 7 °C (12 °F) warmer than the maximum ambient temperatures. However, during the winter months from December through February, there was essentially no difference between the maximum average bridge temperatures and the maximum ambient temperatures. The average daily minimum temperature tended to

remain higher than the minimum ambient temperature. On average, the difference was about 6 °C (10 °F) during summer month, and about 4 °C (8 °F) during the winter month.

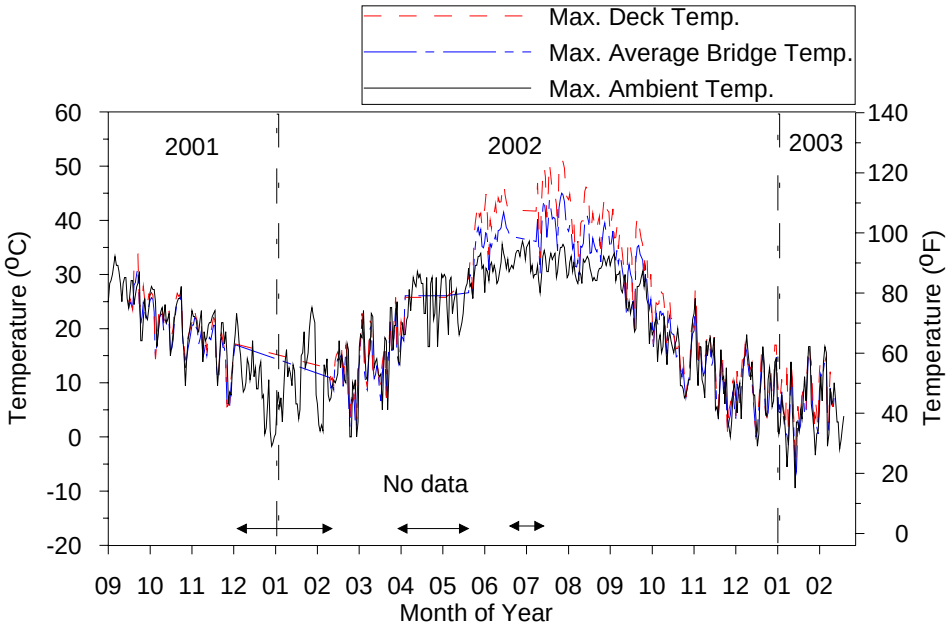

Figure 5.5. Maximum Daily Temperature of Composite Girder B13

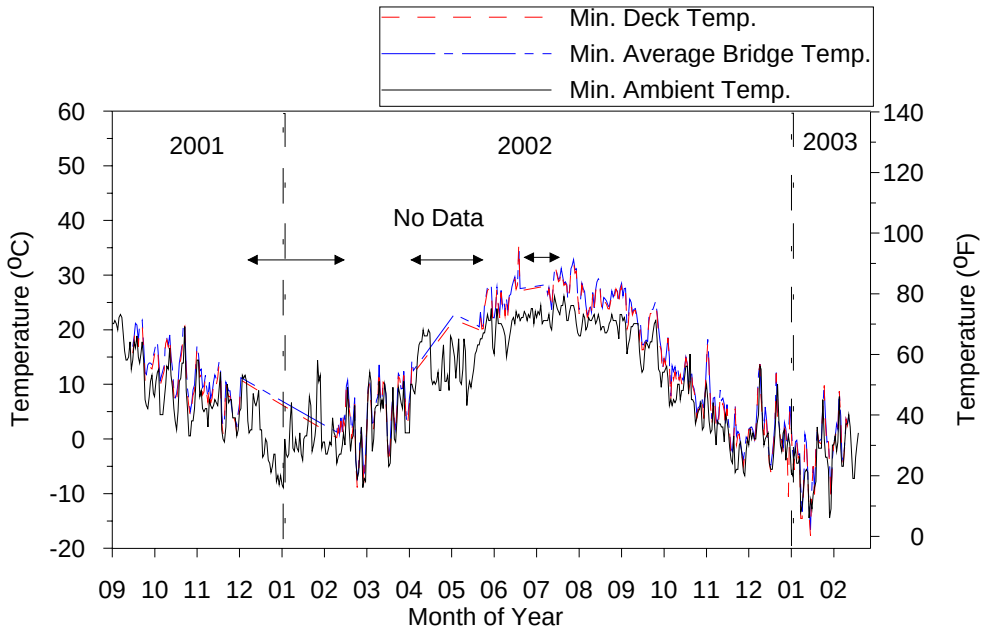

Figure 5.6. Minimum Daily Temperature of Composite Girder B13

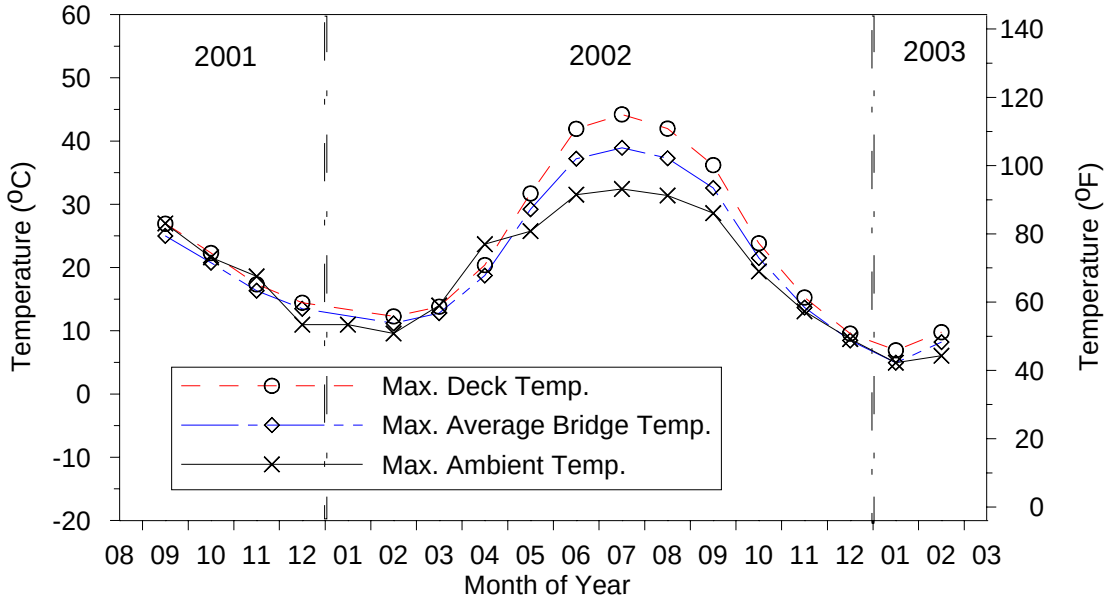

Figure 5.7. Average Maximum Daily Temperature by Month of Composite Girder B13

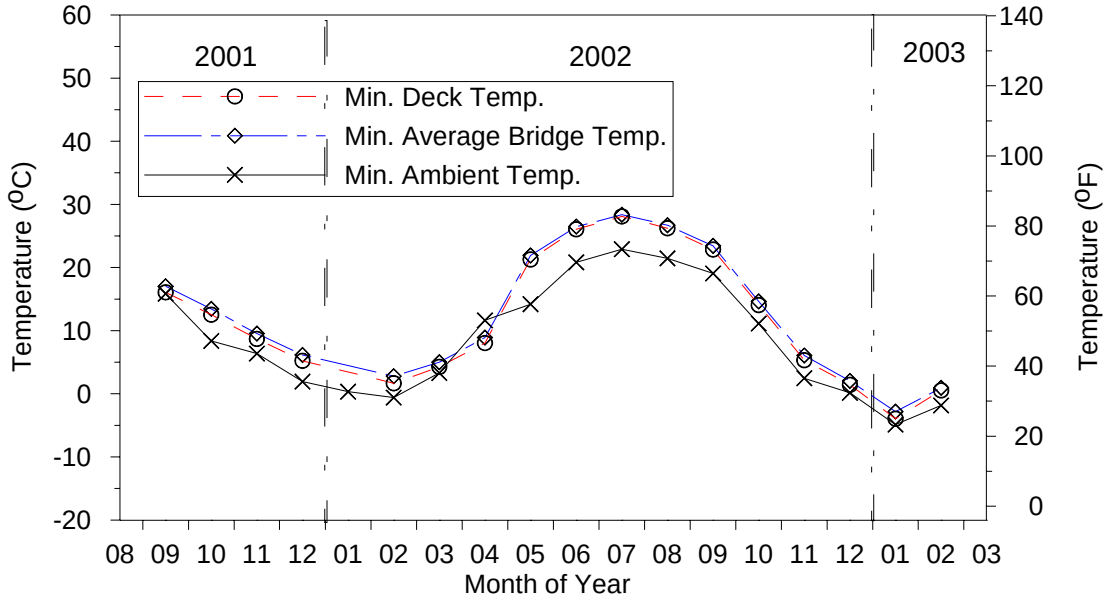

Figure 5.8. Average Minimum Daily Temperature by Month of Composite Girder B13

For the other composite girders, the mean bridge temperature are illustrated in Appendix F including maximum average bridge temperature, minimum average bridge temperature, and daily temperatures averaged by month.

Maximum average bridge temperatures measured on any singe day were 45 °C (118 °F), 44 °C (117 °F), 42 °C(108 °F) and 42 °C(108 °F) for girders B13, B14, B23 and B24, respectively, as listed in Table 5.4. Minimum average bridge temperature measured were 17 °C (63 °F), 14 °C (57 °F), 16 °C(61 °F) and 14 °C(57 °F) for girders B13, B14, B23 and B24, respectively as shown in Table 5.5.

Table 5.4. Comparison of Maximum Measured Temperatures

	Girder Description			
	B13	B14	B23	B24
Absolute Maximum Temperature				
Measured Deck Temperature	51.33	48.09	45.37	43.74
Calculated Average Bridge Temperature	45.01	44.29	42.43	41.70
Ambient Temperature	36.11	36.11	36.11	36.11
Lowest Daily Maximum Temperatures				
Measured Deck Temperature	-4.32	-8.91	-4.91	-9.37
Calculated Average Bridge Temperature	-6.41	-8.26	-6.34	-8.63
Ambient Temperature	-9.44	-9.44	-9.44	-9.44
Highest Average Daily Maximum Temperatures for a Calendar Month				
Measured Deck Temperature	44.22	40.60	39.49	37.46
Calculated Average Bridge Temperature	38.94	37.72	37.23	35.77
Ambient Temperature	32.42	32.42	32.42	32.42
Lowest Average Daily Maximum Temperatures for a Calendar Month				
Measured Deck Temperature	6.91	2.73	5.60	2.25
Calculated Average Bridge Temperature	4.95	3.31	4.71	2.96
Ambient Temperature	4.95	4.95	4.95	4.95
All temperatures in ^{o}C. °F = °C*1.8 + 32				

Table 5.5. Comparison of Minimum Measured Temperatures

	Girder Description			
	B13	B14	B23	B24
Absolute Minimum Temperature				
Measured Deck Temperature	-17.73	-14.35	-17.47	-14.82
Calculated Average Bridge Temperature	-16.59	-13.73	-16.37	-14.35
Ambient Temperature	-14.44	-14.44	-14.44	-14.44
Highest Daily Minimum Temperatures				
Measured Deck Temperature	35.70	36.23	33.95	33.67
Calculated Average Bridge Temperature	34.37	33.58	33.80	31.99
Ambient Temperature	26.11	26.11	26.11	26.11
Lowest Average Daily Minimum Temperatures for a Calendar Month				
Measured Deck Temperature	-3.95	-2.63	-3.40	-3.22
Calculated Average Bridge Temperature	-2.82	-2.08	-2.84	-2.57
Ambient Temperature	-4.89	-4.89	-4.89	-4.89
Highest Average Daily Minimum Temperatures for a Calendar Month				
Measured Deck Temperature	28.10	29.14	25.17	27.00
Calculated Average Bridge Temperature	28.37	28.79	26.07	27.61
Ambient Temperature	22.90	22.90	22.90	22.90
All temperatures in ^{o}C. $°F = °C*1.8 + 32$				

5.3.3. Discussion. As discussed in Section 5.1, different methods for bridge mean temperature are suggested by AASHTO standard specification (1996), AASHTO LRFD Specifications (1994), NCHRP Report 276 (Imbsen et al. 1985) and Gross (1999). Design values are computed and summarized in Table 5.6 based on these methods. Measured average bridge temperatures in this study are also listed in Table 5.6.

It can be found that the designed temperature increases and decreases suggested in the AASHTO Standard Specifications underestimated the maximum increases and decreases that were observed in the bridge. The philosophy of these code provisions is

questionable since the extreme temperatures are independent of the setting temperature. When the setting temperature is very high or very low, this method could underestimate the corresponding temperature increase or decrease. The methods suggested in the LRFD Specification and NCHRP Report 276 Method are also inappropriate for the bridge locations monitored.

Table 5.6. Comparison of Measured Temperatures and Design Temperatures

	Max. Tmep.		Min. Tmep.	
	B13	B14	B13	B14
Historical Climate Data (Ambient Temperatures)				
Extreme Ambient Temp. Ever Recorded	111	111	-15	-15
Avg. Extreme Ambient Temp. for Peak Month	91	91	27	27
Measured Average Bridge Temperatures (9/01 - 02/03)				
Extreme Average Bridge Temp.	113	112	2	7
Avg. Daily Bridge Temp. for Peak Month	102	100	27	28
Setting Temperature	71	71	71	71
Temp. Changes Relative to Setting Temp.	42	41	-69	-64
Design Temperatures				
AASHTO Standard Specifications (1996)	106	106	26	26
AASHTO LRFD Specifications (1994)	80	80	0	0
NCHP Report 276 (Imbsen et al. 1985)	92	92	30.5	30.5
Suggested By Gross (1999)	106	101	6	6
Suggested By Author	111	111	6	6
All temperatures in °F. °C = (°F – 32)/1.8				

A simple approach is suggested for the determination of maximum and minimum design temperatures for the analysis of uniform axial effects by Gross (1999) after monitoring four HPC bridges in Texas. The designed maximum temperatures using this method underestimated the maximum temperatures that were observed in the bridge.

However, the method for estimating minimum temperatures suggested by Gross (1999) is appropriate for the bridge monitored in this study as summarized in Table 5.6.

A modified approach based on the method suggested by Gross (1999) is developed by author to provide more realistic design temperatures than the current methods previously discussed. It is not intended to exactly predict the extreme average bridge temperatures that may occur in the lifetime of a bridge structure. Further experimental data is necessary to validate this approach. The design maximum and minimum temperature can be calculated by the following equations:

$$T_{design,\max} = \frac{1}{2}(T_{July,\max} + T_{all-time,\max}) + 10^{o}F \qquad \text{Equation 5.1}$$

$$T_{design,\min} = \frac{1}{2}(T_{Jan,\min} + T_{all-time,\min}) \qquad \text{Equation 5.2}$$

where,

$T_{July,\max}$ = the average daily maximum ambient temperature in July at the bridge location

$T_{Jan,\min}$ = the average daily minimum ambient temperature in January at the bridge location

$T_{all-time,\max}$ = the maximum ambient temperature ever recorded at the bridge location

$T_{all-time,\min}$ = the minimum ambient temperature ever recorded at the bridge location

The calculated temperatures using above method are illustrated in Table 5.6 and correlate well with the extreme average bridge temperatures monitored in this study. Figure 5.9 illustrates this trend using the modified approach suggested by the author.

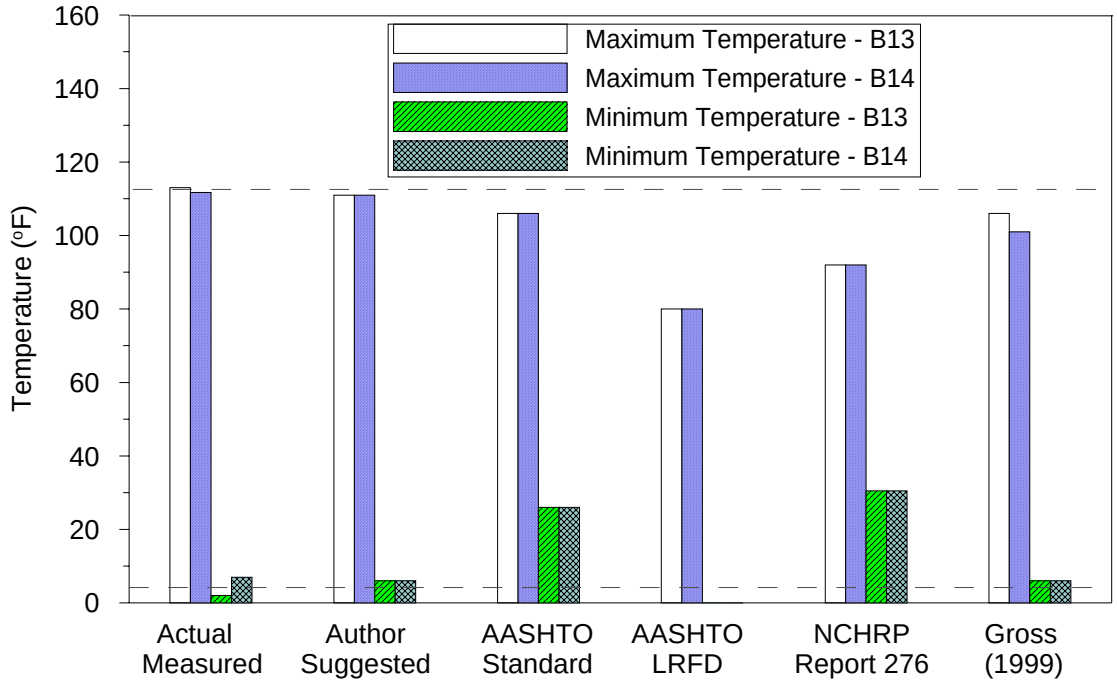

Figure 5.9. Measured Temperatures and Design Temperatures

5.4. THERMAL GRADIENTS

5.4.1. Background. The daily temperature cycle leads to thermal gradients in a structure. During a sunny day, the bridge deck heats up much more quickly than the underside of the bridge and thus a positive thermal gradient results (Imbsen, et al. 1985). The magnitude of this gradient depends on the amount of radiation absorbed by the deck. A darker, rougher deck surface generally has a higher absorptivity than a lighter, smoother surface (Radolli and Green 1975). Positive gradients are typically significant during the summer, ranging from 21 to 31 °C (38 to 55 °F), when the amount of solar radiation is at a maximum (Imbsen et al. 1985).

When a bridge superstructure that had obtained a high temperature during the day experiences a reduction in temperature caused by a cool night, a negative gradient (deck cooler than underside) may develop. Because the surface of bridge deck is typically much

larger than for the rest of the superstructure, the deck loses heat more quickly. Its temperature may drop below the temperature of the rest of the superstructure, resulting in a negative gradient. Since the negative gradient is dependent on the temperature distribution in the structure at the time when cooling begins, as well as the difference between concrete and ambient temperatures, its magnitude is highly variable (Imbsen et al. 1985).

A set of thermal gradients for use as part of the design guidelines were presented in NCHRP report 276 (Imbsen et al. 1985) as shown in Figure 5.10. Thermal gradients are not mentioned in the AASHTO Standard Specifications (1996), but are addressed in detail in the AASHTO LRFD Specifications (1994). In Section 3.12.3 of the LRFD Specifications, design for thermal gradients can be found as shown in Figure 5.11. Actually, the form of the design positive gradient in LRFD specification is a modified version of the positive gradient suggested in the NCHRP report.

In Section 3.4.1 of the LRFD Specification, it can be found that thermal gradients are specified in most of the load combinations. It is also stated in the commentary that, there is general agreement that the in-situ measurements of temperature gradients have yielded a realistic distribution of temperatures through the depths of some types of bridges, but there is very little agreement on the significance of the effect of that distribution. Since cracking, yielding, creep, and other non-linear responses diminish the effects, load factors of less than 1.0 should be considered and there is some basis for lower load factors at the strength and extreme event limit states than at the service limit state.

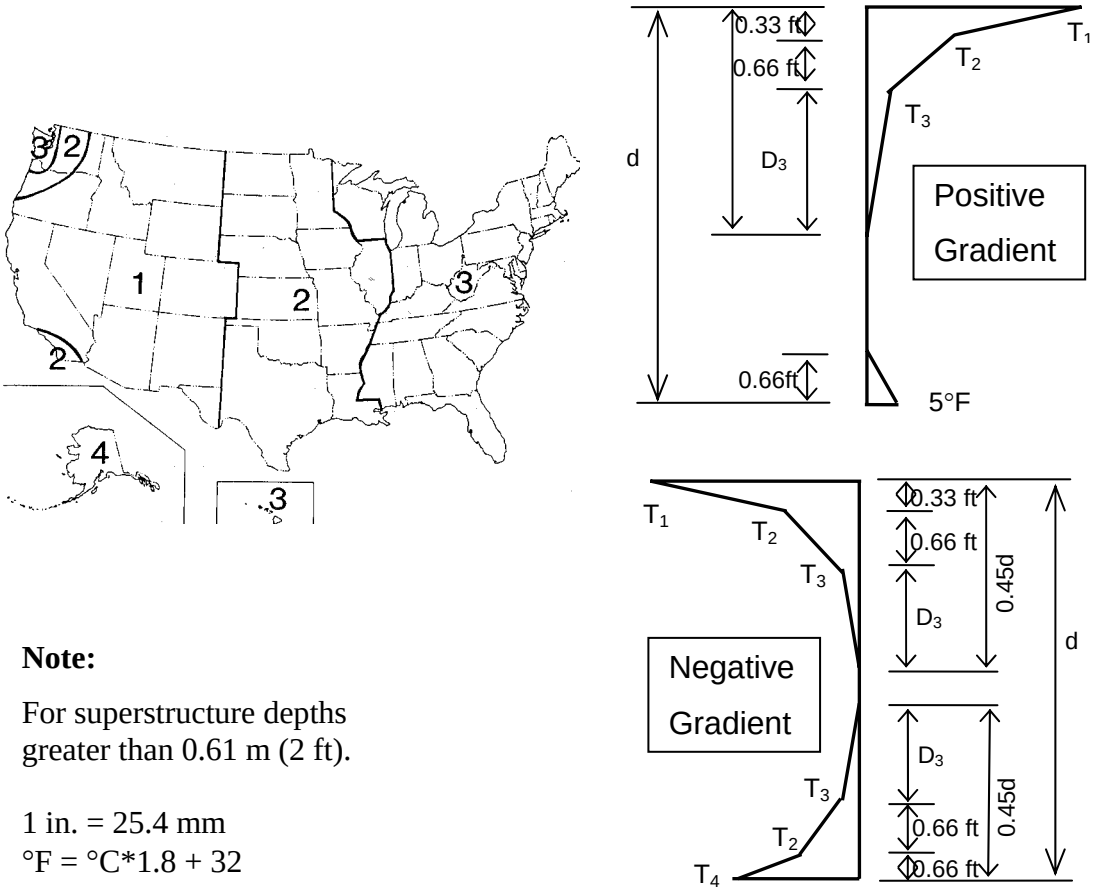

Note:

For superstructure depths greater than 0.61 m (2 ft).

1 in. = 25.4 mm
°F = °C*1.8 + 32

Positive Gradient

Zone	Plain Concrete Surface			2 in. Blacktop			4 in. Blacktop		
	T1	T2	T3	T1	T2	T3	T1	T2	T3
1	54	14	5	43	14	4	31	9	3
2	46	12	4	36	12	4	25	10	3
3	41	11	4	33	11	3	23	11	2
4	38	9	3	29	9	2	22	11	2

Note:
Unit: °F

Negative Gradient

Zone	Plain Concrete Surface				2 in. Blacktop				4 in. Blacktop			
	T1	T2	T3	T4	T1	T2	T3	T4	T1	T2	T3	T4
1	27	7	2	14	22	7	2	15	16	5	1	12
2	23	6	2	10	18	6	2	11	13	5	1	9
3	21	6	2	8	17	6	2	10	12	6	1	8
4	19	5	2	6	15	5	1	8	11	6	1	8

Figure 5.10. Design Thermal Gradients Suggested in NCHRP Report 276 (Imbsen et al. 1985)

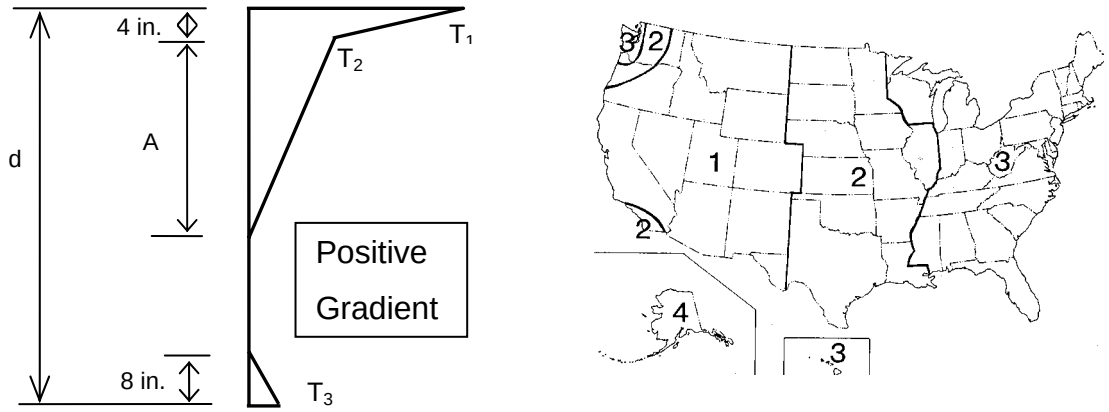

Positive Gradient Unit: °F

Zone	Plain Concrete Surface		2 in. Blacktop		4 in. Blacktop	
	T1	T2	T1	T2	T1	T2
1	54	14	43	14	31	9
2	46	12	36	12	25	10
3	41	11	33	11	23	11
4	38	9	29	9	22	11

Negative Gradient
may be obtained by multiplying positive graient values by -0.5

Note:
1 in. = 25.4 mm
°F = °C*1.8 + 32

Notes:

Dimension "A" shall be taken as:

12.0 in. for concrete superstructures that are 16.0 in. or more in depth

(d-4) in. for concrete superstructures that are less than 16.0 in. in depth

The temperature value T_3 shall be taken as 0.0 unless a site specific study is made to dtermin an appropriate value, but shall not exceed 5°F

Figure 5.11. Design Thermal Gradients Specified in the AASHTO LRFD Specifications

5.4.2. Measurements. In the same manner as for the average bridge temperatures, thermal gradients were measured. Temperatures were recorded at 15 minutes or 1 hour intervals using an automated data acquisition system installed on the bridge.

When the non-composite girders were stored at the precast plant, they were in a outdoor ambient condition. A typical thermal behavior inside the girder is illustrated in Figure 5.12. At the mid-span section of girder B13, temperature at the top fiber reached its peak value at 4:00 PM. Following this, temperatures at all location decreased. The

decreasing rate at the top fiber was higher than that at bottom fiber. Temperatures along the section were close to a constant at 8:00AM in the morning.

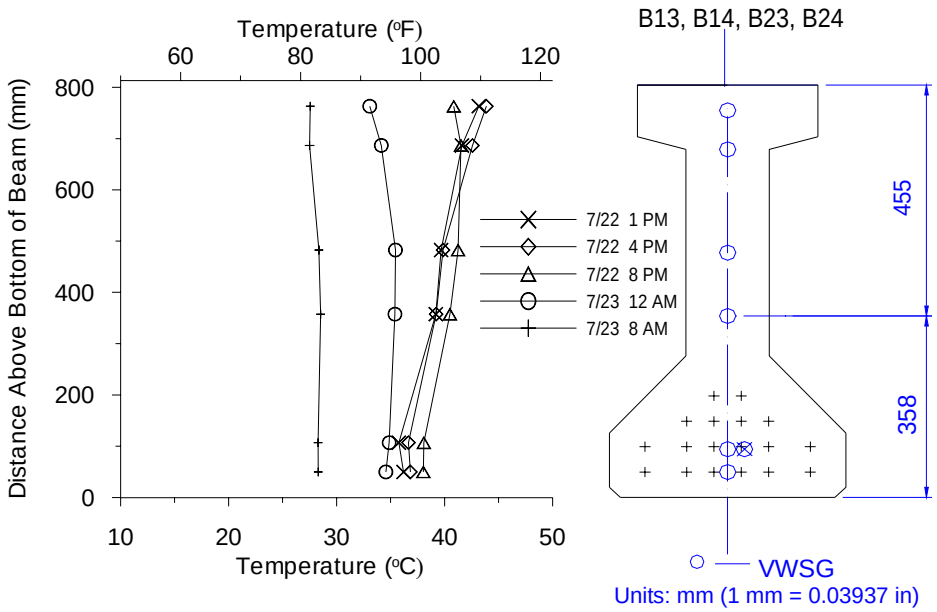

Figure 5.12. Typical Thermal Behavior of Girder B13 in Storage

For the composite girder, typical heating behavior on a sunny summer day and cooling behavior during the subsequent night are shown in Figure 5.13 and Figure 5.14, respectively. On a sunny summer day, at 8:00AM, the temperature along the depth of the section ranged from 23.1 to 24.9 °C (74 to 77 °F). At 12:00PM, at 50 mm (2 in.) below top fiber of the deck, the temperature reached 32.2 °C (90 °F) while the temperature in the girder remained around 24 °C (75 °F). At 4:00PM, the temperature reached 42.1 °C (107 °F) at 50 mm (2 in.) below top fiber of the deck. At the same time, temperature in the girder also increased to 25.8 - 28.1 °C (78 - 83 °F).

A negative gradient exists shortly after sunrise with fairly uniform girder temperatures. Then, the deck heats up quickly by 9.4 °C (17 °F) at noon but changes in

girder temperatures are only 1.6 °C (3 °F). That results in a positive thermal gradient of 8.5 °C (15 °F). In the afternoon, the girder heats up somewhat uniformly while the deck continues to heat at a faster rate than the girder, yielding an increasing of the thermal gradient, which is 16.1 °C (29 °F) at 4:00 PM. When the heat is reradiated to the atmosphere in the late afternoon and early evening hours, the temperature in the deck begins to fall quickly while the girder cools more slowly and uniformly. The deck cools at a more rapid rate due to it higher surface area to volume ratio compared to the girder section. Finally in the early morning a negative gradient was produced.

In a typical cloudy day, thermal behavior of a girder B13 is shown in Figure 5.15. Figure 5.15 illustrates that the thermal gradients at different times of the day varies less than 1.3°C (2°F) since the temperature throughout the entire depth of the section remains relatively constant with variations of only 1.5°C (3°F).

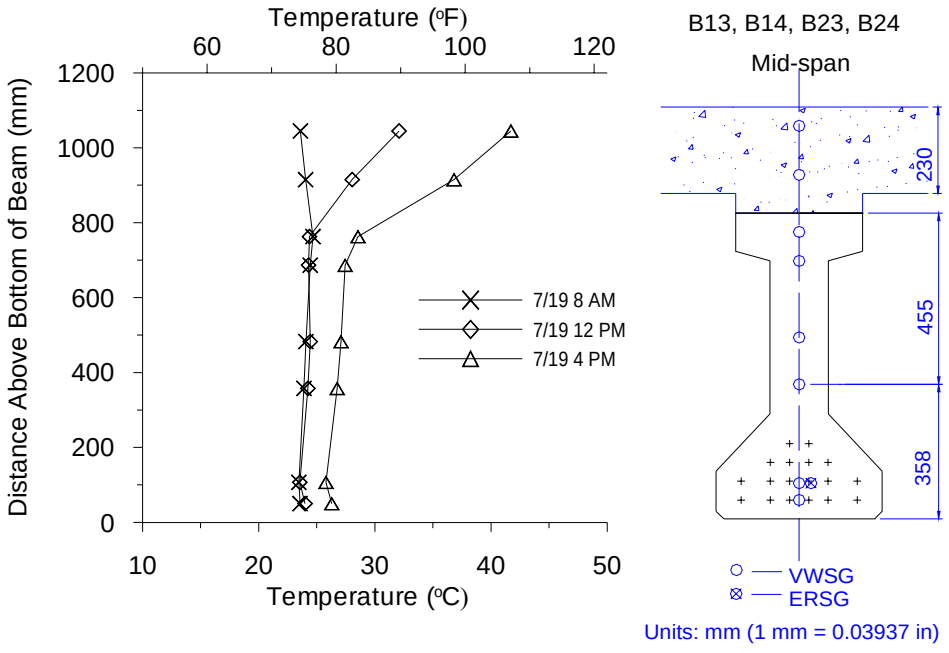

Figure 5.13. Typical Heating Behavior in Girder B13 on a Sunny Summer Day

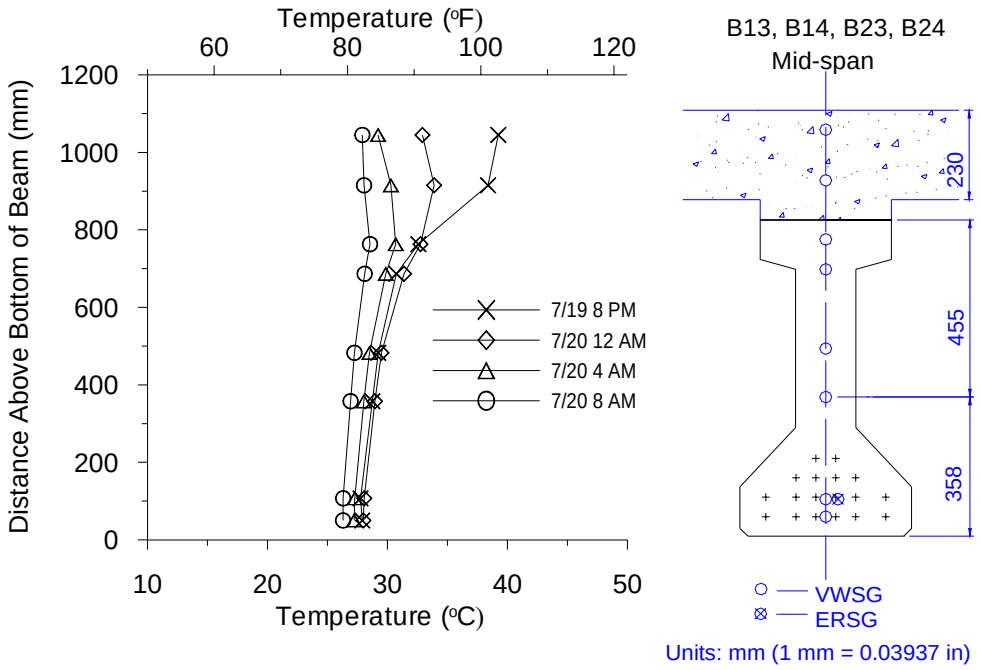

Figure 5.14. Typical Cooling Behavior in Girder B13 Following a Sunny Summer Day

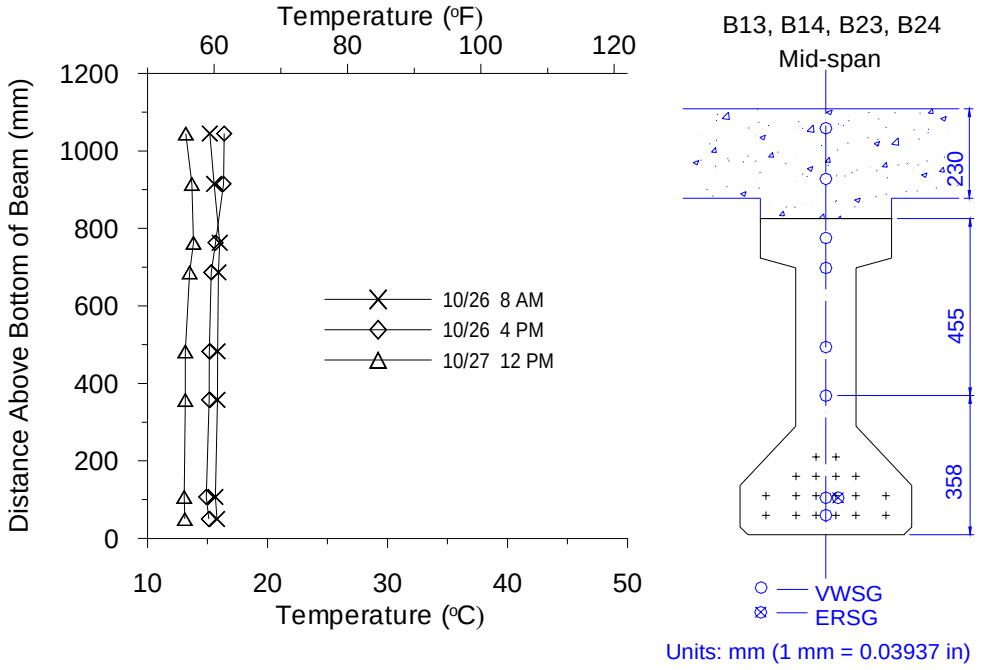

Figure 5.15. Typical Thermal Behavior in Girder B13 on a Cloudy Day

Typical plots of the maximum daily positive and negative thermal gradients measured in the bridge are shown in Figure 5.16 and Figure 5.17. These were obtained from September, 2001 through February, 2003. During this period, at least one set of valid data were obtained for all months of a year. It should be noted that in some days there were no positive gradients especially in winter months. The temperature in the top portion of the bridge section is always lower than the low portion of the bridge section in the winter. This leads to negative thermal gradients throughout the day. Similarly, in the summer months, when the temperature in the top portion of the section is always higher than the lower portion, positive thermal gradients result.

Figure 5.18 illustrates time of maximum daily positive thermal gradients and negative thermal gradients occurrence for girder B13. Maximum daily gradients were averaged by month for the girder and shown in Figure 5.19 for interior girder B13. For the other monitored girders, B14, B23, and B24, thermal gradients recorded are reported in Appendix F.

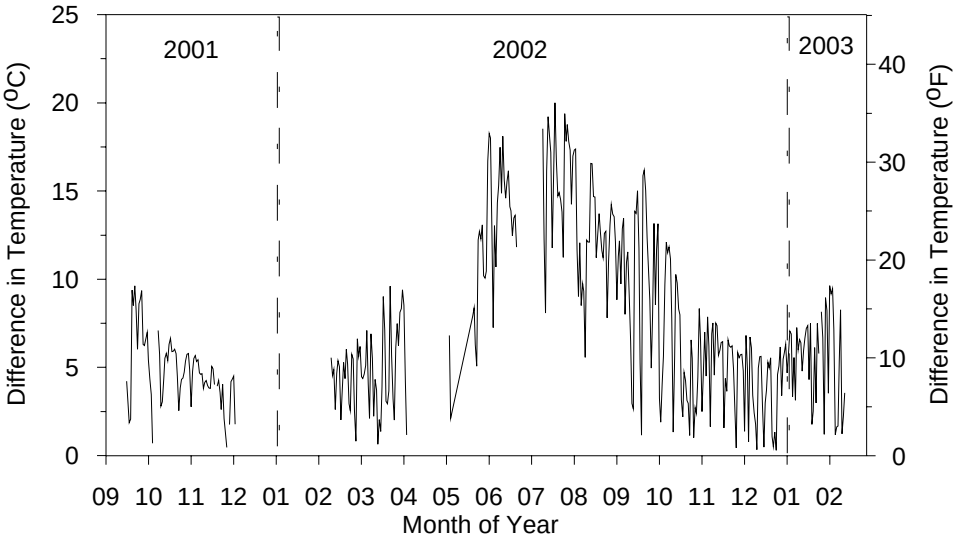

Figure 5.16. Maximum Daily Positive Thermal Gradients for Interior Girder B13

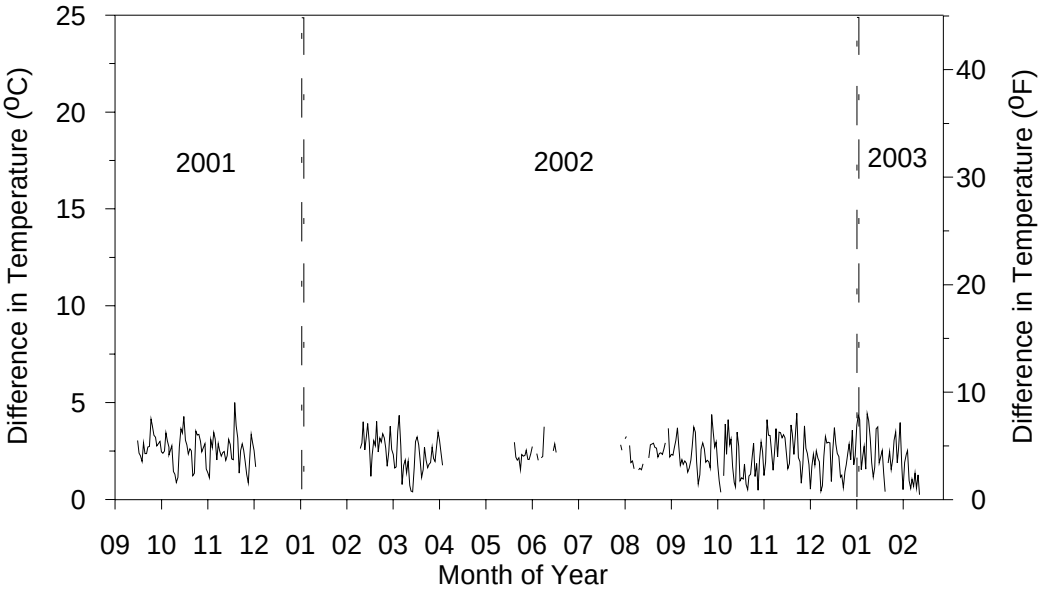

Figure 5.17. Maximum Daily Negative Thermal Gradients for Interior Girder B13

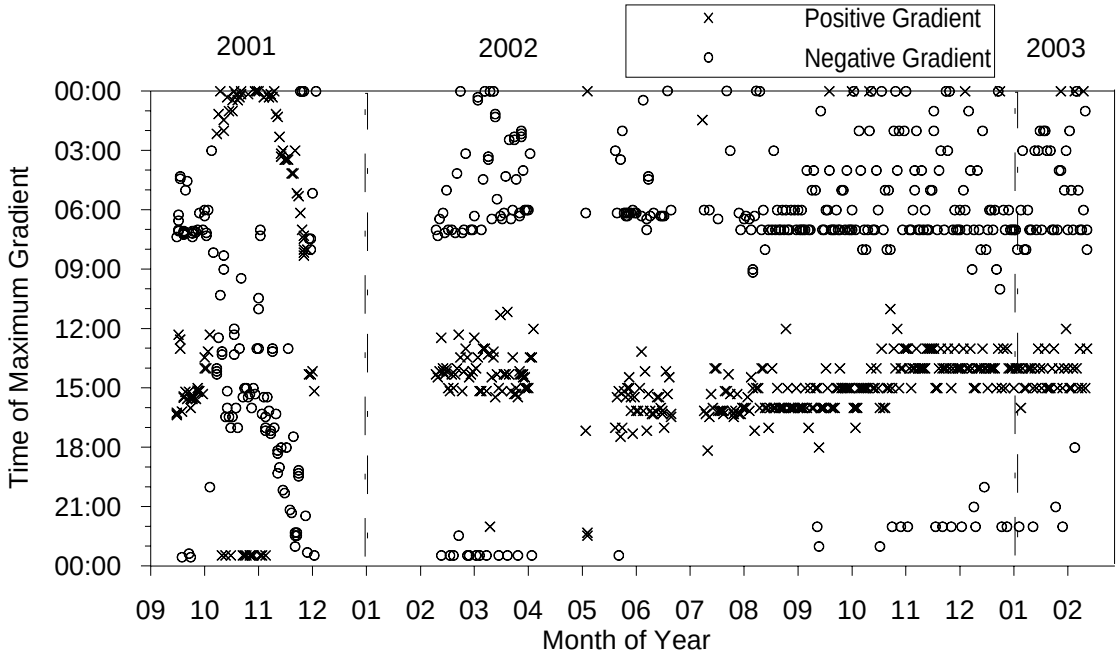

Figure 5.18. Time of Maximum Positive and Negative Gradients for Interior Girder B13

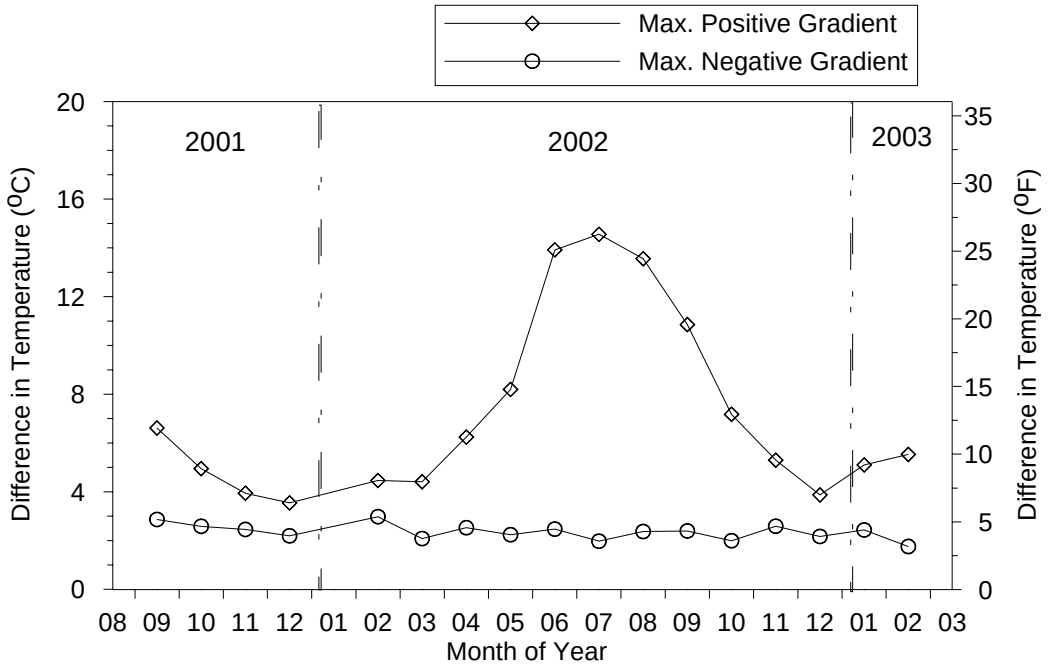

Figure 5.19. Average Maximum Daily Gradients by Month for Interior Girder B13

The magnitude of the maximum positive gradient varied substantially from day to day as illustrated in Figures 5.18 and 5.19. It was only 2.5 °C (5 °F) at one day in winter while it was 20.0 °C (36 °F) at one day in summer. Maximum gradients tended to be higher during summer months because of the intense solar radiation and high ambient temperatures. During fall and winter months, maximum positive gradients could be either high to 9.4 °C (17 °F) or low to 2.5 °C (5 °F), depending on the ambient conditions.

It has been noted that on a few winter days there was no positive gradient visible at any point throughout the day. The maximum positive gradient almost always occurred between 3:00 PM and 6:00 PM during the summer, and between 1:00 PM and 4:00 PM during the winter based on the temperature data obtained.

Similarly, maximum daily negative gradients also varied from day to day. Negative gradients were generally not affected by the time of the year. Often they

occurred sometime during the early morning but the exact time varied substantially from day to day. The average maximum positive gradients were highest during the summer months and lowest during the winter months.

However, the average maximum negative gradients remain relatively constant during the year. Maximum thermal gradients for four monitored girders are summarized in Table 5.7. The maximum positive gradient ranged from 13 to 20 °C (23 to 36 °F), and the peak negative gradients ranged from 4 to 11°C (7 to 20 °F).

Table 5.7. Maximum Thermal Gradients and Their Happening Time

Maximum Measured Thermal Gradients				
Girder	B13	B14	B23	B24
Positive Gradient	20.01	12.86	14.22	10.87
	7/25/02	7/25/02	7/25/02	7/25/02
Negative Gradient	5.01	10.62	3.95	9.53
	11/19/01	1/17/03	10/6/01	1/17/03
Highest Average Measured Thermal Gradients for a Calendar Month				
Girder	B13	B14	B23	B24
Positive Gradient	14.56	9.26	10.11	7.92
	Jul-02	Jul-02	Jul-02	Jul-02
Negative Gradient	2.98	5.61	2.99	5.05
	Feb-02	Jan-03	Jun-02	Jan-03
All thermal gradients in °C. °F = 1.8* °C				

Thermal gradients in interior and adjacent exterior girders had a difference up to 3.9 °C (7 °F) due to the effect of handrail, which was built partly over the exterior girders as shown in Figure 5.20 and Figure 5.21. The differences were compared for different seasons of the year but often occurred at almost the same time of a day. Clearly the

differences in October were very small while in February and July the differences were more significant. Similar phenomena can be observed for the first span and the second span.

For the girders on the same girder line, thermal behavior in the first span girder was compared with that in the second span girder. As shown in Figure 5.22 and Figure 5.23, in February and July the differences were larger [up to 3.9 °C (7 °F)] and varied along the height of the composite girder. In October, the difference along the height of the section was nearly constant. The variation of the difference was less than 1.1 °C (2 °F).

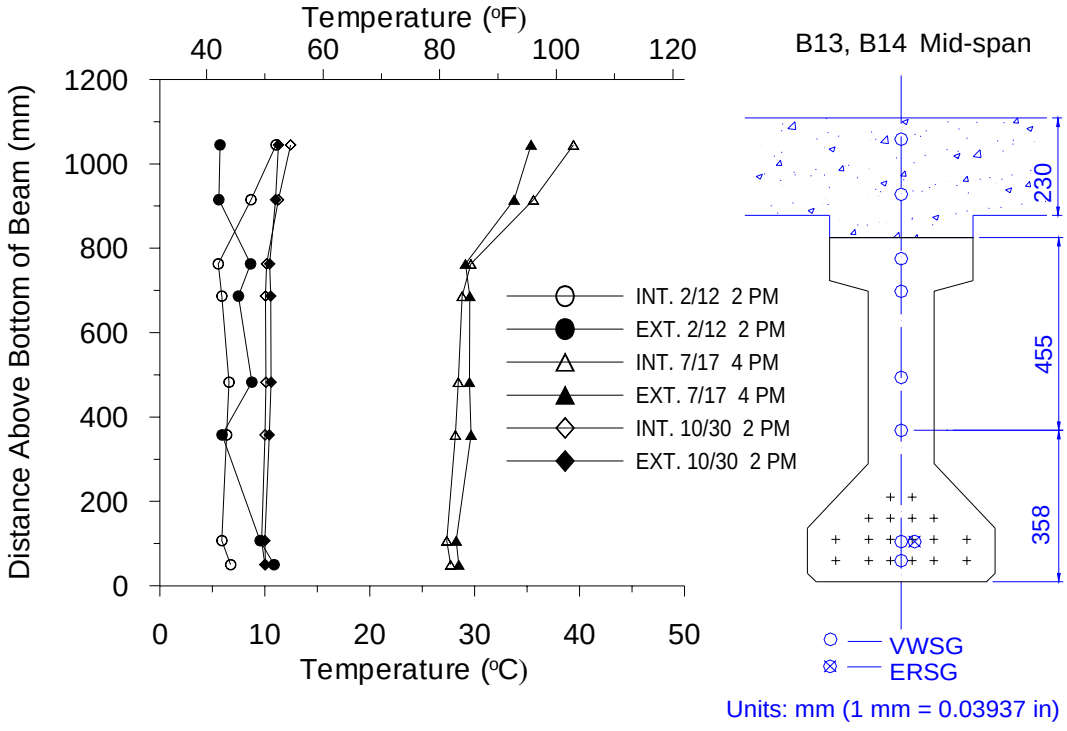

Figure 5.20. Thermal Gradients in Interior and Exterior Girders - B13 and B14

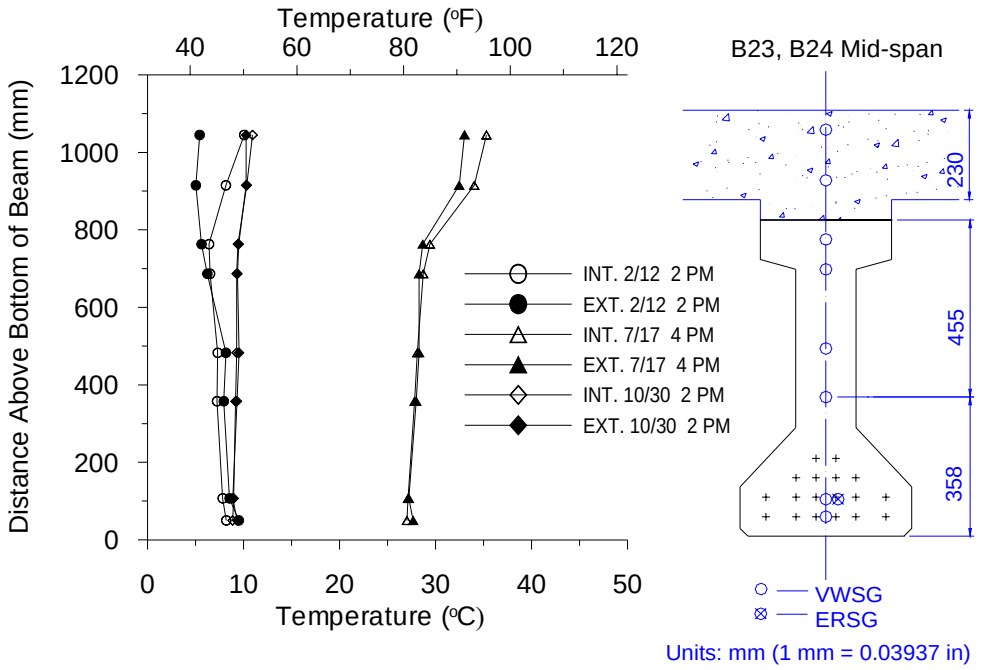

Figure 5.21. Thermal Gradients in Interior and Exterior Girders - B23 and B24

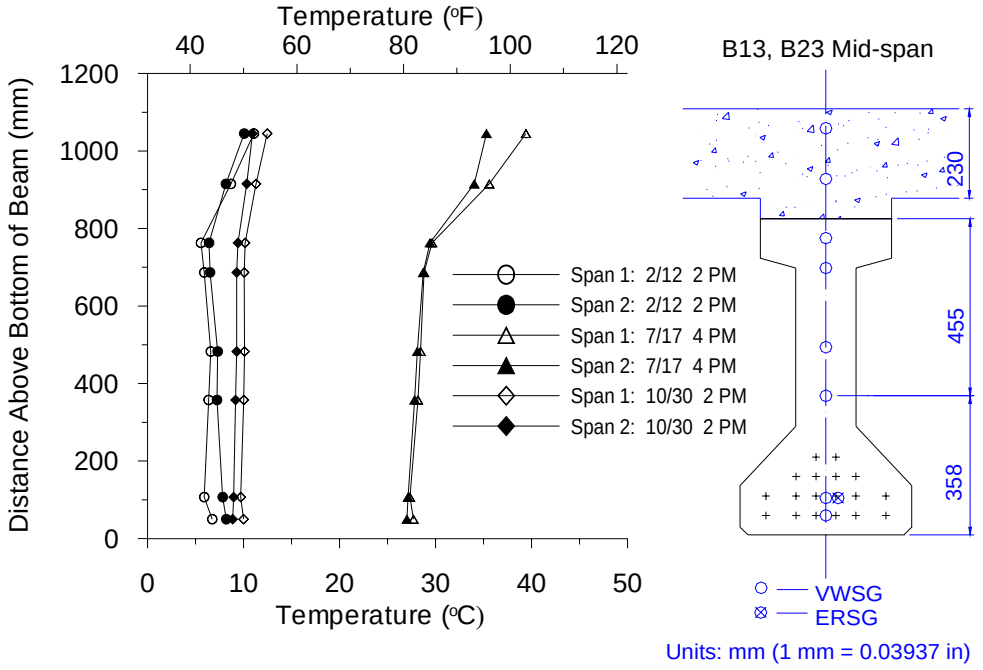

Figure 5.22. Thermal Gradients in Span 1 and Span 2 Girders - B13 and B23

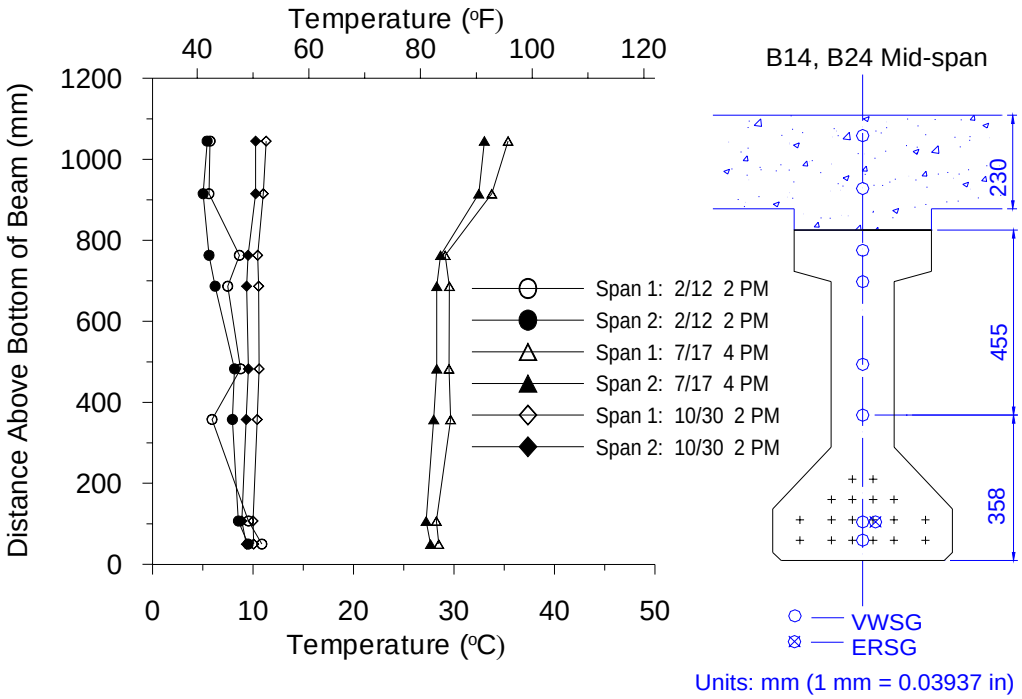

Figure 5.23. Thermal Gradients in Span 1 and Span 2 Girders - B14 and B24

The thermal behavior at different sections of the bridge deck during a sunny summer day is shown in Figure 5.24 and Figure 5.25. Temperature data appears to be different in the heating and cooling of the different sections of the deck.

On a sunny summer day, the temperatures at all section locations were roughly the same at 8:00AM. Temperatures at location B and C are about 4 - 6 °C (7 - 11 °F) higher than that of location of D at 4:00PM. Location D was likely partially shaded from the guard rail resulting in a slightly lower deck temperature, which was about 4.4 °C (8 °F) on a sunny summer day. Therefore, thermal gradients in the exterior girders were smaller than those in the interior girders. On a cloudy day, however, the temperature in the deck kept uniform as in the girders.

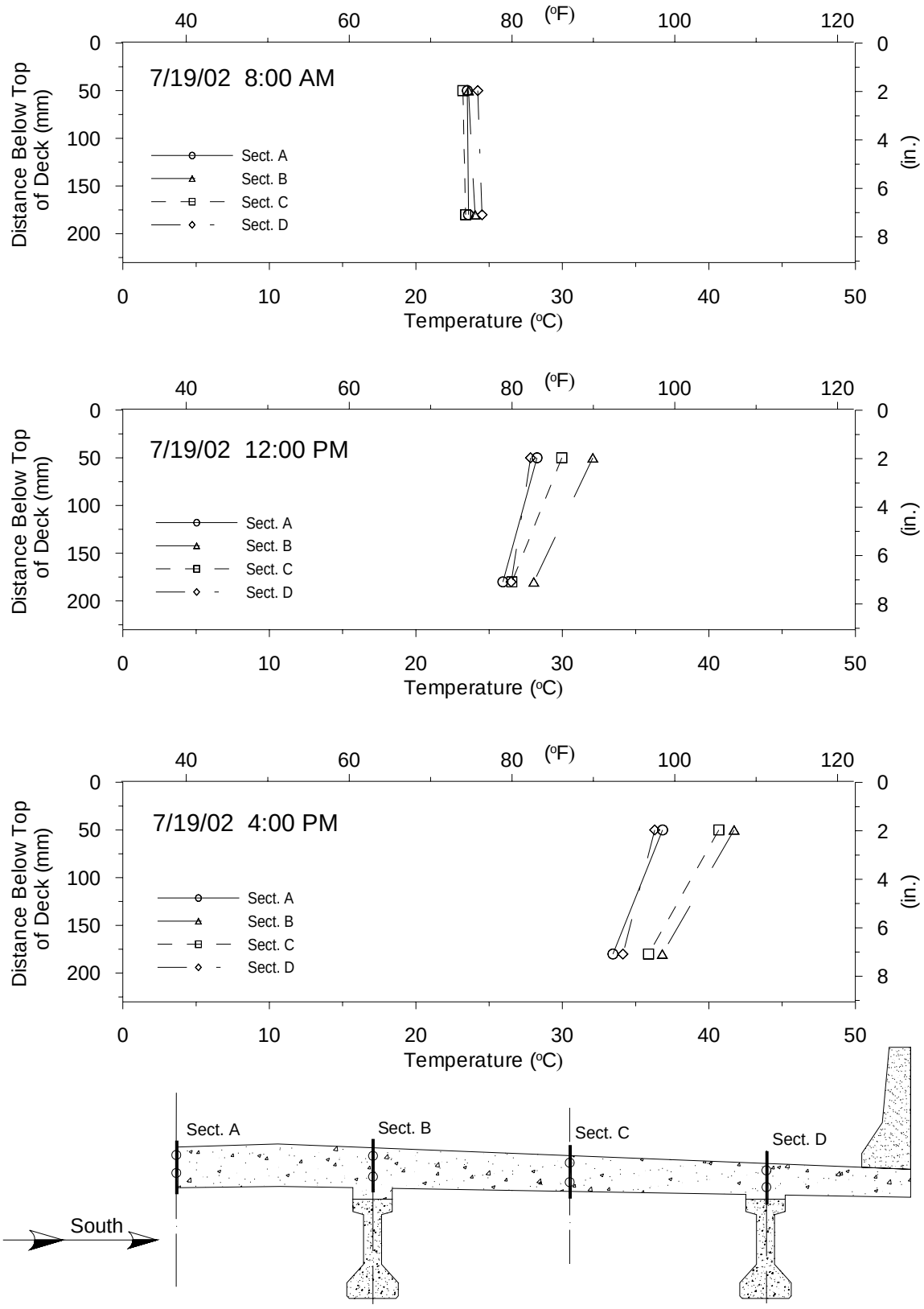

Figure 5.24. Temperatures in the CIP Deck on a Sunny Summer Day

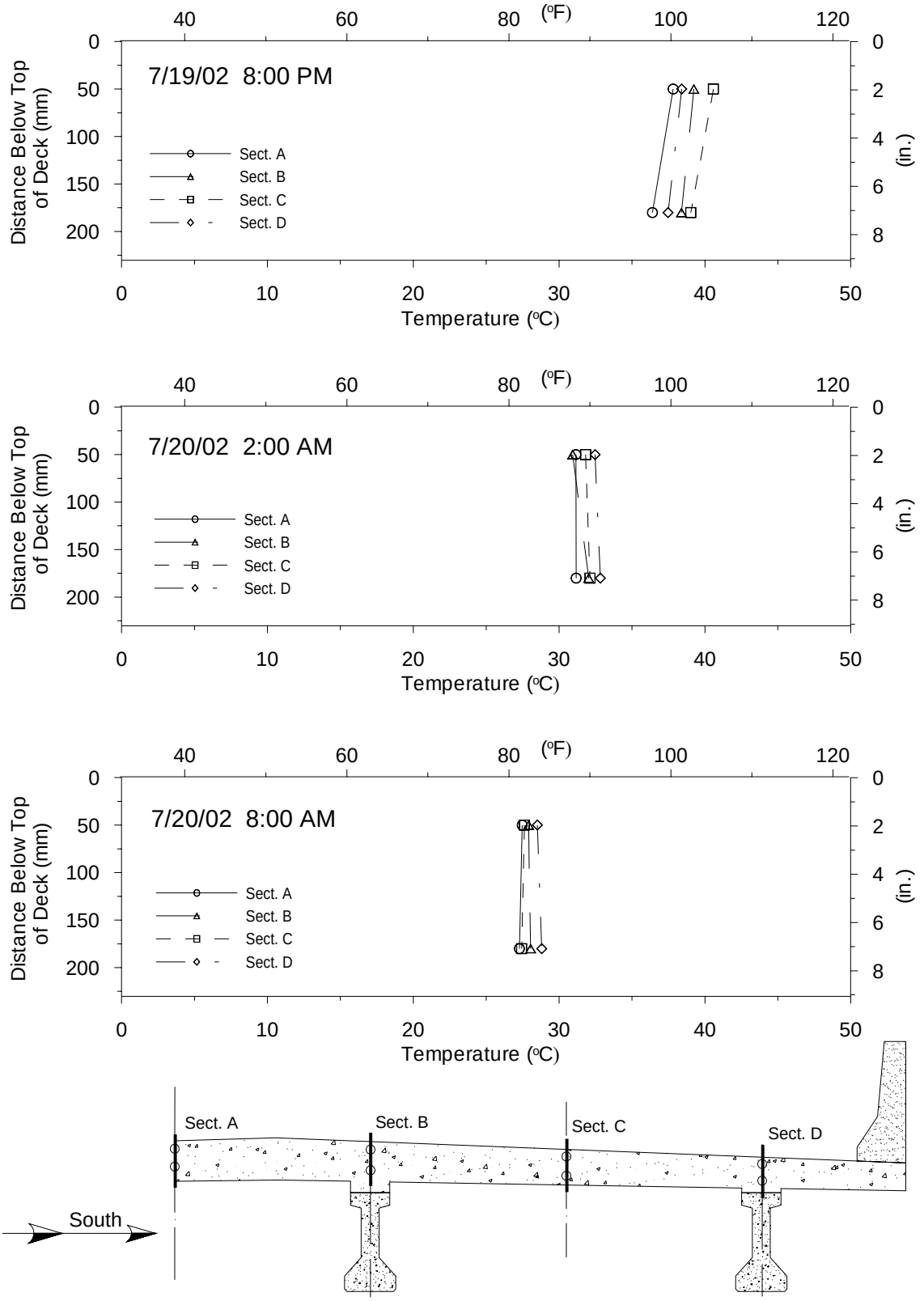

Figure 5.25. Temperatures in the CIP Deck during the Night Following Sunny Summer Day

5.4.3. Discussion. In Figure 5.26 and Figure 5.27, maximum measured positive and negative gradients are compared to the NCHRP 276 method (Imbsen et al. 1985), AASHTO LRFD Specification (1994) and a method suggested by Gross (1999). The maximum measured positive gradients are quite different from those specified by NCHRP, AASHTO and Gross especially at bottom of the deck. Temperature at the lower deck gauge was underestimated by 6.1 °C (11 °F) using the design gradients using all other methods. The shape of the negative measured gradients is similar [less than 2.2 °C (4 °F) difference] to the design negative gradients specified by AASHTO LRFD.

Therefore, only a modified design positive thermal gradient is recommended as shown in Figure 5.28. Note that the temperature at a depth of 0.36 m (14 in.) from the top of the deck is defined as 2.5 °C (4.5 °F) and at 0.10 m (4 in.) from the bottom it is zero. Obviously more studies are needed to check or modify the model, which is developed from this study.

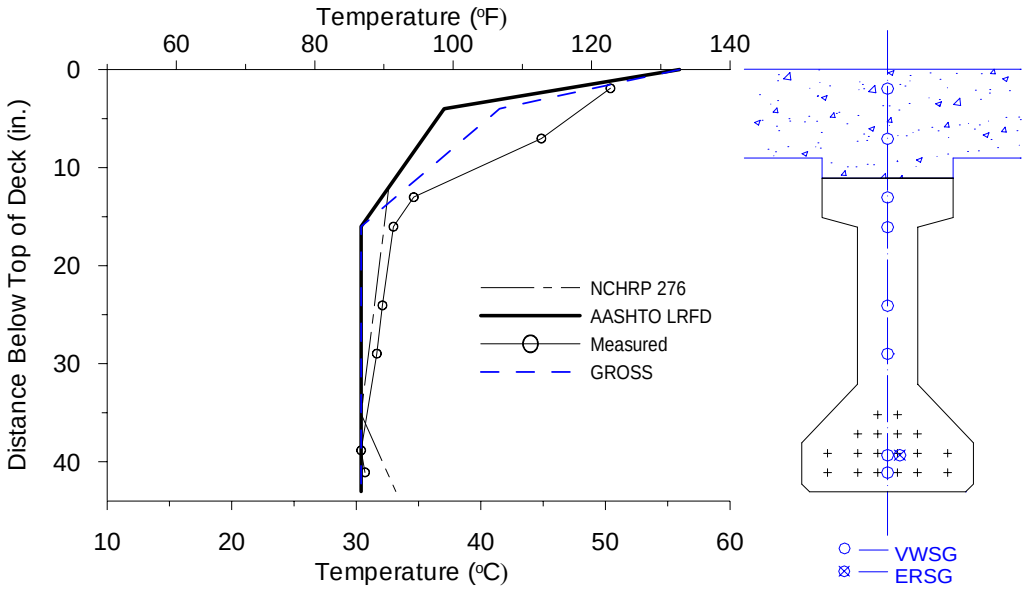

Figure 5.26. Design Positive Gradients and Maximum Measured Positive Gradients

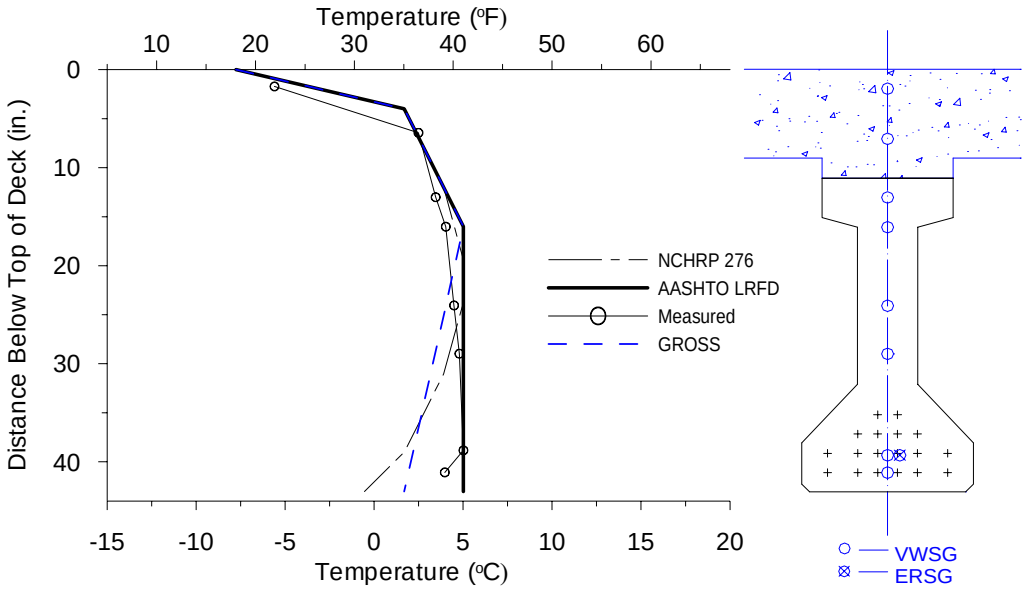

Figure 5.27. Design Negative Gradients and Maximum Measured Negative Gradients

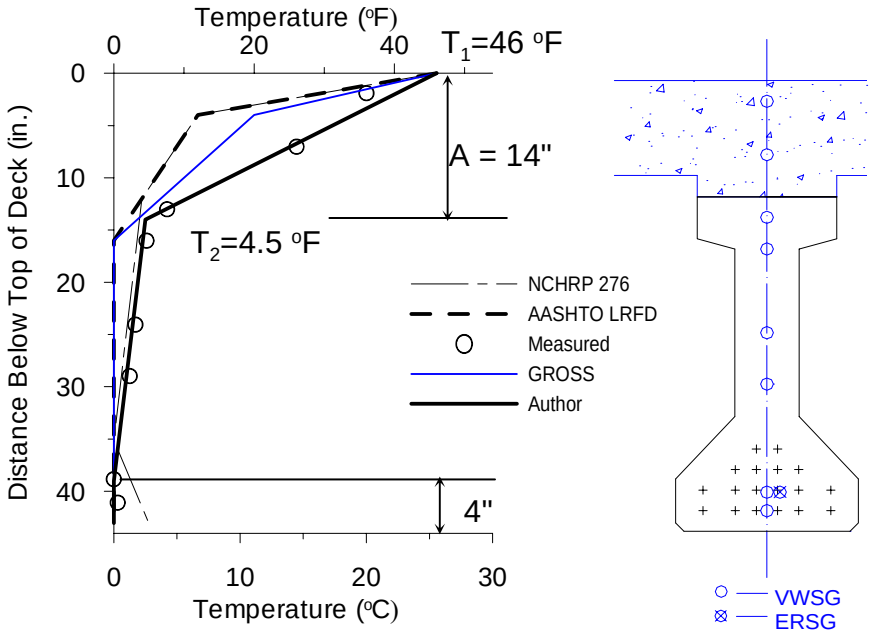

Figure 5.28. Recommended Positive Thermal Gradients

Using the method suggested in AASHTO guide specification on thermal effects in concrete bridge superstructures, the theoretical thermal stresses and strains resulting from

the maximum measured positive gradient in composite girder B13 are shown in Figure 5.29. Based on the measured temperature, full restrained stresses were obtained. Then the stress from release of axial restraint and the stress from release of flexural restraint were obtained using method suggested in AASHTO guide specification. Furthurmore, by combining those three stresses the total thermal stresses were obtained. It may be observed that the calculated strains correlate reasonably well (less than 60 microstrain difference) with the measured strains. Here temperature and strain differences were taken between the 8:00 AM reading on the day of the maximum positive gradient and the 4:00 PM reading. Self equilibrating thermal stresses using different design gradient shapes were compared and illustrated in Figure 5.30.

It can be found that thermal stresses below CIP deck using the design methods cited were all very close [less than 0.7 MPa (100 psi) difference)] to those calculated using measured thermal gradients. However, the stresses using measured thermal gradients were about 4.1 MPa (600 psi) difference from those calculated using known design methods in the deck except the method suggested by the author.

Stresses resulting from unfactored live load and impact are also shown for comparison as illustrated in Figure 5.30. It can be clearly seen thermal stresses at top fiber are only one third of the stressed due to live load and impact. At bottom fiber, thermal stresses were about 1.7 MPa (250 psi) in compression. Thermal stresses at both top fiber and bottom fiber are relatively small in magnitude and unlikely to cause any distress.

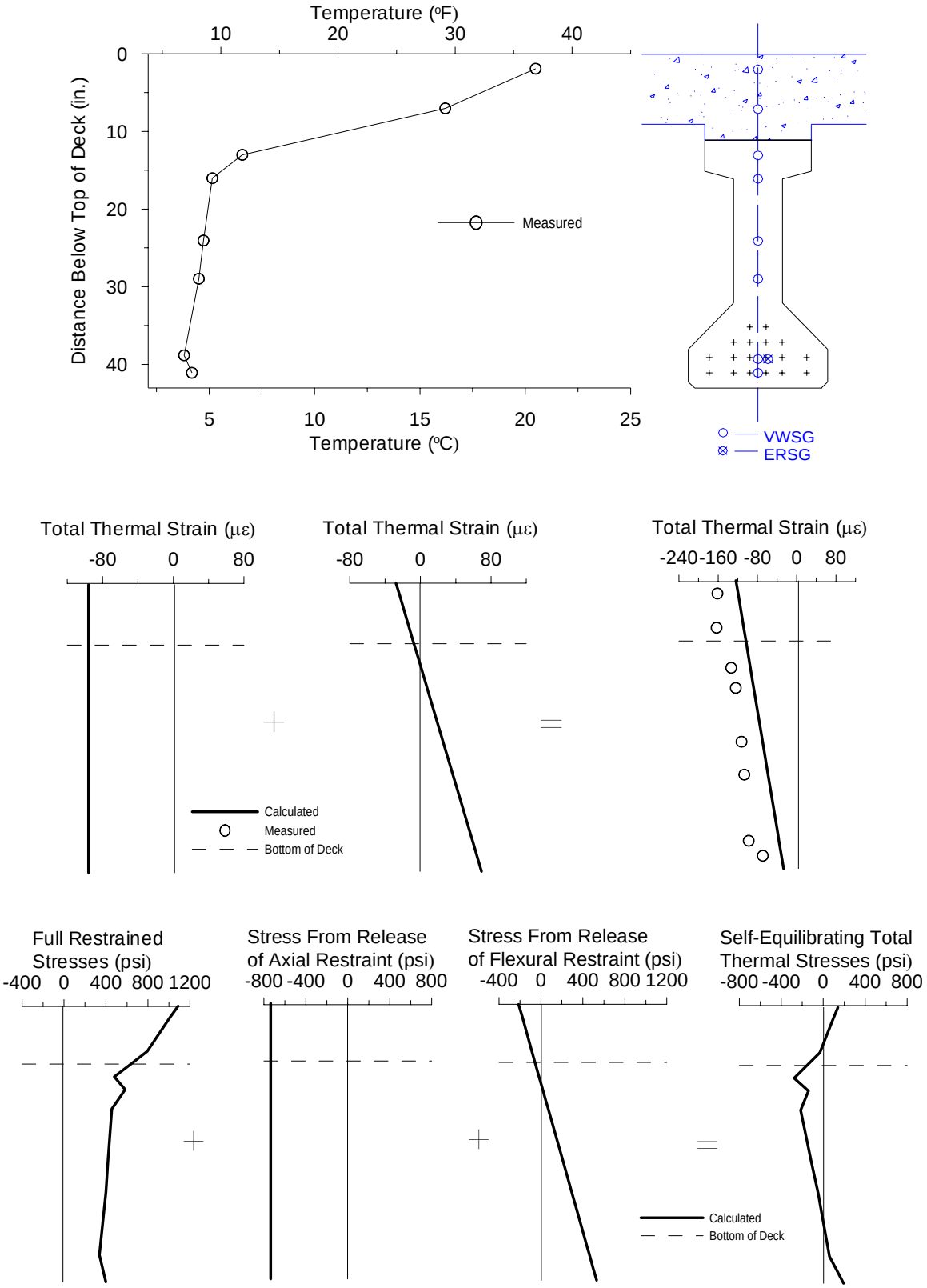

Figure 5.29. Measured and Calculated Thermal Strains and Stresses

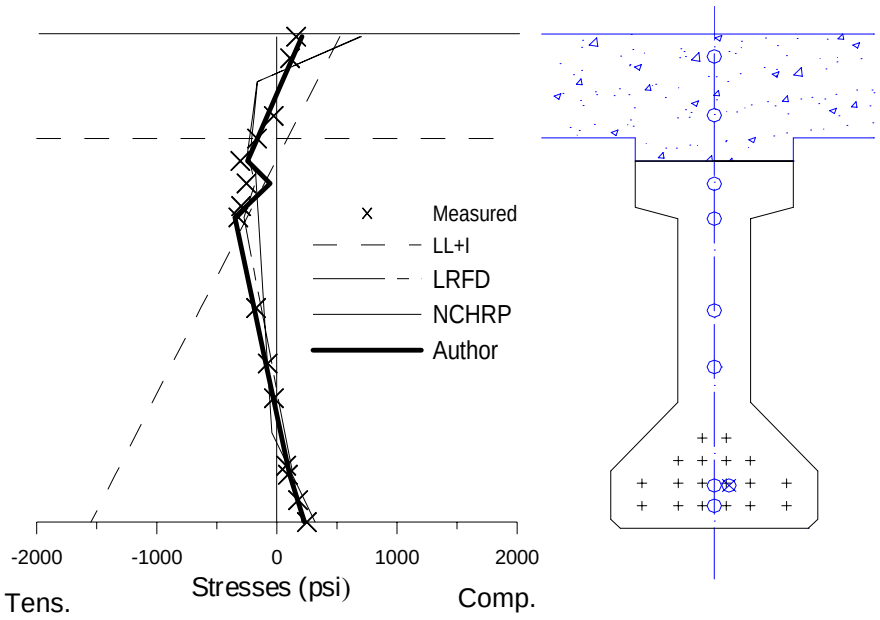

Figure 5.30. Thermal Stress Comparison

5.5. SUMMARY AND CONCLUSIONS

The following conclusions are drawn based on the test results and analysis:

The maximum measured hydration temperature for the HPC prestressed girders was 57 °C (135 °F) and the measured temperature gains after the end of the dormant period ranged from 26 °C (46 °F) to 29 °C (53 °F). Maximum hydration temperatures were not as high as peak suggested value by ACI Committee 363 (1992) which was about 87 °C (190 °F) for concrete used in the girders.

For the HPC girders, equivalent maximum temperature rises ranged from 5.1 to 5.9 °C per 100 kg/m^3 (5.4 to 6.2 °F per 100 lb/yd^3) of cement. For the HPC CIP deck, maximum temperature rise after dormant period was about 18 °C (32 °F). Equivalent maximum temperature rises 5.4 °C per 100 kg/m^3 (5.7 °F per 100 lb/yd^3) of cement, or 4.6 °C per 100 kg/m^3 (4.8 °F per 100 lb/yd^3) of total cementitious material. These

equivalent maximum temperatures are well below values suggested by ACI Committee 363, which was 6 to 8 °C per 100 kg/m^3 (11 to 15 °F per 100 lb/yd^3).

Bridge temperatures were recorded continuously for one and a half years. Maximum temperatures and minimum temperatures are summarized. Maximum average bridge temperatures measured on any singe day were 45 °C (118 °F), 44 °C (117 °F), 42 °C (108 °F) and 42 °C (108 °F) for girders B13, B14, B23 and B24, respectively. Minimum average bridge temperature measured were 17 °C (63 °F), 14 °C (57 °F), 16 °C (61 °F) and 14 °C (57 °F) for girders B13, B14, B23 and B24, respectively.

The maximum temperatures tend to occur during the middle of the summer, typically in July. During this period, the maximum average bridge temperature were approximately 7 °C (12 °F) higher than the maximum ambient temperatures. However, during the winter months from December through February, there was essentially no difference between the maximum average bridge temperatures and the maximum ambient temperatures. The average daily minimum temperature tended to remain higher than the minimum ambient temperature. On average, the difference was about 6 °C (10 °F) during summer months and about 4 °C (8 °F) during the winter months.

The methods for effective bridge temperature suggested in the AASHTO Standard Specification (1996), LRFD Specification (1994) and NCHRP Report 276 Method (Imbsen et al. 1985) are inappropriate for the bridge locations monitored. A modified approach is developed by the author to provide more realistic design temperatures. The calculated temperatures using this suggested method correlate well with the extreme average bridge temperatures obtained in this study.

Maximum measured positive gradients are quite different from those specified by NCHRP, AASHTO and Gross (1999). Temperature at the lower deck gauge was underestimated by 6.1 °C (11 °F) using the design gradients using all other methods but that suggested by the author. The shape of the negative measured gradients is similar [less than 2.2 °C (4 °F) difference] to the design negative gradients specified by AASHTO LRFD.

A modified design positive thermal gradient is recommended as shown previously in Figure 5.29. Note that the temperature at depth of 0.36 m (14 in.) from the top of the deck is defined as 2.5 °C (4.5 °F) and at 0.10 m (4 in.) from the bottom it is zero.

Thermal stresses below the CIP deck using any design methods were very close [less than 0.7 MPa (100 psi) difference)] to those calculated using measured thermal gradients. However, in the deck the stresses using measured thermal gradients were about 4.1 MPa (600 psi) difference from those calculated using known design methods except the method suggested by the author. Thermal stresses at top fiber are only one third of the stressed due to live load (plus impact). At bottom fiber, thermal stresses were about 1.7 MPa (250 psi) in compression. Thermal stresses at both top fiber and bottom fiber are relatively small in magnitude and unlikely to cause any distress.

6. CONCRETE STRAIN MEASUREMENTS

6.1. INTRODUCTION

This Section discusses concrete strain measurements made during this research program. Emphasis is placed on strain measurements related to design calculations as well as measurements that have a significant impact on the overall structural behavior of the bridge and its components.

Strain measurements for the prestressed girders are investigated at several key stages of the construction process. First, the strain behavior in prestressed girders prior to release of prestress is investigated. Then the elastic responses to the release of pretension are considered. After that, the time-dependent strain behavior of the girders after release is discussed. Strain behaviors for the girder during transportation from precast plant to the jobsite and erection are also monitored. Finally, some other elastic responses are examined including deck load application. Strain behavior during live load is discussed in Section 10.

In actual design, concrete stresses are of more importance than concrete strains because concrete stresses are used to control design. In this research program concrete stresses were not measured directly, but estimated by multiplying measured strains by the measured modulus of elasticity.

In some sections, measured stresses or strains are compared with predicted stresses and strains obtained by two methods as described in Table 6.1. The aims are to examine the applicability of the design and analysis method and examine the effects of standard design assumption.

Table 6.1. Stress Comparison Methods

	Measured Stresses	Stresses predicted by Design Method	Stresses predicted by Refined Design Method
Stresses	σ_m	σ_d	σ_{rd}
Variables	E_m, ε_m	E_d, A_d, I_d, …	E_m, A_m, I_m, …
Equations	$\sigma_m = E_m\varepsilon_m$	$\sigma_d = f(E_d, A_d, I_d, \ldots)$	$\sigma_{rd} = f(E_m, A_m, I_m, \ldots)$
E_m – measured modulus of elasticity E_d – modulus of elasticity predicted by standard design equation A_m, I_m – measured section properties; A_d, I_d – designed section properties			

6.2. INTERPRETATION OF GAUGE READINGS

Interpretation of raw strain readings is an important part of the overall data analysis process, and only in a few specific cases can strain readings be used directly without appropriate correction consideration. Generally speaking, temperature effects on the gauge reading must always be accounted for, even if thermal strains are the primary effect being studied. Thus, a temperature reading at the gauge location is essential for each strain reading. Vibrating wire gauges used in this project had a thermistor integrally attached for this purpose.

If compressive strains are positive, the following relationship exists between the reported strain ε_{gauge}, and the actual strain at the gauge location ε_{actual} as shown in Equation 6.1.

$$\varepsilon_{gauge} = \varepsilon_{actual} + (\alpha_{gauge} \cdot (T - T_0)) \qquad \text{Equation 6.1}$$

The second term on the right hand side of the above equation represents the strain not reported by the gauge. If the gauge itself heats up by a temperature change $(T - T_0)$, then the gauge wire expands a corresponding amount and reduces the tension in the

gauge wire. This appears as an apparent additional compressive strain, hence the addition rather than the subtraction of this term in Equation 6.1. This equation can be rearranged in a more useful form as shown in Equation 6.2.

$$\varepsilon_{actual} = \varepsilon_{gauge} - (\alpha_{gauge} \cdot (T - T_0)) \qquad \text{Equation 6.2}$$

Fortunately, the gauges used in this research program were thermally compensated, and had coefficients of thermal expansion (CTE) very similar to those of the concrete in the girders. The CTE of the vibrating wire gauges used in this project was 11.5 με/°C (6.4με/°F).

If thermal effects are to be removed, then Equation 6.3 and Equation 6.4 can be used, where ε_{TER} is the strain with *Thermal Effects Removed*:

$$\varepsilon_{TER} = \varepsilon_{actual} - (\varepsilon_{thermal,axial} + \varepsilon_{thermal,flexural}) \qquad \text{Equation 6.3}$$

$$\varepsilon_{TER} = \varepsilon_{gauge} - (\alpha_{gauge} \cdot (T - T_0)) - (\varepsilon_{thermal,axial} + \varepsilon_{thermal,flexural}) \qquad \text{Equation 6.4}$$

Note that both axial and flexural thermal strains, computed as described in Section 5, must be subtracted from the actual strain. In other words, the removal of thermal strains must consider the temperature distribution through the entire cross-section, rather than just the temperature at the gauge location. Since even thermally compensated gauges only account for temperature changes at the individual gauge location, strains reported from such gauges should still be corrected using this method.

6.3. CONCRETE STRAINS BEFORE RELEASE

6.3.1. Background. Concrete strain behavior before release is usually very complex. Some basic activities inside concrete related to strain changes are listed in

Table 6.2 including autogenous shrinkage, temperature increasing and dereasing, and drying shrinkage.

Table 6.2. Concrete Strain Behavior before Release

Activities inside Concrete	Concrete Deformation	Basic Factors Affecting Strain
Autogenous shrinkage	Small contraction	Mix proportions,
Temperature increasing	Expansion	Size and shape of the member,
Temperature decreasing	Contraction	Ambient conditions,
Drying Shrinkage	Significant contraction	Curing methods, etc.

Although rarely considered in design, concrete strain behavior prior to release can have a large impact on several aspects of behavior for prestressed girders. Strain and strain gradients may cause temporary or permanent deformations in a structural member. Depending on the time at which bond between the strand and the concrete occurs, prestress force in pretensioned members may also be affected by these strains. If the contraction of a concrete member is restrained prior to release, cracking may develop through the cross-section at some locations along the length of the member.

6.3.2. Measurements and Discussion. Concrete strains were measured using vibrating wire strain gauges and were recorded at 5 to 15 minute intervals from the placement of concrete to immediately prior to release. Measurements of hydration temperatures in girders are discussed in Section 5. As discussed previously, strains are monitored with temperature at the same locations. Strains are relative to “baseline” strain readings taken right after placement of concrete.

In Figures 6.1 through 6.11, measured strains and temperatures are shown at different sections of the monitored girders prior to the release of the prestress. Cracking

due to shrinkage that was observed before transfer is also illustrated. As mentioned previously in this study, compressive strains are defined positive while tensile strains are defined as negative.

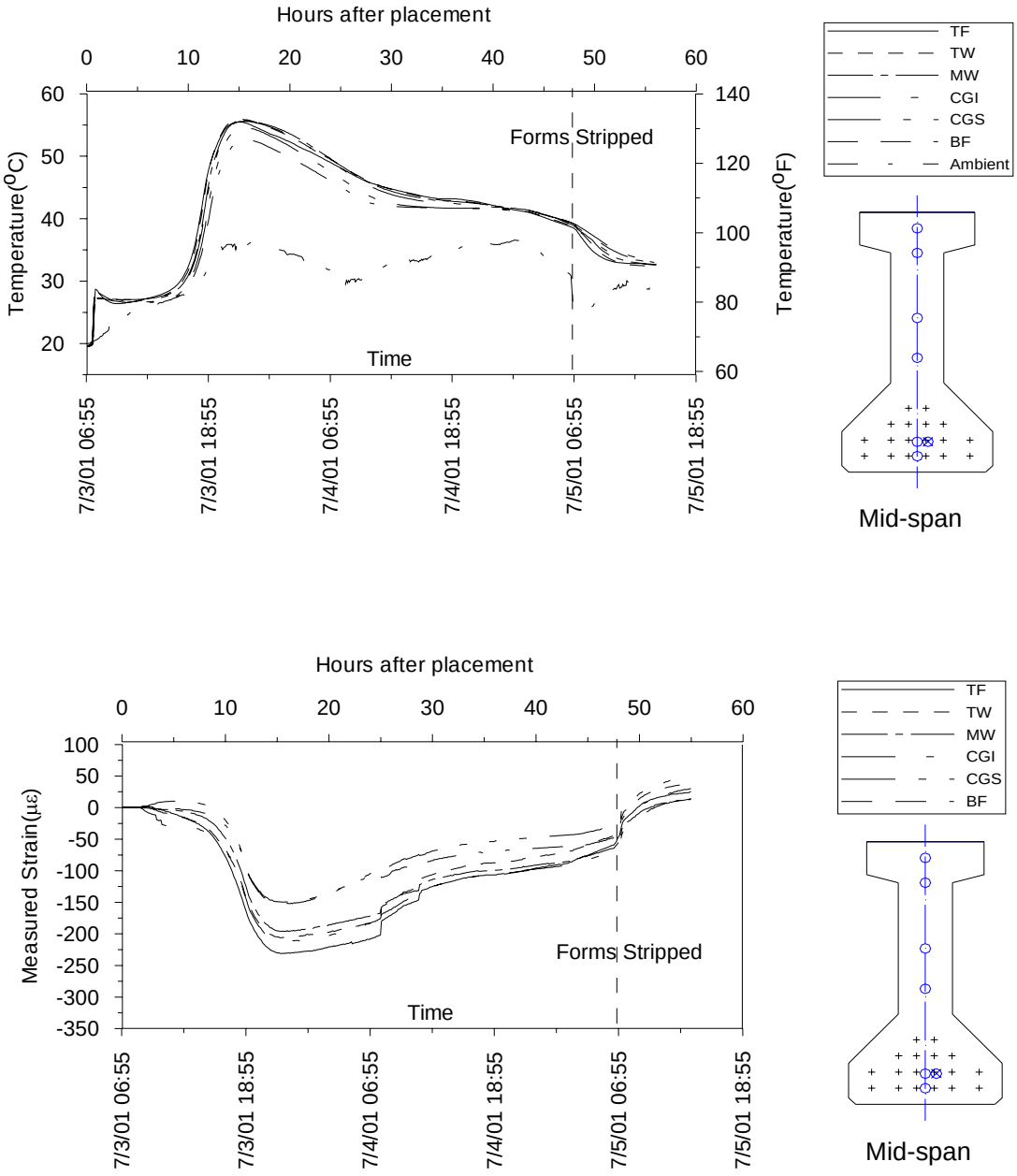

Figure 6.1. Strains and Temperatures at Mid-span of Girder B13 Prior to Release

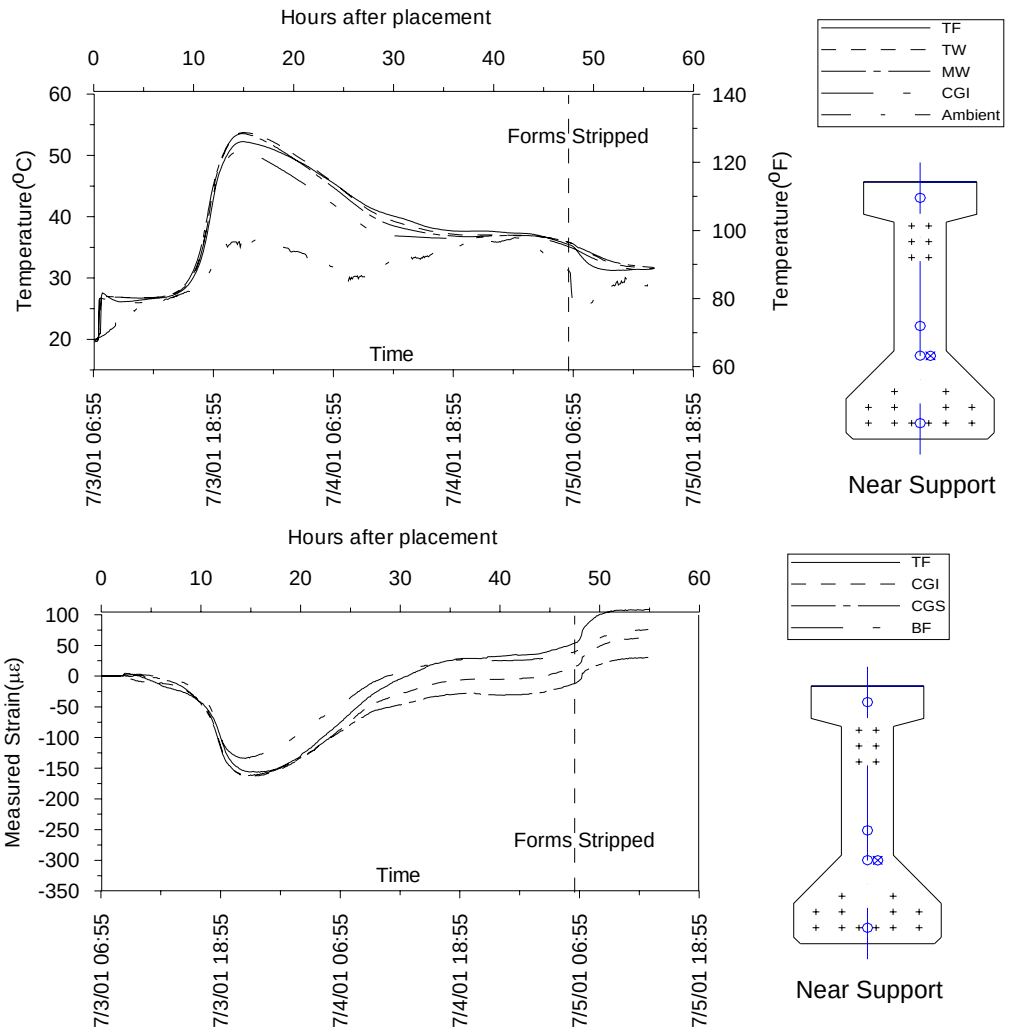

Figure 6.2. Strains and Temperatures at Near End Support of Girder B13 Prior to Release

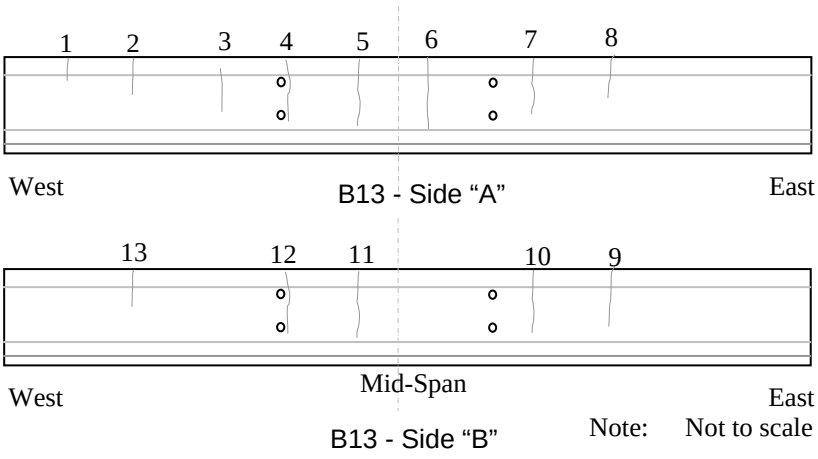

Figure 6.3. Cracking Observed in Girder B13 Prior to Release

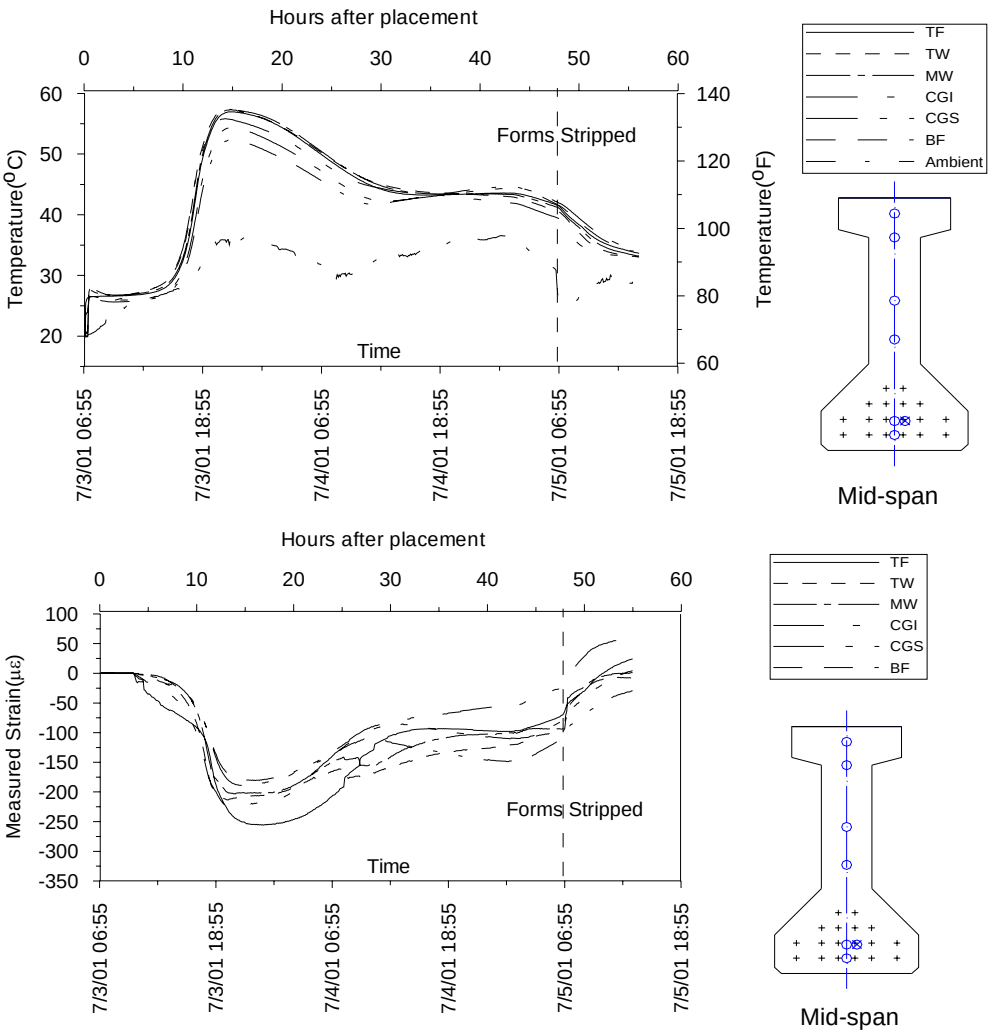

Figure 6.4. Measured Strains and Temperatures at Mid-span of Girder B14 Prior to Release

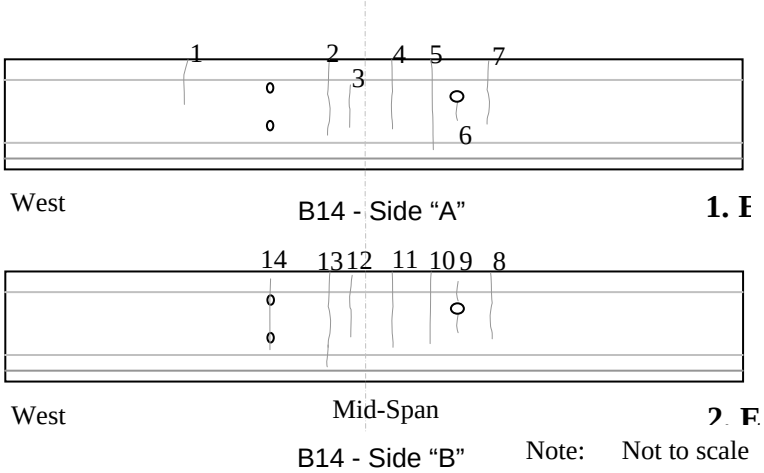

Figure 6.5. Cracking Observed in Girder B14 Prior to Release

It is evident that strain behavior prior to release of strands was quite variable in the four girders, but some basic trends can be found. During the dormant period of hydration, for about 6 hours after the concrete was placed, girder concrete began to expand. As the temperatures increased over the next several hours, the girder concrete also expanded. It is found the expansion was about 40% of the free thermal strain corresponding to the increase in temperature. This implied some restraint from the formwork against expansion of the girder concrete. In general, the expansion was greatest where temperature increases were highest.

A contraction occurs corresponding to the cooling of the girder after the peak of hydration temperature was observed. The contraction continues as the girder cools slowly on the bed. This rate likely increased due to the drying shrinkage of the hardened concrete. In the upper portions of the member, there is a net compressive strain relative to the time of placement of concrete. The contraction at the bottom of the member is much smaller than at the top, indicating the presence of restraint.

Cracking was observed on all four monitored girders as shown in the aforementioned figures. The cracking is evidenced by the sudden apparent increase in tensile strain as illustrated in Figures 6.6 and 6.9.

At the mid-span section of girder B23, the sudden increase of the tensile strain occurred about 33 hours after the placement of concrete. The magnitude of the strain changing ranged from 317 to 616 microstrain. The cracking distribution recorded is illustrated in Figure 6.8. It can be found in this case cracking occurred right at mid-span. The cracking was believed to be caused by the strain gradients along the section when concrete cooling. Since the strain drop happened to all strain gauge locations except the

bottom two, this indicates that the cracking occurred from the top to the center of gravity (c.g.) of the concrete section, as a minimum. It was evidenced by the recorded cracking at the mid-span section.

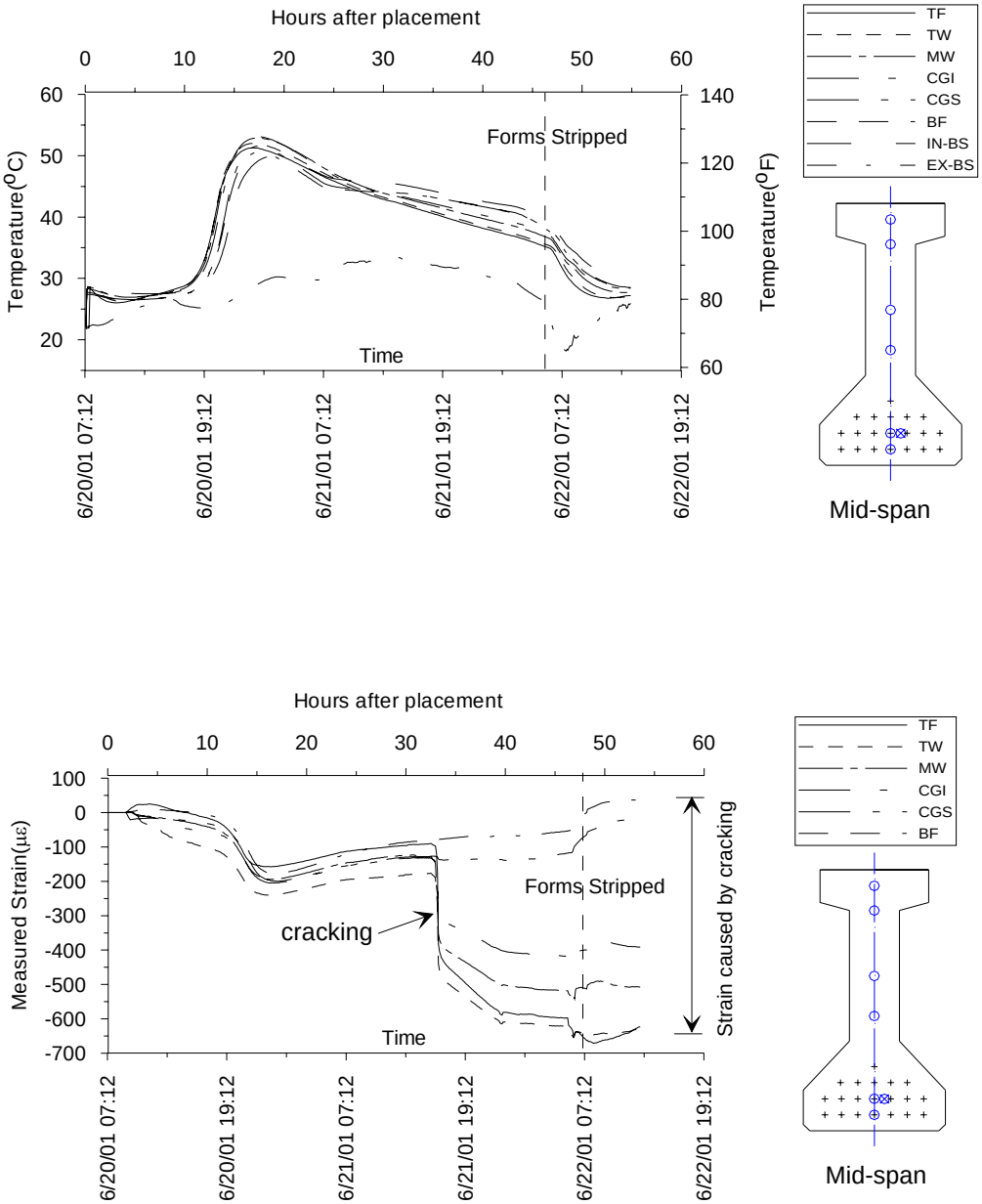

Figure 6.6. Strains and Temperatures at Mid-span of Girder B23 Prior to Release

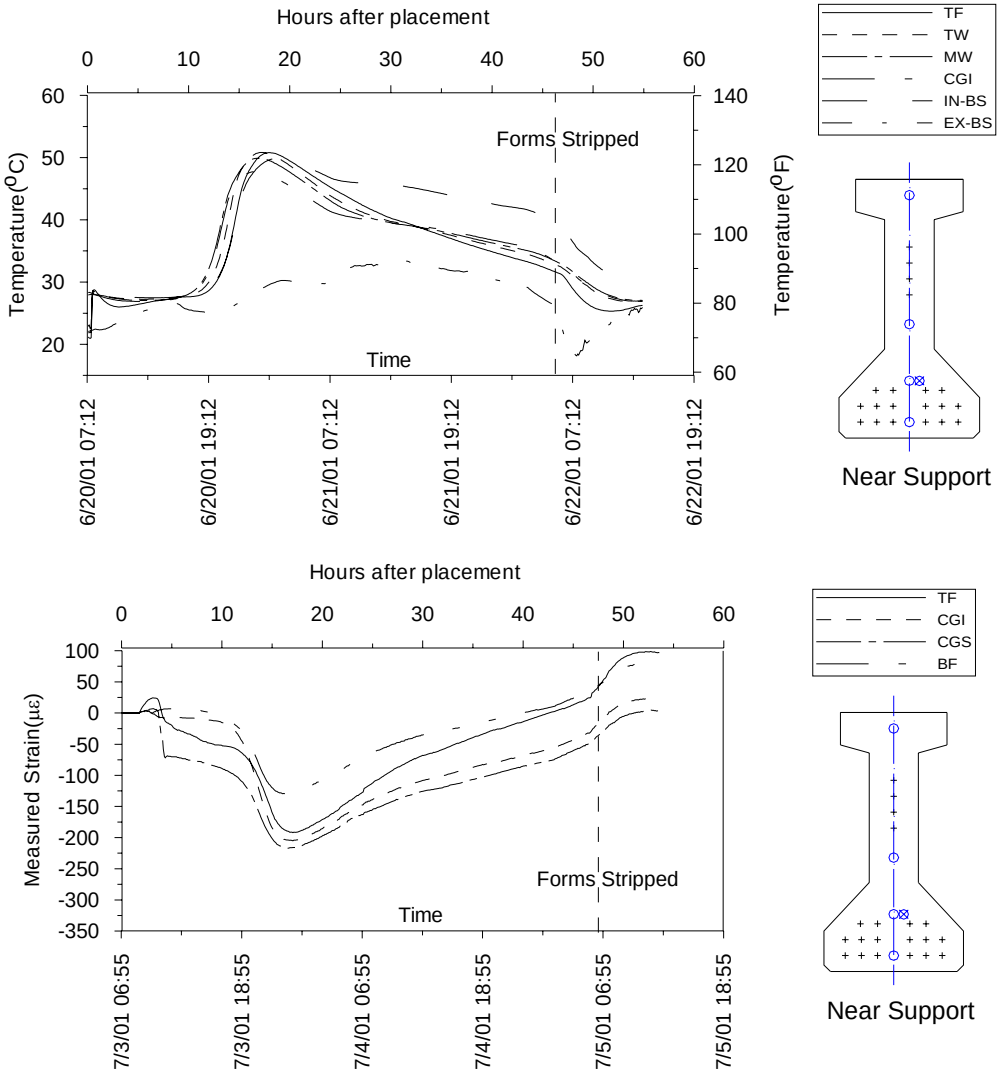

Figure 6.7. Strains and Temperatures at Near End Support of Girder B23 Prior to Release

Figure 6.8. Cracking Observed in Girder B23 Prior to Release

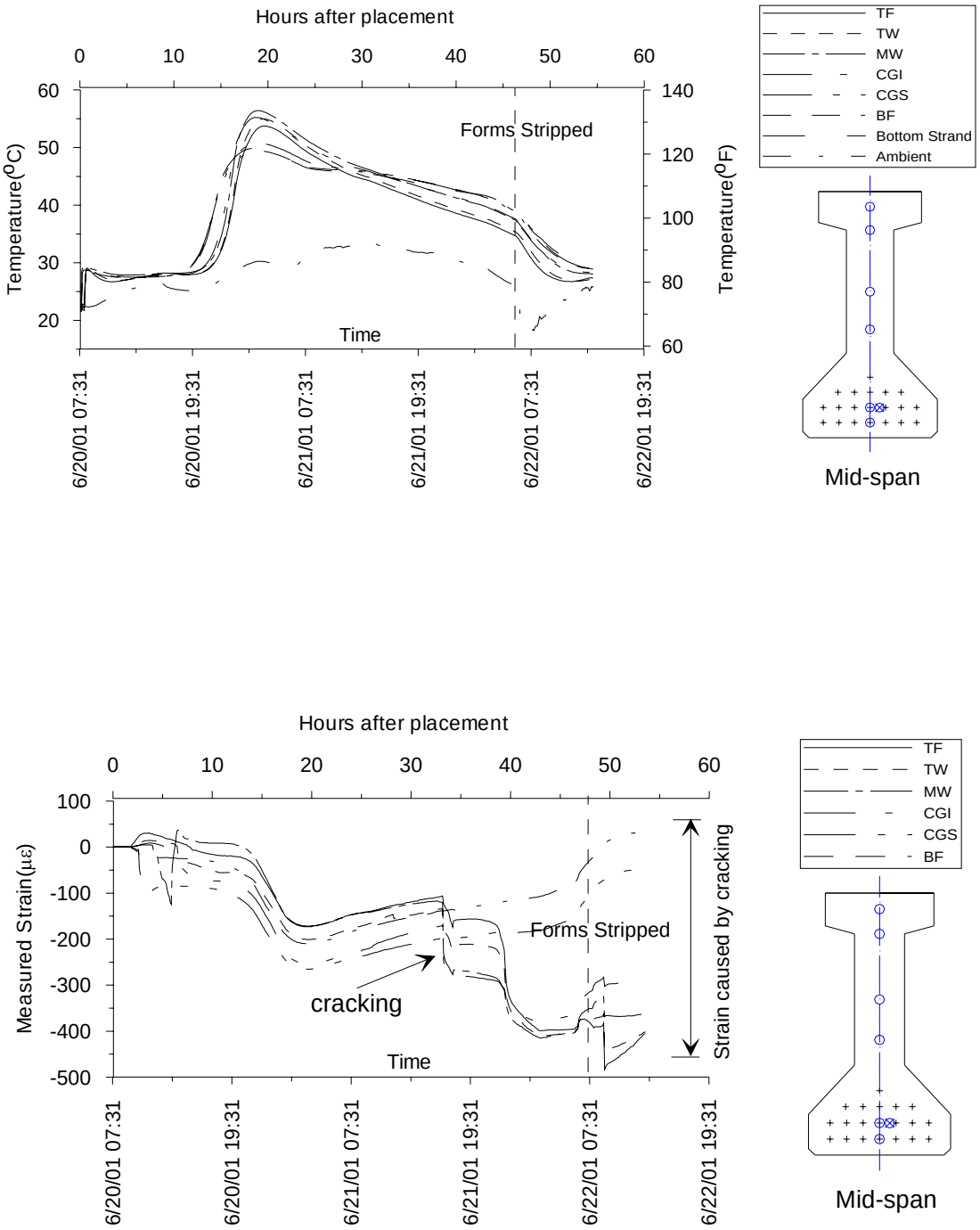

Figure 6.9. Strains and Temperatures at Mid-span of Girder B24 Prior to Release

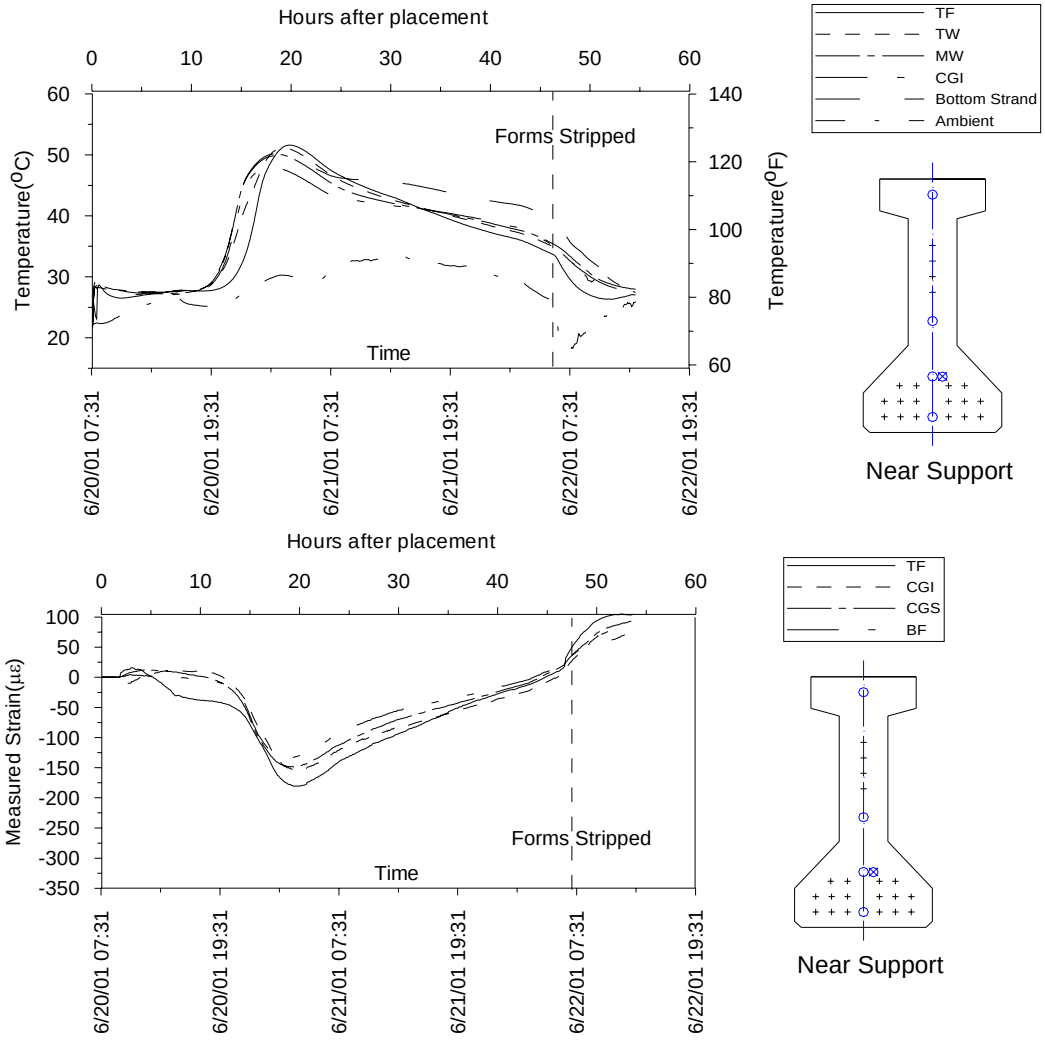

Figure 6.10. Strains and Temperatures at Near End Support of Girder B24 Prior to Release

Figure 6.11. Cracking Observed in Girder B24 Prior to Release

A similar phenomenon as just discussed with girder B23 was observed in girder B24. About 33 hours after the concrete was placed, there was a sudden strain increase. However the magnitude was much smaller than observed in girder B23. The depth of the cracks increased again about 7 hours after initial cracks were observed. The total increase of the strain observed ranged from 258 to 459 microstrain, close to those measured in girder B23. In general, prior to the release of the prestressing strands during the initial hydration period, only small strain levels (less than 100 microstrain) developed depending on ambient conditions. Tensile strain levels then developed preceding the point at which peak hydration temperatures were obtained. Tensile strain levels were higher in the top flange. Their magnitude was about 40% of free thermal strain. Following this, girders continue to contract as they cool. Drying shrinkage adds to contraction in hardened girder. Restraint from formwork reduces contraction, especially at the bottom flange / form interface and may have contributed to the cracking observed.

Initial cracking at mid-span occurred at about 33 hours after the concrete was placed in the two instrumented girders. Crack spacing varied for each girder. A small number of cracks were observed in girders B23, B24 compared to girders B13, B14. Cracks in girder B14 had a smaller crack spacing compared to girder B13. It can be concluded that the number and spacing of cracks were totally case depending.

It is important to note that these cracks closed entirely upon release of prestress and were often impossible to find thereafter. No structural impact was observed in this research program as a result of the formation of these cracks prior to release. To avoid such cracking, it seems the timing during the construction process is the key controllable factor. Girders should be released as soon as possible after required concrete strengths are

obtained. As in this project, the cracking may be avoided if it is released less than 33 hours, about a day and a half after the concrete was placed. Release at 1-day is also more of an industry standard.

6.4. CONCRETE STRAINS AT RELEASE OF PRESTRESS

6.4.1. Background. Checking of concrete stresses at release to ensure they meet allowable limits is one of the most fundamental calculations typically performed in the design of prestressed concrete girders. This check is necessary to ensure that the concrete is not overstressed immediately after release. If tensile stresses exceed the tensile strength of the concrete, flexural cracking may cause the serviceability of the structure to be reduced. If compressive stresses are too high, creep may eventually lead to a sustained-load failure.

The standard design calculations for stresses at release involve comparing extreme fiber stresses to stipulated allowable stresses. The extreme fiber stresses are calculated as the sum of three components: the axial stress resulting from prestressing, the flexural stress resulting from the eccentricity of the prestress, and the flexural stress resulting from the self-weight of the member. Standard equations are given in Equation 6.5 and Equation 6.6 for the extreme bottom and top fibers (assuming compressive stresses are positive). Allowable stresses at release specified by different codes are listed in Table 6.3.

$$\sigma_{rel,bot} = \frac{P}{A} + \frac{P \cdot e \cdot y_{bot}}{I} - \frac{M_{self-wt} \cdot y_{bot}}{I} \leq \sigma_{allowable,rel,comp.} \qquad \text{Equation 6.5}$$

$$\sigma_{rel,top} = \frac{P}{A} - \frac{P \cdot e \cdot y_{top}}{I} + \frac{M_{self-wt} \cdot y_{top}}{I} \geq -\sigma_{allowable,rel,tens.} \qquad \text{Equation 6.6}$$

Table 6.3. Specified Allowable Stresses at Release

Code	ACI, PCI (psi)	AASHTO (psi)
Specified compression stress	$0.6 f'_{ci}$	$0.6 f'_{ci}$
Specified tensile stress	$3\sqrt{f'_{ci}}$	$7.5\sqrt{f'_{ci}}$
Compression stress based on $f'_{ci,design}$	4525	4525
Tensile stress based on $f'_{ci,design}$	261	651
Compression Stress based on $f'_{ci,measured}$ for B13, B14	6314	6314
Tensile stress based on $f'_{ci,measured}$ for B13, B14	308	769
Compression Stress based on $f'_{ci,measured}$ for B23, B24	5857	5857
Tensile stress based on $f'_{ci,measured}$ for B23, B24	296	741
1 psi = 0.00689 MPa		

6.4.2. Measurements and Discussion. As described in Section 3, strain gauges were placed at six different depths in the mid-span section of the girders. A “zero” or “baseline” strain reading was recorded for each instrumented girder just prior to release of prestress, and another set of readings was taken on each girder just after release of prestress. Note that for girders B23 and B24, since cracks were recorded at the gauge locations prior to the release of prestress, strain gauge readings before release included the strain caused by cracking while the readings after release did not because the cracks closed entirely after release. The cracking increased the strain gauge readings and thus the readings were not proper for interpretation for strain due to prestress release. However, to study the later-age behavior of girders B23 and B24, strains monitored by two bottom strain gauges were used for other gauges to correct the effect of cracking and hydration from initial cracking to the release of prestress, assuming same amount of

strains changing for all strain gauges along the section depth at the same section during this period. Therefore, there would be errors which were about 10 - 25% due to this assumption in the strain analysis for girder B23 and B24.

A regression line was fit to the measured release strains for each girder. Measured stresses at release were then estimated using the regression line by multiplying strain values by the measured modulus of elasticity, and comparisons were made with predictions based on design properties and measured properties. A design method and a refined design method are used based on the standard stress equations. The difference between the two prediction methods is listed in Table 6.4. The major differences are refined design method suggested by author uses measured MOE and 2.0% prestress loss before prestress release while AASHTO LRFD uses method specified in the specification. Measured strain data at mid-span and near end-support section are illustrated in Figures 6.12 through 6.19.

Table 6.4. Methods for Prediction of Mid-span Release Stresses

Parameter	Design Method AASHTO LRFD (1994)	Refined Design Method Suggested by Author
Section Properties	Transformed section properties with designed modulus of elasticity	Transformed section properties with Measured modulus of elasticity
Prestress Force/Loss	No loss assumed before release. Elastic shortening loss calculated by approximate method given in AASHTO LRFD Specifications	2.0% loss assumed before release based on measurements. Elastic shortening loss not added because exact analysis using transformed section properties was used.
Modulus of Elasticity	Eq. 1.3 for HSC (ACI 363R-92)	Based on tests of companion specimens

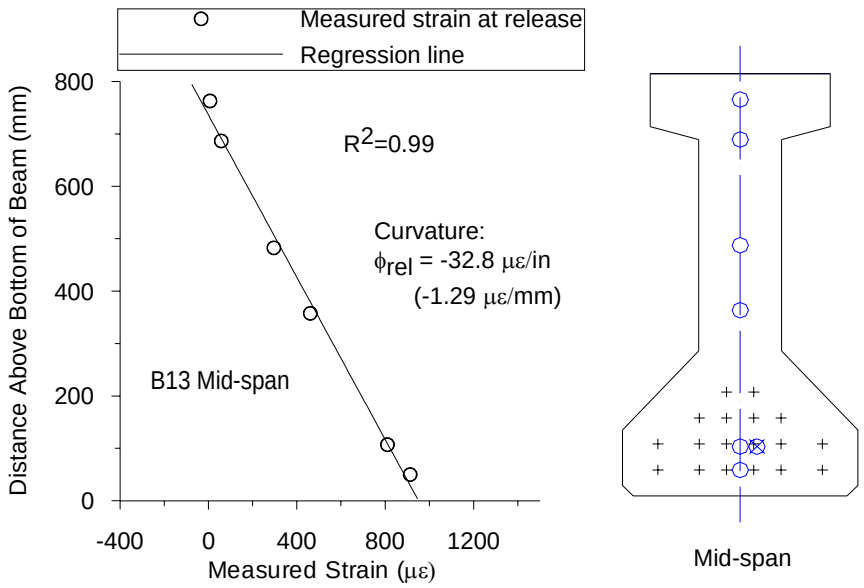

Figure 6.12. Measured Strain at Mid-span of Girder B13 at Release

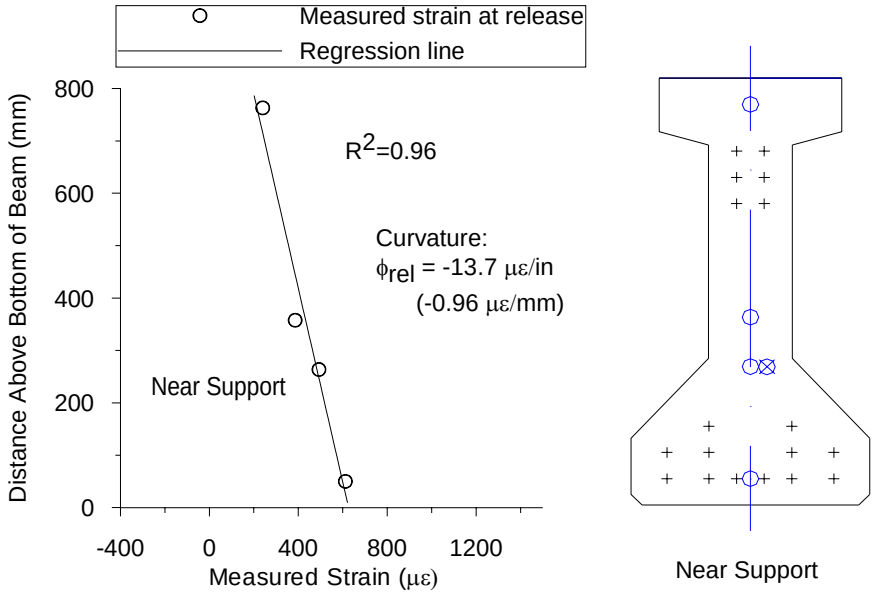

Figure 6.13. Measured Strain at Near End Support Section of Girder B13 at Release

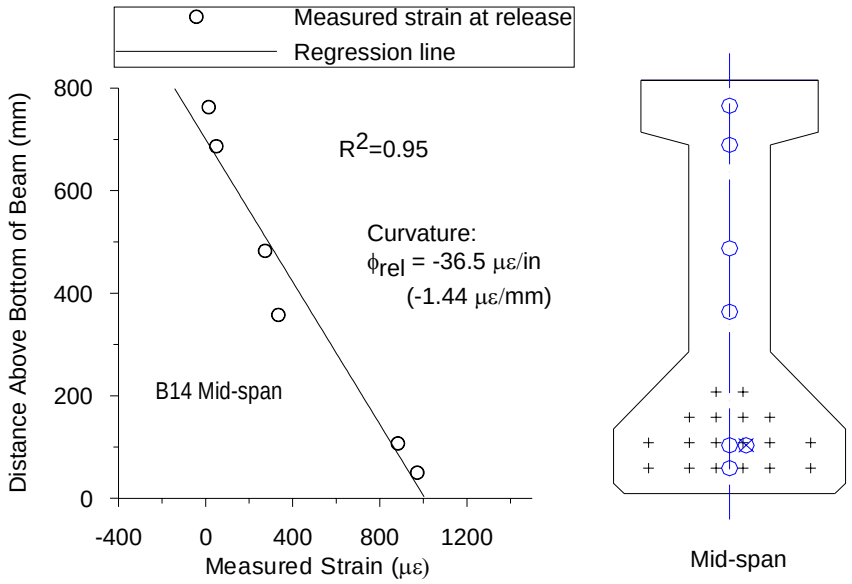

Figure 6.14. Measured Strain at Mid-span of Girder B14 at Release

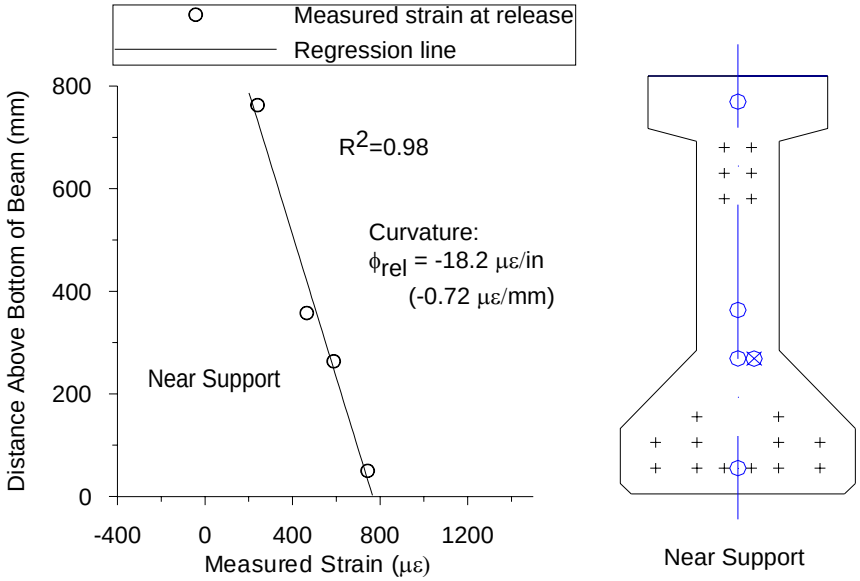

Figure 6.15. Measured Strain at Near End Support Section of B14 at Release

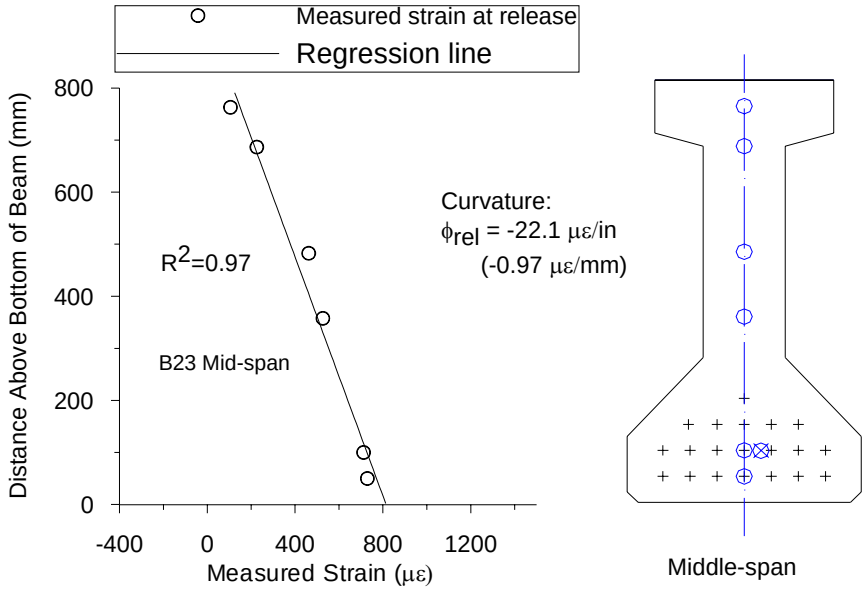

Figure 6.16. Measured Strain at Mid-span of Girder B23 at Release

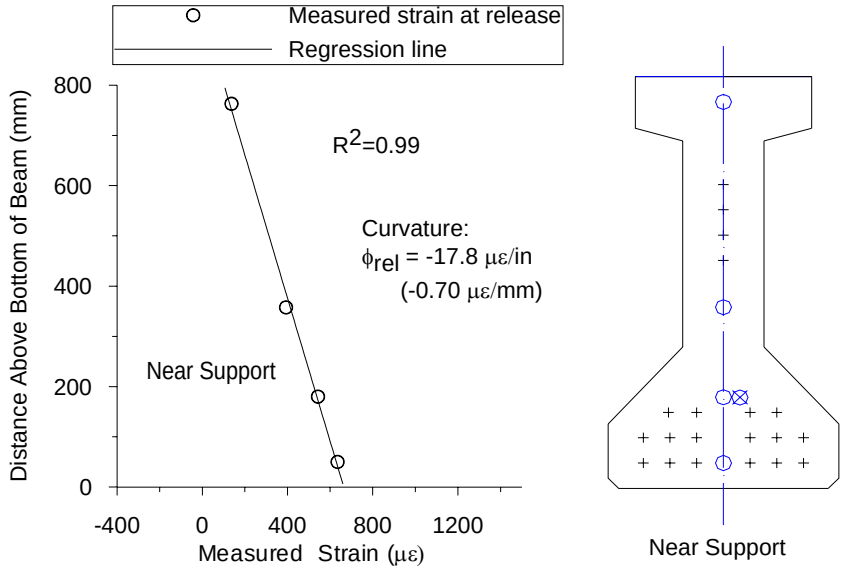

Figure 6.17. Measured Strain at Near End Support Section of Girder B23 at Release

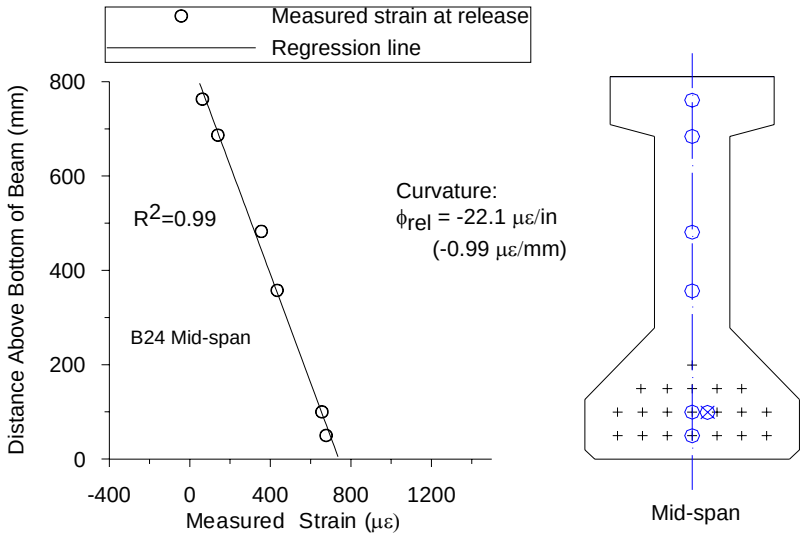

Figure 6.18. Measured Strain at Mid-span of Girder B24 at Release

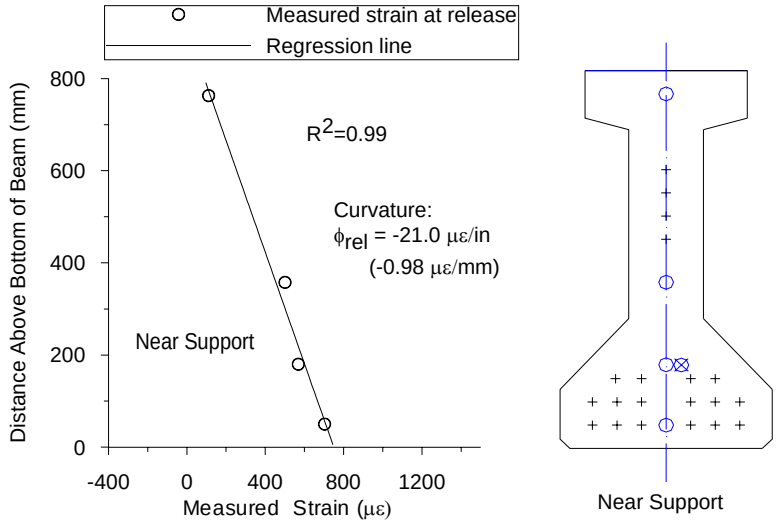

Figure 6.19. Measured Strain at Near End Support Section of Girder B24 at Release

It can be clearly seen that for all cases, the coefficients of determination range from 0.95 to 0.99, very close to 1.0, which means plane section of the girder remains plane. Since girder B13 and girder B14 had the same design, and were cast and released at the same time, the curvatures caused by prestress release at mid-span in the two girder B13 and B14 were 32.8 με/in and 36.5 με/in, respectively. Similarly, curvature was 22.1

με/in for both girders B23 and B24 at mid-span section. Stresses at top and bottom fiber of the section were calculated based on regression line and summarized in Table 6.5.

Table 6.5. Measured Stresses by Regression

Section	Curvature (με/in.)	R^2	Regression Stress Top fiber (psi)	Regression Stress Bottom fiber (psi)
B13-Mid-span	32.8	0.99	-504	4844
B13-Near End	13.7	0.96	953	3189
B14-Mid-span	36.5	0.95	-825	5135
B14-Near End	18.2	0.98	927	3902
B23-Mid-span	22.1	0.97	585	4491
B23-Near End	17.8	0.99	513	3663
B24-Mid-span	22.1	0.97	188	4088
B24-Near End	21.0	0.99	430	4138
Note: Compressive stresses are positive; Tensile stresses are negative. 1 inch = 25.4 mm; 1 ksi = 6.89 MPa				

In Figures 6.20 through 6.23, measured stresses are compared with predictions based on design properties and measured properties. In girder B13, the strains measured are a little higher than the predicted strains by 5 - 15% for all locations along the section. However, since there is tensile stress at the top fiber, it actually means the measured tensile stresses are lower than predicted. At the bottom fiber, measured strain is 16% higher than predicted using the design method, 9% higher than predicted using the refined design method. At the mid-span section of girder B14, both tensile stresses at top fiber and compressive stresses at bottom fiber are higher than predicted. At the top fiber of girder B14, measured tensile stress is 33% higher than predicted using the design method and 23% higher than predicted using the refined design method. At the bottom

fiber of girder B14, measured compressive stress is 21% higher than predicted using the design method and 15% higher than predicted using the refined design method. The regression lines for the measured data are reasonably close to the predicted lines using the design method and refined design method.

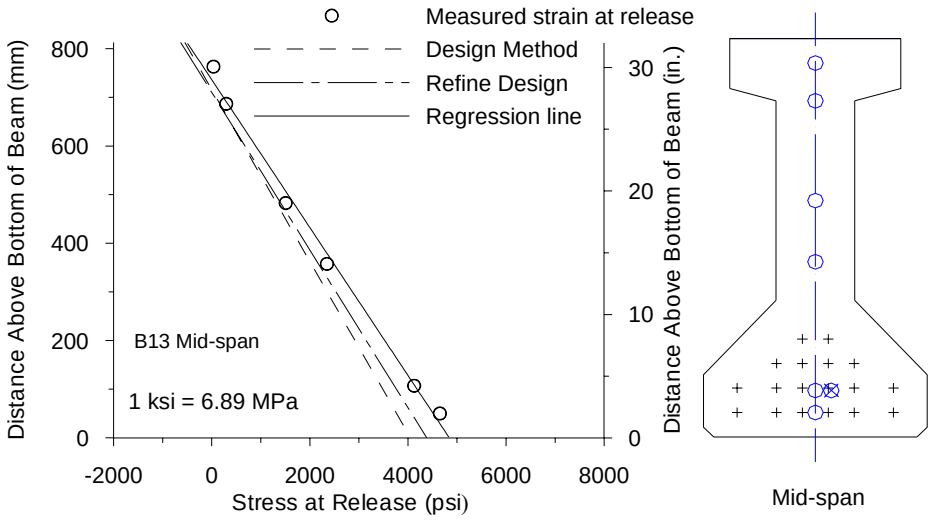

Figure 6.20. Stresses Comparison at Mid-span of Girder B13 at Release

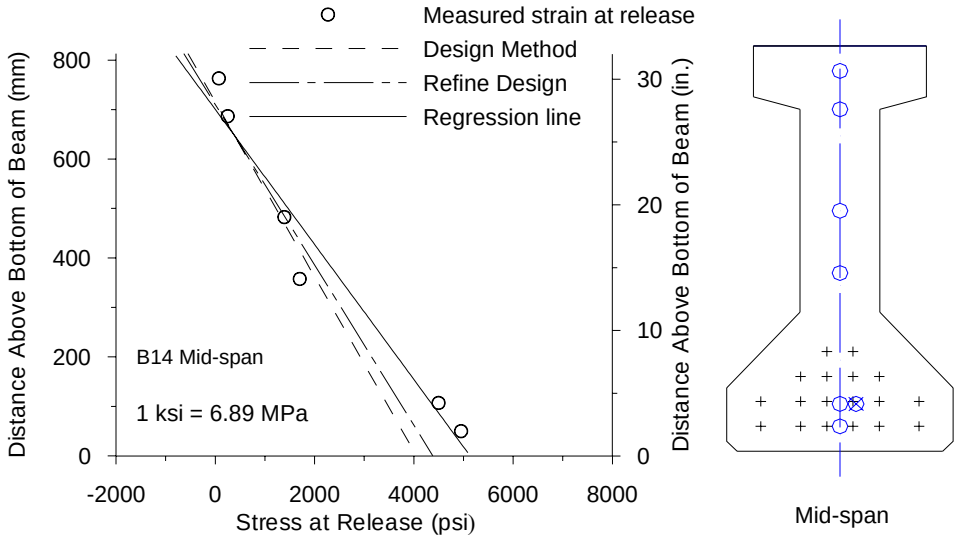

Figure 6.21. Stresses Comparison at Mid-span of Girder B14 at Release

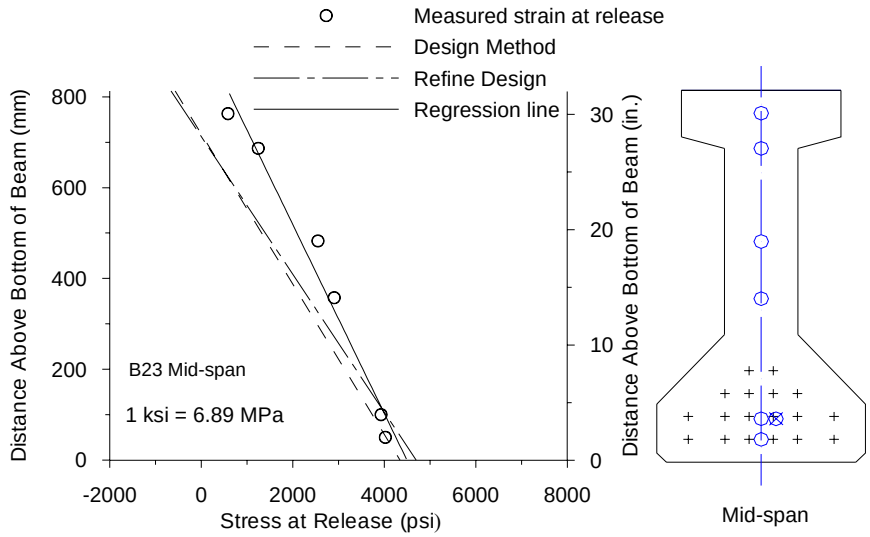

Figure 6.22. Stresses Comparison at Mid-span of Girder B23 at Release

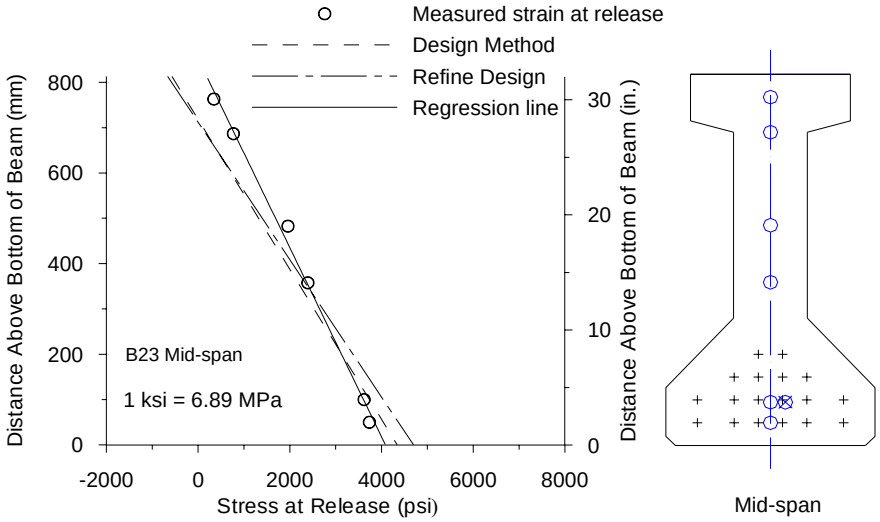

Figure 6.23. Stresses Comparison at Mid-span of Girder B24 at Release

For girders B23 and B24, at mid-span, measured strains at the top fiber are compressive strains. Curvature for measured data is much lower than predicted by about 30%. At the bottom fiber, the compressive stresses for girder B23 is 3% higher than predicted using the design method and 5% higher than predicted using the refined design method. At the mid-span section of girder B24, the compressive stresses at bottom fiber

is 6% higher than predicted using the design method and 15% higher than predicted using the refined design method. As discussed in the beginning of this section, about 10 - 25% errors existed in strain analysis for mid-span section due to cracking prior to release at the gauge locations. At the same time, the restraint of the precasting bed and concrete shrinkage made the process much more complicated for calculation.

However, for most cases, the refined design method provides results closer to measured data than the design method. Measured compressive stresses at the bottom fiber are less than 21% higher than predicted using the design method and 15% higher than predicted using the refined design method. At the top fiber of mid-span, it should be noted that for girder B14, the measured stress was 33% higher than predicted.

It is important to note that measured stresses are sensitive and depend on measured modulus of elasticity data. Therefore, empirical models used to predict the modulus of elasticity will inherently have a significant affect on the accuracy of predicting the measured stresses. It was found that using an empirical model to predict the modulus of elasticity at early-age will usually significantly underestimate the modulus of elasticity by up to 40% (Myers 1998).

Measured and predicted stress results are summarized in Figure 6.24 and Figure 6.25 and compared with allowable stress levels specified in the AASHTO specification. When comparing with allowable stresses, the tensile stresses at top fiber meet requirement at release for all girders expect girder B14. At mid-span of girder B14, tensile stress measured at top fiber is 27% higher than allowable stresses. However there was no cracking observed at mid-span after the release of prestress. The reason can be the restraint from the precasting bed. Before release, the casting bed restrained the

deformation of the girders as discussed before. After the release of the prestress, the restraint (friction between girder and bed) of the bed acted as an additional force on the girder, which led to the higher stresses in the girders. At the same time, prestress losses and shrinkage were different for various girders and led to the complication of this process. It might be the same reason why measured stress at bottom fiber of girder B14 is also 14% higher than allowable stresses and measured stress at bottom fiber of girder B13 is also 7% higher than allowable stresses.

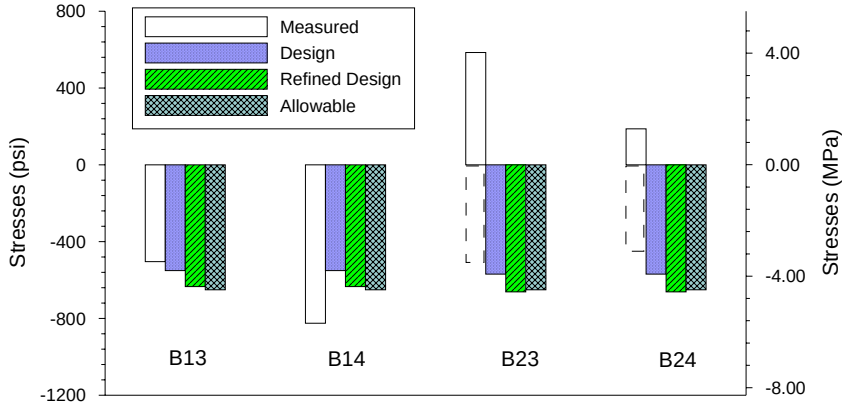

Figure 6.24. Stresses Comparison at Top Fiber of Mid-span Section at Release

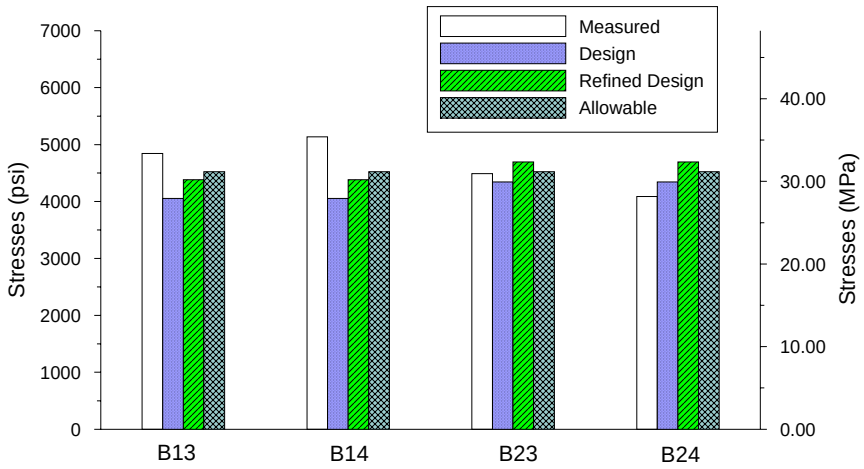

Figure 6.25. Stresses Comparison at Bottom Fiber of Mid-span Section at Release

At mid-span of girders B23 and B24, tensile stresses were expected at the top fiber as shown as dashed lines in Figure 6.24. However, compressive stresses observed at the top fiber based on measured data. The reasons could be combination of errors due to cracking prior to release at the gauge locations, restraint of casting bed, prestress losses, and shrinkage.

6.5. CONCRETE STRAINS IN GIRDERS DURING STORAGE

6.5.1. Background. Due to time-dependent effects, prestressed concrete girders continue to deform after strand release. The time-dependent strains are generally considered in the prediction of prestress losses and girder camber or deflection. In this Section, strain changes during storage are discussed. During this time, only pretensioning force and self-weight load are acting on the member.

The theoretical time-dependent strains at a given section can be computed as a function of the initial elastic strains using the approximate step-function equations adopted by ACI Committee 435 - Deflection of Concrete Building Structures (ACI 435R-95, 1995). The time-dependent strain can be computed as:

$$\varepsilon(y,t) = \left(\frac{1+S_t}{E_{ci}}\right)\cdot\left(\frac{P_0}{A}\right) + \left(\frac{1+S_t}{E_{ci}}\right)\cdot\left(\frac{P_0 \cdot e \cdot y}{I}\right) - \left(\frac{1+C_{ct}}{E_{ci}}\right)\cdot\left(\frac{M_{self-wt} \cdot y}{I}\right) + \varepsilon_{sh,t}$$

Equation 6.7

where, E_{ci} is the modulus of elasticity of the concrete at release; A is the area of the cross section; I is the moment of inertia of the section; y is the distance from the centroid to the location where strain is calculated; e is the eccentricity of the strand; C_{ct} the creep coefficient at time t; $M_{self-wt}$ is the moment caused by self weight of the girder; P_0 is

prestress force at release; $\varepsilon_{sh,t}$ is the shrinkage strain at time *t*; S_t represent the effect of creep, the effects of prestress losses and the interrelation between creep and prestress loss.

The parameter S_t is estimated as:

$$S_t = -\frac{\Delta P}{P_0} + \left(1 - \frac{\Delta P}{2P_0}\right) \cdot C_{ct} \qquad \text{Equation 6.8}$$

where, $\Delta P = P_0 - P_e$; P_0 is prestress force at release; P_e is effective prestress force at time when strain is being computed; C_{ct} the creep coefficient at time *t*.

With the introduction of the above method, the time-dependent strain can be calculated. Sufficient accuracy can usually be obtained if the prestess loss is assumed based on past experience, and the validity of any assumption can be checked by comparing the assumed loss with the calculated strain at the center of gravity (c.g.) of the prestressing strands (Gross, 1999).

6.5.2. Measurements and Discussion. As described in Section 3, strain gauges were placed at six different depths in the mid-span section of the girders. A “zero” or “baseline” strain reading was recorded for each instrumented girder immediately prior to release of prestress. Note that crack formation at the gauge location for girders B23 and B24 prior to release affected the baseline strain readings. The modification same as in Section 6.4 is applied. All of the strains were corrected for thermal effects including thermal gradients along the girder section. During storage, most of the girders stayed at the same locations except some of them were moved for curing. Girder supports were never changed and thus have no effect on the strain measurements. Therefore, the effect of girder supports changing was not considered in this project.

The time-dependent strain behaviors at mid-span section for all four monitored girders are shown in Figures 6.26 through 6.29. As illustrated for girders B13 and B14, the predicted and measured data corresponded well, with 110 - 180 microstrain difference. For girders B23 and B24, the differences between predicted and measured values were more significant, with 200 - 250 microstrain difference. The increase in the measured strains was slower than predicted during the first two months.

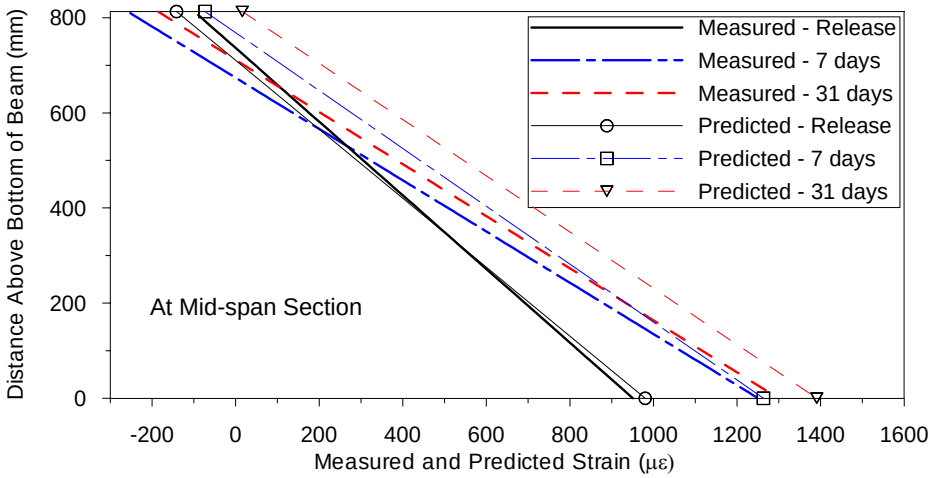

Figure 6.26. Strain at Mid-span of Girder B13 in Storage

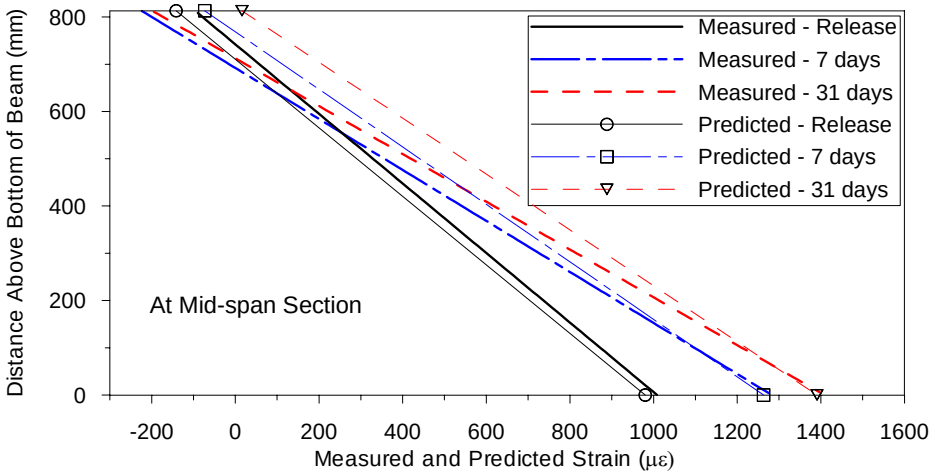

Figure 6.27. Strain at Mid-span of Girder B14 in Storage

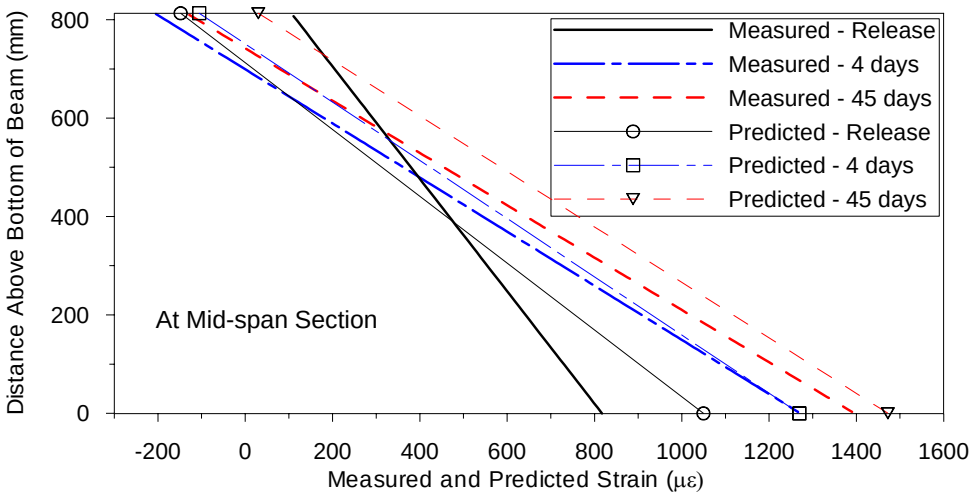

Figure 6.28. Strain at Mid-span of Girder B23 in Storage

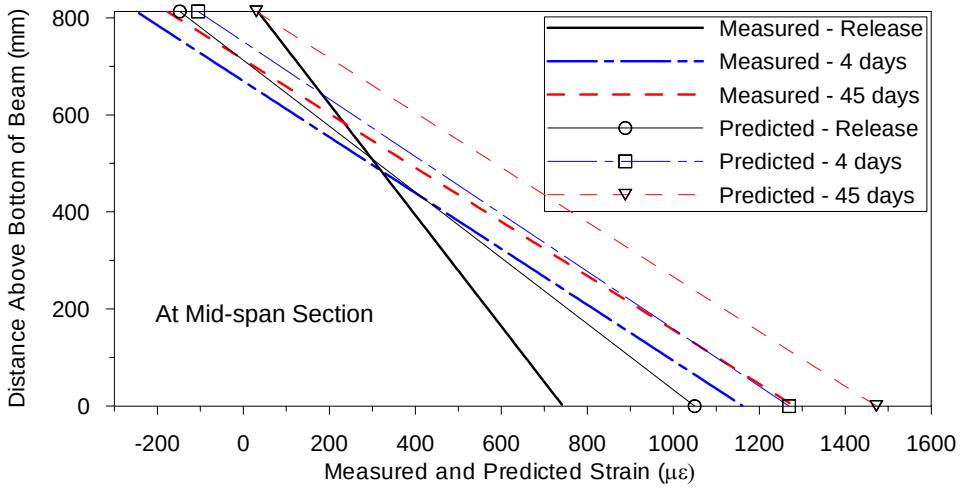

Figure 6.29. Strain at Mid-span of Girder B24 in Storage

The cumulative time-dependent strains are dependent on the baseline reading taken immediately prior to release, similar to measured strain at release. Therefore, these measurements may also include the effect of the release of restraint against shortening of the girder. These measurements may thus be artificially high because the release of restraint appears as an apparent additional compressive strain. This effect does not influence the time-dependent growth of strain.

The potential reasons that time-dependent strain growth was substantially lower than predicted could be the combination of prestress losses, modulus of elasticity, creep, shrinkage, etc.

6.6. STRAINS DUE TO TRANSPORTATION, ERECTION AND DECK

6.6.1 Background. The strain changes within the girder due to transportation, erection and deck are studied in this Section. During transportation from the precast plant to the jobsite girder strains were monitored with no extra load applied on the members except for wind and force caused by acceleration and deceleration of the truck. Strain distributions in the members prior to and after erection are compared in this Section.

Stresses resulting from deck loads are generally computed using a classical mechanics approach. The moment acting at a section is first computed and the stresses at an individual section resulting from the moment are then calculated. For a uniformly distributed load *w*, the resulting stress at mid-span in a simply-supported girder would be computed using following equation:

$$\sigma(y) = -\frac{M \cdot y}{I} = -\frac{(\frac{w \cdot l^2}{8}) \cdot y}{I} \qquad \text{Equation 6.9}$$

Note that *y* is defined as positive below the centroid of the girder for Equation 6.9, and that compressive stresses are assumed to be positive. A positive moment is defined as one causing downward deflection in a simply-supported member.

The uniformly distributed load *w* for different girders is listed in appendix. Since the deck is unshored during construction, the girder alone is assumed to resist the full deck load and the precast girder section properties should be used.

6.6.2 Measurements and Discussion. As described in Section 3, strain gauges were placed at six different depths in the mid-span section of the girders. A "zero" or "baseline" strain reading was recorded for each instrumented girder immediately prior to release of prestress. Note that crack formation at the gauge location for girders B23 and B24 prior to release affect the baseline strain readings, modification same as in Section 6.4 is applied. All the strains were corrected for thermal effects including thermal gradients along the girder section.

Figure 6.30 illustrates the strains in girder B13 and girder B14 respectively before and after transportation. It is evident that the changes were less than 20 microstrain, which were very small in both girders. Similarly, the changes in girders B23 and B24 due to transportation were also very small, less than 25 microstrain.

It required three and a half hours to transport the girders from Bonne Terre, Missouri to the jobsite, near Hayti, Missouri. The strain during transportation at different location in girder B23 was recorded as illustrated in Figure 6.31. The change in strain measured was between -40 to 30 microstrain during transportation.

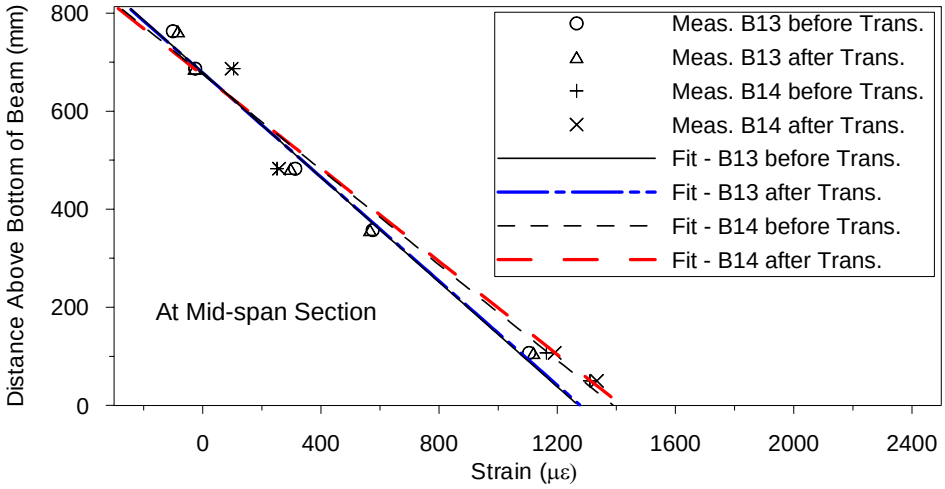

Figure 6.30. Strain at Mid-span of Girders B13 and B14 Before and After Transportation

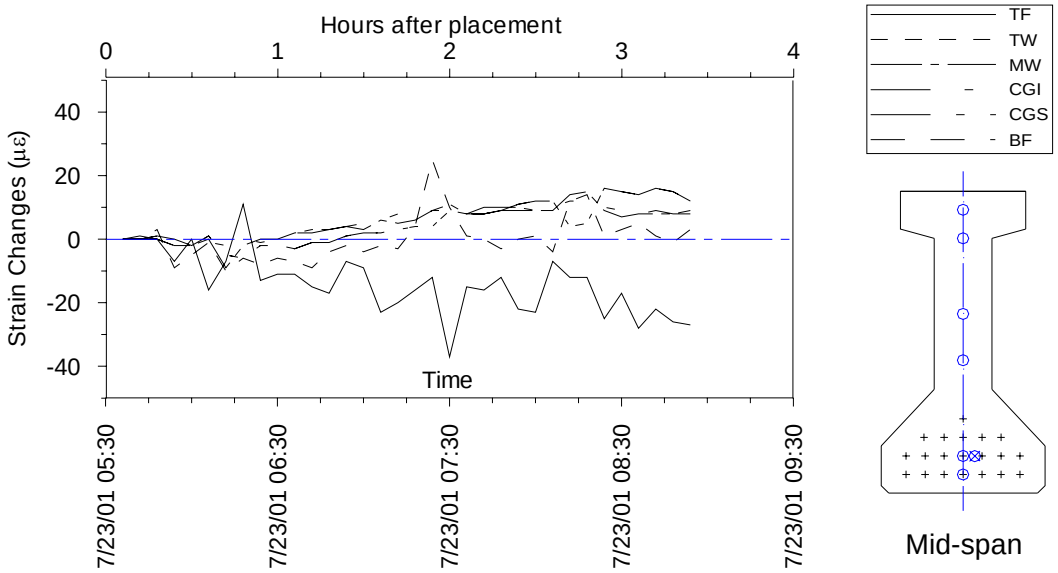

Figure 6.31. Strain Changes during Transportation in Girder B23

Immediately following delivery of the girders to the jobsite, they were erected on the pier bents. Figure 6.32 illustrates the strains in girders B13 and B14 before and after erection. The changes in strain for both girders were minimal as expected (less than 30 microstrain).

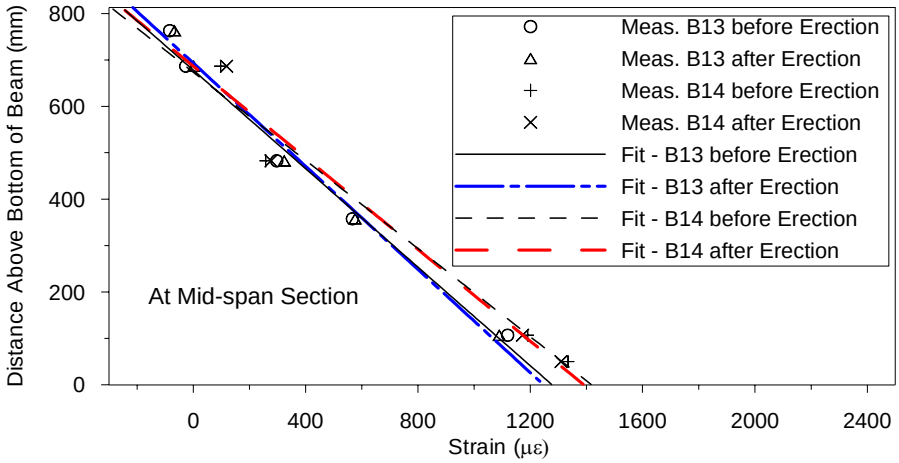

Figure 6.32. Strain Profile Before and After Erection

On November 11th, 2001, the cast-in-place deck was placed beginning at 6:00pm. The casting work was completed by 5:00am the following day. The strains internally within the girders were recorded. As shown in Figure 6.33 and Figure 6.34, at the mid-span section of monitored girders, plane sections before and after deck casting remain plane. Minor differences were observed between interior girder B13 and exterior girder B14.

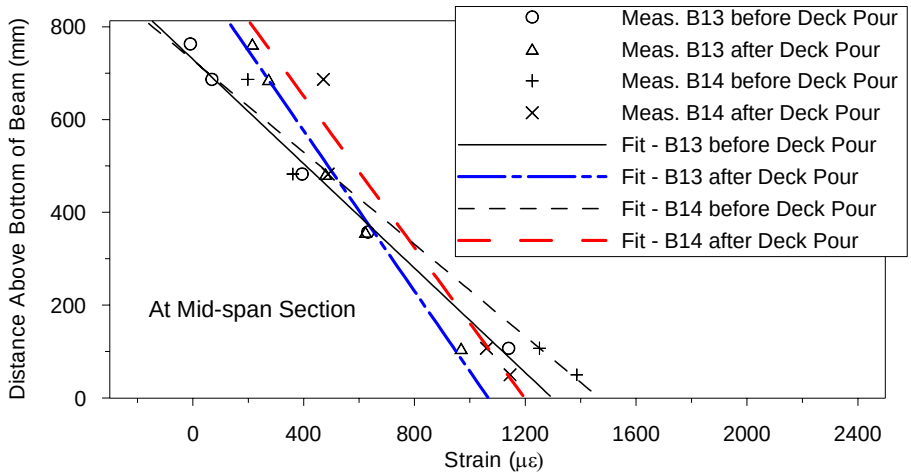

Figure 6.33. Strain Profile Before and After Deck Pour for Girders B13 and B14

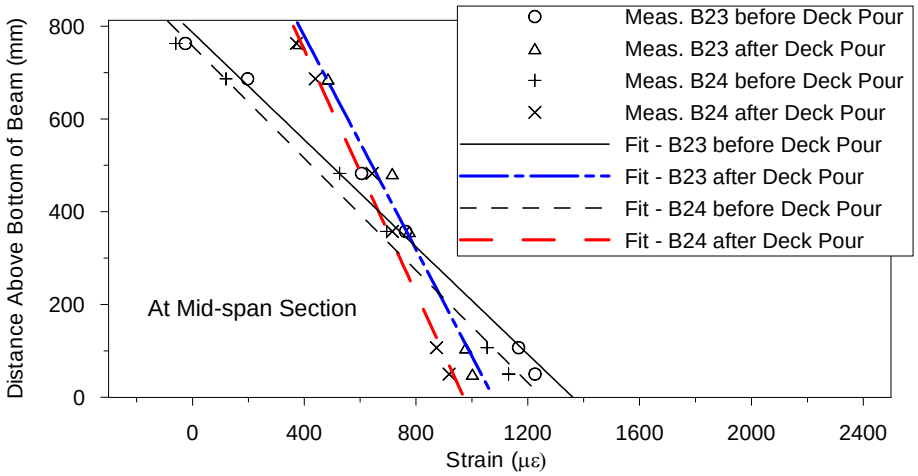

Figure 6.34. Strain Profile Before and After Deck Pour for Girders B23 and B24

Measured strain due to deck load was compared with predicted values as illustrated in Figures 6.35 through 6.38. Predicted values were calculated using the refined design method, which was recommended by the author as discussed in Section 6.3. A small variation between measured and predicted values by less than 15% was observed. Therefore, Equation 6.9 can be used for estimating the stress due to deck load.

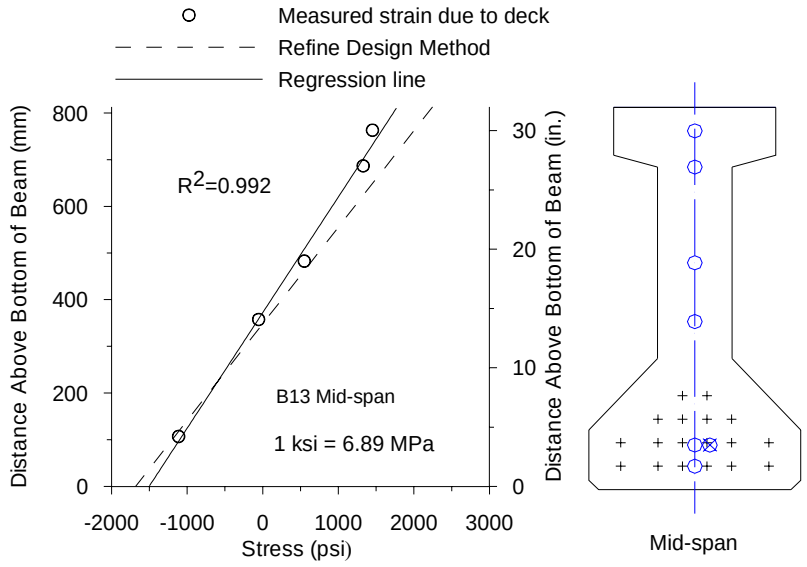

Figure 6.35. Stress Due to Deck Weight for Girder B13

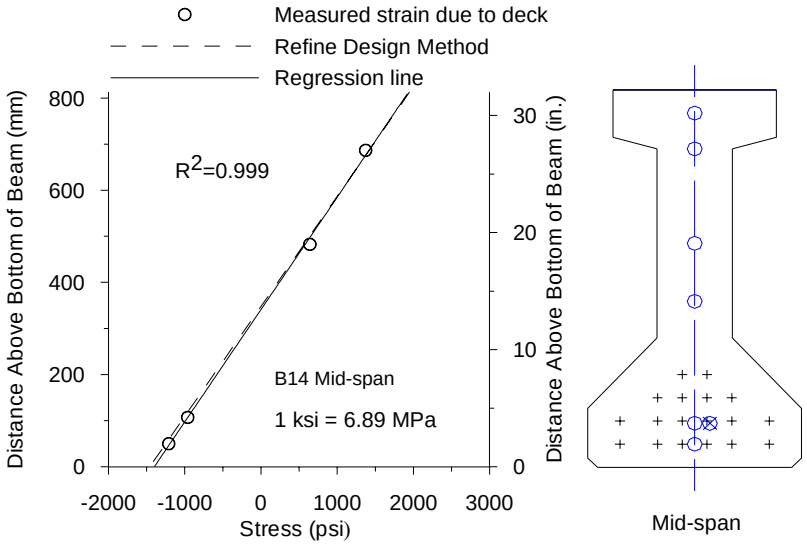

Figure 6.36. Stress Due to Deck Weight for Girder B14

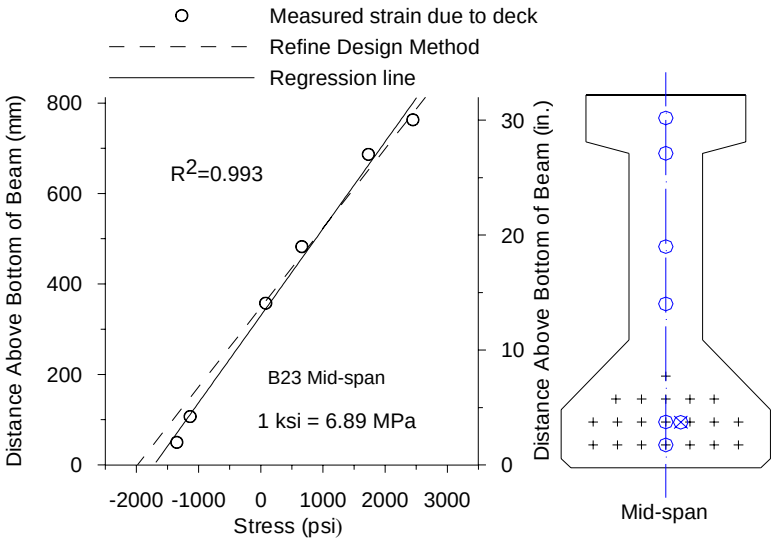

Figure 6.37. Stress Due to Deck Weight for Girder B23

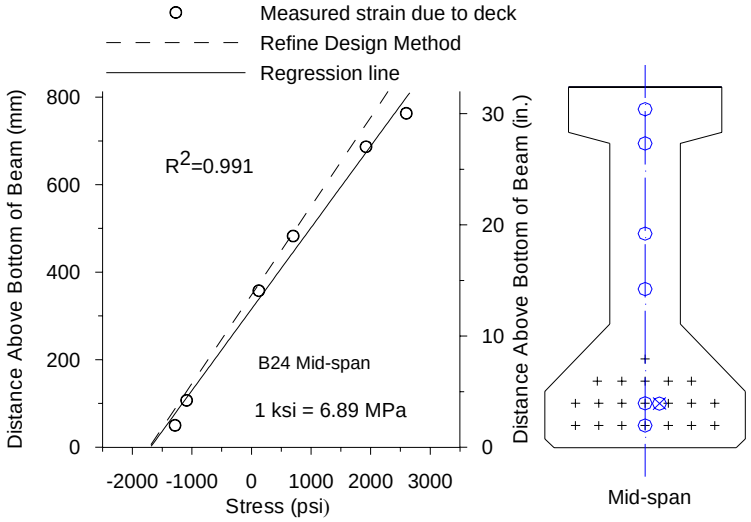

Figure 6.38. Stress Due to Deck Weight for Girder B24

6.7. CONCRETE SURFACE STRAINS AND TRANSFER LENGTH

Prestressing strand and concrete in a pretensioned, prestressed member interact through bond. Without bond, no transfer of forces would occur and the member would not act integrally. For high strength concrete with 15.2 mm (0.6in.) diameter prestressing

strand, the demand on bond is magnified. As a result, numerous researchers have studied prestressing bond, transfer length and development length, over the last half decade.

Development length, l_d, is the shortest bonded length of bar or tendon along which the bar or tendon stress can increase form zero to the stress required for achievement of the full nominal strength at the section under consideration. Development length is the algebraic sum of transfer length and flexural bond length.

Transfer length, l_t, is defined as the bonded tendon length required developing the full effective prestress force f_{pe} in prestressing tendon.

Flexural bond length, l_{fb}, is defined as the distance, in addition to the transfer length, over which the tendon must be bonded to the concrete in order that a stress f_{ps} may develop in the tendon at nominal strength of the member. Note that is the stress in the strand at the ultimate strength of the member. In this project, transfer length was investigated for high strength concrete with 15.2 mm (0.6 in.) diameter prestressing strand.

The concrete surface strain using the DEMEC gauges provided reliable and consistent data. Transfer length was calculated using the 95% average maximum strain (95% AMS) method discussed by Russell (1992).

Figure 6.39 gives the smoothed concrete surface strain data for Girder B13 in first span. Using the 95% AMS method, the transfer length was 361 mm (14.2 in.). Figure 6.40 illustrates the smoothed concrete surface strain for Girder B21 in second span. The transfer length was 475 mm (18.7 in.). These results are consistent with other tests results on prestressed concrete girders with 15.2 mm (0.6 in.) diameter prestressing strand as reported by Barnes et al. (1999).

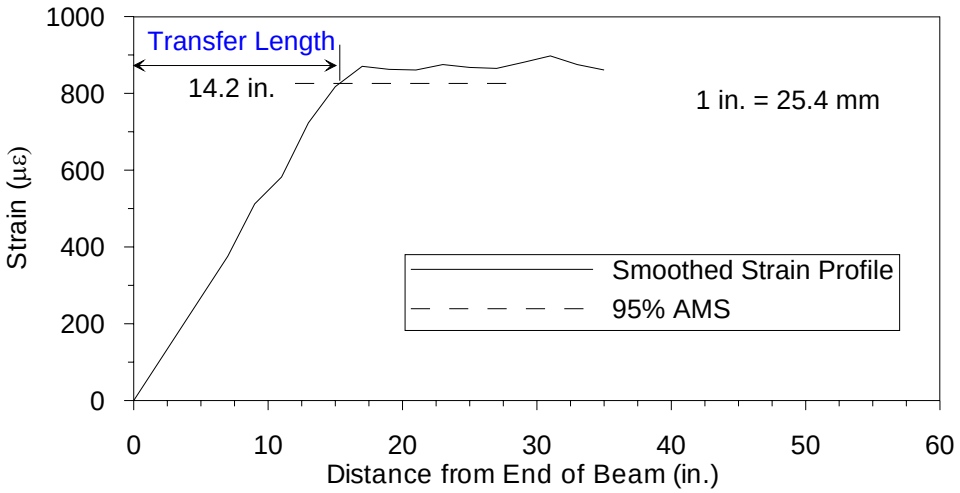

Figure 6.39. Transfer Length for Girder B13

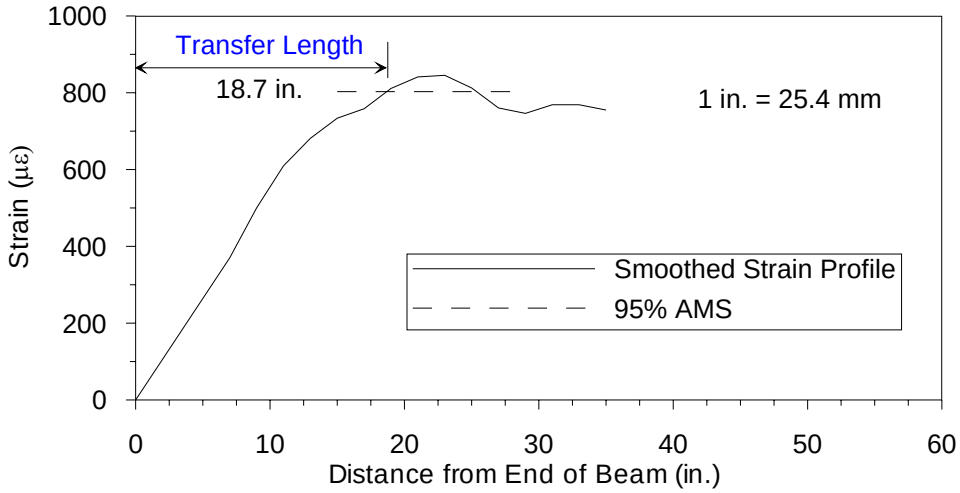

Figure 6.40. Transfer Length for Girder B21

6.8. SUMMARY AND CONCLUSIONS

Concrete strain behavior prior to release is significantly influenced by restraint from formwork and the precasting bed, hydration temperatures, and shrinkage. During hydration, strain gradients in girders were consistent with observed temperature gradients. Measured strains were only 40% of the free thermal strains corresponding to measured temperatures.

Cracking was observed on all instrumented girders prior to release as a result of restraint against shortening due to cooling and drying shrinkage. Number, length and spacing of recorded cracking were case dependent. A sudden increase of the tensile strain was recorded in two instrumented girders while cracking at the same location was observed. The cracking at mid-span occurred at about 33 hours, nearly a day and a half, after the concrete was placed in the two instrumented girders. The sudden strain drop occurred in all strain gauge locations except the bottom two. This indicated that cracks propagated from the top fiber to at least the center of gravity (c.g.) of the section.

These cracks closed entirely upon release of prestress and were often impossible to find thereafter. No structural impact was observed in this research program as a result of the formation of these cracks prior to release. To avoid such cracking, the timing during the construction process is the key controllable factor. Girders should be released as soon as possible after required concrete strengths are obtained. As in this project, the cracking may be avoided if it is released less than 33 hours, about a day and a half after the concrete was placed. Release at 1-day is also more of an industry standard.

Measured strains due to release were fitted linearly. The coefficients of determination ranged from 0.95 to 0.99, which exhibits plane sections prior to the release of prestress remain plane after release. When comparing the recorded data with predicted data, the stresses are sensitive to the modulus of elasticity of the concrete. To avoid error due to modulus of elasticity physical testing of concrete representative of concrete in the member or mix design to be used under match curing is recommended.

The regression lines for the measured data are close to the predicted lines using the design method (AASHTO) and the refined design method presented by the author.

Generally, the refined design method yields improved predicted results than the design method. In some instances, the stresses are higher than predicted stresses and even allowable stresses. The reason can be the restraint from the precasting bed. Before release, the casting bed restrained the deformation of the girders as discussed before. After the release of the prestress, the restraint of the bed acted as an additional force on the girder, which led to the higher stresses in the girders. At the same time, prestress losses, modulus of elasticity, and shrinkage could also contribute to this complicated process.

For most cases, the time-dependent strain behaviors at the mid-span section are much smaller than predicted. The increase in the measured strains was slower than predicted druing the first two months. The prediction method is good for the first month while for the later age the predicted values are far from measured data. The potential reasons that time-dependent strain growth was substantially lower than predicted could be the combination of prestress losses, modulus of elasticity, creep, shrinkage, etc.

The changes in measured strain due to transportation were between -40 to 30 microstrain, which were minimal and thus could be neglected. The changes in measured strain due to erection were less than 30 microstraion. These changes were minimal in all instrumented girders and could be omitted. Measured strain due to deck was compared with predicted values. Small difference (less than 15%) between the two methods was found. Using the theoretical method is precise enough for estimating structural behavior due to deck load for HPC prestressed girders.

7. PRESTRESS LOSS MEASUREMENTS

7.1. INTRODUCTION

7.1.1. General. For prestressed concrete highway bridge girders prestress losses are an important factor related to serviceability conditions. The effective prestress in girders is the nominal jacking force after prestress losses. As a result, losses have a direct impact on concrete stresses development and deflection behavior of the member. A poor estimate of prestress losses can result in a structure where allowable stresses are exceeded or camber and deflection behavior is poorly predicted, such that the serviceability of a structure may be adversely impacted. It should be noted that for bonded members, prestress losses do not impact the ultimate strength of a member.

Loss predictions are needed in order to calculate the required jacking force and to check stresses at different load stages. The most common stages that are checked are:

- Immediately following transfer when tension force is high but compressive strength of concrete is still low.
- In some cases during construction including deck casting.
- At service load after all losses or when most have occurred.

Actual losses are difficult to predict and depend on a number of factors including actual time elapsed, exposure conditions, dimensions of the member, etc. There are several sources of loss in prestressed concrete highway bridge girders. For pretensioned strands, these losses are summarized below in Table 7.1. For post-tensioned tendons, anchorage loss and friction loss should be considered.

Strand relaxation, which is defined as the slight reduction in strand stress under a sustained deformation, results in a time-dependent change in the strand stress. Relaxation

losses can be computed if the relaxation-time relationship is known. This relationship is sometimes supplied by the strand manufacturer, or a well known equation is typically used for 7-wire low relaxation strand to compute this stress change as Equation 7.1 (Gross, 1999). This equation is for low-relaxation strands, which are typically used in the fabrication of prestressed highway girders today, just as in this project.

Table 7.1. Types of Prestress Loss for Pretensioned Strands

Types	Stage of occurrence	Tendon stress loss
Relaxation of tendons (R)	Before and after transfer	$\Delta f_{ps,RE}$
Elastic shortening of concrete (ES)	At transfer	$\Delta f_{ps,ES}$
Creep of concrete (CR)	After transfer	$\Delta f_{ps,CR}$
Shrinkage of concrete (SH)	After transfer	$\Delta f_{ps,SH}$
Thermal effects	During hydration	$\Delta f_{ps,TH}$
TOTAL	Life	$\Delta f_{ps,Total}$

$$\Delta f_{ps,relaxation} = f_{jack} \cdot \left(\frac{\log_{10} t}{45} \right) \cdot \left(\frac{f_{jack}}{f_{py}} - 0.55 \right) \qquad \text{Equation 7.1}$$

The time t is the time after initial stressing and must be taken in hours. The yield stress of the strand f_{py} is typically assumed to be 90% of the nominal ultimate strength of the strand f_{pu}. If the pretensioning force is less than $0.55 f_{py}$, no losses due to relaxation will occur. However, we generally would not design to this pretensiong force level because it is not efficient.

Elastic shortening happens when the prestress force is transferred to the concrete because the concrete member shortens and the steel shortens along with it. For

pretensioned members, elastic shortening losses can be computed exactly using the transformed section. The full prestress force before release P_i is applied and stresses in the transformed section due to prestress and self-weight of the member are computed. In particular, stresses are computed at the center of gravity (c.g.) of the pretensioned strands as in Equation 7.2:

$$f_{cgs} = \frac{P_i}{A_t} + \frac{P_i \cdot e_t^2}{I_t} - \frac{M_{self-wt} \cdot e_t}{I_t} \qquad \text{Equation 7.2}$$

In Equation 7.2, compressive stresses are assumed to be positive and the eccentricity of the strands e_t is assumed to be positive when the c.g. of the strands is below the centroid of the section. Using the principles of strain compatibility, the change in stress in the pretensioned stands can be computed as in Equation 7.3. The exact computation using the transformed section method is equivalent to computation using the net concrete area and prestress force P_0 after elastic shortening loss as in Equation 7.4. In design it is usually considered sufficient to estimate the elastic shortening loss by using gross section properties and an assumed value for P_0 as in Equation 7.5. Effective prestress forces are specified differently in different specifications as presented in Table 7.2.

$$\Delta f_{ES,steel} = n \cdot f_{cgs} = \frac{E_{ps}}{E_{ci}} \cdot f_{cgs} \qquad \text{Equation 7.3}$$

$$f_{cgs} = \frac{P_0}{A_c} + \frac{P_0 \cdot e_c^2}{I_c} - \frac{M_{self-wt} \cdot e_c}{I_c} \qquad \text{Equation 7.4}$$

$$f_{cgs} = \frac{P_0}{A_g} + \frac{P_0 \cdot e_g^2}{I_g} - \frac{M_{self-wt} \cdot e_g}{I_g} \qquad \text{Equation 7.5}$$

Table 7.2. Specified Effective Prestress Forces

Code	Effective Prestress Forces
AASHTO LRFD Specification	$f_{s0} = 0.70 \cdot f_{su}$
AASHTO Standard Specification	$f_{s0} = 0.69 \cdot f_{su}$
PCI Design Handbook	$P_0 = 0.90 \cdot P_i$
f_{su} - Ultimate strength; P_i - Initial prestress force.	

As discussed in Section 4, creep of concrete causes a time-dependent change in strain throughout the depth of the member; where the cross-section is in compression under elastic effects due to application of sustained load, an additional compressive strain will develop over time. Any strand bonded to the concrete section in these compressive regions will shorten along with the concrete such that the tension in the strand is reduced.

Concrete shrinkage will result in a similar time-dependent compressive strain and will also cause a loss of tension in the pretensioning strand.

7.1.2. Measurement of Prestress Losses Using Embedded Gauges.

Measurements of prestressed losses were indirect since changes in stress were not actually measured. Instead, changes in concrete strain at the level of the c.g. of pretensioned strands were measured using embedded strain gauges. The results were converted to prestress losses by multiplying the modulus of elasticity of the prestressed steel as illustrated in Equation 7.6.

$$\Delta f_{ps,measured} = E_{ps} \cdot \varepsilon_{cgs,measured} \qquad \text{Equation 7.6}$$

Modulus of elasticity of the prestressed steel was taken as 193 GPa (28,000 ksi) in Equation 7.6. The modulus of elasticity of the prestressing strands used in this project

was 193 GPa (28,000 ksi) as provided by the manufacturer and that is also the value used for design.

Losses due to relaxation of the strand are not accounted for in this method because these losses do not cause a direct change in strain in the concrete at the level of the strand. Therefore, these losses must be added analytically using the established relaxation-time relationship for the strand as in Equation 7.1. Low relaxation strand is used in this project and minimal error should result from the use of this analytical correction. The baseline measurements were recorded immediately prior to release of prestress. There were some unrecorded prestress losses prior to this time as a result of early-age shrinkage, thermal effects and relaxation. These losses must be added to the total measurements of prestress loss. The corrected measured prestress losses is thus given by Equation 7.7:

$$\Delta f_{ps,total-measured} = E_{ps} \cdot \varepsilon_{cgs,measured} + \Delta f_{ps,relaxation} + \Delta f_{ps,pre-release} \qquad \text{Equation 7.7}$$

All concrete strains reported by the gauges should be corrected by removing the effects of temperature changes and thermal gradients as in Section 6.

7.2. PRESTRESS LOSSES BEFORE RELEASE

7.2.1. Background. Before release of the pretensioned strands, there are three main losses – relaxation of the strand, temperature effects, and concrete shrinkage. These losses directly affect the level of prestress applied to the member. To obtain a more accurate assessment of stresses, these losses should be considered at the corresponding time stage. Elastic shortening losses and long-term losses due to creep are dependent on the initial prestress after losses that occur before release. However, in real design

relaxation and shrinkage are typically calculated as part of the total loss of prestress. Thermal losses are often ignored in design since it is impossible to know the temperature variation between the time of stressing, release, and service stages.

Before the placement of concrete, strands are anchored between the bulkheads at each end of the bed. Each strand is an indeterminate structure. For any temperature change, there will be an axial force developed in the strand such that the total length of the strand does not change. Assuming compressive stresses or losses of tensile stress are positive, since an increase in strand temperature (a positive ΔT) will cause a decrease in tension, the stress loss can be calculated as illustrated in Equation 7.8:

$$\Delta f_{ps,thermal(pre-casting)} = E_{ps} \cdot \alpha_{ps} \cdot \Delta T \qquad \text{Equation 7.8}$$

Temperature changes relative to the strand temperature at jacking should be used if calculating the losses relative to the jacking stress.

Relaxation losses can be computed by using Equation 7.1 as discussed in the previous Section.

When the concrete is placed, the behavior of the strand inside concrete members becomes much more complex. The strand is restrained to varying degrees along the length. Before bond occurs, frictional restraint exists between the fresh concrete and the strand. After bond occurs, restraint keeps changing as concrete gains stiffness.

Thermal and relaxation losses before bond can be assumed to be “locked in” as bond occurs. After bond occurs, relaxation losses can be computed in the same manner as discussed prior to bond. Thermal effects after bond occurs would cause strain changes in both the strand and concrete. After release of pretensioning, thermal losses which occurred between bond and release will be “locked in”.

Variations in the coefficient of thermal expansion will lead to additional stresses along bonded lengths of strand. But because these losses will vary over time as the temperatures in the girder fluctuate, such losses are of a temporary nature. After stripping of the formwork, drying shrinkage may occur from a loss of moisture, causing a shortening of the concrete and thus a loss of prestress.

The losses and computing method presented above are simplification of what is actually a very complex behavior process prior to release. The real behavior is so difficult to model that the above approach is used as an empirical estimation of losses prior to release.

7.2.2. Measurements and Discussion. As described in Section 3, a 445 kN (100 kips) capacity load cell was placed at the bulkhead when jacking. Forces in selected strands were measured from stressing to release for three of the concrete casting dates. For each instrumented strand, the load cell was placed between the strand chuck and the bulkhead at the non-stressing end of the bed as previously shown in Figure 3.5.

Thermocouples were also placed on the instrumented strands in order to measure temperatures at the same instances when strand forces were measured. Two thermocouples were placed on each instrumented strand – one outside the girder and one at least 3 m (9.84 ft) into the girder. Strand forces and temperatures were recorded every 6 minutes.

Strand stresses were measured using a load cell prior to casting. The measured stress at the dead end of the bed should be representative of the stress at any point along the strand. Theoretical thermal losses between stressing and casting were calculated using

Equation 7.8. Relaxation losses were calculated using Equation 7.1. The results are summarized in Table 7.3.

Table 7.3. Prestress Losses Between Jacking and Casting

Pour	Stressing Date	Measured Temperatures		Measured Strand Forces	
		At stressing	Just before casting	At stressing	Just before casting
		(°F)	(°F)	(kips)	(kips)
Pour 2	6/9/01	79.07	72.37	45.3	44.71
Pour 3	6/15/01	89.74	71.42	43.1	42.95
Pour 5	6/28/01	87.33	68.65	45.4	45.35
Average*		85.39	70.81	44.60	44.34
				101.5%	100.9%

Pour	Time between stressing and casting	Measured losses	Analytical Prestress Losses		
			Total	Thermal	Relaxation
	(days)	(ksi)	(ksi)	(ksi)	(ksi)
Pour 2	3.77	2.72	1.68	-1.12	2.81
Pour 3	4.58	0.69	-0.67	-3.08	2.41
Pour 5	4.64	0.23	-0.18	-3.14	2.96
Average*	4.33	1.21	0.28	-2.45	2.72
		0.60%	0.14%	-1.21%	1.35%

°F = °C*1.8 + 32; 1 kip = 4.448 kN; 1 ksi = 6.89 MPa;

* Percentages represent loss as percentage of nominal jacking stress ($0.75f_{pu}$)

Measured losses ranged from 1.58 to 18.75 MPa (0.23 to 2.72 ksi) with an average of 8.34 MPa (1.21 ksi) or 0.60% of the nominal jacking stress. Calculated losses ranged from 4.62 to 11.58 MPa (-0.67 to 1.68 ksi) with an average of 0.28 MPa (1.93 ksi) or 0.14% of the nominal jacking stress.

It can also be found that the initial measured stresses directly after the stressing operation were a little higher than required. On average, initial measured stresses were higher than the nominal jacking stress by an average of 1.5%.

An example of the measured and calculated prestress force changes and measured temperatures over the time period between stressing and casting are shown in Figure 7.1. Strand forces clearly follow the variations in strand temperature, with increases in temperature causing a decrease in strand stress. Basically, the measured prestress force changes follow the same trend as calculated force changes.

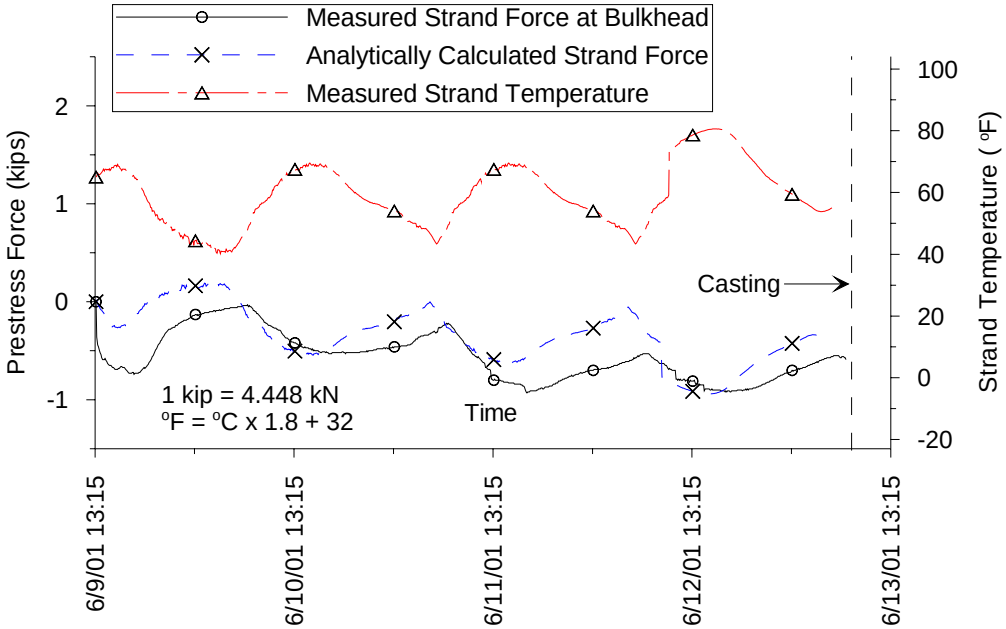

Figure 7.1. Measured Strand Forces and Temperature Before Casting for Pour 2

The measured prestress losses were close to the calculated losses. For some time period, calculated losses were lower than measured. This could be due to other losses that were not included in this analytical calculation model or accounted for. The analytical model accounted for thermal loss and relaxation losses. Friction between strand and

bulkhead may be one additional loss. Since the absolute values of the changes were very small, only 0.60% of nominal jacking stress as measured, the small error in the analytical model appears more pronounced. The difference between the measured and calculated loss tends to be periodical with time, implying the difference mostly related to thermal effect while relaxation loss calculation method does not influence this variation.

After casting, prestress losses are much more complex as discussed in the previous Section, and can not be measured by simply using a load cell on the strand at the bulkhead prior to release of pretensioning. However, the use of a load cell does offer some benefit. The shape of the measured stress curve can provide useful information during this stage.

An example of a measured prestress force changes over time is shown in Figure 7.2 for pour 2. Measured strand temperature inside and outside of the girder are also plotted in Figure 7.2. There is a large degree of symmetry between the temperature history inside of the girder and the measured forces in the strand at the bulkhead. Decreases in the strand force indicate that the strand is trying to lengthen along the member.

A simple analytical model was developed by Gross (1999) to estimate the magnitude of losses between casting and release as shown in Figure 7.3. A coefficient β is introduced to model the increased stiffness considering the effects of fresh concrete, bonded concrete, and the formwork on the free movement of the strand. In the simplified analytical model, β is taken to be constant over distinct intervals between significant events. The strand forces at each bulkhead are considered to be equivalent. Temperature changes are assumed to occur uniformly along the bonded and free lengths of strand. The

coefficient of thermal expansion is also assumed to be the same for the strand. Considering a compatibility requirement of no change in the total strand length, prestress losses due to thermal effects and shrinkage can be computed using Equations 7.9 and Equation 7.10. Relaxation losses between casting and release can be calculated as before casting using Equation 7.1.

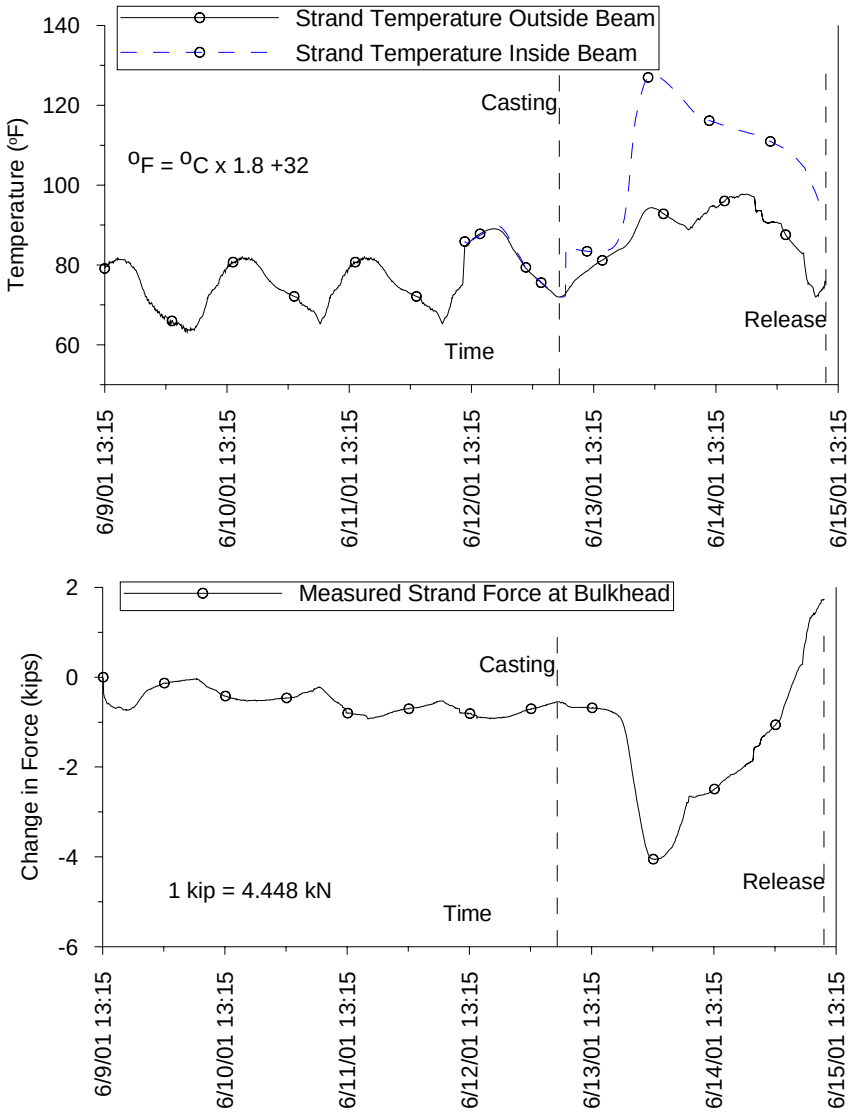

Figure 7.2. Measured Strand Forces and Temperatures Before Release for Pour 2

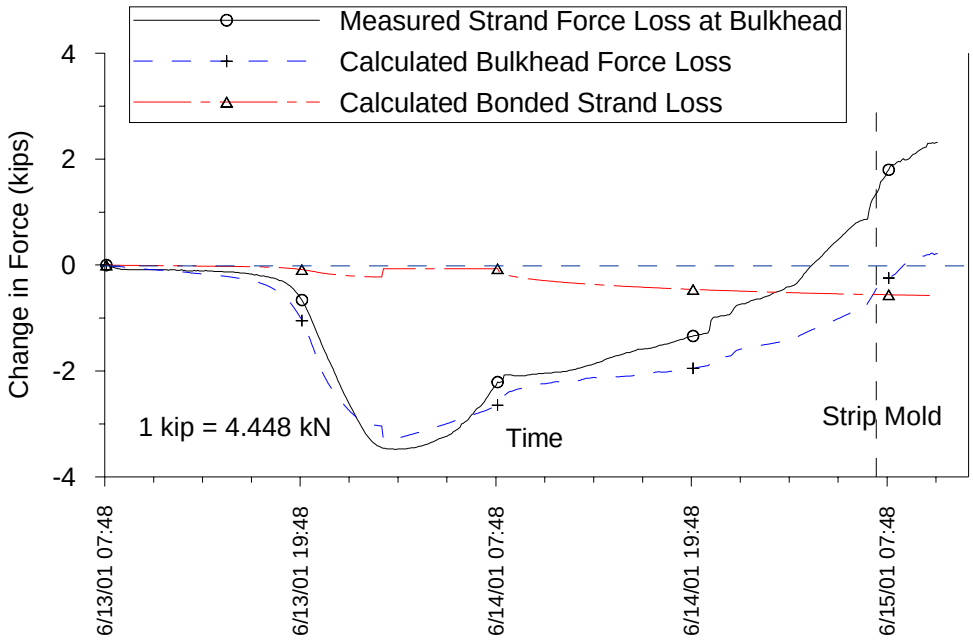

Figure 7.3. Measured Strand Forces and Temperatures Before Release for Pour 2

$$\Delta f_{ps,thermal} = \frac{\alpha \cdot E \cdot (L_f \cdot \Delta T_f + L_b \cdot \Delta T_b)}{\beta \cdot L_f + L_b} \qquad \text{Equation 7.9}$$

$$\Delta f_{ps,shrinkage} = \frac{\varepsilon_{sh} \cdot E \cdot \beta \cdot L_f}{\beta \cdot L_f + L_b} \qquad \text{Equation 7.10}$$

Using a curve matching process, appropriate values of β were determined as those that resulted in analytical curves for force at the bulkhead that exhibited the most agreement with the shape of the curves corresponding to the measured force at the bulkhead. After the most appropriate values of β were determined, changes in the force within the bonded length of strand were computed. Calculated losses using measured force and temperature data are summarized in Table 7.4. The total losses between casting and release ranged from 18.41 to 19.37 MPa (2.67 to 2.81 ksi) with an average of 18.82 MPa (2.73 ksi) or 1.35% of the nominal jacking stress. Shrinkage loss is the main loss among the three components. This is because the relaxation losses are small due to the

short time period and thermal losses are very small due to the minimal thermal changes from casting to release. Thermal effects also results in a small total prestress loss from casting to release.

Table 7.4. Prestress Losses Between Casting and Release

Pour	Stressing Date	Time between cast and release	Outside Strand Temp.		Inside Strand Temp.	
			At casting	Just before release	At casting	Just before release
		(days)	(°F)	(°F)	(°F)	(°F)
Pour 2	6/9/01	2.13	73.04	75.90	84.34	92.62
Pour 3	6/15/01	2.22	72.05	76.44	82.63	85.80
Pour 5	6/28/01	2.27	68.54	83.55	84.15	89.02
Average		2.21	71.20	78.64	83.71	89.15

Pour	Coefficients		Calculated Prestress Losses			
	β_2	$\beta_3 = \beta_4$	Total	Thermal	Relaxation	Shrinkage
			(ksi)	(ksi)	(ksi)	(ksi)
Pour 2	15	70	2.67	0.04	0.27	2.35
Pour 3	10	50	2.70	0.02	0.28	2.40
Pour 5	30	80	2.81	0.04	0.29	2.48
Average			2.73	0.03	0.28	2.41
			1.35%	0.02%	0.14%	1.19%

°F = °C*1.8 + 32; 1 kip = 4.448 kN; 1 ksi = 6.895 MPa;
* Percentages represent loss as percentage of nominal jacking stress ($0.75f_{pu}$)

In summary, the prestress behavior after casting but prior to release is very complicated. However, using a simplified methodology, the prestress losses during this period can be analytically computed. For this project, the losses before release were very small, with an average of 1.95% of the nominal jacking stress. There are several reasons why the value is so low. First, the prestress strands were stressed at a higher temperature

[27 - 32 °C (80 - 90 °F)], usually in afternoon, but concrete was cast in the early morning when the temperature [20 - 22 °C (68 - 72 °F)] was very mild. In this way, the losses caused by strand relaxation and other factors were balanced by decreased temperature, and thus the losses locked in the member before casting were very small, about 0.6% of jacking stress. Second, the strands were all released in the morning with a temperature very close to the temperature when the concrete was cast. Thermal effects during this period therefore were small too. The strands were released shortly after the girder molds were removed before shrinkage developed to a large amount.

Compared with the study on Texas HPC bridges (Gross, 1999), the prestress losses before release in this study are much lower. The reason is that thermal effect contributed much more to the prestress losses before release in Texas bridges than in this study. It is obvious that more research is needed on prestress losses before release. A simple approach needs to be developed for the prestress losses from jacking to release.

7.3. ELASTIC SHORTENING AT RELEASE

7.3.1. Background. Elastic shortening is the loss of prestress associated with shortening of the strand when the concrete member to which it is bonded is compressed. During the transfer of prestress force to the concrete, the stress in the strands is reduced.

The importance of a better estimation of elastic shortening losses is widely recognized. Significant research work has been completed on elastic shortening losses when using normal strength concrete. However, more research is warrented on the elastic shortening losses for members utilizing high performance and/or high-strength concrete.

It should be noted that elastic shortening varies along the length of the member, as a function of the self-weight moment and prestressing layout at each section. Technically elastic shortening should be calculated at each critical section.

Elastic shortening losses are highly dependent on the modulus of elasticity of the concrete at release, because losses are directly related to the stress in the concrete by the modular ratio *n*.

7.3.2. Measurements and Discussion. For all instrumented girders, strain measurements were made using vibrating wire strain gauges embedded in the concrete at the level of the center of gravity (c.g.) of the prestressing strand as discussed at the beginning of this Section. Measured elastic shortening losses are summarized in Table 7.5, in terms of both change in stress and percent loss relative to a nominal jacking stress of 1396 MPa (202.5 ksi).

Table 7.5. Measured Release Strains and Equivalent Elastic Shortening Losses

Girder	Measured Strain	Elastic Shortening Loss	
	(microstrain)	(ksi)	(% of f_{jack})*
B13	810	22.68	11.20%
B14	883	24.72	12.21%
B23	712	19.94	9.84%
B24	656	18.37	9.07%
Average	765	21.43	10.58%
1 ksi = 6.895 MPa; * Relative to nominal jacking stress of 202.5 ksi ($0.75f_{pu}$).			

Measured losses were compared to predicted elastic shortening losses using three methods as illustrated in Table 7.6. Predicted and measured elastic shortening losses are summarized in Table 7.7 and Figure 7.4 in terms of stress change and percent loss.

Table 7.6. Methods for Prediction of Elastic Shortening Losses

Parameter	Exact Analysis	Approximate	Approximate with known modulus
	Equation 7.2	Equation 7.5	Equation 7.5
Section Properties	Transformed section properties	Gross section properties	Gross section properties
Prestress Force	2.0% loss assumed before release based on measurements. Full prestress used for calculations	No loss assumed before release. Effective prestress force after losses assumed to be 70% of force corresponding to ultimate strength of strands, as suggested by AASHTO LRFD	No loss assumed before release. Effective prestress force after losses assumed to be 70% of force corresponding to ultimate strength of strands, as suggested by AASHTO LRFD
Modulus of Elasticity	Based on tests of companion specimens	Eq. 1.3 for HSC (ACI 363R-92)	Based on tests of companion specimens

Table 7.7. Measured and Predicted Elastic Shortening Losses

Girder	Measured losses	Predicted Losses (Stress Loss)			Ratio (Meas. / Pred.)		
		Exact	Approx.	Know E	Exact	Approx.	Know E
B13	22.68	18.75	22.8	18.35	1.210	0.995	1.236
B14	24.72	18.75	22.8	18.35	1.318	1.084	1.347
B23	19.94	18.39	22.49	18.45	1.084	0.887	1.081
B24	18.37	18.39	22.49	18.45	0.999	0.817	0.996
Avg.	21.43	18.57	22.645	18.4	1.153	0.946	1.165
Girder	Measured losses (%)	Predicted Losses (Percent Loss)			Ratio (Meas. / Pred.)		
		Exact	Approx.	Know E	Exact	Approx.	Know E
B13	11.20	9.26	11.26	9.06	1.210	0.995	1.236
B14	12.21	9.26	11.26	9.06	1.318	1.084	1.347
B23	9.84	9.08	11.11	9.11	1.084	0.887	1.081
B24	9.07	9.08	11.11	9.11	0.999	0.817	0.996
Avg.	10.58	9.17	11.18	9.09	1.153	0.946	1.165

All losses shown are in units of ksi; 1 ksi = 6.895 MPa; all percent losses computed as percentage of nominal jacking stress of 202.5 ksi ($0.75f_{pu}$).

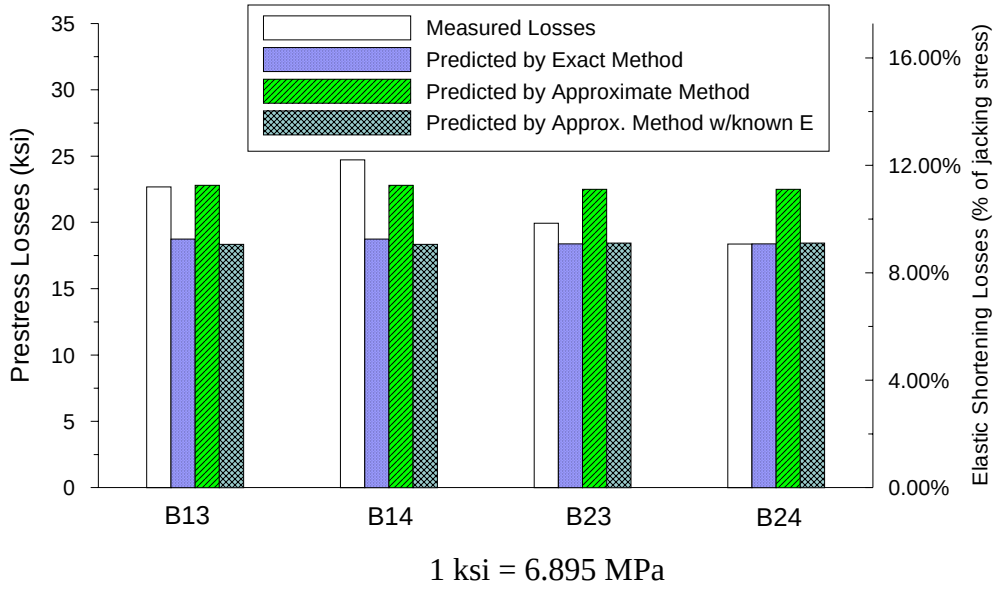

Figure 7.4. Measured and Predicted Elastic Shortening Losses

In general, measured elastic shortening losses were typically higher than losses predicted by the exact method. The reasons should be the same as for high measured strains because they are essentially based on the same measurements. Restraint against shortening of the member prior to release have affected the measurements and caused the measured losses to be artificially augmented. Differences between the actual modulus of elasticity and the values obtained from tests on companion specimens also may have affected the measurements and need further study.

For girders B23 and B24, predicted losses based on the exact method showed good correlation with measured losses. However, for girders B13 and B14, the differences between those two values were larger, about 20 - 30%. This indicates that the restraints affected these two girders more significantly as seen in the strain analysis.

Differences (less than 2%) between the predicted losses based on the approximate method with known modulus and the exact method are very small. Approximate method

using gross section properties resulted in an acceptable estimation for losses at design stage. It is thus recommended that the approximate method based on gross section properties is permissible for the calculation of elastic shortening losses in high-strength concrete designs.

7.4. TOTAL LOSSES

7.4.1. Background. Total losses consist of losses before release, elastic shortening losses, and the time-dependent losses associated with creep, shrinkage, and relaxation. It is true these losses do not affect the ultimate strength of a girder, but do have a significant impact on serviceability. Cracking may occur if the total losses are underestimated. Underestimation or overestimation of the losses may lead to a poor prediction of service camber and deflection. This is more critical for HSC members that often have longer span lengths for a given member depth compared to concrete members with normal strength.

Previous research concluded several methods for total prestress losses estimation and some have been adopted in specifications. The simplest methods are basic lump-sum estimates, in which the magnitude of the total loss is assumed to be a certain value. The methods widely used are the component lump-sum estimation, in which the magnitude of the loss due to each source is estimated separately and the total loss is taken as the sum of the individual components. Some advanced procedures including approximate and incremental time-step methods are often used in conjunction with a personal computer.

In AASHTO Standard Specifications (1996) and the PCI Design Handbook (1999), the basic lump-sum methods are provided. The AASHTO Standard Specifications

suggest a total loss of 310 MPa (45 ksi) for all pretentioned members based on an average design concrete strength of 34 MPa (5000 psi). The PCI Design Handbook specifies that for low relaxation strand, the maximum and minimum total losses are suggested as 207 and 276 MPa (30 and 40 ksi), respectively, although it is implied that the minimum loss may actually be lower.

A refined lump-sum estimate of total losses is provided in the AASHTO LRFD Specifications (1994). The estimates are based on a parametric study by Naaman and Hamza (1993) using a computer time-step analysis. For I-shaped girders, the average time-dependent loss is taken as:

$$\Delta f_{ps,TD}\,(ksi) = 33.0 \cdot \left[1.0 - 0.15 \cdot \frac{f_c^{'} - 6.0}{f_c^{'}}\right] + 6.0 \cdot PPR \qquad \text{Equation 7.11}$$

The partial prestressing ratio PPR is the ratio of prestressed reinforcement to total reinforcement. The lump-sum time-dependent losses should be reduced by 41 MPa (6 ksi) if using low-relaxation strands.

Three of the most common component methods are provided in the AASHTO Standard Specifications, the AASHTO LRFD Specifications, and the PCI Design Handbook as summarized in Table 7.8. These three methods are widely used by designers to predict total prestress losses. Other expressions for the estimation of prestress losses have been developed and are suggested in available literature (Huang 1982, Tadros et al. 1975). Some advanced approaches include the approximate time-step method by Branson (1977) and the incremental time-step method proposed by others (Branson and Ozell 1961, Ghali and Favre 1986, Libby 1990, Naaman 1982, and PCI Committee on Prestress Losses 1975).

Table 7.8. Methods for Total Prestress Losses

	AASHTO Standard	AASHTO LRFD	PCI Design Handbook	GROSS (1999)
$\Delta f_{ps,ES}$	$\frac{E_{ps}}{E_{ci}} \cdot f_{cgp}\ (f_{s0} = 0.69 \cdot f_{su})$	$\frac{E_{ps}}{E_{ci}} \cdot f_{cgp}\quad (f_{s0} = 0.70 \cdot f_{su})$	$\frac{E_{ps}}{E_{ci}} \cdot f_{cgp}\quad (f_{s0} = 0.90 \cdot f_{sj})$	$\frac{E_{ps}}{E_{ci}} \cdot f_{cgp}\quad (f_{s0} = 0.90 \cdot f_{sj})$
$\Delta f_{ps,SH}$	$17.0 - 0.15 \cdot RH$	$17.0 - 0.15 \cdot RH$	$(8.2 \times 10^{-6}) \cdot K_{sh} \cdot E_{ps}$ $\cdot \left(1 - 0.06 \cdot \frac{V}{S}\right) \cdot (100 - RH)$	$\varepsilon^{*}_{sh} \cdot E_{ps}$
$\Delta f_{ps,CR}$	$12.0 \cdot f_{cgp} - 7.0 \cdot f_{cdp}$	$12.0 \cdot f_{cgp} - 7.0 \cdot f_{cdp}$	$K_{cr} \cdot \left(\frac{E_{ps}}{E_c}\right)(f_{cgp} - f_{cdp})$	$K_{cr} \cdot \left(\frac{E_{ps}}{E_c}\right)(f_{cgp} - f_{cdp})$
$\Delta f_{ps,RE}$	$5.0 - 0.10 \cdot \Delta f_{ps,ES}$ $- 0.05 \cdot \Delta f_{ps,SH}$ $- 0.05 \cdot \Delta f_{ps,CR}$	$f_{sj} \cdot \left(\frac{\log_{10} 24 \cdot t_0}{40}\right) \cdot \left(\frac{f_{sj}}{f_{sy}} - 0.55\right)$ $+ 6.0 - 0.12 \cdot \Delta f_{ps,ES}$ $- 0.06 \cdot \Delta f_{ps,SH} - 0.06 \cdot \Delta f_{ps,CR}$	$[K_{re} - J \cdot (\Delta f_{ps,ES} + \Delta f_{ps,SH}$ $+ \Delta f_{ps,CR})] \cdot C$ $(K_{re} = 5.0,\ J = 0.04, C = 1.00)$	$[K_{re} - J \cdot (\Delta f_{ps,ES} + \Delta f_{ps,SH}$ $+ \Delta f_{ps,CR})] \cdot C$ $(K_{re} = 5.0,\ J = 0.04, C = 1.00)$
$\Delta f_{ps,PR}$	Not specified	Not specified	Not specified	$f_{sj} \cdot \left(\frac{\log_{10} 24 \cdot t_0}{40}\right) \cdot \left(\frac{f_{sj}}{f_{sy}} - 0.55\right)$ $+ \frac{1}{3} \cdot E_{ps} \cdot \alpha_{ps} \cdot (T_{peak-hy.} - T_{Stress})$

ll losses in units of ksi. 1 ksi = 6.895 MPa 1 in. = 25.4 mm

Note: f_{cgp} = stress in concrete at c.g. of pretensioned strands at release, ksi; f_{cdp} = stress in concrete at c.g. of pretensioned strands due to applied loads, ksi; f_{sj} = strand stress at jacking, ksi; f_{so} = strand stress just after release, ksi; f_{su} = ultimate strength of the strand, ksi; f_{sy} = yield strength of the strand, ksi; RH = relative humidity in percent; t_0 = time in days between jacking and release; V/S = volume to surface ratio, in. All others can be found as noted before and in corresponding specifications.

Few measurements of long-term prestress losses in actual HPC prestressed highway bridge girders have been documented in available literature. In Texas, the first two HPC bridges were studied and monitored including long-term prestress losses. A set of equations were suggested by Gross (1999) based on the research conducted in Texas and presented in Table 7.8. The expressions presented in Table 7.8 are for pretensioned, low-relaxation strands.

An analytical time-step method was developed based on the procedure outlined by Branson and Kripanarayanan (1971). This method was developed using a computer spreadsheet program and used to predict the time-dependent prestress losses, camber, and deflection for all the instrumented girders. More details about the time-step model and the spreadsheet implemented for this project can be found in Appendix G.

The time-dependent models for creep, shrinkage, and age-strength gain that were developed from companion test data for the high performance concrete girder mix as discussed in Section 4 were used in the time-step method.

Transformed section properties and the actual construction schedules were used for each analysis. Prestress loss before release was considered in the model in the same manner as discussed in Section 7.2. Parameters used in the analysis for each beam are summarized in Appendix D.

Time-dependent losses for each interval were determined by using Equations 7.12 through 7.14. Equation 7.1 was used to calculated relaxation loss. Creep and shrinkage models obtained in Section 4 were used for creep and shrinkage loss calculation. An expression for the total loss at any time is given in Equation 7.15.

$$(\Delta f_{ps,SH})_i = [(\varepsilon_{sh})_t - (\varepsilon_{sh})_{t-\tau}] \cdot E_s \qquad \text{Equation 7.12}$$

$$(\Delta f_{ps,CR})_i = (n \cdot f_c)_{t-\tau}[(C_c)_t - (C_c)_{t-\tau}] \quad \text{Equation 7.13}$$

$$(\Delta f_{ps,RE})_i = (\Delta f_{ps,RE})_t - (\Delta f_{ps,RE})_{t-\tau} \quad \text{Equation 7.14}$$

$$(\Delta f_{ps})_t = \Delta f_{ps,PR} + \sum_{i=1}^{m}\left[(\Delta f_{ps,CR})_i + (\Delta f_{ps,SH})_i + (\Delta f_{ps,RE})_i + (\Delta f_{ps,LD})_i + (\Delta f_{ps,diff-sh})_i\right]$$

Equation 7.15

where,

t = time after release in days (corresponds to the end of time interval m)

m = number of time intervals used to reach time t

τ = differential length of time for interval i

$(n)_{t-\tau}$ = modular ratio of steel to concrete at the beginning of interval i

$(f_c)_{t-\tau}$ = stress in the concrete at CGS at the beginning of time interval i

$(f_c)_{t-\tau}$ = stress in the strands at the beginning of interval i

ε_{sh} = shrinkage strain (use measured data from companion specimens)

C_c = creep coefficient (use measured data from companion specimens)

$\Delta f_{ps,LD}$ = instantaneous losses that occur due to superimposed loads

$\Delta f_{ps,diff-sh}$ = losses due to differential shrinkage

All the others are same as presented previously.

Calculations for a typical time interval began by calculating concrete compressive strength and elastic modulus using equations for the fit curves obtained in Section 4, and then calculating transformed section properties. Incremental losses were calculated using Equations 7.12 through 7.14, summed, and added to the total losses that were determined at the end of the previous time interval as presented in Equation 7.15. Based on the new

value for prestress loss, a new strand stress was determined. This strand stress was used for calculating relaxation and creep losses in the next time interval.

7.4.2. Measurements and Discussion. Long-term prestress losses were successfully measured using embedded vibrating wire strain gauges. Losses were measured using the same procedure as presented in Section 7.2 and were corrected for temperature changes.

Measured long-term losses are summarized in Table 7.9 for all instrumented girders. Pre-release losses (PR) were estimated as described as before and added to the total measurements. Elastic-shortening losses (ES) were discussed in the Section 7.3. The relaxation losses (RE) were estimated analytically. Time-dependent creep losses (CR) and shrinkage losses (SH) were measured till about two years after release. Total time-step long-term prestress losses after release were plotted and shown in Figures 7.5 through 7.8.

Prestress losses were predicted using eight methods as following:

1. Incremental Time-Step with measured parameters
2. Actual girder design using BR200
3. AASHTO LRFD time-dependent lump-sum
4. AASHTO LRFD Components with design parameters
5. AASHTO LRFD Components with measured parameters
6. PCI Design Handbook with design parameters
7. PCI Design Handbook with measured parameters
8. Suggested Method by Gross with measured parameters

Using the above methods, predicted total prestress losses for all four instrumented girders are reported in Tables 7.10 through 7.15 and are plotted in Figures 7.9 through 7.14. Comparisons with measured data were also included in the corresponding tables and figures.

Table 7.9. Measured Total Prestress Losses in Individual Girders by Component

Girder	Days after Release	Loss Components (ksi)				Total Loss (ksi)	Total Loss (% of f_{jack})
		PR	ES	CR+SH	RE		
B13	598	3.04	22.68	13.59	2.90	42.21	20.85%
B14	598	3.04	24.72	12.30	2.73	42.79	21.13%
B23	611	3.39	19.94	17.28	3.11	43.72	21.59%
B24	611	3.39	18.37	14.05	3.24	39.05	19.28%
Average		3.22	21.43	14.30	2.99	41.94	20.71%

All losses shown are in units of ksi; 1 ksi = 6.895 MPa;

All percent losses computed as percentage of nominal jacking stress of 202.5 ksi.

Table 7.10. Losses Calculated as in Actual Girder Designs (AASHTO Standard 9.16.2)

Girder	Loss Components (ksi)				Total Loss (ksi)	Total Loss (% of f_{jack})
	ES	SH	CR	RE		
B13	21.74	6.50	33.40	0.83	62.47	30.85
B14	21.74	6.50	33.40	0.83	62.47	30.85
B23	23.16	6.50	34.91	0.61	65.18	33.07
B24	23.16	6.50	34.91	0.61	65.18	33.07
Average	22.45	6.5	34.155	0.72	63.83	31.96

All losses shown are in units of ksi; 1 ksi = 6.895 MPa;

All percent losses computed as percentage of nominal jacking stress of 202.5 ksi.

Table 7.11. Losses Predicted by the AASHTO LRFD Time-Dependent Lump Sum

Girder	Loss Components (ksi)		Total Loss (ksi)	Total Loss (% of f_{jack})
	ES	SH+CR+RE		
B13	22.57	30.98	53.55	26.44
B14	22.57	30.98	53.55	26.44
B23	22.49	30.98	53.47	26.40
B24	22.49	30.98	53.47	26.40
Average	22.53	30.98	53.51	26.42
All percent losses computed as percentage of nominal jacking stress of 202.5 ksi.				

Table 7.12. Losses Predicted by the AASHTO LRFD Method

AASHTO LRFD Method with Design Parameters						
Girder	Loss Components (ksi)				Total Loss (ksi)	Total Loss (% of f_{jack})
	ES	SH	CR	RE		
B13	22.57	6.50	33.69	4.07	66.84	33.01
B14	22.57	6.50	34.76	4.01	67.84	33.50
B23	22.49	6.50	36.30	3.60	68.89	34.02
B24	22.49	6.50	37.59	3.52	70.10	34.62
Average	22.53	6.50	35.59	3.80	68.42	33.79
AASHTO LRFD Method with Measured Parameters						
Girder	Loss Components (ksi)				Total Loss (ksi)	Total Loss (% of f_{jack})
	ES	SH	CR	RE		
B13	18.16	6.50	34.14	4.53	63.33	31.27
B14	18.16	6.50	35.21	4.47	64.34	31.78
B23	18.45	6.50	36.70	4.06	65.71	32.45
B24	18.45	6.50	38.01	3.98	66.94	33.06
Average	18.31	6.50	36.01	4.26	65.08	32.14
All losses shown are in units of ksi; 1 ksi = 6.895 MPa; All percent losses computed as percentage of nominal jacking stress of 202.5 ksi.						

Table 7.13. Losses Predicted by the Method Suggested by Gross (1999)

Girder	Loss Components (ksi)					Total Loss (ksi)	Total Loss (% of f_{jack})
	PR	ES	CR	SH	RE		
B13	4.15	17.67	5.57	13.90	3.51	44.80	22.12
B14	4.21	17.67	5.57	14.93	3.47	45.86	22.65
B23	3.75	17.92	5.57	15.12	3.46	45.81	22.62
B24	3.96	17.92	5.57	16.42	3.40	47.28	23.35
Avg.	4.02	17.80	5.57	15.09	3.46	45.94	22.69

All losses shown are in units of ksi; 1 ksi = 6.895 MPa;
All percent losses computed as percentage of nominal jacking stress of 202.5 ksi.

Table 7.14. Losses Predicted by the PCI Design Handbook Method

PCI Design Handbook Method with Design Parameters						
Girder	Loss Components (ksi)				Total Loss (ksi)	Total Loss (% of f_{jack})
	ES	SH	CR	RE		
B13	21.69	5.64	22.64	3.00	52.98	26.16
B14	21.69	5.64	24.34	2.93	54.60	26.96
B23	21.61	5.64	23.83	2.96	54.03	26.68
B24	21.61	5.64	25.88	2.87	56.00	27.66
Average	21.65	5.64	24.17	2.94	54.40	26.87
PCI Design Handbook Method with Measured Parameters						
Girder	Loss Components (ksi)				Total Loss (ksi)	Total Loss (% of f_{jack})
	ES	SH	CR	RE		
B13	17.67	5.64	17.05	3.39	43.74	21.60
B14	17.67	5.64	18.32	3.33	44.97	22.21
B23	17.92	5.64	18.55	3.32	45.42	22.43
B24	17.92	5.64	20.15	3.25	46.96	23.19
Average	17.80	5.64	18.52	3.32	45.27	22.36

All losses shown are in units of ksi; 1 ksi = 6.895 MPa;
All percent losses computed as percentage of nominal jacking stress of 202.5 ksi.

Table 7.15. Comparison of Measured and Calculated Total Prestress Losses

Girder	Total Loss(ksi)								
	(1)	(2)	(3)	(4)	(5)	(6)	(7)	(8)	(9)
B13	42.21	44.97	62.47	53.55	66.84	63.33	52.98	43.74	44.80
B14	42.79	45.01	62.47	53.55	67.84	64.34	54.60	44.97	45.86
B23	43.72	46.34	65.18	53.47	68.89	65.71	54.03	45.42	45.81
B24	39.05	46.39	65.18	53.47	70.10	66.94	56.00	46.96	47.28
Avg.	41.94	45.68	63.83	53.51	68.42	65.08	54.40	45.27	45.94

(1) Measured
(2) Incremental Time-Step (Measured Parameters)
(3) Actual Girder Design (BR200)
(4) AASHTO LRFD Time-Dependent Lump-Sum
(5) AASHTO LRFD Components (Design Parameters)
(6) AASHTO LRFD Components (Measured Parameters)
(7) PCI Design Handbook (Design Parameters)
(8) PCI Design Handbook (Measured Parameters)
(9) Suggested Method by Gross (Measured Parameters)

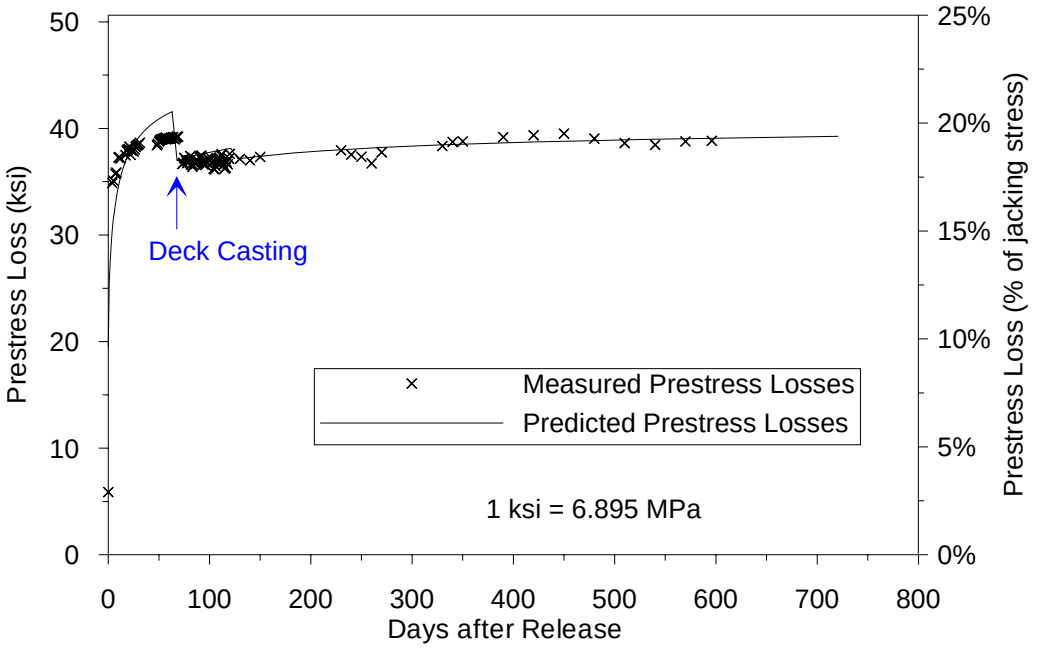

Figure 7.5. Measured and Predicted Time-Step Prestress Losses for Girder B13

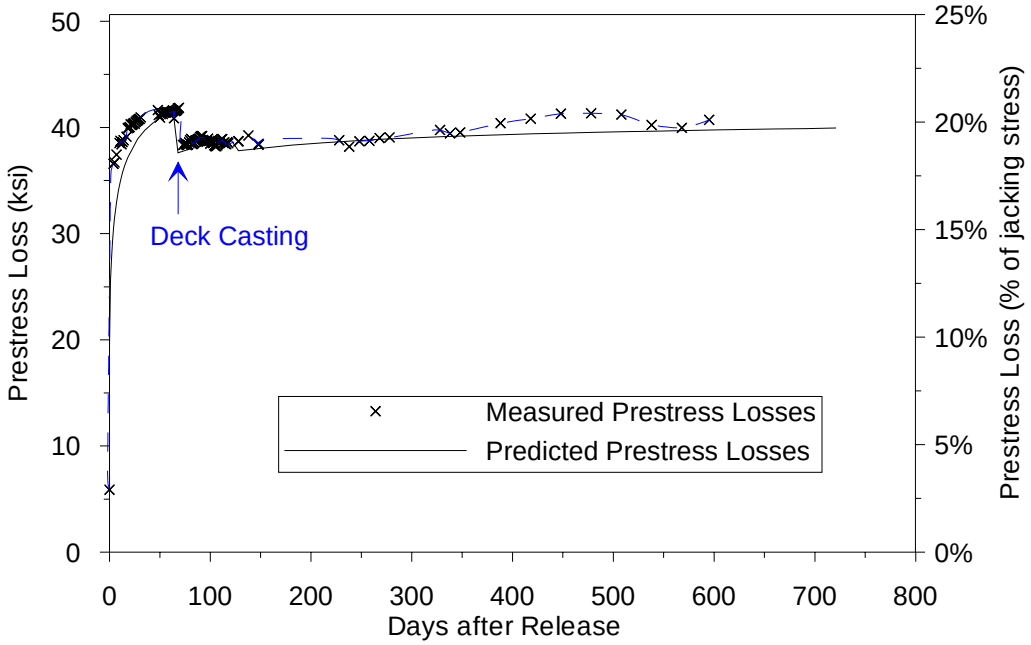

Figure 7.6. Measured and Predicted Time-Step Prestress Losses for Girder B14

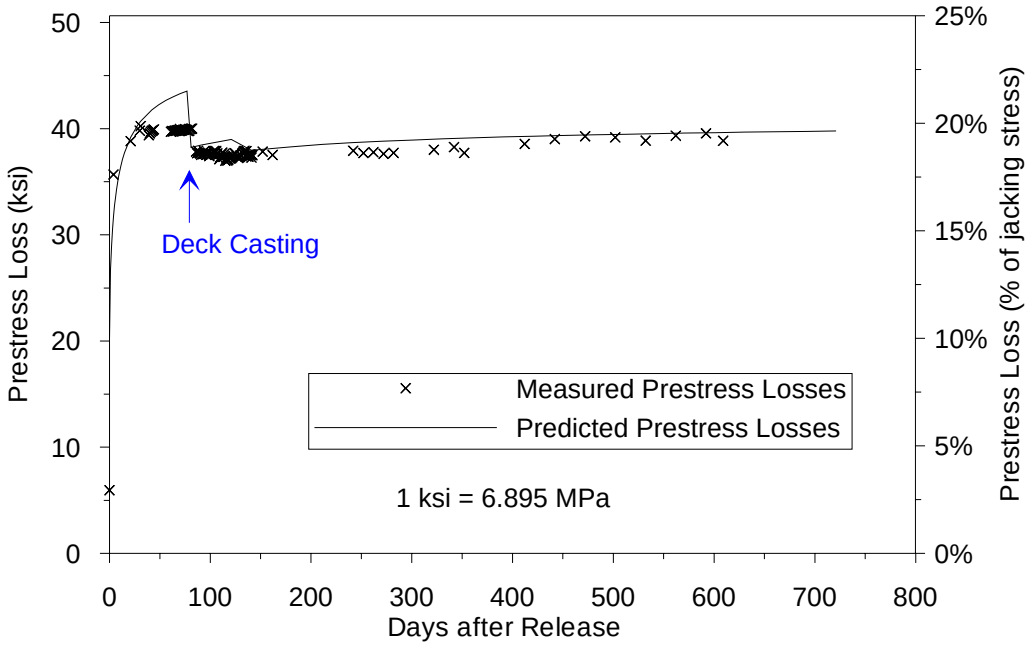

Figure 7.7. Measured and Predicted Time-Step Prestress Losses for Girder B23

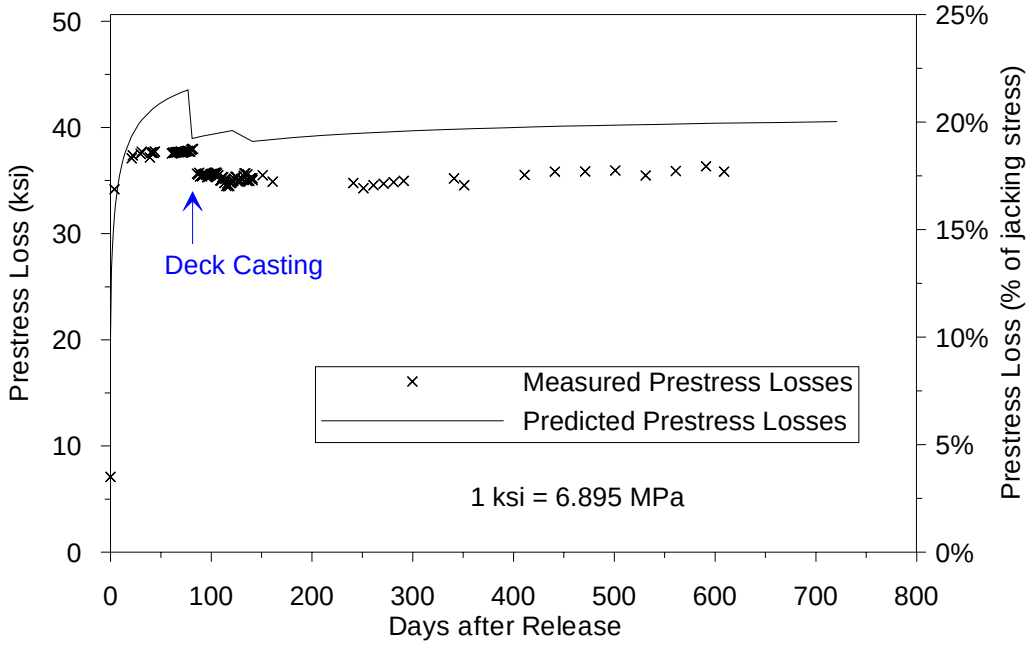

Figure 7.8. Measured and Predicted Time-Step Prestress Losses for Girder B24

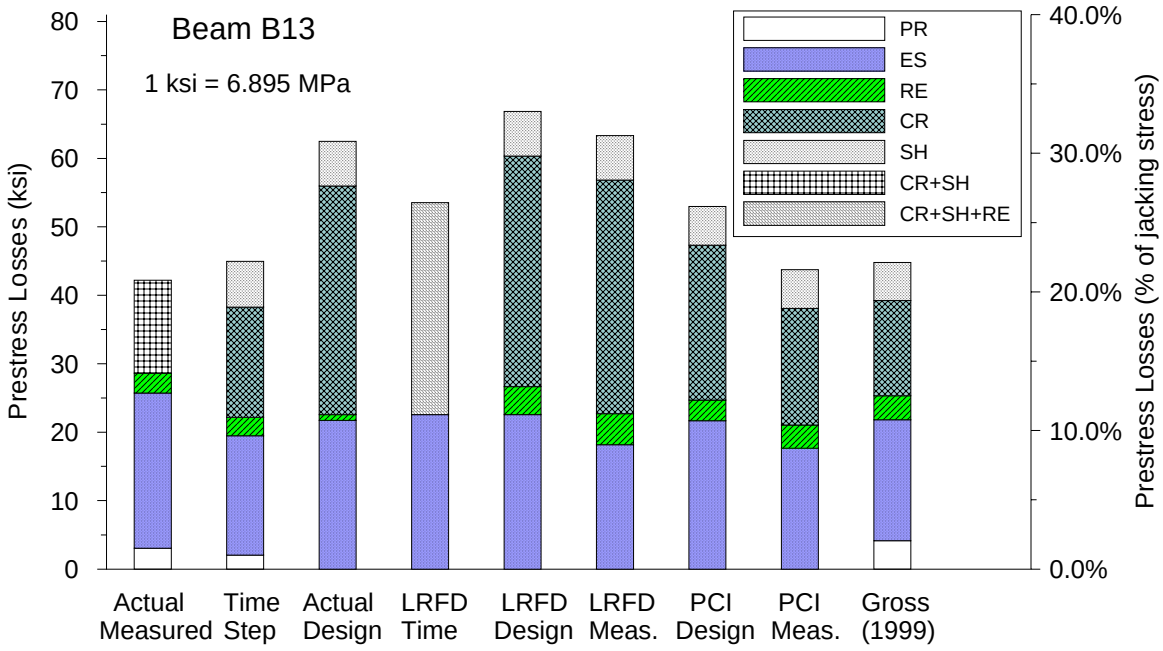

Figure 7.9. Measured and Predicted Total Prestress Losses for Girder B13

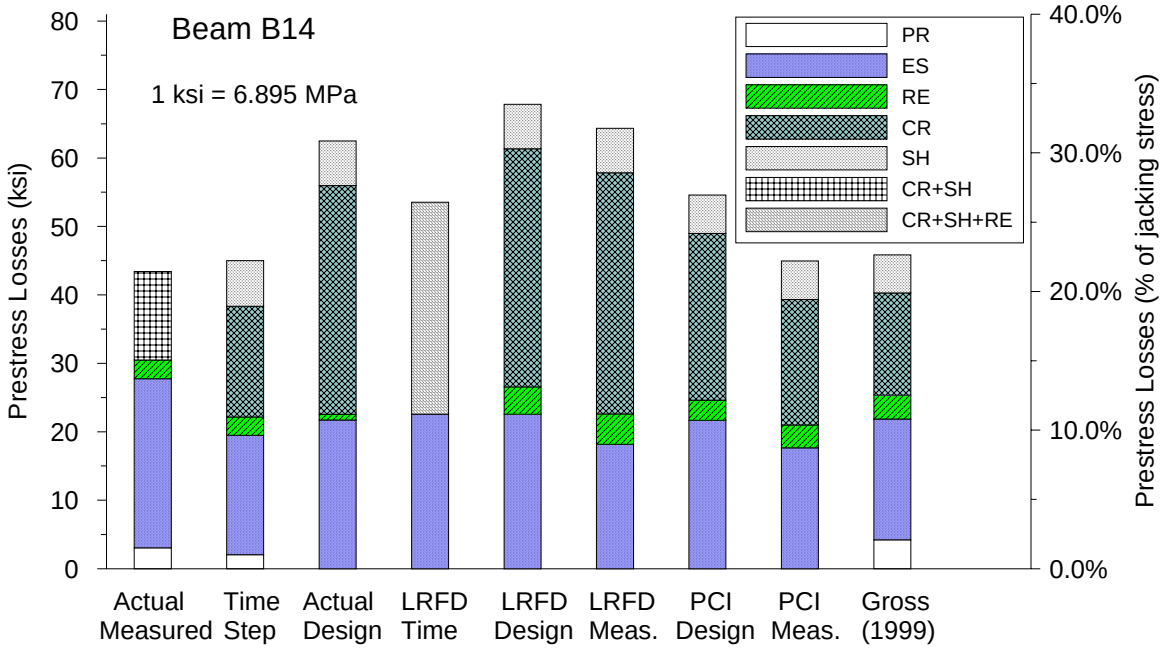

Figure 7.10. Measured and Predicted Total Prestress Losses for Girder B14

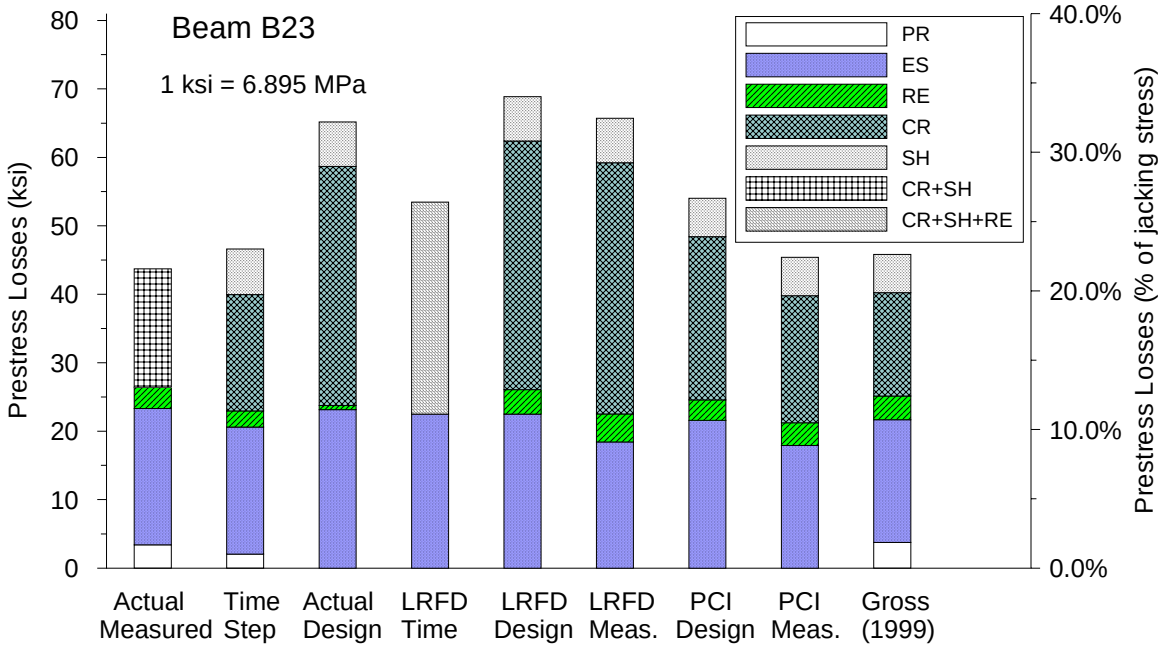

Figure 7.11. Measured and Predicted Total Prestress Losses for Girder B23

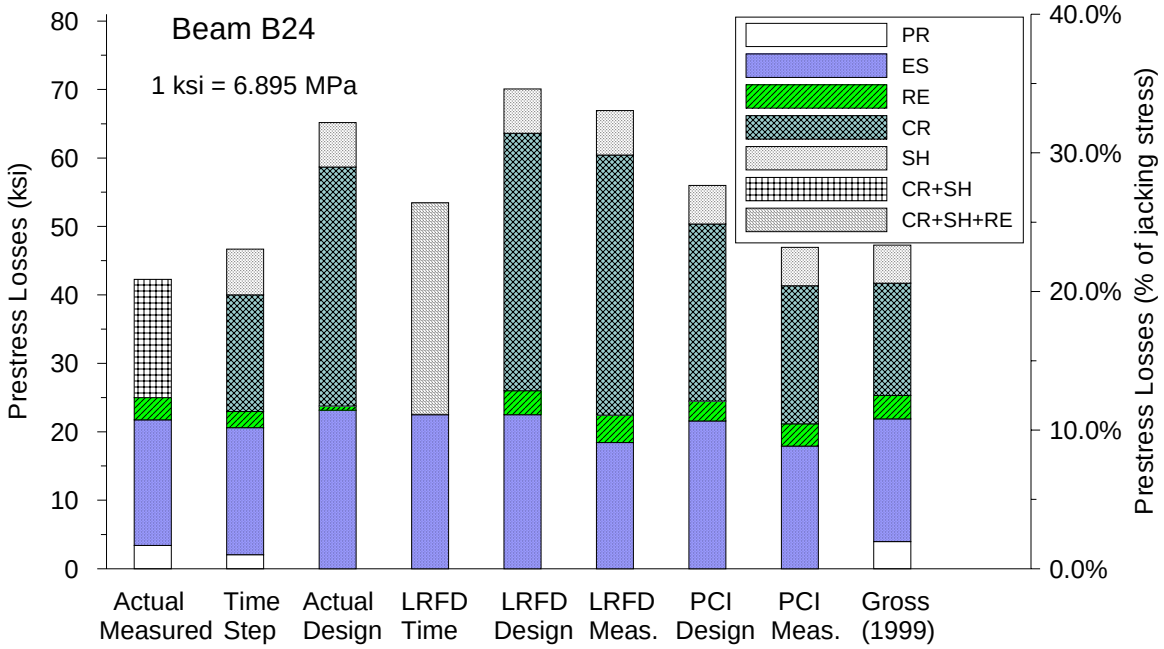

Figure 7.12. Measured and Predicted Total Prestress Losses for Girder B24

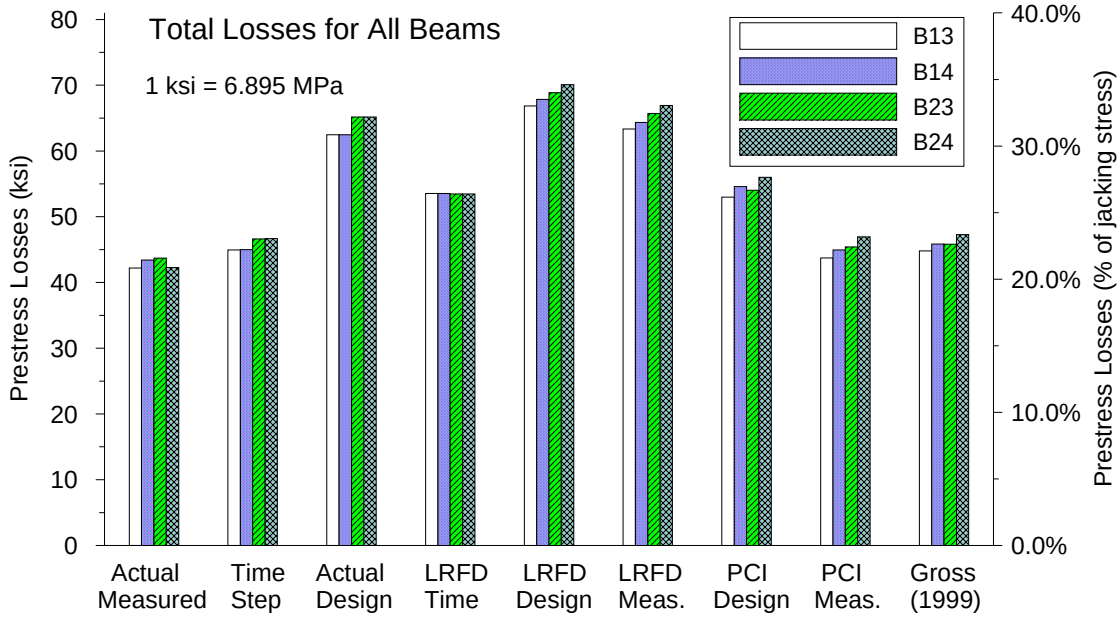

Figure 7.13. Measured and Predicted Total Prestress Losses for All Girders

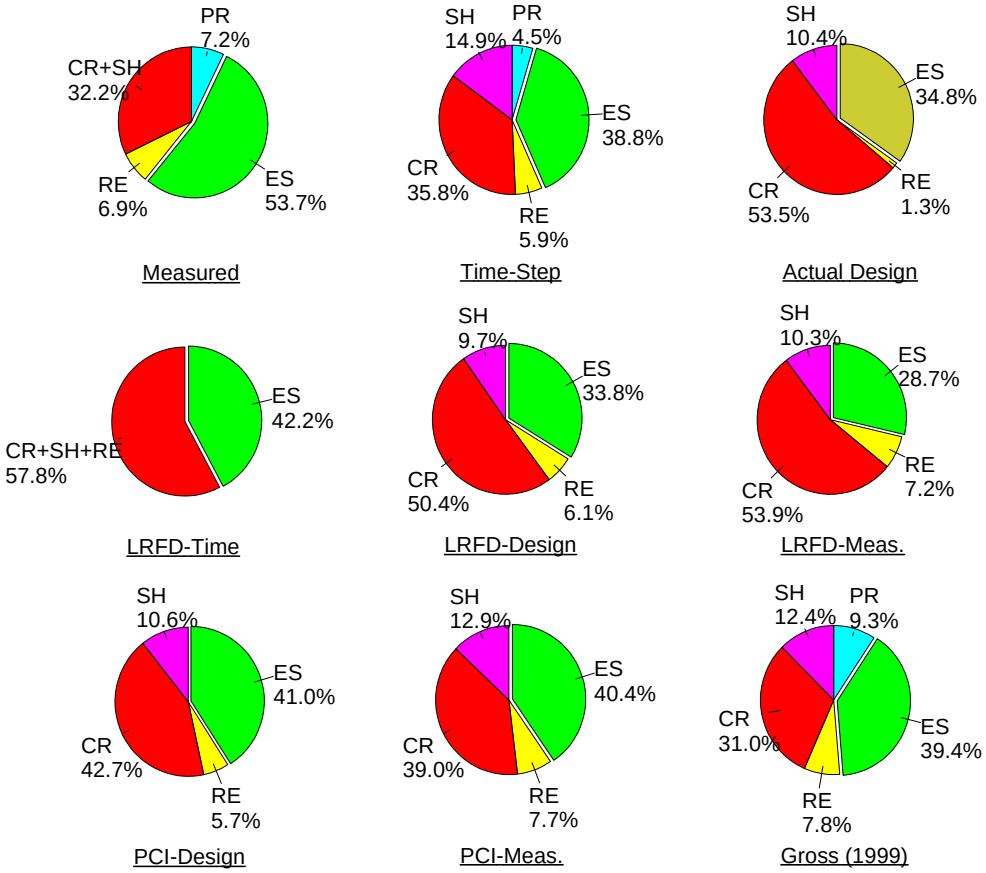

Figure 7.14. Percentage of Prestress Losses Components for Different Methods

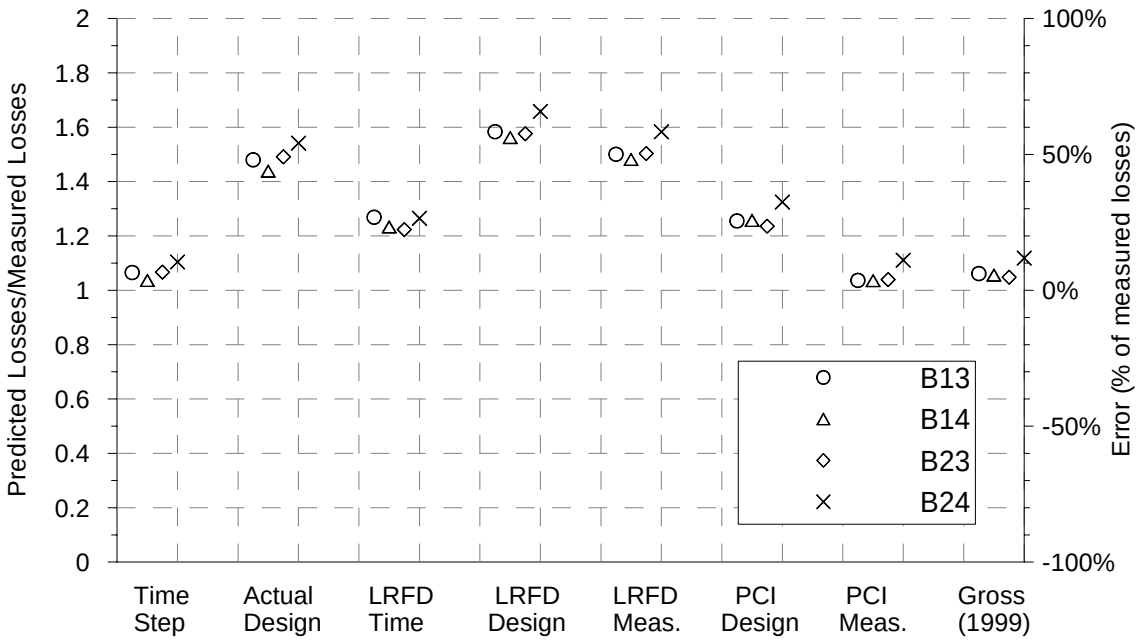

Figure 7.15. Ratio of Predicted Losses to Measured Losses for All Girders

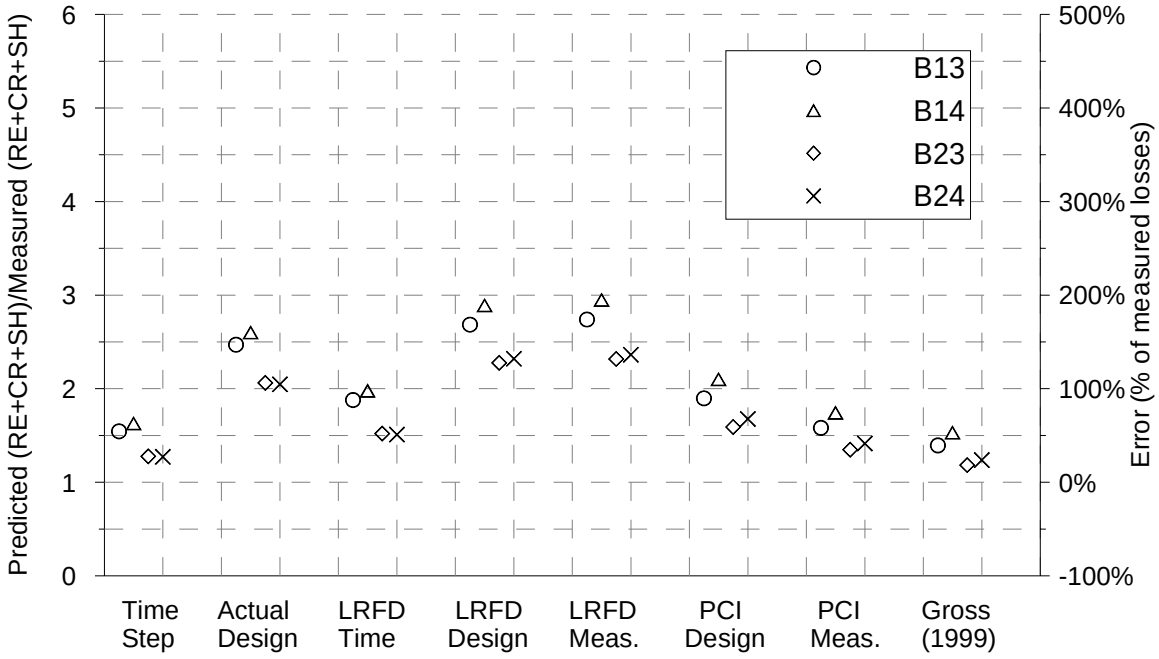

Figure 7.16. Ratio of Predicted Losses After Release to Measured Losses After Release

Total measured losses averaged 289.2 MPa (41.94 ksi), or 20.7% of the nominal jacking stress of 1396 MPa (202.5 ksi). Elastic shortening accounted for the largest portion of the total loss, 53.7% as shown in Figure 5.14. Time-dependent loss due to creep and shrinkage was less than the elastic shortening for measured values in all monitored girders. It is important to notice that losses before release accounted for about 7% of the total measured losses. Measured losses for all four girders were very close.

From the time-history figures of measured losses as illustrated in Figures 7.5 through 7.8, it can be seen that measured losses became stable one year later after release. Predicted time-history of prestress losses correlated very well (4 - 12% difference) with the measured values while using measured material properties in the time-step method. However, even though the total predicted losses were in the range of 4-10% higher than

measured total losses, the predicted elastic shortening losses were 1-29% smaller than measured values while losses due to creep and shrinkage were higher than measured data.

Prestress losses in actual design using program BR200 based on AASHTO Standard Specification are much higher than measured total losses by 45 - 55 %. The difference is mainly caused by estimated losses due to creep and shrinkage while elastic shortening losses in design is very close to the measured values by using match curing system (Myers, 1998). Similarly, predicted losses by AASHTO LRFD are much higher than measured losses by 50 - 60% with overestimated losses due to creep and shrinkage. As shown in Figure 7.16, predicted long-term losses due to relaxation, creep and shrinkage are even 3 times the corresponding measured losses. However, predicted losses by AASHTO LRFD are close to the values in actual design. Using measured material properties resulted in a significantly better estimation than using designed material properties as would be expected.

Predicted losses using the PCI Handbook method with design material properties are close to those computed using the AASHTO LRFD time-dependent lump-sum. Both are higher than measured losses by 22-30% for different girders. The PCI Handbook method and AASHTO LRFD time-dependent lump-sum method are better for design than AASHTO Standard Specification method and AASHTO LRFD design methods.

Predicted losses using the PCI Handbook method with measured material properties are close to those computed by the time-step method, and the method recommended by Gross (1999). Each of these methods is very close to the measured losses with the difference ranging from 4 to 12%. However, it should be noticed that in the measured losses, elastic shortening losses accounted for more than half of the total

losses. As discussed in the previous Section, the higher measured elastic shortening losses was due to the restraint from the casting bed before release. Therefore, the actual losses may be a little lower than the value computed from measured strain data.

Since the time-step method is based on the tested time-dependent material properties, which is not available at design stage, it requires much more accurate empirical time-dependent material properties if this method is used. Even though pre-release losses are not estimated using the PCI method, it still yields a good estimation (less than 15% difference) as well as the method recommended by Gross (1999), which considered pre-release losses.

Based on the analysis above, for prestress precast high performance concrete, girders, PCI Handbook method and the method recommended by Gross (1999) are recommended for prestress losses estimation in design stage. If the prestress losses before release could be considered and concrete material and mechanical can be estimated in a high accuracy level in the design stage, these two methods are very good for exact loss calculation with less than 15% difference from measured values.

7.5. SUMMARY AND CONCLUSIONS

The initial measured stresses at stressing were a little higher than expected. On average, initial measured stresses were higher than the nominal jacking stress by an average of 1.5%.

Strand forces clearly follow the variations in strand temperature, with increases in temperature causing a decrease in strand stress. Basically, the measured prestress force changes follow the same trend as calculated force changes.

The measured prestress losses before concrete casting were close to the calculated losses. For some time period, calculated losses were lower than measured. This could be due to other losses that were not included in the analytical model or accounted for such as friction between strands and casting bed. The analytical model accounted for thermal loss and relaxation losses. Friction between strand and bulkhead may be one additional loss. The difference between the measured and calculated loss tends to be periodical with time, implying the difference mostly related to thermal effect.

For this project, the losses before release were very small, with an average of 1.95% of the nominal jacking stress. There are several reasons why the value is so low. First, the prestress strands were stressed at a higher temperature, usually in afternoon, but concrete was cast in early morning, when the temperature is very low. In this way, the losses caused by strand relaxation and other reasons were even balanced by decreased temperature, and thus the losses locked in the member before casting were only 0.6% of jacking force. Second, the strands were all released in the morning with a temperature very close to the temperature when the concrete was cast. Thermal effects in this period were small too. The strands were released shortly after girders molds removed before shrinkage developed to a large amount.

It is obvious that more research is needed on prestress losses before release. A simple approach needs to be developed for the prestress losses from jacking to release.

Measured elastic shortening losses were typically higher than losses predicted by the exact method. The reasons should be the same as for high measured strains because they are essentially based on the same measurements. Restraint against shortening of the member prior to release have affected the measurements and caused the measured losses

to be artificially augmented. Differences between the actual modulus of elasticity and the values obtained from tests on companion specimens also may have affected the measurements.

For girders B23 and B24, predicted losses based on exact method showed good correlation with measured losses. However, for girders B13 and B14, the differences between those two values are larger. This indicates that the restraints affected these two girders significantly as seen in the strain analysis.

Differences between the predicted losses based on the approximate method with known modulus and the exact method are less than 2%. Approximate method using gross section properties resulted in an acceptable estimation for losses. It is thus recommended that the approximate method based on gross section properties is permissible for the calculation of elastic shortening losses in HSC designs.

Total measured losses averaged 289.2 MPa (41.94 ksi), or 20.7% of the nominal jacking stress of 1396 MPa (202.5 ksi). Elastic shortening accounted for the largest portion of the total loss.

For prestress precast high performance concrete, girders, PCI Handbook method and the method recommended by Gross (1999) are recommended for prestress losses estimation in design stage. If the prestress losses before release could be considered and concrete material and mechanical can be estimated in a high accuracy level in the design stage, these two methods are very good for exact losses calculation with less than 15% difference from measured values.

8. CAMBER AND DEFLECTION MEASUREMENTS

8.1. INTRODUCTION

Even though deflection and camber do not affect the ultimate strength of the bridge, they are very important in the serviceability and constructability of a highway bridge. It is desirable that under dead load, highway bridges should be nearly level or have a slight upward camber. Excessive camber or deflection under full dead load can result in an uneven riding surface. Excessive deflection may also cause ordinary citizens to perceive the structure to be unsafe.

Excessive camber or deflection leads to an uneven riding surface and excessive camber will cause difficulties in satisfying minimum deck thickness requirements in mid-span region. Excessive deflection may also make the riding public feel the structure unsafe. Therefore, deflection behavior should be predicted with a reasonable degree of accuracy in the design stage of the structure.

Camber and deflection are caused mainly by application of prestresss, member self-weight, weight of the bridge deck, superimposed dead loads including guardrails and deck surfacing, live load, thermal gradients, differential shrinkage between cast-in-place deck and girders, and early-age thermal and shrinkage effects in girders prior to detensioning. Creep associated with sustained loads makes the prediction of camber and deflection more complicated.

Many material properties and structural parameters affect camber and deflection. These material properties include modulus of elasticity, unit density, prestress losses, and creep of concrete. Structural parameters include span length, girder spacing, deck thickness, girder cross-section, prestress eccentricity and force, and strand shape.

For bridges with HPC girders, if HPC is used in the design such that span lengths are increased, camber or deflection is magnified as an increase in the square, cube or fourth power of the span length. If HPC is used in design to accommodate larger girder spacing only, camber or deflection can be expected to be higher than for typical designs by a proportional amount. This increase, however, is offset by the potentially higher modulus of elasticity and lower creep coefficients of HSC. Since higher prestress forces are essential for HSC girder designs, more camber due to prestress can be expected in such designs.

In this Section, 4 girders were monitored for camber and deflection behavior and compared with predicted values using both design parameters and measured parameters. Parameters used in the two types of models are listed for each girder in Appendix D.

As discussed in Section 3, a tensioned-wire system and precise surveying system were used for measurement of camber and deflection. Each of these systems proved reliable. The raw measurements, however, required correction for meaningful comparison. Measurement locations for the tensioned-wire system were slightly mislocated from the center of bearing locations due to the drilling operation. In addition measurement points for the precise surveying after erection could not be placed at the center of bearing locations because the locations were blocked by the bent and formwork.

It should also be noted that while the girders were stored at precast plant, support condition varied and required correction. Finally, thermal gradient effect caused fluctuations in deflection behaviors in the girder while in storage as well as under composite action and thus should be corrected. In this Section, all presented measured values are values after correction.

8.2. CAMBER AT RELEASE OF PRESTRESS

8.2.1. General. Camber at release of prestress is an important measurement of deformation in prestressed concrete girders. In many respects, the elastic camber at this stage is an informal measure of the level of prestress acting on the member. This measurement corresponds to the first point on the time-dependent deflection (or camber) curve for a girder, and all points at later ages are, to a large degree, a function of the elastic deformation at this stage.

Camber at release is generally considered to be the sum of two components. The first component Δ_p is due to the eccentricity of the prestressing and generally causes upward camber. The second component Δ_{sw} is due to the self-weight of the member and causes a downward deflection. The mid-span upward camber due to eccentric prestress for a girder with straight strands is given as:

$$\Delta_p = \frac{P_0 \cdot e \cdot L^2}{8EI} \qquad \text{Equation 8.1}$$

Note that this simple equation neglects any change in prestress force along the length of the member. Equations for other very simple layouts can be found in the *PCI Design Handbook* (PCI 1999).

The mid-span deflection due to self-weight of the girder can be predicted by Equation 8.2, which assumes the girder weight to be uniformly distributed along the length of the member and a simple span condition.

$$\Delta_{sw} = \frac{5w_{self-wt} \cdot L^4}{384EI} \qquad \text{Equation 8.2}$$

It is important to note that the self-weight deflection is a function of the fourth power of the span length, while the eccentric prestress camber is only a function of the

square of the span length. This relationship is typical for most prestressed concrete highway bridge girders, and means that the self-weight term increases at a faster rate as span lengths are increased relative to eccentric prestressing forces. It can be shown that for typical designs with very long span to depth ratios, the increase in magnitude of the self-weight term may be greater than the increased magnitude of the prestress term. The result is that net release cambers for very long span-to-depth ratios may actually decrease as spans are increased. Since the dead load deflections (under loads other than the girder self-weight) would be higher, it is quite possible that excessive sag (downward deflection) under full dead load would be present in designs with very large span-to-depth ratios unless carefully considered in design.

8.2.2. Measurements and Discussion. Mid-span camber at release of prestress was measured on a total of 4 girders. The tensioned-wire system, which is described in Section 3, was used for release camber measurements on all girders. A baseline (zero deflection) reading was recorded immediately prior to release, and another measurement was recorded immediately after release. Thermal gradient and measurement location corrections were applied to measured girder cambers.

For prediction, similar methods used for stress analysis as discussed in Section 6 are used for camber estimation. As in Table 8.1, design method and refined design method are used for camber calculation. Measured release cambers are listed in Table 8.2 and plotted in Figure 8.1. It can be found for identically designed girders very similar (less than 5% difference) measured cambers after corrections were obtained at the precast plant. Predicted cambers at release are also summarized in Table 8.2 and plotted in Figure 8.1 for comparison.

Table 8.1. Methods for Prediction of Mid-span Release Camber

Parameter	Design Method AASHTO LRFD (1994)	Refined Design Method Suggested by Author
Section Properties	Transformed section properties with designed modulus of elasticity	Transformed section properties with Measured modulus of elasticity
Prestress Force/Loss	No loss assumed before release. Elastic shortening loss calculated by approximate method given in AASHTO LRFD Specifications	2.0% loss assumed before release based on measurements. Elastic shortening loss not added because exact analysis using transformed section properties was used.
Modulus of Elasticity	Eq. 1.3 for HSC (ACI 363R-92)	Based on tests of companion specimens

Table 8.2. Summary of Measured and Predicted Mid-span Release Cambers

Girder	Measured Release Camber	Predicted Release Camber		Ratio (Meas./Design)	Ratio (Meas./Refined)
		Method (1)	Method (2)		
B13	1.07	1.11	1.10	0.96	0.97
B14	1.10	1.11	1.10	0.99	1.00
B23	1.38	1.71	1.39	0.81	0.99
B24	1.31	1.71	1.39	0.77	0.94

Note: All camber measurements in inches. 1 in.= 25.4 mm
Method (1): Design Method (AASHTO LRFD 1994)
Method (2): Refined Design Method (Suggested by Author)

For girders B13 and B14, measured cambers were very close to the predicted values using both the design method and the refined design method. The difference was only 4% with a minimal value of 0.04 in. For girders B23 and B24, however, the design method yielded much higher camber values than measured values. For girder B24, the predicted camber was 30.5% higher using the design method. Predicted value, however,

using with refined design method were only 6% difference from the measured value. This illustrates the importance of having reliable mechanical and material properties for design.

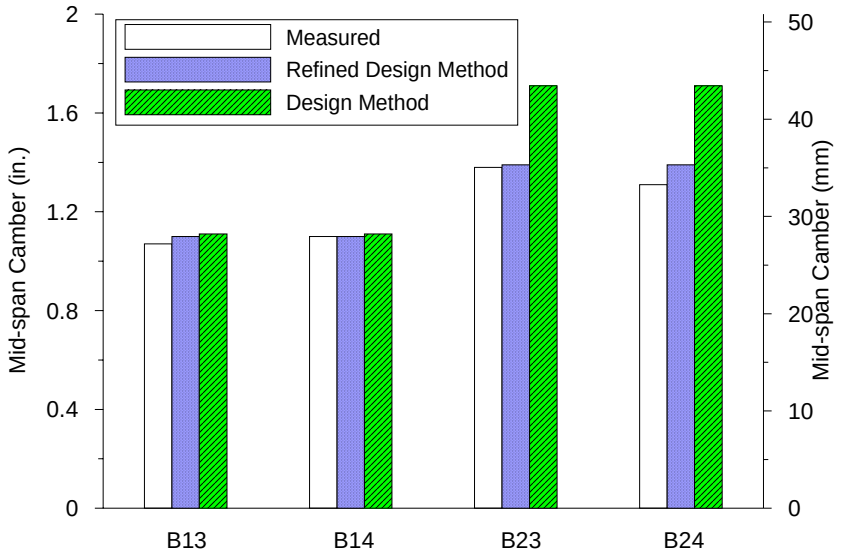

Figure 8.1. Measured and Predicted Mid-span Release Camber

A realistic estimate of the error between the measured and predicted cambers must consider the sum of the absolute values of these components rather than their algebraic sum as shown in Equation 8.3

$$\%Error = \frac{\Delta_{rel} - \Delta_{rel,pred.}}{\left|\Delta_{p,pred.}\right| + \left|\Delta_{self-wt,pred.}\right|} \cdot 100\% \qquad \text{Equation 8.3}$$

The errors computed using the above equation are summarized in Table 8.3. The predicted values used the refined design method with measured material properties. As shown in Table 8.3, the errors ranged from 0 to 4.1% for the four monitored girders, which are within acceptable measure.

Table 8.3. Approximate Error in Prediction of Camber at Release

Girder	Predicted Using Refined Design Method (Suggested by Author)			Measured Release Camber	% Error (Equation 8.3)
	Δ_p	$\Delta_{self\text{-}wt.}$	Δ_{rel}		
B13	1.30	0.20	1.10	1.07	2.0%
B14	1.30	0.20	1.10	1.10	0.0%
B23	1.68	0.29	1.39	1.38	0.5%
B24	1.68	0.29	1.39	1.31	4.1%
Note: All camber measurements in inches. 1 in.= 25.4 mm					

The most significant parameter for higher camber estimation using the design method may be associated with the estimation of the modulus of elasticity. The measured MOE was more than 10% higher than predicted by the equations (ACI 363R-92 1992) used in the design by MoDOT. Errors in estimation of concrete density also significantly contributed to the difference between measured and predicted cambers. By using measured modulus of elasticity, the refined design method yields a very good estimation (less than 4.1% difference) of camber at release for all the four instrumented girders.

It is recommended that predictions of release camber be performed with as much knowledge regarding material and mechanical properties as possible. The use of trial batching and the corresponding determination of material properties is highly recommended, especially for modulus of elasticity and density. When actual determination of these properties is not possible, designers may wish to explore the sensitivity of predictions with respect to specific parameters. Experience from past projects using similar concrete may also help the designer in developing more accurate estimates of material properties than those provided by typical code equations.

8.3. ELASTIC DEFLECTION DUE TO DECK

Elastic deflection due to deck loads are typically computed using a basic classical mechanics formula. If the load is uniformly distributed along the length of the simply supported member, then the resulting deflection is computed as shown in Equation 8.4.

$$\Delta_{deck} = -\frac{5}{48} \cdot \frac{M_{\max}}{EI} \cdot L^2 = -\frac{5w \cdot L^4}{384EI} \qquad \text{Equation 8.4}$$

M_{max} is the maximum moment at the mid-span of the simply-supported member, and negative values represent downward deflections. An accurate prediction under deck loads can be obtained if all parameters are known and if the load is truly uniform. In real bridges, the deck load is generally not perfectly uniformly distributed due to bridge crowns and deck thickness variation (Gross, 1999). The load is dependent on the thickness of the deck, the unit weight of the deck concrete, and the spacing of girders.

The elastic deflection resulting from placement of the cast-in-place deck was measured for four girders using a precise measuring system. The measured and predicted elastic deflections are summarized in Table 8.4 and plotted in Figure 8.2.

Table 8.4. Measured and Predicted Mid-span Deflection Due to Deck Weight

Girder	Measured Deflection	Predicted Deflection		Ratio (Meas./Design)	Ratio (Meas./Refined)
		Method (1)	Method (2)		
B13	0.57	0.797	0.670	0.72	0.85
B14	0.56	0.676	0.582	0.83	0.96
B23	0.86	1.198	0.983	0.72	0.87
B24	0.87	1.022	0.853	0.85	1.02
Note: All camber measurements in inches. 1 in.= 25.4 mm Method (1): Design Method (AASHTO LRFD 1994) Method (2): Refined Design Method (Suggested by Author)					

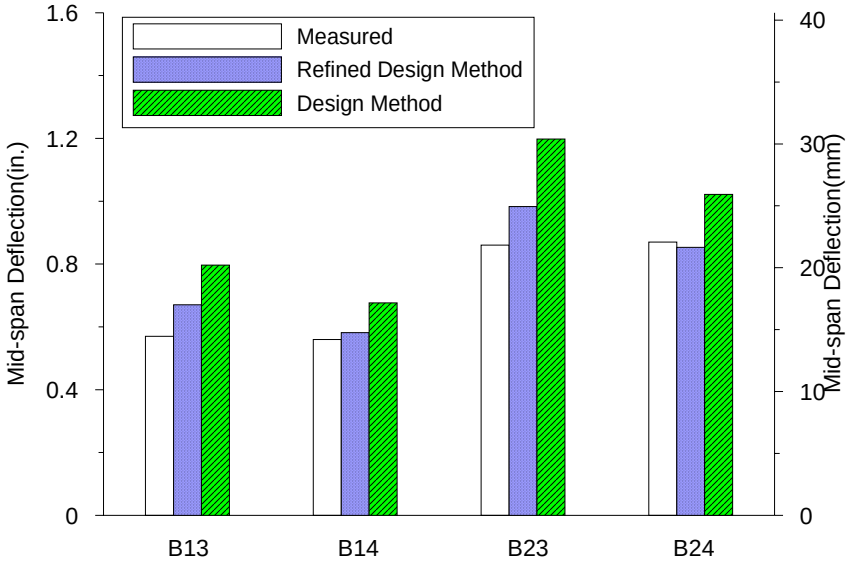

Figure 8.2. Measured and Predicted Mid-span Deflection Due to Deck

Observations regarding measured and predicted elastic deflections due to deck loads are consistent with observations related to measured and predicted stresses due to placement of the cast-in-place deck. As summarized in Table 8.5, errors between measured and predicted deflection, which are from -2 to 15%, are very close to that between measured strain curvature and predicted strain curvature, which are from -4 to 16%.

Table 8.5. Measured and Predicted Deflection and Curvature Due to Deck Weight

Girder	Measured Deflection	Predicted*		Measured Curvature	Predicted*	
		Deflection	Error		Curvature	Error
B13	0.57	0.67	15.0%	18.40	22.000	16.4%
B14	0.56	0.58	3.8%	18.70	19.100	2.1%
B23	0.86	0.98	12.5%	21.54	23.900	9.9%
B24	0.87	0.85	-2.0%	21.60	20.700	-4.3%

Note: All camber measurements in inches. 1 in.= 25.4 mm

* Predicted using Refined Design Method (Suggested by Author)

Girder deflections due to the total deck load were less than predicted, despite the inclusion of time-dependent effects such as creep and shrinkage in the measured deflections. The possible reasons why measured elastic deflection due to deck loads was lower than predicted could be the actual deck thickness. Variations in the actual deck thickness may have contributed to the low deflections. The thickness can be highly variable and lead to variations in the actual deck load (Gross, 1999). It should also be noticed that the deck load at both ends of the girder may be quite different from that on the other parts of the girder because of the large skew of the bridge.

Similar to predicted camber at release, the best way to predict the deflection due to deck is to use of trial batching and the corresponding determination of material properties, especially for modulus of elasticity and density. However, the actual determination of these properties at the design stage is often not available. Experience from past projects using similar concrete may also help the designer in developing more accurate estimates of material and mechanical properties rather than those provided by typical code equation.

8.4. LONG-TERM DEFLECTION BEHAVIOR

8.4.1. General. It is not the individual components of elastic or time-dependent camber and deflection that are of the most interest during the design and construction of prestressed concrete highway bridges. The net camber due to the combined effects of all components is generally much more significant. As discussed in the beginning of this Section, the net camber after erection of the girders is important because it can influence the placement of the cast-in-place bridge deck. The long-term net camber or deflection

under full dead load is important as a serviceability criterion. Excessive camber or defection can result in an uneven riding surface or in a poor aesthetic appearance.

Actually few real guidelines exist for camber and deflection of prestressed concrete highway bridge girders under dead load. The AASHTO Standard Specifications (AASHTO, 1996) do not present any requirements or suggest a range of acceptable behavior for camber and deflection under full dead load. In the commentary of the AASHTO LRFD Specifications (AASHTO, 1994), it is stated that "control of deflections is permitted but not encouraged", and no suggestions for acceptable dead load deflections are provided.

Many standard methods have been proposed in the literature to estimate the long-term deflection behavior of prestressed concrete girders committees (Branson and Ozell 1961, Naaman 1982, and Nilson 1987). There are three basic categories: basic multiplier methods, approximate time-step or advanced multiplier methods, and incremental time-step methods.

Basic multiplier methods provide for the calculation of time-dependent camber or deflection as the algebraic sum of multiples of the elastic components of camber or deflection. This approach is similar to the simple deflection multiplier method recommended in the ACI 318-02 code for time-dependent deflection of reinforced concrete girders. Based on the work of Martin (1977), the PCI Design Handbook (PCI 1999) suggests that the net camber at erection and long-term deflection (or camber) can be estimated by following equations:

$$\Delta_{erection} = 1.80 \cdot \Delta_p - 1.85 \cdot \Delta_{sw} \qquad \text{Equation 8.5}$$

$$\Delta_{long-term} = 2.20 \cdot \Delta_p - 2.40 \cdot \Delta_{sw} - 3.00 \cdot \Delta_{sdl} - 2.30 \cdot \Delta_{cd} \qquad \text{Equation 8.6}$$

Δ_p, Δ_{sw}, Δ_{sdl}, and Δ_{cd} represent the elastic camber or deflection due to initial prestress, member self-weight, superimposed (noncomposite) dead loads, and the weight of the composite deck, respectively. Positive values indicate upward camber and negative values indicate downward deflection.

Approximate time-step procedures and advanced multiplier methods use the same approach as the basic multiplier method, except that the values of the multipliers themselves are determined as part of the calculations. Branson and Kripanarayanan (1971) developed an approximate time-step procedure on this basis that can be applied to a variety of structure types, including prestressed girders with and without composite deck slabs.

More complex incremental time-step procedures have been proposed by many authors and are recommended for use by several committees (ACI 435R-95 1995, Branson and Ozell 1961, Ghali and Favre 1986, Libby 1990, Naaman 1982, and Nilson 1987). These methods are generally considered to be accurate, but as with any approach, the correct modeling of time-dependent material properties is essential.

8.4.2. Measurements and Discussion. Camber and deflection are measured after prestress release as discussed in Section 3 using a tensioned-wire system. After erection of the girders, the precise surveying method was used to monitor camber or deflection.

Measured and predicted camber values at erection and long-term service are summarized in Tables 8.6, 8.7, respectively. As obtained in Sections 8.2 and 8.3, predicted cambers are obtained using the design method and the refined design method. Ratios of measured camber to predicted camber are also listed in Table 8.6 and Table 8.7.

Table 8.6. Measured and Predicted Camber at Erection

Girder	Days	Measured Camber	Predicted Camber		Ratio Meas./Design	Ratio Meas./Refined
			(1)	(2)		
B13	18	1.64	2.13	1.71	0.77	0.96
B14	18	1.75	2.13	1.71	0.82	1.02
B23	31	2.07	2.97	2.19	0.70	0.95
B24	31	1.99	2.97	2.19	0.67	0.91

Note: All camber measurements in inches. 1 in.= 25.4 mm
(1): Design Method (AASHTO LRFD 1994)
(2): Refined Design Method (Suggested by Author)

Table 8.7. Measured and Predicted Long-Term Camber

Girder	Days	Measured Camber	Predicted Camber		Ratio Meas./Design	Ratio Meas./Refined
			(1)	(2)		
B13	598	0.96	1.23	1.15	0.78	0.83
B14	598	0.84	1.35	1.25	0.62	0.67
B23	611	1.01	1.67	1.23	0.60	0.82
B24	611	0.8	1.85	1.37	0.43	0.58

Note: All camber measurements in inches. 1 in.= 25.4 mm
(1): Design Method (AASHTO LRFD 1994)
(2): Refined Design Method (Suggested by Author)

Girders B13 and B14 were erected 18 days after release. The measured cambers at erection were 23% and 18% lower than cambers estimated using the design method for girders B13 and B14, respectively. Measured cambers, however, were only 4% lower and 2% higher than cambers estimated using the refined design method for girders B13 and B14, respectively. Girders B23 and B24 were erected 31 days after the release of prestress. The measured cambers were 30% and 33% lower than cambers estimated using

the design method for girders B23 and B24, respectively. Measured cambers, however, were only 5% and 9% lower than cambers estimated using the refined design method for girders B23 and B24, respectively. The difference is illustrated in Figure 8.3.

For long-term camber at service, measured and predicted cambers at 598 days after prestress release were obtained and compared for girders B13 and B14. The measured cambers were 22% and 38% lower than cambers estimated using the design method for girders B13 and B14, respectively. However, measured cambers were about 17% lower and 33% higher than cambers estimated using the refined design method for girders B13 and B14, respectively.

For girders B23 and B24, measured and predicted long-term camber at 611 days after prestress release are compared as shown in Figure 8.4. The measured cambers were 40% and 57% lower than cambers estimated using the design method for girders B23 and B24, respectively. Measured cambers, however, were about 18% and 42% lower than cambers estimated using the refined design method for girders B23 and B24, respectively.

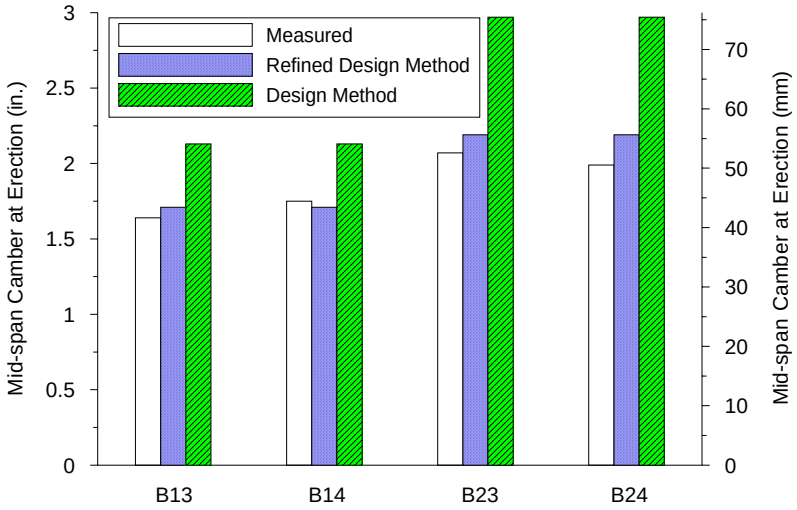

Figure 8.3. Measured and Predicted Camber at Erection

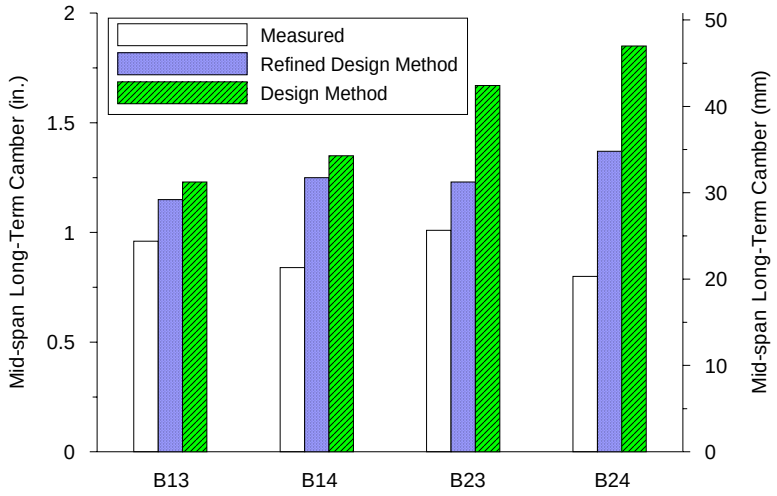

Figure 8.4. Measured and Predicted Long-Term Camber

The complete time-dependent camber and deflection history for each girder was also predicted using an incremental time-step analysis based on measured material properties and the actual construction schedule. Details of this incremental time-step analysis are discussed in Appendix G. Plots of measured and predicted time-dependent camber for each girder are illustrated in Figures 8.5 through 8.8.

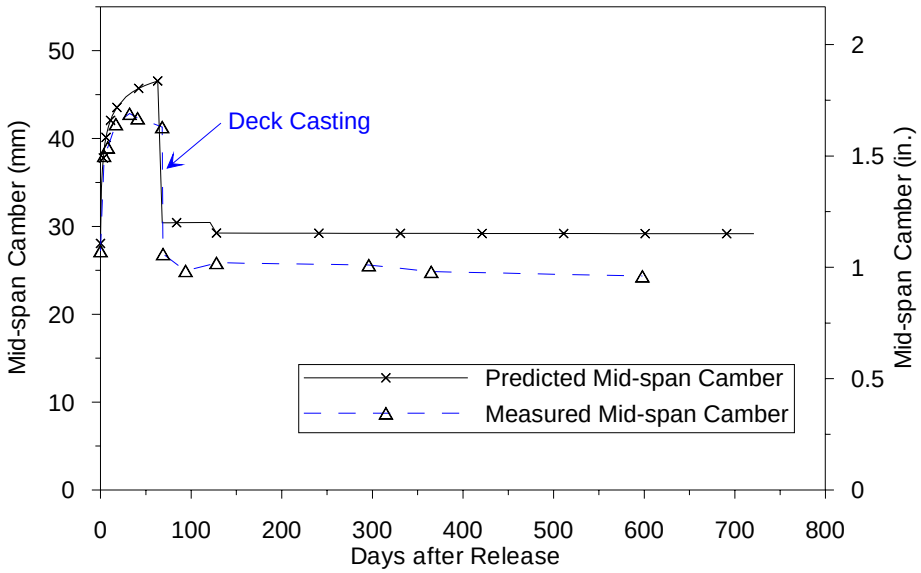

Figure 8.5. Measured and Predicted Long-term Camber for Girder B13

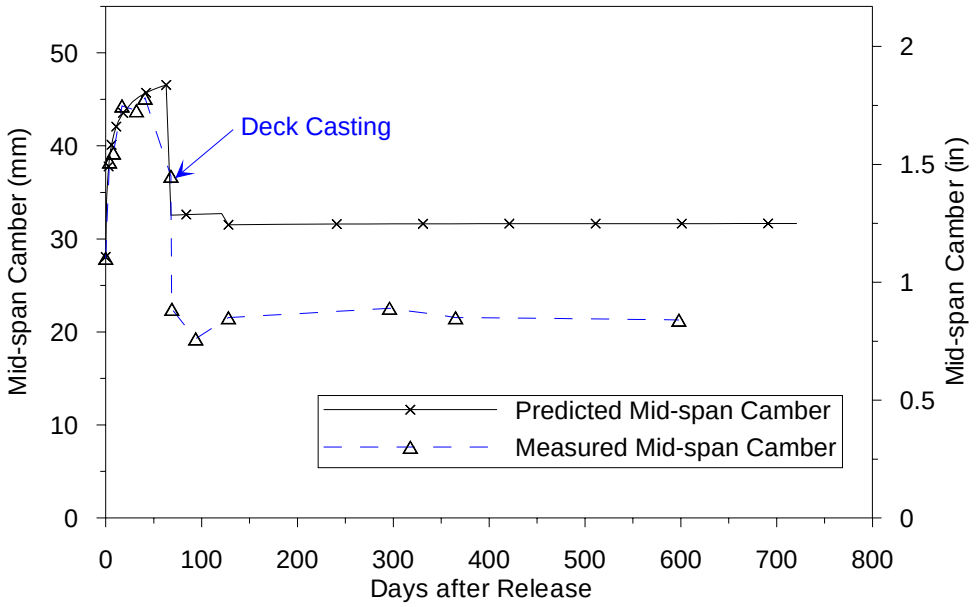

Figure 8.6. Measured and Predicted Long-term Camber for Girder B14

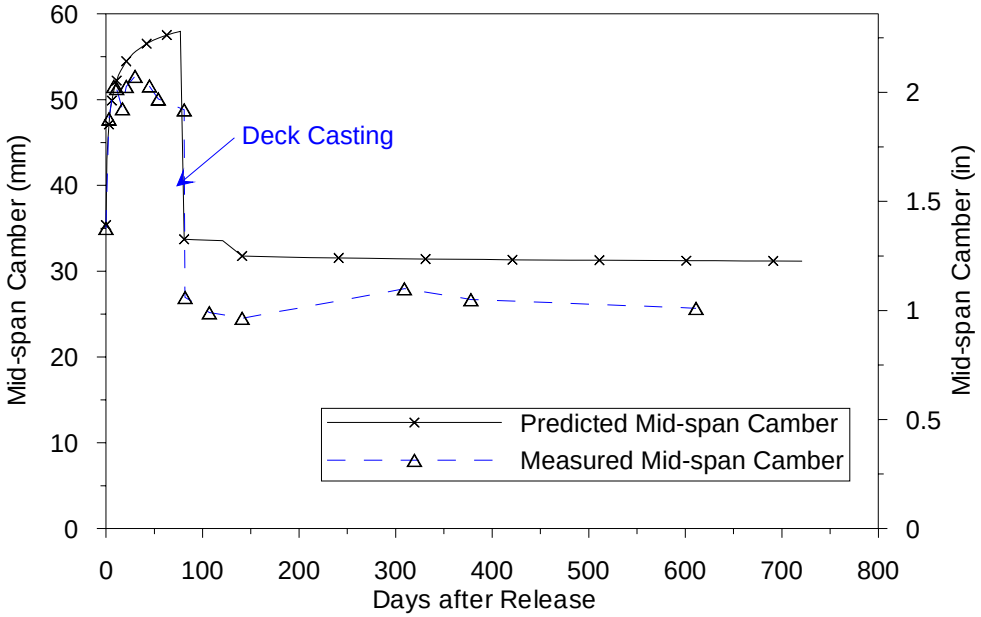

Figure 8.7. Measured and Predicted Long-term Camber for Girder B23

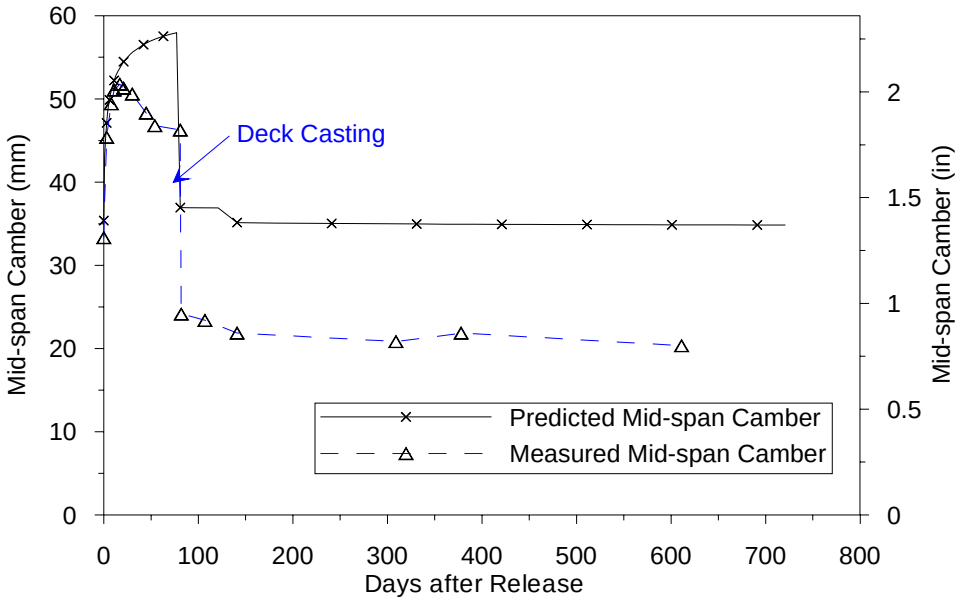

Figure 8.8. Measured and Predicted Long-term Camber for Girder B24

It should be noted that there was generally good agreement between camber values at erection among girders in a given span. That is, the range of values for erection camber among the girders in a span was generally rather small (less than 7%). The measured erection and long-term cambers were substantially lower than the cambers estimated during design by up to 40%. However, the maximum difference between measured and predicted long-term camber was less than 25.4 mm (1 in.). Better correlation existed between the measured values and the predictions based on measured parameters.

The overall range of long-term measured camber values was quite acceptable. None of the four monitored girders exhibited significant downward deflection or excessive upward deflection.

As discussed previously, several important factors have an influence on camber and deflection. It was shown that changes in the initial prestress force and dead loads, as

well as variations in the modulus of elasticity and creep coefficient; all could substantially influence the elastic and time-dependent components of the net camber at erection or long-term service. Increases in the initial prestress force and the creep coefficient, and decrease in the dead loads and modulus of elasticity, would all lead to a higher net camber. Similarly, variations in the opposite direction would lead to a lower net camber.

8.5. SUMMARY AND CONCLUSIONS

Based on the measurement and analysis in this Section, the following observations were made:

Measured camber at release of prestress ranged from 27.2 to 27.9 mm (1.07 to 1.10 in.) for 15.5 m (50.9 ft) long end span girders, 33.3 to 35.1 mm (1.31 to 1.38 in.) for 17.0 m (55.8 ft) long inside span girders. For identical girders measured release cambers were generally very similar in magnitude.

Measured release cambers were lower than predicted release cambers based on either design or measured properties. Differences between measured and predicted release cambers based on designed properties ranged from 0.3 to 10.2 mm (0.01 to 0.40 in.). Meanwhile, differences between measured and predicted release cambers based on measured properties were very small, ranging from 0 to 1.8 mm (0 to 0.07 in.). Differences between measured release camber and predicted release camber based on measured parameters are due in large part to differences between the actual and measured modulus of elasticity for concrete and errors in the refined estimation of the initial prestress force and member self-weight.

Measured elastic deflections due to placement of the cast-in-place deck ranged from 14.2 to 14.5 mm (0.56 to 0.57 in.) for 15.5 m (50.9 ft) long end span girders, 21.8 to 22.1 mm (0.86 to 0.87 in.) for 17.0 m (55.8 ft) long inside span girders. For identical girders measured deflections due to deck weight were generally very similar in magnitude (less than 2% difference).

Measured deflections due to deck load were generally lower than predicted using measured parameters except girder B24. The differences ranged from -0.5 to 3.0 mm (-0.02 to 0.12 in.), which are -2 to 25% of predicted deflections. Meanwhile, the differences between measured and predicted deflection using design parameters ranged from 3.0 to 8.6 mm (0.12 to 0.34 in.), which are 25 to 38% of predicted deflections. Differences between measured and predicted deck deflections are possibly due to variations in the concrete modulus of elasticity and deck thickness, even though these parameters were based on measured values.

Measured camber at erection ranged from 41.7 to 44.5 mm (1.64 to 1.75 in.) for 15.5 m (50.9 ft) long end span girders, 50.5 to 52.6 mm (1.99 to 2.07 in.) for 17.0 m (55.8 ft) long inside span girders. Measured long-term camber ranged from 21.3 to 24.4 mm (0.84 to 0.96 in.) for 15.5 m (50.9 ft) long end span girders, 20.3 to 25.7 mm (0.80 to 1.01 in.) for 17.0 m (55.8 ft) long inside span girders. These long-term measurements show the desired slight upward deflection for all girders.

There was generally good agreement between camber values at erection among girders in a given span. That is, the range of values for erection camber among the girders in a span was generally rather small (less than 7% difference). The measured erection and long-term cambers were substantially lower than the cambers estimated during design by

up to 40%. However, the maximum difference between measured and predicted camber was less than 25.4 mm (1 in.). The overall difference between measured and predicted long-term camber was in an acceptable range. Better correlation existed between the measured values and the predictions based on measured parameters.

9. FABRICATION AND CONSTRUCTION

9.1. INTRODUCTION

In this Section, the fabrication of the precast girders and the construction of the bridge were documented. Construction related issues and concerns are presented. Table 9.1 lists the important dates for the bridge construction and milestones.

Table 9.1. Bridge Construction Timeline

Actions	Start Time and Date	Notes
Girder Pour 1	7:30am, 6/6/2001	Cast B41, B42, B43, B44
Girder Release	10:30am, 6/8/2001	Release B41, B42, B43, B44
Girder Pour 2	7:30am, 6/13/2001	Cast B21*, B22*, B31, B32
Girder Release	10:48am, 6/15/2001	Release B21, B22, B31, B33
Girder Pour 3	7:30am, 6/20/2001	Cast B23*, B24*, B33, B34
Girder Release	12:50pm, 6/22/2001	Release B23, B24, B33, B34
Girder Pour 4	7:30am, 6/26/2001	Cast B51, B52, B53, B54
Girder Release	10:20am, 6/28/2001	Release B51, B52, B53, B54
Girder Pour 5	7:30am, 7/3/2001	Cast B11, B12, B13*, B14*
Girder Release	1:50pm, 7/5/2001	Release B11, B12, B13, B14
Girder Transportation	7/19/2001	Erect Span 3, 4
Girder Transportation	7/23/2001	Transport B13, B14, B23, B24
Girder Erection	10:30am, 7/23/2001	Erect Span 1, 2, 5
Deck Formwork	8/4-8/17/2001	Set up formwork for deck
Deck steel	8/17/2001	Place steel for the deck
Deck Pour	6:30pm, 9/11/2001	Cast CIP deck
* Girders which were instrumented		

9.2. FABRICATION OF PRECAST GIRDERS

A pre-construction meeting was held on January 4th, 2001 at MoDOT District 10 Office in Sikeston, MO. MoDOT, the fabricator, the contractor and UMR researchers participated to clarify any details specific to the construction of the HPC Bridge such as when and how the researchers can access to the bridge and implement instrumentation.

A pre-fabrication meeting prior to fabrication of the precast prestress girders was held on June 1st, 2001 at the precast plant in Bonne Terre, Missouri, 4 days before the beginning of the fabrication. The fabricator, Egyptian Concrete Inc. and the UMR researchers discussed the fabrication schedule of the girders and construction issues. The pre-construction and pre-fabricating meetings were very important for the fabricator, the contractor and researchers because these meetings clarified details of the instrumentation and how that would affect the construction activities. Thus the meetings improved the likelihood for a successful research program throughout the fabrication, construction and monitoring stages.

The bridge girders were fabricated from June 6th through July 26th, 2001. The strands were prestressed before the mild steel was set up as shown in Figure 9.1. Then the concrete was batched and the girders were poured typically 5:30 AM – 7:30 AM in the morning when the ambient temperature was appropriate for concrete placement (see Figure 9.2).

As shown in Figure 9.3, one of the girders cast during the third pour had a void near the end of the member. The void was formed due to lack of vibration near that end when the fabricator vibrated the concrete. The area was patched by the fabricator. To date the repaired defect has not affected the girder behavior in any discernable fashion such as

cracking. It is realized that vibration (internal and external) is important to disperse the concrete thoroughly for fabricating high-strength concrete girders with small geometry and large diameter prestressing strands.

After the steel forms were removed, three to eleven hairline cracks were found on the surface of the girders as shown in Figure 9.4. After transfer, some additional cracks appeared from the top of the girder as illustrated in Figure 9.5. The cracking is discussed in detail in Section 6.

Figure 9.1. Prestressing Strands

a.) Concrete Mixing b.) Casting Concrete

Figure 9.2. Concrete Mix and Pour at Egyptian Concrete

a.) Void Near End of Girder

b.) Blow-up View of Void

c.) Patched Void

Figure 9.3. Void in Girder B24

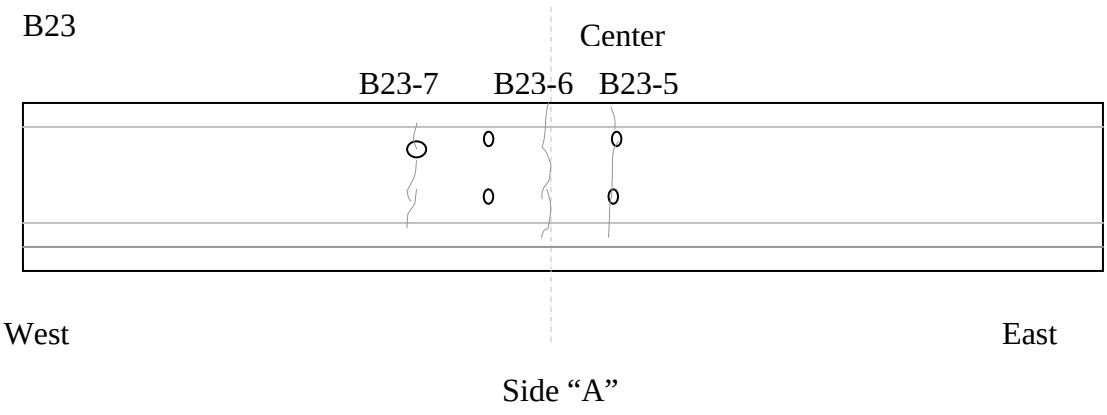

Figure 9.4. Crack Pattern Prior to Strands Release

Figure 9.5. Crack After Strands Release

The girders were moved outdoor for storage and kept cured at Eyption Concrete after release of prestress (see Figure 9.6). During the storage, camber of the girders was measured along with strain and temperature measurements. These girders were shipped to the bridge jobsite after storage and curing on July 23rd, 2001 as illustrated in Figure 9.7.

The shipping of the girders started from 5:00AM to avoid high temperature in the afternoon.

Figure 9.6. Girders Storage at Precast Plant

Figure 9.7. Shipping of the Girders to the Bridge Jobsite

9.3. BRIDGE CONSTRUCTION

A pre-deck construction meeting prior to formwork placement was held on July 31st 2001 in Kennett, MO. Issues including level of instrumentation, staging of instrumentation and casting & placement of concrete issues were discussed. The

construction sequence is documented in Figures 9.8 through 9.15. This included the following process: the bridge girders were erected immediately after they were transported to the jobsite. Following erection of the girders, the formwork for the cast-in-place deck was constructed. Steel in the deck was then placed. On September 11th, 2001 the CIP deck was cast. The bridge handrail was cast in the winter of 2001, after which the bridge construction was complete.

Figure 9.8. Girders Erection

Figure 9.9. Girders on the Bents

Figure 9.10. Formwork and Steel for the Deck

Figure 9.11. Sensors Embedded in the DECK

Figure 9.12. Concrete Placement for the CIP Deck at Jobsite

Figure 9.13. Surface of CIP Deck After Wet Mat Curing

Figure 9.14. Bottom of CIP Deck After Wet Mat Curing

Figure 9.15. Completed Bridge

10. LIVE LOAD TEST PROGRAM

10.1. INTRODUCTION

Bridge A6130 is the first fully HPC superstructure bridge in Missouri. The bridge was instrumented with embedded strain gauges and thermocouples to monitor the early-age and later-age behavior of the structures from construction through service. To investigate the overall behavior of the bridge under live load, a static live load test was developed and carried out in June, 2002. During the live load test, 64 embedded vibrating wire strain gauges (VWSG) were used to acquire the strain rate in the bridge caused by the varying live load conditions. Girder deflections and rotations were also recorded using external sensors and a data acquisition system (DAS). Based on the test results, the load distribution to the girders was studied. The AASHTO specifications live load distribution factor (AASHTO 1994) recommended for design was compared to the measured value. The AASHTO LRFD live load distribution factors (AASHTO 2002) recommended for design were found to be comparable to measured values. Two finite element models were developed using ANSYS and compared with measured values to investigate the continuity level of the Missouri Department of Transportation (MoDOT) interior bent detail.

10.2. LOAD TEST PROGRAM

Concrete strains and girder deflections were the basic components to that were monitored during the load test. An instrumentation program was developed to monitor components of the bridge superstructure during early-age and later-ages to identify trends in the measured and observed behavior as noted in Section 3. A data acquisition system

(DAS-1) with sufficient channels was designed and assembled for the project as described in Chpater 3. Strain gauges were used for the live load test study including VWSG as illustrated in Figure 10.1.

LVDT's and surveying equipment were used for deflection measurement. Seven LVDT's were used for deflection measurement. As shown in Figure 10.2, four were used for the girder mid-span deflection measurement and three were used at the midpoint of the deck between girders. Inclinometers were place on the deck to obtain the slope deformation as shown in Figure 10.2. A second data acquisition system (DAS-2) was shipped from the Univ. of Missouri-Rolla (UMR) to the bridge site to acquire data from the LVDT's and inclinometers. Due to clearance heights on the underside of the bridge and the presence of water below span 2 through 4, the LVDT's could only be used for Span 1. Therefore, surveying equipment was used to measure the deflection of the second span girders as highlighted in Figure 10.2. It may be noted that the surveying equipment was ultimately not precise enough (more than 110% difference between two readings for the same case) for the deflection measurements of Span 2 due to the stiff nature of the bridge and relatively short span lengths.

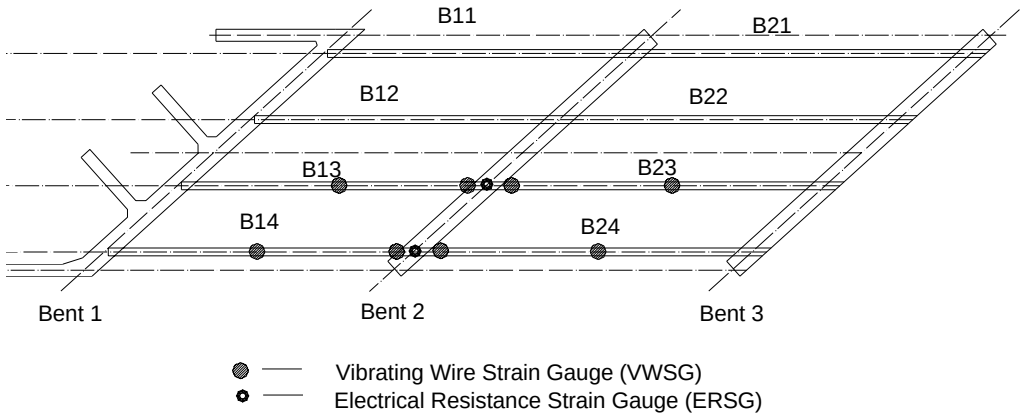

Figure 10.1. Strain Gauge Connected with DAS-1

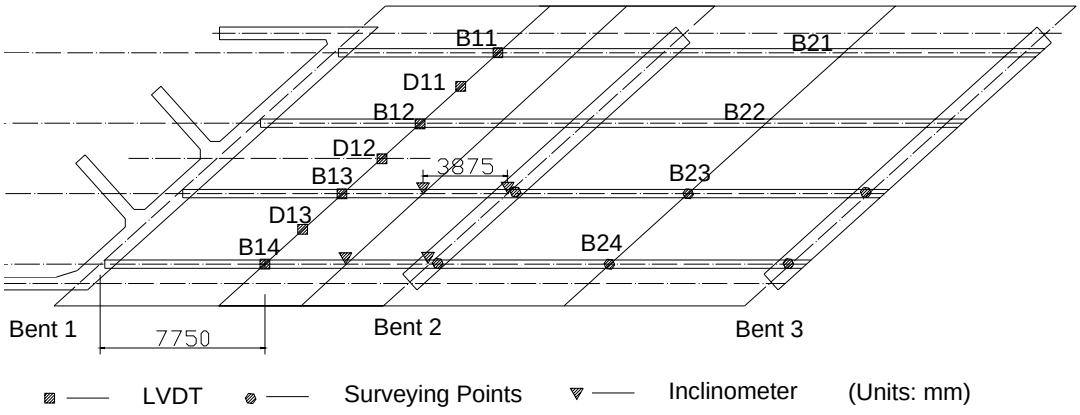

Figure 10.2. Deformation Measurement Points for Live Load Test

Two MoDOT dump trucks were of identical configuration as shown in Figure 10.3. A SHD 5935 truck loaded up to 201.6 kN (47380 lb) and a SHD 6032 truck loaded up to 218.8 kN (49220 lb) were used in the live load test. Axle weights were obtained prior to load testing using Missouri District 10 weight scales and shown in Figure 10.3.

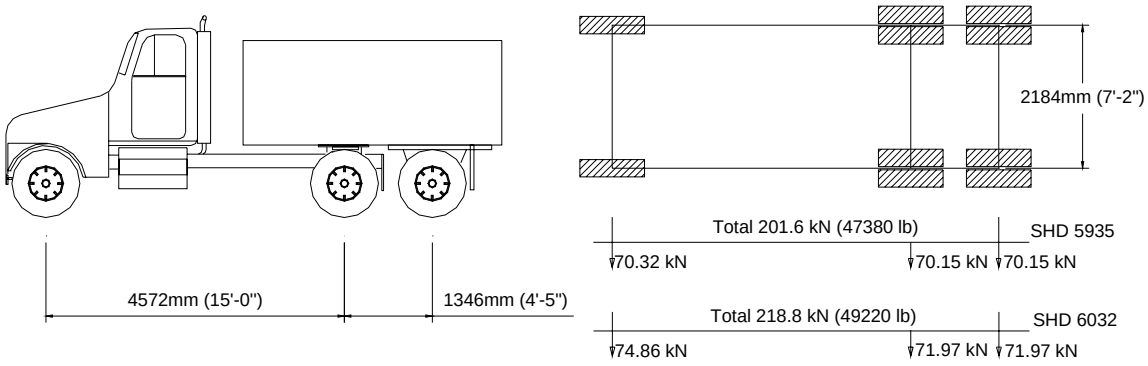

Figure 10.3. Dump Truck for Live Load Test

Six load cases were implemented for the load test. The truck location in each case is described in Table 10.1 where the trucks were centered based on axle weight. These load cases were selected to study both load distribution across the width of the bridge and

bent rotation at the interior bent. In addition to the live load test results reported herein, later-age live load testing is planned as part of the long-term monitoring program to investigate time-dependant effects on the response of the bridge.

Table 10.1 Load Case Description

Load Case	Description
A	One truck centered over mid-span of girder B13
B	One truck centered over mid-span of girder B12
C	Two trucks centered over mid-span of girder B13; Clear transverse distance between two axles of two trucks is 0.6 m.
D	One truck centered over mid-span of girder B13 and one truck centered over mid-span of girder B23
E	Two trucks centered over mid-span of girder B23; Clear transverse distance between two axles of two trucks is 0.6 m.
F	One truck centered over mid-span of girder B23

Figure 10.4 shows a typical load case that the dump truck stops at mid-span of the girder. Figures 10.5 through 10.10 illustrate load cases that were planned as part of the live load testing program.

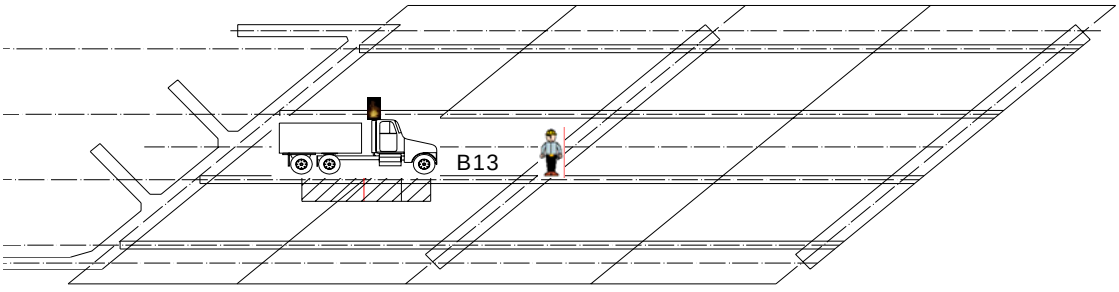

Figure 10.4. Dump Truck Stop at Mid-span of a Girder

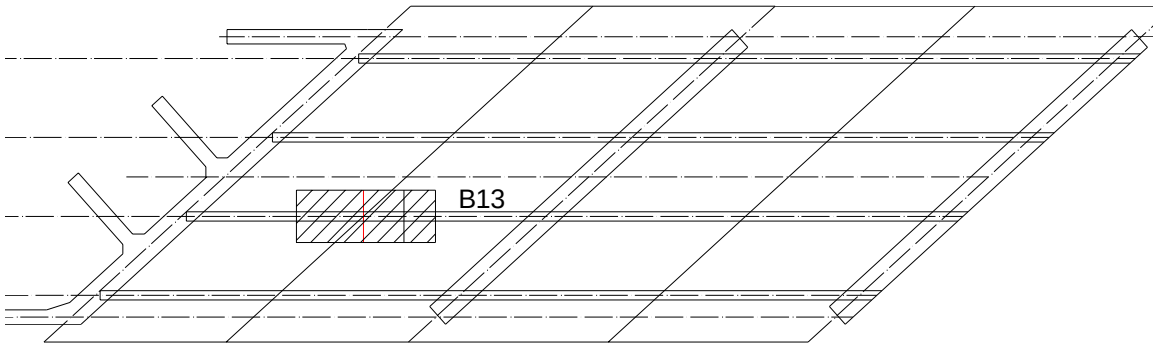

Figure 10.5. Load Case A

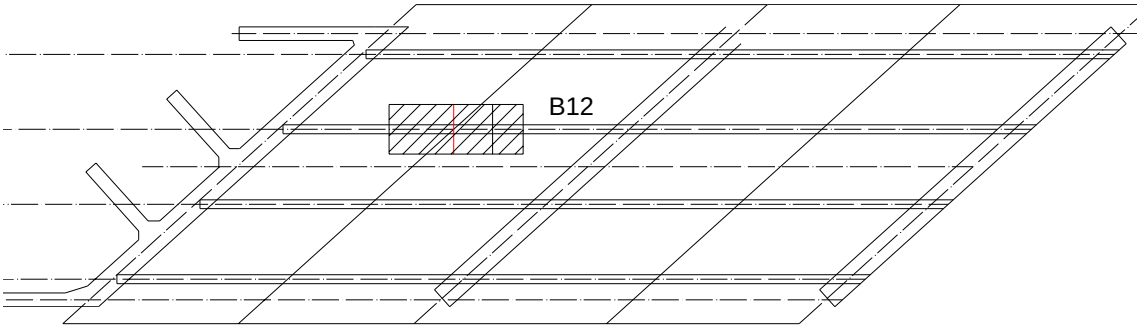

F

igure 10.6. Load Case B

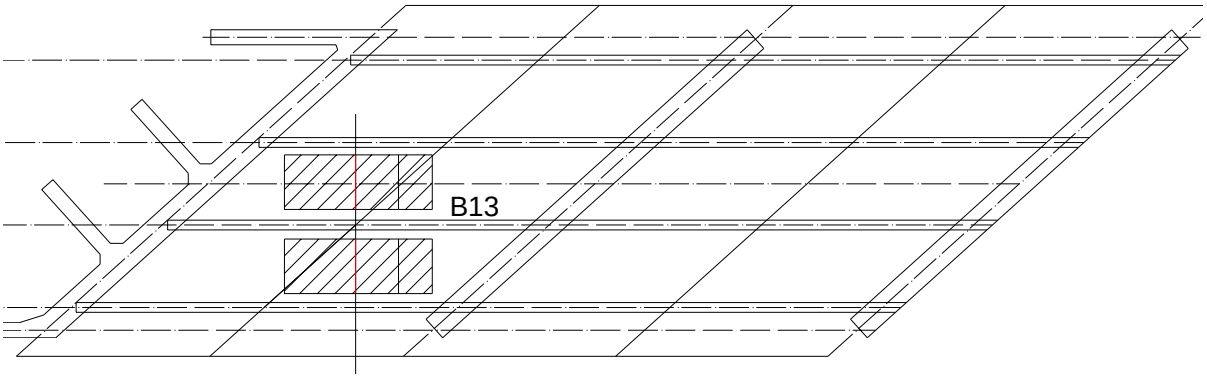

Figure 10.7. Load Case C

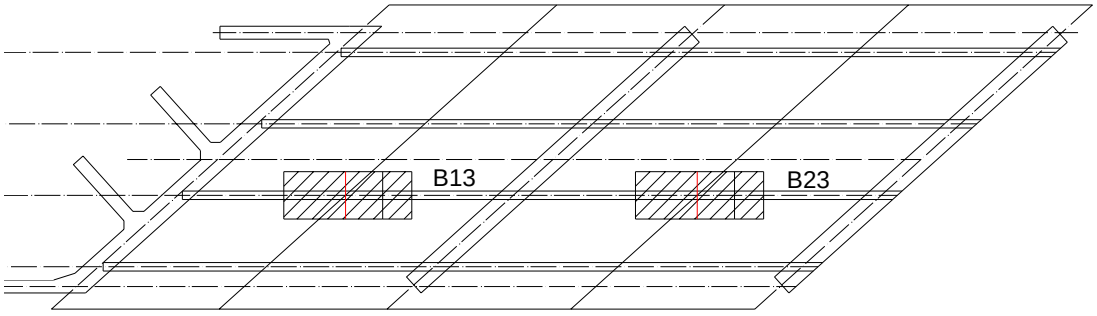

Figure 10.8. Load Case D

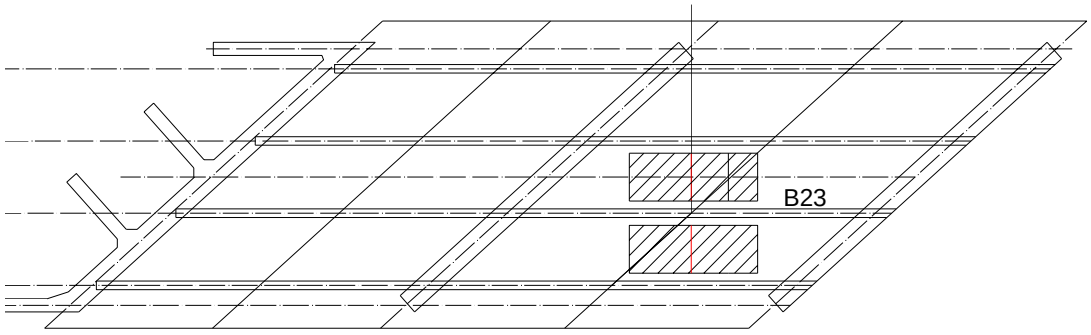

Figure 10.9. Load Case E

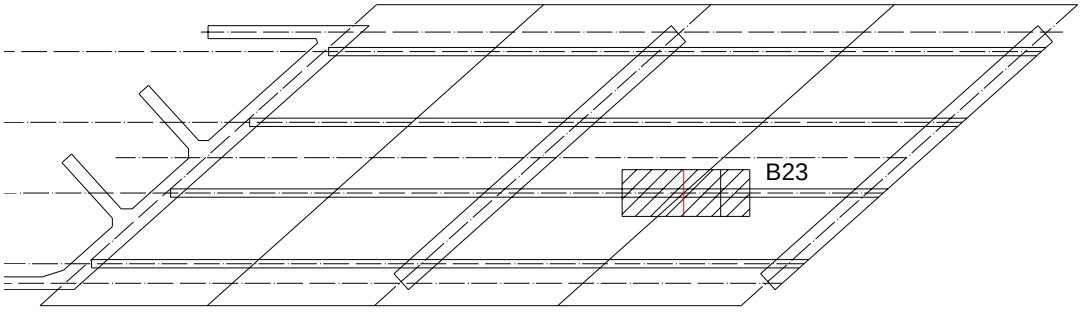

Figure 10.10. Load Case F

10.3. LIVE LOAD TEST RESULTS

After download of field data acquired by DAS-1 and DAS-2, the girder deflections and section curvatures were obtained. Several characteristics of the

constructed HPC bridge were then investigated, including the load distribution, the serviceability, and continuity across the interior bents.

10.3.1. Deflection. The LVDT's used for monitoring Span 1 offered prescise results [± 0.025 mm (± 0.001 in.)] summarized in Table 10.2. The surveying equipment used for Span 2 was accurate to [± 1 mm (± 0.04 in.)]. The accuracy of these measurements were therefore not precise enough based on the measured deflection readings to be presented herein. For load cases A, B and C, the deflection of girders B11, B12, B13 and B14 are presented in Figures 10.11 through 10.13.

Load case A was centered on girder B13, while load case B was centered on girder B12. From the deflection results observed and presented in the aforementioned figures, there is very good correlation (less than 2% difference) between girders B12 and B13 respectively for the adjacent load case A and B that are nearly symmetric. These values are not exactly identical due to the non-consistent deck thickness along the width and length of the bridge. The measured deflection at mid-span of the deck between girders demonstrated the same trend.

Table 10.2. Deflection Results for Girders and Deck

Load Case	Deflection (mm)						
	B11	B12	B13	B14	D11	D12	D13
A	0.048	0.213	0.678	0.157	0.097	0.498	0.500
B	0.282	0.663	0.234	-0.020	0.531	0.594	-0.005
C	0.152	0.508	1.026	0.511	0.269	0.841	0.988
D	0.013	0.135	0.625	0.112	0.010	0.434	0.536
E	-0.102	-0.249	-0.185	-0.216	-0.229	-0.203	-0.231
F	-0.043	-0.188	-0.175	-0.211	-0.160	-0.168	-0.226
"+" is downward deflection; "-" is upward deflection; 1 mm = 0.03937 in.							

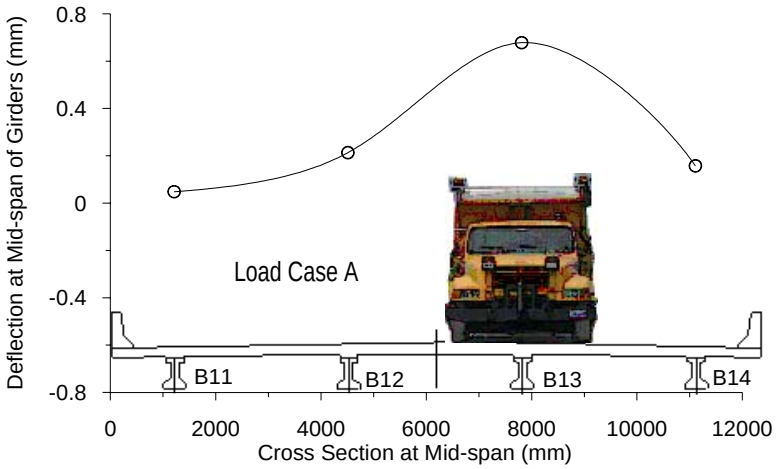

Figure 10.11. Deflection at Mid-span of Girders - Load Case A

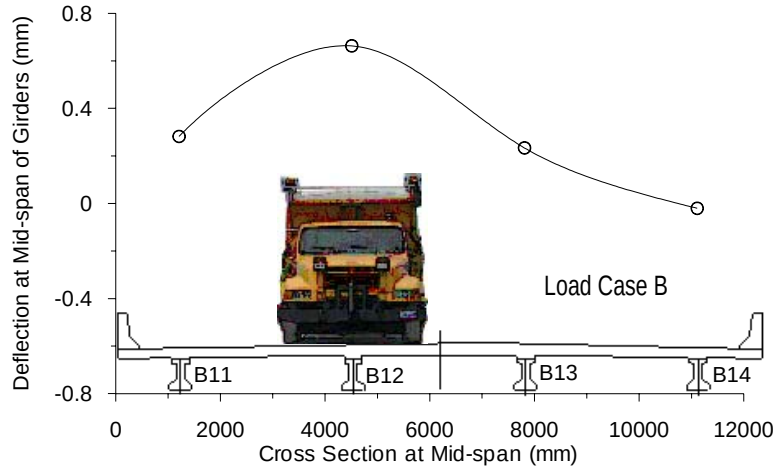

Figure 10.12. Deflection at Mid-span of Girders - Load Case B

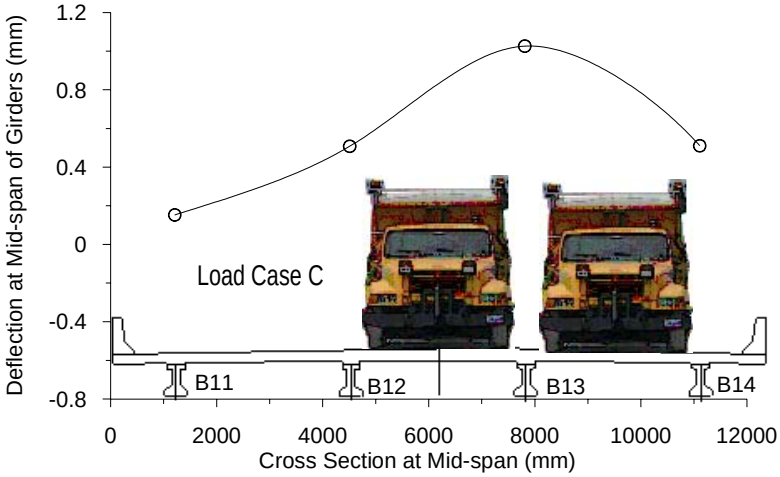

Figure 10.13. Deflection at Mid-span of Girders - Load Case C

For load case C, the deflection at mid-span of girder B13 as illustrated in Figure 10.13 is larger than in load case A and B due to the increase in live load represented by applying two trucks with the weight illustrated in Figure 10.3. Load case D may be considered as the sum of load case A and load case F. Therefore, the mid-span deflection for load case D should be 0.503 mm (0.020 in.), which is the sum of 0.678 mm (0.027 in.) and -0.175 mm (-0.007). The actual measured response was 0.625 mm (0.025 in.) with a difference of 19% from calculated from load case A and F. The difference is attributed to a slight loading location error, which is less than 100 mm (4 in.). The truck locations for load case A and load case F were not positioned in identical locations as for load case D in the field though the error is less than 100 mm (4 in.). For load case E and load case F, there were negative mid-span deflections for the girders in the first span, signifying that the continuity connection at the interior bent is neither perfectly fixed nor simple supported at the bent line.

10.3.2. Section Curvature. Live load test results at different locations are detailed in Table 10.3. Interior girders B13 and B23 are considered in the table. The response of exterior girders B14 and B24 to the live load was minimal (less than 0.0005 με/mm). As detailed in Table 10.3, some data were not indicated because the strain values along the section depth were smaller than 3 με; therefore, section curvatures based on these strain measurements were not practicable.

As previously noted, strain gauges were embedded at various depths across the section. The curvature was determined from the slope of a linear trend line fit based on the recorded strain data as illustrated in Figures 10.14 through 10.19. Using the composite section properties and modulus of elasticity of the concrete from match cured

specimens, the moment at the section was determined. The results are detailed in Table 10.3.

Figures 10.14 through 10.19 present typical strain profile at the mid-span section and near-end support section. The curvature values obtained by curve fitting the test data are also presented in the figures. Thermal effects were investigated, but determined to be minimal (strains due to thermal effects were less than 5% of those due to live load) and not impact the curvature results shown in Table 10.3.

Table 10.3. Measured Curvature and Moment

Load case	Girder	Mid-span Curvature (με/mm)	Near-end Support Curvature (με/mm)	Mid-span Moment (kN-m)	Near-end Support Moment (kN-m)
A	B13	0.0392	-0.0335	143.26	-122.38
	B23	-0.0075	-0.0236	-27.45	-86.19
B	B13	0.0278	-0.0340	101.55	-124.16
	B23	N/A	N/A	N/A	N/A
C	B13	0.0158	-0.0214	57.70	-78.06
	B23	N/A	N/A	N/A	N/A
D	B13	0.0187	N/A	68.31	N/A
	B23	0.0599	N/A	218.79	N/A
E	B13	-0.0432	-0.0421	-157.88	-153.63
	B23	0.1030	N/A	376.07	N/A
F	B13	-0.0419	-0.0456	-153.17	-166.67
	B23	0.0844	-0.0497	308.16	-181.59

Note: N/A means not available; Moments are computed from curvature.

1 kN = 224.8 lb; 1 mm = 0.03937 in.

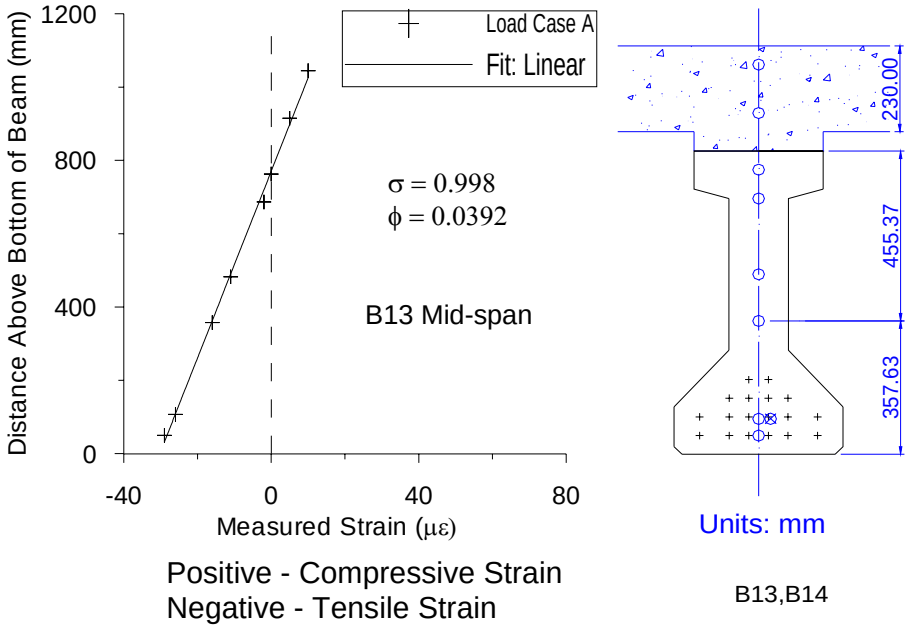

Figure 10.14. Strain Profile at Girder B13 Mid-span Section - Load Case A

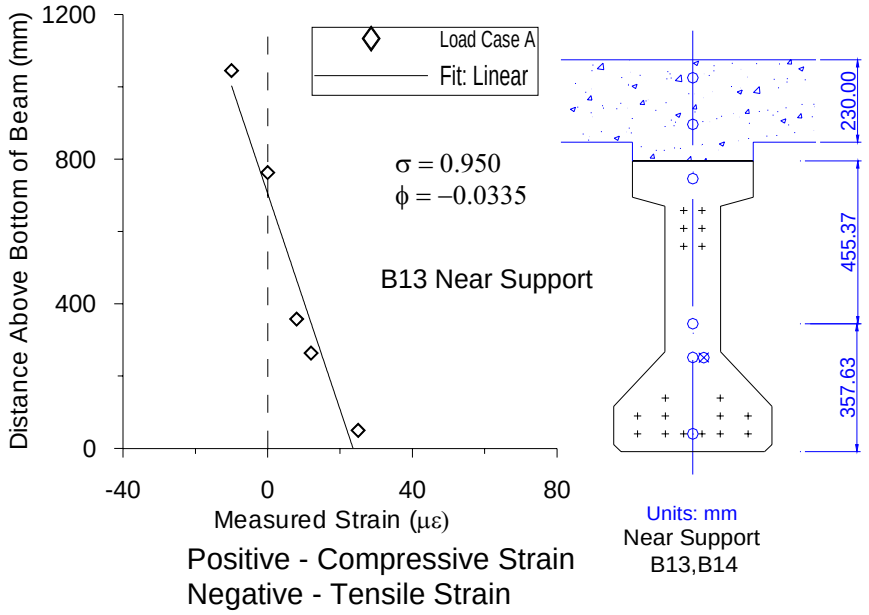

Figure 10.15. Strain Profile at Girder B13 Near-end Support Section - Load Case A

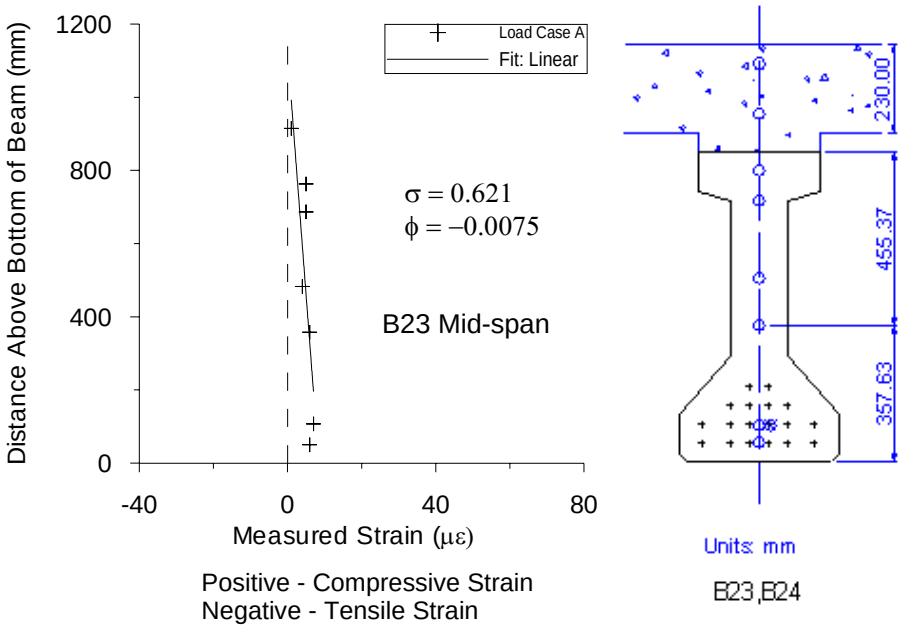

Figure 10.16. Strain Profile at Girder B23 Mid-span Section - Load Case A

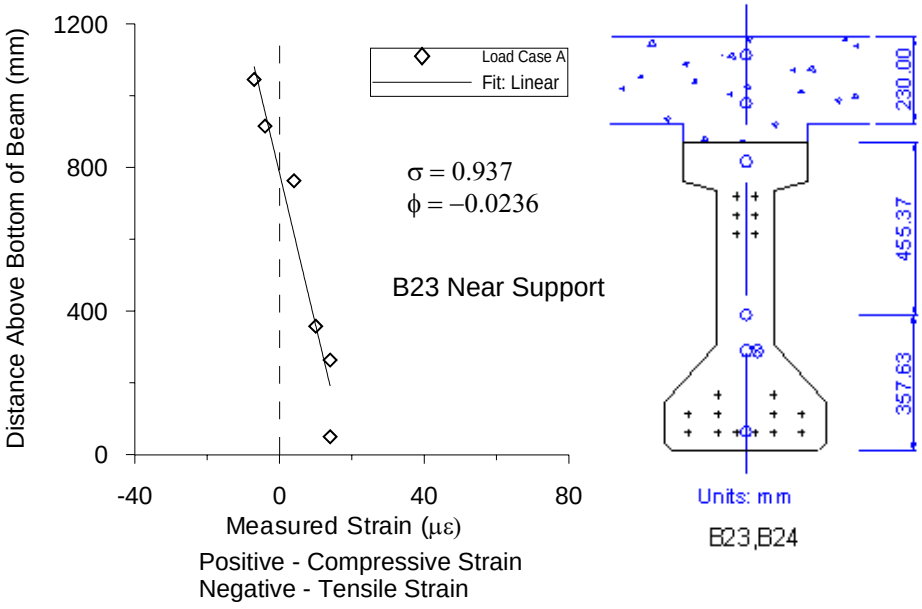

Figure 10.17. Strain Profile at Girder B23 Near-end Support Section - Load Case A

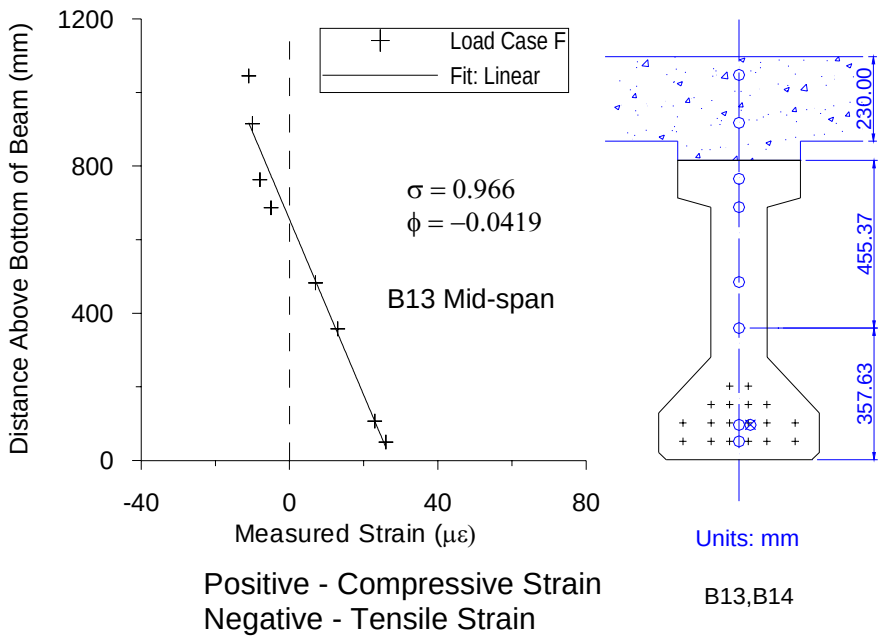

Figure 10.18. Strain Profile at Girder B13 Mid-span Section - Load Case F

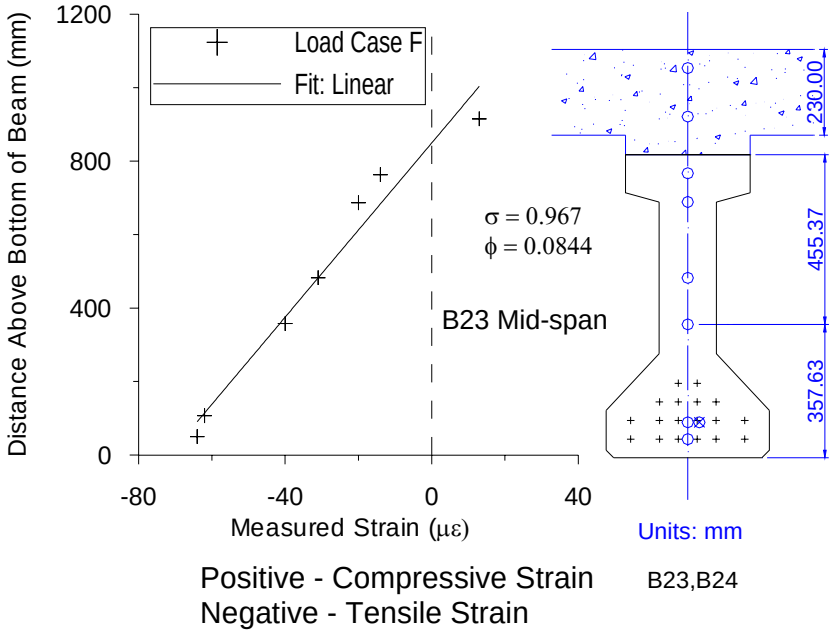

Figure 10.19. Strain Profile at Girder B23 Mid-span Section - Load Case F

From the strain profiles, it can be seen that the embedded strain gauges provided valid readings even when the maximum strain responses along the section were less than

10 με as shown in Figure 10.16. The strain profiles for much of the bridge cross-sections exhibited a very close linear relationship. The squared coefficients of determination are near 1.00 for fitting the load test results ranging from 0.92 to 0.97 as shown in Figures 10.17 through 10.19. The fitted straight lines also proved the girder theory assumption that plane sections remain plane for the composite section.

10.3.3. Load Distribution Factor. The live load distribution factors for design were attained from AASHTO 3.23.2 and 3.23.1 (AASHTO 1994) and AASHTO LRFD 4.6.2.2 (AASHTO 2002). For moment calculation with two lanes loaded, the recommended AASHTO distribution factor for exterior girders B11 and B14 is 1.614 and for interior girders B12 and B13 is 1.969. Both are controlled by fatigue of the girders due to live load and they are used for design of the girders. Applying AASHTO Table 3.23.3 to consider skew effects of the support, the reduction factor of 0.88 is found. This reduces the distribution factors to 1.420 for girders B11 / B14 and 1.735 for girders B12 / B13, respectively. Similarly using AASHTO LRFD, distribution factors were 0.73 and 0.61 for girder B13 / B12 considering two lanes loaded and one lane loaded, respectively. There is no specification on fatigue effect on load distribution factor in LRFD.

For each live load case in the load test, mid-span deflection of the four girders monitored in Span 1 was measured with LVDT's. To examine the distribution of load across the bridge, individual girder deflections were totaled, and then each individual girder response was divided by this total. The result is a fraction of the total bridge response that each individual composite girder carried. To avoid confusion with load distribution factor as defined in the AASHTO specification, a calculated term entitled load distribution coefficient is used to represent the fraction of the load that causes the

maximum response in any individual girder for that particular truck crossing. The responses used for calculation can be strain or deflection (Neely 2000). Based on deflection data, the load distribution coefficient for span one girders B11, B12, B13 and B14 can be obtained as listed in Table 10.4. Load case E and load case F are not listed because trucks were placed in the second span only for these two cases.

Table 10.4. Load Distribution Factor and Tested Load Distribution Coefficient

	AASHTO Load Distribution Factor			Load Distribution Coefficient			
Girder	AASHTO Standard Two Lanes Loaded	AASHTO LRFD Two Lanes Loaded	AASHTO LRFD One Lane Loaded	Load Case A 1 truck	Load Case B 1 truck	Load Case C 2 trucks	Load Case D 1 truck
B11	1.420	0.774	0.643	0.044	0.243	0.139	0.014
B12	1.735	0.731	0.608	0.194	0.572	0.462	0.152
B13	1.735	0.731	0.608	0.618	0.202	0.934	0.707
B14	1.420	0.774	0.643	0.144	-0.018	0.465	0.126

As illustrated in Table 10.4, the maximum load distribution coefficient is 0.934 for girder B13. Load distribution factors based on AASHTO LRFD were comparable to the tested distribution coefficients. Minor variation (less than 5%) was expected since the tests trucks were not located according to the designed lanes, but rather located to acquire the worst case factor for the specific girder studied. An additional factor also included the short span and large skew of the bridge. These account for why some coefficients were slightly higher than the calculated factors by AASHTO LRFD. Load distribution factors found based on AASHTO specification are substantially higher than the live load test result values obtained and illustrated in Table 10.4. Live load distribution factors specified by AASHTO (1996, 1998) design codes were about 2.4 times using AASHTO

LRFD. Therefore, AASHTO (1996, 1998) design codes are too conservative for the live load distribution factor calculation and subsequently the load rating in terms of strength limit requirements. This finding is consistent with other load test results on prestressed concrete bridges as reported by Cai et al. (2002). Based on the load test conducted herein, AASHTO LRFD provides more appropriate load distribution factors for design (less than 20% difference from measured values).

10.3.4. Continuity. One of the unique features of this HPC bridge is that it is designed with a continuity detail (see Figure 10.20) that was developed in the 1970's in Missouri for conventional normal strength prestressed / precast concrete bridges. The ends of the girders are cast integrally with the bent and cast-in-place deck. This load test provided the opportunity to investigate the behavior of this detail in conjunction with HPC and 15.2 mm (0.6 in.) diameter prestressing strands.

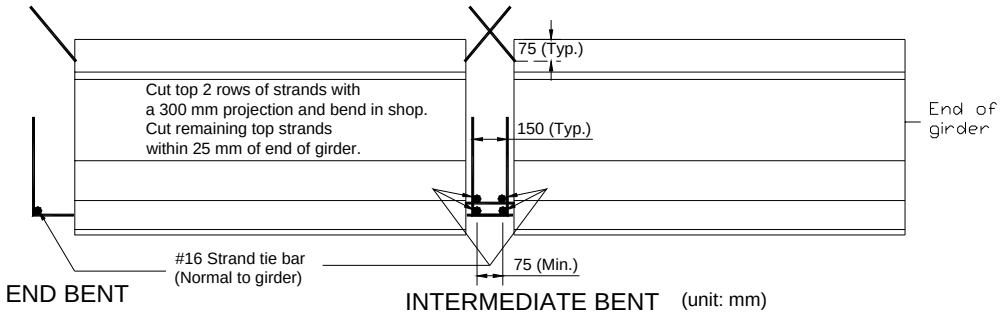

Figure 10.20. Intermediate Bent / End Bent Continuity Detailing

The girders were designed as simply supported members prior to casting the cast-in-place deck and bent continuity detail. After the girders and bent were cast integrally, they were designed as a continuous beam structure. From the data above, it may be noted that for each load case negative moment develops at the near-end support section. To

investigate the boundary condition, using ANSYS two finite element models were developed and analyzed, only considering girders B13, B23 and half of B33 using the composite section, applying load as live load multiplied by the load distribution coefficient measured in the tests. Measured material properties were used in the analysis as shown in Table 10.5. These models were used to compare the continuity level of the MoDOT interior bent detail to measured values. Since the test results were all available at each instrumented section for load case A, load case A was studied using finite element method (FEM). Two models were developed for comparison. The first model is a continuous beam model and the second is a model where the girder is fixed at the bent (beams fixed at bent model) as illustrated in Table 10.5. The FEM analysis results and test results are listed in Table 10.5. Deflections and slopes in the test results were obtained from LVDT and inclinometers while the moments were calculated from section curvatures presented in Table 10.3.

As illustrated in Table 10.5 and Figure 10.21, the moment at mid-span section of girder B13 due to live load is only 3% less than that of the fixed end model and is about 50% less than that of the continuous beam model. Use of the continuous beam approach for design would naturally yield less accurate results than using fixed end model by underestimating the interior bent negative moment by 9% and overestimating the mid-span positive moment by 100%. The fixity level of the interior bent is nearly fixed based upon the rotation and moment levels measured and predicted by the beam fixed at bent model. It therefore is advisable to consider the girder continuity as fully fixed. To simplify the design calculations, the fixed end model is conservative and acceptable for calculating both positive and negative moment in the loaded span for the continuity detail

used. For the conjunctive girder in the adjacent span (Span 2), a continuous beam model is conservative for design if Span 1 is the only span loaded; a continuous beam model will provide conservative design moments for the adjacent girders in Span 2.

Table 10.5. Test Results and FEM Results

	Continuous Beams (FEM)	Test Results	Beams Fixed at Bent (FEM)
Model	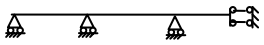	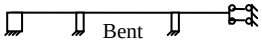	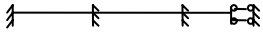
B13 mid-span deflection	1.694 mm	0.678 mm	0.539 mm
Slope at bent 2	0.0140°	0.004°	0°
Slope at ¼ point	0.0137°	0.007°	0.0057°
B13 mid-span moment	286.9 kN-m	143.26 kN-m	146.7 kN-m
B13 near support moment	-110.9 kN-m	-122.38 kN-m	-178.8 kN-m
B23 near support moment	-149.2 kN-m	-86.19 kN-m	0 kN-m
B23 mid-span moment	-69.0 kN-m	-27.45 kN-m	0 kN-m
Material Properties: Girders: f_c' = 80.3 MPa E_c = 47520 MPa Deck: f_c' =39.8 MPa E_c = 39989 MPa			

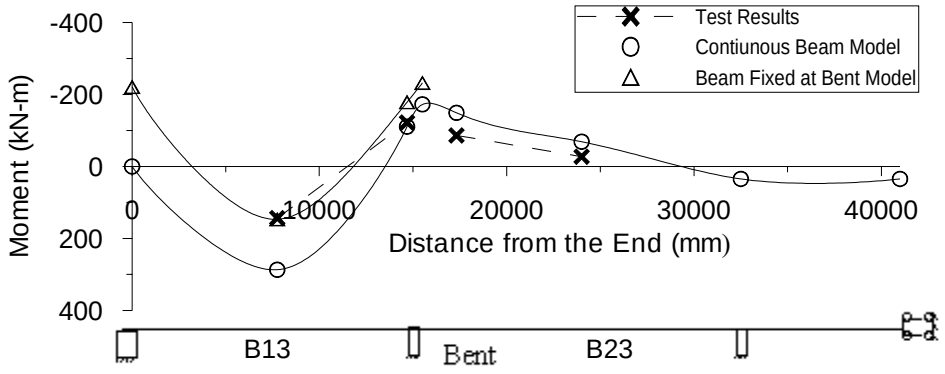

Figure 10.21. Moment Diagram for FEM Model and Test Results

It may be noted that at the time of load testing no deterioration or cracking was observed around the bent detail or within the deck system. Over time should cracking develop in this region due to temperature effects or overload, the observed field behavior of the bridge may deviate from fully fixed model due to softening in the bent region. However, the system should allow enough redistribution of moments to accommodate slight variations between the model assumption and field behavior. Cracking in the continuity region will be closely monitored; if it occurs, the influence of this effect will be studied as supplemental later-age load tests are conducted along with time-dependant effects.

10.4. CONCLUSIONS

As described herein, a static live load test was undertaken for a recently completed HPC bridge in Missouri. The following conclusions are drawn based on the test results observed and FEM's developed:

The load test results were found to correlate to analytic models, both in terms of deflection and strain data. The LVDT were very accurate [± 0.025 mm (± 0.001 in.)] and responded to minor variation in applied load single vehicular loading. Due to the small nature of the applied live load, high girder stiffness and short relative span lengths, deflection readings were small. Subsequently, surveying equipment used for deflection measurements was not viable.

From the strain profiles, it can be seen that the embedded strain gauges provided valid readings even when the maximum strain responses along the section were less than 10 με as shown in Figure 10.16. The strain profiles for much of the bridge cross-sections

exhibited a close linear relationship. The squared coefficients of determination were nearly 1.00 for fitting the load test results ranging from 0.92 to 0.97 as shown in Figures 10.17 through 10.19. The fitted straight lines also proved the girder theory assumption that plane sections remain plane for the composite section.

The tested actual bridge live load distribution coefficients were found to be comparable to the live load distribution factors calculated using the AASHTO LRFD specifications (2002). The AASHTO LRFD specification (2002) appears appropriate for HPC bridges is recommended instead. Live load distribution factors specified by AASHTO Standard Specification were about 2.4 times using AASHTO LRFD. Therefore, AASHTO Standard Specification is too conservative for the live load distribution factor calculation and subsequently the load rating in terms of strength limit requirements. Based on the load test conducted herein, AASHTO LRFD provides more appropriate load distribution factors (less than 20% difference from measured values) and thus is recommended for design.

The test and analysis results demonstrated that the MoDOT continuity detail at the interior bent can be considered as fixed based upon the rotation and moment levels measured and predicted by the beam fixed at bent model. It therefore is advisable to consider the girder continuity as fully fixed for these types of bridge systems. To simplify the design calculations, the fixed end model is conservative and acceptable for calculating negative moment in the loaded span for the continuity detail used. This assumes there would not be softening in the negative moment region of the bent detail due to cracking from temperature variations or overloads over time.

11. OPTIMIZED MODOT SECTIONS FOR HSC BRIDGE GIRDERS

11.1. INTRODUCTION

In the early applications of prestressed concrete, designers developed their own "best" girder cross section to use for different projects. This led to different girder shapes for different bridges and thus the girder formwork could not be reused. To improve economy of construction, girder shapes were standardized by the Prestressed Concrete Institute (PCI). In the 1950s, girder Types I through IV were developed followed by Types V and VI in the 1960s. Following the original adoption of the standard AASHTO-PCI shapes, individual states developed their own standard sections for efficiency and economy. In 1980, FHwA initiated an investigation to identify new optimized sections for major prestressed concrete girders.

Previous studies identified the advantages of utilizing high-strength concrete (HSC) in highway bridges (Rabbat and Russell 1982). Comparisons showed that by increasing the girder concrete compressive strength from 35 to 48 MPa (5000 to 7000 psi), the maximum span capability of AASHTO girders was increased by about 15%. In the project studied by Capenter (1980), it indicated that span capabilities of various girder cross sections could be increased through the utilization of higher strength concretes. For the same span length, the number of girders in a cross section could be reduced by up to 30% when utilizing a higher strength concrete (Gross, 1999). Figure 11.1 illustrated this point, Texas Department of Transportation (TxDOT) reduced the number of girders from 7 using conventional concrete to 4 using HSC over a given span length. It was found, however, that at very high concrete strength levels, the maximum available prestressing force limited the advantages of high-strength concrete.

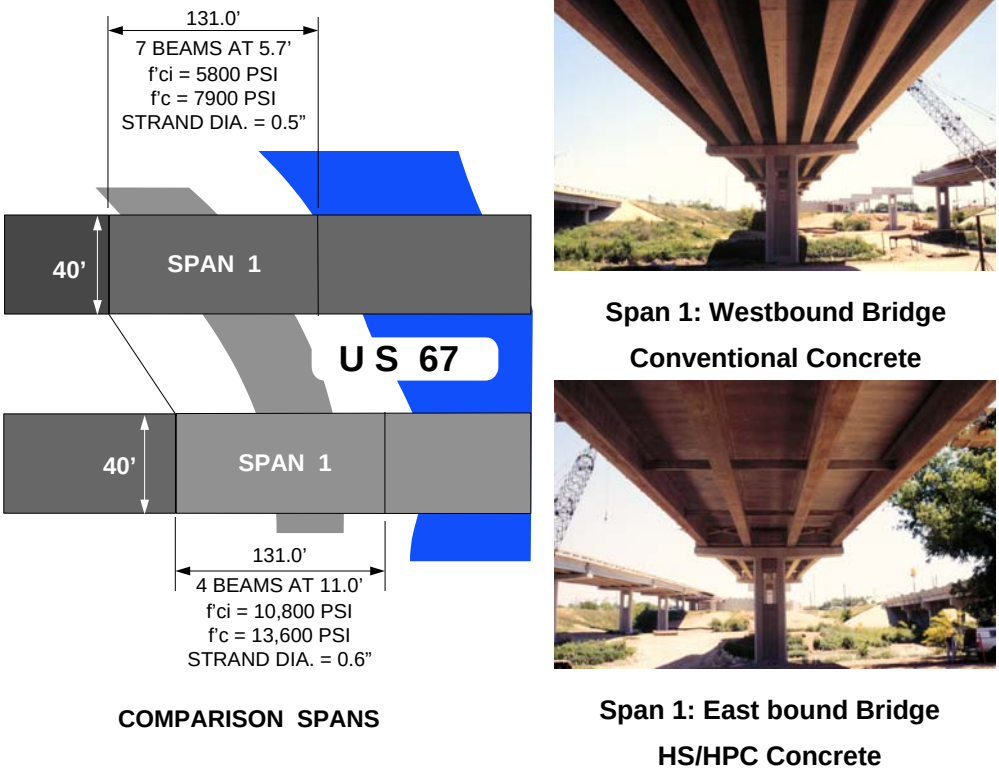

Figure 11.1. North Concho River US 87 & S.O. RR Overpass Comparison Spans of HS/HPC Girders and Conventional Strength Girders (Myers and Yang 2001)

The use of high-strength concrete in long span, simply supported, precast, prestressed, concrete girders was investigated in a series of parametric studies by Zia et al. (1989). It indicated that longer span lengths can be achieved with higher strength concretes. However, when the compressive strength was increased beyond a certain strength level which was 69 MPa (10,000 psi) found by Zia et al. (1989), there was little or no benefit to be gained for current section shapes. It is also found that smaller sections utilizing higher-strength concrete could be used in place of larger sections with lower-strength concretes. A girder spacing of 2.4 m (8 ft) was the most cost-effective design for about 60% of the span range of a given girder section in the cost analysis study. For the longest span length, a 1.8 m (6 ft) spacing was the most cost-effective.

The feasibility of using high-strength concrete in prestressed concrete girders was evaluated by Bruce et al. (1994). The investigation concluded that structural members utilizing concrete with a compressive strength up to 69 MPa (10,000 psi) can be designed conservatively using the AASHTO Standard Specifications (1989).

In the study conducted by Construction Technology Laboratories (CTL) in 1997 (Russell et al. 1997), it was reported that the use of existing girder cross sections with concrete compressive strengths up to 69 MPa (10,000 psi) allow longer span lengths and more economical structures. To effectively utilize higher strength concretes, additional prestressing force which can be calculated for specific cases must be applied to the cross section.

In this study, some cross sections were identified as having a high degree of structural efficiency and also being cost-effective. These sections were reported as follows: CTL Bulb-Tee, PCI Bulb-Tee, Florida Bulb-Tee, AASHTO Section Type VI, Washington Series, Texas Box U54, and Nebraska Sections. Cross-sectional dimensions of these girders are illustrated in Figure 11.2.

As a conclusion in the CTL study, the Bulb-Tee was recommended to be considered as a national standard for span lengths from 24 to 61 m (80 to 200 ft). However, the Washington and Colorado sections are equivalent up to span lengths of 37 m (120 ft), and the Florida and University of Nebraska sections are slightly more economical for span lengths greater than 46 m (150 ft).

AASHTO girder Type II, III, and IV are shown in Figure 11.3 for comparison with MoDOT girder sections. Cost effectiveness will also be studied for AASHTO girder sections using high-strength concrte.

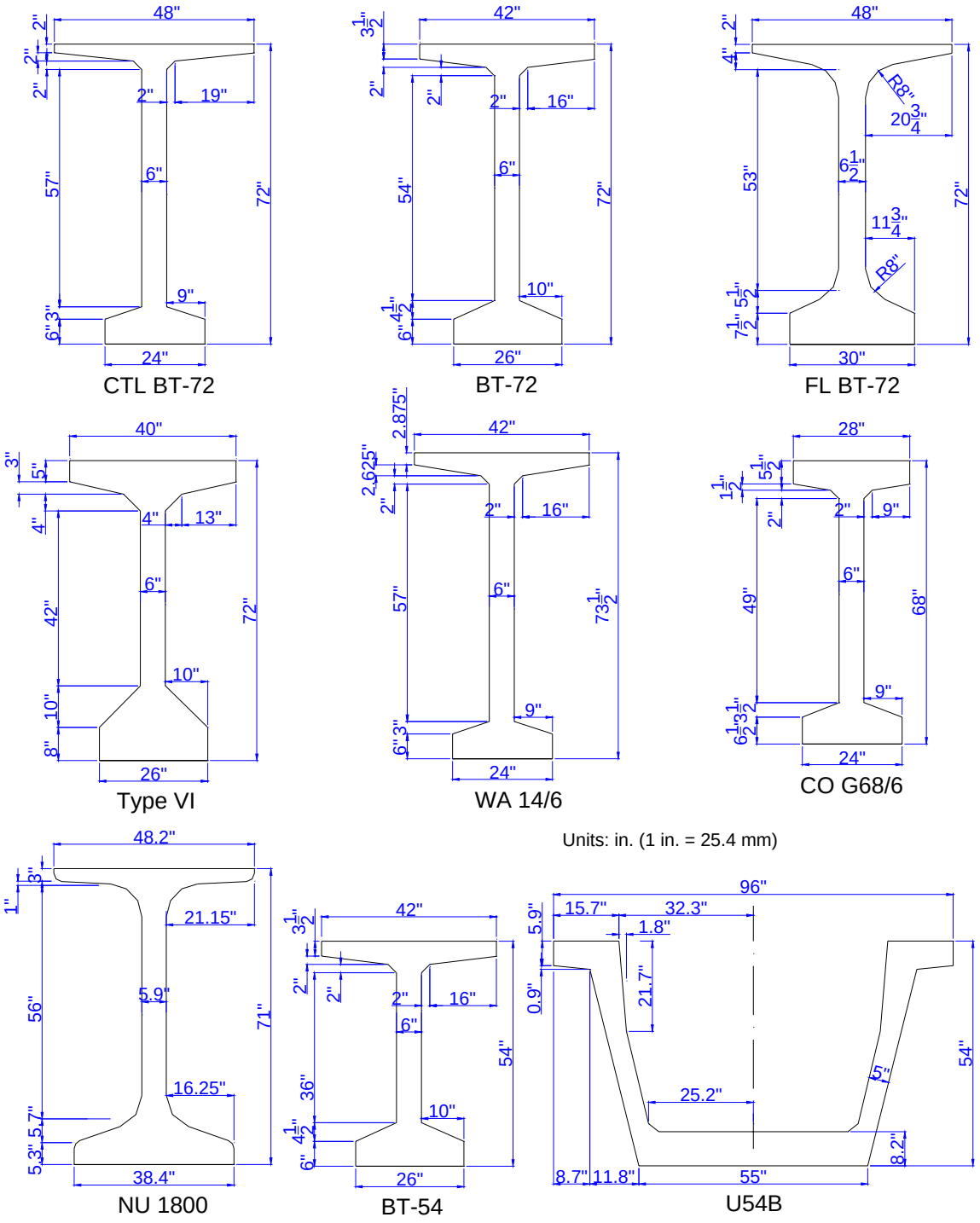

Figure 11.2. Cost-effective Cross Section in CTL Study

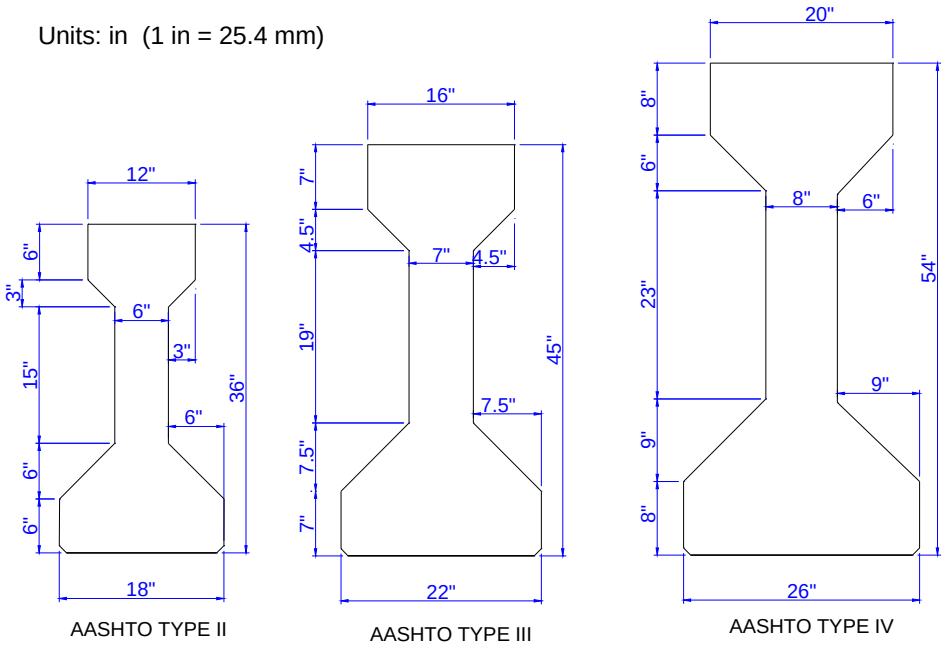

Figure 11.3. AASHTO Cross Sections for Prestressed Concrete Girders

MoDOT has several standard shapes including Type 2, Type 3, Type 4, Type 6 and Type 7. The dimensions of these sections are shown in Figure 11.4. It may be observed that MoDOT Section Type 7 is very close to PCI Section BT-72 in terms of geometry poperties while MoDOT Section Type 6 is close to PCI Section BT-54 and AASHTO Section Type IV. The CTL study concluded that the PCI Section BT-72 was the most cost-effective cross-section for span lengths up to 45.7 m (150 ft) at all concrete compressive strengths. In this study, MoDOT Section Type 7 will be compared with PCI Section BT-72. In addition MoDOT Section Type 6 will be studied along with PCI Section BT-54.

The objectives for this optimization study were as follows:

- Identify the limitations of existing MoDOT girder cross sections relative to the use of high-strength concrete in simple span structures.

- Define existing factors that serve to limit the applications of high-strength concrete in bridge girders.
- Examine the feasibility of modified cross sections that can be used to take advantage of the higher strength concrete that are currently available.

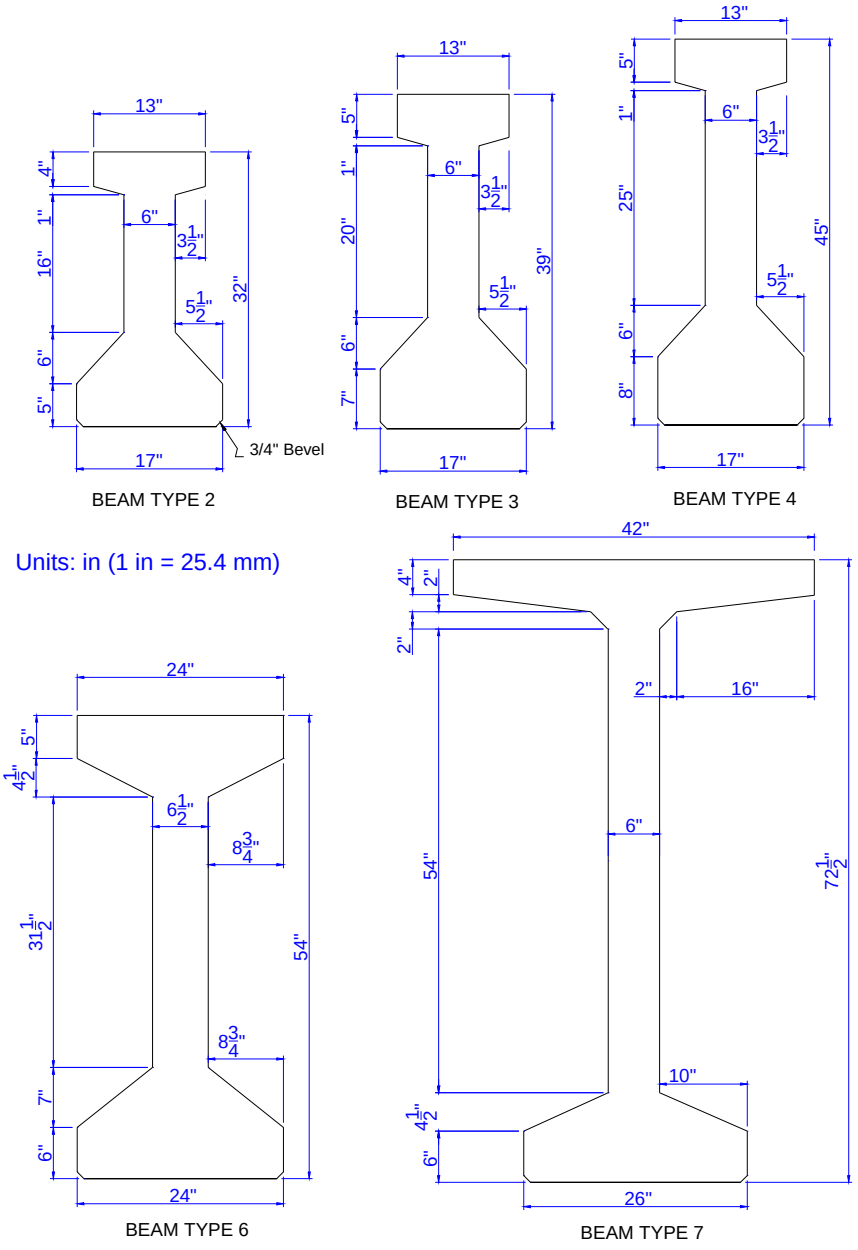

Figure 11.4. MoDOT Sections for Prestressed Concrete I-Girders

11.2. PROGRAM FOR OPTIMIZATION

Based on the computer program BRIDGE developed for the “FHwA Optimization Study”(Russell et al. 1997), a Visual Basic program named PCBRIDGE was developed by the author. The required input of the program consists of girder span, spacing and cross section, concrete and strand characteristics, and relative cost of materials. The program determines deck thickness and deck reinforcement, required number of prestressing strands, and a cost index per unit surface area of bridge deck. The program also provides section properties, moments, stress levels, and deflections. Some operation windows of the program PCBRIDGE are shown in Figure 11.5.

The following parameters were considered in the PCBRIDGE program:

- Girder spacing. No maximum spacing was placed on the girders. Minimum spacing considered was that which corresponded to the flanges of the two girders touching each other.
- Span Lengh. Spans in excess of 24.4 m (80 ft) were considered.
- Deck thickness. Deck thickness varied with girder spacing according to a predetermined design.
- Concrete strength. Concrete strength of the girders at 28 days was varied from 41 MPa (6000 psi) upward in increments of 14 MPa (2000 psi) with no upper limit. Release strength was taken as 75% of the 28-day strength.

For the purposes of making the cost comparisons for different sections, the relative unit costs for in-place materials were taken as reported for “FHwA Optimization Study” (Russell et al. 1997):

Concrete (girder and deck)	1 unit/unit of weight of concrete

Strands	8 unit/unit of weight of concrete
Reinforcing Steel	9 unit/unit of weight of concrete
Epoxy-Coated Reinforcing Steel	12 unit/unit of weight of concrete

The following default assumptions were made in the PCBRIDGE program:

- Design conforms to AASHTO Specifications. Live load consists of HS 20-44 loading. Girders are simply supported. Design is based on a typical interior girder. Concrete deck is CIP and acts compositely with the girder. Deck formwork is supported on the girder. The transformed area of strands was neglected.
- Concrete compressive strength of the deck is constant and equal to 28 MPa (4000 psi) at 28 days. If the compressive strength of the concrete in the deck limited the design, the strength was increased. Strands are Grade 270 with a 12.7 mm (0.5 in.) diameter and have an idealized trilinear stress-strain curve. Strands are spaced at 51 mm (2 in.) centers with a minimum 51 mm (2 in.) concrete surface to center of the strand spacing.
- Total prestress losses equal 310 MPa (45,000 psi). However, it is possible that with higher strength concrete, the prestress losses may be lower. This would have beneficial effect in reducing the number of strands (Russell et al. 1997).
- Relative unit costs of materials and labor are constant for each cost analysis. The effect of increased costs for higher strength materials is investigated in a separate phase of the project. Cost analysis comparisons are for the precast girder and the CIP deck only. Costs of substructure and approach fills are not considered.
- Design is based on flexural strength at mid-span. It is assumed that the compressive and tensile stresses that would develop at the ends of the girders if all

strands were straight can be handled by the draping of strands, by additional top strands at the ends of the girders or debonding some strands at the ends of the girders. Selected girder designs were checked for shear and found to have adequate strength based on existing design requirements.

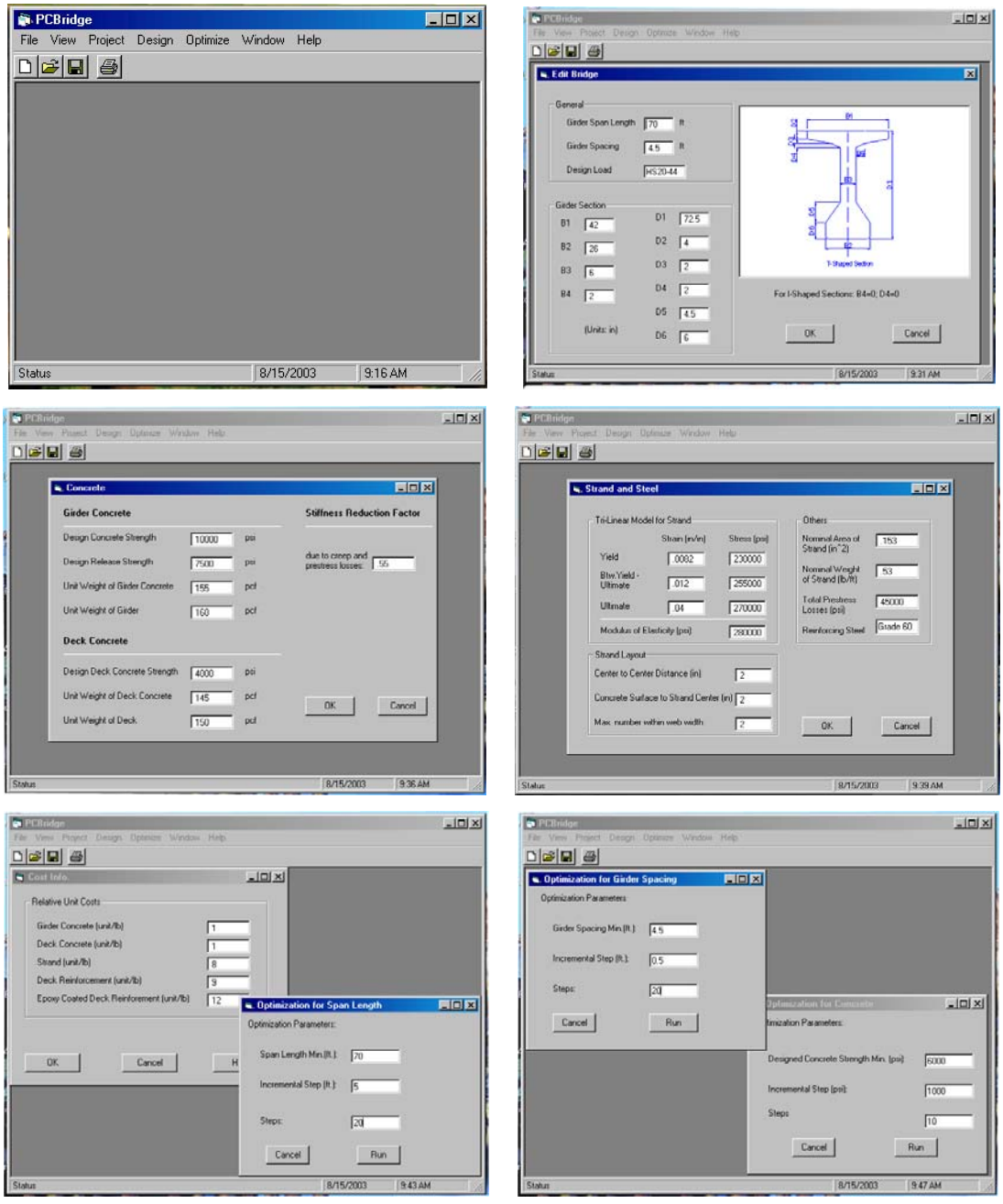

Figure 11.5. Operation Windows for Program PCBRIDGE

11.3. ANALYSIS OF EXISTING CROSS SECTIONS

11.3.1. Cross Section Efficiency Factors and Ratios. Based on minimizing the area of the section for a given section modulus, an efficiency factor for prestressed sections has been developed by Guyon (1953). This efficiency factor ρ is defined as:

$$\rho = \frac{r^2}{y_t \cdot y_b} \qquad \text{Equation 11.1}$$

where

r = radius of gyration of section

y_t, y_b = distance from center of gravity to top and bottom fibers, respectively

The efficiency factors for the various sections shown in Figure 11.2, AASHTO Section Type II through VI, and MoDOT sections are plotted in Figure 11.6 with respect to depth of section.

An efficiency ratio for I-sections was used to study the section efficiency (Russell et al. 1997). The efficiency ratio α is defined as:

$$\alpha = \frac{3.46 \cdot S_b}{A \cdot h} \qquad \text{Equation 11.2}$$

where

S_b = section modulus for bottom fibers

A = cross-sectional area

h = depth of section

The efficiency ratios for the various sections shown in Figure 11.2, AASHTO Section Type II through VI, and MoDOT sections are plotted in Figure 11.7 with respect to depth of section.

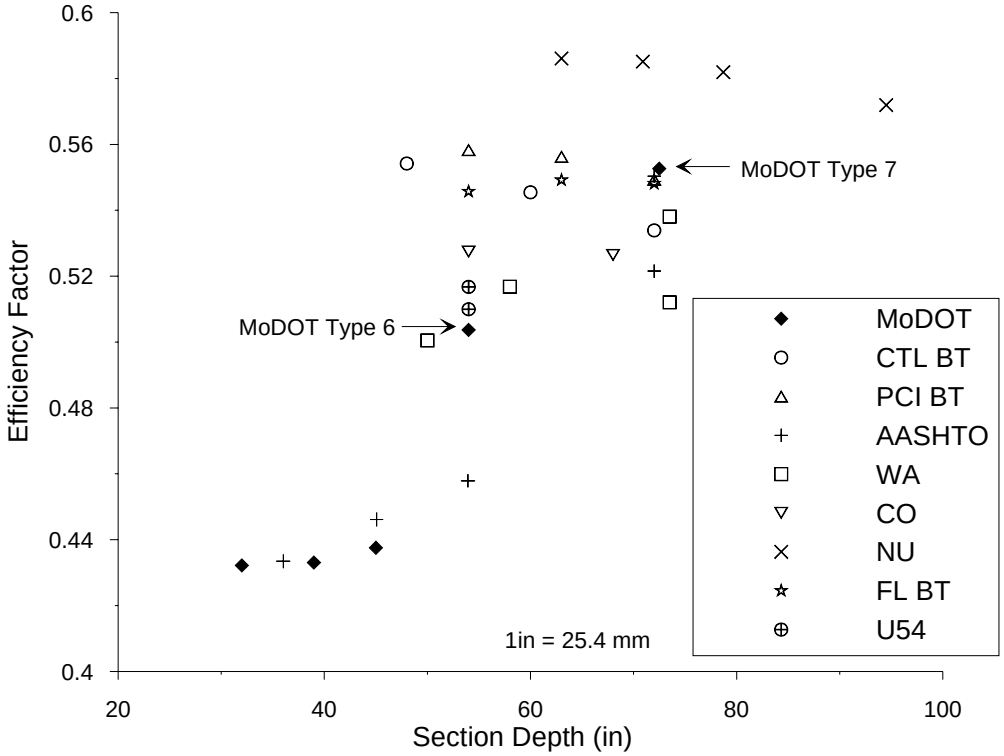

Figure 11.6. Cross Section Efficiency Factors

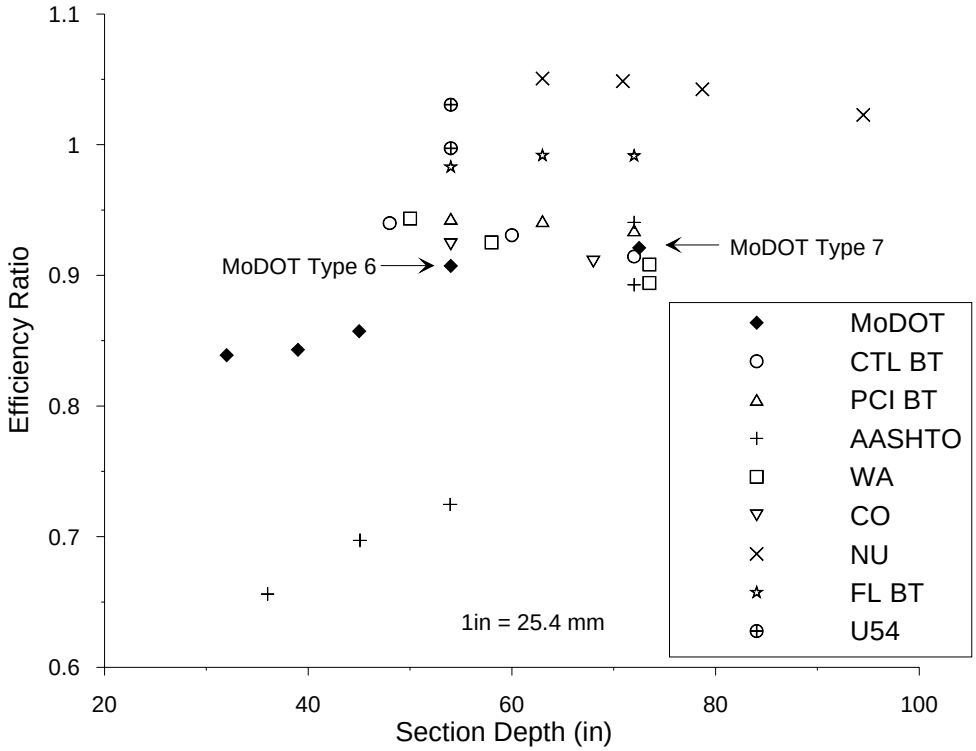

Figure 11.7. Cross Section Efficiency Ratios

From Figures 11.6 and 11.7, efficiency factor and ratio for MoDOT Section Type 7 are found to be very close to those of PCI Section BT-72. Meanwhile, the efficiency factor for MoDOT Section Type 6 is much lower than that of PCI Section BT-54. But the efficiency ratio for MoDOT Section Type 6 is lower than that of PCI Section BT-54. MoDOT Section Type 2 through Type 4 has much higher efficiency ratios than AASHTO Section Type II through Type IV.

11.3.2. Optimum Cost Index Charts. Using computer program PCBRIDGE, a cost-efficiency analysis of various cross sections can be performed. As shown in Figure 11.8, the cost index per unit surface area of the bridge deck can be plotted versus span length for a given cross section. At various girder spacings, different cost curves result as shown by the solid lines in Figure 11.8.

If the end points of each individual cost curve are joined, an optimum cost curve can be obtained as shown by the dashed line in Figure 11.8. This optimum cost curve indicates the least cost index for a particular span and varies as a function of girder spacing. It may be observed that for a given span, cost index per square foot of bridge deck decreases as girder spacing increases.

The cost chart in Figure 11.8 is for a bridge utilizing PCI Section BT-72 with 28-day girder concrete strength of 69 MPa (10,000 psi). At other girder concrete strengths, additional optimum cost curves can be computed using program PCBRIDGE by changing concrete strength parameters only. Figure 11.9 is a plot of the optimum cost curves for a MoDOT Section Type 7 at 41, 55, 69, 83, and 96 MPa (6000, 8000, 10000, 12000, and 14000 psi).

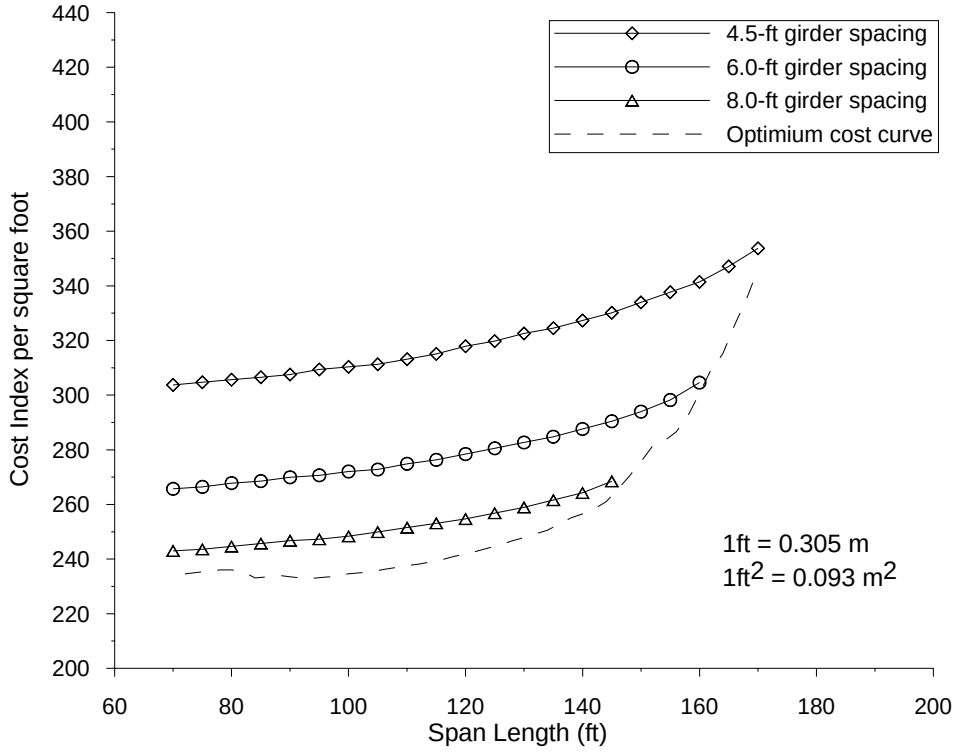

Figure 11.8. Cost Chart for a PCI Section BT-72 at 10,000 psi (69 MPa)

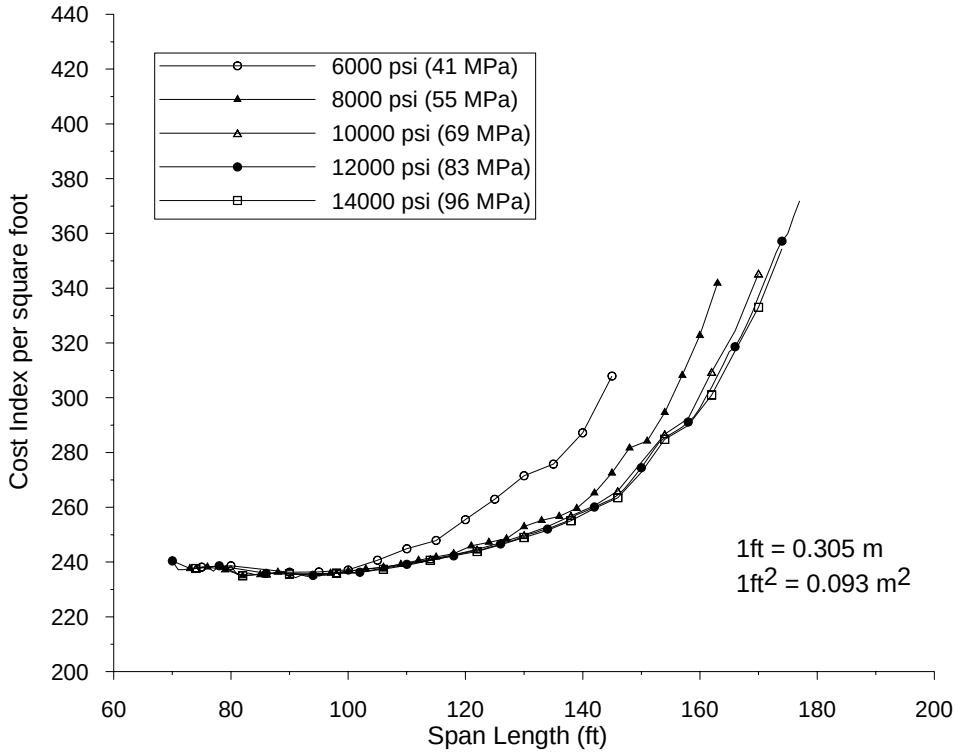

Figure 11.9. Cost Chart for a MoDOT Section Type 7

Although Figure 11.9 represents one particular cross section, MoDOT Section Type 7, the results and relationships are consistent with other sections. It illustrates the benefits and limitations of high-strength concrete for existing cross section of precast, prestressed bridge girders.

For spans less than 27.4 m (90 ft), the cost index per square foot of bridge deck remains constant for different concrete compressive strengths. For these spans, the higher concrete strength would allow for more prestressing and therefore, greater girder spacing and reduction in the cost index. However, the controlling condition for these spans is initial prestress transfer. For a given span, there is a point where additional prestressing will cause tension in the top fibers regardless of the concrete strength. The dead load at prestress transfer is constant for a given span and cross section, and independent of the final in-place girder spacing. As a result, no benefit is realized by using concrete compressive strengths greater than 41 MPa (6000 psi) at these span lengths.

For spans exceeding 30.5 m (100 ft) when concrete strengths are less than 55 MPa (8000 psi), and spans exceeding 33.5 m (110 ft) when concrete strengths exceed 55 MPa (8000 psi), the higher strength concrete allows larger prestressing and, as a result, greater girder spacings for a given span, thus reducing unit cost.

A cost chart for MoDOT Section Type 7 also shows that cost benefits vary as a function of span length and girder concrete strength. For example, a 55 MPa (8000 psi) girder has a 2% lower cost index than a corresponding 41 MPa (6000 psi) girder at a span length of 33.5 (110 ft), but a 9% lower unit cost at a span length of 42.7 m (140 ft). These cost benefits continue to increase as the span length increases, reaching a maximum of 16% at a span length of 45.4 m (149 ft). At this point, the lower strength girder has

reached its maximum span length, while the higher strength girders still has additional capacity. In other words, another benefit of high-strength concrete is the ability to achieve great span lengths.

11.3.3. Span Length. The effect of concrete strength on the maximum span capacity is shown in Figures 11.10 and 11.11 for MoDOT sections (Type 2, Type 3, Type 4, Type 6, Type 7). For AASHTO sections (Type II, Type III, Type IV, Type VI), the effect is shown in Figure 11.12 and Figure 11.13.

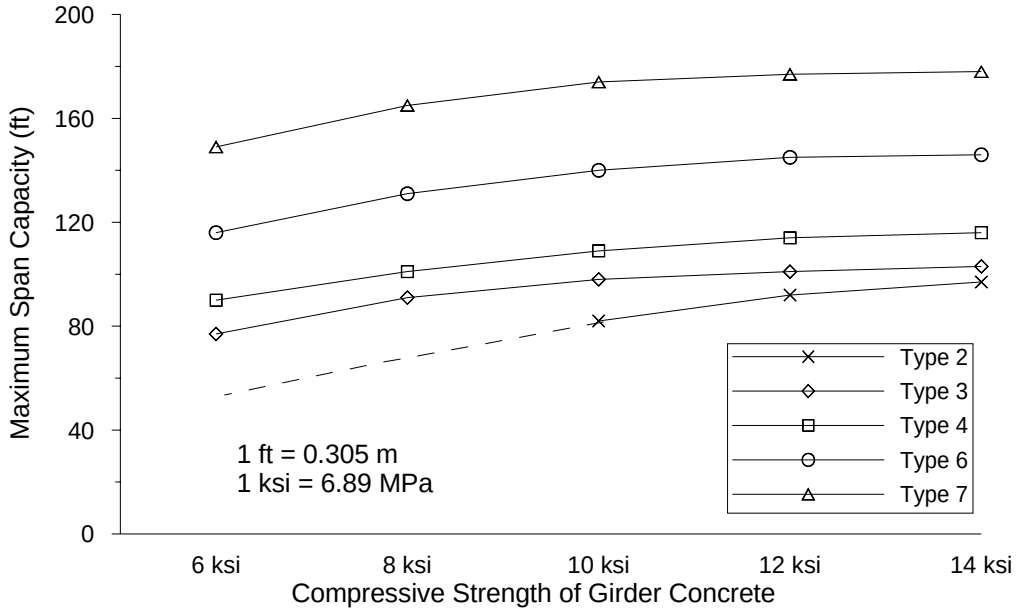

Figure 11.10. Maximum Span Capacity of MoDOT Sections

With the increase of concrete strength, the maximum span capacity is increased for various cross sections. From 41 MPa (6000 psi) to 96 MPa (14,000 psi), maximum span capacity is increased by 33% for MoDOT Section Type 3, and 19% for MoDOT Section Type 7. The increase decreases with the increasing of the concrete strength and ultimately flattening out at a concrete strength of 83 MPa (12,000 psi). The maximum

available prestressing force limits the advantages of high-strength concrete. Because the program can only analyze bridges with a span length higher than 21.3 m (70 ft), MoDOT Section Type 2 using concrete strength at 41 MPa (6000 psi) and 55 MPa (8000 psi) can not be designed using the program. From the trend of the curve, it may be observed that span capacity of MoDOT Section Type 2 using concrete strength at 41 MPa (6000 psi) and 55 MPa (8000 psi) is smaller than 21.3 m (70 ft).

For MoDOT Sections, Type 2, Type 3 and Type 4 can be used for span length less than 36.6 m (120 ft) while Type 6 and Type 7 are most appropriate for span length from 36.6 m (120 ft) to 54.9 m (180 ft).

As shown in Figure 11.11 and Figure 11.13, the increasing of maximum span capacity for smaller sections is greater than deeper sections. The increasing of maximum span capacity decreases for each succeeding 14 MPa (2000 psi) increase in girder compressive strength.

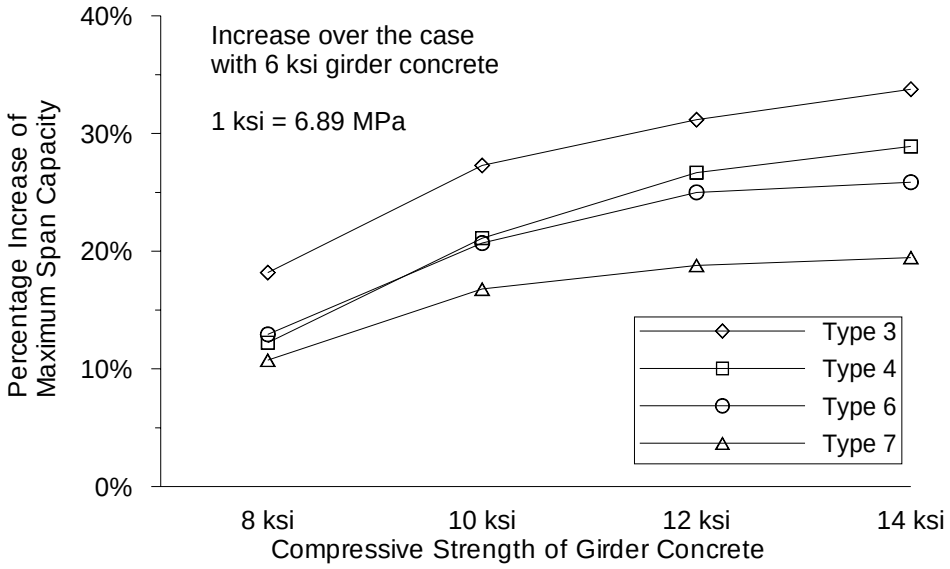

Figure 11.11. Maximum Span Capacity Increasing of MoDOT Sections

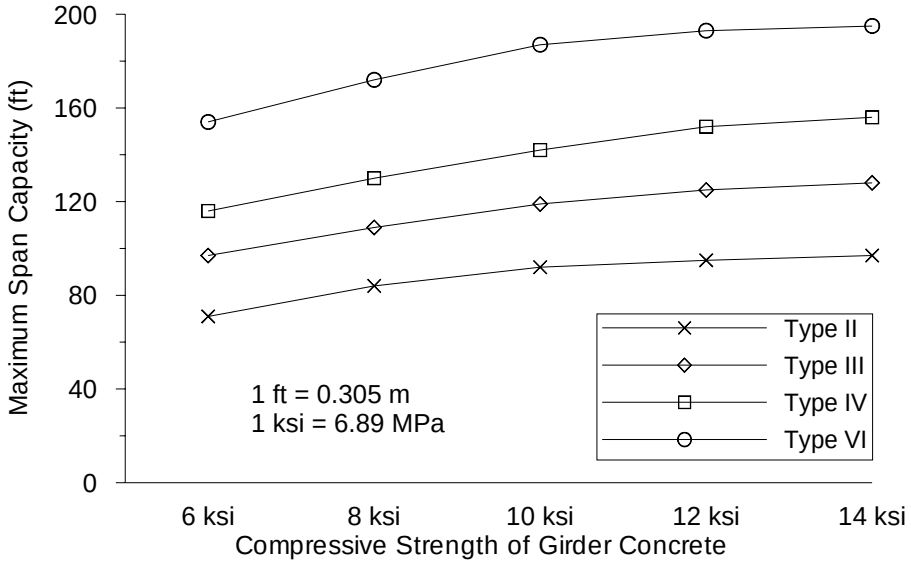

Figure 11.12. Maximum Span Capacity of AASHTO Sections

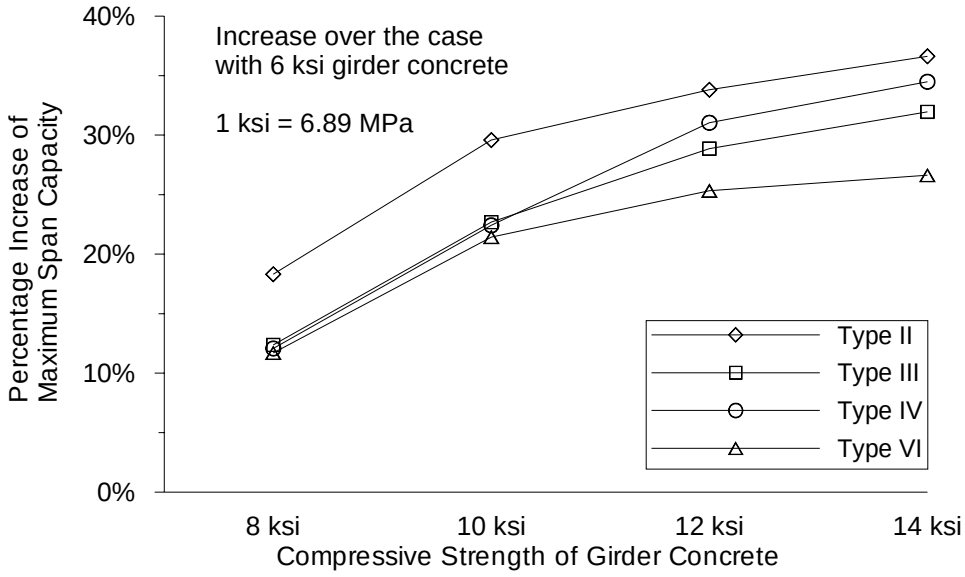

Figure 11.13. Maximum Span Capacity Increasing of AASHTO Sections

The primary cause of these diminishing returns is the decreasing strand eccentricity. The increasing of girder compressive strengths will lead to inefficient strand layouts. Once strands are placed within the web, the efficiency of a section begins to decrease rapidly.

A secondary cause for the diminishing returns is the deck concrete compressive strength. In calculating the composite section properties and service load stresses, the PCBRIDGE program employs a transformed section. As girder strength increases and deck strength remains constant, the composite section properties decrease, with a corresponding increase in service load stresses for the same span and girder spacing.

From Figure 11.14, it may be observed that for MoDOT Section Type 6, girder spacing for effective design is 1.2 m (4 ft) to 3.1 m (10 ft). The most effective design girder spacing is 1.8 m (6 ft) to 2.4 m (8 ft).

For MoDOT Section Type 7 as shown in Figure 11.15, when the span length is less than 39.6 m (130 ft), girder spacing from 2.4 m (8 ft) to 3.1 m (10 ft) is the most effective design. When span length is greater than 39.6 m (130 ft), girder spacing 1.8 m (6 ft) to 2.4 m (8 ft) is the most effective design. For same span length, higher concrete strength can reduce the girder number with larger girder spacing.

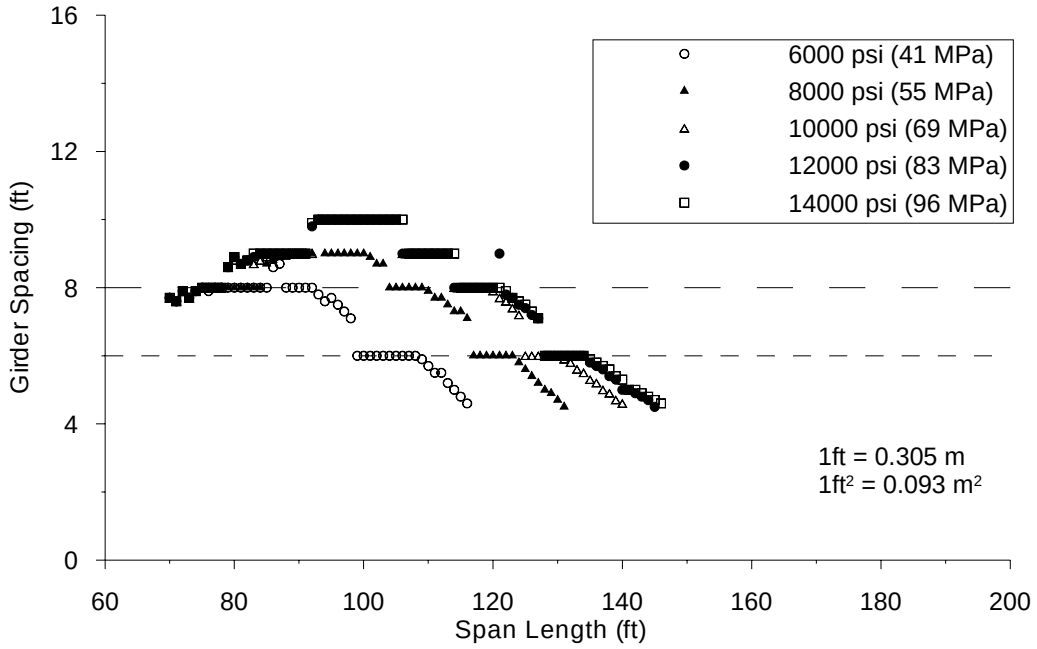

Figure 11.14. Girder Spacing for MoDOT Section Type 6

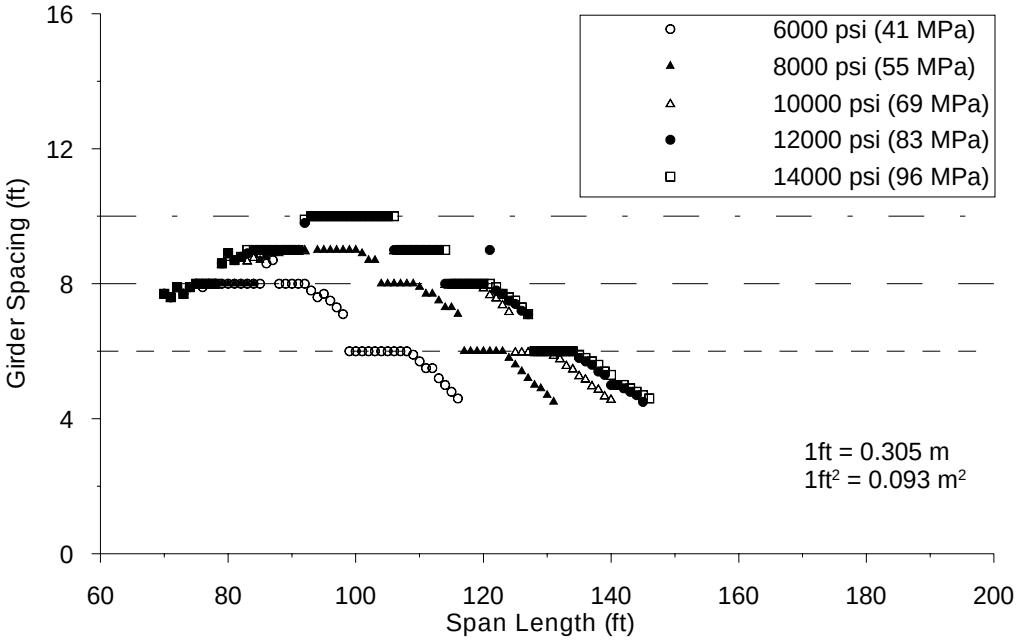

Figure 11.15. Girder Spacing for MoDOT Section Type 7

11.3.4. Comparison of Cross Sections. In this Section, various specific cross sections will be compared to identify which characteristics of existing girder cross sections are more important when using of high-strength concrete. Cost charts for the sections analyzed are included in Appendix H.

11.3.4.1 MoDOT Type 6 and Type 7. The following curing conditions were investigated for the precast concrete. Figure 11.16 shows the optimum cost curves of MoDOT Section Type 6 at various concrete strengths. Compared with Figure 11.9, the behavior of MoDOT Section Type 6 is similar with that of a MoDOT Section Type 7.

It may be noted that shallower sections with higher strength concretes can be used in place of deeper sections with lower strength concretes. In Figure 11.16, optimum cost curve for a MoDOT Section Type 7 of 41 MPa (6000 psi) concrete is included. Up to a span length of 27.4 m (90 ft), a MoDOT Section Type 6 with 41 MPa (6000 psi) is cost effective replacement over a MoDOT Section Type 7 with 41 MPa (6000 psi). For a span

length greater than 27.4 m (90 ft) but less than 33.5 m (110 ft), a MoDOT Section Type 6 with 55 MPa (8000 psi) is a cost effective replacement over a MoDOT Section Type 7 with 41 MPa (6000 psi). For a span length greater than 33.5 m (110 ft) but less than 39.6 m (130 ft), MoDOT Section Type 6 with 69 MPa (10,000 psi) can be used in place of MoDOT Section Type 7 with 41 MPa (6000 psi). This concept is useful for replacement of existing bridges.

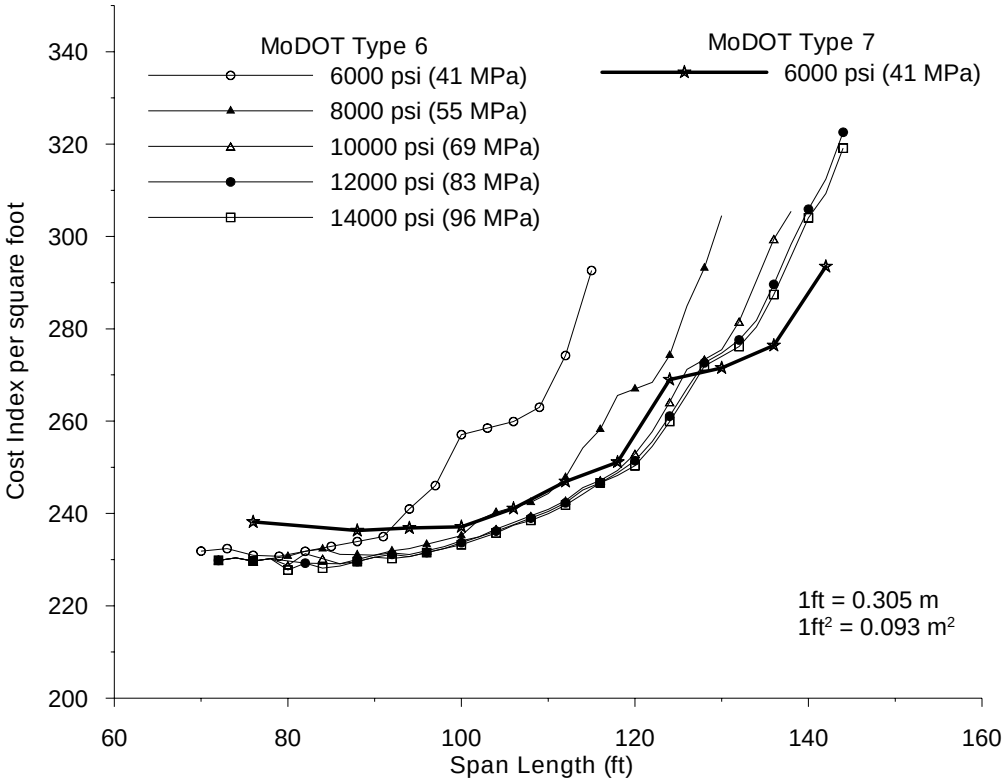

Figure 11.16. Comparison of MoDOT Section Type 6 and Type 7

11.3.4.2 MoDOT Type 6, Type 7 and PCI BT-54, BT-72. The PCI Bulb-Tee Section BT-72 is recommended as the basis for cost comparison by Russell et al. (1997). The PCI Bulb-Tee shapes are the accepted national standard and Section BT-72 exhibits cost-effectiveness for spans from 24.4 to 45.7 m (80 to 150 ft).

As shown in Figure 11.17, MoDOT Section Type 6 exhibits greater cost-effectiveness than a PCI Section BT-54. When the concrete strength is less than 55 MPa (8000 psi), the different is as small as 4%. The difference increases with the increase in concrete strength. This may be attributed to the larger top flange of Section BT-54 compared to that of MoDOT Section Type 6. The bottom flanges of the two sections are very similar with a difference of 2% in area. It also shows that smaller top flanges with high-strength concrete can be used in place larger top flanges when using higher strength concretes.

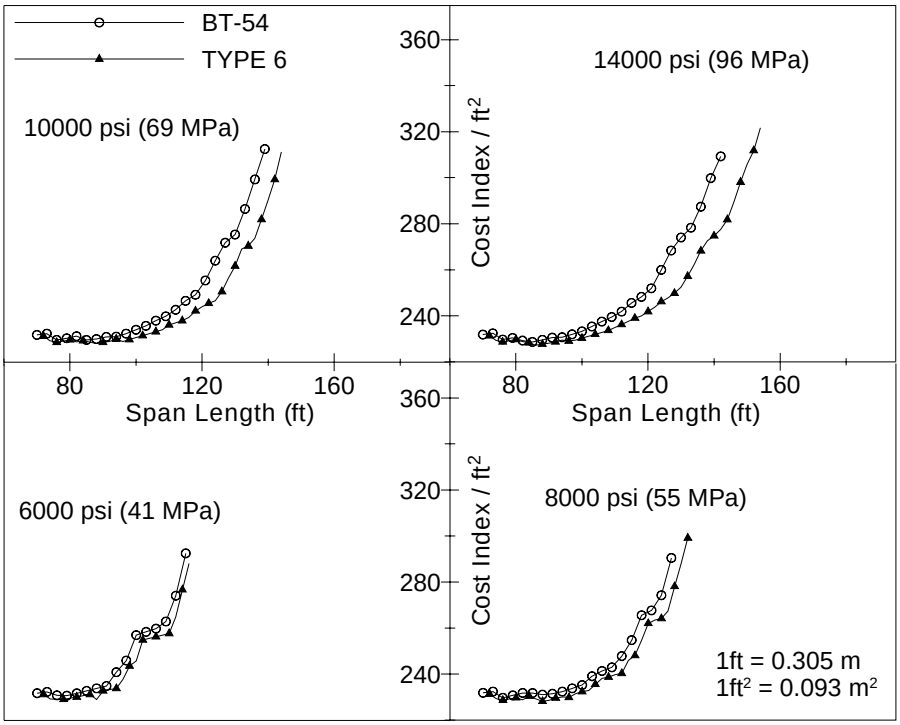

Figure 11.17. Comparison of MoDOT Section Type 6 and PCI Section BT-54

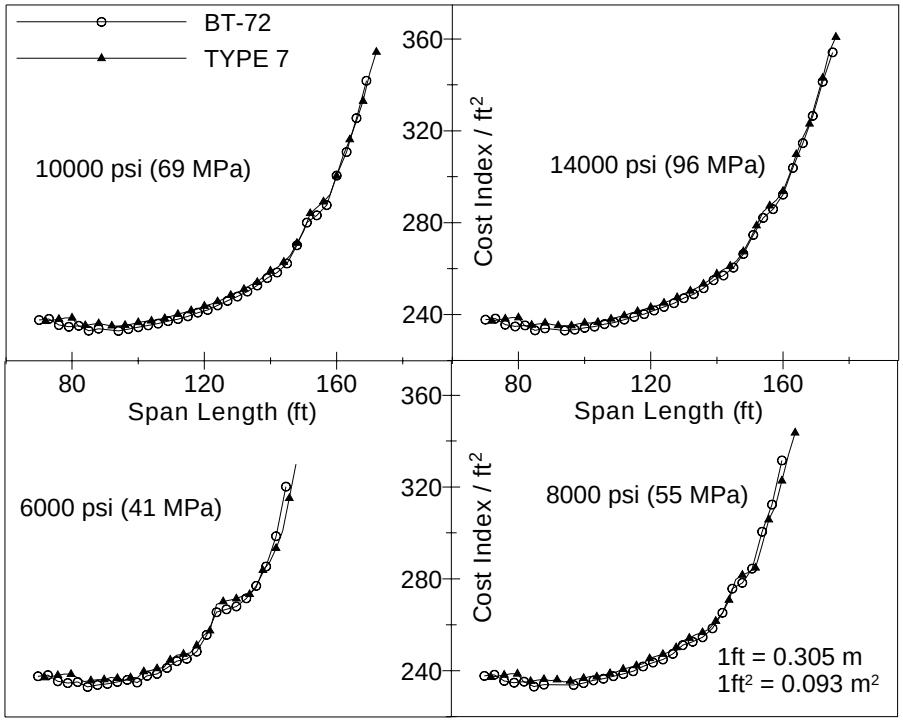

Figure 11.18. Comparison of MoDOT Section Type 7 and PCI Section BT-72

It may be observed that a MoDOT Section Type 7 has almost no difference compared to PCI Section BT-72 in terms of cost effectiveness (see Figure 11.18). From "FHwA Optimization Study" (Russell et al. 1997) PCI Section BT-72 was concluded as the most cost effective cross section for span lengths up to 45.7 m (150 ft) at all concrete strengths compared to other similar sections. Therefore, the MoDOT Section Type 7 may also be categorized as the most cost effective cross section for span lengths up to 45.7 m (150 ft) at all concrete strength levels.

11.3.4.3 MoDOT sections and AASHTO sections. Smaller depth sections are not discussed in "FHwA Optimization Study" (Russell et al. 1997). In Figure 11.19, MoDOT Section Type 3, Type 4, AASHTO Section Type II and Type III are compared in this Section.

The MoDOT Section Type 4 is more cost effective than the AASHTO Section Type III even though they have same depth of 1143 mm (45 in.). The reason is that AASHTO Section Type III has a wider web which can still only accommodate 2 strands per row. At the same time, the bottom flange of the MoDOT Section Type 4 can accommodate one additional row of strands compared to the AASHTO Section Type III. Compared to MoDOT Section Type 4, however, AASHTO Section Type III has a larger maximum span capacity due to its wider flange and web.

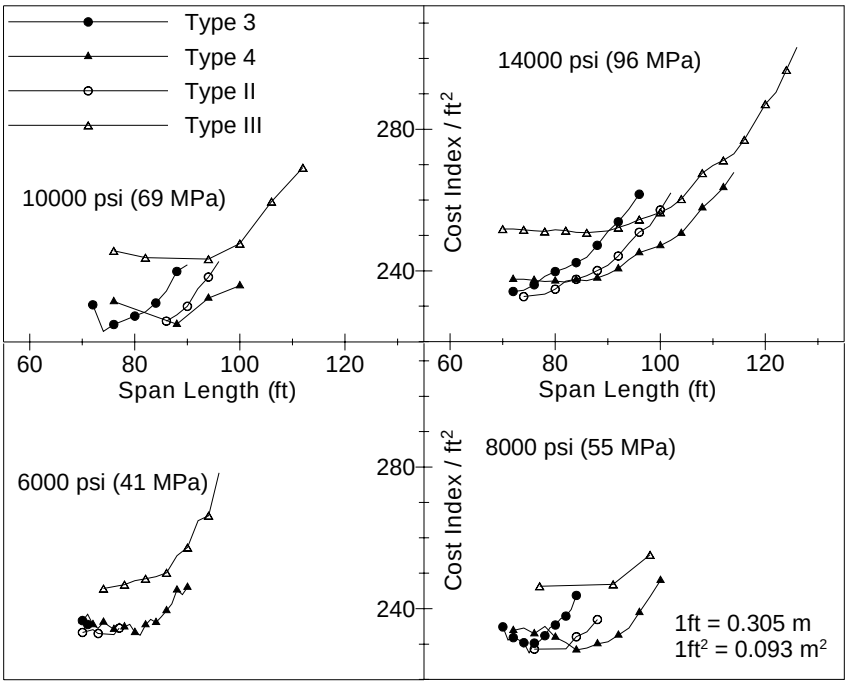

Figure 11.19. Comparison of MoDOT Sections and AASHTO Sections

11.4. ANALYSIS OF MODIFIED CROSS SECTIONS

From the previous study (Zia et al. 1989 and Russell et al. 1997), it is found there is a strength level beyond which high-strength concrete can not be effectively utilized. The advantages of high-strength concrete are limited by two major factors.

One limitation is the bottom flange of the section. The chief structural benefit of higher strength concrete is the greater amount of prestressing force that can be imposed on the section. However, the physical dimension of the section's bottom flange limits the amount and location of prestressing strands. The efficiency of the section will fall dramatically when the bottom flange reaches its capacity for total number of strands. To overcome this limitation, modifications to the cross sections are studied in this Section including bottom flange geometry, strand strength, strand spacing, and strand size.

The other limitation is the cost effectiveness of the deck with large girder spacing. There is a point at which the increase in unit deck costs alone begins to outweigh the savings in unit girder costs with larger girder spacing. A reinforced concrete deck is not cost effective and limits the benefits of higher strength concrete in the girder for long-span decks (Russell et al. 1997). This limitation is beyond the scope of this study and not investigated.

11.4.1. Bottom Flange Geometry. Modifying the bottom flange geometry allows a larger number of strands within the flange and thus more efficient strand placement. In this Section, the MoDOT Section Type 6 and Type 7 are studied using 1860 MPa (270 ksi), 12.7 mm (0.5 in.) diameter prestressing strands with 51 mm (2 in.) center to center spacing. Two strands were allowed within each row of the web.

As shown in Figure 11.20, two modifications were studied for both MoDOT Section Type 6 and Type 7. Modification No. 1 is increase flange thickness 51 mm (2 in.) without changing the section depth. Modification No. 2 is increase the section depth 51 mm (2 in.). Figures 11.21 and 11.22 compare optimum cost curves for the MoDOT Section Type 6 and Type 7 at various concrete strengths, respectively.

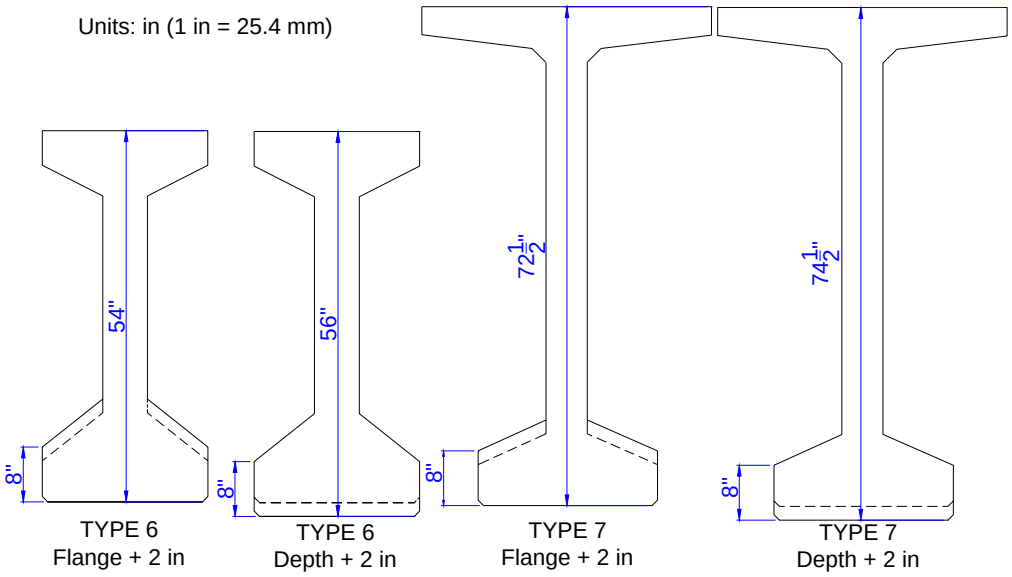

Figure 11.20. Bottom Flange Modification of MoDOT Section Type 6 and Type 7

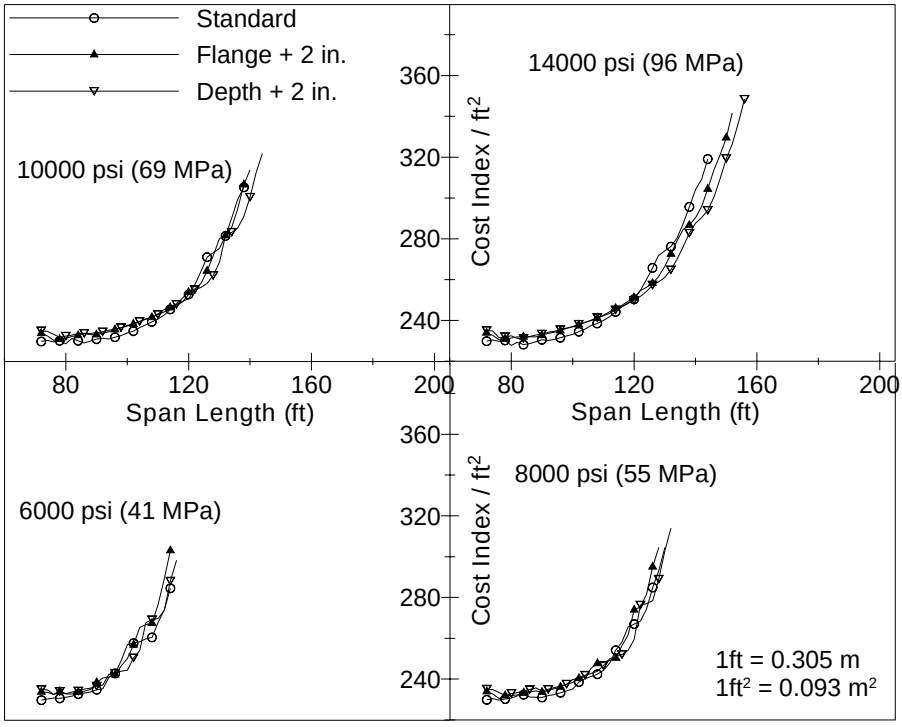

Figure 11.21. Comparison of Modified and Standard MoDOT Type 6 Section

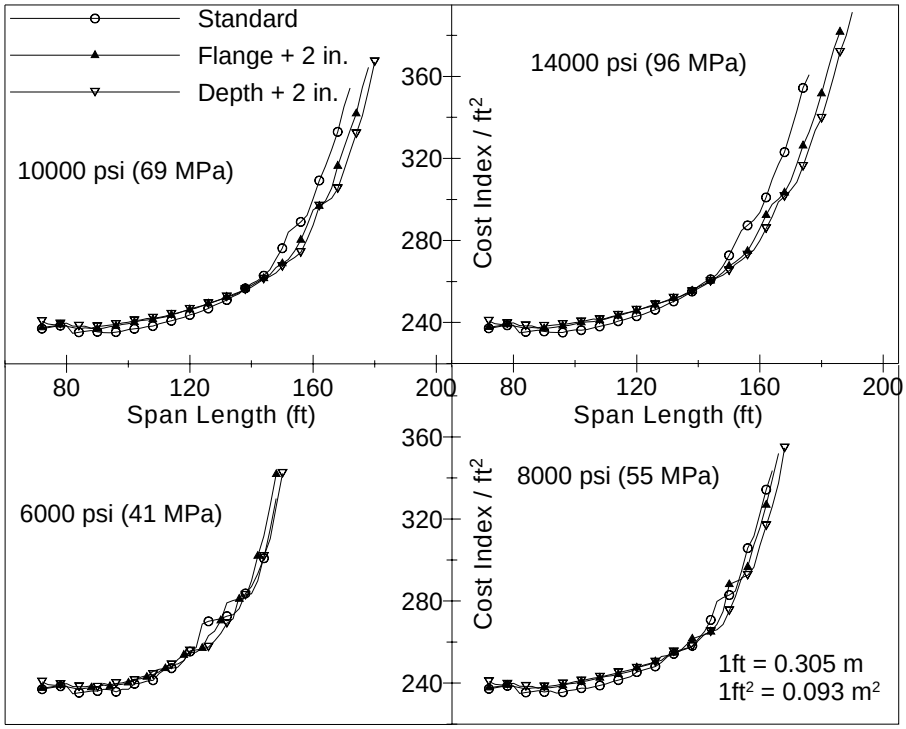

Figure 11.22. Comparison of Modified and Standard MoDOT Type 7 Section

For the MoDOT Section Type 6, both modifications have a minimal effect (less than 3%) on optimum cost curves with strength up to 69 MPa (10,000 psi). Benefits may be observed on the 96 MPa (14,000 psi) plot where both modifications are more cost effective at span length in excess of 36.6 m (120 ft). Increasing the depth 51 mm (2 in.) is more cost effective than increasing flange thickness 51 mm (2 in.) alone. However, the difference between these two options is less than 2%.

In the case of MoDOT Section Type 7, both modifications have minimal effect (less than 2%) on optimum cost curves for a strength level of 41 MPa (6000 psi). For 55 MPa (8000 psi) concrete strength, both modifications results in a slightly more cost effective section than the original MoDOT Section Type 7 by more than 5%. Benefits of modified sections are realized at concrete strengths in excess of 55 MPa (8000 psi) and

span length in excess of 42.7 m (140 ft). The difference between the two modified sections is less than 3% because both accommodate the same maximum number of strands within their bottom flange.

11.4.2. Strand Strength. Increasing the strand strength allows for greater prestressing. In this Section, MoDOT Section Type 6 and Type 7 are studied using 12.7 mm (0.5 in.) diameter prestressing strands with 51 mm (2 in.) center to center spacing. Two strands were allowed within each row of the web. Cost effectiveness of cross sections using strands with strength of 1860 MPa (270 ksi) are compared with sections using 2070 MPa (300 ksi) strands. It should be noted that 2070 MPa (300 ksi) strands are not available in the United States while they are manufactured and used in Japan. In this Section, 2070 MPa (300 ksi) strands are studied for the possible future application.

Figures 11.23 and 11.24 compare optimum cost curves for the MoDOT Section Type 6 and Type 7 at various concrete strengths, respectively, when the strand tensile strength is increased from 1860 MPa (270 ksi) to 2070 MPa (300 ksi).

From these figures, it may be observed that the strand tensile strength increase has the largest impact about 16% on the 96 MPa (14,000 psi) plot and the smallest impact about 2% on the 41 MPa (6000 psi) plot. This behavior is consistent with the conclusion that the bottom flange size limits the effectiveness of higher concrete strengths because both methods increase the total prestressing forces. More effective prestressing can be placed within the cross section with a greater strand strength and ultimately greater prestressing force for the same area of steel. The span length can be increase by about 3.0 m (10 ft) using 2070 MPa (300 ksi) strands compared to using 1860 MPa (270 ksi) strands for both MoDOT Section Type 6 and Type 7.

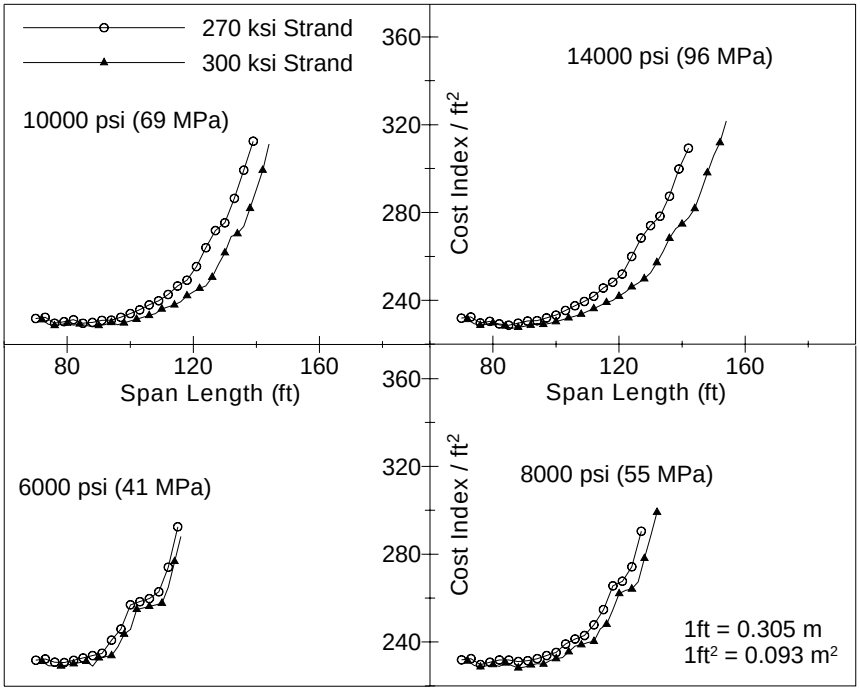

Figure 11.23. Comparison of Strand Tensile Strength for MoDOT Section Type 6

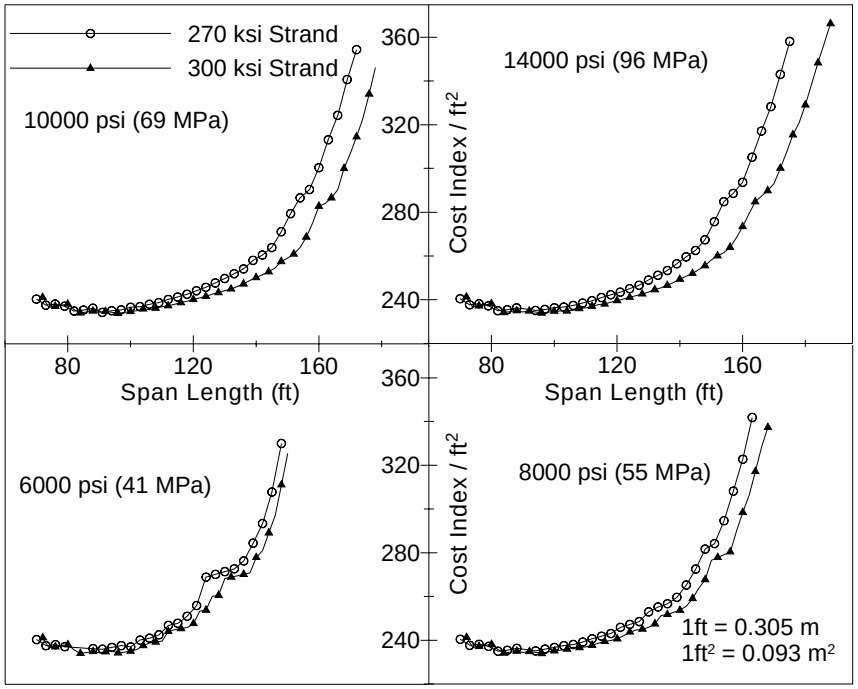

Figure 11.24. Comparison of Strand Tensile Strength for MoDOT Section Type 7

11.4.3. Strand Spacing and Size. Employing larger strand size and smaller spacing can also overcome the bottom flange physical limitation. This allows a greater prestressing force within the bottom flange. However, with closer strand spacing, special attention should be paid to the bond behavior, transfer length and development length.

In this Section, MoDOT Section Type 6 and Type 7 are studied using 1860 MPa (270 ksi), prestressing strands. Two strands were allowed within each row of the web. Strand spacing of 51 mm (2 in.) and spacing of 38 mm (1.5 in.) were studied in this Section. Three different strand sizes, 12.7 mm (0.5 in.) diameter, 15.2 mm (0.6 in.) diameter and 17.8 mm (0.7 in.) diameter strands, were considered.

As shown in Figures 11.25 through 11.28, both strand spacing and size have the largest impact about 26% on 96 MPa (14,000 psi) concrete strength and the smallest impact about 2% on 41 MPa (6000 psi) concrete strength. This behavior is again consistent with the conclusion that the bottom flange size limits the effectiveness of higher concrete strengths. With smaller strand spacing or larger strand size, up to 30% more prestressing force can be placed within the cross section. For 96 MPa (14,000 psi) concrete strength plot in different cases, span length capacities are all increased dramatically by up to 25%.

When using concrete with strength higher than 69 MPa (10,000 psi), the benefits are obvious with span in excess of 36.6 m (120 ft) for both MoDOT Section Type 6 and Type 7 Sections. Therefore, for MoDOT sections, using small strand spacing or large strand side can yield cost effective design when the concrete strength is higher than 69 MPa (10,000 psi) and span length is in excess of 36.6 m (120 ft).

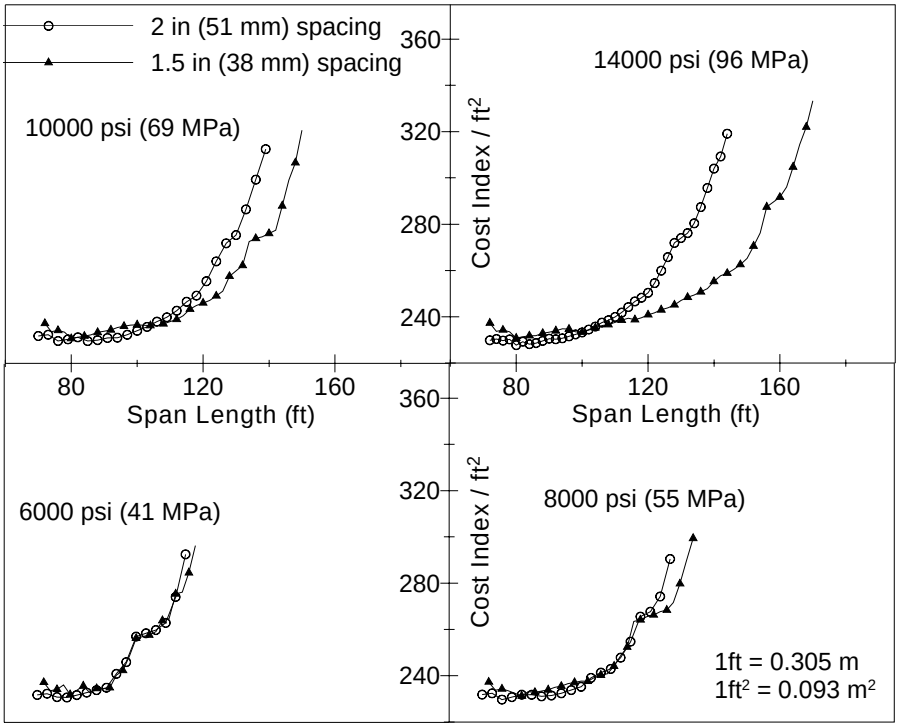

Figure 11.25. Comparison of Strand Spacing for MoDOT Section Type 6

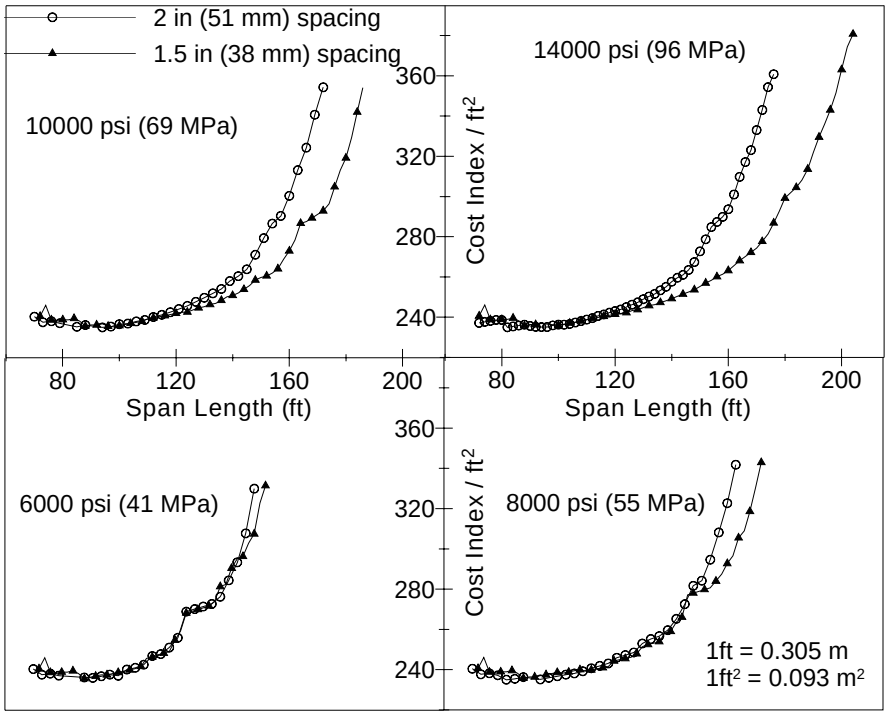

Figure 11.26. Comparison of Strand Spacing for MoDOT Section Type 7

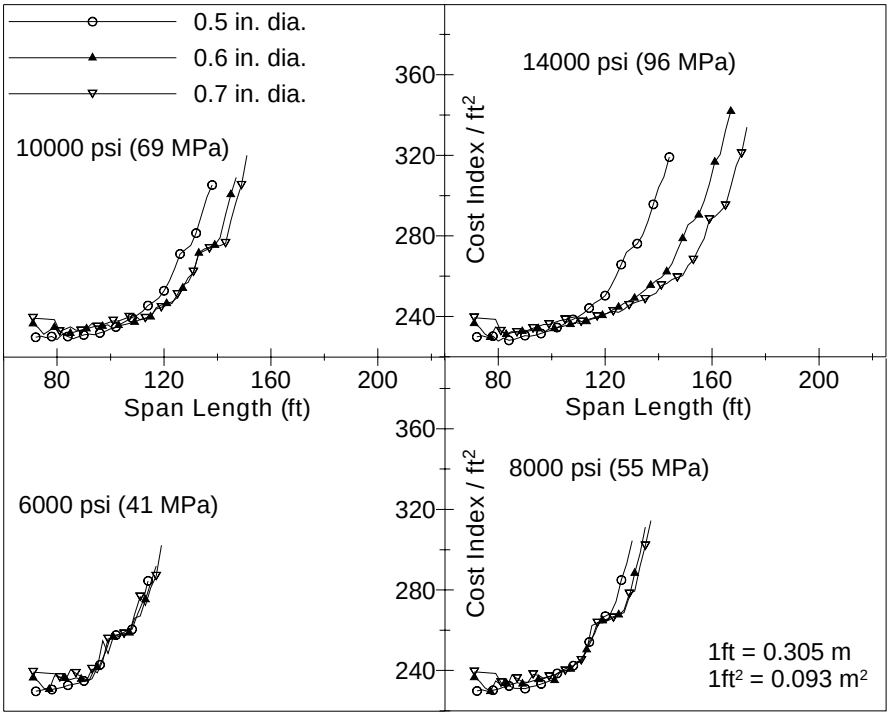

Figure 11.27. Comparison of Strand Diameter on MoDOT Section Type 6

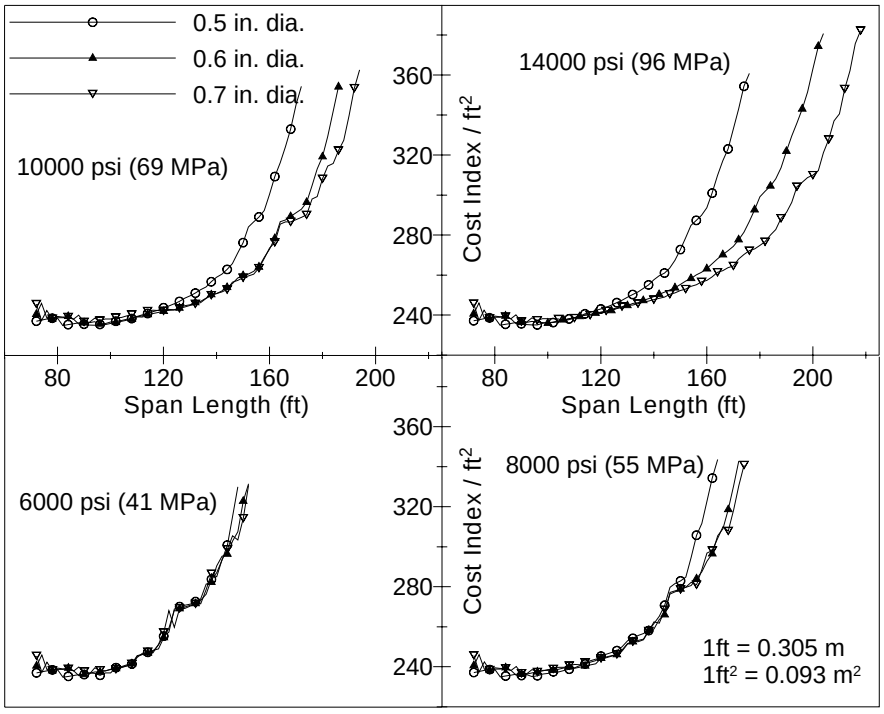

Figure 11.28. Comparison of Strand Diameter on MoDOT Section Type 7

11.5. SUMMARY AND CONCLUSIONS

Based on the discussion in this Section, the following conclusions are made:

For all MoDOT sections using 12.7 mm (0.5 in.) diameter Grade 270 strand at 51 mm (2 in.) centers, the maximum useful concrete compressive strength was in the range of 69 to 83 MPa (10,000 to 12,000 psi). Above this strength level, sufficient prestressing forces need to be supplied within the cross section to take advantage of any higher concrete compressive strengths.

With the increase of concrete strength, the maximum span capacity is increased for various cross sections by up to 33%. From 41 MPa (6000 psi) to 96 MPa (14,000 psi), maximum span capacity is increased by 33% for MoDOT Section Type 3, and 19% for MoDOT Section Type 7. The increase is diminishes with increase in the concrete strength and ultimately flattening out at a concrete strength of 83 MPa (12,000 psi). The maximum available prestressing force limits the advantages of using high-strength concrete.

MoDOT Section Type 7 is the most cost effective cross section for span lengths up to 45.7 m (150 ft) at all concrete strengths comparing with other existing MoDOT cross sections.

A shallower MoDOT section using higher-strength concrete can be more cost effective than a deeper section with a lower strength concrete. This is useful for replacement of existing bridges or new bridges with clearance requirements.

Bottom flange modifications have a small impact on optimum cost curves for MoDOT Section Type 6. In the case of MoDOT Section Type 7, benefits of bottom flange modifications are realized at concrete strengths in excess of 55 MPa (8000 psi) and

span length in excess of 42.7 m (140 ft). The difference between the two modified sections is minimal because both accommodate the same maximum number of strands within their bottom flange.

The impact of increasing strand tensile strength from 1860 to 2070 MPa (270 to 300 ksi) was dependent on girder concrete strength. The benefits of higher strand tensile strength were minimal at a concrete strength of 41 MPa (6000 psi). The span length can be increase by about 3.0 m (10 ft) with higher grade strand for both MoDOT Section Type 6 and Type 7.

The effect of strand spacing and size was dependent on concrete strength. With smaller strand spacing or larger strand size, up to 30% more prestressing force can be placed within the cross section. For 96 MPa (14,000 psi) concrete strength, span length capacities are all increased dramatically by up to 25%. When using concrete with strength higher than 69 MPa (10,000 psi), the benefits are obvious with span in excess of 36.6 m (120 ft) for both MoDOT Section Type 6 and Type 7 compared to using normal strength concrete, which has a strength less than 41 MPa (6000 psi).

12. SUMMARY, CONCLUSIONS AND RECOMMENDATIONS

12.1. SUMMARY OF PRIMARY FINDINGS

The most important findings in this research program are as follows:

1. MoDOT Bridge A6130 consisting of prestressed concrete was successfully constructed in Missouri using high performance concrete. Concrete with designed release strength of 52 MPa (7542 psi) and designed 56-day strength of 70 MPa (10,152psi) was attained successfully at prestressing plant. According to FHwA HPC performance grade and measured material properties of HPC used in this bridge, precast girder concrete conformed to Grade 2 HPC while the cast-in-place deck concrete conformed to Grade 1 HPC.
2. The relationships between modulus of elasticity, splitting tensile strength and compressive strength were studied for both lightweight concrete and normal weight concrete. The following equations are recommended and yield a better prediction than existing empirical equations. These are not intended to be specific to a given mix design/mix constituent, but rather an average starting empirical equation for the design engineer with limited mix design/mix constituent information.

   For light weight concrete:

$$E_c = (w/145)^{1.5}[42090(f_c^{'})^{0.5} + 854100]\ (psi) \qquad \text{Equation 4.1}$$

   For normal weight concrete:

$$E_c = (w/145)^{1.5}[43780(f_c^{'})^{0.5} + 141300]\ (psi) \qquad \text{Equation 4.2}$$

   For both light weight and normal weight concrete:

$$f_{sp} = 2.59(f_c^{'})^{0.62}\ (psi) \qquad \text{Equation 4.3}$$

3. Creep and shrinkage were found to be lower than predicted using ACI Committee 209 Guidelines. Fit curves represent the measured data well and were recommended for estimation of creep coefficient and shrinkage strain.
4. The maximum measured hydration temperature for the HPC girders was 57 °C (135 °F). Equivalent maximum temperature rises for both girder and deck concrete were well below values suggested by ACI Committee 363 (1992) due to the supplementary cementitious materials used and higher SA/V ratio of the MoDOT Type 2 Section.
5. The methods for determination of effective bridge temperature suggested in the AASHTO Standard Specification (1996), LRFD Specification (1994) and NCHRP Report 276 Method (1985) are inappropriate for the bridge locations monitored. A modified approach was developed by the author to provide more realistic design temperatures. The calculated temperatures using this suggested method correlated well with the extreme average bridge temperatures monitored in this study.
6. Maximum measured positive gradients are quite different from those specified by NCHRP (1985), AASHTO (1994) and Gross (1999). Temperature at the lower deck gauge was underestimated by 6.1 °C (11 °F) using the design gradients using all other methods. A modified design positive thermal gradient is recommended by the author and proved to yield better estimation of the maximum measured positive gradient. The shape of the negative measured gradients is reasonably similar[less than 2.2 °C (4 °F) difference] to the design negative gradients specified by AASHTO LRFD (1994). Thermal stresses at top fiber are only one third of the stresses due to live load (plus impact). At bottom fiber, thermal stresses were about

1.7 MPa (250 psi) in compression. Thermal stresses at both top fiber and bottom fiber are relatively small in magnitude and unlikely to cause any distress.

7. Concrete strain behavior prior to release was significantly influenced by restraint from formwork and precasting bed, hydration temperatures, and shrinkage. Sudden increase of the tensile strain was measured and at the same place cracking was observed prior to release as a result of restraint against shortening due to cooling and drying shrinkage. Number, length and spacing of recorded cracking were totally case dependent. These cracks closed entirely upon release of prestress and were often impossible to find thereafter. No structural impact was observed in this research program as a result of this cracking.
8. Generally, the refined design method yields better predicted results compared to the AASHTO design methods in calculating strain behavior, prestress losses, deflections and cambers.
9. In some cases, the stresses observed in concrete after release were higher than predicted stresses, even exceeding allowable stresses. One of the reasons was the effect of restraint from the casting bed. Before release, the casting bed restrained the deformation of the girders. After the release of the prestress, the restrain of the bed acted as an additional force on the girder, which led to the higher stresses in the girders.
10. The time-dependent strain behaviors at the mid-span section were found to be much smaller than predicted. Increases in the measured strains were slower than predicted for the first two months after fabrication. The prediction method suggested by the

author was accurate for the first month; however at later-age it was difficult to predict the strain behavior.

11. Total measured losses averaged 289.2 MPa (41.94 ksi), approximately 20.71% of the nominal jacking stress of 1396 MPa (202.5 ksi). Elastic shortening accounted for the largest portion of the total loss. Prestress losses before release in this study were found to be minimal.
12. For prestress precast high performance concrete girders, the PCI Handbook method and method recommended by Gross (1999) are recommended for prestress losses estimation in design stage. Moreover, they are accurate for exact loss calculation once the measured material properties are available.
13. Measured release cambers were lower than predicted based on either design or measured properties with differences ranging from 0 to 10.2 mm (0 to 0.40 in.). Differences between measured release camber and predicted release camber based on measured parameters are due in large part to errors in the refined estimation of the initial prestress force and member self-weight.
14. There was generally good agreement (less than 7% difference) between camber values at erection among girders in a given span. Better correlation existed between the measured values and the predictions based on measured parameters.
15. The measured erection and long-term cambers were substantially lower than the cambers estimated during design by MoDOT by up to 40%. However, the overall difference between measured and predicted long-term camber was in an acceptable range. Improved correlation existed between the measured values and the predictions based on measured parameters.

16. The actual bridge live load distribution coefficients by field load testing were found to be comparable to the live load distribution factors calculated using the AASHTO LRFD specifications (1994), but significantly lower than those factors calculated using the AASHTO standard specification (1996). The distribution factors recommended by AASHTO (1996) appeared to be overly conservative based on the live load test herein. Therefore, the AASHTO specification design codes are generally too conservative for the live load distribution factor calculation and subsequently the load rating in terms of strength limit requirements using these design guides. The AASHTO LRFD specification appears appropriate for HPC bridges is recommended instead.
17. The test and analysis results demonstrated that the MoDOT continuity detail at the interior bent is nearly fixed based upon the rotation and moment levels measured and predicted by the beam fixed at bent model. It therefore is advisable to consider the girder continuity as fully fixed for these types of bridge systems. To simplify the design calculations, the fixed end model is conservative and acceptable for calculating negative moment in the loaded span for the continuity detail used. This assumes there would not be softening in the negative moment region of the bent detail due to cracking from temperature variations or overloads over time.
18. For all MoDOT sections using 12.7 mm (0.5 in.) diameter Grade 270 strand at 51 mm (2 in.) centers, the maximum useful concrete compressive strength was in the range of 69 to 83 MPa (10,000 to 12,000 psi). Above this strength level, sufficient prestressing force can not be supplied within the cross section to take advantage of any higher concrete compressive strengths.

19. The maximum available prestressing force limited the advantages of high-strength concrete. To take full advantage, cross sections can be modified by increasing bottom flange thickness and utilizing higher strand strength, smaller strand spacing or larger strand size.
20. The HPC deck proved to be a durable mix with low shrinkage, good scaling resistance and low chloride permability.

12.2. RECOMMENDATIONS FOR FUTURE RESEARCH

Following future research areas are recommended:

1. For better prediction of structural behavior, a database should be developed for the material properties of different HPC mixes using local materials, especially for modulus of elasticity, shrinkage, and creep.
2. More research is needed on prestress losses before release. A simple approach needs to be developed for the prestress losses from jacking to release.
3. Additional measurements of bridge temperatures at various locations in Missouri and other states are important. To set up a data base for thermal gradients is necessary for better estimation of thermal gradients at different geographical locations.
4. Additional live load tests are useful for investigating long-term behavior of HPC bridges considering lower creep properties of HPC and high performance deck concrete.

5. New standard shapes should be considered and investigated by MoDOT, should they have a desire to use and implement HSC over 83 MPa (12,000 psi) with larger prestressing strands.
6. Good quality control is needed in placing high performance concrete decks to insure the mix remains durable and does not develop excessive cracking.

APPENDIX A.

GAUGES NUMBERING AND WIRE LENGTH

Table A.1. Gauge Identification Designations

ITEMS	IDENTIFICATION			
Embedded Gauge Number	Type		Range	Named
	Deck VW		001-100	001-008
	Girder VW		101-200	101-156
	Girder ER		201-250	201-208
	Girder TC		251-300	251-257; 261-267
	Deck TR		301-400 (Corresponding VW # + 300)	301-308
	Girder TR		401-500 (Corresponding VW # + 300)	401-456
Girders and Decks Designation	Girder: *Bmn* CIP Deck: *Dmn*		Where *B* = beam, *m* = span #, *n* = beam line # Separate the deck as several small decks between bents and girders Where *D* = deck, *m* = span #, *n* = small girder line # of the two lines	
Embedded Gauge Depth	TD		Top Deck (2 in. below top fiber of deck)	
	BD		Bottom Deck (2 in. above bottom fiber of deck)	
	TF		Top Flange (2 in. below top fiber)	
	TW		Top of Web	
	MW		Middle of Web	
	BW		Bottom of Web	
	CGI		c.g. of Noncomposite I-shaped Girder	
	CGS		c.g. of Prestressed Strands	
	BF		Bottom Flange (2 in. above bottom surface)	
Longitudinal Location of Embedded Gauges	M		Mid-span	
	Sm		Near the Support at Bent *m*	
	Sm,n		Near Bent *m, n* meters. from end of girder	
Gauge Type	Embedded Gauges	VW	Vibrating Wire Strain Gauge	
		TC	Thermocouple	
		ER	Bonded Electric Resistance Strain Gauge	
		TR	Thermistor (integral with Vibrating Wire Strain Gauge)	
	Other Gauges	DEMEC	Surface Mechanical Strain Gauges	
		T-W	Tensioned – Wire Deflection System	
		PSS	Precise Survey System of Deflection	
		LC	Load Cells	
DAS	CR23X			

Table A.2. VWSG Numbering and Wire Length

Girder VW (including those in the deck over the Girder)			
VW #101 B13-M-TD	VW #115 B14-M-TD	VW #129 B23-M-TD	VW #143 B24-M-TD
VW #102 B13-M-BD	VW #116 B14-M-BD	VW #130 B23-M-BD	VW #144 B24-M-BD
VW #103 B13-M-TF	VW #117 B14-M-TF	VW #131 B23-M-TF	VW #145 B24-M-TF
VW #104 B13-M-TW	VW #118 B14-M- TW	VW #132 B23-M-TW	VW #146 B24-M- TW
VW #105 B13-M-MW	VW #119 B14-M-MW	VW #133 B23-M-MW	VW #147 B24-M-MW
VW #106 B13-M-CGU	VW #120 B14-M-CGU	VW #134 B23-M-CGU	VW #148 B24-M-CGU
VW #107 B13-M-CGS	VW #121 B14-M-CGS	VW #135 B23-M-CGS	VW #149 B24-M-CGS
VW #108 B13- M-BF	VW #122 B14- M-BF	VW #136 B23- M-BF	VW #150 B24- M-BF
VW #109 B13-S-TD	VW #123 B14-S-TD	VW #137 B23-S-TD	VW #151 B24-S-TD
VW #110 B13-S-BD	VW #124 B14-S-BD	VW #138 B23-S-BD	VW #152 B24-S-BD
VW #111 B13-S-TF	VW #125 B14-S-TF	VW #139 B23-S-TF	VW #153 B24-S-TF
VW #112 B13-S-CGU	VW #126 B14-S-CGU	VW #140 B23-S-CGU	VW #154 B24-S-CGU
VW #113 B13-S-CGS	VW #127 B14-S-CGS	VW #141 B23-S-CGS	VW #155 B24-S-CGS
VW #114 B13-S-BF	VW #128 B14-S-BF	VW #142 B23-S-BF	VW #156 B24-S-BF
Notes:			
B13, #101-#108: 17m	B14, #115-#122: 27m	B23, #129-#136: 17m	B24, #143-#150: 27m
B13, #109-#114: 6m	B14, #123-#128: 15m	B23, #137-#142: 6m	B24, #151-#156: 15m

Table A.3. VWSG and ERSG Numbering and Wire Length

Deck VW (not including those in the deck over the Girder)	
VW #001 D12-M-TD	
VW #002 D12-M-BD	
VW #003 D13-M-TD	D12, mid-span: #1-#2 11m
VW #004 D13-M-BD	D13, mid-span: #3-#4 18m
VW #005 D22-M-TD	D22, mid-span: #5-#6 11m
VW #006 D22-M-BD	D23, mid-span: #7-#8 18m
VW #007 D23-M-TD	
VW #008 D23-M-BD	

Girder ERSG	
ER #201 B13-M-CGS	
ER #202 B13-S-CGS	B13, mid-span: #201 —— 18m
ER #203 B14-M-CGS	B13, near-support: #202 —— 8m
ER #204 B14-S-CGS	B14, mid-span: #203 —— 27m
ER #205 B23-M-CGS	B14, near-support: #204 —— 15m
ER #206 B23-S-CGS	
ER #207 B24-M-CGS	B23, mid-span: #205 —— 18m
ER #208 B24-S-CGS	B23, near-support: #206 —— 8m
ER #211 C13-TF	B24, mid-span: #207 —— 27m
ER #212 C13-MW	B24, near-support: #208 —— 15m
ER #213 C13-BF	C13, #211, 212, 213 —— 5.5m
ER #214 C14-TF	C14, #214, 215, 216 —— 12m
ER #215 C14-MW	
ER #216 C14-BF	

Table A.4. Thermocouple Numbering and Wire Length

Girder Thermocouple (including those in the deck)	
TC #251B21-TD	TC #261B22-TD
TC #252B21-BD	TC #262B22-BD
TC #253B21-TF	TC #263B22-TF
TC #254B21-TW	TC #264B22-TW
TC #255B21-MW	TC #265B22-MW
TC #256B21-BW	TC #266B22-BW
TC #257B21-BF	TC #267B22-BF

Note:

#251-#257: 7m (23ft) #261-#267: 13m (42ft)

APPENDIX B.

GAUGE LOCATIONS IN THE GIRDERS AND DECK

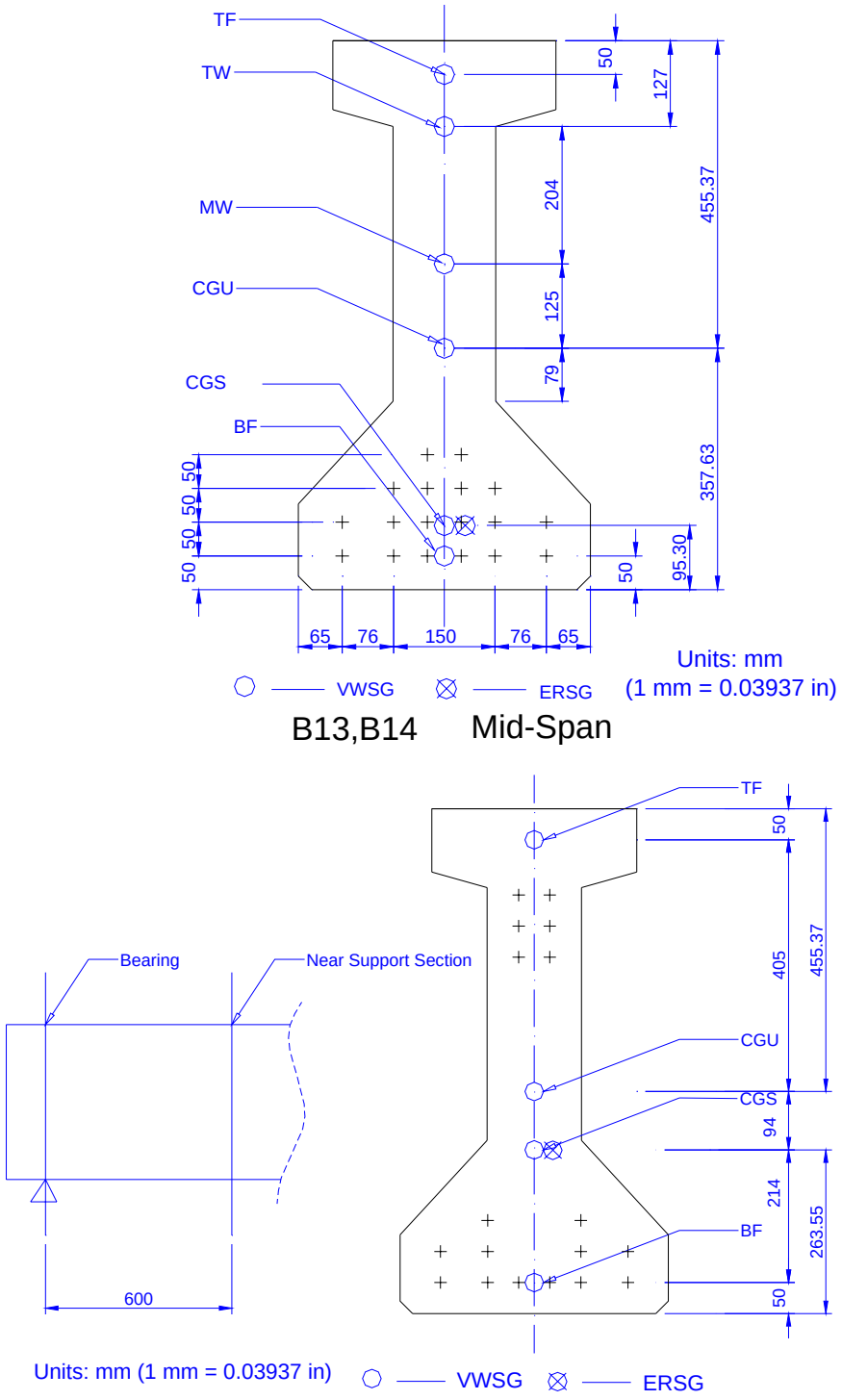

Figure B.1. Gauges Location in Girders B13 and B14

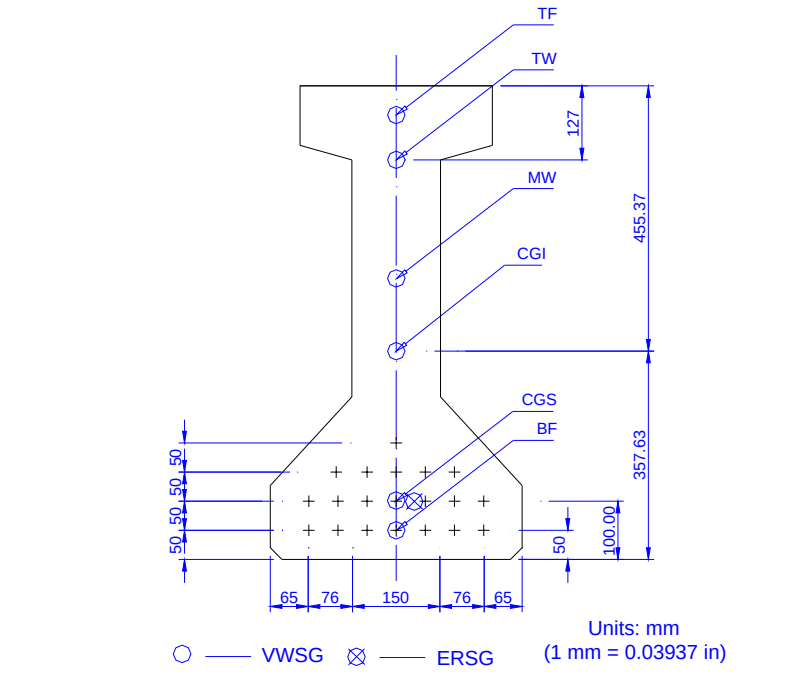

B23,B24 Mid-span

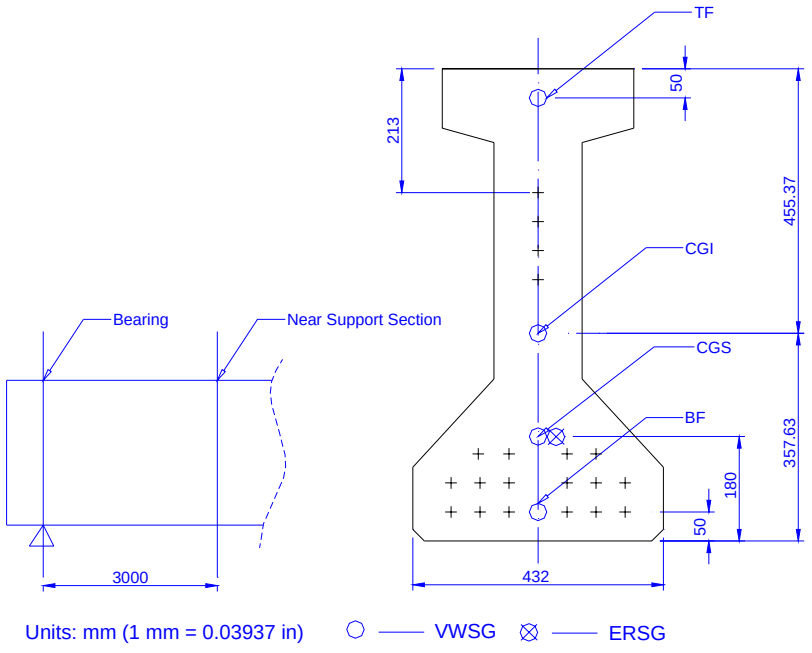

B23,B24 Near Support

Figure B.2. Gauges Location in Girders B23 and B24

Location of Gauges

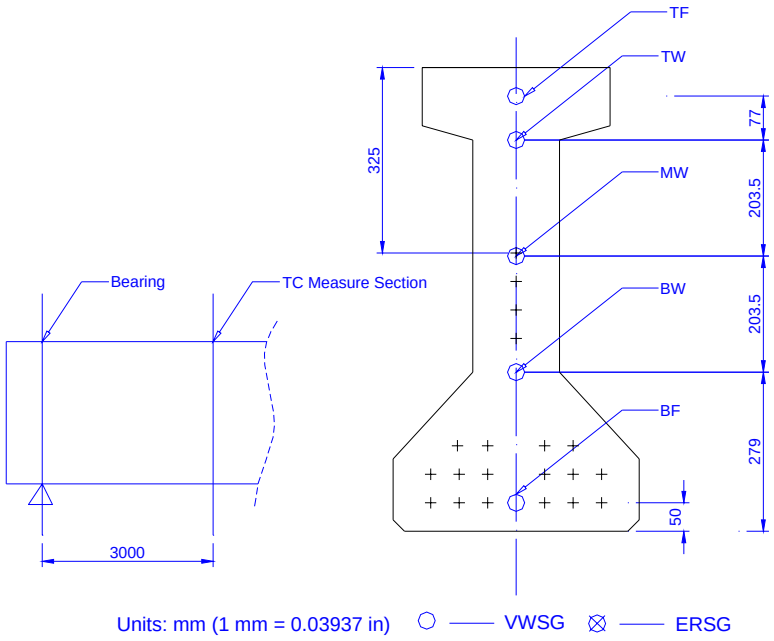

Figure B.3. Gauges Location in Girders B21 and B22

Table B.1. Gauges Location in Girders B13

		West		East
VWSG				
TD	DECK	**101**		**109**
BD		**102**		**110**
TF	GIRDER	**103**		**111**
TW		**104**		
MW		**105**		
CGI		**106**		**112**
CGS		**107**		**113**
BF		**108**		**114**
		M		**S1**

		West		East
ERSG				
TD	DECK			
BD				
TF	GIRDER			
TW				
MW				
CGI				
CGS		**201**		**202**
BF				
		M		**S1**

Table B.2. Gauges Location in Girders B14

West East

VWSG

TD	DECK	**115**	**123**
BD		**116**	**124**
TF	GIRDER	**117**	**125**
TW		**118**	
MW		**119**	
CGI		**120**	**126**
CGS		**121**	**127**
BF		**122**	**128**
		M	**S2**

West East

ERSG

TD	DECK		
BD			
TF	GIRDER		
TW			
MW			
CGI			
CGS		**203**	**204**
BF			
		M	**S2**

West East

Table B.3. Gauges Location in Girders B21

West			East
TC			
TD	**251**		DECK
BD	**252**		
TF	**253**		GIRDER
TW	**254**		
MW	**255**		
BW	**256**		
BF	**257**		
S2,2m		**M**	

Table B.4. Gauges Location in Girders B22

West			East
TC			
TD	**261**		DECK
BD	**262**		
TF	**263**		GIRDER
TW	**264**		
MW	**265**		
BW	**266**		
BF	**267**		
S2,2m		**M**	

West	East

Table B.5. Gauges Location in Girders B23

West East

VWSG

TD	**137**	**129**	DECK
BD	**138**	**130**	
TF	**139**	**131**	GIRDER
TW		**132**	
MW		**133**	
CGI	**140**	**134**	
CGS	**141**	**135**	
BF	**142**	**136**	
	S2	**M**	

West East

ERSG

TD			DECK
BD			
TF			GIRDER
TW			
MW			
CGI			
CGS	**206**	**205**	
BF			
	S2	**M**	

West East

Table B.6. Gauges Location in Girders B24

West East

VWSG

TD	**151**	**143**	DECK
BD	**152**	**144**	
TF	**153**	**145**	GIRDER
TW		**146**	
MW		**147**	
CGI	**154**	**148**	
CGS	**155**	**149**	
BF	**156**	**150**	
	S2	**M**	

West East

ERSG

TD			DECK
BD			
TF			GIRDER
TW			
MW			
CGI			
CGS	**208**	**207**	
BF			
	S2	**M**	

West East

Table B.7. Gauges Location in Deck D12

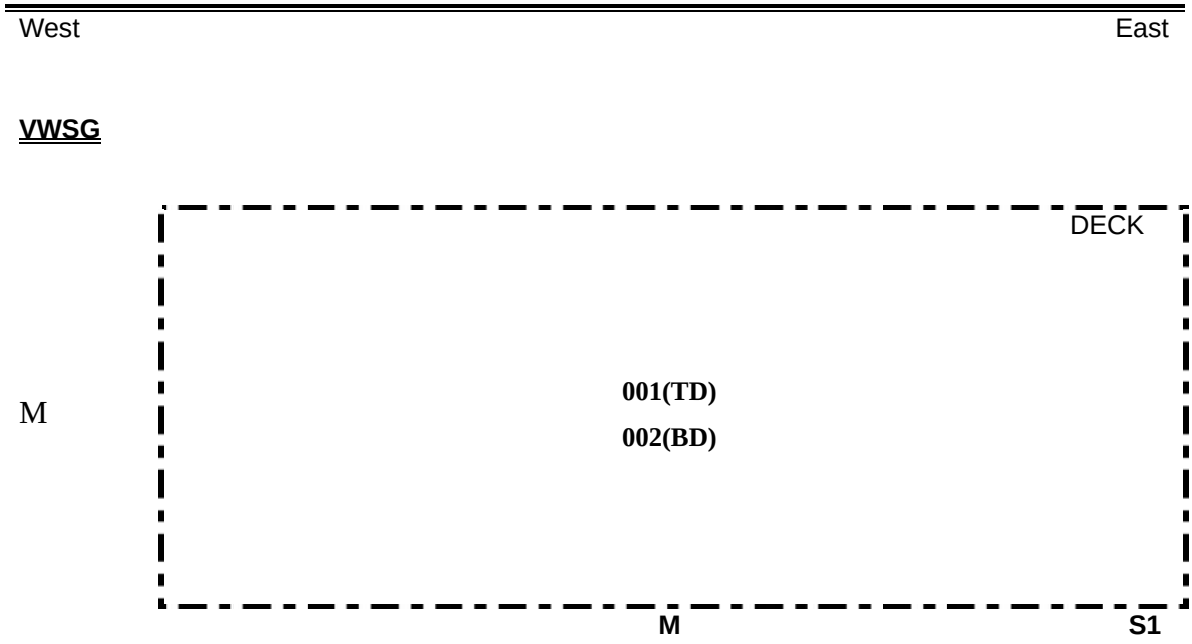

Table B.8. Gauges Location in Deck D13

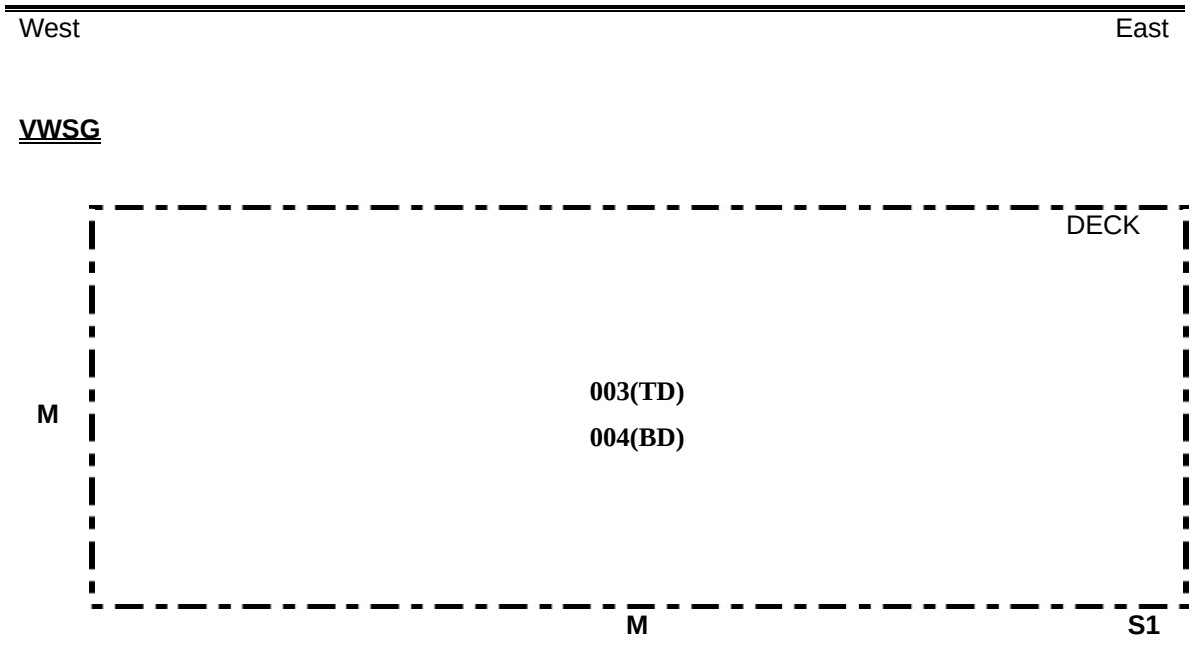

Table B.9. Gauges Location in Deck D22

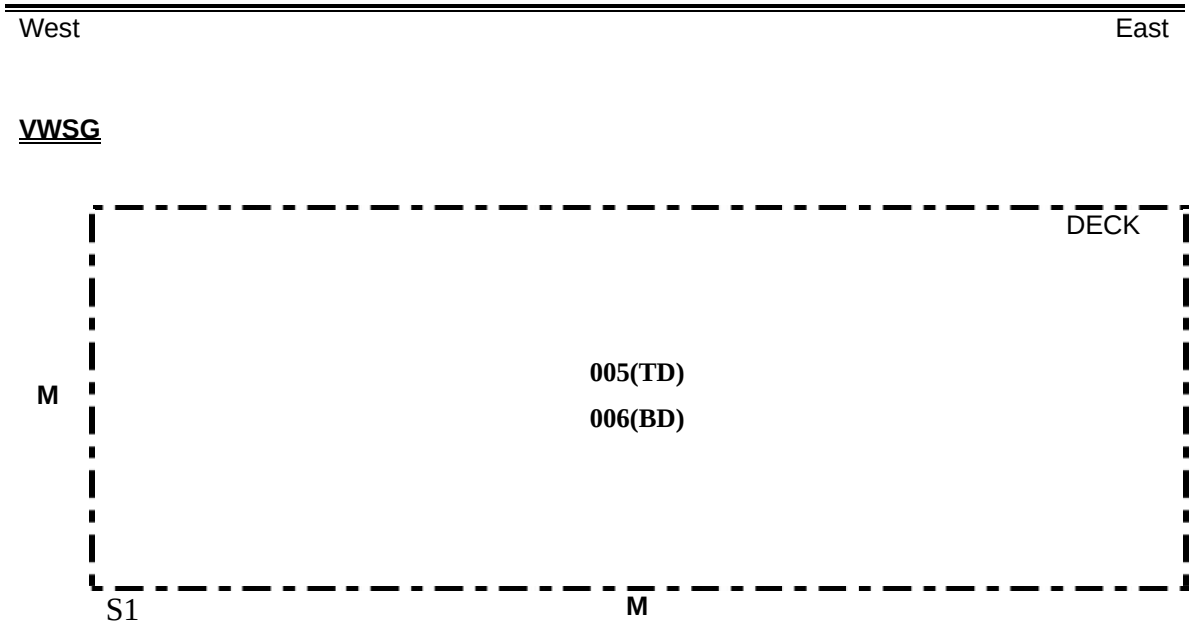

Table B.10. Gauges Location in Deck D23

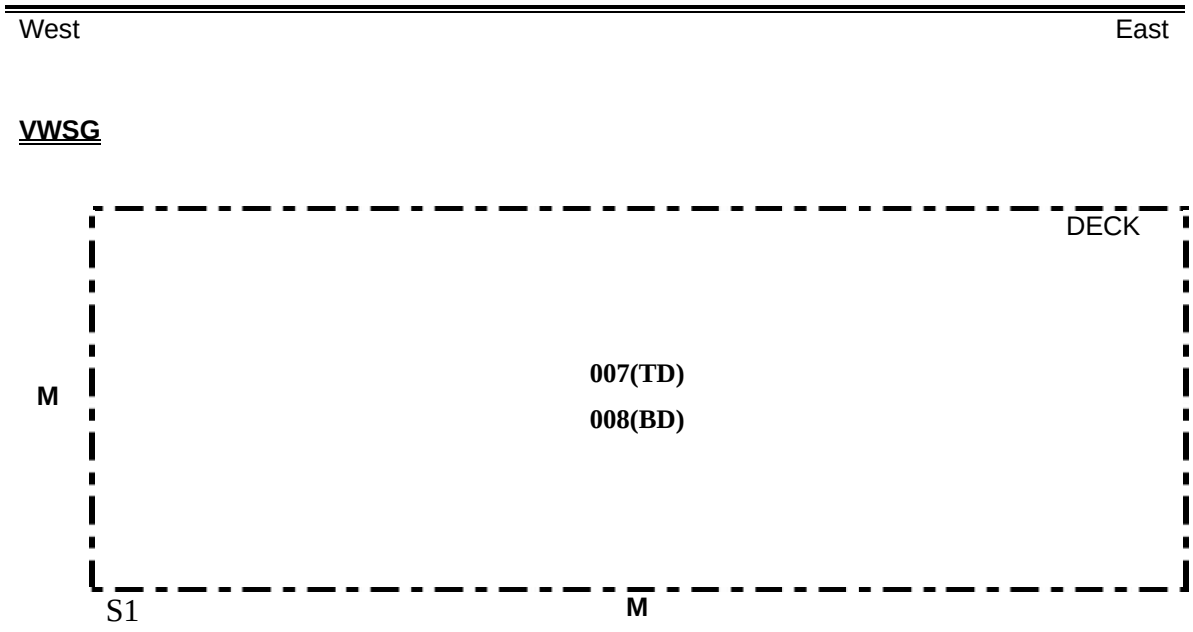

APPENDIX C.

PROGRAM FOR DAS CR23X

```
;{CR23X}
;
*Table 1 Program
  01: 3600      Execution Interval (seconds)

;AM416#1--ERSG

1:  Do (P86)
 1: 43       Set Port 3 High

2:  Beginning of Loop (P87)
 1: 0        Delay
 2: 14       Loop Count

3:  Do (P86)
 1: 71       Pulse Port 1

4:  Delay w/Opt Excitation (P22)
 1: 3        Ex Channel
 2: 0        Delay W/Ex (units = 0.01 sec)
 3: 1        Delay After Ex (units = 0.01 sec)
 4: 0        mV Excitation

5:  Full Bridge (P6)
 1: 1        Reps
 2: 23       200 mV, 60 Hz Reject, Slow Range
 3: 7        DIFF Channel
 4: 3        Excite all reps w/Exchan 3
 5: 2500     mV Excitation
 6: 1        Loc [ mVperV    ]
 7: 1.0      Mult
 8: 0.0      Offset

6:  Z=F (P30)
 1: 2.06     F
 2: 00       Exponent of 10
 3: 2        Z Loc [ GF        ]

uStrain=4e3/GF*mVperV/(1-2*0.001*mVperV)

7:  Z=X*F (P37)
 1: 3        X Loc [ uStrain   ]
 2: 1        F
 3: 4     -- Z Loc [ AM1ER_1   ]

8:  End (P95)

9:  Do (P86)
 1: 53       Set Port 3 Low

10:  Do (P86)
 1: 10       Set Output Flag High (Flag 0)

11:  Set Active Storage Area (P80)
 1: 1        Final Storage Area 1
 2: 1        Array ID

12:  Real Time (P77)
 1: 1110     Year,Day,Hour/Minute (midnight =
0000)

13:  Sample (P70)
 1: 14       Reps
 2: 4        Loc [ AM1ER_1   ]

;AVW4--VWSG: AM416#2,3,4,5

14:  Do (P86)
 1: 44       Set Port 4 High

;AM416#2

15:  Beginning of Loop (P87)
 1: 0        Delay
 2: 16       Loop Count

16:  Do (P86)
 1: 71       Pulse Port 1

17:  Vibrating Wire (SE) (P28)
 1: 1        Reps
 2: 5        SE Channel
 3: 1        Excite all reps w/Exchan 1
 4: 5        Starting Freq. (units = 100 Hz)
 5: 10       End Freq. (units = 100 Hz)
 6: 500      No. of Cycles
 7: 10       Rep Delay (units = 0.01 sec)
 8: 131   -- Loc [ AM5ST_1   ] ;
 9: 4062.4   Mult ;
10: 0.0      Offset ;

18:  Excite-Delay (SE) (P4)
 1: 1        Reps
 2: 15       5000 mV, Fast Range
 3: 1        SE Channel
 4: 1        Excite all reps w/Exchan 1
 5: 1        Delay (units 0.01 sec)
 6: 2500     mV Excitation
 7: 147   -- Loc [ AM5TC_1   ] ;
 8: 0.001    Mult
 9: 0.0      Offset

19:  Polynomial (P55)
 1: 1        Reps
 2: 147   -- X Loc [ AM5TC_1   ]
 3: 147   -- F(X) Loc [ AM5TC_1   ]
 4: -104.78  C0
 5: 378.11   C1
 6: -611.59  C2
 7: 544.27   C3
 8: -240.91  C4
```

```
 9: 43.089   C5

20:  End (P95)

21:  Do (P86)
 1: 10       Set Output Flag High (Flag 0)

22:  Set Active Storage Area (P80)
 1: 1        Final Storage Area 1
 2: 5        Array ID

23:  Real Time (P77)
 1: 1110     Year,Day,Hour/Minute (midnight =
0000)

24:  Sample (P70)
 1: 16       Reps
 2: 147      Loc [ AM5TC_1   ]

25:  Sample (P70)
 1: 16       Reps
 2: 131      Loc [ AM5ST_1   ]

;AM416#3

26:  Beginning of Loop (P87)
 1: 0        Delay
 2: 16       Loop Count

27:  Do (P86)
 1: 71       Pulse Port 1

28:  Vibrating Wire (SE) (P28)
 1: 1        Reps
 2: 6        SE Channel
 3: 1        Excite all reps w/Exchan 1
 4: 5        Starting Freq. (units = 100 Hz)
 5: 10       End Freq. (units = 100 Hz)
 6: 500      No. of Cycles
 7: 10       Rep Delay (units = 0.01 sec)
 8: 67    -- Loc [ AM3ST_1   ] ;
 9: 4062.4   Mult ;
10: 0.0      Offset ;

29:  Excite-Delay (SE) (P4)
 1: 1        Reps
 2: 15       5000 mV, Fast Range
 3: 2        SE Channel
 4: 1        Excite all reps w/Exchan 1
 5: 1        Delay (units 0.01 sec)
 6: 2500     mV Excitation
 7: 83    -- Loc [ AM3TC_1   ]
 8: 0.001    Mult
 9: 0.0      Offset

30:  Polynomial (P55)
 1: 1        Reps
 2: 83    -- X Loc [ AM3TC_1   ]
 3: 83    -- F(X) Loc [ AM3TC_1   ]
 4: -104.78  C0
 5: 378.11   C1
 6: -611.59  C2
 7: 544.27   C3
 8: -240.91  C4
 9: 43.089   C5

31:  End (P95)

32:  Do (P86)
 1: 10       Set Output Flag High (Flag 0)

33:  Set Active Storage Area (P80)
 1: 1        Final Storage Area 1
 2: 3        Array ID

34:  Real Time (P77)
 1: 1110     Year,Day,Hour/Minute (midnight =
0000)

35:  Sample (P70)
 1: 16       Reps
 2: 83       Loc [ AM3TC_1   ]

36:  Sample (P70)
 1: 16       Reps
 2: 67       Loc [ AM3ST_1   ]

;AM416#4

37:  Beginning of Loop (P87)
 1: 0        Delay
 2: 16       Loop Count

38:  Do (P86)
 1: 71       Pulse Port 1

39:  Vibrating Wire (SE) (P28)
 1: 1        Reps
 2: 7        SE Channel
 3: 1        Excite all reps w/Exchan 1
 4: 5        Starting Freq. (units = 100 Hz)
 5: 10       End Freq. (units = 100 Hz)
 6: 500      No. of Cycles
 7: 10       Rep Delay (units = 0.01 sec)
 8: 18    -- Loc [ AM2ST_1   ] ;
 9: 4062.4   Mult ;
10: 0.0      Offset ;

40:  Excite-Delay (SE) (P4)
 1: 1        Reps
 2: 15       5000 mV, Fast Range
 3: 3        SE Channel
```

```
 4: 1       Excite all reps w/Exchan 1
 5: 1       Delay (units 0.01 sec)
 6: 2500    mV Excitation
 7: 51   -- Loc [ AM2TC_1   ]
 8: 0.001   Mult
 9: 0.0     Offset

41:  Polynomial (P55)
 1: 1       Reps
 2: 51   -- X Loc [ AM2TC_1   ]
 3: 51   -- F(X) Loc [ AM2TC_1   ]
 4: -104.78  C0
 5: 378.11   C1
 6: -611.59  C2
 7: 544.27   C3
 8: -240.91  C4
 9: 43.089   C5

42:  End (P95)

43:  Do (P86)
 1: 10      Set Output Flag High (Flag 0)

44:  Set Active Storage Area (P80)
 1: 1       Final Storage Area 1
 2: 2       Array ID

45:  Real Time (P77)
 1: 1110    Year,Day,Hour/Minute (midnight =
0000)

46:  Sample (P70)
 1: 16      Reps
 2: 51      Loc [ AM2TC_1   ]

47:  Sample (P70)
 1: 16      Reps
 2: 18      Loc [ AM2ST_1   ]

;AM416#5

48:  Beginning of Loop (P87)
 1: 0       Delay
 2: 16      Loop Count

49:  Do (P86)
 1: 71      Pulse Port 1

50:  Vibrating Wire (SE) (P28)
 1: 1       Reps
 2: 8       SE Channel
 3: 1       Excite all reps w/Exchan 1
 4: 5       Starting Freq. (units = 100 Hz)
 5: 10      End Freq. (units = 100 Hz)
 6: 500     No. of Cycles
 7: 10      Rep Delay (units = 0.01 sec)
 8: 99   -- Loc [ AM4ST_1   ] ;
 9: 4062.4  Mult ;
10: 0.0     Offset ;

51:  Excite-Delay (SE) (P4)
 1: 1       Reps
 2: 15      5000 mV, Fast Range
 3: 4       SE Channel
 4: 1       Excite all reps w/Exchan 1
 5: 1       Delay (units 0.01 sec)
 6: 2500    mV Excitation
 7: 115  -- Loc [ AM4TC_1   ]
 8: 0.001   Mult
 9: 0.0     Offset

52:  Polynomial (P55)
 1: 1       Reps
 2: 115  -- X Loc [ AM4TC_1   ]
 3: 115  -- F(X) Loc [ AM4TC_1   ]
 4: -104.78  C0
 5: 378.11   C1
 6: -611.59  C2
 7: 544.27   C3
 8: -240.91  C4
 9: 43.089   C5

53:  End (P95)

54:  Do (P86)
 1: 54      Set Port 4 Low

55:  Do (P86)
 1: 10      Set Output Flag High (Flag 0)

56:  Set Active Storage Area (P80)
 1: 1       Final Storage Area 1
 2: 4       Array ID

57:  Real Time (P77)
 1: 1110    Year,Day,Hour/Minute (midnight =
0000)

58:  Sample (P70)
 1: 16      Reps
 2: 115     Loc [ AM4TC_1   ]

59:  Sample (P70)
 1: 16      Reps
 2: 99      Loc [ AM4ST_1   ]


;Thermocouple--AM25T

60:  Do (P86)
 1: 42      Set Port 2 High
```

```
61:  Do (P86)
 1: 71       Pulse Port 1

62:  AM25T  Multiplexer (P134)
 1: 16       Reps @@12
 2: 21       10 mV, 60 Hz Reject, Slow Range
 3: 1        Channel
 4: 6        DIFF Channel
 5: 22       Exchan 2, 60 Hz Reject
 6: 1        Clock Control
 7: 2        Reset Control
 8: 1        Type T (Copper-Constantan)
 9: 163      Ref Temp (Deg. C) Loc [ RefTemp    ]
10: 164      Loc [ TC_1      ]
11: 1.0      Mult
12: 0.0      Offset

63:  Do (P86)
 1: 52       Set Port 2 Low

64:  Do (P86)
 1: 10       Set Output Flag High (Flag 0)

65:  Set Active Storage Area (P80)
 1: 1        Final Storage Area 1
 2: 6        Array ID

66:  Real Time (P77)
 1: 1110     Year,Day,Hour/Minute (midnight =
0000)

67:  Sample (P70)
 1: 16       Reps
 2: 164      Loc [ TC_1      ]

68:  Serial Out (P96)
 1: 71       Destination Output

69:  Serial Out (P96)
 1: 62     -- Destination Output

*Table 2 Program
  02: 0.0000    Execution Interval (seconds)

*Table 3 Subroutines

End Program
```

APPENDIX D.

GIRDER PARAMETERS

Table D.1. Parameters for Girders

	Parameter	Design	Measured
Material Properties	$f'_{ci,\ beam}$	Specified design strength	Measured strength at release
	$f'_{c,\ beam}$	Specified design strength	Measured strength at 56d
	$f'_{c,\ CIP\ deck}$	Specified design strength	Measured strength at 28d
	$E_{ci,\ beam}$	$1{,}000{,}000+40{,}000(f'_c)^{0.5}$	Measured strength at release
	$E_{c,\ beam}$	$1{,}000{,}000+40{,}000(f'_c)^{0.5}$	Measured strength at 56d
	$E_{c,\ CIP\ deck}$	$57{,}000(f'_c)^{0.5}$	Measured strength at 28d
	ρ_{beam}	Assume 150pcf	Measured unit weight
	$\rho_{CIP\ deck}$	Assume 150pcf	Measured unit weight
Section Properties	$A_{beam\ (untrans.)}$	Gross section properties	Gross section properties
	$I_{beam\ (untrans.)}$	Gross section properties	Gross section properties
	$y_{bot,beam\ (untrans.)}$	Gross section properties	Gross section properties
	$A_{beam\ (release)}$	Transformed section with design $E_{ci,\ beam}$	Transformed section with measured $E_{ci,\ beam}$
	$I_{beam\ (release)}$	Transformed section with design $E_{ci,\ beam}$	Transformed section with measured $E_{ci,\ beam}$
	$y_{bot,\ beam\ (release)}$	Transformed section with design $E_{ci,\ beam}$	Transformed section with measured $E_{ci,\ beam}$
	$A_{beam\ (final)}$	Transformed section with design $E_{c,\ beam}$	Transformed section with measured $E_{c,\ beam}$
	$I_{beam\ (final)}$	Transformed section with design $E_{c,\ beam}$	Transformed section with measured $E_{c,\ beam}$
	$y_{bot,\ beam\ (final)}$	Transformed section with design $E_{c,\ beam}$	Transformed section with measured $E_{c,\ beam}$
	$A_{composite}$	Composite section with gross section	Composite section with measure $E_{c,\ beam}$
	$I_{composite}$	Composite section with gross section	Composite section with measure $E_{c,\ beam}$
	$y_{bot,\ composite}$	Composite section with gross section	Composite section with measure $E_{c,\ beam}$
Dead loads and Mid-span Moments	$w_{beam\ self\text{-}wt}$	Calculated based on design	Actual concrete and steel
	$w_{CIP\ deck}$	Calculated based on design	Actual concrete and steel
	$w_{composite\ DL}$	Uniform composite DL, due to barrier curb and FWS.	Uniform composite DL, due to barrier curb and FWS.
	$M_{beam\ self\text{-}wt}$	$wL^2/8$	$wL^2/8$
	$M_{CIP\ deck}$	$wL^2/8$	$wL^2/8$
	$M_{composite\ DL}$	$wL^2/8$	$wL^2/8$
Structural Layout, Geometry	L(beam)	Length specified in drawings	Length specified in drawings
	L(bearings)	Length specified in drawings	Length specified in drawings
	Beam spacing	Width specified in drawings.	Width specified in drawings.
	Beam Gap	Width specified in drawings.	Measured width in field
	Deck thickness	Specified in drawings.	Measured thickness in field

Table D.2. Parameters for Girder B13

	Parameter	Unit	Design	Measured
Material Properties	$f'_{ci,\ beam}$	*psi*	7,542 (52 MPa)	10524
	$f'_{c,\ beam}$	*psi*	10,153 (70 MPa)	11647
	$f'_{c,\ CIP\ deck}$	*psi*	4,016 (28 MPa)	5804
	$E_{ci,\ beam}$	*ksi*	4474	6184
	$E_{c,\ beam}$	*ksi*	5030	6775
	$E_{c,\ CIP\ deck}$	*ksi*	3632	5647
	ρ_{beam}	*pcf*	150	150
	$\rho_{CIP\ deck}$	*pcf*	150	150
Section Properties	$A_{\ beam\ (untransformed)}$	in^2	310.6	310.6
	$I_{\ beam\ (untransformed)}$	in^4	33978	33978
	$y_{\ bot,beam\ (untransformed)}$	*in*	14.1	14.1
	$A_{\ beam\ (release)}$	in^2	336.9	333.0
	$I_{\ beam\ (release)}$	in^4	37323	36842
	$y_{\ bot,\ beam\ (release)}$	*in*	13.7	13.7
	$A_{\ beam\ (final)}$	in^2	333.4	331.9
	$I_{\ beam\ (final)}$	in^4	36891	36704
	$y_{\ bot,\ beam\ (final)}$	*in*	13.7	13.8
	$A_{\ composite}$	in^2	999.3	1054.3
	$I_{\ composite}$	in^4	176779	179964
	$y_{\ bot,\ composite}$	*in*	30.2	30.6
Dead loads and Mid-span Moments	$w_{\ beam\ self\text{-}wt}$	*kip/ft*	0.324	0.324
	$w_{\ CIP\ deck}$	*kip/ft*	1.239	1.239
	$w_{\ composite\ DL\ (incl.\ rail)}$	*kip/ft*	0.529	0.529
	$M_{\ beam\ self\text{-}wt}$	*ft-kips*	98.6	98.6
	$M_{\ CIP\ deck}$	*ft-kips*	376.9	376.9
	$M_{\ composite\ DL\ (incl.\ rail)}$	*ft-kips*	160.9	160.9
Structural Layout and Geometry	L(beam)	*ft*	50.26 (15.320 m)	50.26 (15.320 m)
	L (center to center bearings)	*ft*	49.33 (15.035 m)	49.33 (15.035 m)
	Beam spacing	*in.*	10.83 (3.300 m)	10.83 (3.300 m)
	Gap between beams	*in.*	7.09 (180 mm)	7.09 (180 mm)
	Thickness of CIP deck	*in.*	9.06 (230 mm)	9.06 (230 mm)

Note:
1 in = 25.4 mm;
1 ksi = 6.895 MPa

Table D.3. Construction of Girder B13

Beam Type	Type 2, group 2	
Section Type	I	**Notes:**
Strand Size	0.6 in	
# of Strands (Pretensioned)	18	
cgs of Strands (center; end)	4.22”; 11.22”	
Construction schedule	Time	
Cast (beam concrete placed)	7/3/01 7:30 am	
Forms Stripped	7/5/01 9:00 am	
Released	7/5/01 2:00 pm	
Erected	7/23/01	
Deck Cast	9/11/01	
Safety Barrier Curb Cast	N/A	

Table D.4. Parameters for Girder B14

	Parameter	Unit	Design	Measured
Material Properties	$f'_{ci,\ beam}$	*psi*	7,542 (52 MPa)	10524
	$f'_{c,\ beam}$	*psi*	10,153 (70 MPa)	11647
	$f'_{c,\ CIP\ deck}$	*psi*	4,016 (28 MPa)	5804
	$E_{ci,\ beam}$	*ksi*	4474	6184
	$E_{c,\ beam}$	*ksi*	5030	6775
	$E_{c,\ CIP\ deck}$	*ksi*	3632	5647
	ρ_{beam}	*pcf*	150	150
	$\rho_{CIP\ deck}$	*pcf*	150	150
Section Properties	$A_{beam\ (untransformed)}$	in^2	310.6	310.6
	$I_{beam\ (untransformed)}$	in^4	33978	33978
	$y_{bot,beam\ (untransformed)}$	*in*	14.1	14.1
	$A_{beam\ (release)}$	in^2	336.9	333.0
	$I_{beam\ (release)}$	in^4	37323	36842
	$y_{bot,\ beam\ (release)}$	*in*	13.7	13.7
	$A_{beam\ (final)}$	in^2	333.4	331.9
	$I_{beam\ (final)}$	in^4	36891	36704
	$y_{bot,\ beam\ (final)}$	*in*	13.7	13.8
	$A_{composite}$	in^2	973.9	1026.7
	$I_{composite}$	in^4	174778	178009
	$y_{bot,\ composite}$	*in*	29.9	30.4
Dead loads and Mid-span Moments	$w_{beam\ self\text{-}wt}$	*kip/ft*	0.324	0.324
	$w_{CIP\ deck}$	*kip/ft*	1.075	1.075
	$w_{composite\ DL\ (incl.\ rail)}$	*kip/ft*	0.529	0.529
	$M_{beam\ self\text{-}wt}$	*ft-kips*	98.6	98.6
	$M_{CIP\ deck}$	*ft-kips*	327.0	327.0
	$M_{composite\ DL\ (incl.\ rail)}$	*ft-kips*	160.9	160.9
Structural Layout and Geometry	L(beam)	*ft*	50.26 (15.320 m)	50.26 (15.320 m)
	L (center to center bearings)	*ft*	49.33 (15.035 m)	49.33 (15.035 m)
	Beam spacing	*in.*	10.83 (3.300 m)	10.83 (3.300 m)
	Gap between beams	*in.*	7.09 (180 mm)	7.09 (180 mm)
	Thickness of CIP deck	*in.*	9.06 (230 mm)	9.06 (230 mm)

Note:
1 in = 25.4 mm;
1 ksi = 6.895 MPa

Table D.5. Construction of Girder B14

Beam Type	Type 2, group 2	
Section Type	I	**Notes:**
Strand Size	0.6 in	
# of Strands (Pretensioned)	18	
cgs of Strands (center; end)	4.22”; 11.22”	
Construction schedule	Time	
Cast (beam concrete placed)	7/3/01 7:30 am	
Forms Stripped	7/5/01 9:00 am	
Released	7/5/01 2:00 pm	
Erected	7/23/01	
Deck Cast	9/11/01	
Safety Barrier Curb Cast	N/A	

Table D.6. Parameters for Girder B21

	Parameter	Unit	Design	Measured
Material Properties	$f'_{ci,\ beam}$	*psi*	7,542 (52 MPa)	11937
	$f'_{c,\ beam}$	*psi*	10,153 (70 MPa)	12509
	$f'_{c,\ CIP\ deck}$	*psi*	4,016 (28 MPa)	5804
	$E_{ci,\ beam}$	*ksi*	4474	7761
	$E_{c,\ beam}$	*ksi*	5030	7628
	$E_{c,\ CIP\ deck}$	*ksi*	3632	5647
	ρ_{beam}	*pcf*	150	150
	$\rho_{CIP\ deck}$	*pcf*	150	150
Section Properties	$A_{beam\ (untransformed)}$	in^2	310.6	310.6
	$I_{beam\ (untransformed)}$	in^4	33978	33978
	$y_{bot,beam\ (untransformed)}$	*in*	14.1	14.1
	$A_{beam\ (release)}$	in^2	340.5	340.5
	$I_{beam\ (release)}$	in^4	37962	37962
	$y_{bot,\ beam\ (release)}$	*in*	13.7	13.7
	$A_{beam\ (final)}$	in^2	336.6	336.6
	$I_{beam\ (final)}$	in^4	37447	37447
	$y_{bot,\ beam\ (final)}$	*in*	13.7	13.7
	$A_{composite}$	in^2	977.0	977.0
	$I_{composite}$	in^4	176373	176373
	$y_{bot,\ composite}$	*in*	29.9	29.9
Dead loads and Mid-span Moments	$w_{beam\ self\text{-}wt}$	*kip/ft*	0.324	0.324
	$w_{CIP\ deck}$	*kip/ft*	1.075	1.075
	$w_{composite\ DL\ (incl.\ rail)}$	*kip/ft*	0.529	0.529
	$M_{beam\ self\text{-}wt}$	*ft-kips*	98.6	98.6
	$M_{CIP\ deck}$	*ft-kips*	327.0	327.0
	$M_{composite\ DL\ (incl.\ rail)}$	*ft-kips*	160.9	160.9
Structural Layout and Geometry	L(beam)	*ft*	55.18 (16.820 m)	55.18 (16.820 m)
	L (center to center bearings)	*ft*	54.33 (16.560 m)	54.33 (16.560 m)
	Beam spacing	*in.*	10.83 (3.300 m)	10.83 (3.300 m)
	Gap between beams	*in.*	7.09 (180 mm)	7.09 (180 mm)
	Thickness of CIP deck	*in.*	9.06 (230 mm)	9.06 (230 mm)

Note:
1 in = 25.4 mm;
1 ksi = 6.895 MPa

Table D.7. Construction of Girder B21

Beam Type	Type 2, group 3	
Section Type	I	**Notes:**
Strand Size	0.6 in	
# of Strands (Pretensioned)	20	
cgs of Strands (center; end)	4.00”; 8.20”	
Construction schedule	Time	
Cast (beam concrete placed)	6/13/01 7:30 am	
Forms Stripped	6/15/01 9:00 am	
Released	6/15/01 11:00 am	
Erected	7/23/01	
Deck Cast	9/11/01	
Safety Barrier Curb Cast	N/A	

Table D.8. Parameters for Girder B22

	Parameter	Unit	Design	Measured
Material Properties	$f'_{ci,\ beam}$	*psi*	7,542 (52 MPa)	11937
	$f'_{c,\ beam}$	*psi*	10,153 (70 MPa)	12509
	$f'_{c,\ CIP\ deck}$	*psi*	4,016 (28 MPa)	5804
	$E_{ci,\ beam}$	*ksi*	4474	7761
	$E_{c,\ beam}$	*ksi*	5030	7628
	$E_{c,\ CIP\ deck}$	*ksi*	3632	5647
	ρ_{beam}	*pcf*	150	150
	$\rho_{CIP\ deck}$	*pcf*	150	150
Section Properties	$A_{beam\ (untransformed)}$	in^2	310.6	310.6
	$I_{beam\ (untransformed)}$	in^4	33978	33978
	$y_{bot,beam\ (untransformed)}$	*in*	14.1	14.1
	$A_{beam\ (release)}$	in^2	340.5	340.5
	$I_{beam\ (release)}$	in^4	37962	37962
	$y_{bot,\ beam\ (release)}$	*in*	13.7	13.7
	$A_{beam\ (final)}$	in^2	336.6	336.6
	$I_{beam\ (final)}$	in^4	37447	37447
	$y_{bot,\ beam\ (final)}$	*in*	13.7	13.7
	$A_{composite}$	in^2	1002.4	1002.4
	$I_{composite}$	in^4	178399	178399
	$y_{bot,\ composite}$	*in*	30.1	30.1
Dead loads and Mid-span Moments	$w_{beam\ self\text{-}wt}$	*kip/ft*	0.324	0.324
	$w_{CIP\ deck}$	*kip/ft*	1.239	1.239
	$w_{composite\ DL\ (incl.\ rail)}$	*kip/ft*	0.529	0.529
	$M_{beam\ self\text{-}wt}$	*ft-kips*	98.6	98.6
	$M_{CIP\ deck}$	*ft-kips*	376.9	376.9
	$M_{composite\ DL\ (incl.\ rail)}$	*ft-kips*	160.9	160.9
Structural Layout and Geometry	L(beam)	*ft*	55.18 (16.820 m)	55.18 (16.820 m)
	L (center to center bearings)	*ft*	54.33 (16.560 m)	54.33 (16.560 m)
	Beam spacing	*in.*	10.83 (3.300 m)	10.83 (3.300 m)
	Gap between beams	*in.*	7.09 (180 mm)	7.09 (180 mm)
	Thickness of CIP deck	*in.*	9.06 (230 mm)	9.06 (230 mm)

Note:
1 in = 25.4 mm;
1 ksi = 6.895 MPa

Table D.9. Construction of Girder B22

Beam Type	Type 2, group 3	
Section Type	I	**Notes:**
Strand Size	0.6 in	
# of Strands (Pretensioned)	20	
cgs of Strands (center; end)	4.00”; 8.20”	
Construction schedule	Time	
Cast (beam concrete placed)	6/13/01 7:30 am	
Forms Stripped	6/15/01 9:00 am	
Released	6/15/01 11:00 am	
Erected	7/23/01	
Deck Cast	9/11/01	
Safety Barrier Curb Cast	N/A	

Table D.10. Parameters for Girder B23

	Parameter	Unit	Design	Measured
Material Properties	$f'_{ci,\ beam}$	*psi*	7,542 (52 MPa)	9762
	$f'_{c,\ beam}$	*psi*	10,153 (70 MPa)	12808
	$f'_{c,\ CIP\ deck}$	*psi*	4,016 (28 MPa)	5804
	$E_{ci,\ beam}$	*ksi*	4474	6409
	$E_{c,\ beam}$	*ksi*	5030	6534
	$E_{c,\ CIP\ deck}$	*ksi*	3632	5647
	ρ_{beam}	*pcf*	150	150
	$\rho_{CIP\ deck}$	*pcf*	150	150
Section Properties	$A_{beam\ (untransformed)}$	in^2	310.6	310.6
	$I_{beam\ (untransformed)}$	in^4	33978	33978
	$y_{bot,beam\ (untransformed)}$	*in*	14.1	14.1
	$A_{beam\ (release)}$	in^2	340.5	337.0
	$I_{beam\ (release)}$	in^4	37962	37513
	$y_{bot,\ beam\ (release)}$	*in*	13.7	13.7
	$A_{beam\ (final)}$	in^2	336.6	333.7
	$I_{beam\ (final)}$	in^4	37447	37075
	$y_{bot,\ beam\ (final)}$	*in*	13.7	13.7
	$A_{composite}$	in^2	1002.4	1028.6
	$I_{composite}$	in^4	178399	178981
	$y_{bot,\ composite}$	*in*	30.1	30.4
Dead loads and Mid-span Moments	$w_{beam\ self\text{-}wt}$	*kip/ft*	0.324	0.324
	$w_{CIP\ deck}$	*kip/ft*	1.239	1.239
	$w_{composite\ DL\ (incl.\ rail)}$	*kip/ft*	0.529	0.529
	$M_{beam\ self\text{-}wt}$	*ft-kips*	98.6	98.6
	$M_{CIP\ deck}$	*ft-kips*	376.9	376.9
	$M_{composite\ DL\ (incl.\ rail)}$	*ft-kips*	160.9	160.9
Structural Layout and Geometry	L(beam)	*ft*	55.18 (16.820 m)	55.18 (16.820 m)
	L (center to center bearings)	*ft*	54.33 (16.560 m)	54.33 (16.560 m)
	Beam spacing	*in.*	10.83 (3.300 m)	10.83 (3.300 m)
	Gap between beams	*in.*	7.09 (180 mm)	7.09 (180 mm)
	Thickness of CIP deck	*in.*	9.06 (230 mm)	9.06 (230 mm)

Note:
1 in = 25.4 mm;
1 ksi = 6.895 MPa

Table D.11. Construction of Girder B23

Beam Type	Type 2, group 3	
Section Type	I	**Notes:**
Strand Size	0.6 in	
# of Strands (Pretensioned)	20	
cgs of Strands (center; end)	4.00”; 8.20”	
Construction schedule	Time	
Cast (beam concrete placed)	6/20/01 7:30 am	
Forms Stripped	6/22/01 9:00 am	
Released	6/22/01 1:00 pm	
Erected	7/23/01	
Deck Cast	9/11/01	
Safety Barrier Curb Cast	N/A	

Table D.12. Parameters for Girder B24

	Parameter	Unit	Design	Measured
Material Properties	$f'_{ci,\ beam}$	*psi*	7,542 (52 MPa)	9762
	$f'_{c,\ beam}$	*psi*	10,153 (70 MPa)	12808
	$f'_{c,\ CIP\ deck}$	*psi*	4,016 (28 MPa)	5804
	$E_{ci,\ beam}$	*ksi*	4474	6409
	$E_{c,\ beam}$	*ksi*	5030	6534
	$E_{c,\ CIP\ deck}$	*ksi*	3632	5647
	ρ_{beam}	*pcf*	150	150
	$\rho_{CIP\ deck}$	*pcf*	150	150
Section Properties	$A_{beam\ (untransformed)}$	in^2	310.6	310.6
	$I_{beam\ (untransformed)}$	in^4	33978	33978
	$y_{bot,beam\ (untransformed)}$	*in*	14.1	14.1
	$A_{beam\ (release)}$	in^2	340.5	337.0
	$I_{beam\ (release)}$	in^4	37962	37513
	$y_{bot,\ beam\ (release)}$	*in*	13.7	13.7
	$A_{beam\ (final)}$	in^2	336.6	333.7
	$I_{beam\ (final)}$	in^4	37447	37075
	$y_{bot,\ beam\ (final)}$	*in*	13.7	13.7
	$A_{composite}$	in^2	977.0	1002.1
	$I_{composite}$	in^4	176373	176998
	$y_{bot,\ composite}$	*in*	29.9	30.2
Dead loads and Mid-span Moments	$w_{beam\ self\text{-}wt}$	*kip/ft*	0.324	0.324
	$w_{CIP\ deck}$	*kip/ft*	1.075	1.075
	$w_{composite\ DL\ (incl.\ rail)}$	*kip/ft*	0.529	0.529
	$M_{beam\ self\text{-}wt}$	*ft-kips*	98.6	98.6
	$M_{CIP\ deck}$	*ft-kips*	327.0	327.0
	$M_{composite\ DL\ (incl.\ rail)}$	*ft-kips*	160.9	160.9
Structural Layout and Geometry	L(beam)	*ft*	55.18 (16.820 m)	55.18 (16.820 m)
	L (center to center bearings)	*ft*	54.33 (16.560 m)	54.33 (16.560 m)
	Beam spacing	*in.*	10.83 (3.300 m)	10.83 (3.300 m)
	Gap between beams	*in.*	7.09 (180 mm)	7.09 (180 mm)
	Thickness of CIP deck	*in.*	9.06 (230 mm)	9.06 (230 mm)

Note:
1 in = 25.4 mm;
1 ksi = 6.895 MPa

Table D.13. Construction of Girder B24

Beam Type	Type 2, group 3	
Section Type	I	**Notes:**
Strand Size	0.6 in	After formwork removed, a void near the end of the beam was found due to lack of vibration. The void was patched and has not affected the beam behavior as monitored.
# of Strands (Pretensioned)	20	
cgs of Strands (center; end)	4.00"; 8.20"	
Construction schedule	Time	
Cast (beam concrete placed)	6/20/01 7:30 am	
Forms Stripped	6/22/01 9:00 am	
Released	6/22/01 1:00 pm	
Erected	7/23/01	
Deck Cast	9/11/01	
Safety Barrier Curb Cast	N/A	

APPENDIX E.

CREEP AND SHRINKAGE PLOTS

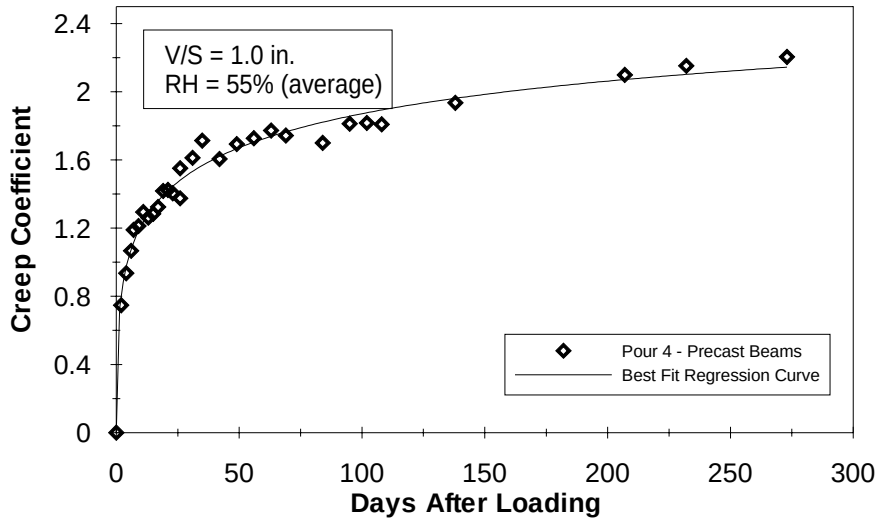

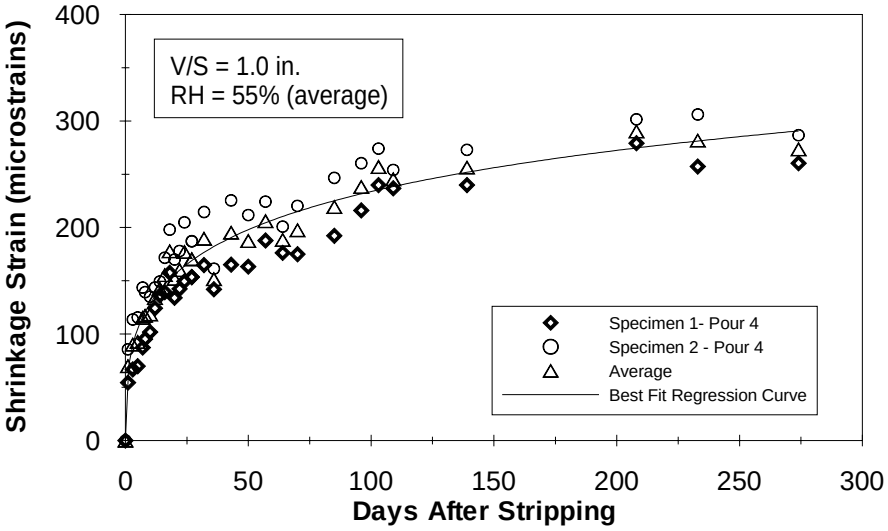

Figure E.1. Creep and Shrinkage of Pour 4 Girder Concrete

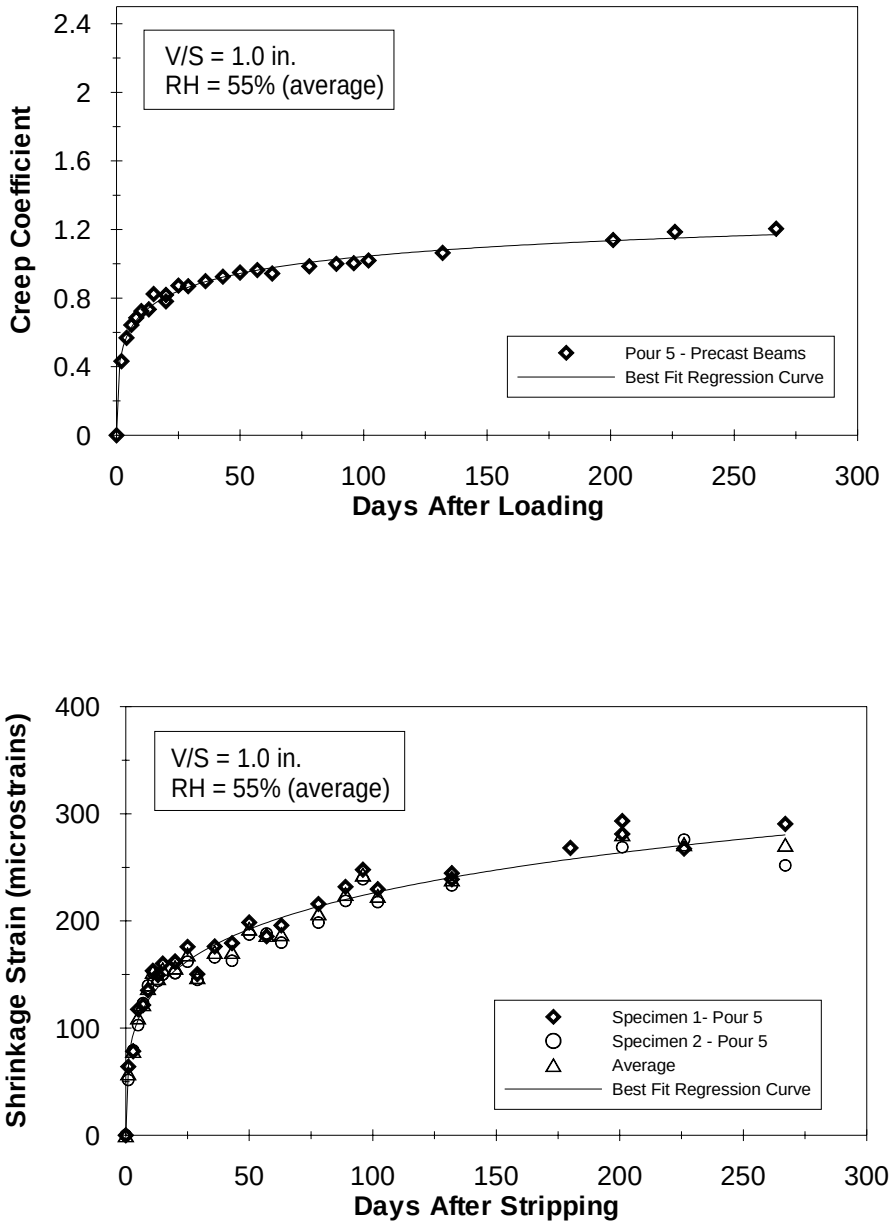

Figure E.2. Creep and Shrinkage of Pour 5 Girder Concrete

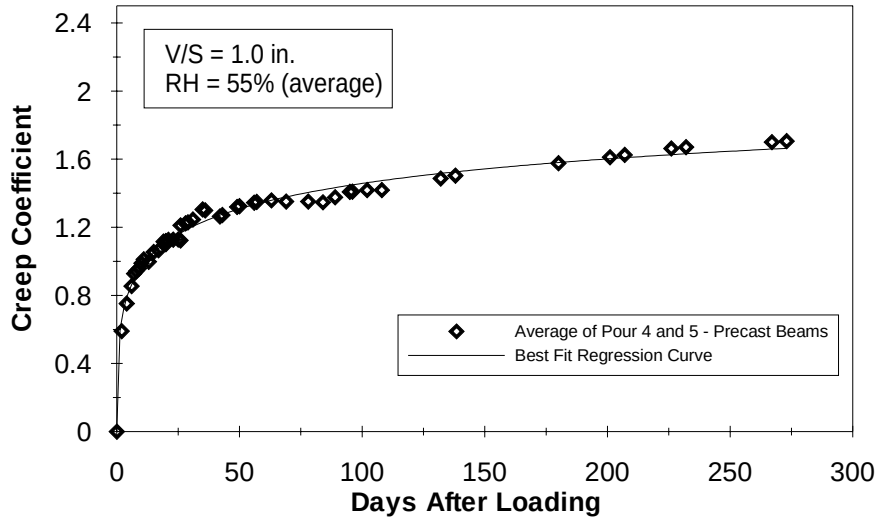

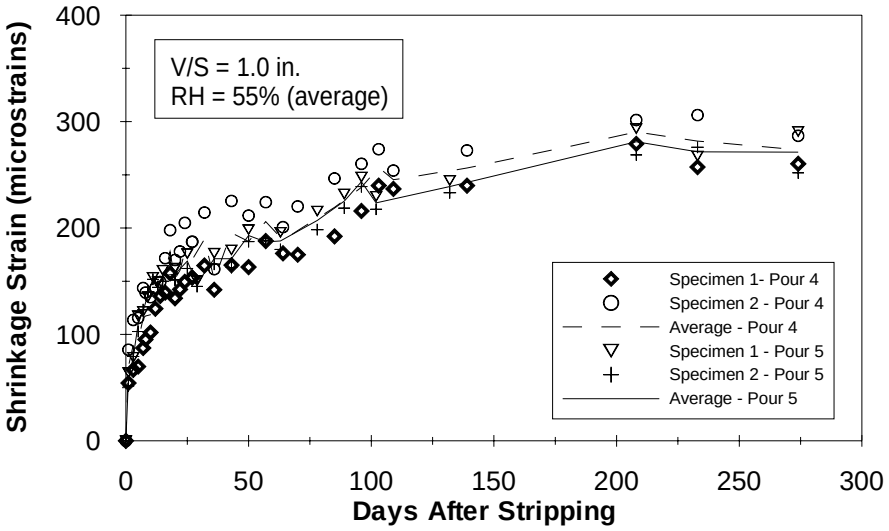

Figure E.3. Average of Creep and Shrinkage for Girder Concrete

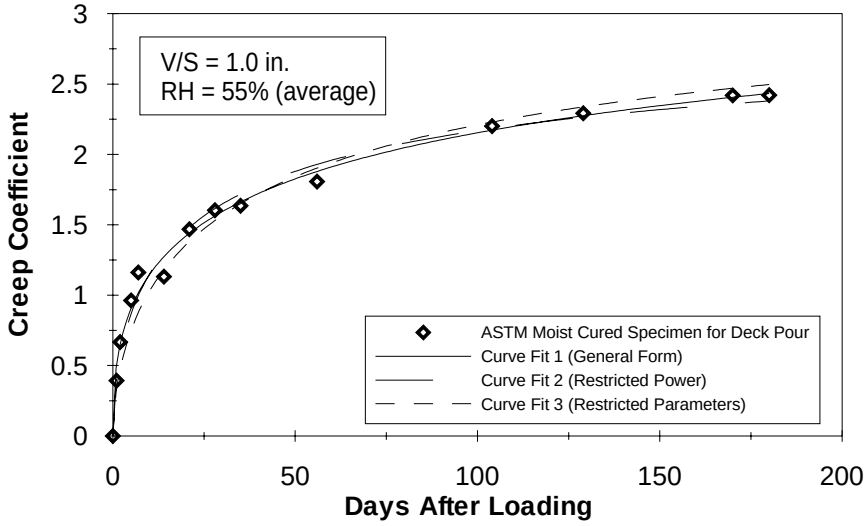

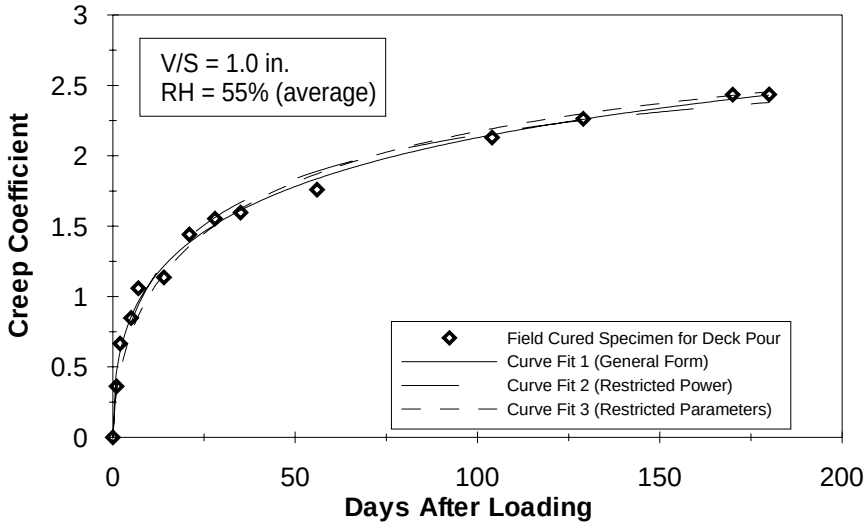

Figure E.4. Creep Coefficient for Deck Concrete

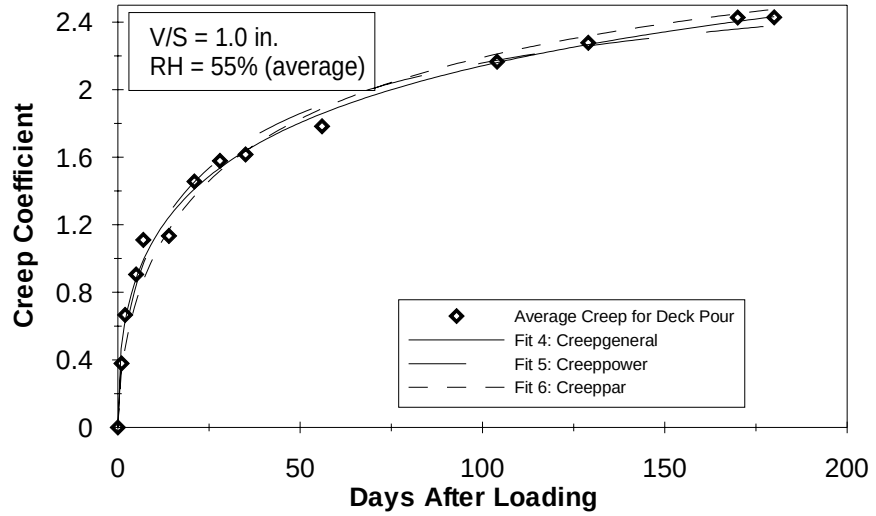

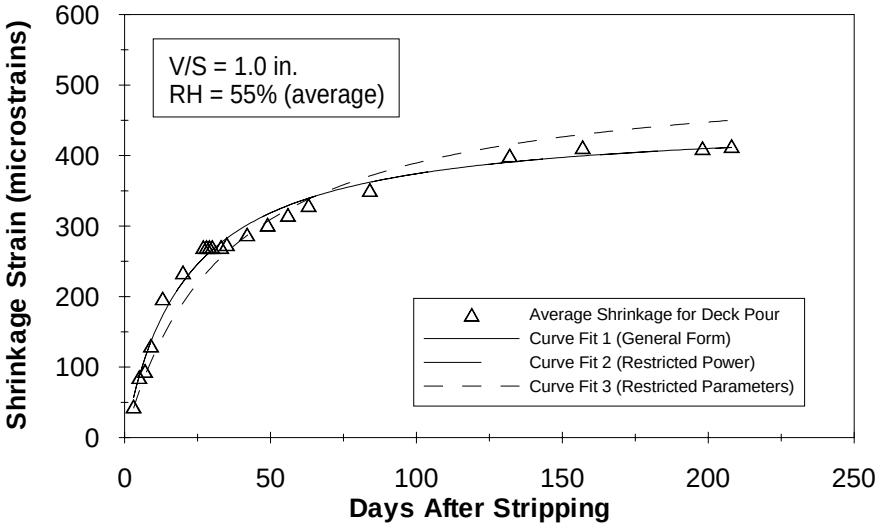

Figure E.5. Creep and Shrinkage of Deck Concrete

APPENDIX F.

BRIDGE TEMPERATURE MEASUREMENT

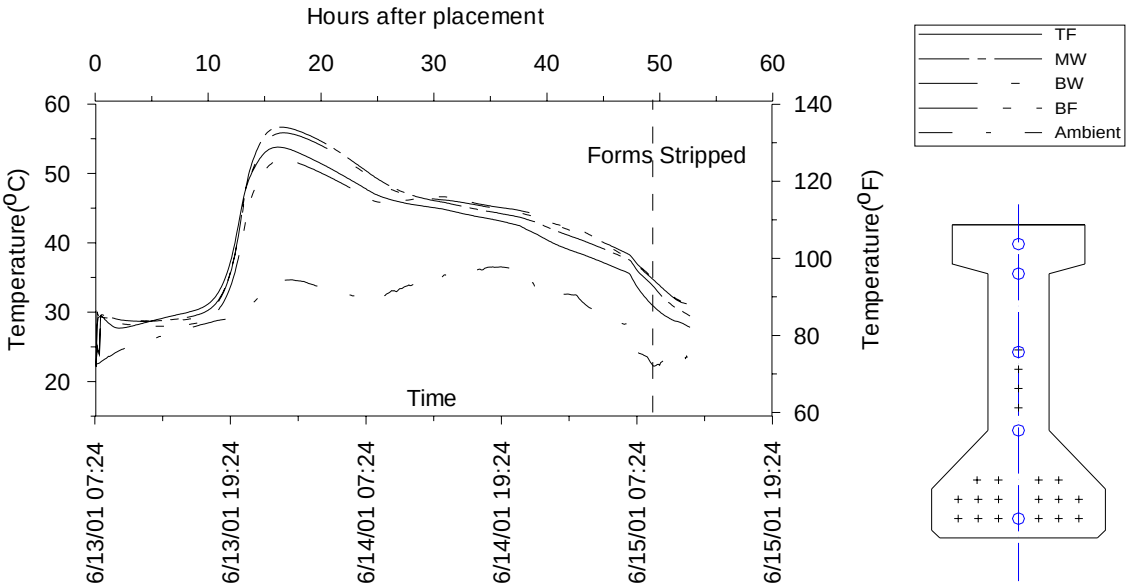

Figure F.1. Measured Hydration Temperatures in Girder B21

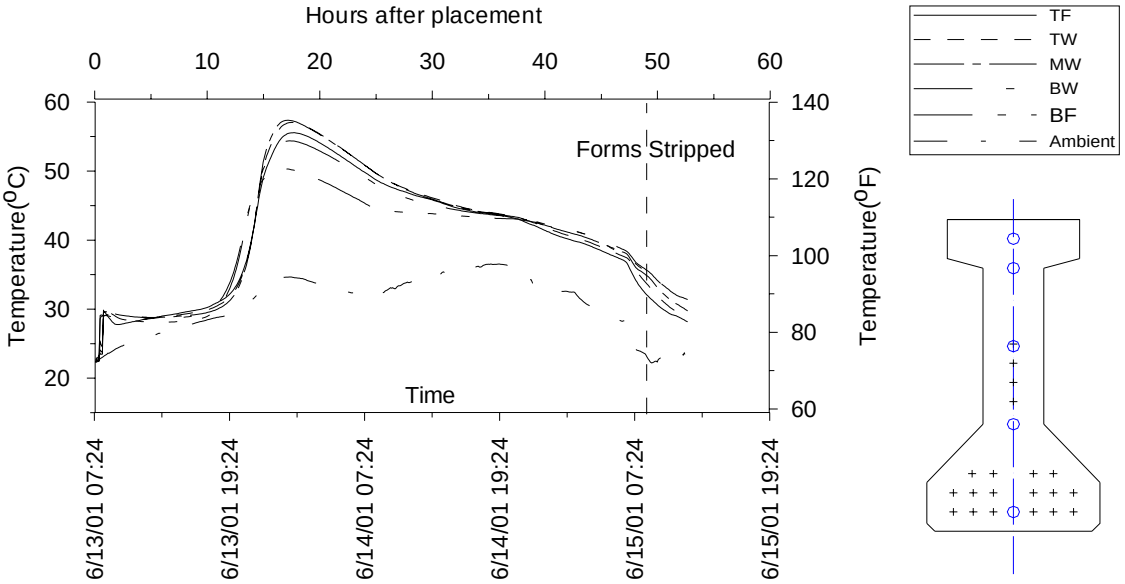

Figure F.2. Measured Hydration Temperatures in Girder B22

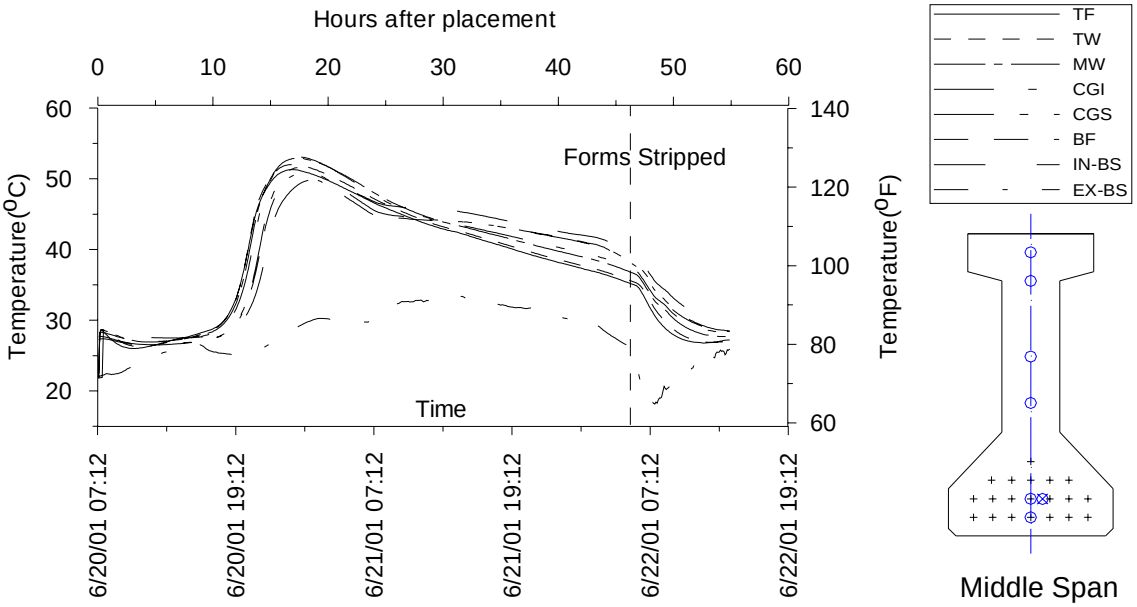

Figure F.3. Measured Hydration Temperatures in Mid-Span Section of Girder B23

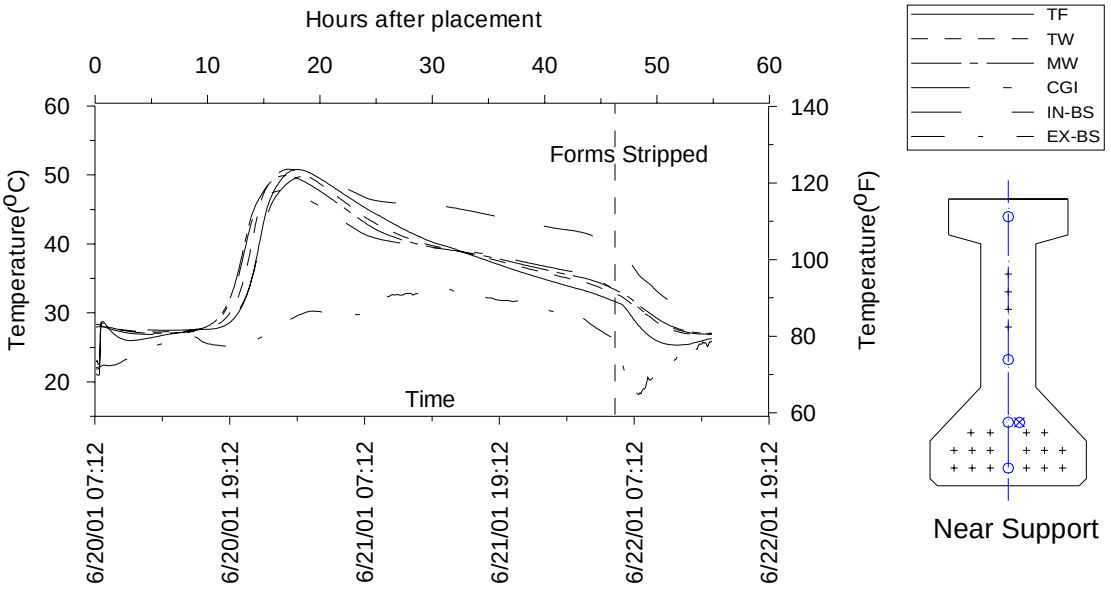

Figure F.4. Measured Hydration Temperatures in Near Support Section of Girder B23

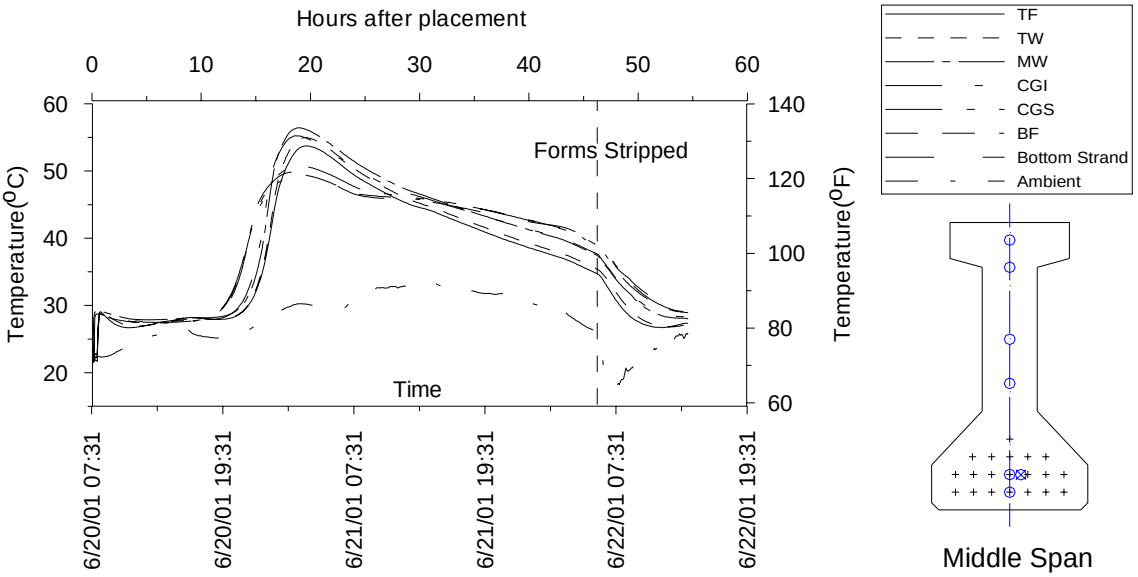

Figure F.5. Measured Hydration Temperatures in Mid-Span Section of Girder B24

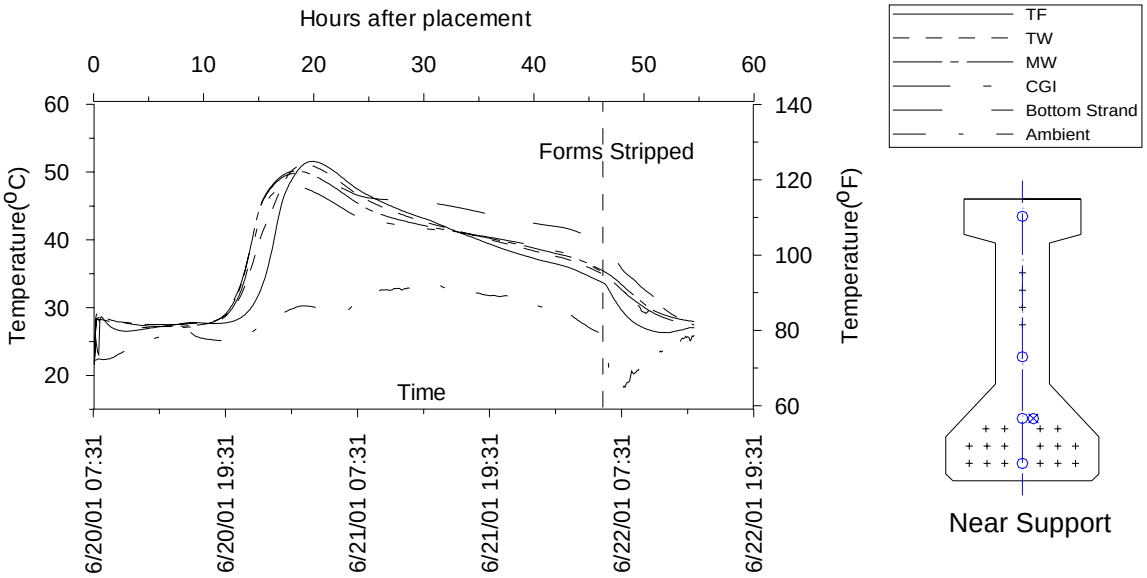

Figure F.6. Measured Hydration Temperatures in Near Support Section of Girder B24

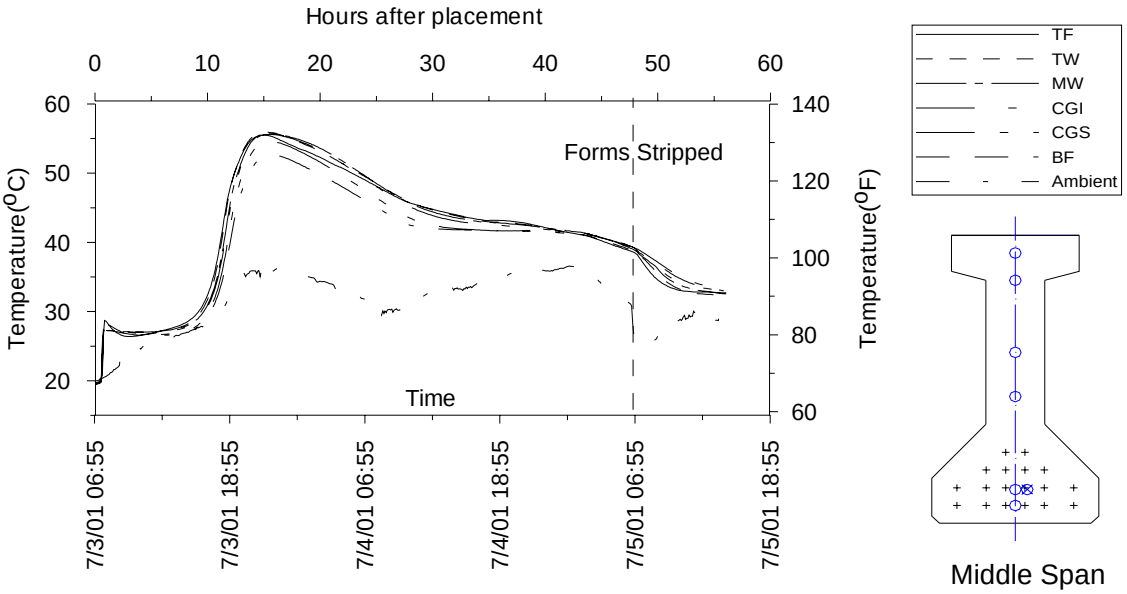

Figure F.7. Measured Hydration Temperatures in Mid-Span Section of Girder B13

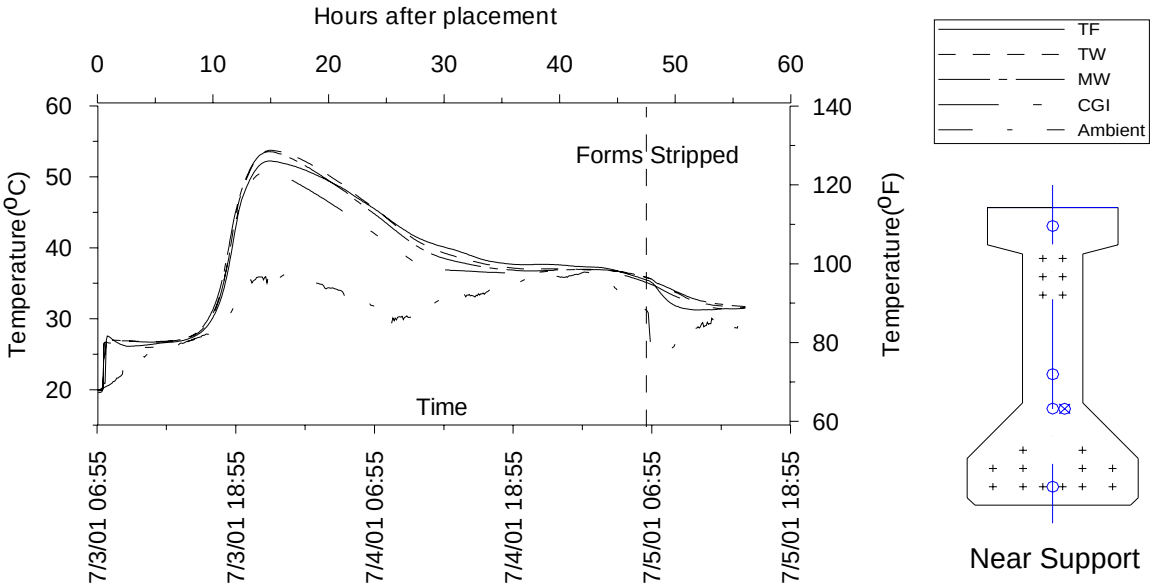

Figure F.8. Measured Hydration Temperatures in Near Support Section of Girder B13

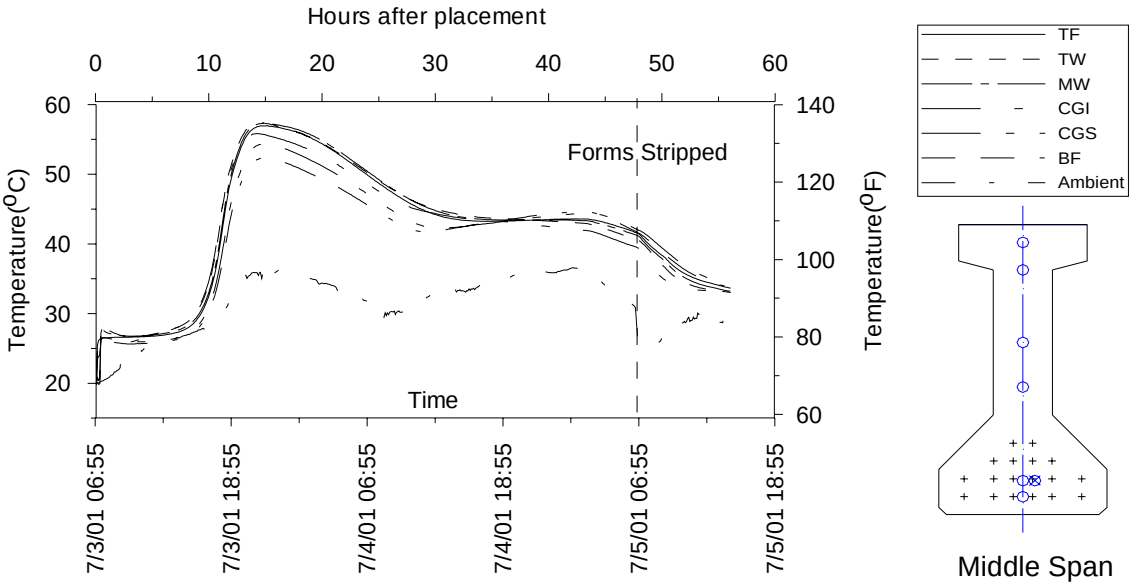

Figure F.9. Measured Hydration Temperatures in Mid-Span Section of Girder B14

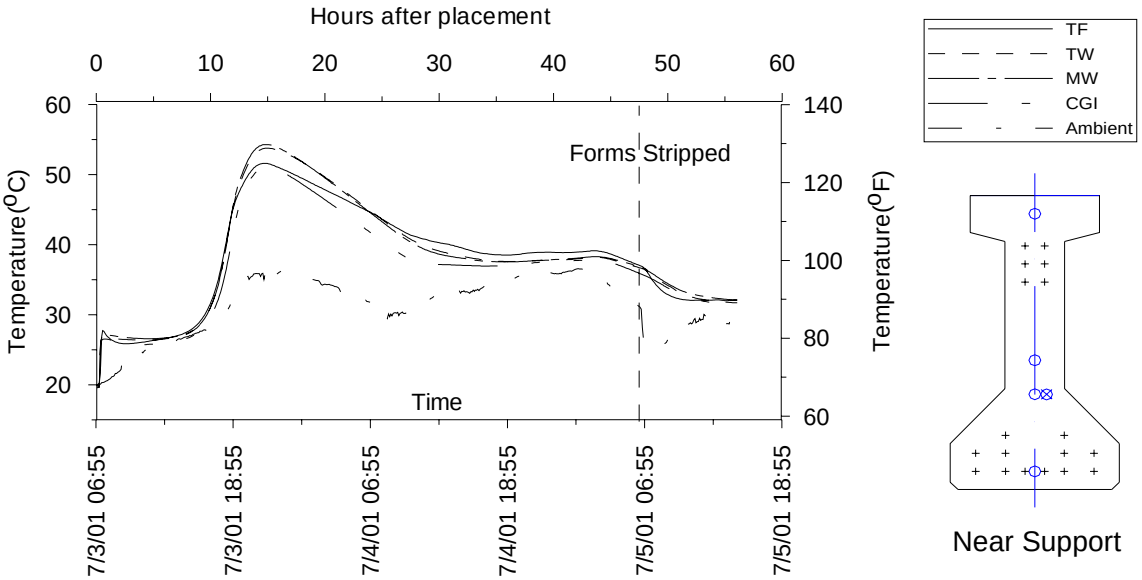

Figure F.10. Measured Hydration Temperatures in Near Support Section of Girder B14

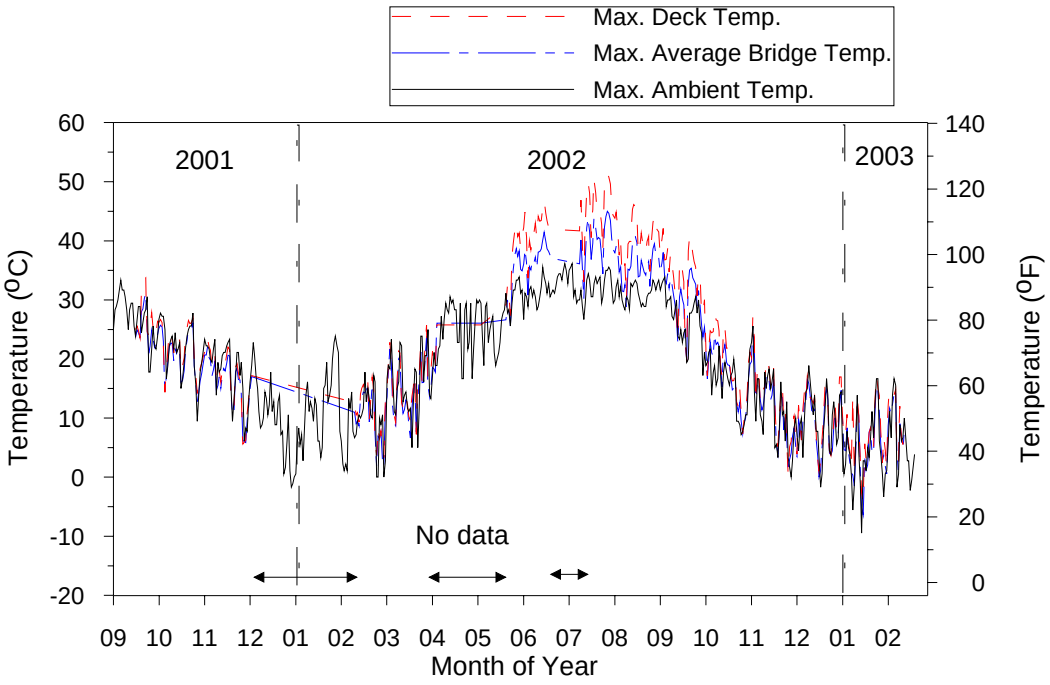

Figure F.11. Maximum Daily Temperature of Composite Girder B13

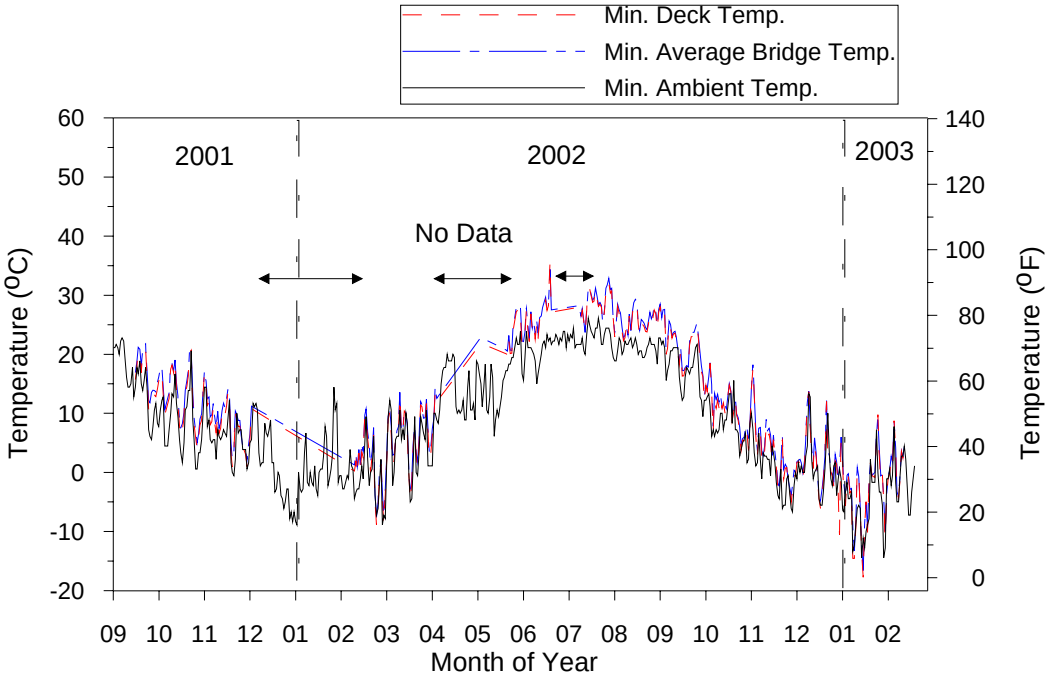

Figure F.12. Minimum Daily Temperature of Composite Girder B13

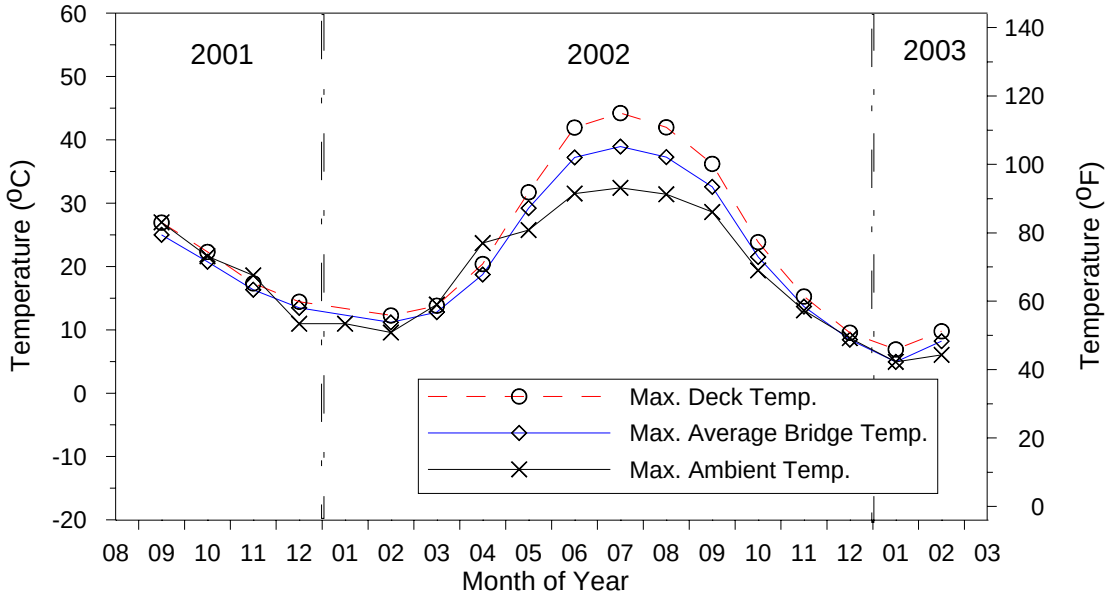

Figure F.13. Average Maximum Daily Temperature by Month of Composite Girder B13

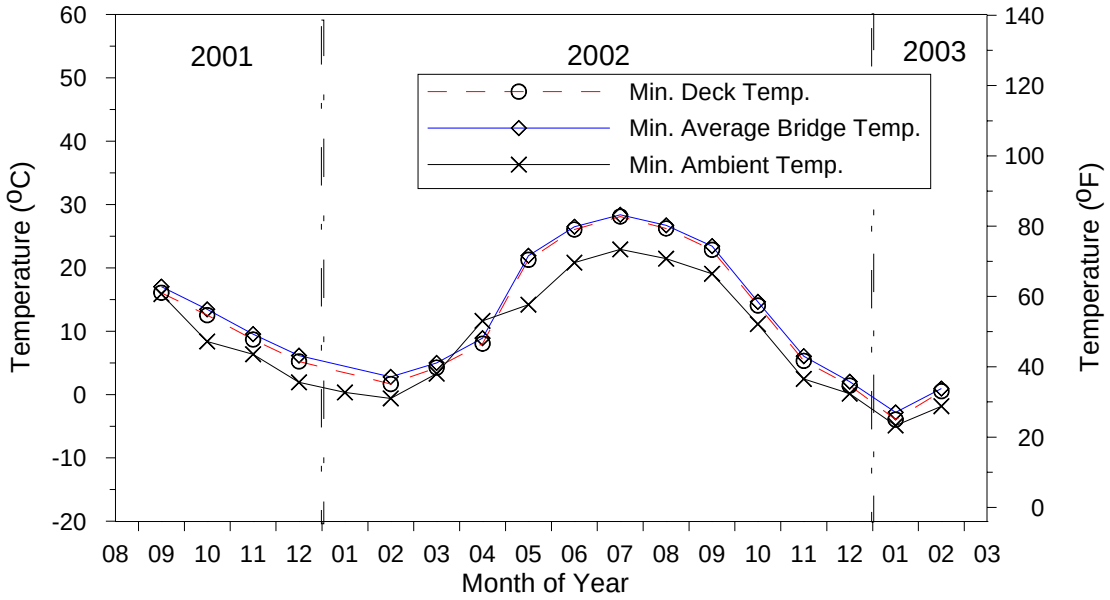

Figure F.14. Average Minimum Daily Temperature by Month of Composite Girder B13

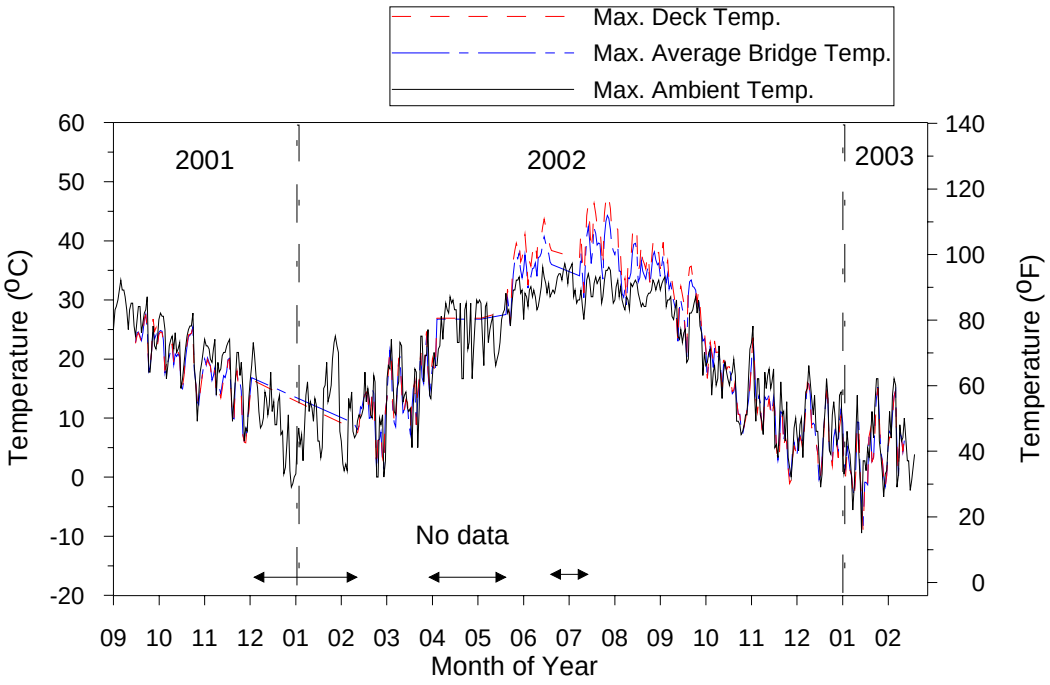

Figure F.15. Maximum Daily Temperature of Composite Girder B14

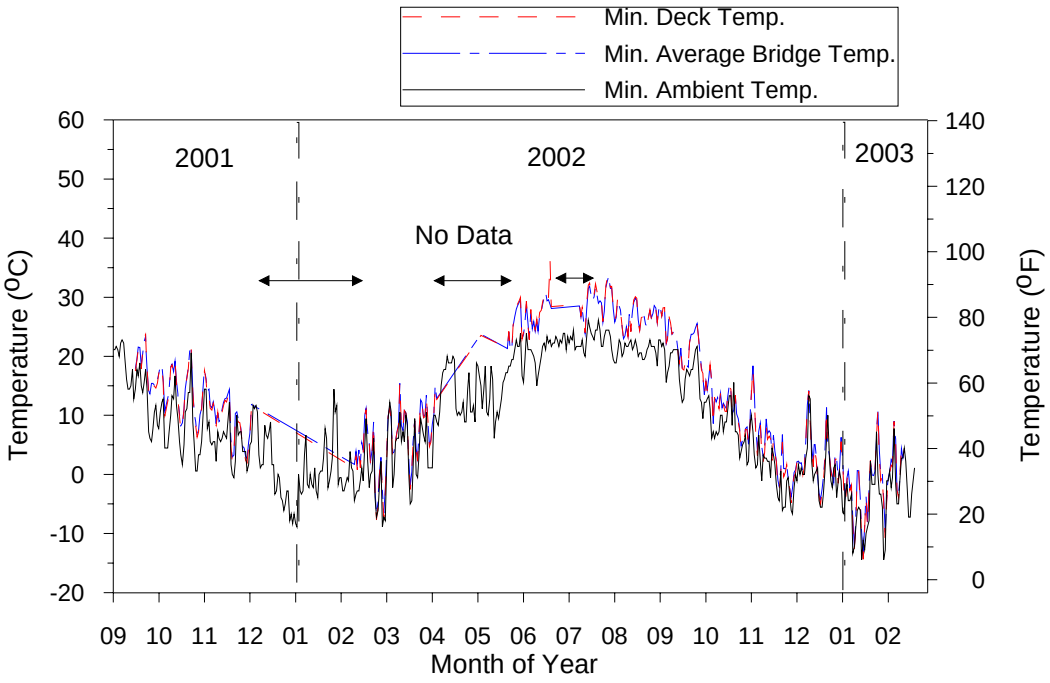

Figure F.16. Minimum Daily Temperature of Composite Girder B14

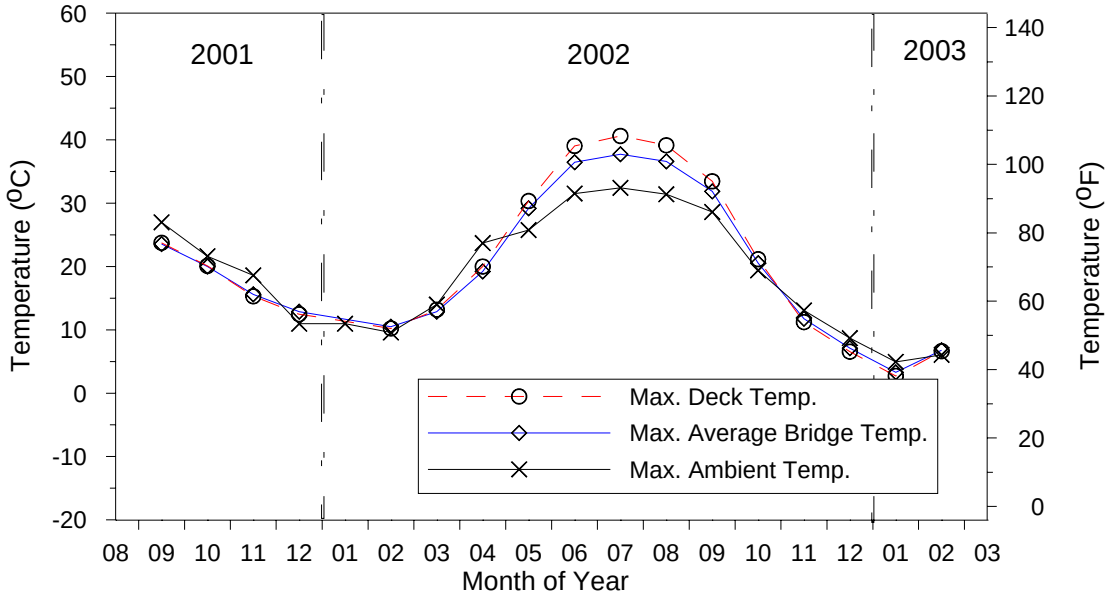

Figure F.17. Average Maximum Daily Temperature by Month of Composite Girder B14

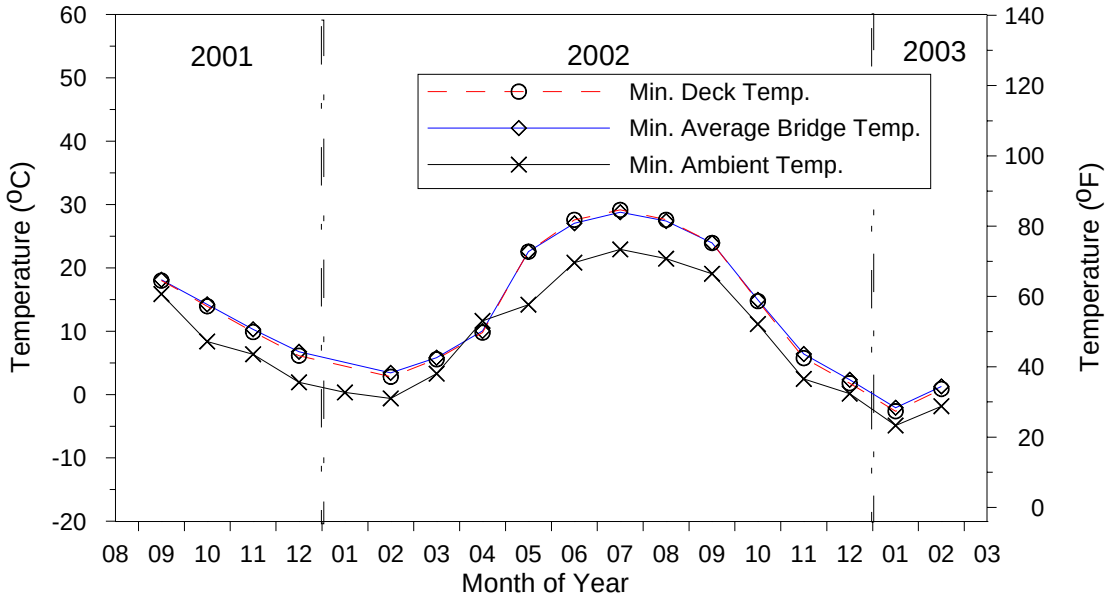

Figure F.18. Average Minimum Daily Temperature by Month of Composite Girder B14

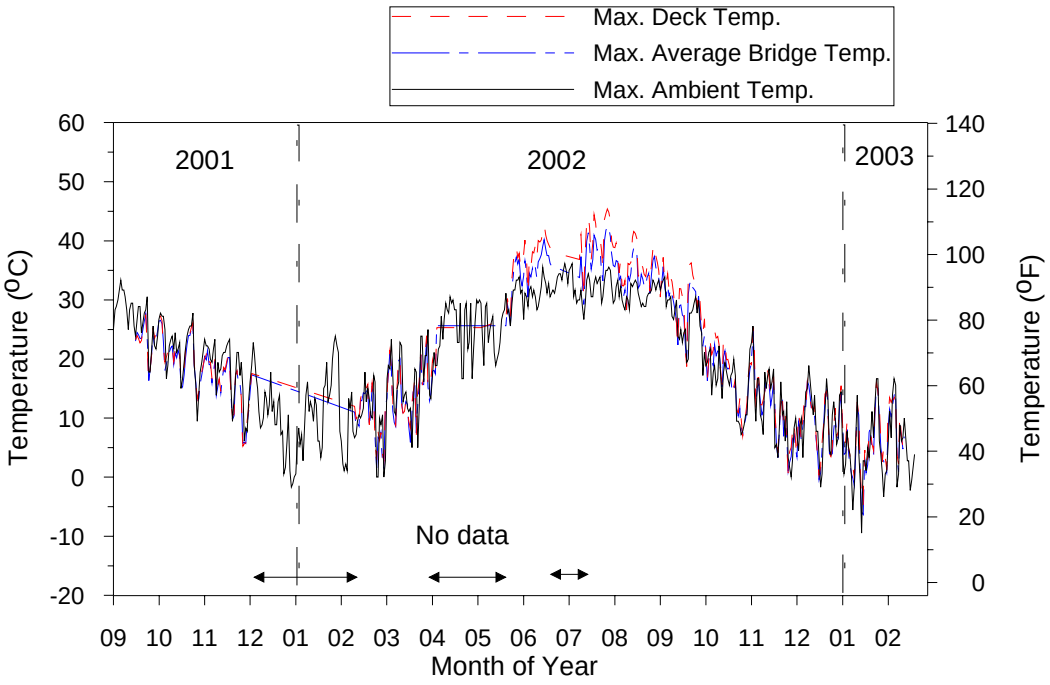

Figure F.19. Maximum Daily Temperature of Composite Girder B23

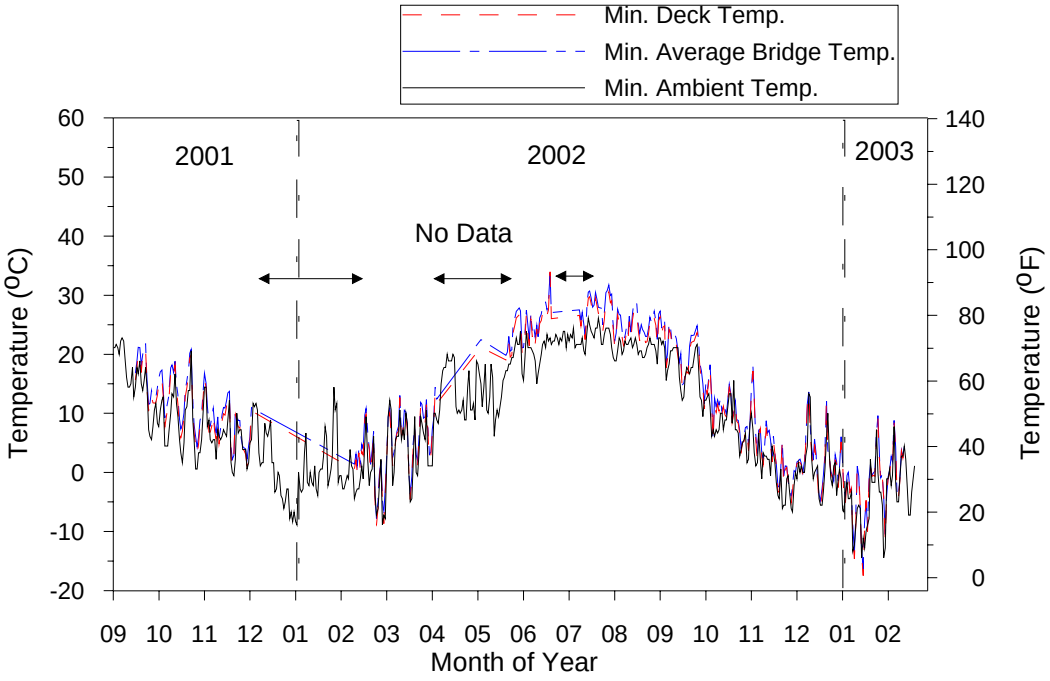

Figure F.20. Minimum Daily Temperature of Composite Girder B23

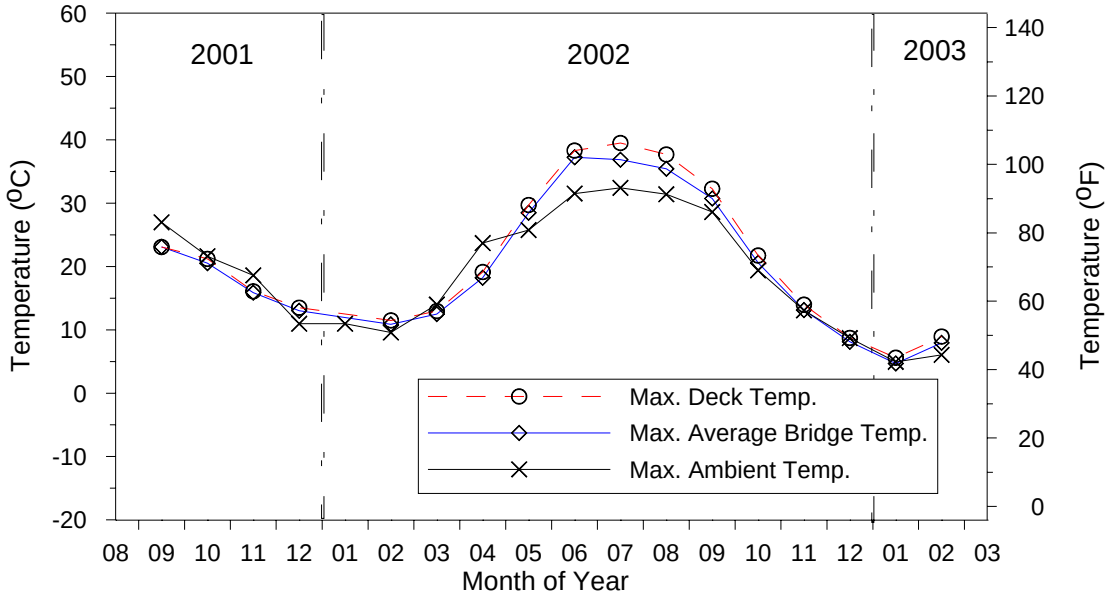

Figure F.21. Average Maximum Daily Temperature by Month of Composite Girder B23

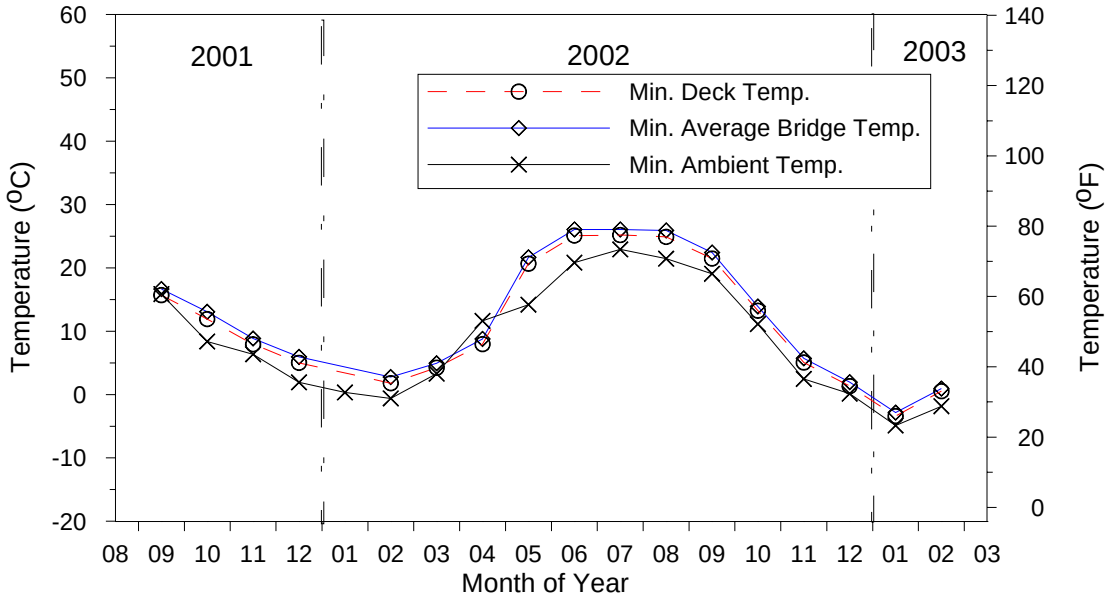

Figure F.22. Average Minimum Daily Temperature by Month of Composite Girder B23

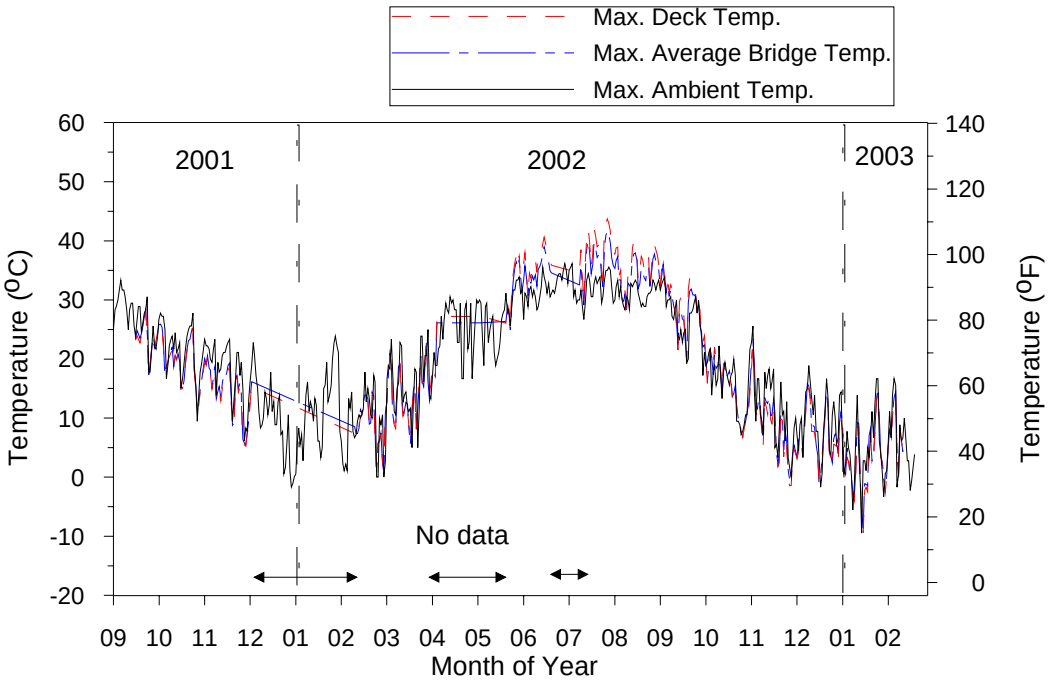

Figure F.23. Maximum Daily Temperature of Composite Girder B24

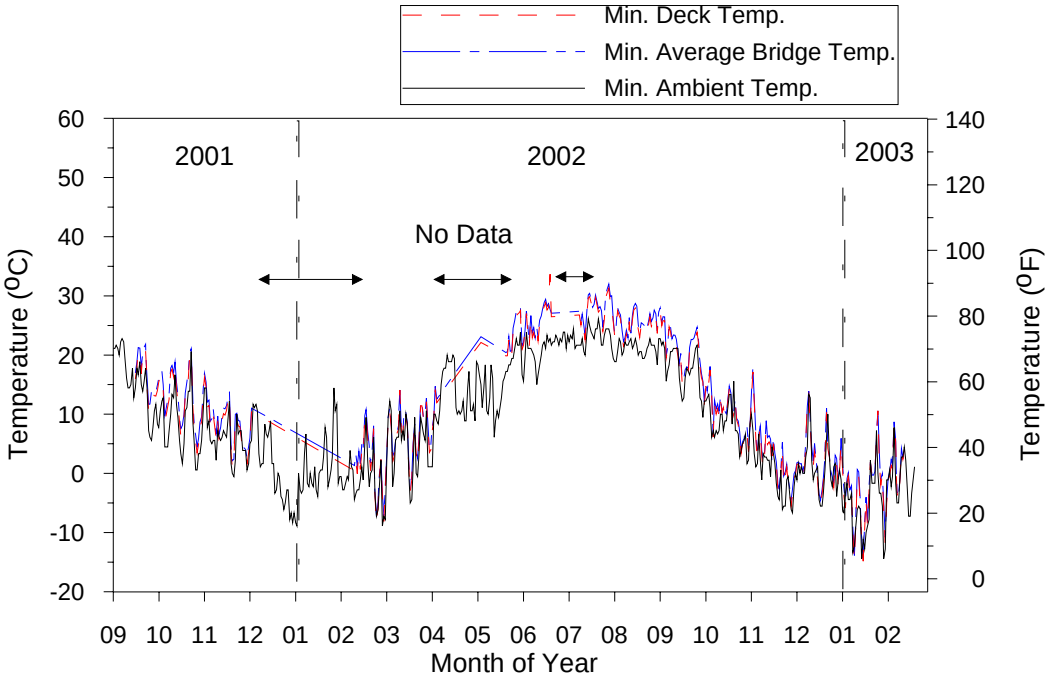

Figure F.24. Minimum Daily Temperature of Composite Girder B24

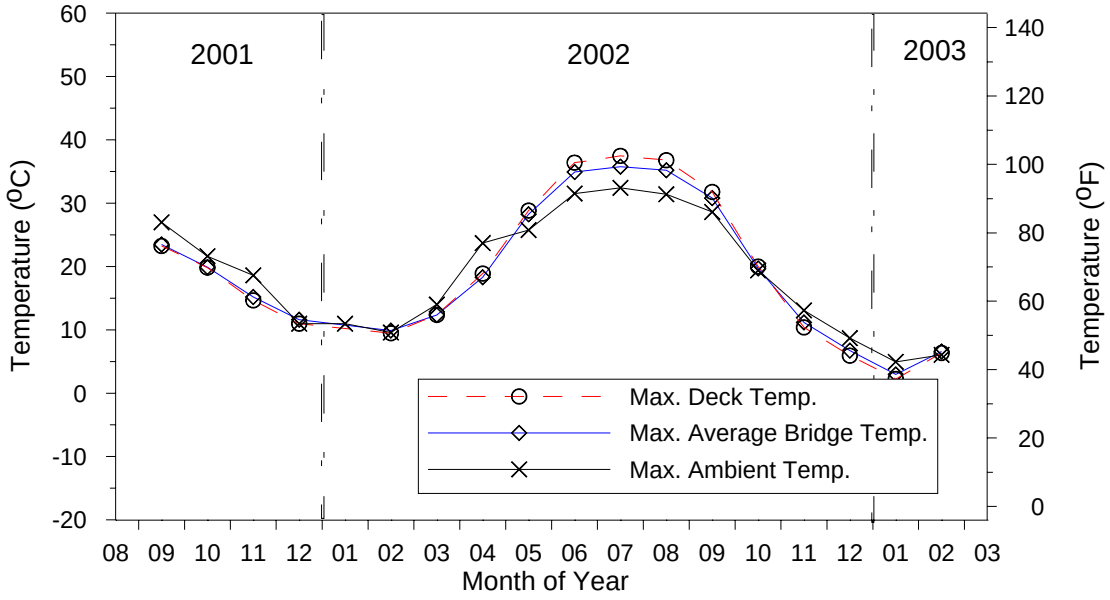

Figure F.25. Average Maximum Daily Temperature by Month of Composite Girder B24

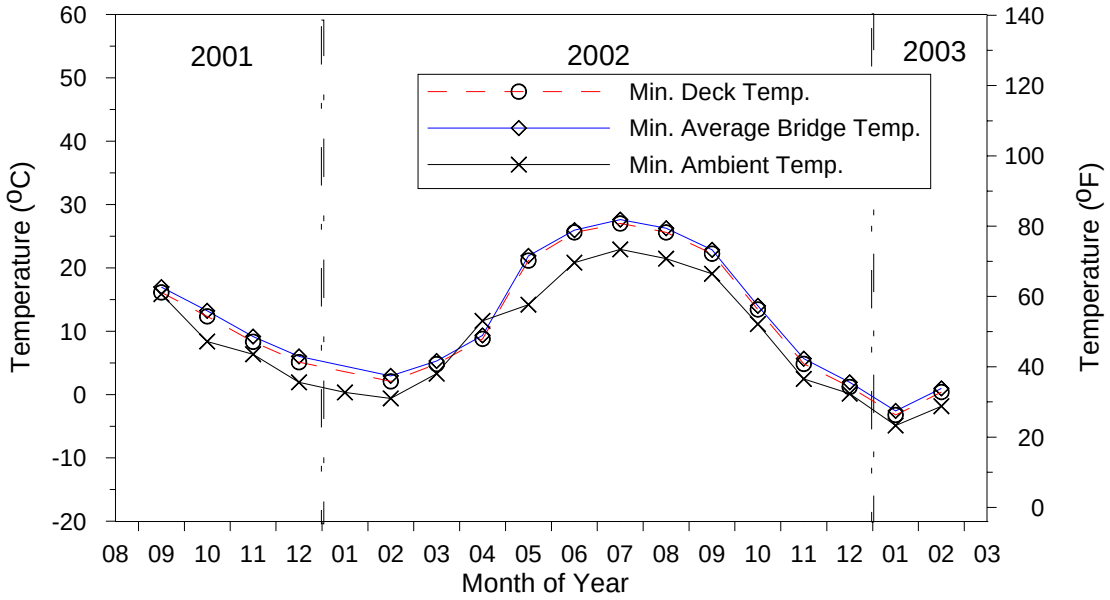

Figure F.26. Average Minimum Daily Temperature by Month of Composite Girder B24

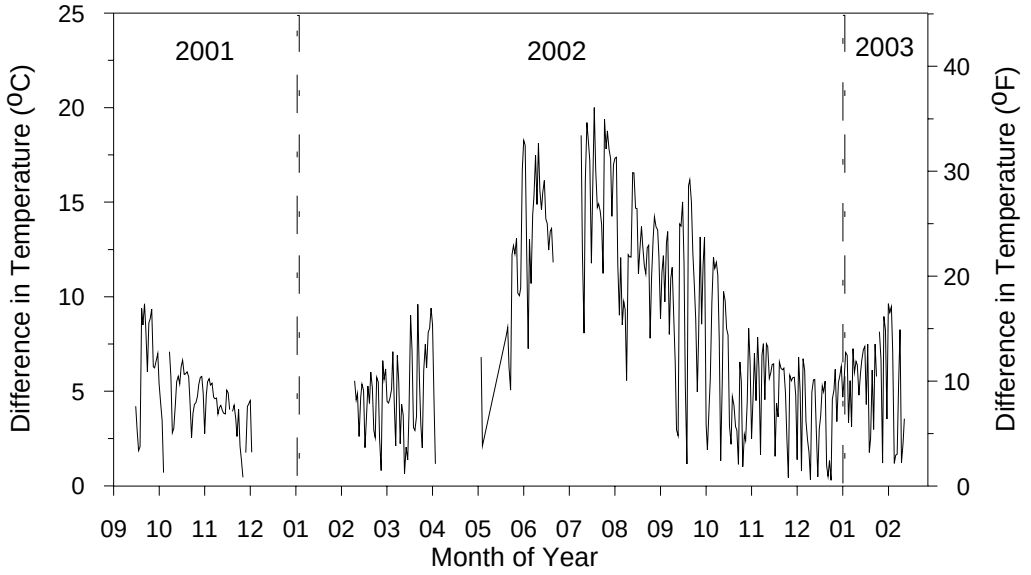

Figure F.27. Maximum Daily Positive Thermal Gradients for Interior Girder B13

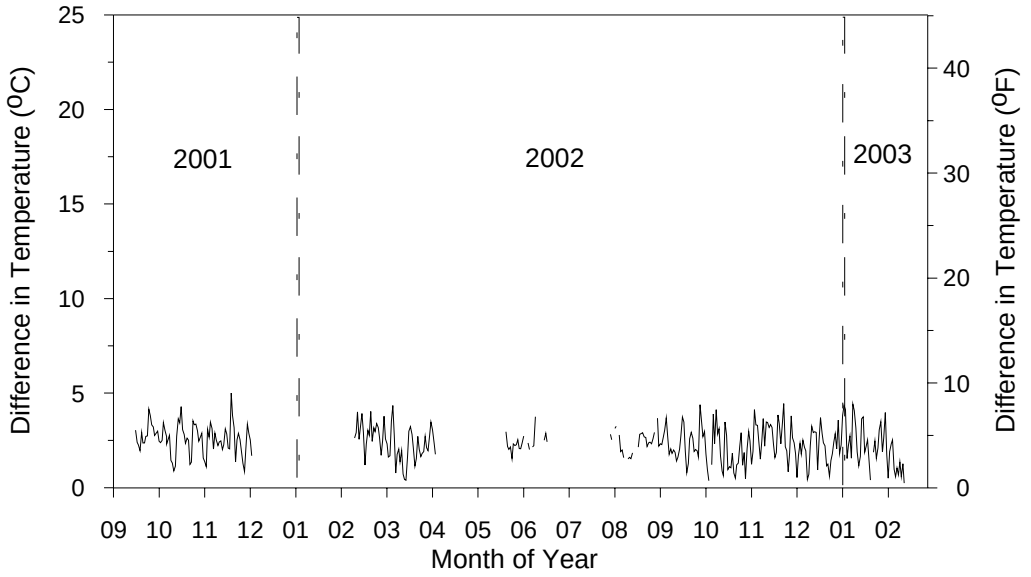

Figure F.28. Maximum Daily Negative Thermal Gradients for Interior Girder B13

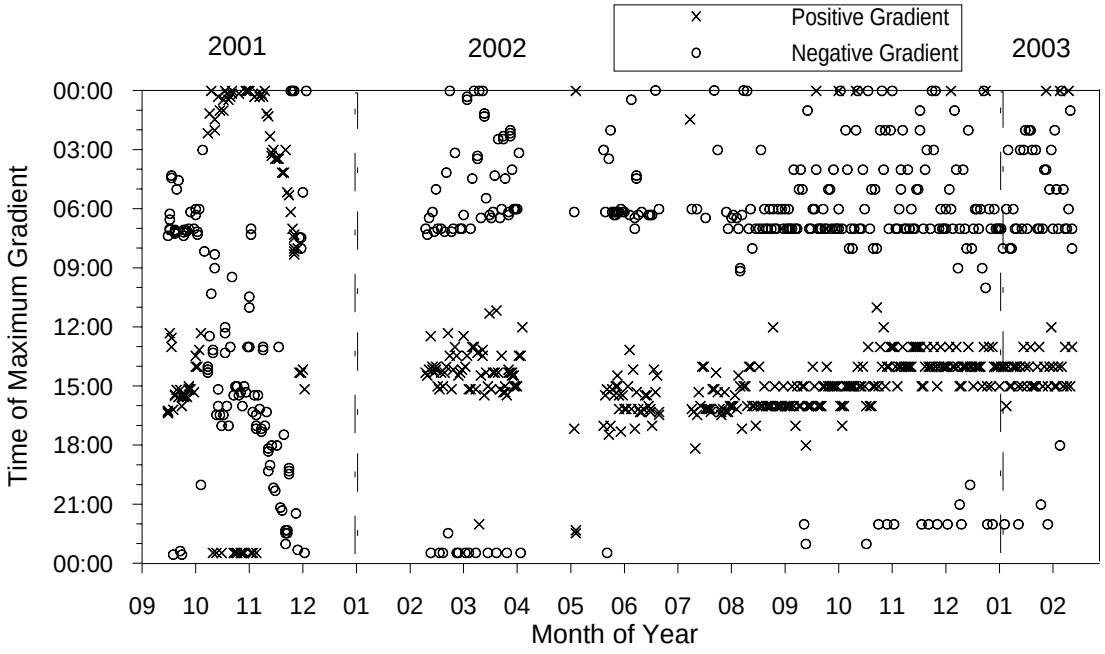

Figure F.29. Time of Maximum Positive and Negative Gradients for Interior Girder B13

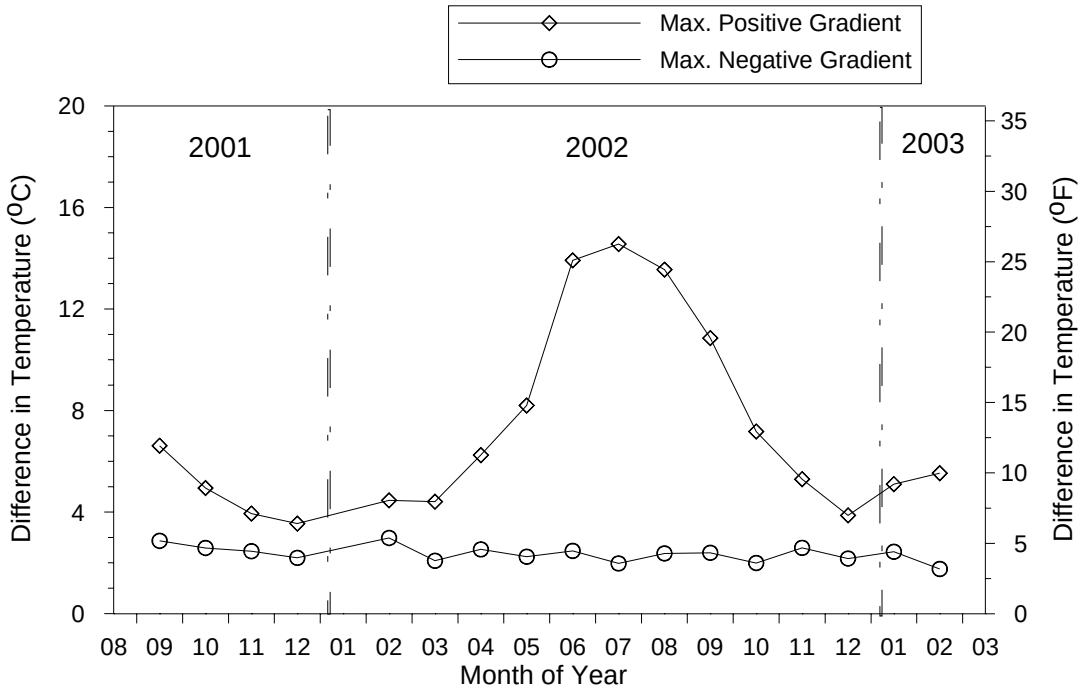

Figure F.30. Average Maximum Daily Gradients by Month for Interior Girder B13

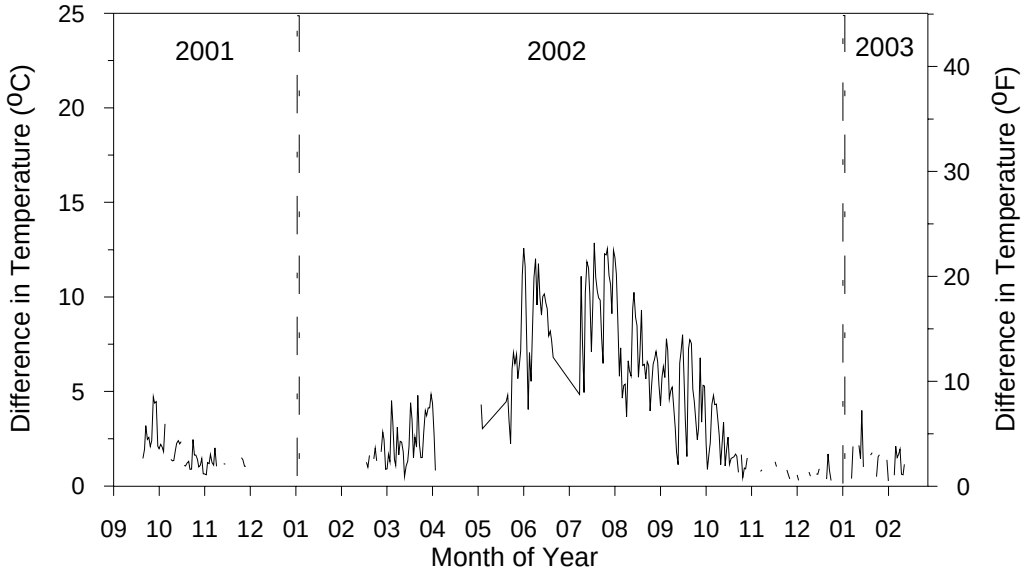

Figure F.31. Maximum Daily Positive Thermal Gradients for Interior Girder B14

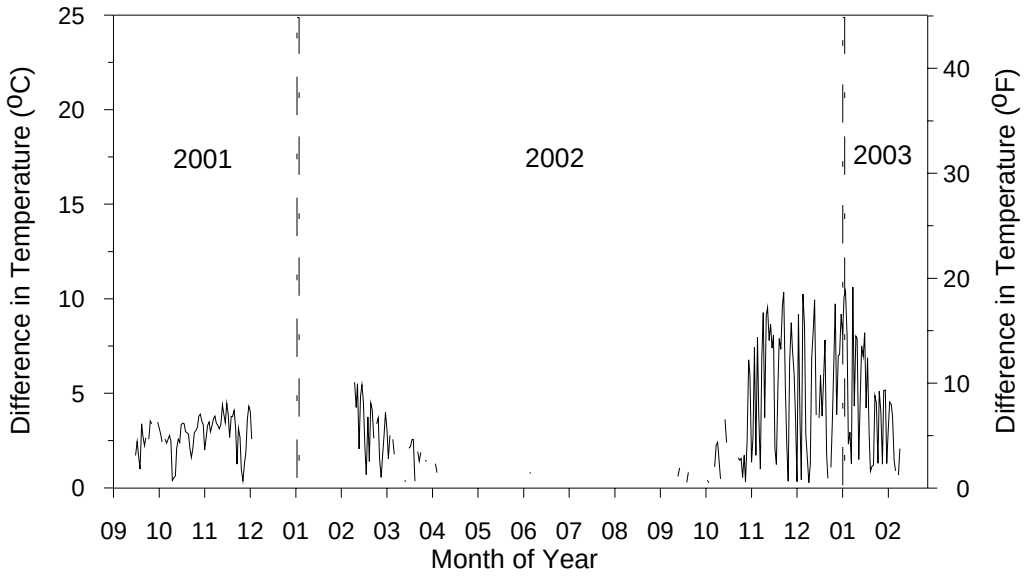

Figure F.32. Maximum Daily Negative Thermal Gradients for Interior Girder B14

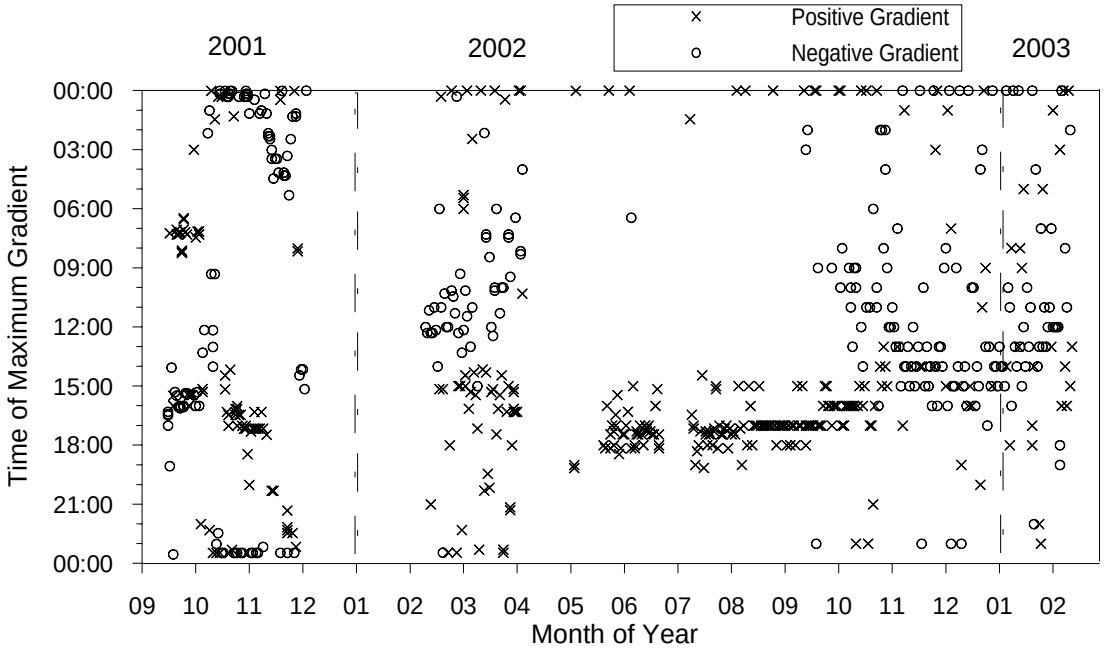

Figure F.33. Time of Maximum Positive and Negative Gradients for Interior Girder B14

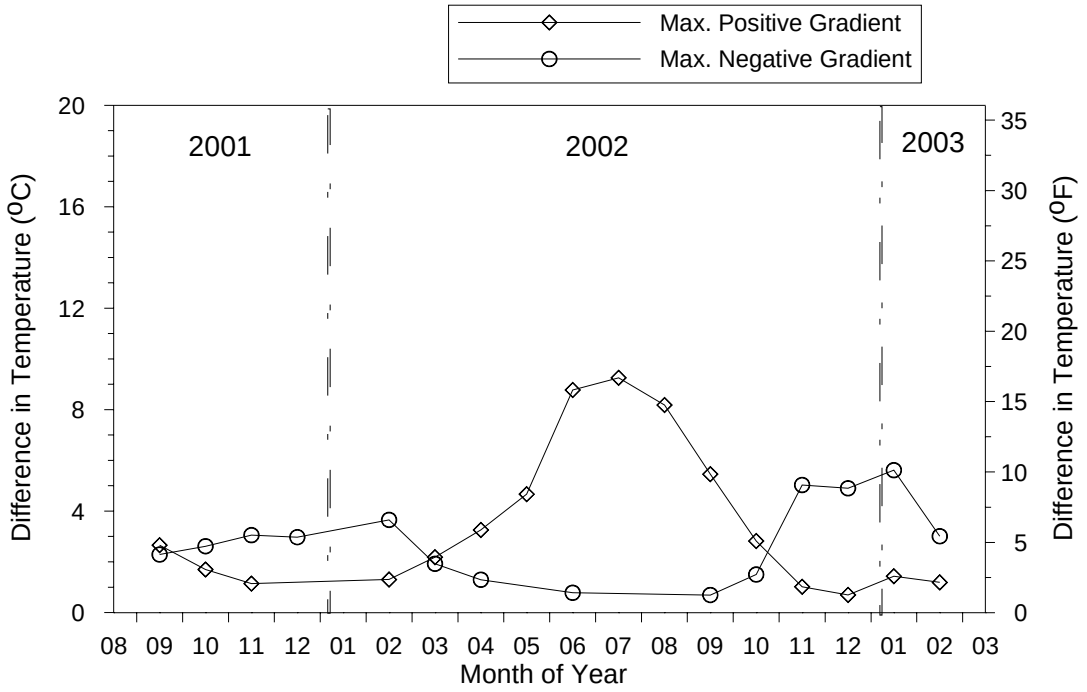

Figure F.34. Average Maximum Daily Gradients by Month for Interior Girder B14

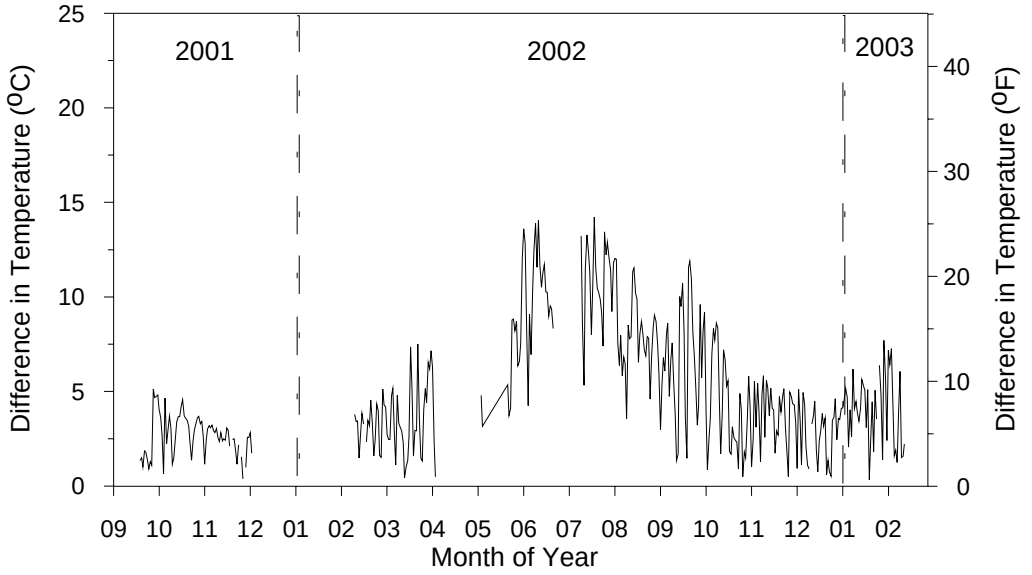

Figure F.35. Maximum Daily Positive Thermal Gradients for Interior Girder B23

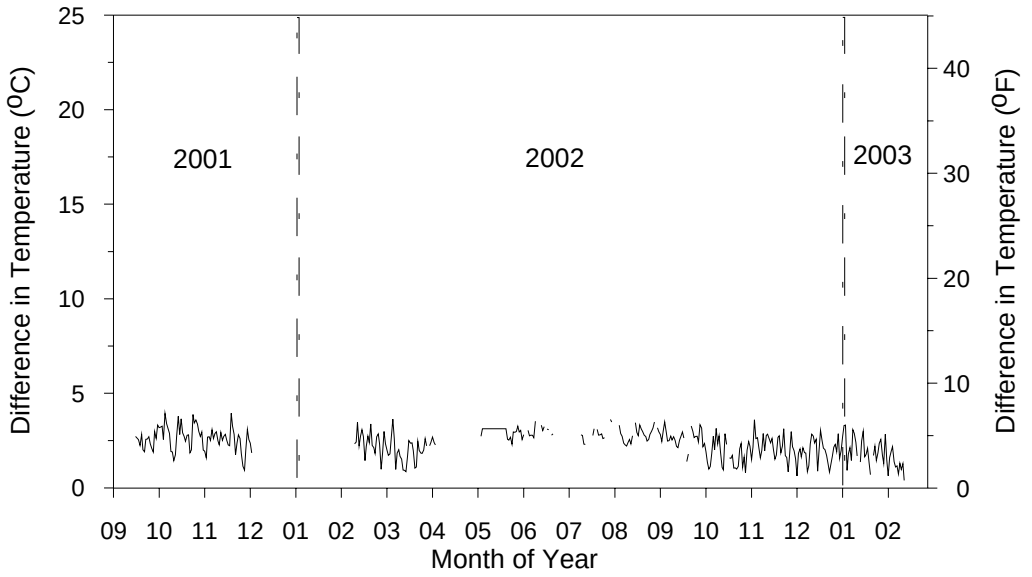

Figure F.36. Maximum Daily Negative Thermal Gradients for Interior Girder B23

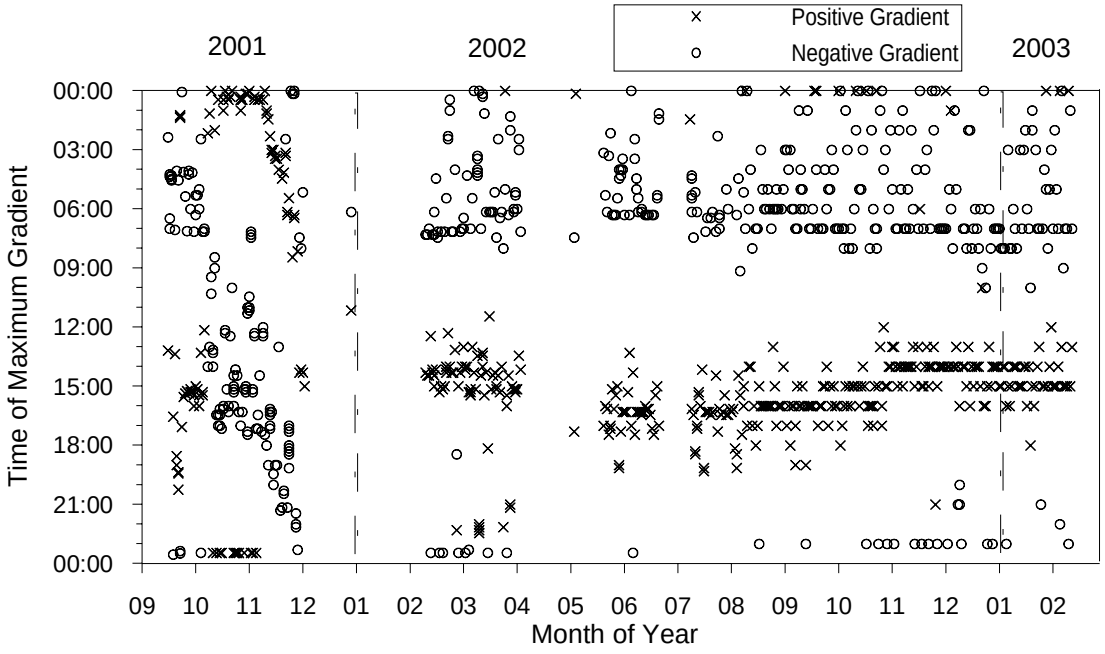

Figure F.37. Time of Maximum Positive and Negative Gradients for Interior Girder B23

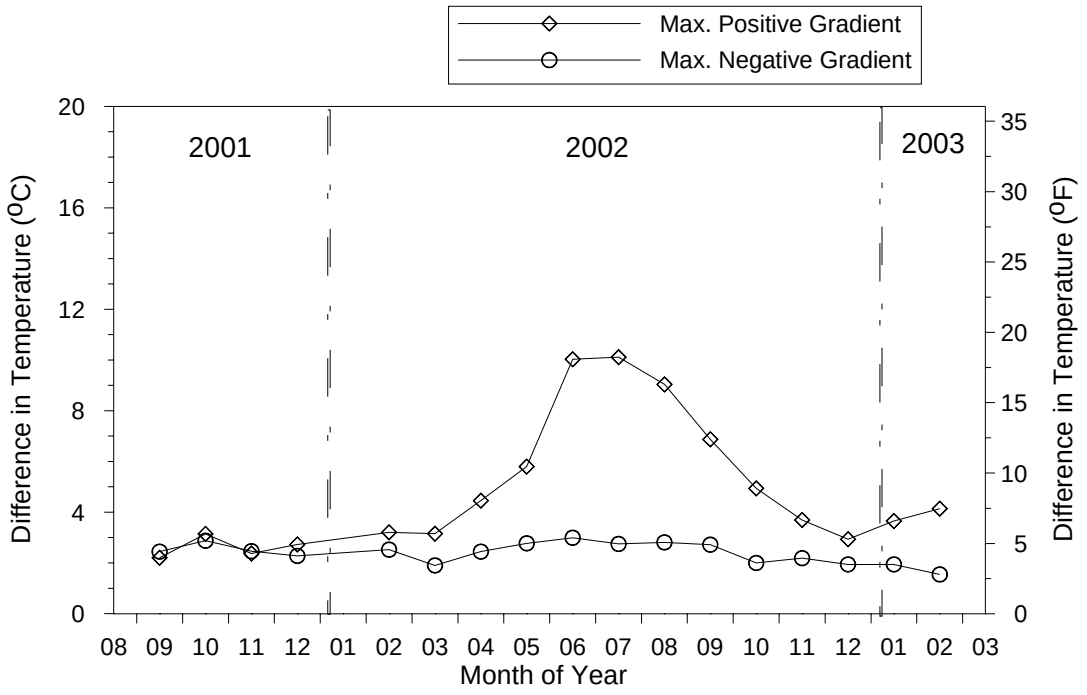

Figure F.38. Average Maximum Daily Gradients by Month for Interior Girder B23

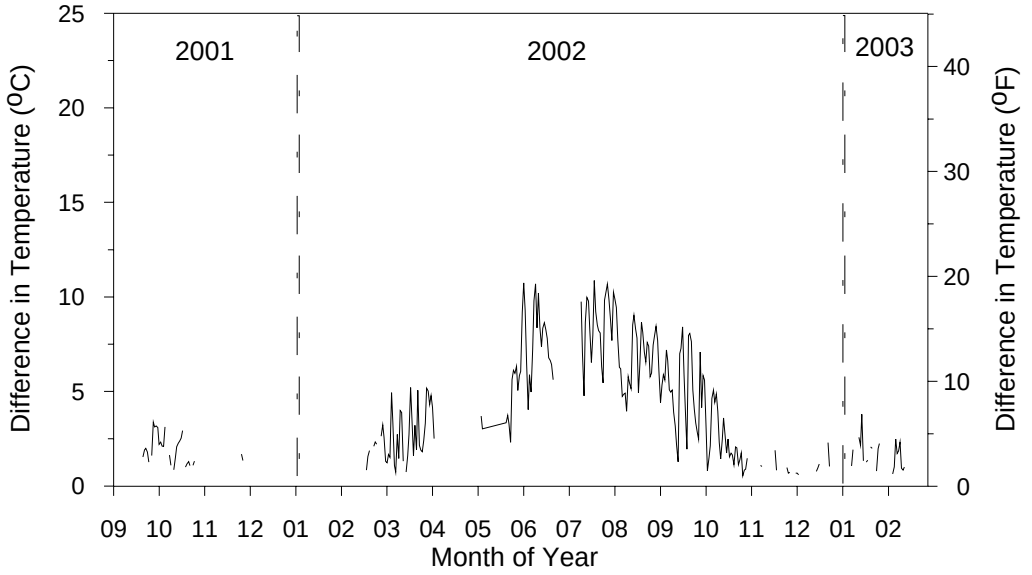

Figure F.39. Maximum Daily Positive Thermal Gradients for Interior Girder B24

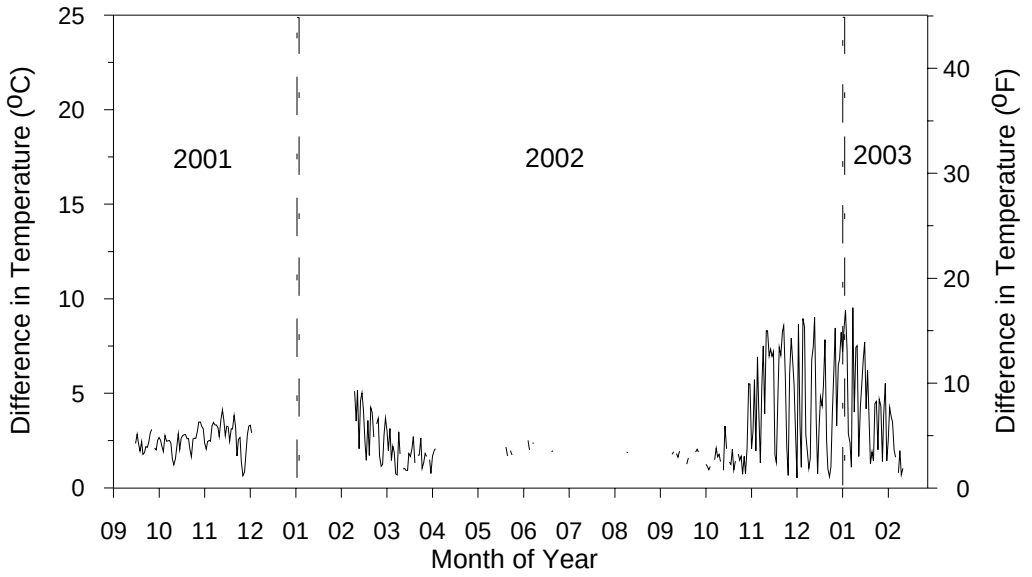

Figure F.40. Maximum Daily Negative Thermal Gradients for Interior Girder B24

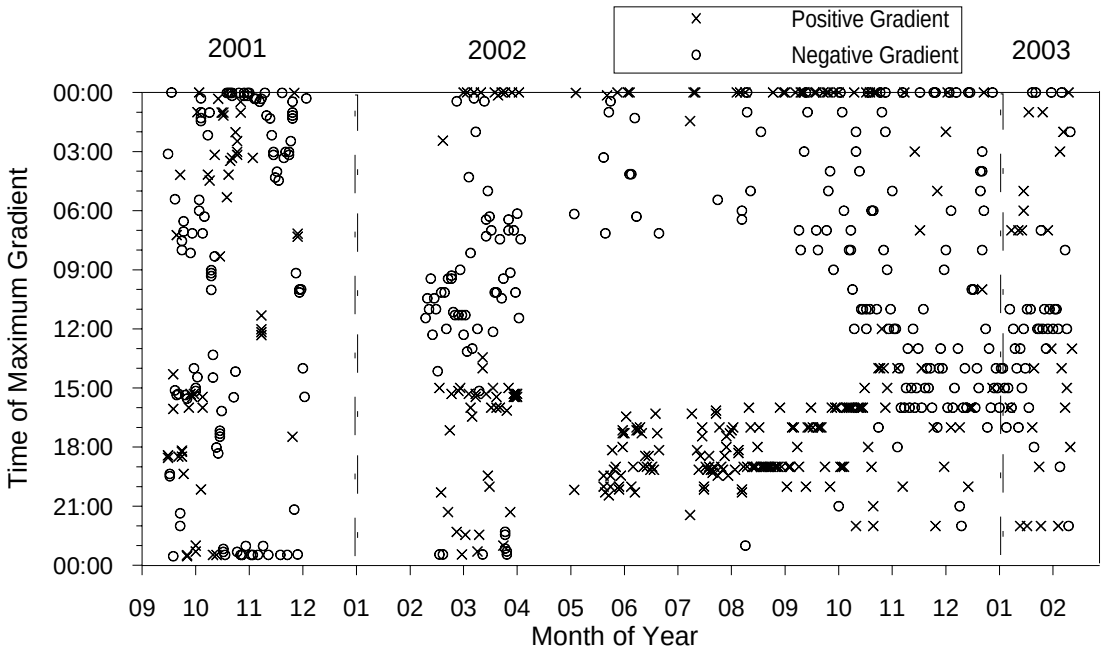

Figure F.41. Time of Maximum Positive and Negative Gradients for Interior Girder B24

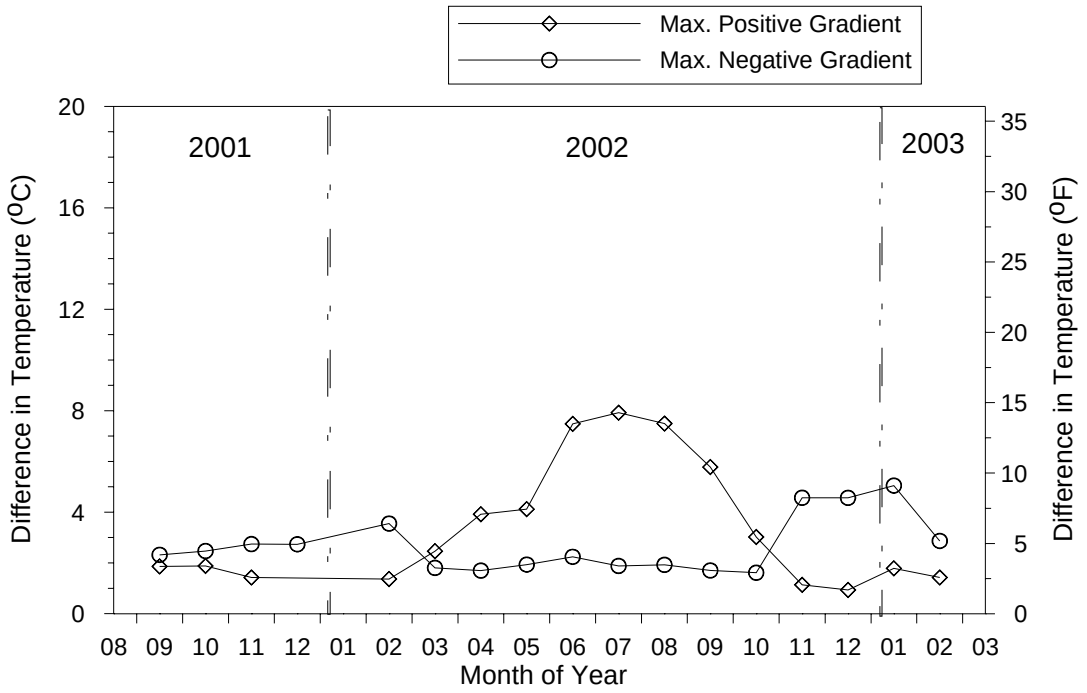

Figure F.42. Average Maximum Daily Gradients by Month for Interior Girder B24

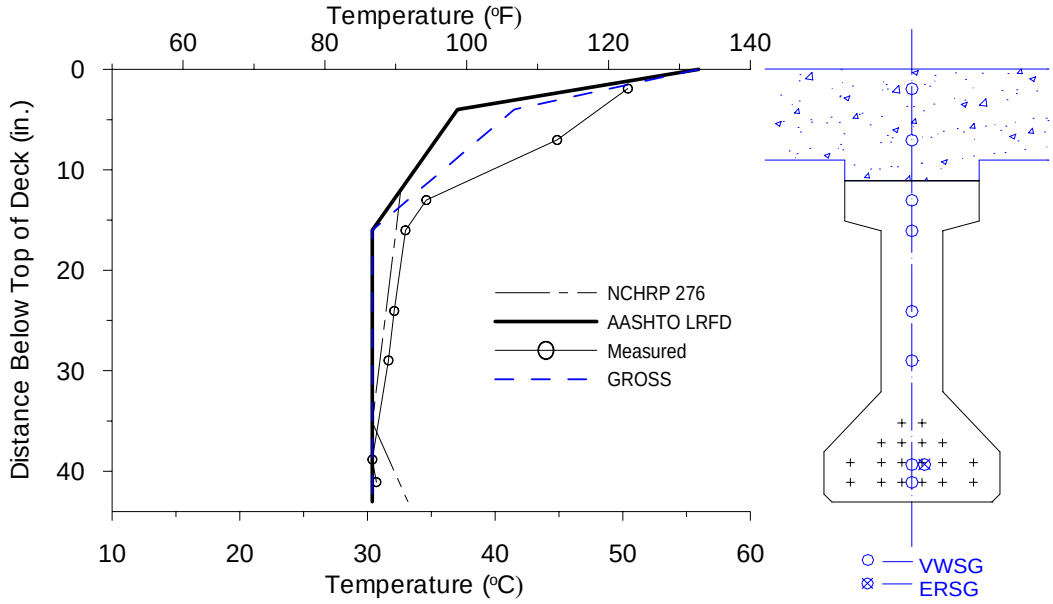

Figure F.43. Design Positive Gradients and Maximum Measured Positive Gradients in Girder B13

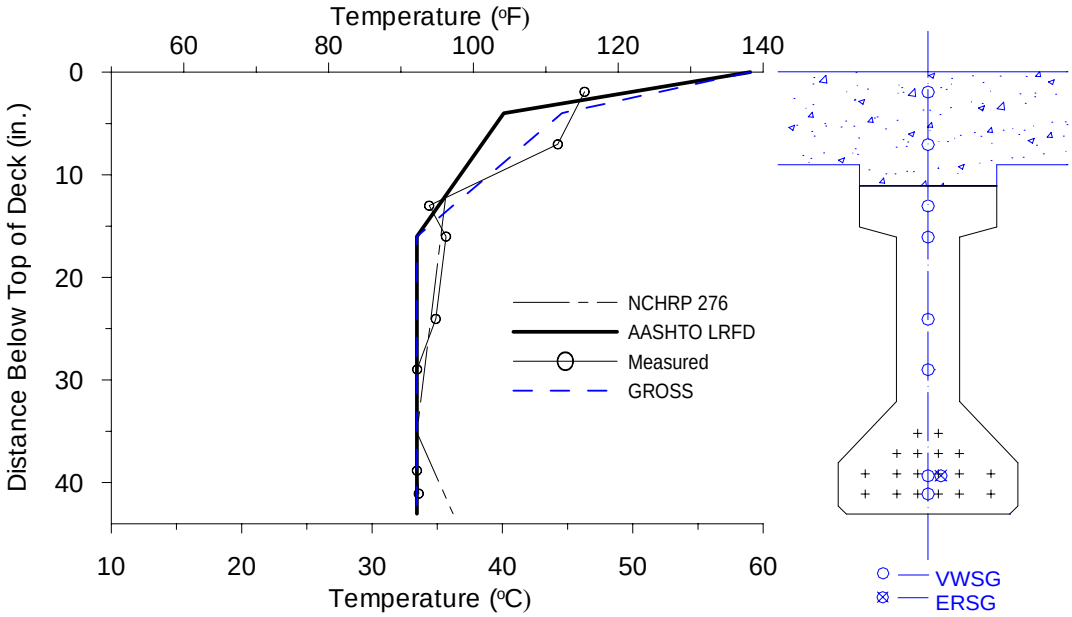

Figure F.44. Design Positive Gradients and Maximum Measured Positive Gradients in Girder B14

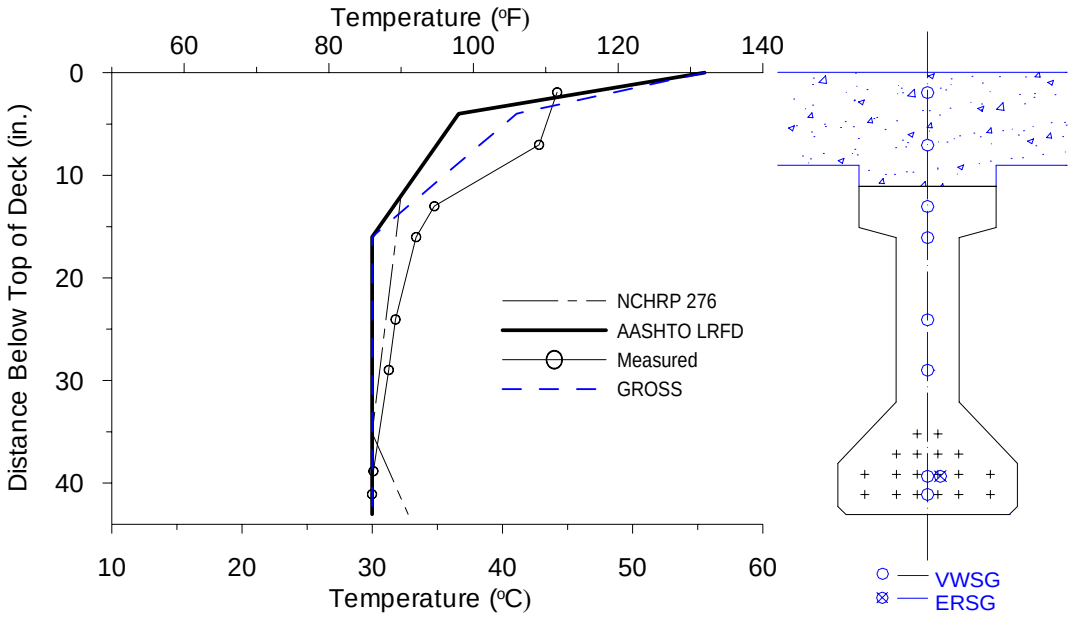

Figure F.45. Design Positive Gradients and Maximum Measured Positive Gradients in Girder B23

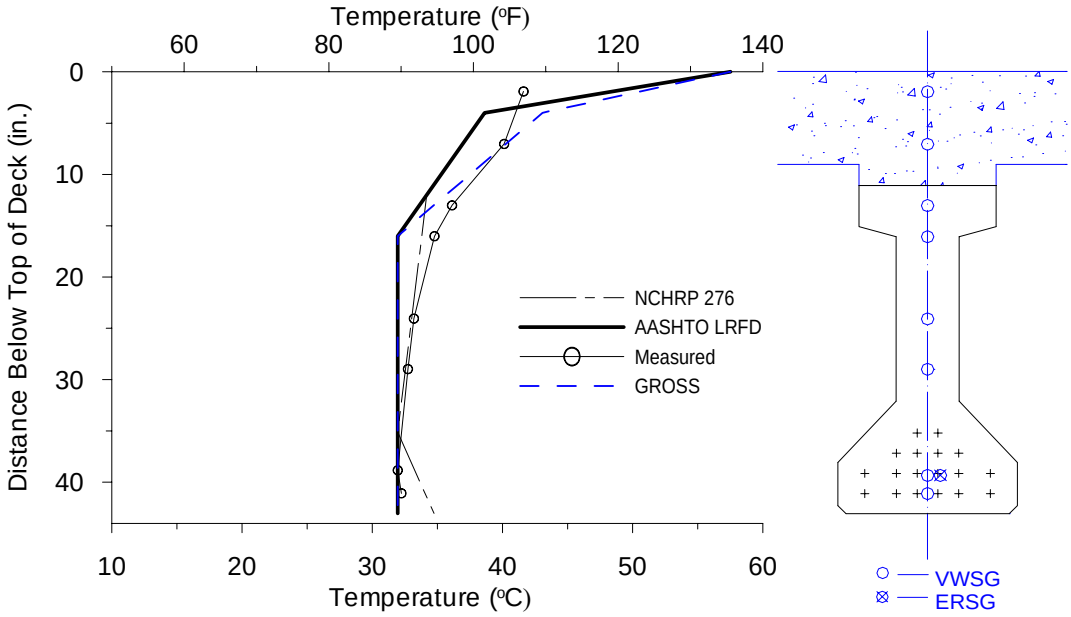

Figure F.46. Design Positive Gradients and Maximum Measured Positive Gradients in Girder B24

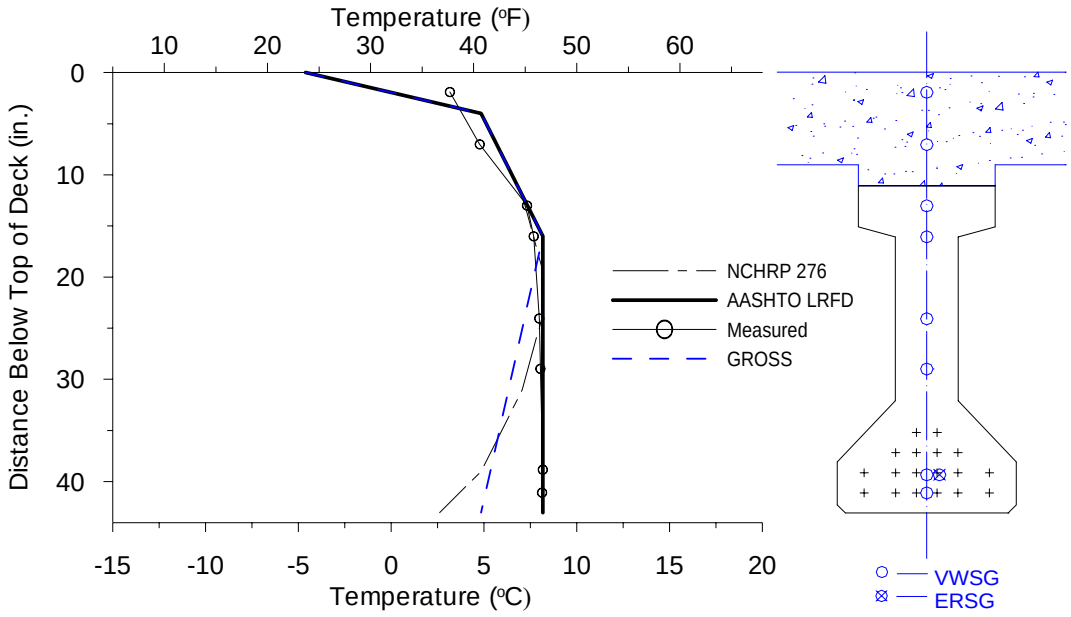

Figure F.47. Design Negative Gradients and Maximum Measured Negative Gradients in Girder B13

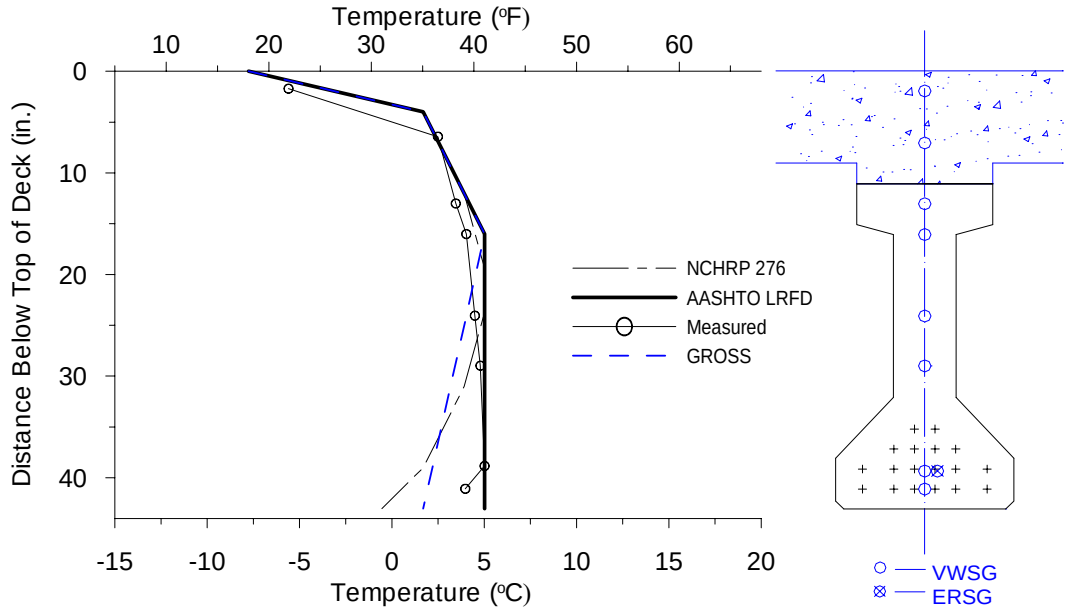

Figure F.48. Design Negative Gradients and Maximum Measured Negative Gradients in Girder B13

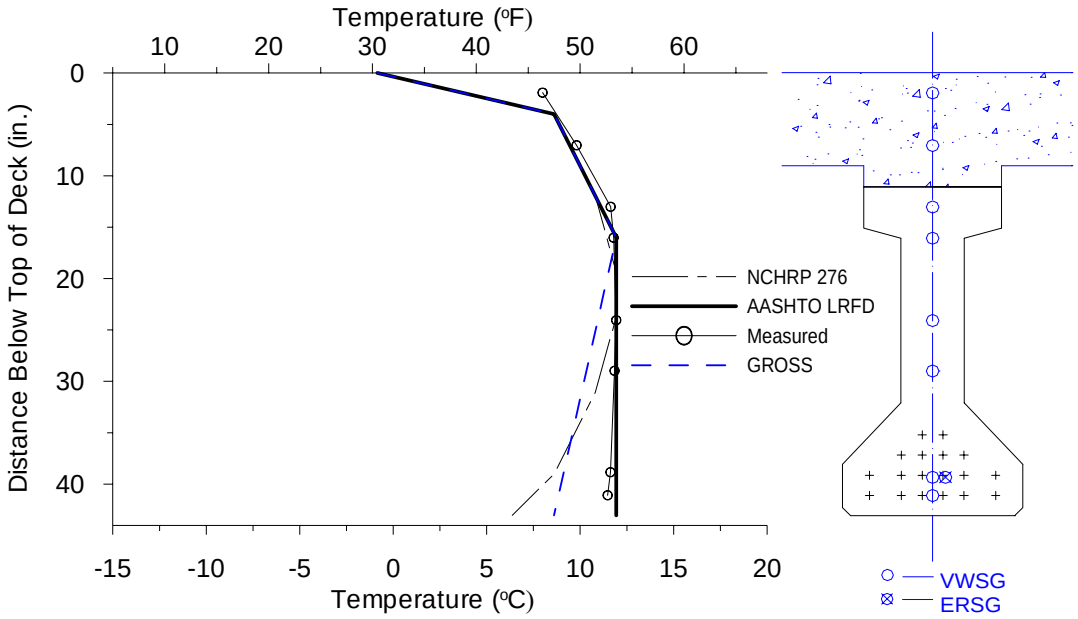

Figure F.49. Design Negative Gradients and Maximum Measured Negative Gradients in Girder B23

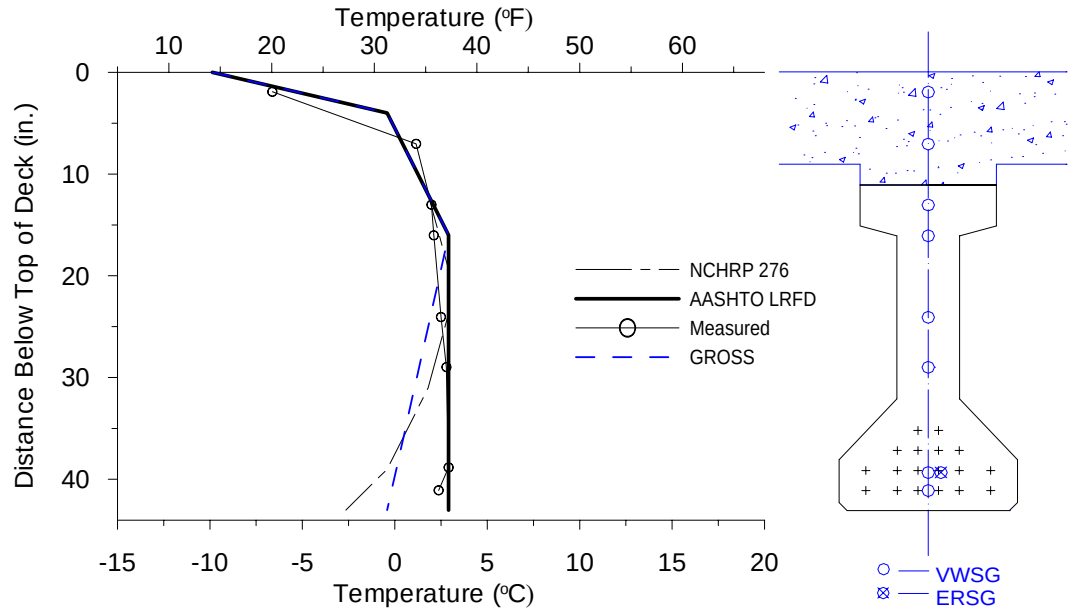

Figure F.50. Design Negative Gradients and Maximum Measured Negative Gradients in Girder B24

APPENDIX G.

TIME-STEP METHOD FOR PRESTRESS LOSSES AND DEFLECTION

Time-Step Model

An incremental time-step model was developed by the author for the prediction of long-term camber and prestress loss in the beams monitored in this study. The model was developed and programmed for use on a computer spreadsheet. It is based on the general procedure outlined by Libby (1990), Byle and Burns (1998).

The model is based on elastic bending theory (i.e. plane sections remains plane) and can be used to analyze behavior at a single cross-section. Superposition of elastic and time-dependent stresses and strains is assumed to hold, and the effects from each type of force or applied load are computed separately. This includes forces due to pretensioning, post-tensioning, self-weight of the member, placement of cast-in-place deck, and placement of the traffic rails on the composite section.

In this model, deformations that result from time-dependent creep and shrinkage deformations are computed. Elastic forces and loads are applied in time steps of zero duration. The effects of composite action after placement of the bridge deck are modeled by computing deformations in the beam and slab separately, as if there was no composite action.

Losses due to creep and shrinkage deformations of the cross-section, and due to the relaxation of steel, are computed during each time-interval. The remaining stress at the end of the interval is assumed to be the stress at the beginning of each subsequent interval.

Deformations are only computed at the mid-span section of the simply-supported girders. This effective curvature was computed for each component of camber or deflection based on the shape of the curvature diagram under the corresponding elastic

force. This simplification is assuming only that the shape of the curvature diagram due to each source of force or load remains the same over time. This approach should not result in a major loss of accuracy because mid-span curvatures are computed exactly, and the curvatures at sections near mid-span contribute much more to the deflection of a simply – supported member than the curvatures near the beam ends.

Measured material properties, determined from tests on companion specimens, were used in the analyses for each girder. The creep-time, shrinkage-time, strength-time, and modulus-strength relationships developed for each beam or concrete mix in Section 4 were used to continuously model the beam concrete properties at all times.

Transformed section properties and the actual construction schedules were used for each analysis. Prestress loss before release was considered in the model in the same manner as discussed in Section 7.2. Parameters used in the analysis for each beam are summarized in Appendix D. The spreadsheet is shown as follows:

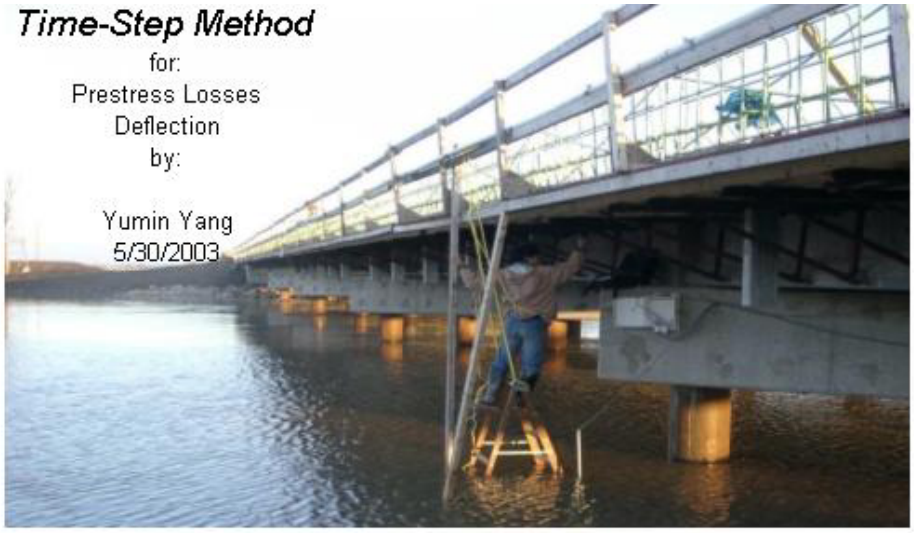

Welcome to Analysis of Prestress losses,
Deflection and Camber of precast prestress concrete girders.

Briefly:

The page is arranged with the calculation to the left. User instructions in the middle and workings to the right.

Blue underlined cells are input.

Command buttons is Visual Basic Command.

For precast prestressed concrete girders

Basic Information Input

Developed by Yumin Yang @May, 2003 UMR

Project:	Bridge A6130			For:	Girder Concrete	
By:	YYM	Date:	5/30/2003	File:		

INPUT	Beam No.	B13-Interior Beam, Span 1				
Material Properties	**Concrete**			**Prestressing Strands**		
	f_c' (beam)	70	MPa	f_{pu}	1860	MPa
	f_{ci}' (beam)	52	MPa	$f_{jacking}$	1396	MPa
	f_c' (deck)	28	MPa	E_{ps}	193060	MPa
	E_c (beam)	34682	MPa	A_{ps}	138.7	mm^2
	E_{ci} (beam)	30848	MPa	No.	18	
	E_c (deck)	25042	MPa	$Y_{b,ps}$	107.2	mm
	w(concrete density)	2481	kg/m^3			
Geometry	Length L	15.036	m			
Section Properties	**Non-Composite**			**Composite**		
	B1	330	mm	B6	2591	mm
	B2	152	mm			
	B3	432	mm			
	B4	89	mm			
	B5	140	mm			
	D1	813	mm	D7	230	mm
	D2	102	mm	D8	50	mm
	D3	25	mm			
	D4	407	mm			
	D5	152	mm			
	D6	127	mm			
Load:						
	w (beam)	4.73	kN/m			
	w (deck)	18.09	kN/m			
	w (DL,composite)	7.72	kN/m			
	w (other)	0	kN/m			

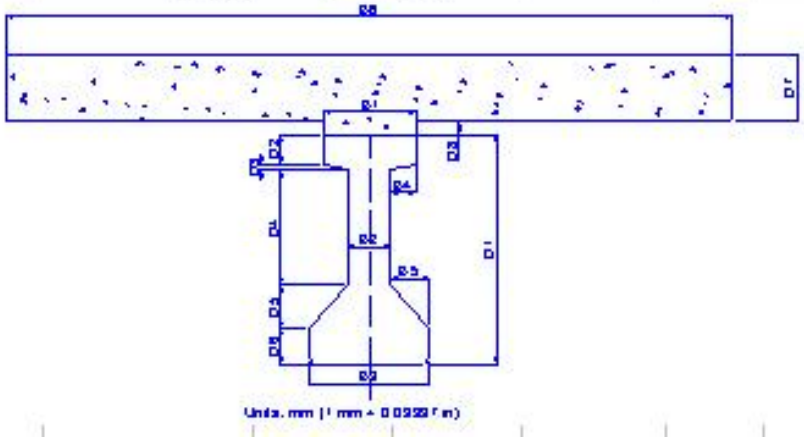

For precast prestressed concrete girders

Section Properties

Developed by Yumin Yang @May, 2003 UMR

Project:	Bridge A6130			For:	Girder Concrete
By:	YYM	Date:	5/30/2003	File:	D:\yumin\PC208W\Instru-pc208\Prestrssr

INPUT

Beam No. B13-Interior Beam, Span 1

Material Properties	Concrete			Prestressing Strands		
	f_c' (beam)	70	MPa	f_{pu}	1860	MPa
	f_{ci}' (beam)	52	MPa	$f_{jacking}$	1396	MPa
	f_c' (deck)	28	MPa	E_{ps}	193060	MPa
	E_c (beam)	34682	MPa	A_{ps}	138.7	mm²
	E_{ci} (beam)	30848	MPa	No.	18	
	E_c (deck)	25042	MPa	$Y_{b,ps}$	107.2	mm
				Area	2496.6	mm²

Section Properties	Non-Composite			Composite		
	B1	330	mm	B6	2591	mm
	B2	152	mm			
	B3	432	mm			
Input Section Data	B4	89	mm			
	B5	140	mm			
	D1	813	mm	D7	230	mm
	D2	102	mm	D8	50	mm
	D3	25	mm			
	D4	407	mm			
	D5	152	mm			
	D6	127	mm			

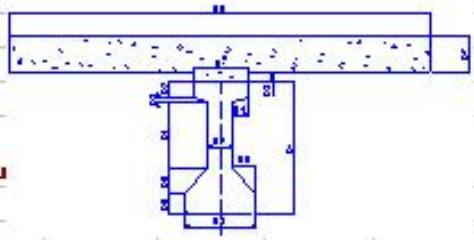

If A, I, $Y_{b,i}$ is known, input below, otherwise, calcu

Calculate

Cases	A (mm²)	I (mm⁴)	$Y_{b,i}$ (mm)
Gross Section	200797.0	1.42E+10	356.93
Non-Composite at release (trans.)	213925.2	1.5E+10	341.61
Non-Composite final (transformed)	212197.9	1.49E+10	343.51
Composite section (transformed)	654400.6	7.4E+10	769.71

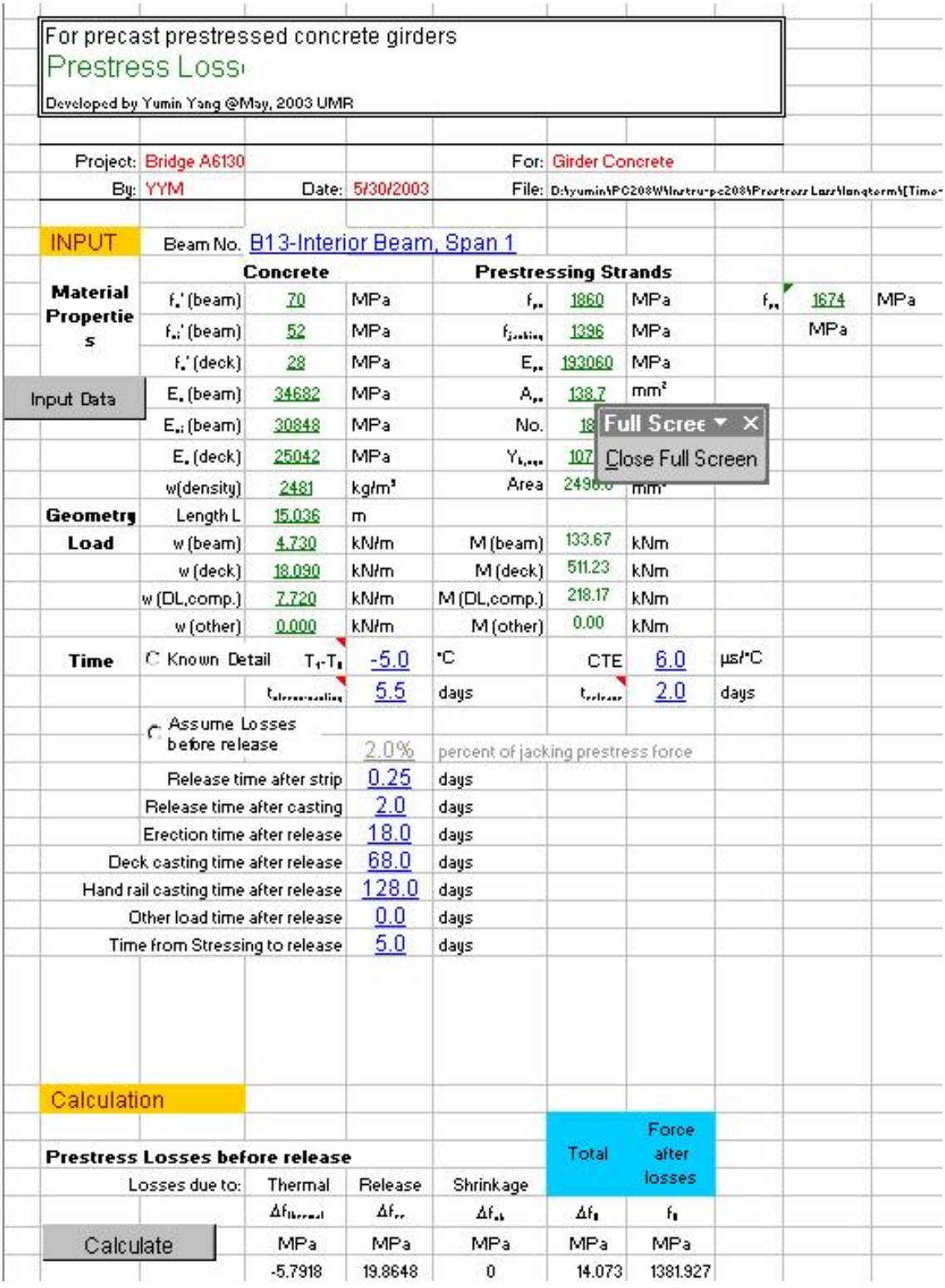

For precast prestressed concrete girders

Prestress Loss

Developed by Yumin Yang @May, 2003 UMR

Project: Bridge A6130 For: Girder Concrete

By: YYM Date: 5/30/2003 File: D:\yumin\PC208W\Instru-pc208\Prestress Loss\longterm\[Time-

INPUT Beam No. B13-Interior Beam, Span 1

		Concrete			Prestressing Strands				
Material Properties	f_c' (beam)	70	MPa	f_{pu}	1860	MPa	f_{py}	1674	MPa
	f_{ci}' (beam)	52	MPa	$f_{jacking}$	1396	MPa		MPa	
	f_c' (deck)	28	MPa	E_{ps}	193060	MPa			
Input Data	E_c (beam)	34682	MPa	A_{ps}	138.7	mm^2			
	E_{ci} (beam)	30848	MPa	No.	18				
	E_c (deck)	25042	MPa	$Y_{bs,ps}$	107				
	w(density)	2481	kg/m^3	Area	2496.6	mm^2			
Geometry	Length L	15.036	m						
Load	w (beam)	4.730	kN/m	M (beam)	133.67	kNm			
	w (deck)	18.090	kN/m	M (deck)	511.23	kNm			
	w (DL,comp.)	7.720	kN/m	M (DL,comp.)	218.17	kNm			
	w (other)	0.000	kN/m	M (other)	0.00	kNm			
Time	Known Detail	T_i-T_s	-5.0	°C	CTE	6.0	μs/°C		
		$t_{slab\ cast\ to\ release}$	5.5	days	$t_{cr,creep}$	2.0	days		
	Assume Losses before release		2.0%	percent of jacking prestress force					
	Release time after strip		0.25	days					
	Release time after casting		2.0	days					
	Erection time after release		18.0	days					
	Deck casting time after release		68.0	days					
	Hand rail casting time after release		128.0	days					
	Other load time after release		0.0	days					
	Time from Stressing to release		5.0	days					

Full Scree ▾ ×

Close Full Screen

Calculation

Prestress Losses before release				Total	Force after losses
Losses due to:	Thermal	Release	Shrinkage		
	$\Delta f_{thermal}$	Δf_{re}	Δf_{sh}	Δf_s	f_s
Calculate	MPa	MPa	MPa	MPa	MPa
	-5.7918	19.8648	0	14.073	1381.927

Prestress Losses after release					Total	Force after losses		For Graph
Time after release		Shrinkage	Creep	Release			Loads	
	t	$\Delta f_{shrinkage}$	Δf_{creep}	$\Delta f_{release}$	Δf_s	f_s	Δf_{loads}	Δf_s
	days	MPa	MPa	MPa	MPa	MPa	MPa	MPa
Release	0							
Erection	18.0							
Deck load	68.0							
Handrail	128.0							
other loads								
Time-History						1381.927		
Release	0	0.00	0.000	0.000	120.39	1261.54	120.39	134.46
	1	4.32	36.622	0.697	41.64	1219.90	0	176.10
		3.59	11.251	0.590	15.43	1204.47	0	191.53
		3.03	6.968	0.511	10.51	1193.96	0	202.04
		2.59	5.102	0.451			0	210.19
		2.24	3.993	0.403			0	216.83
		1.96	3.258	0.365			0	222.41
		1.73	2.735	0.333	4.80	1168.80	0	227.20
		2.91	4.388	0.590	7.88	1160.91	0	235.09
		2.35	3.414	0.511	6.27	1154.64	0	241.36
		1.94	2.765	0.451	5.15	1149.49	0	246.51
	15	1.63	2.303	0.403	4.33	1145.15	0	250.85
Erection	18	2.00	2.838	0.535	5.37	1139.78	0	256.22
	28	4.38	6.375	1.381	12.13	1127.65	0	268.35
	35	1.90	2.925	0.736	5.56	1122.08	0	273.92
	42	1.39	2.237	0.617	4.24	1117.84	0	278.16
	49	1.06	1.784	0.531	3.37	1114.47	0	281.53
	56	0.83	1.466	0.466	2.77	1111.70	0	284.30
	63	0.67	1.232	0.416	2.32	1109.38	0	286.62
Deck Loa	68	0.41	0.769	0.271	-31.72	1141.10	-33.2	254.90
	77	0.61	0.846	0.445	1.90	1139.20	0	256.80
	121	1.05	1.611	1.040	3.70	1133.12	0	262.88
Handrail	128	0.18	0.294	0.207	-6.76	1139.87	-7.437	256.13
	181	0.93	1.454	1.283	3.67	1136.21	0	259.79
	211	0.33	0.570	0.572	1.47	1134.74	0	261.26
	241	0.25	0.461	0.497	1.21	1133.53	0	262.47
	391	0.09	0.213	0.301	0.61	1129.58	0	266.42
	511	0.05	0.139	0.229	0.42	1127.65	0	268.35
	601	0.04	0.108	0.194	0.34	1126.55	0	269.45
	721	0.03	0.081	0.161	0.27	1125.38	0	270.62
Total Losses	**MPa**	46.10	111.14	18.35	255.37	255.37	-40.61	
	ksi	6.69	16.12	2.66	37.04	37.04	-5.89	
Losses with compensation for elastic change due to superimposed dead load:				**CR+SH+RE+PR**		**44.97**	**MPa**	

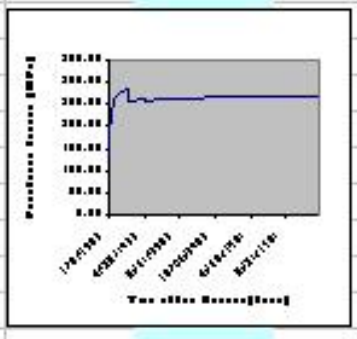

For precast prestressed concrete girders

Deflection

Developed by Yumin Yang @May, 2003 UMR

Project:	Bridge A6130		For:	Girder Concrete		
By:	YYM	Date: 5/30/2003	File:	D:\yumin\PC208W\Instru-pc208\Prestress Loss\long-term\[Time		

INPUT Beam No. B13-Interior Beam, Span 1

Input Data

		Concrete		Prestressing Strands				
Material Properties	f_c' (beam)	70	MPa	f_{pu}	1860	MPa	f_{py} 1674	MPa
	f_{ci}' (beam)	52	MPa	$f_{jacking}$	1396	MPa		
	f_c' (deck)	28	MPa	E_p	2E+05	MPa		
	E_c (beam)	34682	MPa	A_{ps}	138.7	mm²		
	E_{ci} (beam)	30848	MPa	No.	18			
	E_c (deck)	25042	MPa	$Y_{b,ps}$	107.2	mm		
	w(density)	2481	kg/m³	Area	2497	mm²		
Geometry	Length L	15.036	m					
Load	w (beam)	4.730	kN/m	M (beam)	133.67	kNm		
	w (deck)	18.090	kN/m	M (deck)	511.23	kNm		
	w (DL,comp.)	7.720	kN/m	M (DL)	218.17	kNm		
	w (other)	0.000	kN/m	M (other)	0.00	kNm		
Time	◉ Known Detail	T_i-T_d	-5.0	°C	CTE	6.0	με/°C	
		$t_{storage,casting}$	5.5	days	$t_{release}$	2.0	days	
	○ Assume Losses before release		2.00%	percent of jacking prestress force				
	Release time after strip		0.25	days				
	Release time after casting		2.0	days				
	Erection time after release		18.0	days				
	Deck casting time after release		68.0	days				
	Hand rail casting time after release		128.0	days				
	Other load time after release		0.0	days				
	Time from Stressing to release		5.0	days				

Calculation

Prestress Losses before release

Losses due t	Thermal	Release	Shrinkage	Total	Force after losses
	$\Delta f_{thermal}$	Δf_{re}	Δf_{sh}	Δf_s	f_s
Calculate	MPa	MPa	MPa	MPa	MPa
	-5.79	19.86	0.00	14.07	1381.93

Deflection Calculation						Time-step Defl.	Time-step Defl.	Total Deflection	For Graph
Time after release		Beam Weigh	Prestress	Deck	Rail				
	t	Δ_{beam}	Δ_{ps}	Δ_{deck}	Δ_{rail}	$(\Delta_{ps})_i$	$(\Delta_{di})_i$	Δ_{total}	Δ_{total}
	days	mm	mm	mm	mm	mm	mm	mm	mm
Release	0	-4.96	33.02						
Erection	18.0								
Deck load	68.0			-17.03					
Handrail	128.0				-1.39				
other loads									
Time-History								33.02	
Release	0	-4.96	33.02			0.00	0.00	28.06	1.10
	1					7.89	-1.54	34.41	1.35
	2					2.59	-0.53	36.48	1.44
	3					1.67	-0.35	37.80	1.49
	4					1.22	-0.26	38.76	1.53
	5					0.95	-0.20	39.51	1.56
	6					0.78	-0.17	40.12	1.58
	7					0.65	-0.14	40.63	1.60
	9					1.05	-0.23	41.45	1.63
	11					0.82	-0.18	42.08	1.66
	13					0.66	-0.15	42.60	1.68
	15					0.55	-0.12	43.03	1.69
Erection	18					0.68	-0.15	43.55	1.71
	28					1.54	-0.35	44.74	1.76
	35					0.71	-0.16	45.29	1.78
	42					0.55	-0.13	45.71	1.80
	49					0.44	-0.10	46.05	1.81
	56					0.36	-0.08	46.33	1.82
	63					0.30	-0.07	46.56	1.83
Deck Load	68			-17.03		1.06	-0.20	30.40	1.20
	77					0.32	-0.31	30.41	1.20
	84					0.22	-0.21	30.42	1.20
	91					0.19	-0.18	30.42	1.20
	121					0.63	-0.61	30.44	1.20
Handrail	128				-1.39	0.31	-0.12	29.25	1.15
	181					0.66	-0.67	29.24	1.15
	211					0.26	-0.27	29.23	1.15
	241					0.21	-0.22	29.22	1.15
	271					0.17	-0.18	29.22	1.15
	301					0.15	-0.15	29.21	1.15
	451					0.08	-0.08	29.19	1.15
	481					0.07	-0.07	29.19	1.15
	511					0.06	-0.07	29.18	1.15
	631					0.04	-0.05	29.17	1.15
	661					0.04	-0.04	29.17	1.15
	691					0.04	-0.04	29.17	1.15
	721					0.04	-0.04	29.16	1.15
Total (mm) =		-4.96	33.02	-17.03	-1.39	28.55	-9.03		

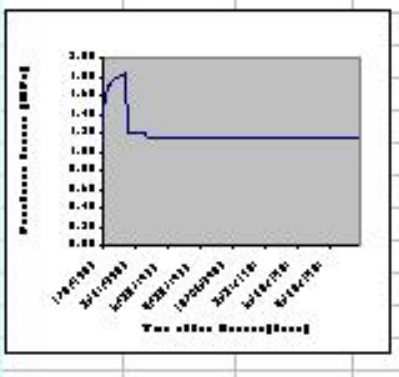

APPENDIX H.

OPTIMUM COST CURVE FOR SECTION OPTIMIZATION

Table H.1. Existing Cross Section Properties

Agency	Girder Type	Depth (in.)	Web (in.)	Area (in^2)	Inertia (in^4)	y_t (in.)	y_b (in.)	S_t (in^3)	S_b (in^3)	ρ	α
MoDOT	Type 2	32	6	311.5	33955	18	14.05	1892	2417	0.432	0.839
	Type 3	39	6	382.5	62001	21.9	17.06	2826	3634	0.433	0.843
	Type 4	45	6	429.5	93474	25.5	19.52	3669	4789	0.438	0.857
	Type 6	54	6.5	644.1	236105	28.1	25.89	8399	9120	0.504	0.907
	Type 7	72.5	6	787.4	571047	34.9	37.58	16353	15196	0.553	0.921
CTL	BT-48	48	6	557	177736	23.5	24.47	7554	7263	0.554	0.940
	BT-60	60	6	629	308722	29.6	30.41	10433	10152	0.545	0.931
	BT-72	72	6	701	484993	35.6	36.36	13608	13339	0.534	0.914
PCI	BT-54	54	6	659	268077	26.4	27.63	10166	9702	0.558	0.943
	BT-63	63	6	713	392638	30.8	32.12	12740	12224	0.556	0.942
	BT-72	72	6	767	545894	35.4	36.6	15421	14915	0.549	0.934
AASHTO	Type II	36	6	367	50778	15.8	20.3	3222	2506	0.433	0.656
	Type III	45	7	566	127111	20.4	24.7	6243	5142	0.446	0.697
	Type IV	54	8	786	259918	24.7	29.3	10535	8882	0.458	0.725
	Type VI	72	8	1085	733320	35.6	36.38	20587	20157	0.522	0.893
	Mod.VI	72	6	941	671088	35.6	36.44	18872	18416	0.550	0.940
Washington	80/6	50	6	513	159191	27.2	22.76	5844	6994	0.501	0.943
	100/6	58	6	591	256560	30	27.99	8549	9166	0.517	0.925
	120/6	73.5	6	688	475502	37.7	35.82	12619	13275	0.512	0.908
	14/6	73.5	6	736	534037	35.3	38.2	15129	13980	0.538	0.894
Colorado	G54/6	54	6	631	242592	27.3	26.67	8876	9096	0.527	0.924
	G68/6	68	6	701	426575	34	34.01	12550	12543	0.526	0.910
Nebraska	1600	63	5.9	852	494829	32.6	30.36	15160	16299	0.586	1.051
	1800	70.9	5.9	898	659505	36.7	34.18	17960	19295	0.585	1.049
	2000	78.7	5.9	944	849565	40.7	37.96	20853	22381	0.582	1.042
	2400	94.5	5.9	1038	1E+06	48.8	45.66	27109	28997	0.572	1.023
Florida	BT-54	54	6.5	785	311765	28.1	25.89	11091	12042	0.546	0.983
	BT-63	63	6.5	843	458521	32.9	30.12	13945	15223	0.549	0.992
	BT-72	72	6.5	901	638672	37.6	34.36	16968	18588	0.548	0.991
Texas	U54A	54	10.2	1022	379857	30.1	23.88	12611	15907	0.517	0.997
	U54B	54	10.2	1118	403878	31.5	22.46	12805	17982	0.510	1.031

1 in = 25.4 mm; 1 in^2 = 645 mm^2; 1 in^3 = 16390 mm^3; 1 in^4 = 416,000 mm^4

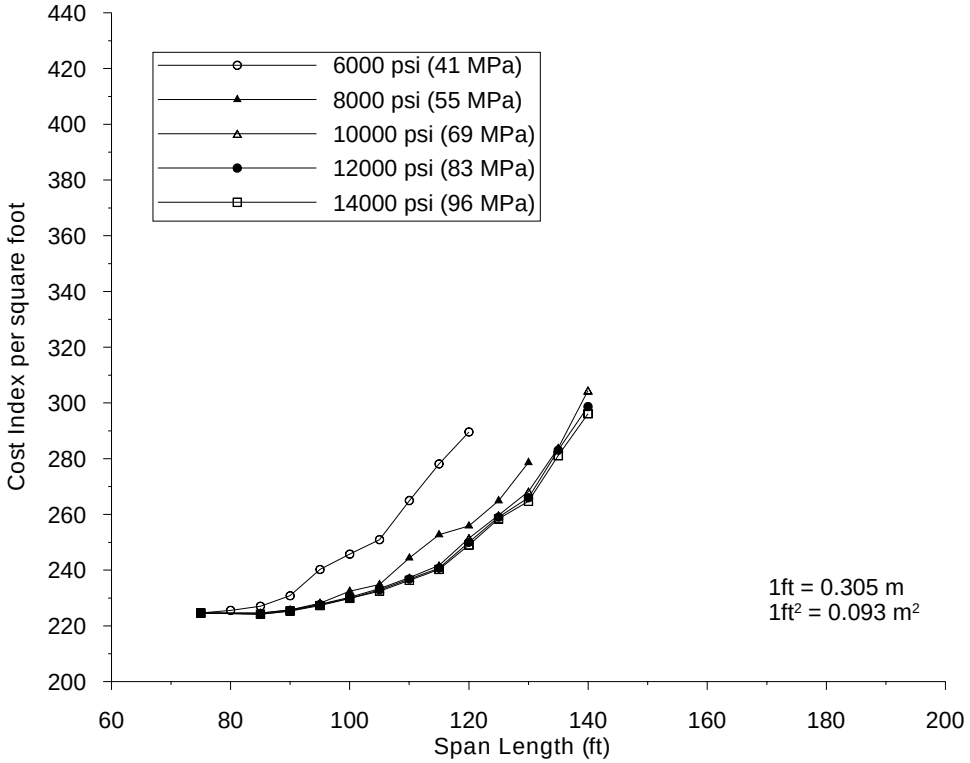

Figure H.1. Cost Chart for a PCI Section BT-54

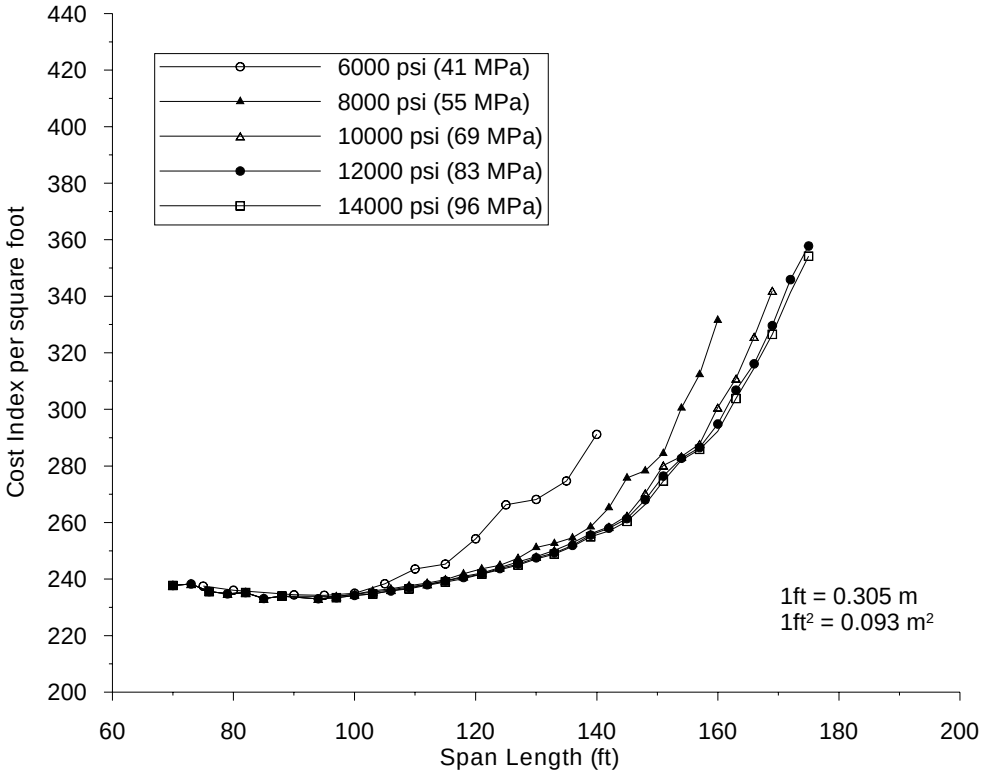

Figure H.2. Cost Chart for a PCI Section BT-72

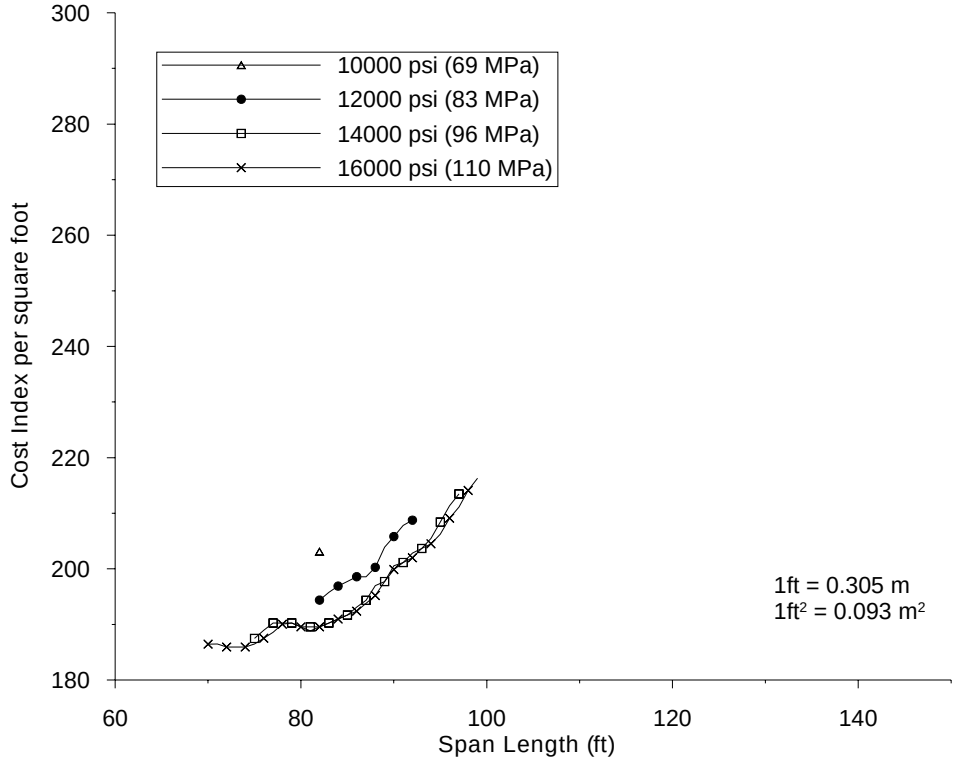

Figure H.3. Cost Chart for a MoDOT Type 2

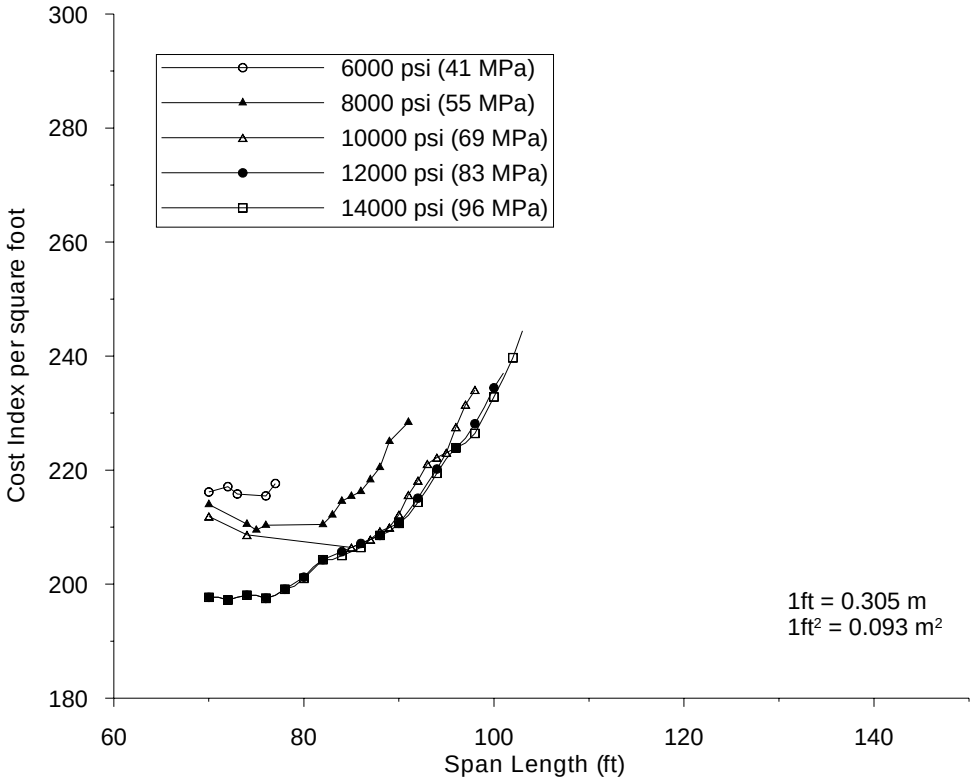

Figure H.4. Cost Chart for a MoDOT Type 3

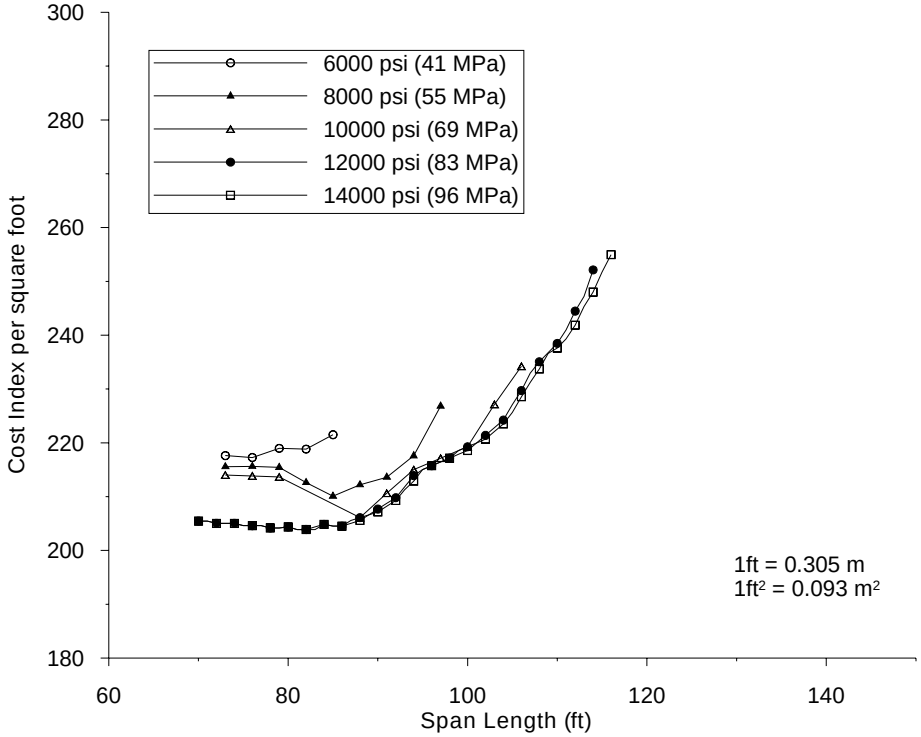

Figure H.5. Cost Chart for a MoDOT Type 4

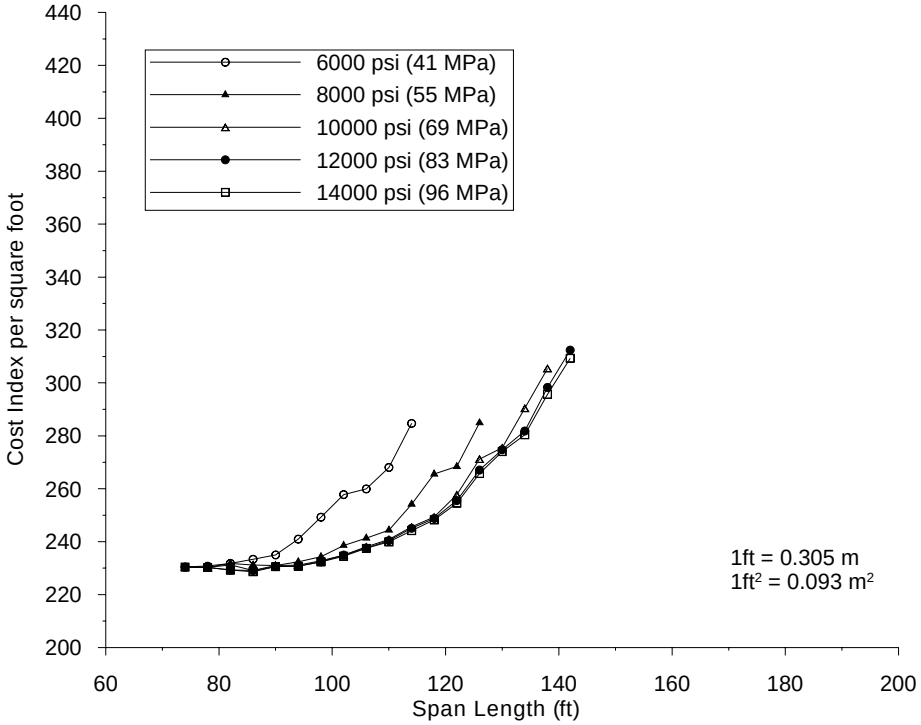

Figure H.6. Cost Chart for a MoDOT Type 6

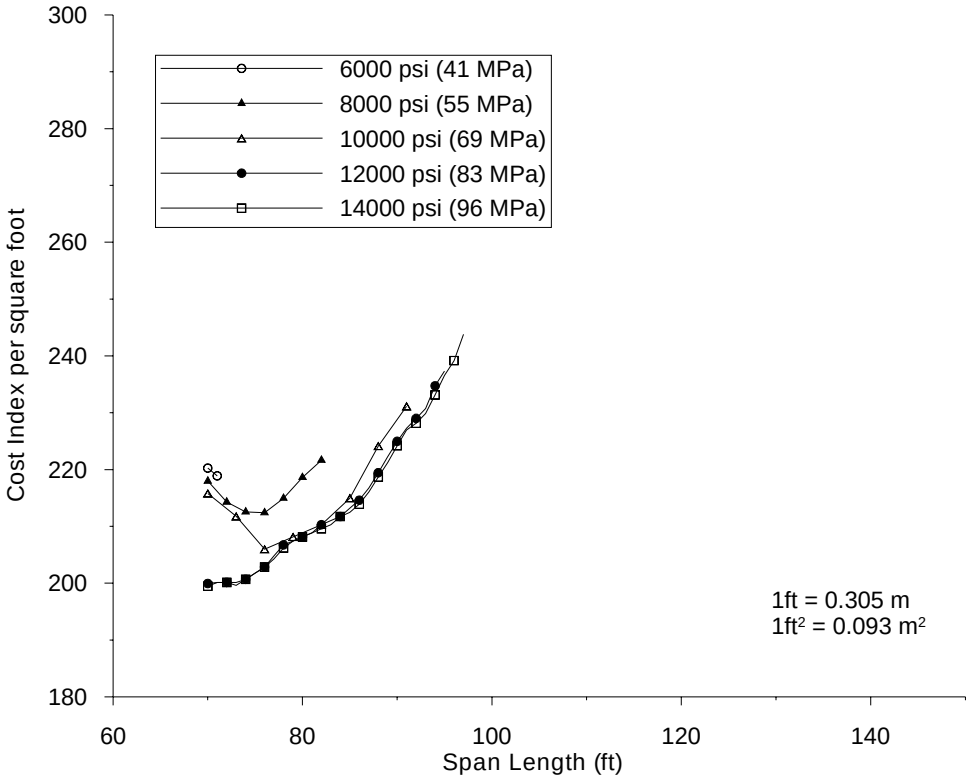

Figure H.7. Cost Chart for a AASHTO Type II

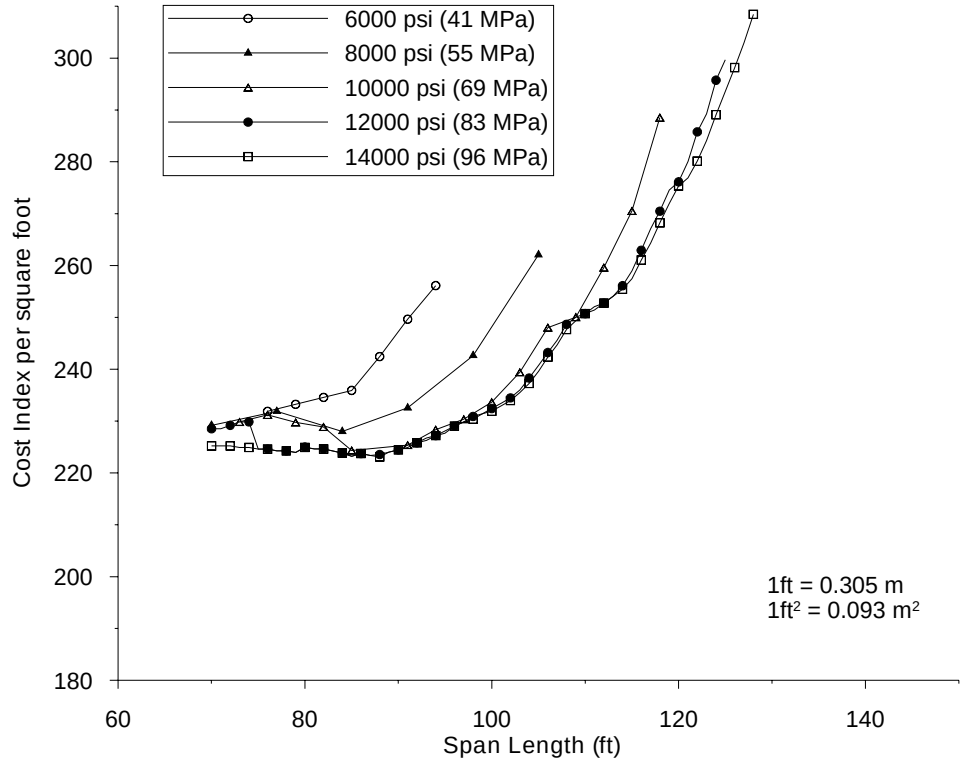

Figure H.8. Cost Chart for a AASHTO Type III

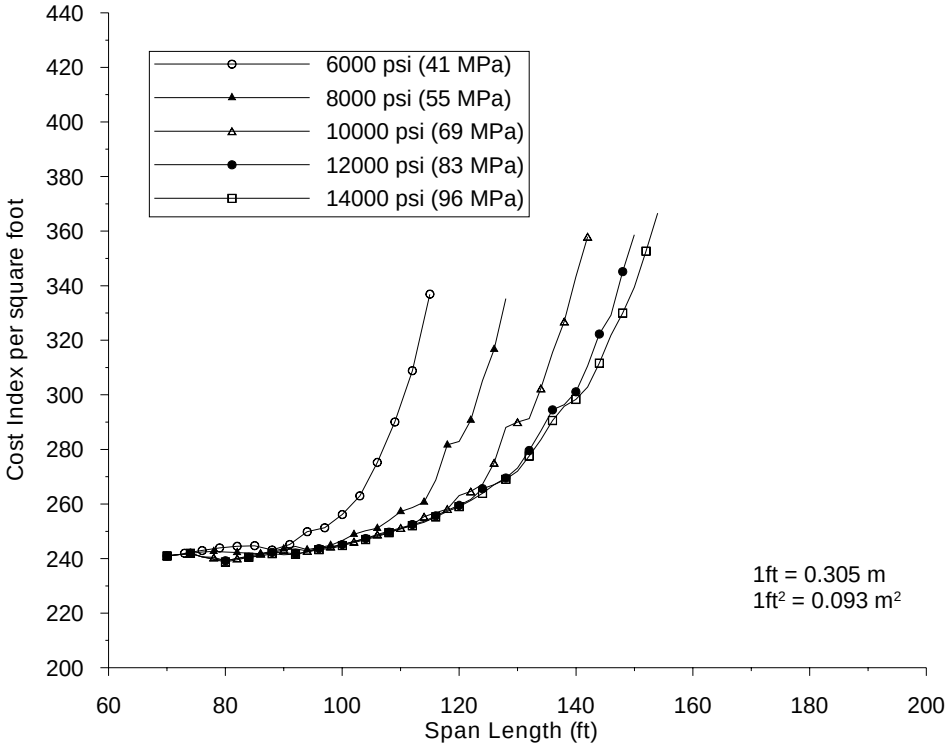

Figure H.9. Cost Chart for a AASHTO Type IV

BIBLIOGRAPHY

American Association of State Highway and Transportation Officials (1994), "AASHTO LRFD Bridge Design Specifications," American Association of State Highway and Transportation Officials, Washington, DC.

American Association of State Highway and Transportation Officials (2002), "AASHTO LRFD Bridge Design Specifications (Interim Revision)," American Association of State Highway and Transportation Officials, Washington, DC.

American Association of State Highway and Transportation Officials (1994), "Guide Specifications for Distribution of Loads for Highway Bridges," American Association of State Highway and Transportation Officials, Washington, DC.

American Association of State Highway and Transportation Officials (1989), "Standard Specifications for Highway Bridges," 14th edition, American Association of State Highway and Transportation Officials, Washington, DC.

American Association of State Highway and Transportation Officials (1996), "Standard Specifications for Highway Bridges," 16th edition, American Association of State Highway and Transportation Officials, Washington, DC.

American Concrete Institute (ACI 116R-90) (1990), "Cement and Concrete Terminology," American Concrete Institute, Detroit, Michigan.

American Concrete Institute (ACI 209R-92) (1992), "Prediction of Creep, Shrinkage, and Temperature Effects in Concrete Structures," American Concrete Institute, Detroit, Michigan.

American Concrete Institute (ACI 318-99) (1999), "Building Code Requirements for Structural Concrete," American Concrete Institute, Detroit, Michigan.

American Concrete Institute (ACI 318-02) (2002), "Building Code Requirements for Structural Concrete," American Concrete Institute, Detroit, Michigan.

American Concrete Institute (ACI 363R-92) (1992), "State-of-the-Art Report on High Strength Concrete," American Concrete Institute, Detroit, Michigan.

American Concrete Institute (ACI 363.2R-98) (1998), "Guide to Quality Control and Testing of High-Strength Concrete," American Concrete Institute, Detroit, Michigan.

American Concrete Institute (ACI 435R-95) (1995), "Control of Deflection in Concrete Structures," American Concrete Institute, Detroit, Michigan.

Aitcin, P.C. and Neville, A. (1993), "High-Performance Concrete Demystified," Concrete International, January, Vol. 15, No. 1, pp. 21-26.

ASTM C 31/C 31 M - 00 (2000), "Standard Practice for Making and Curing Concrete Test Specimens in the Field," American Society for Testing and Materials, West Conshohocken, Pennsylvania.

ASTM C 39/C 39M – 01 (2001), "Standard Test Method for Compressive Strength of Cylindrical Concrete Specimens," American Society for Testing and Materials, West Conshohocken, Pennsylvania.

ASTM C 157 – 93 (1993), "Test Method for Length Change of Hardened Hydraulic-cement Mortar and Concrete Specification for Sheet Materials for Curing Concrete," American Society for Testing and Materials, West Conshohocken, Pennsylvania.

ASTM C 192/C 192 M – 00 (2000), "Standard Practice for Making and Curing Concrete Test Specimens in the Laboratory," American Society for Testing and Materials, West Conshohocken, Pennsylvania.

ASTM C 469 - 94 (1994), "Standard Test Method for Static Modulus of Elasticity and Poisson's Ratio of Concrete in Compressive," American Society for Testing and Materials, West Conshohocken, Pennsylvania.

ASTM C 490 - 93a (1993), "Practice for Use of Apparatus for the Determination of Length Change of Hardened Cement Paste, Mortar and Concrete," American Society for Testing and Materials, West Conshohocken, Pennsylvania.

ASTM C 496 - 96 (1996), "Test Method for Splitting Tensile Strength of Cylindrical Concrete Specimens," American Society for Testing and Materials, West Conshohocken, Pennsylvania.

ASTM C 512 - 87 (1994), "Test Method for Creep of Concrete in Compression," American Society for Testing and Materials, West Conshohocken, Pennsylvania.

ASTM C 666 - 92 (1992), "Test Method for Resistance to Rapid Freezing and Thawing," American Society for Testing and Materials, West Conshohocken, Pennsylvania.

ASTM C 672 - 92 (1992), "Test Method for Scaling Resistance of Concrete Surfaces Exposed to Deicing Chemicals," American Society for Testing and Materials, West Conshohocken, Pennsylvania.

ASTM C 944 - 95 (1995), “Test Method for Abrasion Resistance of Concrete or Mortar Surfaces by the Rotating-Cutter Method,” American Society for Testing and Materials, West Conshohocken, Pennsylvania.

ASTM C 1202 - 94 (1994), “Test Method for Electrical Indication of Concrete’s Ability to Resist Chloride Ion Penetration,” American Society for Testing and Materials, West Conshohocken, Pennsylvania.

Barnes, R. W., Burns, N. H., and Kreger, M. E. (1996), “Development Length of 0.6-Inch Prestressing Strand in Standard I-Shaped Pretensioned Concrete Beams,” Center for Transportation Research, The University of Texas at Austin, Research Report 1388-1, Austin, Texas.

Barr, P., Fekete, E., Eberhard, J., Stanton, B., Khaleghi, B., Hsieh, J. (2000), “High Performance Concrete in Washington State SR 18/SR 516 Overcrossing: Interium Report on Girder Monitoring,” FHWA Report FHWA-RD-00-070, 137 pp.

Barrios, A. O., Burns, N. H., and Carrasquillo, R. L. (1996), “Behavior of High Strength Concrete Pretensioned Girders During Transfer of Prestressing Forces,” Center for Transportation Research, The University of Texas at Austin, Research Report 580-1, Austin, Texas.

Branson, D. E. (1977), “Deformation of Concrete Structures,” McGraw-Hill, New York.

Branson, D. E. and Kripanarayanan, K. M. (1971), “Loss of Prestress, Camber, and Deflection of Non-composite and Composite Prestressed Concrete Structures,” PCI Journal, September/October, Vol. 16, No. 5, pp. 22-52.

Branson, D. E. and Ozell, A. M. (1961), “Camber in Prestressed Concrete Beams,” PCI Journal (Proceedings), June, Vol. 57, No. 12, pp. 1549-1574.

Bruce, R. N., Martin, B. T., Russell, H. G., and Roller, J. J. (1994), “Feasibility Evaluation of Utilizing High-Strength Concrete in Design and Construction of Highway Bridge Structures,” Louisiana Transportation Research Center, Research Report FHWA/LA-92/282, Baton Rouge, Louisiana.

Burns, N.H., Gross, S.P., and Byle, K.A. (1997), “Instrumentation and Measurements – Behavior of Long-Span Prestressed High Performance Concrete Bridges,” Proceedings of the PCI/FHWA, International Symposium on High Performance Concrete, New Orleans, Louisiana.

Byle, K. A., Burns, N. H., and Carrasquillo, R. L. (1998), “Time-Dependent Deformation Behavior of Prestressed High Performance Concrete Bridge Beams,” Center

forTransportation Research, The University of Texas at Austin, Research Report 580-6, Austin, Texas.

Cai, C. S., Shahawy, M., Peterman, R. J (2002). “Effect of Diaphragm on Load Distribution in Prestressed Concrete Bridges,” Transportation Research Board 81st Annual Meeting, Conference Proceedings - CD Rom, Washington, D.C.

Carpenter, J. E. (1980), “Applications of High-Strength Concrete for Highway Bridges,” Public Roads, Vol. 44, No. 2, pp. 76-83.

Cohen, M. D., Zhou, Y., and Dolch, W. L. (1992), "Non-Air-Entrained High-Strength Concrete - Is It Frost Resistant?" ACI Materials Journal, Jul-Aug, Vol. 89, No. 4, pp 406-415.

FHWA (1997a). Alabama. Highway 1199 Over Uphaupee and Bulger Creek, Macon County. Publication No. FHWA-RD-97-055.

FHWA (1997b). Georgia. Bridge Over Interstate 75, Henry County, Tentative Site. Publication No. FHWA-RD-97-057.

FHWA (1997c). Nebraska. 120th Street and Giles Road Bridge, Sarpy County. Publication No. FHWA-RD-97-058.

FHWA (1997d). New Hampshire. Route 104 Bridge Over the Newfound River, Bristol. Publication No. FHWA-RD-97-059.

FHWA (1997e). .New Hampshire . Route 3A Bridge Over the Newfound River, Bristol. Publication No. FHWA-RD-97-088.

FHWA (1997f). .North Carolina . U.S. 401 Over the Neuse River, Wake County. Publication No. FHWA-RD-97-060.

FHWA (1997g). Texas. Louetta Road Overpass State Highway 249, Houston. Publication No. FHWA-RD-97-063.

FHWA (1997h). Texas. San Angelo Bridge U.S. Route 67, San Angelo. Publication No. FHWA-RD-97-062.

FHWA (1997i). Virginia. Route 40 Over the Falling River, Lynchburg District. Publication No. FHWA-RD-97-065.

FHWA (1997j). Virginia. Virginia Avenue Over the Clinch River, Richlands. Publication No. FHWA-RD-97-064.

FHWA (1997k). Washington. Eastbound State Route 18 Over State Route 515, King County. Publication No. FHWA-RD-97-066.

Forster, S. W. (1994), "High-Performance Concrete – Stretching the Paradigm," Concrete International, October, Vol. 16, No. 10, pp. 33-34.

French, C. W. and Mokhtarzadeh, A. (1993), "High Strength Concrete: Effects of Materials, Curing and Test Procedures on Short-Term Compressive Strength," PCI Journal, Vol. 38, No. 3, May-June, pp. 76-87.

Ghali, A. and Favre, R. (1986), "Concrete Structures, Stresses and Deformations," Chapman Hall, London.

Goodspeed, C. H.,Vanikar, S., and Cook, R. A. (1996), "High-Performance Concrete Defined for Highway Structures," Concrete International, Feb, Vol. 18, No. 2, pp. 62-67.

Gross, S.P. (1999). "Field Performance of Prestressed High Performance Concrete Highway Bridges in Texas," Dissertation, University of Texas at Austin.

Gross, S.P., Burns, N.H. (1999). "Field Performance of Prestressed High Performance Concrete Highway Bridges in Texas," The University of Texas at Austin, CTR Preliminary Research Report 580/589-2.

Guyon, Y. (1953). "Prestressed Concrete," John Wiley and Sons, New York.

Huang, T. (1982), "Study of Prestress Losses Conducted by Lehigh University," PCI Journal, September/October, Vol. 27, No. 5, pp. 48-61.

Imbsen, R. A., Vandershof, D. E., Schamber, R. A., and Nutt, R. V. (1985), "Thermal Effects in Concrete Bridge Superstructures," NCHRP Report No. 276, Transportation Research Board, Washington, DC.

Lachemi, M., Lessard, M., and Aitcin, P. C. (1996), "Early-Age Temperature Developments in a High-Performance Concrete Viaduct, High-Strength Concrete: An International Perspective," ACI SP-167, American Concrete Institute, Detroit, Michigan, pp. 149-174

Libby, J. R. (1990), "Modern Prestressed Concrete," 5th Edition, Van Nostrand Reinhold, New York.

Martin, L. D. (1991), "A rational Method for Estimating Camber and Deflection in Precast Prestressed Members," PCI Journal, January/February, Vol. 22, No. 1, pp. 100-108

Mindness, S.,Young, J.F. (1981), "Concrete," Prentice Hall Inc., Englewood Cliffs, New Jersey.

Myers, J. J. (1998), "Production and Quality Control of High Performance Concrete in Texas Bridge Structures," Dissertation, University of Texas – Austin.

Myers, J. J. (2000), "HPC for Bridge A6130-Route 412 Pemiscot County," Research Project Statement, Investigation Number RI00-002, University of Missouri-Rolla.

Myers, J. J. (1999), "How to Achieve a Higher Modulus of Elasticity," HPC Bridge Views, FHWA Sponsored, NCBC Co-Sponsored Newsletter, Issue No.5, September/October.

Myers, J. J., and Carrasquillo, R.L. (2000), "Influence of Hydration Temperature on the Durability and Mechanical Property Performance of HPC Prestressed / Precast Beams," National Research Council, Journal of the Transportation Research Board, 1696, Vol. 1, pp. 131-142.

Myers, J. J., Carrasquillo, Ramon L. (1997), "Quality Control & Quality Assurance Program for Precast Plant Produced High Performance Concrete U-Beams," Proceedings of the PCI/FHWA, International Symposium on High Performance Concrete, New Orleans, Louisiana.

Myers J. J., Kleinhans, D.D. (2003), "A Simplified Thermal Stress Analysis Approach Developed for the Practicing Bridge Engineer," Precast/Prestressed Concrete Institute (Submitted for Consideratrion).

Myers J. J., Yang Y. (2001), "Practical Issues for the Application of High Performance Concrete to Highway Structures," American Society of Civil Engineering – Journal of Bridge Engineering, November/December, Vol. 6, No. 6, pp. 613-627.

Naaman, A. E. (1982), "Prestressed Concrete Analysis and Design - Fundamentals," McGraw-Hill, New York.

Naaman, A. E. and Hamza, A. M. (1993), "Prestress Losses in Partially Prestressed High Strength Concrete Beams," PCI Journal, June/July, Vol. 38, No. 3, pp. 98-114.

Nawy, E. G. (2001), "Fundamentals of High Performance Concrete," 2nd edition, John Wiley & Sons, New York.

Neely, W. D. (2000), "Evaluation of the In-Service Performance of the Tom's Creek Bridge," MS Thesis. Virginia Polytechnic Institute and State University.

Neville, A. M. (1981), "Properties of Concrete," Third Edition, Pitman Publishing, London.

Nilson, A. H. (1987), "Design of Prestressed Concrete," John Wiley and Sons, New York.

Precast/Prestressed Concrete Institue. (1999), "PCI Design Handbook," PCI, Chicago, Illinois.

PCI Committee on Prestress Losses. (1975), "Recommendations for Estimating Prestress Losses," PCI Jounal, July/August, Vol. 20, No. 4, pp. 43-75.

Priestley, M. J. N. (1978), "Design of Concrete Bridges for Temperature Gradients," ACI Journal, Vol. 75, No. 5, pp. 209-217

Rabbat, B. G., Takayanagi, T., and Russell, H. G. (1982), "Optimized Sections for Major Prestressed Concrete Bridge Girders," U.S. Department of Transportation, Federal Highway Administration, Report N. FHWA/RD-82/005, Washington, DC, 178 pp.

Rabbat, B. G., and Russell, H. G. (1982), "Optimized Sections for Precast, Prestressed Bridge Girders," PCI Journal, July/August, Vol. 27, No. 4, pp. 88-104.

Radolli, M. and Green, R. (1975), "Thermal Stresses in Concrete Bridge Superstructures Under Summer Conditions," Transportation Research Record, Transportation Research Board, No. 547, pp. 23-36.

Reynolds, J.C. and Emanuel, J. H. (1974), "Thermal Stresses and Movements in Bridges," Journal of the Structural Division (ASCE), American Society of Civil Engineers, Vol. 100, No. ST1, pp. 63-78

Russell, B. W. (1992), "Design Guidelines for Transfer, Development and Debonding of Large Diameter Seven Wire Strands in Pretensioned Concrete Girders," Doctoral Thesis, The University of Texas at Austin, Austin, Texas.

Russell, H. G., Volz, J. S., and Bruce, R. N. (1997), "Optimized Sections for High- Strength Concrete Bridge Girders," Publication No. FHWA-RD-95-180, Federal Highway Administration, McLean, Virginia.

Shah, S.P. and Ahmad, S. H. (1994), "High Performance Concrete: Properties and Applications," McGraw-Hill, New York.

Stark, D. (1989), "Durability of Concrete in Sulfate-Rich Soils," Research and Development Bulletin RD097, Portland Cement Association, Skokie, Illinois, 14 pp.

Tadros, M. K., Ghali, A., and Dilger, W. H. (1975), "Time-Dependent Prestress Loss and Deflection in Prestressed Concrete Members," PCI Journal, May/June, Vol. 20, No. 3, pp. 86-98.

Yang, Y., Myers, J.J. (2003), "Live Load Test Results of Missouri's First High Performance Concrete Superstructure Bridge," National Research Council, Transportation Research Record – Journal of the Transportation Research Board (Accepted), Washington DC, 12 Pages.

Yang, Y. Myers, J. J. (2003), "Thermal Behavior of Missouri's First High Performance Concrete Superstructure Bridge," Proceedings for the 3rd International Symposium on High Performance Concrete, October 19-22, Orlando, Florida, 14 Pages.

Yang, Y. M., Shen, Ji, Myers, J. J. (2002), "Instrumentation Plan and Early-Age Monitoring of High Performance Concrete Bridge Girders in Missouri," Transportation Research Board, 81st Annual Meeting, January 13-17, 2002, Washington, DC.

Zia, P., Schemmel, J. J., and Tallman, T. E. (1989), " Structural Applications of High-Strength Concrete," North Carolina Center for Transportation Engineering Studies, Report No. FHWA/NC/89-006, Raleigh, North Carolina.

Zia, P., Leming, M. L., Ahmad S. H., Schemmel, J. J., Elliott, R. P. and Naaman, A. E. (1993), "Mechanical Behavior of High-Performance Concretes," Vol. 1: Summary Report. SHRP-C-361, Strategic Highway Research Program, National Research Council, Washington, DC, xi, pp. 98.

Zia, P., Ahmad, Shuaib, and Leming, Michael (1997), "High-Performance Concretes: A State-of-Art Report (1989 – 1994) FHWA-RD-97-030," Federal Highway Administration, McLean, Virginia.